Advanced Laboratory Testing for Offshore Pile Foundations under Monotonic and Cyclic Loading

A thesis submitted in partial fulfilment of the requirements of

the Doctor of Philosophy (PhD) degree

and the Diploma of Imperial College (DIC) in the Faculty of Engineering

By

Tingfa Liu

Department of Civil and Environmental Engineering

Imperial College London

October 2018

DECLARATION

The work presented in this thesis was carried out in the Geotechnics Section of the Department of Civil and Environmental Engineering at Imperial College London. This thesis is the result of my own work and any quotation from, or description of the work of others is acknowledged herein by reference to the sources, whether published or unpublished. No part of this thesis has been or is being concurrently submitted for any such degree, diploma or other qualification.

Tingfa Liu

London, October 2018

Abstract

Laboratory experimental research is described that supported the PISA Joint Industry monopile design project and a smaller scale international investigation into the ageing behaviour of micro-piles driven in sands. The study focused on the soils encountered at the PISA test sites, including the stiff high *OCR*, low plasticity, glacial till sampled at Cowden (Humberside, UK), and a silica-dominated fine marine sand retrieved from Dunkirk (Northern France). Tests were also conducted on sands from two other sites at Blessington (Ireland) and Larvik (Norway).

Working in conjunction with parallel research by Ushev (2018), four important aspects of the PISA test sites' soil conditions were studied: (i) Stress-strain-stiffness behaviour from the initial linear elastic range (Y_1) over the full non-linear range and up to final critical states; (ii) Stiffness and shear strength anisotropy; (iii) Response to cyclic loading; and (iv) Soil-soil/steel interface shearing.

Hollow Cylinder and fully-instrumented Bishop-Wesley triaxial apparatuses were employed in the Author's tests that revealed the Cowden till's shear strength and stiffness anisotropy, both of which impact on the interpretation of the lateral loading behaviour observed in the large scale PISA field tests. Extensive monotonic drained triaxial tests were conducted on reconstituted Dunkirk sand to characterise its highly non-linear small-strain stiffness characteristics, considering the effects of state as well as stress history (*OCR*), effective stress level and evolving anisotropy. The sand's Y_1 and Y_2 kinematic surfaces were depicted and tracked in effective stress space. The effects of end restraint in triaxial testing were also examined carefully, before exploring the large strain behaviour of Dunkirk sand and interpreting the results with a critical state and state parameter approach.

The monotonic testing was followed by an extensive programme of drained cyclic triaxial tests on Dunkirk sand that applied up to 10^4 cycles to demonstrate how the samples' state, stress history, mean cyclic stress ratio and cyclic amplitude affected the sand's response to repetitive loading. Cyclic strain accumulation flow and dilation characteristics were found to vary significantly with all of the above factors. The detailed response could not be depicted accurately by simple cyclic dilation models that consider only the mean cyclic stress ratio. Cyclic threshold conditions were characterised in terms of two kinematic yielding surfaces that correlated with those

seen under monotonic loading conditions. Additional experiments on pre-cycled samples demonstrated that the repetitive loading enhanced the sand's monotonic shear strength and stiffness characteristics.

The associated study of sand-steel interface shearing employed Bishop ring shear tests to impose large shear displacements that revealed a notable dependence of the shear resistances and dilation angles on normal stress levels and ageing times, and so provide significant insights into the ageing mechanisms that boost the axial capacities of steel piles driven in sandy soils.

Information from the Author's test programmes contributed to the pile ageing JIP test interpretation and was central to the successful modelling of the PISA field tests undertaken by other members of the Imperial College team.

Acknowledgements

I would like to express my sincere gratitude to my supervisor, Professor Richard Jardine for his invaluable support, encouragement and constructive critiques over the past four years. The research presented in this thesis has benefited enormously from his guidance on critical and integrated thinking, as well as meticulous attitude towards writing and presenting.

The research was funded by an IC-CSC scholarship (No. 201406210049) and partly by Ørsted through the Post-PISA Experimental Project. Their financial support is acknowledged. I am also grateful to the IC PISA team led by Professor Lidija Zdravković, and especially to Dr. David Taborda for involving me in calibrating the PISA sand model. Professor Catherine O'Sullivan kindly granted me access to the QicPic and microscope devices. Her useful guidance and supervision is much appreciated. My sincere thanks go to Dr. Stavroula Kontoe and Professor Matthew Coop for their insightful comments and useful discussions during the thesis examination and on many other occasions. I am also indebted to Professors Liming Hu and Qingbo Wen at Tsinghua University for their continuing support and encouragement.

The fruitful experimental research was made possible with contributions from several current and previous colleagues. Dr. Emil Ushev was a great company in the office, lab and field, and kindly taught me through many experimental techniques and useful tricks. Important guidance from Drs. Amandine Brosse, Amin Aghakouchak and Satoshi Nishimura is highly appreciated particularly regarding RCHCA operation and result interpretation. I also thank Dr. Róisín Buckley for the field work opportunities as well as the serious "hot-pot" talks on piling studies. Thanks are also due to Mr. Ken Vinck, who made an excellent contribution to the Dunkirk sand study and took care of my tests when I was away, and to Mr. Haoruo Chen who produced very useful sand-steel interface experiments. I wish to thank Dr. Masahide Otsubo for sharing his knowledge on shear velocity testing and analysis, Drs. Khalid Ai-Haj and Tom Shire for the useful discussions on filter paper testing, and Mr. Santiago Quinteros for sharing his expertise in interface shear experiments as well as insights into broad engineering practice.

Sincere gratitude goes to the technical and administrative team in the section and

the department. I am heavily indebted to Mr. Steven Ackerley, who has so often prioritised my endless and obsessive requirements in the lab. I also thank Mr. Graham Keefe for responding to my (frequent) steel interface needs, and Mr. Alan Bolsher for his help particularly in dealing with the block samples. Support from Mr. Duncan Parker and Mr. Stef Karapanagiotidis at different stages of the research is also appreciated. I am also grateful to Ms. Sue Feller for her essential “espresso” salvation, and to Miss Fionnuala Dhonnabhain for her essential support throughout the years.

It has been a privilege and wonderful experience being part of the Geotechnics family and the tea/coffee/beer club. I wish to thank the very kind, supportive and helpful colleagues I met here. Special thanks are due to Drs. Wenjie Cui, Sarah Tallett-Williams and Vasiliki Tsaparli for the very important life advice.

Last but not least, I am indebted to my parents and parents-in-law for their invaluable encouragement, and to my sisters, who supported the family through the difficult times. Finally, I wish to thank my beloved wife Ling, for supporting me through the long research and writing-up period, and bestowing a very enjoyable and fruitful PhD life in London.

Table of contents

Nomenclature

Symbols

α	Angle between the vertical and the direction of σ_1
$\alpha_{d\sigma}$	Angle between the vertical and the direction of $\Delta\sigma_1$
$\beta_1 \quad \beta_3$	Parameters to quantify level of stress non-uniformity in HCA testing
δ'_{peak}	Soil-interface frictional angle at peak
$\delta'_{20\ mm}$	Soil-interface frictional angle at 20 mm shearing displacement
δ'_{cv}	Soil-interface frictional angle at constant volume condition
μ	Coefficient of viscosity
ν	Poisson's ratio
ρ	Bulk density
ϕ_p'	Peak angle of shear resistance
ϕ_u'	Ultimate angle of shear resistance
γ	Shear strain
w	Angular frequency, $w = 2\pi f$
σ_n	Normal stresses
σ_v'	Vertical effective stress
σ_h'	Horizontal effective stress
σ_1	Major principal stress
σ_2	Intermediate principal stress
σ_3	Minor principal stress
τ	Shear stress
ε_1	Major principal strain
ε_2	Intermediate principal strain
ε_3	Minor principal strain
ε_{vol}	Volumetric strain
ε_a	Axial strain
ε_r	Radial strain
ε_s	Shear strain, defined as $2/3(\varepsilon_a - \varepsilon_r)$ in triaxial testing

η	Mean cyclic stress ratio, $\eta = q_{mean}/p_0'$
λ ζ	Parameters for defining power law critical state line
ψ	State parameter (= e - e_{cs})
A_d	Dilatancy constant
b	Intermediate principal stress factor, $b = (\sigma_2 - \sigma_3)/(\sigma_1 - \sigma_3)$
B	Elastic stiffness parameter
C_c	Semi-logarithmic compressibility (= $\Delta e/\Delta\log(\sigma_v)$)
C_{LC}	Linear compressibility index (= $\Delta e/\Delta\sigma_v$)
C_α	Secondary compressibility ratio (= $\Delta e/\Delta\log(t)$)
C_ε	Creep strain ratio (= $\Delta\varepsilon_a/\Delta\log(t)$)
C_u	Uniformity coefficient
D	Torsional damping ratio of the specimen
D_a	Torsional damping ratio of the active mass
D_p	Torsional damping ratio of the passive system
D_r	Torsional damping ratio of the reaction system
D_{50}	Particle diameter corresponding to 50% cumulative mass
D^p D^t	Plastic or total dilation ratio
E	Young's modulus
e	Void ratio
e_{max} e_{min}	Maximum and minimum void ratio
e_{cs}	Void ratio at critical state
F_a	Axial force applied in HCA
f	Frequency
$f(e)$	Void ratio function
G	Shear modulus
G_s	Specific gravity
H	Specimen height
I_p	Plasticity index
I_G	Grading index

I.D	Inner diameter of HCA specimen
J_a	Rotational inertia of the active mass
J_p	Rotational inertia of the passive system
J_r	Rotational inertia of the reaction system
k_c^b k_c^d	State parameter constants for bounding surface and dilatancy surface on the triaxial compression side
K_o	Earth pressure at rest
K_a	Torsional spring constant of the active mass
K_p	Torsional spring constant of the passive system
K_r	Torsional spring constant of the reaction system
L_s L_c	Shortest and longest wavelength for roughness analyses
M_{cs}	Stress ratio at critical state, = $(q/p')_{cs}$
M_T	Applied torque in HCA or ring shear testing
N	Number of cyclic shearing cycle
N_f	Number of cycle to failure
O.D	Outer diameter of the HCA specimen
p_r	Reference atmospheric pressure (101.33 kPa)
p'	Mean effective stress ratio, $p' = (\sigma_1' + \sigma_2' + \sigma_3')/3$
p_i	Inner cell pressure
p_o	Outer cell pressure
q	Deviatoric stress, = $(\sigma_1' - \sigma_3')$ (HCA stress space) = $(\sigma_v' - \sigma_h')$ (Triaxial testing)
q_{mean}	Mean cyclic deviatoric stress
q_{cyc}	Cyclic amplitude deviatoric stress
q_c	CPT cone resistance
R_d	Relative density
R_{CLA}	Centre-line average roughness
R_{RMS}	Root mean square roughness
r_i	Inner radius of HCA specimen
r_o	Outer radius of HCA specimen
S_u	Undrained shear strength

T	Period in cyclic loading
w_s	Shrinkage limit

Abbreviations

BE	Bender Element
BRE	Building Research Establishment
bgl.	Below ground level
CNL	Constant Normal Load (stress)
CNS	Constant Normal Stiffness
CNV	Constant Volume
COV	Coefficient of Variation
CPT	Cone Penetration Test
CSL	Critical State Line
CT	Computational Tomography
CRSP	Constant Rate Strain Pump
CSR	Cyclic Stress amplitude Ratio
DOF	Degree of Freedom
DSS	Direct Simple Shear test or apparatus
GWL	Ground Water Level
HCA	Hollow Cylinder Apparatus
HCATC	HCA testing applying Triaxial Compression conditions
HCASS	HCA Simple Shear testing
ICL	Imperial College London
ICRCHCA	Imperial College Resonant Column Hollow Cylinder Apparatus
LBS	Local Boundary Surface
LICRCHCA	Large Imperial College Hollow Cylinder Apparatus
LVDT	Linear Variable Differential Transformer
MARKII ICHCA	Mark II Imperial College Hollow Cylinder Apparatus
MCC	Modified Cam Clay
NGI	Norwegian Geotechnical Institute

OCR	Over-Consolidation Ratio
PB	Small stress-strain Probing tests in triaxial or HCA
PISA	Pile-Soil Analysis project
PSD	Particle Size Distribution curve
RC	Resonant Column
SCPT	Seismic Cone Penetration Test
TRIAX	Software for controlling triaxial, HCA or ring shear testing
TXC	Triaxial Compression test
TXE	Triaxial Extension test
Y_1 Y_2 Y_3 Y_4	Yielding surfaces 1-4 of the multiple yielding surface framework (Jardine, 1992)

Lists of Figures

Lists of Tables

CHAPTER 1 Introduction

1.1 Research background

Offshore energy exploitation is crucial to many economies in Europe and Asia. Extensive research and development is underway to help advance offshore geotechnical engineering to meet the technical challenges posed by moving into deeper water and extending the life of existing assets (Jardine, 2018). Piled foundations are extensively used as supporting structures for many offshore oil and gas platforms and wind turbines. These foundations are subjected to axial, lateral and moment loadings, which combine monotonic and cyclic components. Their combined actions significantly increase the complexity of geomechanics analyses undertaken to assure their safe and economical design.

Conventional design guidelines for the prediction of pile capacity and displacements under monotonic loading are known to offer lower-than-desired levels of reliability, and further uncertainties exist concerning how cyclic loading should be considered in practice.

Several research projects have been established to tackle these complex geomechanics problems. Outcomes from projects involving the Imperial College Geotechnics Group have led to the development of design guidelines, such as the Imperial College Pile (ICP) design methods for axially loaded piles in sands and clays (Jardine *et al.*, 2005), new axial design method for driven piles in chalk (Buckley, 2018, Jardine *et al.*, 2018), advanced methods of numerical analysis (Potts & Zdravković, 1999, 2001) and the PISA design methods tailored for laterally loaded large diameter monopiles (Byrne *et al.*, 2017). Other important aspects concerning pile behaviour, for example installation, ageing and axial cyclic effects, have also been examined (Chow *et al.*, 1998, Jardine & Standing, 2012, Carroll *et al.*, 2017). A brief review is presented below of two of these piling research projects to which the Author's laboratory-based research programme has contributed.

PIle Soil Analysis project (PISA) and beyond

The PISA project was a three-year joint industry project (JIP) that aimed to develop better design methods for laterally loaded large diameter monopiles. The project was run through the Carbon Trust's Offshore Wind Accelerator programme and led by Ørsted (formerly DONG Energy), with financial and technical support from around 10 other offshore wind developers. The scientific contributions of the project were provided by an Academic Work Group (AWG) that consisted of Oxford University (OU), Imperial College London (ICL) and University College Dublin (UCD).

The project involved benchmarking medium-scale field testing campaigns, bespoke 3D finite element modelling and development of a new design method, as well as advanced site characterisation and laboratory element testing (Byrne *et al.*, 2015b, Zdravković *et al.*, 2015, Byrne *et al.*, 2017). The field tests were carried out at two selected sites involving stiff glacial clay till at Cowden, Humberside (UK) and dense sand at Dunkirk in Northern France. In total 28 heavily instrumented piles with varied diameters (D = 0.273 m, 0.762 m and 2.0 m), embedded lengths (between 1.43 m and 10.5 m) and wall thickness (from 7 mm to 38 mm) were driven and tested under predominantly monotonic loading, with supplementary one-way and two-way cyclic loading.

Supporting 3D finite element analyses were carried out with the ICFEP code (Potts & Zdravković, 1999) and two advanced constitutive models, an extended generalised Modified Cam Clay (MCC) variant and a bounding surface plasticity model, were adopted respectively to reproduce the behaviour of the low plasticity Cowden till and Dunkirk sand. The responses of the rigid piles were analysed with sophisticated ICFEP finite element modelling (Zdravković *et al.*, 2015) that incorporated the laboratory testing by Ushev (2018) and the Author and gave excellent fits to the field tests.

Simplified 1-D design models were also developed that extend from the conventional *p-y* approach by incorporating additional soil reaction components of distributed moment along the pile shaft as well as a horizontal force and moment at the pile base, as shown in Figure 1-1. These additional components were found essential to representing accurately the behaviour of the laterally loaded large diameter (D) but low length (L) to diameter ratio (L/D) monopiles (Byrne *et al.*, 2017, Burd *et al.*, 2017).

Two design methods, namely a rule-based method and a numerical-based method,

were proposed in the PISA project. Byrne *et al.* (2017) demonstrated how these methods were applied for analysing the pile tests at the Cowden till site, while Burd *et al.* (2017) illustrated the design aspects of monopile foundations based principally on the outcomes from the Dunkirk pile tests and analyses. One example is demonstrated in Figure 1-2 that compares the experimentally measured and numerically modelled load-displacement response and bending moment profile.

Advanced laboratory studies were required to establish the soil profiles at the two sites and characterise facets of the soils' behaviours that were critical for finite element analyses. Ushev (2018) characterised the monotonic and cyclic shearing behaviour of the stiff low-plasticity Cowden till, while the Author focused on stiffness and undrained shear strength anisotropy of Cowden till and several aspects of the behaviour of Dunkirk sands, including the sand's monotonic compression and shearing behaviour, stiffness anisotropy and response to drained cyclic loading. The laboratory studies were integrated with the outcomes from the extensive site investigation activities carried out at the two sites.

The research has been progressed in several phases. The Author and Ushev (2018) provided key initial inputs to the PISA project's first phase, which subsequently progressed through the PISA-2 programme to consider various ground profiles (including layered soils) and loading conditions (in particular cyclic loading). Much of the work described by the Author and Ushev (2018) was undertaken as part of a post-PISA laboratory research project (2016-2017) that was partially funded by Ørsted to extend the laboratory studies beyond the scope initially set out for PISA.

Grenoble-Tech/NGI/Imperial College joint micro-pile project

Following earlier studies reported by Jardine *et al.* (2006), Karlsrud *et al.* (2014), Rimoy *et al.* (2015) and Gavin *et al.* (2015), a joint Grenoble-Tech/NGI/Imperial College micro-pile project was established to investigate the ageing mechanisms that affect the axial capacities of open-ended steel piles driven in sands (Carroll *et al.*, 2017, 2018). A total of 51 micro-pile tests were performed at three sand sites, Larvik (in Norway), Dunkirk (in France) and Blessington (in Ireland), where extensive industrial scale tests on piles driven in sands were performed, based on which the ageing trends of axial capacity have been established, as shown in Figure 1-3. The micro-piles tested in this project had outer diameters from 48 to 60 mm and average contact lengths

between 1.75 m and 2.4 m, and were made of different types of steel, including stainless, galvanised and mild steel. Piles were tested with a range of initial shaft surface roughnesses.

The outcomes from the tests performed after ageing periods from 0.1 day to 696 days provided new evidence as to how the ageing behaviour is affected by ground condition (sand properties, deposit density and groundwater level), pile diameter, steel type and surface roughness. The results also examined the ageing hypotheses posed previously by Chow *et al.* (1998) and Jardine *et al.* (2006). The effects of pile driving procedures and installation effects, were also assessed. The results also led to a re-evaluation of some of the parameters employed in the current design approaches (such as the ICP-05, Jardine *et al.* (2005)) to better incorporate the effects of the above factors.

Laboratory sand-steel interface tests that could reproduce pile installation process were required to characterise the interface shearing properties of the sands present at the three sites against interfaces with prescribed steel types and roughness conditions. Further research was also called for to examine the separate or coupled effects of some of the identified factors on interface shearing behaviour under well-controlled laboratory conditions. A suitable study was integrated into the Author's PhD programme.

1.2 Research objectives and methodology

The above research projects provided the background to the Author's laboratory-based research programme. Before considering the Author's overall research aims, it is useful to point out the distinctly different features of soil conditions considered in axially and laterally loaded piles, as demonstrated schematically in Figures 1-4 and 1-5.

The study of axially loaded piles' capacity under static or cyclic loading particularly concerns the behaviour at the soil-steel interface and the stress-strain-stiffness behaviours of the soils adjacent to the piles, which is modified considerably by driven pile installation. Previous research by Aghakouchak (2015) demonstrated the importance of reproducing representative soil conditions in element tests to aid the interpretation of axially loaded pile behaviour. In contrast, laterally

loaded piles mobilise large volumes of soils in their active and passive zones during loading. While installation process remain influential, the lateral responses are more predominantly affected by the mass behaviour of the soils in their initial 'in-situ' states.

The Author's research involved four geo-materials: Cowden till and the Dunkirk, Fontainebleau, Blessington and Larvik sands. The locations at which they were sampled are indicated in Figure 1-6. The research undertaken focused on three main objectives.

(1) Investigating the anisotropic behaviour of the over-consolidated low plasticity stiff Cowden till, adding to the research programme by Ushev (2018). This involved three main activities:
   a. Characterising the anisotropic linear and non-linear stiffness and undrained shear strength of the material under 4-dimensional stress space;
   b. Establishing the anisotropic stiffness profile of the Cowden site over the depths where the PISA laterally loaded piles were embedded; and
   c. Revealing the differences in the anisotropic features of the Cowden till's behaviour and those of high-plasticity stiff clays as identified by Gasparre (2005), Nishimura (2006), Minh (2006), Brosse (2012) and Hosseini Kamal (2012).

(2) Investigating comprehensively the multi-faceted behaviour of the Dunkirk sands to support the PISA and post-PISA research projects. Four key aspects that were addressed were:
   a. Characterising the sands' cross-anisotropic linear elastic stiffnesses using upgraded laboratory apparatus and techniques, and establishing the Dunkirk site's anisotropic stiffness profiles;
   b. Investigating the materials' highly non-linear, stress- and strain-dependent stiffness characteristics from small strain range ($<10^{-3}$ %) up to failure;
   c. Determining the materials' failure and critical state behaviours, stress-dilation relationships and critical state lines. These features were crucial to the numerical simulations of the PISA Dunkirk pile tests under monotonic loading;
   d. Exploring the drained cyclic shearing and post-cycling behaviour of Dunkirk sands, enabling future re-interpretation and modelling of the PISA Dunkirk cyclic tests.

(3) Investigating the compression and sand-steel interface shearing behaviour of the sands present around the shafts of driven steel piles, with three strands of work:
   a. Quantifying the significant mutation of sands subjected to high pressure compression and large-displacement interface shearing;
   b. Assessing the effects of several key factors on sand-steel interface shearing properties; and
   c. Exploring ageing effects on sand-steel interface shearing behaviour and examining some of the pile ageing hypotheses from a laboratory perspective.

The Author also supported two MSc projects that produced supplementary information to the above research programme. The projects included:

(1) Investigation of the behaviour of Dunkirk sand under triaxial drained monotonic shearing conditions over a full strain range, as completed by Vinck (2016) and partly integrated into Chapters 5 and 6; and
(2) Characterisation of the sand-steel interface shearing behaviour of Dunkirk and Blessington sands and the ageing effects, as completed by Chen (2017a) and included in Chapter 4.

Research methodology and interpretive frameworks

The research programme employed advanced laboratory apparatuses and techniques developed in the Geotechnics section of Imperial College London, as later described in Chapter 2. The testing outcomes were interpreted by reference to five established frameworks for characterising soil behaviour:

(1) Cross-anisotropic linear elastic stiffness theory, as described in Section 3.2.1 and applied in Chapter 3 for Cowden till and Chapter 5 for Dunkirk sands;

(2) Visco-elasticity theory, as briefly described in Section 2.3.3 and applied for interpreting shear stiffness and damping properties of Cowden till from resonant column testing in Chapter 3;

(3) The multiple kinematic yield surface conceptual model proposed by Jardine (1992) and Kuwano & Jardine (2007) (see Section 5.2.2) that was applied to interpret the pre-failure characteristics of Dunkirk sand, as described in Chapters 5 and 7;

(4) The critical state framework and the state parameter-based approach (reviewed in

Section 6.2) that were employed for interpreting large-strain monotonic shearing behaviour of Dunkirk sands presented in Chapter 6 and drained cyclic behaviour reported in Chapter 7.

(5) The cross-anisotropic *q-p′-b-α* framework that has been employed since Hight *et al.* (1983) to characterise shear strength anisotropy of soils through Hollow Cylinder testing. The latter was employed for investigating undrained shear strength properties of Cowden till, as described in Chapter 3.

1.3 Thesis structure and layout

The thesis is divided into eight chapters. Background information and a brief supporting literature review is included in most chapters. Key research questions and hypotheses are posed at the start of each main experimental chapter, followed by detailed interpretation and discussion that is structured to answer these questions.

Chapter 1 sets out the Author's research background, objectives and methodology and provides an overview of the related piling research projects.

Chapter 2 provides detailed descriptions of the site conditions, soil materials, testing apparatuses and techniques. The in-situ profiles of the PISA testing sites at Cowden and Dunkirk are introduced, followed by descriptions of the site investigation and sampling campaigns as well as the outcomes. The principles, capabilities and limitations of the apparatuses employed in the Author's research are described, including the modifications and optimisations implemented to enable the intended monotonic and cyclic tests to be conducted.

Chapter 3 presents the research into the anisotropic stiffness and undrained shear strength of the Cowden glacial till through HCA and advanced triaxial testing. Challenges encountered in specimen formation and the corresponding counter-measures are described. Potential issues of sampling disturbance and bias are assessed. Discussion and interpretation follows on the completed set of tests. The anisotropic stiffness characteristics of the Cowden site are reported and their implications regarding the response of predominantly laterally loaded piles are discussed.

Chapter 4 investigates the high pressure compression, crushing and sand-steel

interface shearing behaviour of the four sands as investigated through oedometer, direct shear and Bishop ring shear testing. Discussion is presented first on the 1D oedometer compression and crushing characteristics of the Dunkirk and Fontainebleau NE34 sands, before moving to consider the small- and large-displacement interface shearing behaviours of the three sands (Dunkirk, Blessington and Larvik). Factors affecting sand-steel interface shearing behaviour are discussed, and the several pile aging hypotheses proposed by Chow *et al.* (1997) and Jardine *et al.* (2006) are examined based on the laboratory outcomes.

Chapter 5 characterises the pre-failure behaviour of Dunkirk sands under triaxial conditions. Interpretation of the testing outcome focuses on the materials' consolidation, creep, pre-failure stiffness characteristics and yield surfaces. Sets of power law correlations are obtained to express the stress-dependent and anisotropic small-strain stiffness behaviour. The effects of end restraint on stiffness characteristics are discussed. The cross-anisotropic stiffness characteristics of Dunkirk sand are described and the stiffness profiles applying to the Dunkirk site are discussed.

Chapter 6 progresses the reporting on the experiments set out in the previous chapter to summarise Dunkirk sands' large-strain shearing behaviour. The influences of effective stress level, specimen density and over-consolidation (*OCR*) are addressed and further discussion is presented on the effects of end restraint on shear strength and volumetric behaviour. Critical state line (CSL) are reported, which allowed further interpretation employing a state-parameter approach.

Chapter 7 extends the investigation of Dunkirk sand's mechanical behaviour to consider its long-term drained cyclic loading response and post-cycling shearing response under triaxial conditions. Technical aspects regarding the stress-controlled cyclic tests and the steps required to obtain reliable cyclic strain and stiffness measurements are appraised. Detailed discussion is presented on the cyclic strain rates and accumulation patterns, the evolving trends of cyclic shear stiffness, and the characteristics of post-cycling monotonic shear stiffness and strength. The effects of specimen density, mean cyclic stress ratio (q_{mean}/p_0') and cyclic stress amplitude ratio (q_{cyc}/p_0') are highlighted as well as those of the effective stress history (*OCR*).

Chapter 8 summarises the main outcomes and key findings from the Author's research and identifies those aspects that require further investigation.

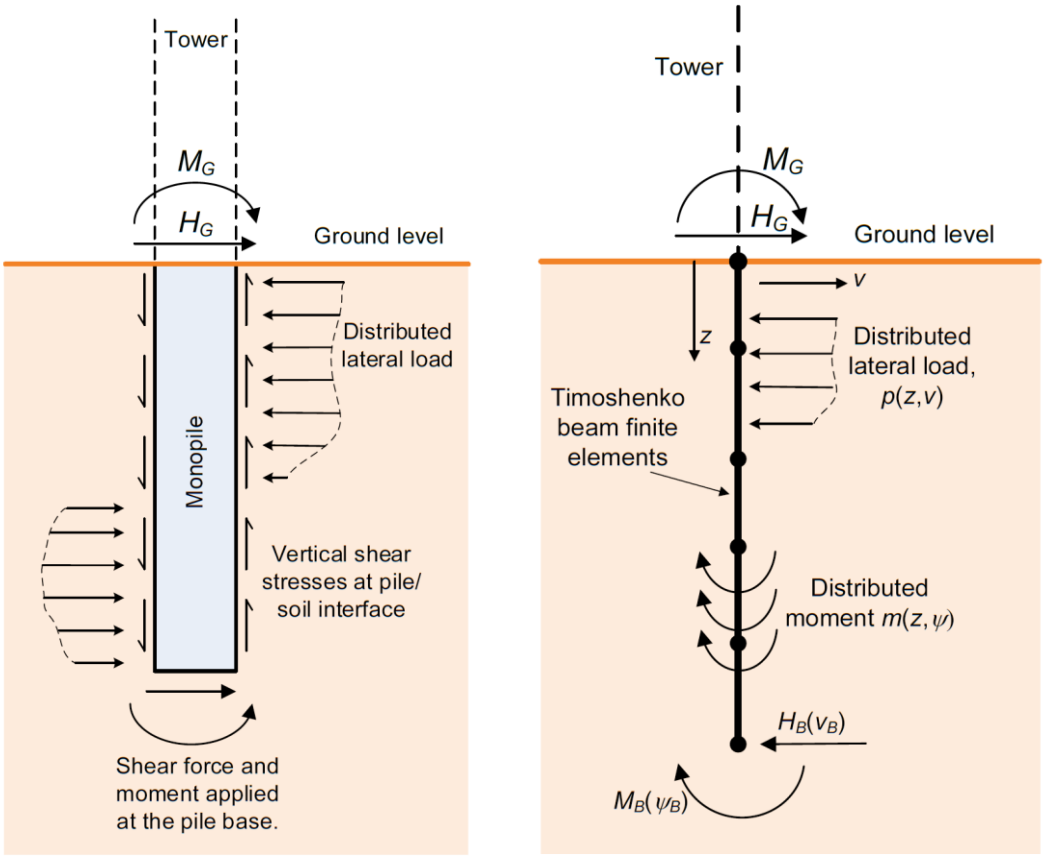

Figure 1-1 Soil reaction components identified in the PISA design method (left) and the 1D simplified finite element model (right) (Byrne *et al.*, 2017)

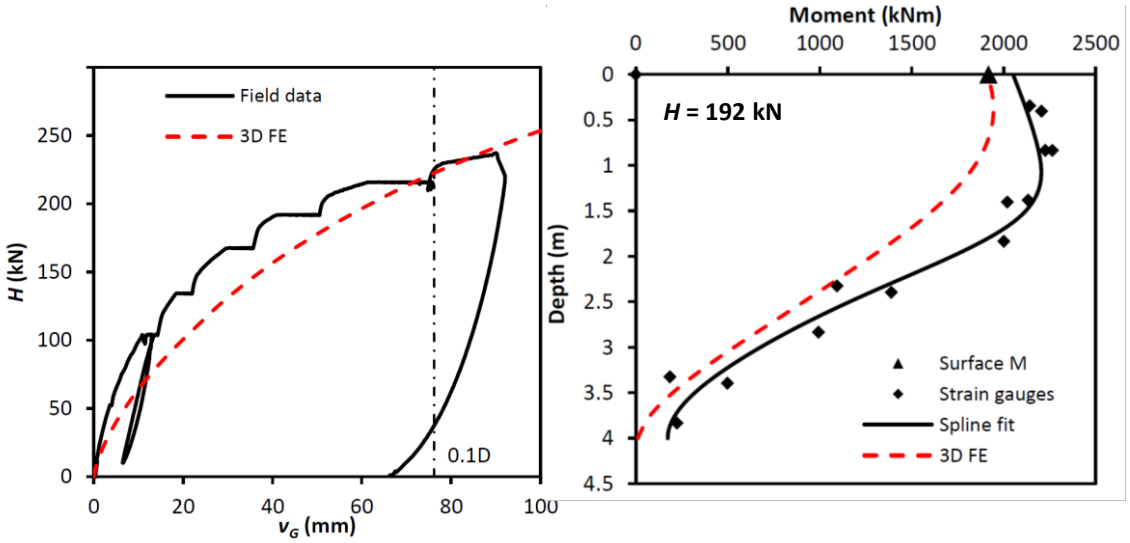

Figure 1-2 Measured and simulated horizontal load-displacement (H-v_G) response (left) and bending moment-depth distribution under H = 192 kN (right) for a medium sized PISA pile driven at Dunkirk with D = 0.762 m and L = 4 m tested under lateral and moment loading (Burd *et al.*, 2017), see Taborda *et al.* (2018) for further cases

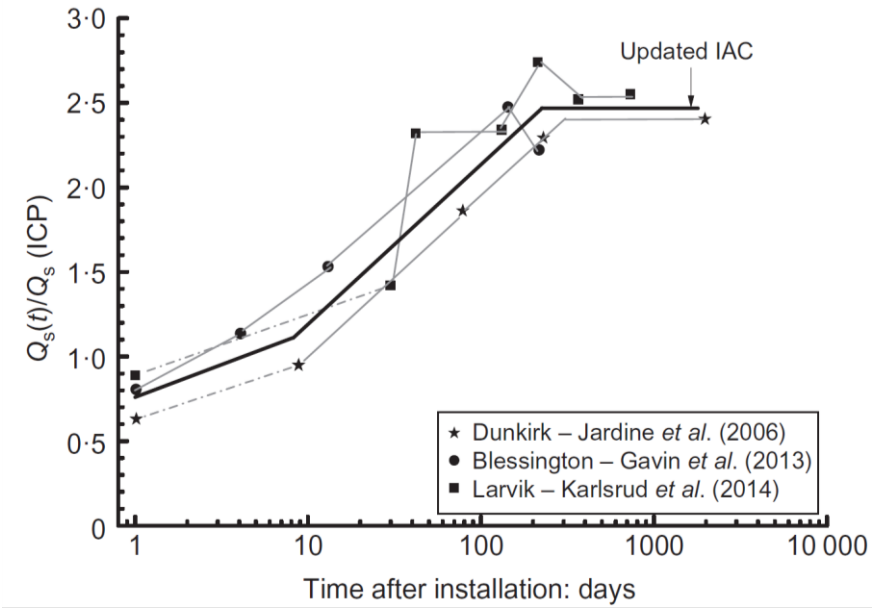

Figure 1-3 Ageing trends of axial capacity of industrial scale piles driven at Dunkirk, Blessington and Larvik sites (Rimoy *et al.*, 2015)

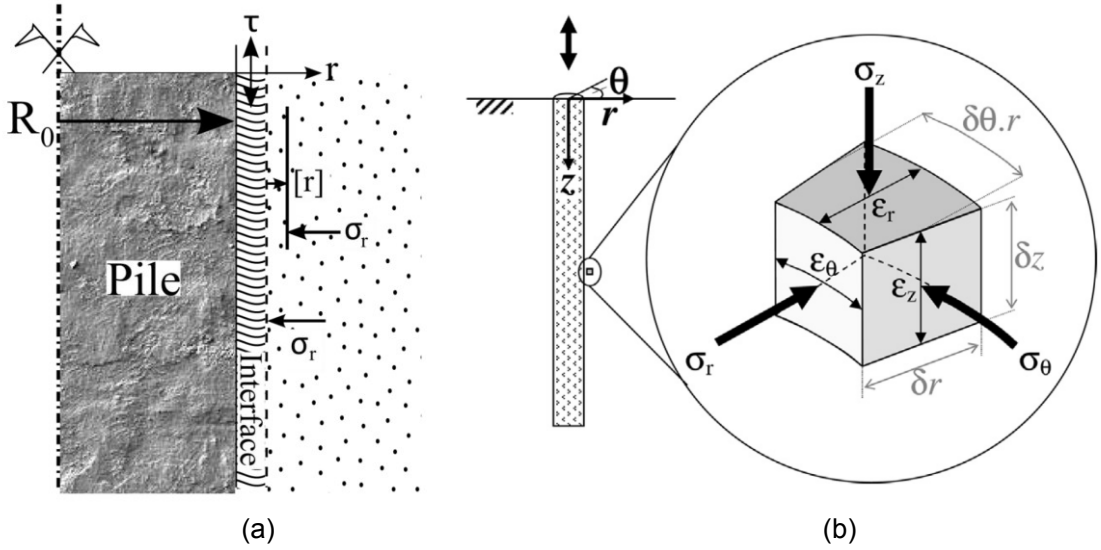

Figure 1-4 Stress regimes around axially loaded piles: (a) soil-pile shaft interface regime; (b) stress and strain conditions of soil elements adjacent to pile shaft

(Sim *et al.*, 2013, Aghakouchak, 2015)

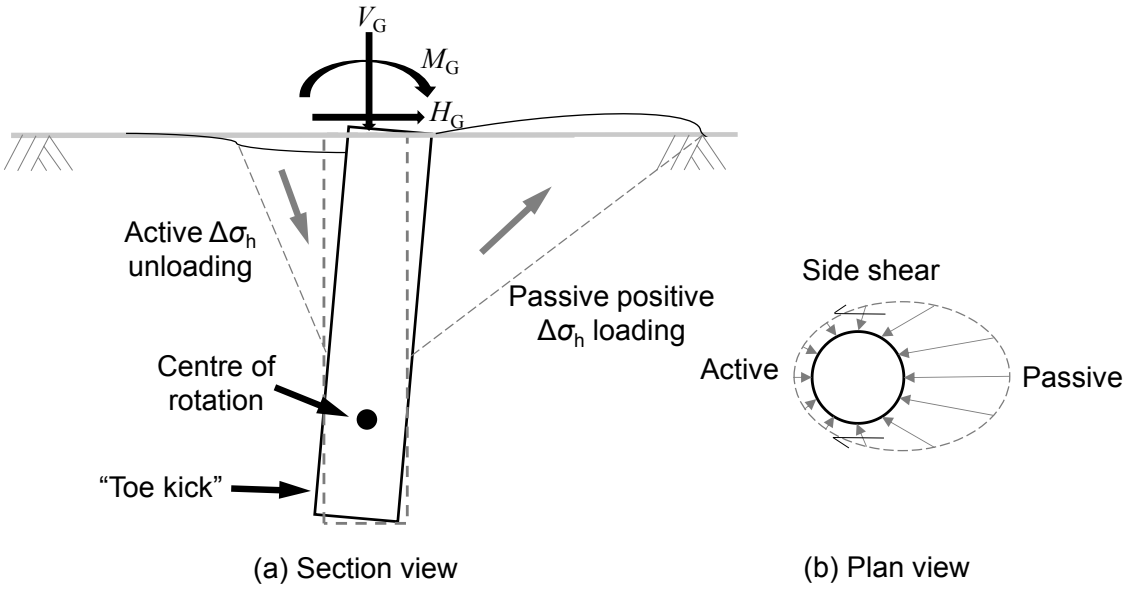

Figure 1-5 Stress regimes developed around a laterally loaded rigid monopile

Figure 1-6 Locations of the soils involved in the laboratory-based research programme

CHAPTER 2
PISA testing sites, soils, apparatus and techniques

2.1 Introduction

The PISA project focused on the two test sites' reference soils: the ductile low plasticity stiff clay till present at Cowden in North-eastern England and the dense fine sand found at the Port Ouest test area of Dunkirk in Northern France. Systematic laboratory testing programmes were carried out to characterise ground conditions and soil behaviour, generating the parameters and inputs essential for the interpretive analyses of the field tests and finite element simulations.

This chapter reviews first the ground conditions at the Cowden till and Dunkirk sand sites, integrating outcomes from historic and recent site investigation activities and laboratory testing programmes. Sampling campaigns aiming to retrieve good quality soil samples for laboratory testing are also described. Detailed descriptions are then given of the series of testing apparatus and techniques adopted in the Author's study, including a resonant column hollow cylinder apparatus (RCHCA), fully instrumented Bishop-Wesley automated stress-path triaxial apparatuses and Bishop ring shear apparatus. The capabilities and limitations of these apparatuses are addressed.

2.2 PISA testing sites and materials

Ushev (2018) described the geological history and formation of the Cowden glacial till and provided full details of the site conditions and soil properties, integrating results from his extensive laboratory testing with earlier studies summarised by Powell & Butcher (2003). Earlier characterisation of the Dunkirk site was documented by Chow (1997) and later Jardine *et al.* (2006), and their work has been supplemented by investigations carried out for the PISA project. This section briefly resummarises the two sites' ground conditions and soil profiles as well as the sampling campaigns and their outcomes. Attention is focused on the variations in soil density, ground water pressures and earth pressure coefficients (K_o) which are critical in setting the in-situ conditions for numerical analyses.

2.2.1 Cowden site (North-eastern England) and Cowden till

Site conditions and profiles

The Cowden site is located in the northeast of England, and it offers deep layers of clay matrix dominated glacial tills. The Cowden site was selected for the Building Research Establishment's (BRE) programme of studies on glacial tills from the 1970s onwards. Research teams from BRE, Imperial College London (Lehane, 1992) and Norwegian Geotechnical Institute (NGI) (Karlsrud *et al.*, 2014), also conducted field tests at the site, which has been extensively investigated using a wide range of in-situ and laboratory techniques, as summarised by Powell & Butcher (2003).

The upper section of the Cowden profile, in which the PISA piles were tested, comprises mainly stony low plasticity glacial till down to around 12 m, below which lies a layer of silty sand and deeper till layers. The phreatic surface was found to be at 1.0 m through recent piezometer measurements for the PISA site investigation. The pore water pressure profile shown in Figure 2-1 indicates partially under-drained conditions between 5 m to 12 m, principally due to the presence of the sand layer. An upper weathered layer exists and the transition to unweathered till was found at 4.8 m depth in visual inspections made by Ushev (2018) on his rotary core specimens. High values of K_o had been interpreted by Powell & Butcher (2003), as shown in Figure 2-1. However the PISA team's interpretation led to a limit of 1.5 for K_o in the upper 5 m, as higher values were believed to be unrealistic when considering the prior geological process of glacial deposition and the presence of extensive vertical fissuring in the

upper weathered layer.

Figure 2-2 plots the profiles of index properties reported by Ushev (2018) and maximum elastic shear stiffnesses established from various laboratory and in-situ measuring techniques. The upper weathered layer exhibited slightly higher plastic and liquid limits (around 18% and 36% respectively), and generally stable trends were noted in the deeper, unweathered, layers. Particle size distribution analyses indicated an average clay content of about 30% and gravel content around 10%. Most particles larger than 2 mm comprise chalk (45~76%), sandstones, igneous rock fragments and shale. Chapter 3 presents detailed photographic records of the erratic fissures and gravel inclusions observed by the Author in the specimen trimming and preparation stage of his tests on the till.

As shown in Figure 2-2, the elastic shear stiffnesses determined from in-situ seismic CPT (SCPT) measurements broadly match those from laboratory multi-directional bender element measurements on specimens re-consolidated to estimated in-situ stresses. The shear velocity based results, however, were located consistently above the equivalent shear stiffness trends inferred from undrained triaxial compression and extension Young's moduli, by assuming an isotropic linear elastic model. The divergent trends indicate potentially anisotropic stiffness behaviour, and led to a further investigation through a programme of hollow cylinder (HCA) tests and small-strain triaxial probing tests, as described later in Chapter 3.

PISA *sampling campaigns at Cowden*

Two campaigns that aimed to retrieve high quality samples for laboratory testing were carried out at Cowden for the PISA project. The first, rotary, coring campaign was carried out in May to June 2014, by Concept Drilling Service Ltd assisted by Dr. Emil Ushev. The triple-barrel, wireline, Geobor-S sampling system was employed to take 100 mm outer diameter cores and four boreholes were drilled down to 13.0 m. Parts of the drilled cores were heavily disturbed due to the presence of stones, fissures, plant roots and other inclusions, resulting in a relatively low overall satisfactory sampling recovery rate of 42%. Ushev (2018) presented detailed photographic records of the extracted cores and their corresponding quality categories.

The recovered good quality samples were mainly tested by Dr. Emil Ushev as part of his doctoral research programme, with the other experiments by GEOLABs to

characterise the material's index properties, compressibility and undrained triaxial strength and stiffness, as part of the initial laboratory testing programme performed for the PISA project. Some remaining preserved cores were tested by the Author to further investigate the material's elastic stiffness anisotropy through triaxial stress probing tests.

The stock of good quality rotary cores from the first sampling campaign was not considered sufficient. An additional block sampling campaign was undertaken by SOCOTEC (formerly Environmental Scientifics Group, ESG) with Dr. Emil Ushev from January to February 2015. The detailed procedures for block sampling were similar to those documented by Gasparre (2005), Nishimura (2006) and Ushev (2018), and Figure 2-3 illustrates some of the key steps.

In total eighteen soil blocks were retrieved from two trial pits from six levels (coded A to F) down to 3.5 m. All were located within the weathered layer. The spatial distribution of the sampling locations is shown in Figure 2-4. Each block had dimensions of around 350 mm×350 mm×350 mm and an approximate weight of 110 kg. It should be noted that although many blocks were available from the shallow layers (sets A and B in Figure 2-4), these were not employed in the main testing programmes due to their heavily fissured nature, as well as concerns regarding the effects of plant roots and vegetation. The major groups of research tests by Ushev (2018) and the Author were concentrated on blocks from layers E (3.0 m depth) and F (3.5 m depth), which were less affected by these inconvenient features.

2.2.2 Dunkirk site (Northern France) and Dunkirk sands

Site conditions and profiles: historic and recent data

The Dunkirk test site is located in Northern France. It forms part of the extended beach area formed at the ZIP Les Huttes Industrial zone developed in the Port Ouest area. The site has been used as a testing site for earlier research projects which focused particularly on driven pile behaviour in sands. These projects include: the 1980s French CLAROM/IFP project (Brucy *et al.*, 1991), an Imperial College/BRE pile project in mid-1990s (Chow, 1997), the GOPAL project (Parker *et al.*, 1999), an HSE funded Imperial College project (Jardine *et al.*, 2006, Jardine & Standing, 2012), the SOLCYP project nearby at Loon-Plage (Puech *et al.*, 2012), the PISA project (Byrne *et*

al., 2015a, Zdravković *et al.*, 2015), and the Grenoble-Tech/NGI/Imperial College micro-pile project (Carroll *et al.*, 2017). Figure 2-5 presents the timeline of the field testing studies and the 'parallel' laboratory programmes on Dunkirk sand launched at Imperial College.

Historical site investigation data reported by Chow (1997) showed that the top 3 m of the deposit was a hydraulic fill sand layer, underlain by a Flandrian sand layer that extended from 3 m to 30 m depth. The Flandrian sand layer was divided by several organic layers between the sand units. The average relative densities of the hydraulic sand fill and the Flandrian sand layer were reported by Chow (1997) as 100% and 75%, respectively. The water table was reported at 4 m depth by that time. The updated site investigation work carried out by the PISA project confirmed the general features of the site profiles reported in the earlier studies, but indicated that 20 years later and at a location around 100 m away, the CPT measurements and shear stiffnesses were higher and that the water table was found at a greater depth of 5.4 m (PISA Academic Work Group, 2017).

Possible differences in site conditions noted in the above two sets of site investigations are indicated in Figure 2-6, comparing traces of CPT cone resistance q_c and downhole maximum shear stiffness G_{vh} from seismic CPT (SCPT) measurements. It is clear that the q_c and G_{vh} profiles from the recent PISA measurements plot above those from the earlier site investigations. The increased cone resistance and stiffness of the deposit may reflect spatial variations, the effects of long-term natural drainage, sand ageing with time, or a combination of these factors.

Sampling at Dunkirk and the materials for laboratory testing

A sampling campaign was attempted at the Dunkirk site for PISA in May to June 2014 by Concept Drilling Service Ltd., employing the same Geobor-S triple barrel coring technique as at Cowden. However, the drilling team was not able to obtain good quality cores in the sand deposit and the sampling campaign ended with no suitable samples for further laboratory testing. Three boreholes were drilled down to 12 m, 10 m and 20 m, and the average total recovery rates were 20%, 57% and 60%, respectively. Examples of poor and promising "intact" cores are shown in Figure 2-7. The samples were mostly heavily disturbed and contaminated by drilling fluid and were thus disqualified for further testing. Therefore, laboratory characterisation of

Dunkirk sand had to rely on reconstituted samples collected on several occasions by the Author's supervisor at the site.

Three earlier sampling campaigns have been conducted at the Dunkirk site. In 1988, the French CLAROM research consortium retrieved satisfactory pushed and rotary samples from a borehole down to 26.4 m and retained these in 0.11 m diameter, 0.7 m long plastic tubes (Chow, 1997). Some of these samples were used in the doctoral research by Chow (1997) and Kuwano (1999). Figure 2-8 summarises the particle distribution curves and D_{50} values found from samples taken at five depths, indicating generally consistent gradings throughout the top 12 m. This batch of sand was referred to Dunkirk sand Batch 1.

Another batch of Dunkirk sand was sampled at the site in 2002 from a trial pit dug down to 0.8 m. The collected material was air-dried and sieved to remove shell fragments and other large inclusions. This batch of sand was tested by Aghakouchak (2015) in his doctoral project and by the Author in the triaxial tests performed for the PISA project (see Chapter 5). Additional high pressure oedometer tests as well as sand-steel ring shear and direct shear tests were also performed on this material by Chen (2017a) and the Author (see Chapter 4). This batch of sand is named as Dunkirk sand Batch 2 for later reference.

A third batch of Dunkirk sand was retrieved at the same site in 2013 from a shallow pit (around 0.5 m), and is referred as Batch 3. Figure 2-9 summarises gradings of the three batches of Dunkirk sand from shallow depth. The materials sampled in different periods and from near-by locations had very similar gradings. Vinck (2016) carried out index property tests and drained monotonic triaxial tests on Batch 3 and highlighted subtle differences between Batches 2 and 3 in terms of shear strength and stiffness as well as critical state behaviour. The Batch 3 material was also employed by the Author for the study of long-term drained cyclic shearing behaviour of Dunkirk sand (see Chapter 7).

2.2.3 Figures

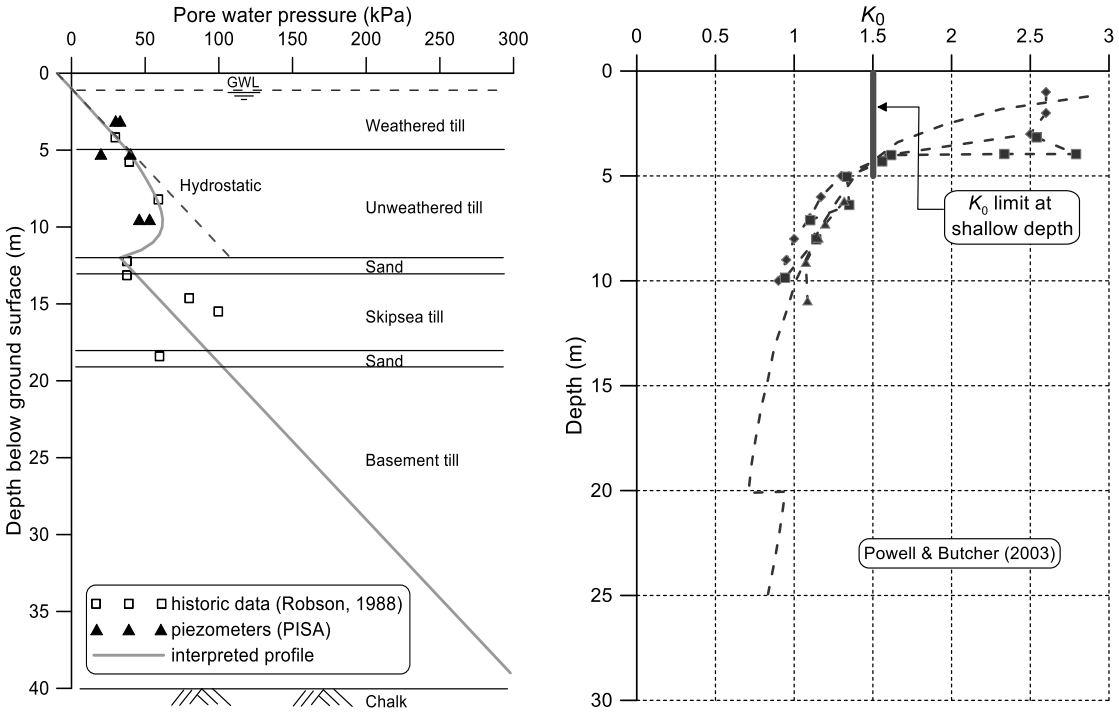

Figure 2-1 Cowden site ground profile: pore water pressure (left); K_o profile (right) (PISA Academic Work Group, 2017, Ushev, 2018)

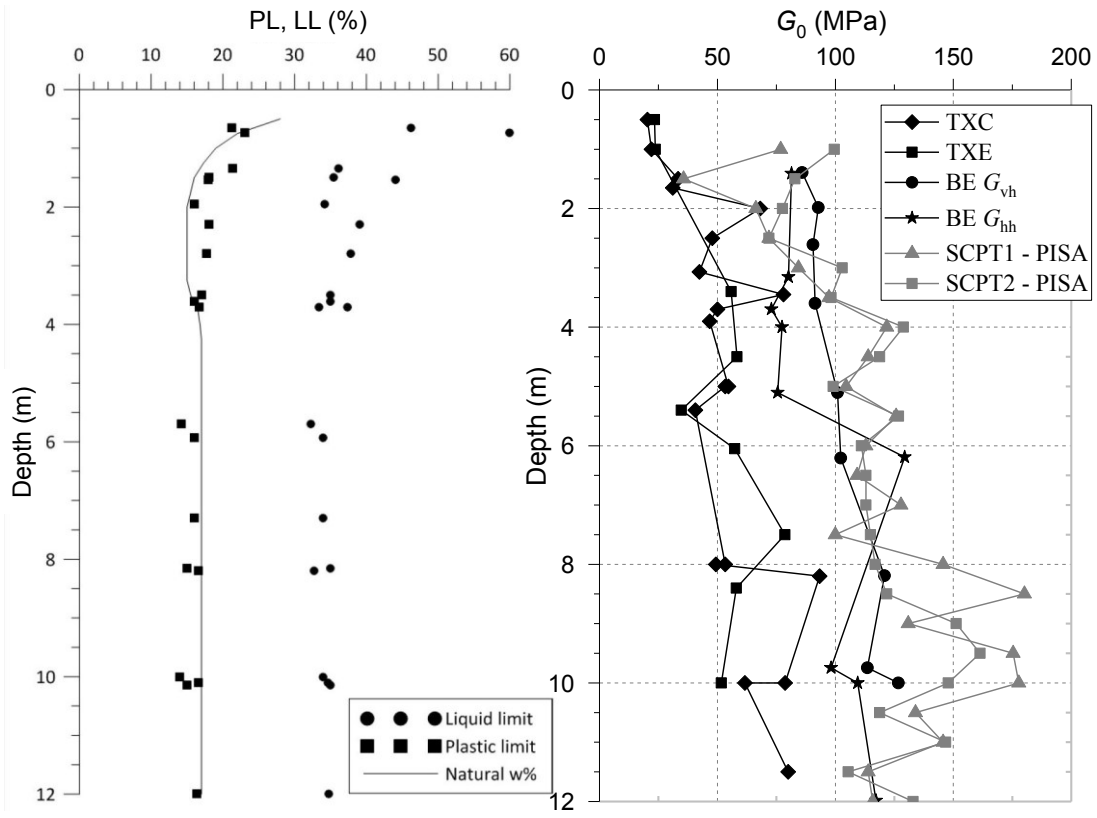

Figure 2-2 Cowden soil profile: plastic and liquid limit (left); maximum shear stiffness (right) (Ushev, 2018)

Figure 2-3 Sampling procedures for retrieving intact Cowden till block samples (Ushev, 2018)

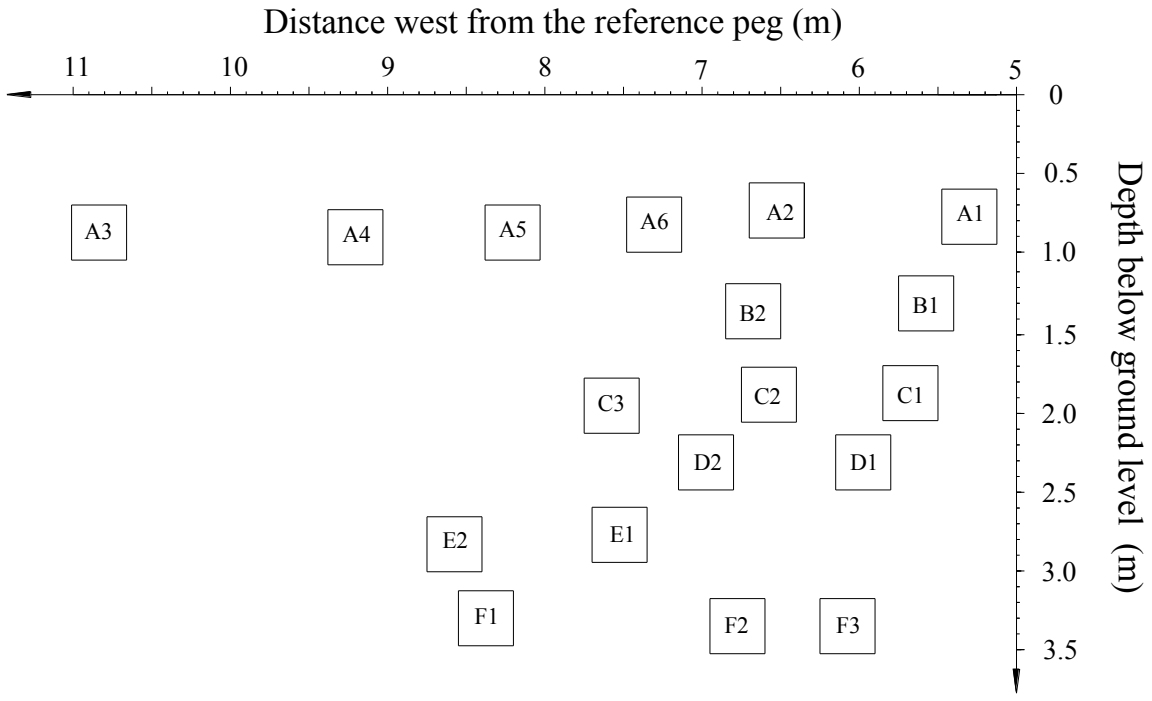

Figure 2-4 Spatial distribution of the Cowden block samples (size: 350 mm×350 mm×350 mm), noted that Blocks E1 and E2 being the soil blocks employed in the Author's testing programme on Cowden till described in Chapter 3

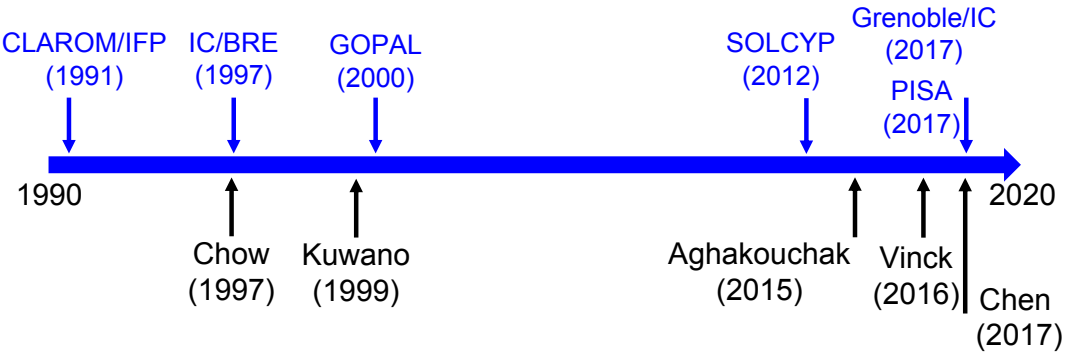

Figure 2-5 Field piling studies (top) performed at the Dunkirk site and the laboratory research programmes (bottom) on Dunkirk sand carried out at Imperial College

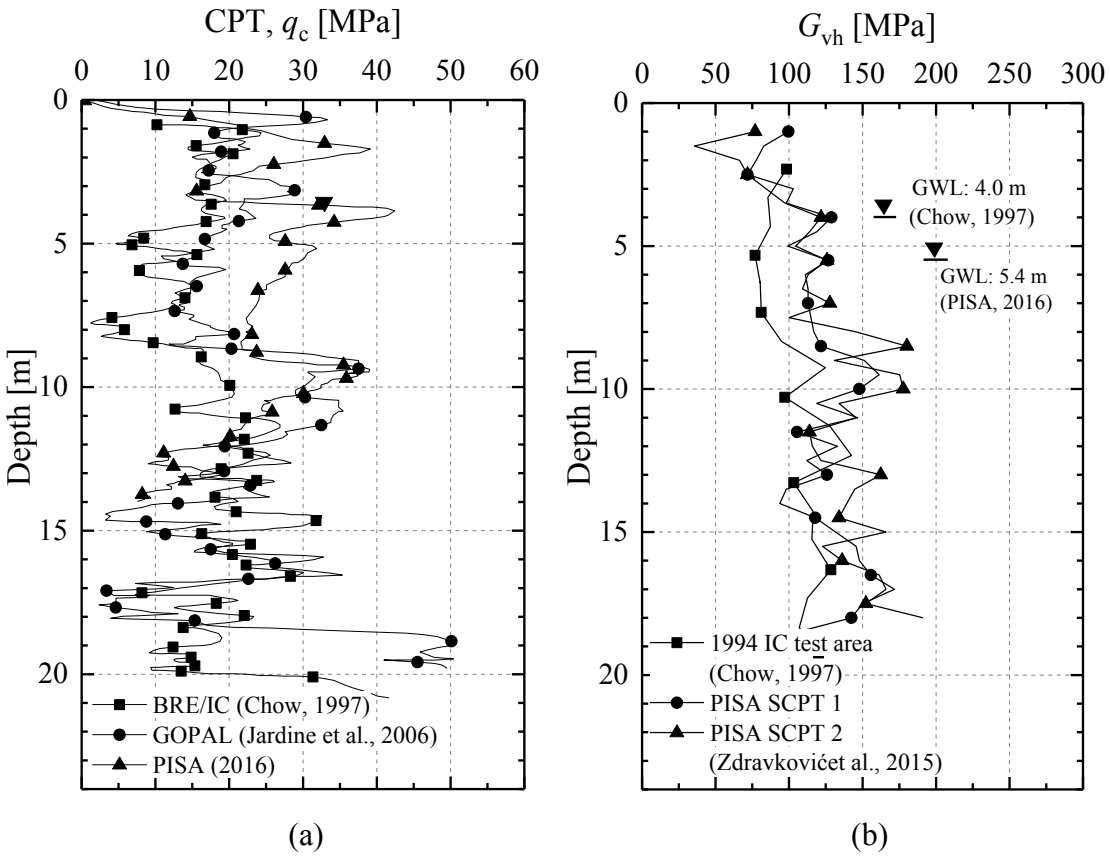

Figure 2-6 Dunkirk ground profile: (a) CPT cone resistance, q_c; (b) downhole maximum elastic shear stiffness, G_{vh}, noting the differences in the ground water level (GWL) as well as the q_c and G_{vh} traces between the measurements made by around 20 years apart

Figure 2-7 Examples of drilled (a) poor quality and (b) promising 'intact' cores retrieved from the PISA rotatory core sampling campaign at the Dunkirk site

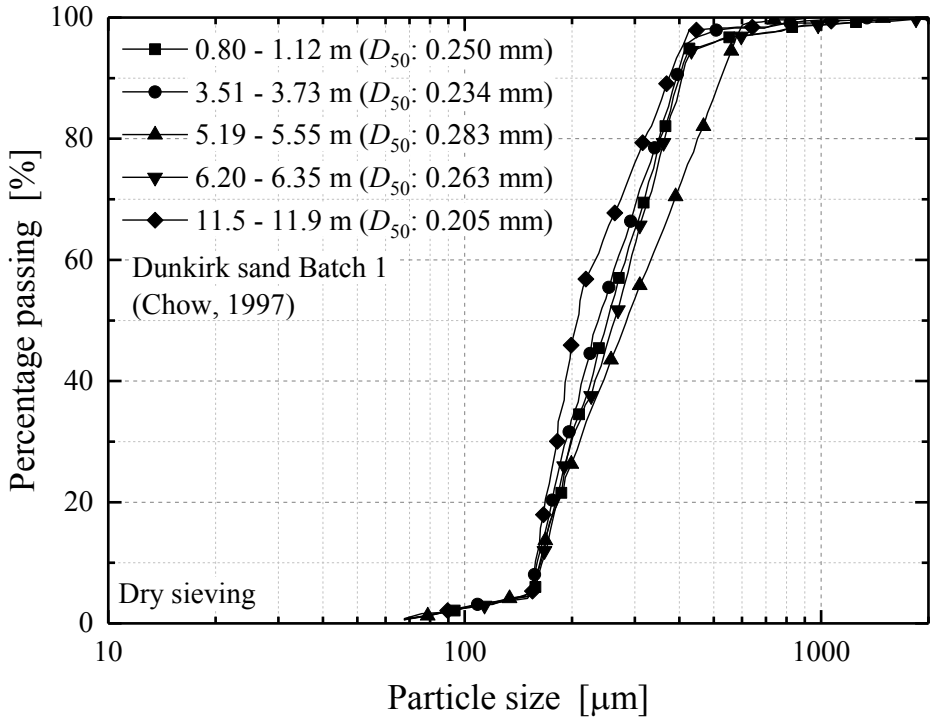

Figure 2-8 Particle size distributions and D_{50} values for Dunkirk sand Batch 1 from varied depths (Chow, 1997)

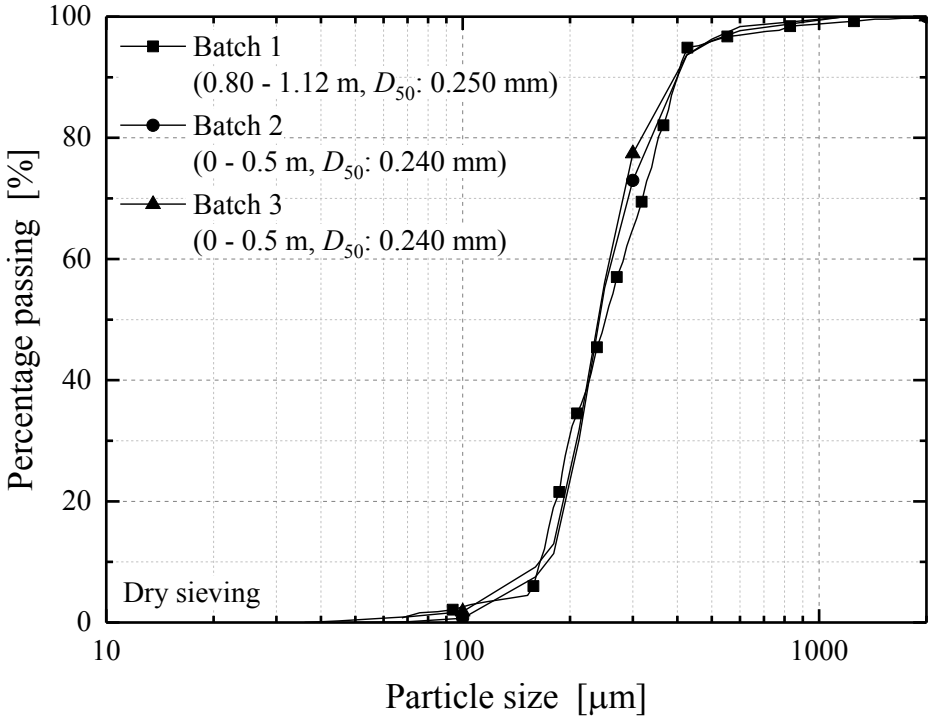

Figure 2-9 Particle size distributions and D_{50} values for the three batches of Dunkirk sand sampled from shallow depths

2.3 Testing apparatuses and techniques

The Author's research programme involved testing with apparatuses that included the Imperial College Resonant Column Hollow Cylinder Apparatus (ICRCHCA), Bishop-Wesley type automated stress-path triaxial apparatuses and Bishop ring shear apparatuses. This section presents first an introduction to hollow cylinder testing, followed by detailed descriptions of the employed apparatuses and related techniques employed in the research, addressing their capabilities and limitations as well as modifications implemented for the Author's testing.

2.3.1 Hollow cylinder testing: assumptions and limitations

Hollow Cylinder Apparatus (HCA) element testing on soil samples has long been appreciated at Imperial College as a robust approach for assessing mechanical anisotropy in advanced soil characterisation (see from Hight *et al.* (1983) to Brosse *et al.* (2017)). Four external boundary stresses are imposed on HCA specimens: axial force (F_a), torque (T) plus inner (p_i) and outer (p_o) cell pressures, as illustrated in Figure 2-10. These external actions generate stresses and strains that distribute non-uniformly within HCA specimens. Such spatial distributions of stress and strain conditions cannot be solely determined from force equilibrium or displacement compatibility formulations. Assumptions have to be introduced to solve the HCA tests as boundary value problems and characterise the stress and strain states as representing a soil element.

Assumptions

Two important assumptions are involved in the derivation of the stress and strain states in HCA specimens (Hight *et al.*, 1983, Porovic, 1995, Nishimura, 2006, Brosse, 2012).

Stress boundary condition Radial friction generated at the specimen ends induced by the rigid rough plattens is neglected, i.e. $\tau_{zr} = 0$, and therefore the specimen is assumed to be free of radial restraint while deforming. This assumed condition is required to be compatible with the condition of zero shear stress at the inner and outer side membranes, i.e. $\tau_{rz} = \tau_{r\theta} = 0$. However, at specimen ends, friction in the radial direction cannot be effectively eliminated, as the plattens need to have sufficient roughness to transmit torsional (circumferential) loading to the specimens by means of rough porous stones, often supplemented by shear vanes. As explained later, the radial

restraint invoked by rough plattens is one of the main causes of the non-uniformities in HCA specimens.

Constitutive correlation Isotropic linear elastic models were adopted from the onset to derive average stresses and strains across HCA specimens and so represent the conditions applying to an equivalent soil element. As demonstrated by Nishimura (2006), similar solutions can also be developed for cross-anisotropic linear elastic materials. Further numerical modelling may be undertaken with a wide range of elastic-plastic or more advanced constitutive modes, see for example by Zdravkovic & Potts (2005).

Nishimura (2006) and Brosse (2012) discuss other assumptions which are often made regarding the stress conditions within HCA specimens and the corresponding strains, which include the following:

Assumptions regarding stresses

(a) Simplified treatments of HCA tests may assume that in a horizontal cross-section, the axial stress (σ_z) is uniform and does not vary in the radial (r) or circumferential (θ) direction.

$$\frac{\partial \sigma_z}{\partial r} = 0 \quad \frac{\partial \sigma_z}{\partial \theta} = 0 \tag{2.1}$$

(b) In the same way, it is often assumed that end effects are negligible so that the circumferential stress (σ_θ) is only dependent of the radius from the symmetric z-axis and does not vary in the height (z) and circumferential (θ) direction.

$$\frac{\partial \sigma_\theta}{\partial z} = 0 \quad \frac{\partial \sigma_\theta}{\partial \theta} = 0 \tag{2.2}$$

(c) No shear stress can be generated on the side membranes and is usually neglected in the radial direction at the specimen ends. Shear stress is assumed to be only generated in the torsional (circumferential) direction ($\tau_{z\theta}$).

$$\tau_{rz} = 0 \quad \tau_{r\theta} = 0 \tag{2.3}$$

(d) The distribution of torsional shear stress is independent of z and θ.

$$\frac{\partial \tau_{z\theta}}{\partial z} = 0 \quad \frac{\partial \tau_{z\theta}}{\partial \theta} = 0 \tag{2.4}$$

(e) The only body force is gravity, which acts in the axial (vertical) direction.

Assumptions regarding strains

HCA specimens are often assumed to maintain right cylindrical shapes while being subjected to compression or extension in the axial direction, combined with torsional twisting. The following assumptions on strains then apply.

(a) The symmetry around the vertical *z*-axis is maintained and all the normal strain components show no variation with regard to the circumferential (θ) direction.

$$\frac{\partial \varepsilon_z}{\partial \theta} = 0 \qquad \frac{\partial \varepsilon_r}{\partial \theta} = 0 \qquad \frac{\partial \varepsilon_\theta}{\partial \theta} = 0 \tag{2.5}$$

(b) The specimens deform uniformly in horizontal cross-sections and the axial strain component (ε_z) is independent of *r*.

$$\frac{\partial \varepsilon_z}{\partial r} = 0 \tag{2.6}$$

(c) During torsional rotation a vertical cross-section maintains planar so the circumferential strain (ε_θ) varies linearly with *r* and *z*.

$$\frac{\partial \varepsilon_\theta}{\partial r} = \text{const} \qquad \frac{\partial \varepsilon_\theta}{\partial z} = \text{const} \tag{2.7}$$

It is important to note that several of the above simplifying assumptions may be discarded when full 3-D numerical analyses that employ realistic boundary conditions are carried out in conjunction with sophisticated soil models, see for example by Zdravkovic & Potts (2005).

Analysis of stress and strain

The stress and strain components reported from HCA tests usually represent averaged values taken across the HC specimen to represent the states expected in a single soil element. The formulations for calculating the average stresses depend on the assumptions made and the way of averaging. Following the approach of Hight *et al.* (1983), the equations used in the current study for the calculation of the average stress components are listed as following.

$$\overline{\sigma_z} = \frac{\int_0^H \sigma_z dz}{\int_0^H dz} = \frac{F_a}{\pi(r_o^2 - r_i^2)} + \frac{p_o r_o^2 - p_i r_i^2}{r_o^2 - r_i^2} \tag{2.8}$$

$$\overline{\sigma_{\mathrm{r}}} = \frac{\int_{r_{\mathrm{i}}}^{r_{\mathrm{o}}} \sigma_{\mathrm{r}} dr}{\int_{r_{\mathrm{i}}}^{r_{\mathrm{o}}} dr} = \frac{p_{\mathrm{o}} r_{\mathrm{o}} + p_{\mathrm{i}} r_{\mathrm{i}}}{r_{\mathrm{o}} + r_{\mathrm{i}}} \tag{2.9}$$

$$\overline{\sigma_{\theta}} = \frac{\int_{r_{\mathrm{i}}}^{r_{\mathrm{o}}} \sigma_{\theta} dr}{\int_{r_{\mathrm{i}}}^{r_{\mathrm{o}}} dr} = \frac{p_{\mathrm{o}} r_{\mathrm{o}} - p_{\mathrm{i}} r_{\mathrm{i}}}{r_{\mathrm{o}} - r_{\mathrm{i}}} \tag{2.10}$$

$$\overline{\tau_{\mathrm{z}\theta}} = \frac{T}{\int_0^{2\pi} \int_{r_{\mathrm{i}}}^{r_{\mathrm{o}}} r^2 dr d\theta} = \frac{3M_{\mathrm{T}}}{2\pi(r_{\mathrm{o}}^3 - r_{\mathrm{i}}^3)} \tag{2.11}$$

Where F_{a} and M_{T} are the axial force and torque, respectively. H represents the specimen's height, and r_{o} and r_{i} respectively the outer and inner radius. p_{o} and p_{i} denote the outer and inner cell pressure.

Vaid *et al.* (1990) proposed an alternative approach of averaging over the volume of the specimen. The formulations made for calculating the average torsional stress $\tau_{\mathrm{z}\theta}$ also differ depending whether elasticity or full plasticity is assumed. Equation (2.11) above may be regarded as a plasticity solution and it satisfies the condition of thermodynamics equilibrium (Nishimura, 2006). Adopting a linear elastic soil model leads instead to the following.

$$\overline{\tau_{\mathrm{z}\theta}} = \frac{4M_{\mathrm{T}}(r_{\mathrm{o}}^3 - r_{\mathrm{i}}^3)}{3\pi(r_{\mathrm{o}}^4 - r_{\mathrm{i}}^4)(r_{\mathrm{o}}^2 - r_{\mathrm{i}}^2)} \tag{2.12}$$

Considering the specimen dimensions adopted in the Author's tests, the differences in $\overline{\tau_{z\theta}}$ of using Equations (2.11) and (2.12) are no greater than 2.6%. Some researchers, for example, Yang *et al.* (2007), adopted the average value of the above elastic and plastic solution as the torsional shear stress.

Similarly, the strain components and the volumetric strain are defined through the following equations (Hight *et al.*, 1983).

$$\overline{\varepsilon_{\mathrm{z}}} = \frac{\int_0^H \varepsilon_{\mathrm{z}} dz}{\int_0^H dz} = -\frac{\Delta H}{H} \tag{2.13}$$

$$\overline{\varepsilon_{\mathrm{r}}} = \frac{\int_{r_{\mathrm{i}}}^{r_{\mathrm{o}}} \varepsilon_{\mathrm{r}} dr}{\int_{r_{\mathrm{i}}}^{r_{\mathrm{o}}} dr} = -\frac{\Delta r_{\mathrm{o}} - \Delta r_{\mathrm{i}}}{r_{\mathrm{o}} - r_{\mathrm{i}}} \tag{2.14}$$

$$\overline{\varepsilon_{\theta}} = \frac{\int_{r_{\mathrm{i}}}^{r_{\mathrm{o}}} \varepsilon_{\theta} dr}{\int_{r_{\mathrm{i}}}^{r_{\mathrm{o}}} dr} = -\frac{\Delta r_{\mathrm{o}} + \Delta r_{\mathrm{i}}}{r_{\mathrm{o}} + r_{\mathrm{i}}} \tag{2.15}$$

$$\overline{\gamma_{\mathrm{z}\theta}} = \frac{\int_0^{2\pi} \int_{r_{\mathrm{i}}}^{r_{\mathrm{o}}} \gamma_{\mathrm{z}\theta} r dr d\theta}{\int_0^{2\pi} \int_{r_{\mathrm{i}}}^{r_{\mathrm{o}}} \gamma_{\mathrm{z}\theta} dr d\theta} = -\frac{2\Delta\theta(r_{\mathrm{o}}^3 - r_{\mathrm{i}}^3)}{3H(r_{\mathrm{o}}^2 - r_{\mathrm{i}}^2)} \tag{2.16}$$

$$\varepsilon_{\mathrm{vol}} = \overline{\varepsilon_{\mathrm{z}}} + \overline{\varepsilon_{\mathrm{r}}} + \overline{\varepsilon_{\theta}} \tag{2.17}$$

Where Δh, Δr_{o} and Δr_{i} denote the change of the specimen's height, outer radius and inner radius, respectively. Meanwhile, the sample is assumed to deform as an idealised right cylinder, and its dimensions can be determined through the externally measured change of height (ΔH), sample volume (ΔV) and the inner cavity volume (ΔV_{i}) through the equations below.

$$H = H_0 - \Delta H \tag{2.18}$$

$$r_{\mathrm{i}} = r_{\mathrm{i}0} \sqrt{\frac{1 - \Delta V_{\mathrm{i}} / V_{\mathrm{i}0}}{1 - \Delta H / H_0}} \tag{2.19}$$

$$r_{\mathrm{o}} = r_{\mathrm{o}0} \sqrt{\frac{1 - (\Delta V + \Delta V_{\mathrm{i}}) / (V_0 + V_{\mathrm{i}0})}{1 - \Delta H / H_0}} \tag{2.20}$$

Where H_0, V_0 and $V_{\mathrm{i}0}$ are respectively the specimen's initial height, volume and inner volume. As the strains are defined as positive in compression, the above variations are regarded as positive as specimen height, radius or volume decreases.

Principal stress and strain and other parameters

Referring to Figure 2-11, the principal stresses and strains can be defined with the averaged stress and strain components stated above with the following equations.

$$\sigma_1 = \frac{\sigma_z + \sigma_\theta}{2} + \sqrt{\left(\frac{\sigma_z - \sigma_\theta}{2}\right)^2 + {\tau_{z\theta}}^2}$$
$$\sigma_2 = \sigma_r \tag{2.21}$$
$$\sigma_3 = \frac{\sigma_z + \sigma_\theta}{2} - \sqrt{\left(\frac{\sigma_z - \sigma_\theta}{2}\right)^2 + {\tau_{z\theta}}^2}$$

$$\varepsilon_1 = \frac{\varepsilon_z + \varepsilon_\theta}{2} + \sqrt{\left(\frac{\varepsilon_z - \varepsilon_\theta}{2}\right)^2 + \left(\frac{\gamma_{z\theta}}{2}\right)^2}$$
$$\varepsilon_2 = \varepsilon_r \tag{2.22}$$
$$\varepsilon_3 = \frac{\varepsilon_z + \varepsilon_\theta}{2} - \sqrt{\left(\frac{\varepsilon_z - \varepsilon_\theta}{2}\right)^2 + \left(\frac{\gamma_{z\theta}}{2}\right)^2}$$

The following stress parameters and equations are often adopted to describe the specimen's stress state.

$$\alpha = \frac{1}{2}\tan^{-1}\left(\frac{2\tau_{z\theta}}{\sigma_z - \sigma_\theta}\right) \tag{2.23}$$

$$b = \frac{\sigma_2 - \sigma_3}{\sigma_1 - \sigma_3} \tag{2.24}$$

$$q = \sigma_1 - \sigma_3 \tag{2.25}$$

$$p = \frac{\sigma_1 + \sigma_2 + \sigma_3}{3} \qquad p' = p - u \tag{2.26}$$

Where α is the angle between the direction of the major principal stress (σ_1) and the vertical axis; b denotes the intermediate stress factor; q represents the deviatoric stress; p, p', u are respectively the mean stress, mean effective stress and pore water pressure.

Other related stress parameters are expressed below.

$$t = \frac{\sigma_1 - \sigma_3}{2} \tag{2.27}$$

$$s = \frac{\sigma_1 + \sigma_3}{2} \qquad s' = s - u \tag{2.28}$$

$$\phi_{mob}' = \sin^{-1}\left(\frac{\sigma_1' - \sigma_3'}{\sigma_1' + \sigma_3'}\right) = \sin^{-1}\left(\frac{t}{s'}\right) \tag{2.29}$$

Non-uniformities in HCA testing

HCA specimen geometry inevitably introduces non-uniformity in stresses and strains within the specimens that can lead to deviations between responses of single soil elements and those represented by the averaged stress and strain components. These issues were explored in the course of developing HCA equipment by Hight *et al.* (1983) and Saada (1988) among others, and in interpreting test outcomes (see for example by Menkiti (1995), Porovic (1995) and Rolo (2004) among others).

Two factors are regarded as the main sources of non-uniformities in HCA testing. The first is associated with the curvature of the specimen wall. The stress components developed within HC specimens are likely to vary along *z*- or *r*-axis and the deviations between the averaged and distributed stresses depend on specimen geometries (r_o, r_i and H) and the imposed external loads (p_o, p_i and M_T). In particular, excessively non-uniform σ_r distributions arise if a large difference exists between the inner and outer cell pressure. The shear stress $\tau_{z\theta}$ transmitted through the rough plattens is also inevitably non-uniform, especially if the specimen wall thickness is relatively large compared to the average radius.

The end constraint invoked by the rigid rough plattens is the other major cause of the stress and strain non-uniformity. As in triaxial testing, rough plattens restrict free deforming and result in highly non-uniform straining close to the ends. Friction present in the radial direction of the platten generates unwanted τ_{rz} or $\tau_{r\theta}$ stresses, which cannot be balanced by any complementary shear components. However, according to the St.Venant principle, the effects of end constraint can be significantly alleviated, provided that certain height to diameter (H/D) criteria can be satisfied. Careful section of specimen geometries is therefore required.

The non-uniformities in HCA testing have been investigated through numerical approaches to help optimise specimen geometries and assess potential deviations between the observed stress-strain-stiffness responses interpreted from tests and true single-element soil behaviour. Analyses of HCA tests as boundary value problems are themselves critically dependent on the constitutive models adopted. The outcomes can provide useful insights regarding the non-uniformities and the resultant errors in terms of strength and stiffness. Accurate assessments, however, require appropriate soil constitutive models to be selected and calibrated to the soils studied.

Saada & Townsend (1981) proposed criteria for HCA allowable specimen geometries based on linear elasticity analyses.

$$H \geq 5.44\sqrt{r_o^2 - r_i^2} \quad n = \frac{r_i}{r_o} \geq 0.65 \tag{2.30}$$

The above criteria provide preliminary guidance on specimen geometry selection, although may be regarded as conservative as analyses based on linear elasticity constitutive laws tends to overestimate the stress non-uniformities developed in highly nonlinear geo-materials (Brosse, 2012).

Hight *et al.* (1983) reported rigorous finite element (FE) analyses of the non-uniformities present in HCA specimens and applied the results as guidance in developing the Large Imperial College Hollow Cylinder Apparatus (LICHCA). Two constitutive models were adopted in the analyses, including linear elastic and strain hardening modified Cam-clay model. The following parameters, β_1 and β_3, were defined to quantify the level of stress non-uniformity.

$$\begin{aligned} \beta_1 &= \frac{\left|\bar{\sigma}^* - \bar{\sigma}\right|}{\sigma_L} \\ \beta_3 &= \frac{\int_a^b \left|\sigma(r) - \bar{\sigma}^*\right| dr}{(b-a)\sigma_L} \end{aligned} \tag{2.31}$$

Where a and b are the specimen's inner and outer radius, respectively. $\bar{\sigma}$ is the average of stress output from FE simulations, $\bar{\sigma}^*$ averaged stress calculated from Equations (2.8) to (2.11) and σ_L a measure of average stress level. $\sigma(r)$ is the distribution of the normal or shear stress component across the wall, namely along the r-axis. Figure 2-12 demonstrates schematically the defined stress variables, also quoted is the evolving trends of the two parameters against radius ratio (a/b) from Hight *et al.* (1983)'s analyses on the $\tau_{z\theta}$ component. It is clear that the non-uniformities reduce as the specimen wall becomes thinner.

Apart from assessing suitable specimen geometries, the loading conditions and stress states that may result in severe non-uniformities can be identified through numerical simulations. Symes (1983) established two 'no-go' zones where excessive non-uniformities can be expected when stress paths approach stress states with either (α = 0, b = 1) or (α = 90°, b = 0), which lead to large cell pressure difference (p_o-p_i)

across the wall. Hight *et al.* (1983) set lower and upper bounds for p_o/p_i as between 0.9 and 1.2 in their testing with the LICHCA.

Numerical analyses considering other geometries and constitutive models have also been investigated, with particular emphases on the effects of non-uniformities on strength parameters and stiffness, see for examples by Menkiti (1995), Porovic (1995), Rolo (2004) and Zdravkovic & Potts (2005) among others. The outcomes from these studies generally conformed with earlier findings by Hight *et al.* (1983) but also highlighted the complexities in assessing the magnitudes of errors induced by non-uniformities in terms of effective stress path, strength or stiffness parameters.

The Resonant Column Hollow Cylinder Apparatus (RCHCA) employed in the Author's tests accommodates soil specimens with 19 mm inner radius (r_i), 35.5 mm outer radius (r_o) and 195 mm height, giving radius ratio r_i/r_o of 0.54. As indicated in Figure 2-12, compared with LICHCA (Hight *et al.*, 1983) specimens (r_i = 100 mm, r_o = 125 mm, H = 250 mm), the RCHCA specimens have a smaller radius ratio and a lower diameter-wall thickness ratio and are therefore expected to encounter greater non-uniformities due to greater wall curvature. These features were confirmed by Zdravkovic & Potts (2005), who further argued that if non-uniformities of HCA testing were to be interpreted and assessed in terms of engineering parameters, both the diameter-wall thickness ratio and sample height should be considered. Their numerical simulations demonstrated that the deviations in stress path, stress-strain and stiffness responses between the RCHCA test and an 'ideal' simulated test were significantly reduced by the RCHCA specimens' relatively large height to diameter ratio.

However, as recognised by the earlier studies, numerical assessments of HCA non-uniformities are highly dependent on the constitutive models adopted and are affected by a range of factors, including soil stress history and conditions, stress path for consolidation and shearing. Other features, such as anisotropy and rate effects of soils may also require consideration. Although beyond the current research scope, the Modified Cam Clay (MCC) model (Roscoe & Burland, 1968) with nonlinear Hvorslev surface (Tsiampousi *et al.*, 2013), which was adopted to simulate the PISA pile testing at Cowden, might be employed to represent the behaviour of Cowden till and assess soil-specific errors induced by the non-uniformities in HCA testing.

Apart from specimen dimensions and stress conditions discussed above, another

important source of non-uniform stress and strain distributions in HC specimens exists in the non-uniformities or heterogeneities of tested specimens, especially when testing natural clays. Aged stiff natural clays tend to develop macro-fabric and meso-structure features during shearing that manifest as fissures, shear bands or other forms of discontinuities (see for examples in the studies by Nishimura (2006), Minh (2006) and Brosse (2012)). Non-uniformities in these HCA samples tend to be more severe than reconstituted specimens as straining tends to be modified at failure by pre-existing fissures, bedding features or discontinuities. In the cases of Cowden till, as presented in Chapter 3, the non-uniformities of the specimens were mostly due to the presence of fissured zones and randomly distributed heterogeneities (gravels, voids, etc.). Detailed assessment or quantification of how non-uniformities affect the tested specimens is difficult to make. However, the observed mechanical responses from HCA testing could still be regarded as representing of the behaviour of natural soils, provided that the specimen volume is sufficiently large to be treated as representative element volume (REV).

2.3.2 Imperial College Resonant Column HCA (ICRCHCA)

The ICRCHCA was manufactured in 1991 by Soil Dynamics Instruments Inc., in conjunction with Imperial College. The general configuration was based on a design by Professor Vincent P. Drnevich but was modified to comprise an all-stainless steel construction and include at the base a new biaxial load cell developed between Maywood Instrument Ltd. and Imperial College. The system was also linked to the control system developed at Imperial College. The apparatus is equipped with a Hardin oscillator which enables the determination of soil dynamic properties (shear stiffness $G_{z\theta}$ and damping ratio) under generalised stress states independently of quasi-static loading. The apparatus and control algorithms have been continuously upgraded and enhanced at Imperial College for studies of a range of soils, including intact and reconstituted stiff clays (Nishimura, 2006, Brosse, 2012), sands and silts (Porovic, 1995, Aghakouchak, 2015) under both monotonic and cyclic shearing conditions.

The apparatus can accommodate testing hollow soil specimens with two sets of geometries, 71 mm O.D (outer diameter) and 38 mm I.D (inner diameter) or 100 mm O.D and 71 mm I.D. The specimen height is constrained to be between around 165 mm and 195 mm due to the presence of the proximity transducers and the Hardin oscillator.

As higher specimens with larger H/D ratios are generally favoured in HCA testing, the first geometry was commonly used in the earlier studies and was adopted in the Author's programme.

The apparatus mainly consists of a loading and transmission system, transducers and instruments, signal conditioning and data logging units, a resonant column (RC) system, as well as software and algorithms for test control. The schematic diagram of the general configuration is shown in Figure 2-13 and is detailed below. The resonant column (RC) system and testing procedures are presented in the next section.

Loading and transmission

The apparatus adopts a compressed air to apply axial load and water pressures to the specimen, while torque is applied mechanically through a rotary table controlled with a stepper motor and transmitted through a gear and chain system, as seen in Figure 2-13.

Compressed air (with maximum stable pressure around 820 kPa) is supplied through a central compressor and is further regulated using a Manostat pneumatic valve before connecting to the main pressure supply of the apparatus. The additional pneumatic valve filters off fluctuations in the pressure system and more importantly, sets an upper limit (700 kPa) to the apparatus's operation pressure, which is critical for safety reasons since the strength of the acrylic cylinder chamber enclosing the outer cell is limited.

The outer cell water pressure is generated through direct contact between the pressured air and cell water, while the inner cell and pore water pressures are generated through Imperial College volume-gauges that convert air pressure to water pressure. The pressures are regulated through Watson-Smith electro-pneumatic Manostat controllers, which are mobilised through digital stepper motors and enable high resolution pressure control of 0.07 kPa per pulse.

The axial load is generated via a double-acting Bellofram through differentiated air pressures in its bottom and top chamber. The Bellofram is fixed to a cross-beam and clamped to two tie rods. Air pressure in the bottom Bellofram chamber is regulated manually and maintained constant throughout the tests. The air pressure in the top chamber is regulated by an electro-pneumatic unit, which is controlled from programmed close-loop feedback control algorithms.

Torque is generated by a stepper motor and rotary table system and transmitted to the top of the specimen through a gear reduction system and a loading ram, as shown in Figure 2-14. The gear system and stepper motor was set up in a way that each full rotation (360˚) requires 5760000 pulses, so the rotation can be controlled in 6.25×10^{-5} degrees steps. Torque transmission to the loading ram is enhanced by six bolts that tighten the rotatory gear against the loading shaft. Torque transmission through the specimen is provided by friction between the sintered bronze annular drainage disks and the specimen ends, the coupling between which is further enhanced by adopting annular disks with eight evenly distributed thin metal vanes that are penetrated about 4 mm into the specimen. Although not used in the Author's programme, a rotary tension cylinder is available to apply additional tension force through a wire to embrace the rotatory table. This auxiliary set-up was found to be essential in Aghakouchak (2015)'s cyclic tests as it helped to reduce compliance and alleviate backslash of the gear when applying load reversals.

Transducers, instruments and their performance

The transducers and instruments employed in the ICRCHCA apparatus are summarised in Table 2-1, including the dual-axis (pressure balanced) load cell, water pressure transducers, volume-gauges and proximity transducers, also listed are their performances in terms of resolution and precision. The methods for calibrating the transducers were as outlined by Nishimura (2006).

A dual-axis combined load cell is used to measure axial force F_a and toque M_T at the base of the specimen. The capacity for measuring axial load is around 4 kN and 180 Nm for torque. The load cell is subject to a moderate level of cross-coupling as the load and torque measurements are not fully independent. The cross-coupling terms were found by linear regression of the calibration data. The correlation coefficients obtained in the Author's calibration were very close to those found by previous researchers, gaining confidence in the load cell's condition and long-term stability.

Axial displacement is measured with a canteliver strain-gauge device which is fixed to the beam supporting the load Bellofram and sits on a cross-bar that moves together with the loading shaft, as seen in Figure 2-13. Because the displacement is monitored away from the specimen, the measurements are not immune from system compliance invoked by the loading and transmission parts, as well as the deflection of

the tie rods. System compliance was checked as part of the calibration process and is discussed further in the following subsection.

Water pressure transducers are used to determine inner and outer cell pressures and specimen pore water pressure. Imperial College volume-gauges, which also serve as air/water interfaces, were adopted to measure volume changes of the specimen and the inner cell. Volume compliance in the volume-gauges and connecting tubes in the course of pressure changes or long-term testing was characterised through a series of calibration tests with a dummy sample, as later discussed in Section 2.3.7. However, the resulting errors in strain measurements were concluded to marginal and were therefore not applied to correct the testing outcomes.

Platten-to-platten rotation at the specimen top end is determined by a pair of non-contacting proximity transducers, as shown in Figure 2-14. A light aluminium cam with weight of 460 g is fixed to the porous disk at the specimen top and serves as the metallic target for the proximity transducers. The cam has logarithmically curved profiles which give linear correlations between the angle of rotation and the angle and the distance between the side and the proximity transducer. The proximity transducers are fixed diametrically opposite at the top a supporting cage, which is carefully adjusted prior to testing to achieve the best resolution voltage range of around 800 mV. Two new cams were manufactured for the Author's testing as the existing unit suffered corrosion at the corner edges, probably due to their occasional contact with cell water in their long-run use. The new cams have almost identical dimensions, edge shape and weight, and the calibration coefficients were found to be similar.

On the basis of the performance of each individual transducer listed in Table 2-1, the resolution and precision of the strain components (ε_z, ε_r, ε_θ, $\gamma_{z\theta}$) can be estimated using the approximation approach described by Nishimura (2006). A resolution and precision range of $(1\text{-}4)\times10^{-4}$ % was generally found for all the strain components, assuming a standard specimen size of O.D = 71 mm, I.D = 38 mm and H = 190 mm. Despite the fact that the individual external and 'semi-local' instrument measurements made with the ICRCHCA are less accurate than those that can be obtained with local LVDTs in the triaxial tests described later, the system offers acceptable overall strain measurement performance. There remain, however, unquantified errors associated with sample-end effects (bedding) and possible tilting under load.

Test control, signal conditioning and data acquisition

The ICRCHCA test control and data acquisition systems were upgraded by Dr. Amin Aghakouchak to operate with the in-house software TRIAX (Toll, 2002), which is also employed for triaxial, ring shear and other testing. The software receives and records real-time measuring data from the transducers, and embeds closed-loop feed-back control algorithms to regulate the electro-pneumatic controllers or constant displacement rate screw pumps with stepper motor pulses so that targeted stress or strain conditions can be reached.

The TRIAX software allows flexible definitions for the test variables and control parameters. These features are critical to the HCA testing described here, which requires simultaneous control over a series of variables. Care is needed to choose appropriate values for control tolerances and maximum steps to avoid problems of over- or under-shooting. The software also offers other options for refining test control and optimising testing outcomes.

Signal processing is conducted through a 16 bit analogue-digital (A/D) MSL converter that transforms analogue signals from the instruments to digital signals before being sent to the software. The A/D converter has four DC voltage ranges, namely ±20 mV, ±150 mV, ±1.3 V, ±10 V (Kuwano, 1999), and provides a theoretical resolution of 0.625 μV at its best. The signal processing unit enables high quality test measurement and control that are of particular importance for interpreting soil small strain behaviour (Gasparre *et al.*, 2014).

Modifications implemented and other issues

The apparatus was in working order when the Author commenced his testing and no major modification was implemented on its hardware. Effort was mostly focused on optimising the test control system operating with the TRIAX programme.

Torsional shear control was updated by introducing the number of stepper motor pulses as a direct control variable so that the shearing can be readily applied in both stress-control and strain control manner. Since the angle of rotation is directly correlated to stepper motor pulses, the number of steps can be viewed as an external measure of the rotation angle.

Meanwhile, as noted by previous researchers, the ICRCHCA has some particular

difficulties including: (i) an air-diffusion problem created by having a free-air water interface within the cell chamber, and (ii) its system compliance, as discussed below.

Air diffusion and countermeasure During testing, the outer cell chamber is only half filled with de-aired water, since the electronic parts of the Hardin oscillator and proximity transducers are not water-proof and cannot be immersed in pressurised water. Due to the presence of a large area of direct contact between air and water, the pressurised air tends to dissolve in the water and slowly migrate through the latex membrane enclosing the specimen, reducing its degree of saturation and resulting in errors in pore water pressure and sample volume measurements. This issue is most significant when testing coarse materials, although it can also impact long-term tests on low permeability clays.

As suggested by previous researchers, diffusion can be addressed by regularly replacing the outer cell water with fresh de-aired water. This must be achieved without disturbing the specimen. An auxiliary water tank is required for this purpose, where de-aired water with a similar volume (around 10 litres) to the outer cell water is stored for around 6 to 12 hours to let the water temperature equilibrate to the ambient temperature in the lab. Water in the tank is then pressured into the outer cell chamber from the bottom and outflow is drained though a pipe fixed close to the chamber water level.

Great care is needed to choose appropriate inflow pressure and outflow rate values to avoid disturbance to the outer cell pressure and maintain a stable water level. The load cell and volume-gauge readings are monitored to verify that negligible disturbance is imposed on the specimen by the flushing process. A needle value was added to the outlet tube to attain a fine control of the flow rate. In the Author's tests, each replacement of the 10 litre water volume cell took around 1 hour. The water change process was usually performed on a daily basis, but was avoided before initiating any critical testing stage, in particular the final shearing.

System compliance Two major sources of system compliance of the ICRCHCA were identified associated with applying axial and torsional loading.

As shown in Figure 2-13, the ICRCHCA has an axial configuration, with most of its functioning units aligned along a central rod. As the axial displacement is determined externally at the top of the apparatus, errors inevitably arise from the

deflection of the tie rods, cross-beams and the outer cell chamber as well as the compliance of the porous stones, load cell, Hardin oscillator, loading rods and rams.

Calibration tests was performed to assess the axial compliance of the apparatus using a hollow cylinder dummy sample machined from rigid PVC (Young's modulus around 3.0 GPa). The sample was enclosed by outer and inner membranes and was set up in a normal testing way, allowing determination of compliances from axial loading and unloading as well as from the volume-gauges. The first set of axial calibration tests concerned compliance during pressurising the cell fluids. The axial load was maintained zero and the cell and inner cell pressure were raised simultaneously from 40 kPa up to 600 kPa and brought down to 320 kPa. Axial displacements were recorded after each pressure level, as plotted in Figure 2-15. The second set of tests investigated compliance associated with axial loading and unloading while maintaining constant cell and inner cell pressure. Three cell pressure levels (400 kPa, 500 kPa and 600 kPa) were examined and the recorded accumulated displacements are presented in Figure 2-16.

Figures 2-15 and 2-16 indicate clear trends of axial compliance with levels of cell pressure and deviatoric load. The trends can be expressed by approximately linear correlations, although hysteretic responses were also observed in the unloading loops that extended to the extension side. As shown in Figure 2-16, the load-displacement correlation coefficients generally decreased with cell pressure level, indicating stiffer response under high cell pressure conditions. The coefficients obtained were found to match well those established by Nishimura (2006) from compression calibration tests on a hollow brass cylinder sample with Young's modulus around 140 GPa.

The attained coefficients obtained from the calibration tests were adopted to correct the axial displacement measurements recorded in the Author's tests.

System compliance may also rise when applying torsion, primarily from slippage at the chain and rotatory rotary table as well as other transmission pieces. Assessment of the torsional compliance requires a special set-up with calibration rods. Since torsional strains are determined precisely from the 'semi-local' proximity transducers, no torsional compliance calibrations were made in the Author's programme. However, the effects of torsional compliance on shear stress-strain response and stiffness are illustrated through an HCA simple shear test on Cowden till, as shown in Figure 2-17.

Torsional strains determined from the ‘external’ stepper motor suggested a much softer stress-strain response over the small strain range than those measured by the proximity transducers, although the two trends tended to converge when shear strains exceeded 1%.

Table 2-1 Summary of the transducers employed in the ICRCHCA and their performance in terms of resolution and precision

CH	Variable [unit]	Transducer type	Manufacturer	Measuring range [unit]		Resolution[1] [unit]		Precision[2] [unit]	
				Voltage	*Eng.*	Voltage	*Eng.*	Voltage	*Eng.*
1	Axial force [N]	Dual-axis load cell	Maywood Instruments Ltd.	-2213.4 ~ 13280 [mV]	$-1\times10^3 \sim 6\times10^3$ [N]	0.040 [mV]	0.018 [N]	0.27 [mV]	0.122 [N]
12	Torque [Nm]	Dual-axis load cell	Maywood Instruments Ltd.	-3860 ~ 3860 [mV]	-180 ~ 180 [Nm]	0.043 [mV]	0.001 [Nm]	0.128 [mV]	0.003 [Nm]
3	Pore water pressure [kPa]	Water pressure transducer	Sensotec THE/708-11	-14988.6 ~ 0 [μV]	0 ~ 1034.2 [kPa]	0.625 [μV]	0.040 [kPa]	0.680 [μV]	0.047 [kPa]
4	Outer cell pressure [kPa]	Water pressure transducer	Sensotec THE/708-11	-14988.6 ~ 0 [μV]	0 ~ 1034.2 [kPa]	0.625 [μV]	0.040 [kPa]	0.566 [μV]	0.039 [kPa]
7	Inner cell pressure [kPa]	Water pressure transducer	Keller series 27	-50251 ~ 0 [μV]	0 ~ 1000 [kPa]	0.625 [μV]	0.012 [kPa]	3.568 [μV]	0.071 [kPa]
5	Axial displacement [mm]	Canteliver strain-gauge	MPE LSC Transducer	-35714 ~ 0 [μV]	0 ~ 25 [mm]	0.625 [μV]	0.0004 [mm]	1.429 [μV]	0.001 [mm]
6	Sample volume [cm^3]	Volume gauge	Imperial College	0 ~ 38641 [μV]	0 ~ 50 [mL]	0.625 [μV]	0.0008 [mL]	0.692 [μV]	0.0009 [mL]
8	Inter cell volume [cm^3]	Volume gauge	Imperial College	0 ~ 35714 [μV]	0 ~ 50 [mL]	0.625 [μV]	0.0009 [mL]	1.429 [μV]	0.002 [mL]
9	Rotation [°]	Proximity transducer	Kaman KD-2310 4S	2580.6 [mV]	0 ~ 40 [˚]	0.038 [mV]	0.0005 [˚]	0.196 [mV]	0.003 [˚]
10	Rotation [°]	Proximity transducer	Kaman KD-2310 4S	1877.9 [mV]	0 ~ 40 [˚]	0.038 [mV]	0.0007 [˚]	0.095 [mV]	0.002 [˚]

Notes: [1]: Resolution values of the water pressure, displacement and volume transducer were determined over the best resolution range provided by the 16-bit A/D converter; resolution of the load/torque cell and proximity transducers were defined as the resolved smallest division from 200 readings recorded over the pressure range of the tests. [2]: Precision was determined as the standard deviation of 200 readings.

2.3.3 Resonant column system and derivation of soil dynamic parameters

The ICRCHCA is equipped with a Hardin oscillator with which resonant column tests can be performed to determine the soil specimen's dynamic parameters (elastic shear modulus G and damping ratio D) independently of the quasi-static loading system. As part of the hybrid HCA system, the resonant column testing produces an independent stiffness dataset that can be further integrated with stiffness data obtained from laboratory or in-situ shear velocity measurements as well as laboratory quasi-static testing with high resolution local instruments, see for examples by Gasparre *et al.* (2007b) and Brosse *et al.* (2016). The principles and procedures for resonant column testing with this equipment, as well as the appropriate interpretation approaches, were elaborated by Nishimura (2006) and Brosse (2012), and are briefly discussed below.

Testing principle, set-up and procedure

The resonant column testing units are configured in a fixed-base-spring-top design. The top of the tested specimen is incorporated with the Hardin oscillator and is excited in a torsional mode, generating vibrations in the z-θ direction, while the specimen bottom is fixed to a rigid base. Torsional excitation propagates through the specimen and the reflective waves are recorded. Assuming the wave propagates as if in a continuum, the dynamic properties of the specimen can be derived based on the input and output waves, together with appropriate boundary conditions.

The general set-up and electrical connections for resonant column testing in the ICRCHCA are illustrated in Figure 2-18. A sinusoidal input signal is generated by a Thurlby-Thandar programmable function generator and is sent through the specimen from a control box connected to the electro-magnetic oscillator after being amplified. The acceleration of the soil specimen is recorded by an accelerometer coupled to the Hardin oscillator. The output voltages and accelerations are amplified and sent back to the control box from where the voltage and acceleration are measured using a voltmeter.

The frequency of the input signal is slowly adjusted and the resonance frequency is determined by observing the coupled input and output voltage signal using the X-Y mode of a Hameg oscilloscope. Resonance is reached when the input and output signals have an angular phase difference of 90˚, manifesting as a right ellipse in a Lissajous figure. The input frequency is recorded as the resonant frequency f_{res}.

Interpreting the shear modulus and damping ratio requires readings of the input voltage of the Hardin oscillator V_{tor} and the output voltage of the accelerometer V_{acc}, as well as the specimen's dimensions (height and inner and outer radius) and bulk density ρ_{bulk}. It is common to undertake a series of measurements covering a range of input voltages to assess how dynamic shear moduli vary with the dynamic shear strain level.

Theory and parameter derivation

In resonant column testing, wave propagation through a soil specimen is regarded as a boundary value problem and the derivation of shear modulus and damping properties requires a constitutive relationship, stress equilibrium conditions and boundary conditions (Drnevich, 1978, Ashmawy & Drnevich, 1994, Nishimura, 2006, Brosse, 2012), as described below.

Constitutive relationship and stress equilibrium condition The visco-elastic constitutive equation of the Kelvin-Voigt type is used to correlate shear stress $\tau_{z\theta}$ and strain $\gamma_{z\theta}$.

$$\tau_{z\theta} = G\gamma_{z\theta} + \mu\frac{\partial\gamma_{z\theta}}{\partial t} \tag{2.32}$$

Where G is the elastic shear stiffness and μ is the coefficient of viscosity. Applying Newton's first law and introducing $\theta(z, t)$ as the soil element rotation, the propagation of shear wave can be expressed as:

$$\frac{\partial^2\theta}{\partial t^2} = \frac{G}{\rho}\frac{\partial^2\theta}{\partial z^2} + \frac{\mu}{\rho}\frac{\partial^3\theta}{\partial z^2\partial t} \tag{2.33}$$

Where ρ is soil density. The damping ratio D is defined as:

$$D = \frac{\mu w}{2G} \tag{2.34}$$

Where w is the circular frequency of oscillation. The solution of the above shear wave propagation can be obtained as:

$$\theta(z,t) = (C_1 e^{iaz} + C_2 e^{-iaz})e^{iwt} \tag{2.35}$$

Where C_1 and C_2 are constants to be determined from boundary conditions, and the parameter a is defined as:

$$a^2 = \frac{\rho w^2}{G(1+2Di)} \tag{2.36}$$

Boundary conditions Historically, resonant column tests in the ICRCHCA were interpreted with models employing a single degree of freedom (1-DOF) or three degrees of freedom (3-DOF) (Nishimura, 2006, Brosse, 2012), as shown in Figure 2-19, and it has been recognised that the 3-DOF model could better cater for system compliance and generate more accurate solutions. Nishimura (2006) demonstrated the difference of interpreting the RCHCA using 1-DOF model and 3-DOF model in terms of resultant shear stiffness ($G_{z\theta}$) and damping ratio (D) varied with resonance frequency (f_{res}). For the Cowden till studied here (from 3 m depth, see Chapter 3), the resonance frequency of the samples at their estimated in-situ stresses were located in the range of 125-130 Hz. The resultant $G_{z\theta}$ from the 1-DOF model were found to be 0.2-1.3% higher than those from the 3-DOF model, while damping ratios D were noted to be 2.7-3.8% lower.

The 3-DOF model considers three components in the apparatus which are represented with the following equations.

Passive system

$$K_{\mathrm{p}}\theta_{\mathrm{p}} + C_{\mathrm{p}}\frac{\partial\theta_{\mathrm{p}}}{\partial t} + J_{\mathrm{p}}\frac{\partial^2\theta_{\mathrm{p}}}{\partial t^2} - GI\left.\frac{\partial\theta}{\partial z}\right|_{z=0} - \eta I\left.\frac{\partial^2\theta}{\partial z\partial t}\right|_{z=0} = 0 \tag{2.37}$$

Reaction system

$$K_{\mathrm{r}}\theta_{\mathrm{r}} + K_{\mathrm{a}}(\theta_{\mathrm{r}} - \theta_{\mathrm{a}}) + C_{\mathrm{r}}\frac{\partial\theta_{\mathrm{r}}}{\partial t} + C_{\mathrm{a}}\left(\frac{\partial\theta_{\mathrm{r}}}{\partial t} - \frac{\partial\theta_{\mathrm{a}}}{\partial t}\right) + J_{\mathrm{r}}\frac{\partial^2\theta_{\mathrm{r}}}{\partial t^2} = -T_0\sin(wt) \tag{2.38}$$

Active system

$$K_{\mathrm{a}}(\theta_{\mathrm{a}} - \theta_{\mathrm{r}}) + C_{\mathrm{a}}\left(\frac{\partial\theta_{\mathrm{a}}}{\partial t} - \frac{\partial\theta_{\mathrm{r}}}{\partial t}\right) + J_{\mathrm{a}}\frac{\partial^2\theta_{\mathrm{a}}}{\partial t^2} + GI\left.\frac{\partial\theta}{\partial z}\right|_{z=H} + \eta I\left.\frac{\partial^2\theta}{\partial z\partial t}\right|_{z=H} = T_0\sin(wt) \tag{2.39}$$

Where θ represents rotation of a soil element at the depth z and instant t. θ_{a}, θ_{r} and θ_{p} represents rotation of the active, reaction and passive system at an instant t, respectively. J, K and C respectively denote rotational inertia, torsional stiffness and torsional damping coefficient and the subscript a, r and p signify the active, reaction and passive system. The above equation can be expressed in complex space by using:

$$\theta_{\mathrm{a}} = A_{\mathrm{a}} e^{\mathrm{iwt}} \quad \theta_{\mathrm{r}} = A_{\mathrm{r}} e^{\mathrm{iwt}} \quad \theta_{\mathrm{p}} = A_{\mathrm{p}} e^{\mathrm{iwt}} \tag{2.40}$$

Rewriting the equations into the following matrix form:

$$\begin{bmatrix} A_{\mathrm{p}} \\ A_{\mathrm{a}} \\ A_{\mathrm{r}} \end{bmatrix} = \begin{bmatrix} y_{11}+iz_{11} & y_{12}+iz_{12} & y_{13}+iz_{13} \\ y_{21}+iz_{21} & y_{22}+iz_{22} & y_{23}+iz_{23} \\ y_{31}+iz_{31} & y_{32}+iz_{32} & y_{33}+iz_{33} \end{bmatrix} \begin{bmatrix} 0 \\ T_0/Jw^2 \\ -T_0/Jw^2 \end{bmatrix} \tag{2.41}$$

A transfer function H can be introduced and the solution can be written as

$$H = \frac{A_a Jw^2}{T_0} = y_{22} + y_{23} + i(z_{22} + z_{23}) \tag{2.42}$$

$$MMF_{\mathrm{a}} = |H| = \sqrt{(y_{22}+y_{23})^2 + (z_{22}+z_{23})^2} \tag{2.43}$$

$$\phi_a = \arg(H) = \arctan\left(\frac{z_{22}+z_{23}}{y_{22}+y_{23}}\right) \tag{2.44}$$

Detailed values of y_{ii}, z_{ii}, $\mathrm{i} \in [1,2,3]$ are given by Ashmawy & Drnevich (1994) and Nishimura (2006). Finally, soil elastic shear stiffness G and damping ratio D can be solved from the following functions.

$$f_{\mathrm{ares}} = f_{\mathrm{ares}}(G, D) \tag{2.45}$$

$$MMF_{\mathrm{ares}} = MMF_{\mathrm{ares}}(G, D) \tag{2.46}$$

Where f_{ares} and MMF_{ares} represent the resonant frequency and the magnification factor at the resonance.

2.3.4 Bishop-Wesley automated stress-path triaxial apparatus

Two types of hydraulic stress-path triaxial apparatus were employed in the Author's research programme, namely a '38 mm' type for testing solid soil specimens with nominal 38 mm diameter and a '100 mm' type for 100 mm diameter sample. The apparatuses inherit features from the original design by Bishop & Wesley (1975) and have been continuously upgraded with advanced transducers and control systems. This subsection presents a brief overview of the triaxial apparatuses and more details can be found in recent PhD studies by Gasparre (2005), Hosseini Kamal (2012), Al-Haj (2014) and Aghakouchak (2015). Ushev (2018) recently presents the most up-to-date assessment of the apparatuses' performance and provides further details particularly on the newly developed radial strain measuring system (Ackerley *et al.*, 2016) and the modifications he implemented for testing the ductile Cowden till.

General set-up and features

The general configuration of the triaxial apparatus is shown in Figure 2-20. Table 2-2 presents a detailed summary of their key features. As a re-engineered version of the standard '38 mm' triaxial apparatus, the '100 mm' apparatus provides generally better resolution and accuracy in stress control and strain measurement as well as greater scope for testing larger soil specimens and deploying more local instruments.

Similar to the ICRCHCA system, the cell, pore water and ram pressure of the triaxial apparatus is applied separately through air-water or air-oil Bellofram interfaces that convert air pressure into water or oil pressure. Air pressure is regulated by Watson-Smith electro-pneumatic controllers and stepper motors that are controlled by computer software and provide a pressure resolution of 0.07 kPa per pulse. The maximum pressure generated by the interfaces is constrained by the pressure of the central compressed air supply, although the pressure can be further elevated with a pressure multiplier. The apparatuses are also equipped with a constant rate strain pump (CRSP) for strain-controlled constant rate loading. Meanwhile, silicone oil is used in the '100 mm' apparatus to drive the ram instead of water, so as to extend the hardware's durability. However, this step also diminishes the system's mobility in applying quick loading steps. The '100 mm' triaxial has a higher platten-to-specimen area ratio (2:1), offering higher deviatoric stresses if they are required to fail high strength or stiffness materials, for example chalk.

Unlike the HCA testing, the effects of end restraint can be significantly alleviated in triaxial testing by imposing lubrication between the specimen ends and the rigid plattens. This was achieved in the Author's tests by means of lubrication disks consisting of layers of latex membrane sandwiched with silicone grease or high vacuum grease. Furthermore, more uniform radial straining at the specimen ends can be achieved by using over-size plattens that can accommodate a certain amount of radial deformation before being suffering from stress concentrations at the platten edges. The lubrication layers and over-sized plattens can be implemented in the Bishop-Wesley apparatuses.

Another important aspect that affects principally soil small strain behaviour is the connection between load cell and specimen top cap. Gasparre *et al.* (2014) summarised the several commonly used schemes, including rigid connection, pin connection, suction cap connection, half-ball only and half-ball with suction cap connection. It was argued that the half-ball with suction cap connection provided best outcome from their experimental data. Other schemes, for example epoxy connection (Escribano, 2014) have also been used in recent research. The half-ball with suction cap connection was employed in the main run of the Author's tests using the '38 mm' triaxial while the rigid connection type was used in the tests with '100 mm' triaxial apparatuses. In both scenarios, generally satisfactory agreements were achieved of the axial and radial strains measured at different locations, as later shown in Figure 2-25.

The computer software TRIAX (Toll, 2002) is employed for test control, monitoring and recording and an MSL 16 bit A/D convertor was used for data acquisition. The software and convertor are as described earlier in Section 2.3.2.

The systems deployed were able to apply and monitor long-term cyclic loading conditions in the Author's tests on Dunkirk sand (see Chapter 7), covering a wide range of stress conditions and making full measurements in each shearing cycle, with a loading frequency of 0.0083 Hz and period of 2 minutes. Aghakouchak (2015) employed similar testing systems for his undrained cyclic tests on Dunkirk sand and adopted faster shearing cycles with frequency of 0.016 Hz (1/60 s), while slower loading with a frequency of 0.0033 Hz and period of 5 minutes was adopted in the undrained cyclic tests on Cowden till by Ushev (2018). A new cyclic triaxial apparatus capable of applying much faster loading motions (> 1 Hz) has become available at Imperial College recently. The new device, however, has distinctively different

configurations from those of the Bishop-Wesley type adopted in the Author's research.

Transducers, instruments and their performance

As summarised in Table 2-2, the triaxial apparatuses are heavily instrumented with full sets of pressure transducers as well as external and local strain sensors. The configurations of the external transducers are similar for the '38 mm' and '100 mm' apparatus, while the latter is equipped with more sets of axial and radial LVDTs and can readily accommodate other instruments, including the multi-directional bender elements and pore water pressure probes.

Table 2-3 presents a detailed summary of the transducers and instruments used in the two types of triaxial apparatus, listing their working range, calibration coefficient and sensitivity. The best theoretical resolution provided by the 16 Bit A/D convertor is calculated and converted to the resolution of stress or strain variables each transducer corresponds to. The best theoretical resolution of the A/D converter corresponds to the first DC voltage range, namely ±20 mV, and the engineering resolution R is calculated via the following equation.

$$R = S \times \frac{2r}{2^B - 1} \tag{2.47}$$

Where S is calibration coefficient, r is voltage range, B is the minimum number of Bits and is taken as 16 for the convertor used. The results indicate that both types of triaxial apparatuses are capable of providing high resolution stress and strain measurements. For the external transducers, the best resolution range is sufficiently large and easy to locate. However, the highest resolution range of the local LVDTs is located over a relatively small span and operator dexterity is required to ensure that the test runs over this optimal range.

Throughout the Author's testing programme, effort has been expensed to enhance radial strain measurements in both types of apparatus. Figure 2-21 shows a diagram of the radial-belt used in the '38 mm' apparatus. It was often noted that the radial-belt could suffer from delayed response during consolidation or shearing stages, resulting in significant errors or uncertainties in the attempts to determine Poisson's ratio or other variables that require precise radial strain data. Close inspection revealed that in the original design of the radial-belt, the free 'sliding' motion between the LVDT and the inner core tended to be restrained by friction between the holder and the moving

armature. The situation was aggravated as the LVDT could not stay perfectly horizontal due to its self-weight and therefore the LVDT and the core became slightly misaligned. The problem was solved by adding a carefully calibrated mass to one end of the LVDT (as shown in Figure 2-21) to balance its self-weight so that the LVDT and the core can stay well-aligned over the small radial strain range. The outcome of the modification is shown in Figure 2-22, taking an example from a small amplitude (q_{cyc} = 6.7 kPa) drained cyclic triaxial compression test. The upgraded radial-belt was able to capture very small cyclic radial strains when the specimen was cyclically sheared around its K_o stress condition.

The radial strain measurements in the '100 mm' triaxial adopted a measuring system recently developed by Ackerley *et al.* (2016). Ushev (2018) implemented further modifications to the original design to enable testing ductile Cowden till that required large shear strains to fail. An overview of the radial measuring system and other instruments deployed in the '100 mm' triaxial in shown in Figure 2-23 (a). A small modification to the system was suggested by the Author while calibrating the radial LVDTs using a set-up shown in Figure 2-23 (c). It was found that the radial strain measurements were sensitive in compression to the position of the supporting base of the LVDT core (shown in Figure 2-23 (b)). If the base was supported at too low a location, as shown in Figure 2-24, the calibration trend over the compression size tended to diverge from the trend of the extension size. This problem was solved by modifying the supporting base from a flat shape to a cone shape to avoid interference between the inner parts of the LVDT. A smooth calibration curve covering the whole range was then obtained.

Figure 2-25 shows recorded axial and radial strains in a consolidation stage of a '100 mm' triaxial test on Dunkirk sand. The radial strains were measured with the upgraded radial strain measuring system. The results show encouraging agreement between the strains measured in the central portion of the specimen at three locations 120˚ evenly apart, although the radial strains manifest more scatter overall than the axial data.

As mentioned earlier, the triaxial apparatuses are equipped with full sets of multi-directional bender elements that enable measurements of dynamic shear velocity independently of the quasi-static loading. A typical set of bender element signal recorded in the Author's test on Dunkirk sand is shown in Figure 2-26. A basic

approach of interpreting bender element signal in time-domain and determining shear stiffnesses requires specimen density, distance between the signal transmitter and receiver as well as arrival time (Kuwano, 1999, Kuwano & Jardine, 2002b). Many researchers, for example Alvarado & Coop (2012) and Otsubo (2017), adopted alternative time-domain or frequency-domain approaches. Yamashita *et al.* (2009) and Clayton (2011) reviewed the variables and uncertainties associated with bender element testing and data interpretation. Throughout the Author's programme, the time-domain approach based on first-peak arrival time was used.

Table 2-2 Summary of the key features of the '38 mm' and '100 mm' Bishop-Wesley type automated stress-path triaxial apparatus

	Specimen dimension	Cell/pore water pressure system	Ram pressure system	Transducers & instruments	
				External	Local
'38 mm'	*D*: 38 mm *H*: 76 mm *V*: 86.2 cm^3	1. Air-water interface (maximum: 820 kPa) 2. Can be amplified up to 1.2 MPa 3. Control resolution: 0.07 kPa	1. Air-water interface (maximum: 820 kPa) 2. Constant rate strain pump (CRSP) (maximum: 1.8 MPa) 3. Ram-to-specimen area ratio: 1:1	1. Three pressure transducers (cell, pore water, ram) 2. Displacement transducer 3. Volume-gauge 4. Temperature transducer	1. Load cell 2. Two axial LVDTs 3. Radial-belt 4. Mid-height PWP probe
'100 mm'	*D*: 100 mm *H*: 200 mm *V*: 1570.8 cm^3	1. Air-water interface (maximum: 820 kPa) 2. Can be amplified up to 1.2 MPa 3. Control resolution: 0.07 kPa	1. Air-oil interface (maximum: 820 kPa) 2. Constant rate strain pump (CRSP) (maximum: 1.8 MPa) 3. Ram-to-specimen area ratio: 2:1	1. Three pressure transducers (cell, pore water, ram) 2. Displacement transducer 3. Volume-gauge 4. Temperature transducer	1. Load cell 2. Three axial LVDTs 3. Three radial LVDTs 4. Three pairs of bender elements 5. Mid-height PWP probe

Notes:

1. Air pressure into the air-water or air-oil interfaces is regulated by Watson-Smith electro-pneumatic controllers and stepper motors;
2. Platten type includes rough or lubricated platten with standard size or over-sized;
3. Connection type between load cell and specimen top includes rigid connection, pinned connection, suction cap connection, half-ball only connection and suction cap and half-ball connection, see Gasparre *et al.* (2014) for details;
4. Computer software TRIAX is used for test control, monitoring and data recording, and data acquisition is through 16 Bit Datascan 7220 Analogue to Digital (A/D) convertors.

Table 2-3 Summary of the transducers and instruments deployed in the '38 mm' and '100 mm' triaxial apparatuses

Transducer type	Manufacturer /type	*App.*	Range [unit]		Calibration factor [unit]	Sensitivity [unit]	Resolution unit			
			Voltage	*Eng.*			Range	Limit	*Eng.*	*Variable*
Cell/pore pressure	RS Components	38 mm 100 mm	50 mV	1000 kPa	0.02 kPa/μV	0.05 mV/kPa	1	400 kPa	0.01 kPa/bit	0.01 kPa/bit
							2	1000 kPa	0.09 kPa/bit	0.09 kPa/bit
Ram pressure			50 mV	2500 kPa	0.05 kPa/μV	0.02 mV/kPa	1	1000 kPa	0.03 kPa/bit	0.03 kPa/bit
							2	2500 kPa	0.23 kPa/bit	0.23 kPa/bit
Mid-height probe	Druck PDCR 81		55 mV	1000 kPa	0.018 kPa/μV	0.06 mV/kPa	1	360 kPa	0.01 kPa/bit	0.01 kPa/bit
							2	1000 kPa	0.08 kPa/bit	0.08 kPa/bit
Displacement	Soil Tech Ltd, and others	38 mm	35 mV	25 mm	0.0007 mm/μV	1.4 mV/mm	1	14 mm	0.4 μm/bit	0.0006 %/bit
							2	25 mm	3.2 μm/bit	0.0042 %/bit
		100 mm					1	14 mm	0.4 μm/bit	0.0002 %/bit
							2	25 mm	3.2 μm/bit	0.0016 %/bit
Volume gauge	Imperial College	38 mm	35 mV	50 cm^3	0.0014 cm^3/μV	0.7 mV/cm^3	1	28 cm^3	0.85 mm^3/bit	0.001%/bit
							2	50 cm^3	6.4 mm^3/bit	0.0074 %/bit
	Imperial College	100 mm	35 mV	100 cm^3	0.0028 cm^3/μV	0.35 mV/cm^3	1	56 cm^3	1.7 mm^3/bit	0.0001%/bit
							2	100 cm^3	12.8 mm^3/bit	0.0008 %/bit
Load cell	Applied Measurements Ltd, STALC3 series	38 mm	28 mV	5 kN	0.176 N/μV	5.6 mV/kN	1	3.7 kN	0.11 N/bit	0.10 kPa/bit
							2	5 kN	0.85 N/bit	0.75 kPa/bit
			10 mV	5 kN	0.4769 N/μV	2 mV/kN	1	5 kN	0.31 N/bit	0.27 kPa/bit
		100 mm	10 mV	5 kN	0.4456 N/μV	2 mV/kN	1	5 kN	0.31 N/bit	0.04 kPa/bit
			27 mV	5 kN	0.1861 N/μV	5.6 mV/kN	1	3.7 kN	0.11 N/bit	0.01 kPa/bit
							2	5 kN	0.85 N/bit	0.11 kPa/bit
			27 mV	25 kN	0.9317 N/μV	1 mV/kN	1	20 kN	0.61 N/bit	0.08 kPa/bit
							2	25 kN	4.6 N/bit	0.58 kPa/bit

Continued Table 2-3 Summary of the transducers and instruments deployed in the '38 mm' and '100 mm' triaxial apparatuses

Transducer type	Manufacturer /type	*App.*	Range [unit]		Calibration factor [unit]	Sensitivity [unit]	Resolution [unit]			
			Voltage	*Eng.*			Range	Limit	*Eng.*	*Variable*
Axial LVDT	Imperial College	38 mm	±5 V	±5 mm	0.001 mm/mV	1000 mV/mm	1	0.02 mm	0.0006 μm/bit	1.22×10^{-6} %/bit
							2	0.15 mm	0.0046 μm/bit	9.16×10^{-6} %/bit
							3	1.3 mm	0.0397 μm/bit	7.93×10^{-5} %/bit
							4	5 mm	0.1526 μm/bit	3.05×10^{-4} %/bit
Radial-belt							1	0.02 mm	0.0006 μm/bit	8.03×10^{-7} %/bit
							2	0.15 mm	0.0046 μm/bit	6.02×10^{-6} %/bit
							3	1.3 mm	0.0397 μm/bit	5.22×10^{-5} %/bit
							4	5 mm	0.1526 μm/bit	2.00×10^{-4} %/bit
Axial LVDT		100 mm	±5 V	±5 mm	0.001 mm/mV	1000 mV/mm	1	0.02 mm	0.0006 μm/bit	9.10×10^{-7} %/bit
							2	0.15 mm	0.0046 μm/bit	6.83×10^{-6} %/bit
							3	1.3 mm	0.0397 μm/bit	5.92×10^{-5} %/bit
							4	5 mm	0.1526 μm/bit	2.28×10^{-4} %/bit
Radial LVDT							1	0.02 mm	0.0006 μm/bit	1.22×10^{-6} %/bit
							2	0.15 mm	0.0046 μm/bit	9.16×10^{-6} %/bit
							3	1.3 mm	0.0397 μm/bit	7.93×10^{-5} %/bit
							4	5 mm	0.1526 μm/bit	3.05×10^{-4} %/bit

Notes:

(1) Resolution calculated based on the four DC voltage ranges (20 mV, 150 mV, 1.3 V, 5 V) of the 16 bit A/D convertor;

(2) Engineering resolution of each transducer corresponds to the stress or strain measured, i.e., axial strain for displacement transducer and axial LVDT, volumetric strain for volume-gauge, radial strain for radial LVDTs, and deviatoric stress q for load.

(3) The gauging length of the axial LVDT is 50 mm and 67 mm in the '38 mm' and '100 mm' triaxial apparatus respectively.

(4) Calculations are based on the dimensions of the standard '38 mm' and '100 mm' triaxial specimens listed in Table 2-2.

2.3.5 Bishop ring shear apparatus

Bishop type soil-soil or soil-interface ring shear testing (Bishop *et al.*, 1971) has been employed to study the residual shear strength of soils. Applications include landslide slope stability analysis (Lupini *et al.*, 1981, Lemos, 1986, Tika *et al.*, 1996), determining soil-interface shearing resistance for driven piles in sands and clays (Jardine *et al.*, 2005, Yang *et al.*, 2010, Barmpopoulos *et al.*, 2010, Ho *et al.*, 2011), and investigating critical state behaviour and particle breakage in granular media undergoing very large shear strains (Coop *et al.*, 2004). The apparatus's capabilities and limitations for the purposes of characterising soil-interface shearing response in comparison with other types of interface shearing devices are reviewed later in Table 4-1.

The schematic diagram of the apparatus and its set-up is shown in Figure 2-27. Bishop *et al.* (1971) documented the apparatus's working principles, design and performance as well as specimen preparation methods and testing procedures. A major upgrading programme on the apparatus has recently been completed by Mr. Steve Ackerley and Dr. Emil Ushev, which included the following key modifications (Ushev, 2018).

a. Enhanced displacement and load measurements with improved accuracy and stability;
b. An upgraded torsional shearing system equipped with a stepper motor driven by a function generator so that the shearing rates imposed can be flexibly adjusted;
c. Replacement of the dead load system (see Figure 2-27) for applying normal stress with a pressure actuator which provides precise and continuous stress control through the Windows-based software TRIAX.

The apparatus can have several configurations for soil-soil or soil-interface testing, see the examples given by Bishop *et al.* (1971) and Ho *et al.* (2011). The commonly used lower interface configuration, as illustrated in Figure 2-28, was used in the Author's testing programme on fine sand materials under saturated condition. In this set-up, the bottom plate and interface are assembled and fixed to the rotating table and the inner and outer confining rings are fixed above the interface. The tested materials are pluviated or placed into the gap provided by the confining rings in a few layers (usually 2 or 3) and tapped uniformly to reach the height or density target for each

layer. A porous stone with evenly distributed brass vanes is then placed above the prepared specimen, located above are the torque arm and other connecting pieces for applying normal stresses (see Figure 2-27).

When testing with the lower interface set-up, the inner and outer confining moulds are firmly attached to the interface beneath in during consolidation stage, while a gap between the confining rings and the interface has to be opened during shearing stage so that the measurement of torsional force is not affected by friction between the confining rings and interfaces. The gap is opened through the guided linking yoke and the width of the opening is dependent of the gradings of the tested material (usually 0.1 mm for fine sands). The opening results in unwanted material loss during shearing, which inevitably affects the determination of volume change and dilation. In tests that shear to very large distances (a few metres), the opened gap may be temporarily closed to minimise material escape (Yang *et al.*, 2010).

When the gap is opened, a pull-up force has to be applied to the confining rings to detach the confining rings from the interface. The pull-up force, which is measured by the top proving rings in Figure 2-27, corresponds to the friction between the soil specimen and the walls of the confining rings. The friction should be compensated in consolidation stages so that the contact stress at the interface is close to the target normal stress. The recorded friction, which commonly fluctuates as shearing evolves, should also be taken into account when calculating the normal stress and interface shearing angle.

As recommended by Bishop *et al.* (1971), the normal stress σ_n' and the shear stress τ are assumed to be uniformly distributed across the rotary shearing plane, and the calculation of shearing angle δ' can be simplified as:

$$\tan\delta' = \frac{3M_T(r_1 + r_2)}{2W(r_1^2 + r_1 r_2 + r_2^2)} \tag{2.48}$$

Where r_1 and r_2 is the inner and outer radius of the specimen, respectively; M_T is the total torque and W is net normal load, after accounting for friction at the inner and outer confining rings.

2.3.6 Other devices employed in the current research

QicPic device

The QicPic laser-based imaging system was employed by the Author to aid the particle-scale depiction and analyses of the sand materials' size and shape, as described later in Chapter 4. The QicPic system analyses a great number of laser-projected images of a dynamic flow of moving particles, and obtain depictions of particle size and shape that is statistically representative of realistic three-dimensional measures (Altuhafi & Coop, 2011, Altuhafi *et al.*, 2013). This technique has the advantage of examining a large number of particles over relatively short times, while other true 3-D scanning methods, for example micro-CT, are more time-consuming and challenging.

An overview of the QicPic system is demonstrated in Figure 2-29. A critical step in QicPic measurement is to obtain well dispersed particle flows to reduce the occurrence of particle overlapping or depositing with preferential alignments under gravity. A GRADIS dry gravity dispersing unit (as shown in Figure 2-29) is used for measuring particle size greater than 100 μm while a LIXELL water circulation system is adopted for particle size less than 100 μm. When using the dry feeding unit, the particles pass through an inclined vibrating feeder unit to attain a well-dispersed particle flow with a certain speed before dropping under gravity into the dispersing shaft. The particle flow is then aligned though a tapered section before dropping through the imaging unit. A vacuum-extraction unit is attached to the end of system to create downward air flow through the shaft to further disperse the particles and facilitate their random orientation. The laser scanning has an exposure time of less than 1 ns to avoid motion blur and the detector camera operates at up to 450 frames per second, enabling it to image a large number of particles in a short span of time.

From the obtained 2D images, particle size can be calculated in different ways, including the $d^{\text{Feret-min}}$ and $d^{\text{Feret-max}}$ which respectively is the minimum and maximum distance between two parallel lines touching the particle on opposite sides, and the d^{EQPC} diameter which is the diameter of the equivalent circle covering the same area as that of a particle. Previous researchers, such as Yang *et al.* (2010) and Altuhafi & Coop (2011), noted that the PSD curves based on the different diameter indexes are different and the Feret-min usually gives the closest match to conventional sieving tests.

Some shape measures are defined in the QicPic system (Altuhafi *et al.*, 2013) and

are in the subsequent discussion, including:

a. Aspect ratio (AR), defined as $d^{\text{Feret-min}}/\ d^{\text{Feret-max}}$;

b. Convexity ratio (C_x), the ratio between the imaged particle area and the area of the convex hull;

c. Sphericity (S^{QP}), ratio between the perimeter of the equivalent circle covering the same area as the particle, to the perimeter of the particle.

Figure 2-30 presents examples of binary images of Dunkirk sand Batch 2 particles and the corresponding size and shape parameters determined from QicPic measurements.

Surface roughness measuring devices

A Taylor Hobson Talysurf profilometer was employed to quantify the surface roughnesses of the steel interfaces used in the sand-interface shearing tests reported in Chapter 4. The general set-up of the device is shown in Figure 2-31. The profilometer moved at a constant rate of 0.5 mm/s and surface profile was gauged with a stylus in the front. Roughness parameters, including the commonly used centre-line average roughness (R_{CLA}) and root mean square roughness (R_{RMS}), can be determined from the gauged surface profiles through the following equations.

$$R_{CLA} = \frac{1}{l_r}\int_0^{l_r} |z(x)|\, dx \tag{2.49}$$

$$R_{RMS} = \sqrt{\frac{1}{l_r}\int_0^{l_r} z^2(x) dx} \tag{2.50}$$

Where l_r is sampling length and $z(x)$ is profile height from reference mean profile line.

The selection of appropriate measuring length, filtering method and cut-off values in surface roughness measurements is a subtle process. A mathematical filtering process is required to exclude wavelengths above or below a particular frequency, while the cut-off values set the ranges of wavelength over which a filter becomes effective. In the measurements, it is required to prescribe a shortest wavelength as the low cut-off (L_s) and longest wavelength (L_c) as the high cut-off. Figure 2-32 shows two sets of roughness measurements made on one steel interface and demonstrates how the selection of measuring lengths and cut-offs affect the interpreted surface profiles and the resultant R_{CLA} values. The measurement made with a long measuring length (100

mm) and high cut-off values (L_s: 0.025 mm, L_c: 25 mm) captured abrupt peaks and troughs along the measuring length, but failed to depict surface variations over local areas. On the other hand, the 5 mm length measurement with lower cut-off values (L_s: 0.0025 mm, L_c: 0.8 mm) showed overall smaller profile variations but sensed at high "resolution" the profile fluctuations over smaller measuring ranges, resulting in lower overall R_{CLA} value.

The steel interfaces used in the Author's tests vary from polished smooth pieces with R_{CLA}<1.2 μm to rough ones with R_{CLA} in the range of 10-15 μm, which were formed by air-abrading the interfaces with hard (hardness Mohs 9) and highly angular Guyson fused aluminium oxide (Al_2O_3) materials with grain size around 1.8 mm. The surface finish was predominantly controlled by the size and angularity of the blast media used and the sand-blasting process was of relatively less fine control. The roughened surfaces were therefore expected to exhibit randomly distributed peaks and troughs without following regular patterns of waviness or texture. Therefore, large cut-off values (L_s: 0.025 mm, L_c: 25 mm) were favoured to capture these abrupt peaks and troughs, which could dominate the sand-steel interface shearing behaviour. A relatively long measurement length (100 mm) was also used so that the uniformity of the surface finish can be regularly checked. Relatively small profile variations over local areas might not be fully represented in these measurements, as seen in Figure 2-32. However, this was believed to be less important as the sizes of these minor surface variations were significantly smaller than those of the tested sand grains (see Chapter 4).

2.3.7 Issues related to laboratory testing

Effects of temperature fluctuation

It has been emphasised by Jardine (2013) that a very stable temperature environment is one of the stringent conditions required to ensure the best performance of the advanced strain sensors and generate representative data for characterising soils' complex behaviours. While all the tests reported herein were performed in temperature controlled laboratories, the performance of the air-conditioning systems installed in different labs varied and assessment was therefore made of the effects of temperature fluctuation and the possible countermeasures against such effects.

Figure 2-33 presents the apparent axial creep strain trends recorded in two tests performed in laboratories (Lab 1 and Lab 2) with air-conditioning systems of having different performance levels. Lab 1 refers to the Main Laboratory at the Geotechnics Section which was updated around five years ago to offer a controlled temperature of 20 ˚C with fluctuations within ±0.3 ˚C. Lab 2 refers to the Teaching Laboratory within which the temperature could fluctuate around 21 ˚C by up to ±1.5 ˚C. Temperatures fluctuate in cycles with periods of 1 day and 30 minutes in Lab 1 and Lab 2, respectively. The tests performed in Lab 1 were largely unaffected by its minor temperature fluctuations and exhibited very clear residual creep strain trends. Although perceivable through discernible general trends, the Lab 2 test environment led to fluctuating apparent strain cycles whose periods matched the temperature variations.

When testing in laboratories with less capable air-conditioning systems (as in Lab 2), countermeasures may be applied to reduce temperature changes in the cell chamber, or around other testing components such as pressure transducers and volume-gauges. One approach is to use bubble wrap and aluminium foil as insulation/reflection layers to cushion environmental temperature change. As shown in Figure 2-34, a trial of this approach in the Lab 2 led to very positive effects and this approach was also applied by the Author in the Lab 1 for the most sensitive triaxial probing tests on Cowden till.

Short and long-term compliance of the pore water pressure system

In both the ICRCHCA and Bishop-Wesley triaxial apparatus, the pore water pressure system is driven by the Imperial College type volume-gauges and the measured pore water volume changes are taken as representing the volume change of the specimen. However, it was recognised that the volume-gauges were subjected to a moderate level of compliance or "leakage" and the recorded volume-gauge readings may not accurately reflect the volume change of the specimen. The compliance of the volume-gauges mainly arise from the deformation of the Bellofram and the rubber layers sealed inside. Other components consisting of the pore water pressure system may also attribute to the compliance effects and result in unrepresentative sample volume measurements, including expansion or contraction of the connecting plastic tubes, possible leakage through the ball values, residual air compressed in the de-aired water or trapped in the porous stone used.

In HCA or triaxial apparatuses equipped with only external volume measurements

or partial sets of local strain sensors, volume compliance check and calibration is often recommended as an initial step to assess system performance and produce calibration coefficients for volume correction.

Such calibration exercises were carried out in the beginning of the Author's testing programme with one of the '38 mm' triaxial apparatus. The pore water pressure system was first flushed with de-aired water for a few times. A steel solid dummy sample and an underlying saturated standard porous stone were installed on the pedestal and enclosed by a latex membrane. The "saturation" stage was performed by arising the pore water pressure from 20 kPa to 300 kPa at a rate of 60 kPa/hour, and from 300 kPa to 700 kPa at the same rate but with a pause of at least 72 hours after each 100 kPa pressure increment. The cell pressure was varied at the same rate and a constant p' of 20 kPa was maintained throughout the stages.

Figure 2-35 shows the variations of volume-gauge readings in the pressuring and hold stage, with the positive sign representing water in the volume-gauge being pushed out from the volume-gauge and into the pore water pressure system. Also indicated in the plot is the identified long-term compliance rate established by linear regression of the recorded data while holding 300 kPa pore water pressure. On the other hand, Figure 2-36 plots trends of volume-gauge readings recorded as the pore water pressure was increased from 300 kPa to 600 kPa. The trends were approximated by linear regressions and the slopes were identified as short-term compliance rates.

Figure 2-37 summarises the rates of short-term compliance (mL/100 kPa) and long-term compliance (mL/day) at varied pore water pressure levels. The compliance rates were noted to be pressure-dependent and generally decreased as pore water pressure increased, suggesting the measuring system becomes stiffer under high pore water pressures.

Adopting the same set-up, two "consolidation" and "swelling" cycles were applied to the dummy sample and porous stone while holding constant 300 kPa pore water pressure. As the steel dummy sample had polished smooth surfaces, any volume change in the system was believed to be primarily due to membrane penetration into the rough porous stone, which had a diameter (D) of 38 mm and thickness (t) of 5 mm. Figure 2-38 plots the trends of volume-gauge readings against effective stress level, with the negative sign denoting water being pushed into the volume-gauge.

Following the approach adopted by Kuwano & Jardine (2002a) and assuming the porous stone could be treated as incompressible under the tested stress levels, the unit membrane penetration into the porous stone v_{MP} is determined as $\Delta V/(\pi Dt)$ and the v_{MP}-log(σ_h') trends can be approximately fitted by linear trends. The slope of trends is denoted as C_{MP}, representing unit membrane penetration per log cycle of change in horizontal stress σ_h'. Averaging the data of the later three stages shown in Figure 2-38 led to a C_{MP} value of 0.077 mm for the used porous stone with rough and coarse surface. For comparison, Kuwano & Jardine (2002a) reported a C_{MP} of 0.015 mm for membrane penetration with a loose specimen of fine Ham River sand with D_{50} = 0.27 mm.

Such calibrated short- and long-term compliance rates and volume changes induced by membrane penetration were not necessary in tests with full set of local instruments, from which sample volumetric strains could be determined with high accuracy without being affected by system compliances or membrane penetrations. Nevertheless, improved understanding of these issues helped to explain the commonly noted discrepancies of specimen volume change from local and external measurements, and justify the 'unusual' external volume trends noted in the long-term drained cyclic triaxial tests on sands where the identification of terminal densities is particularly important, as further demonstrated in Chapter 7.

2.3.8 Figures

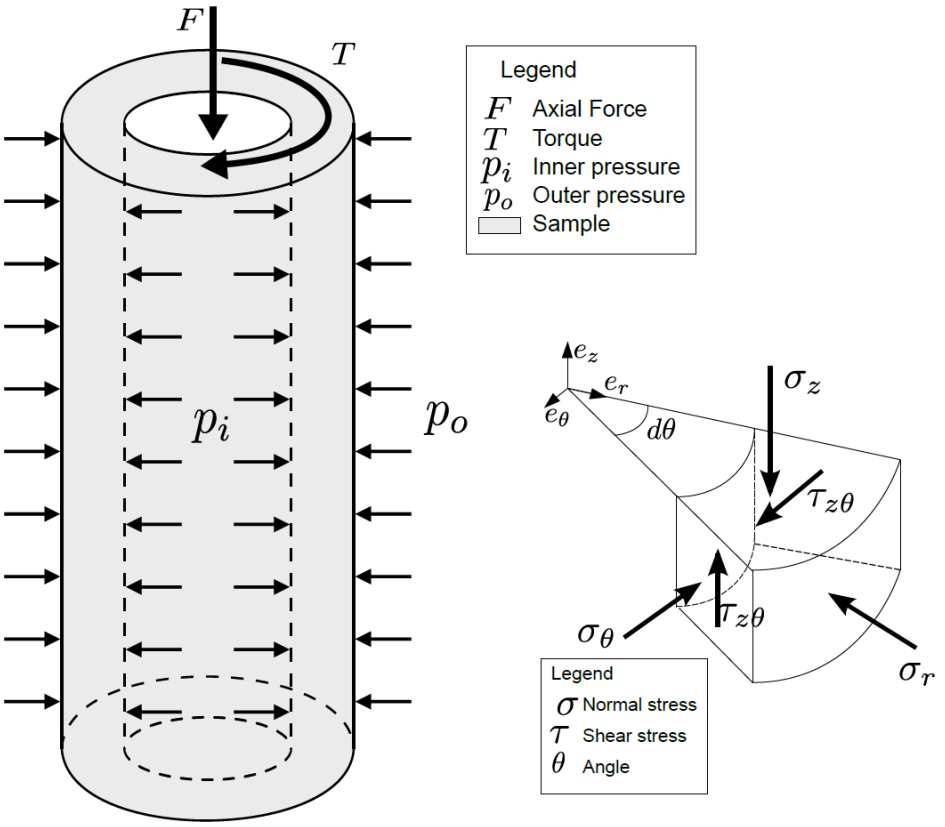

Figure 2-10 Hollow cylinder testing: applied external stress conditions and representative stress state as an equivalent soil element (Brosse, 2012)

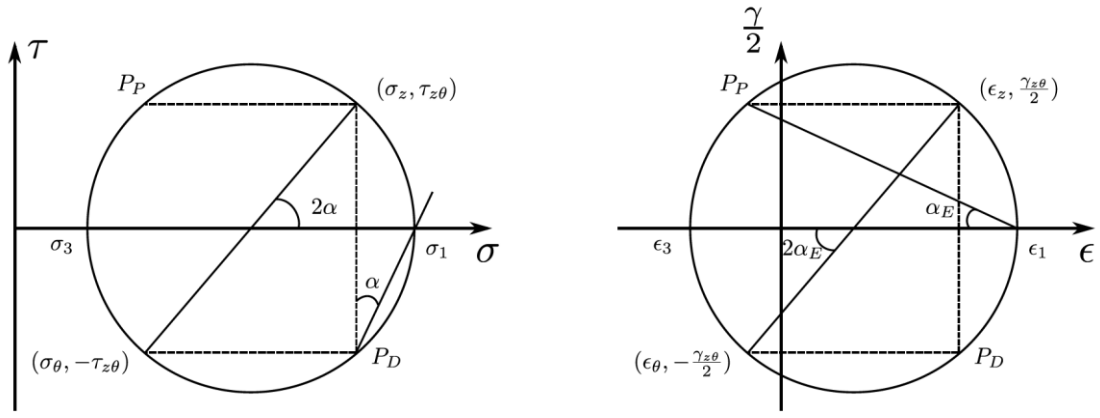

Figure 2-11 Stress and strain state in a hollow cylinder (HCA) specimen. P_P refers to the pole in terms of plane orientation and P_D in stress or strain direction (Brosse, 2012)

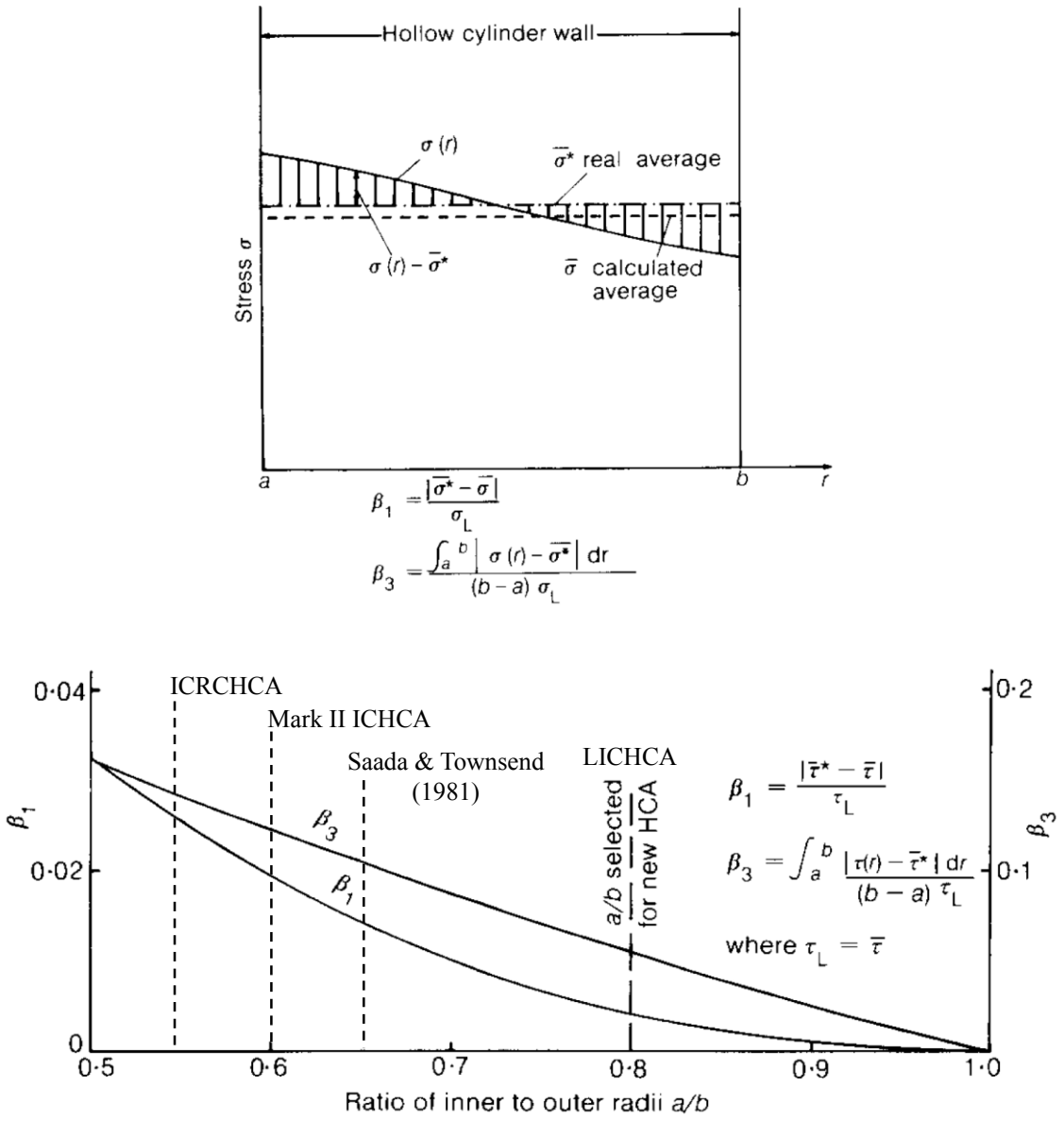

Figure 2-12 Parameters (β_1, β_3) defined to quantify stress non-uniformities across a hollow cylinder specimen wall and the attained evolving trends of the parameters against radius ratio (r_i/r_o) while assessing the shear stress (Hight *et al.*, 1983), also indicated are the radius ratios of the three HCAs at Imperial College

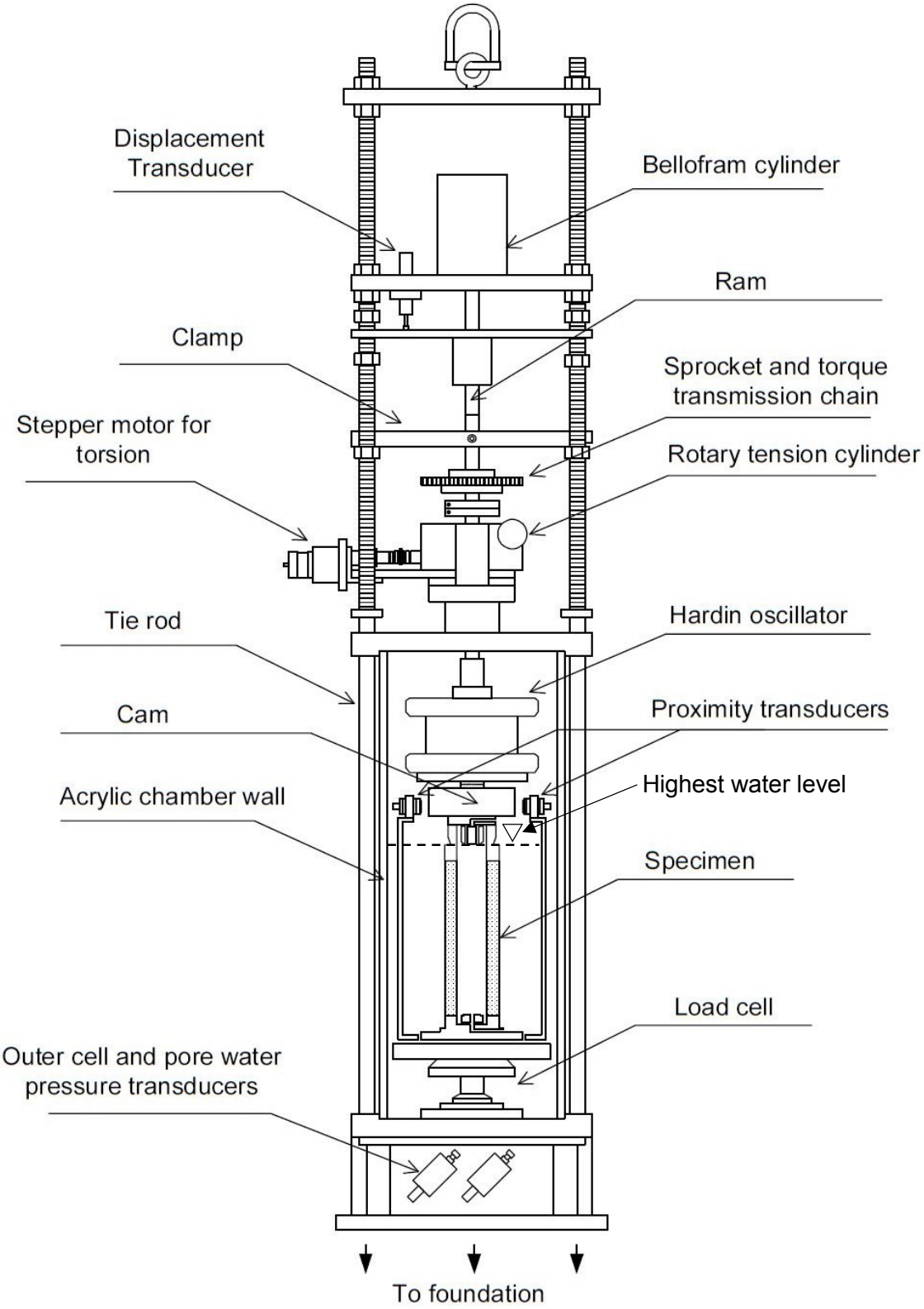

Figure 2-13 Configuration of the Imperial College Resonant Column Hollow Cylinder Apparatus (ICRCHCA) (Nishimura, 2006)

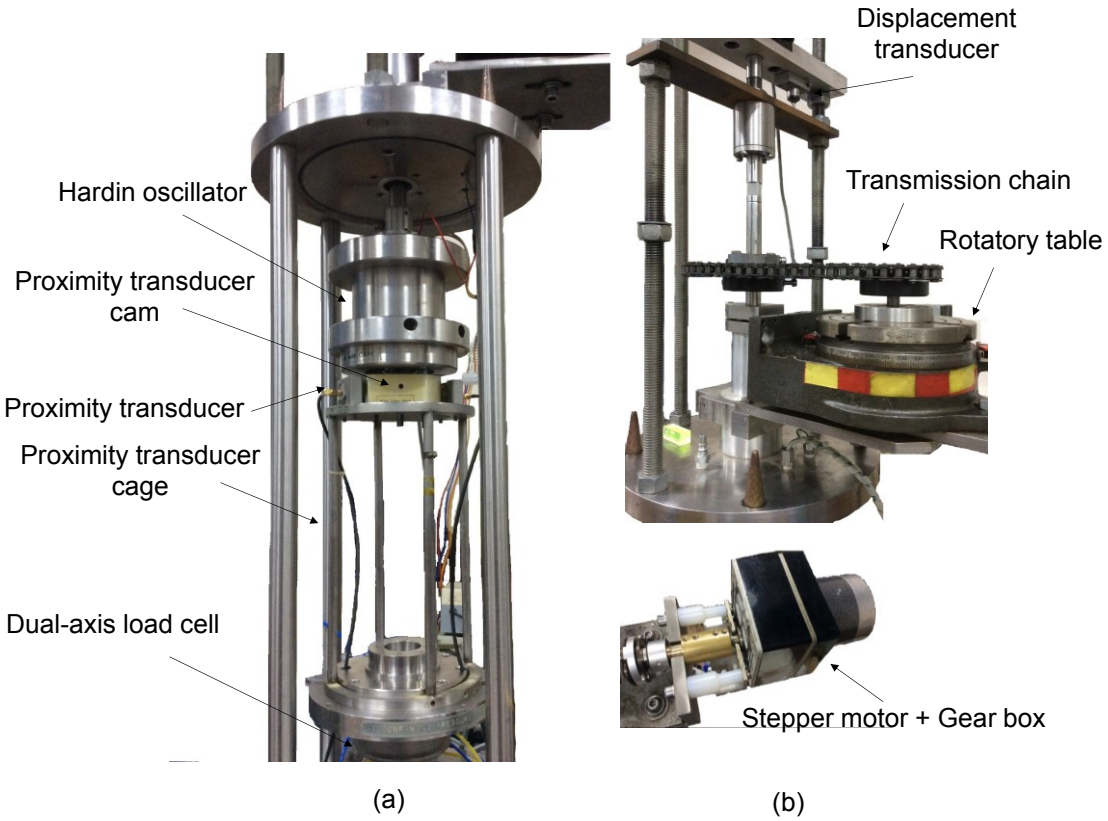

Figure 2-14 ICRCHCA: (a) general set-up of the proximity transducers; (b) torsion generation and transmission units

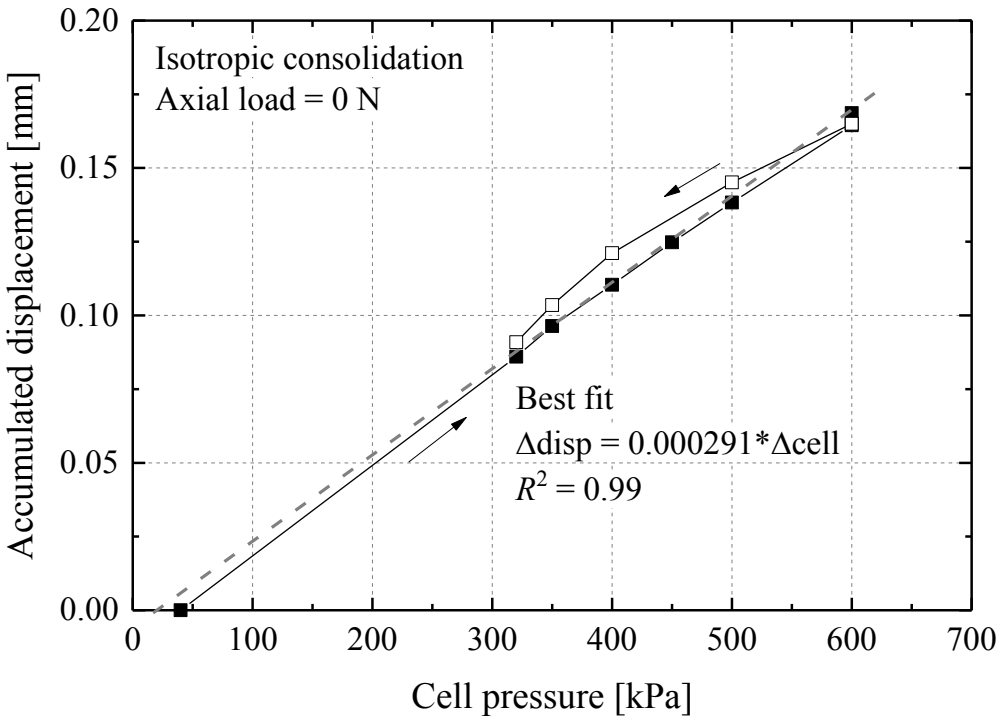

Figure 2-15 Accumulated axial displacement in pressuring the cell chamber while keeping zero deviatoric load on a rigid dummy sample

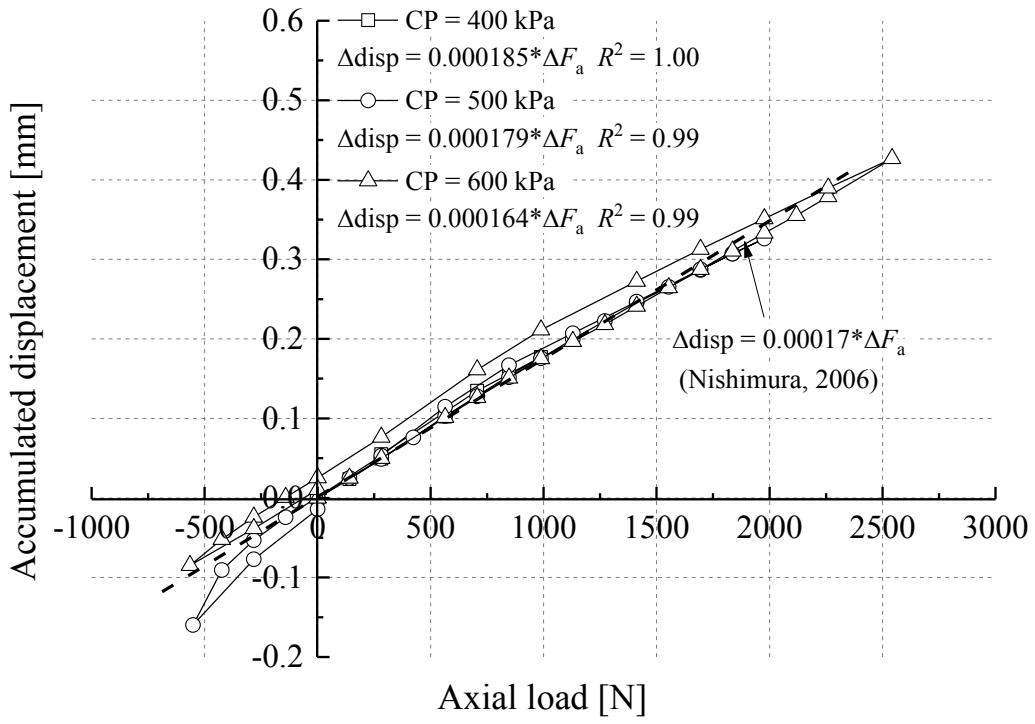

Figure 2-16 Accumulated axial displacement in loading and unloading a rigid dummy sample at three cell pressure levels

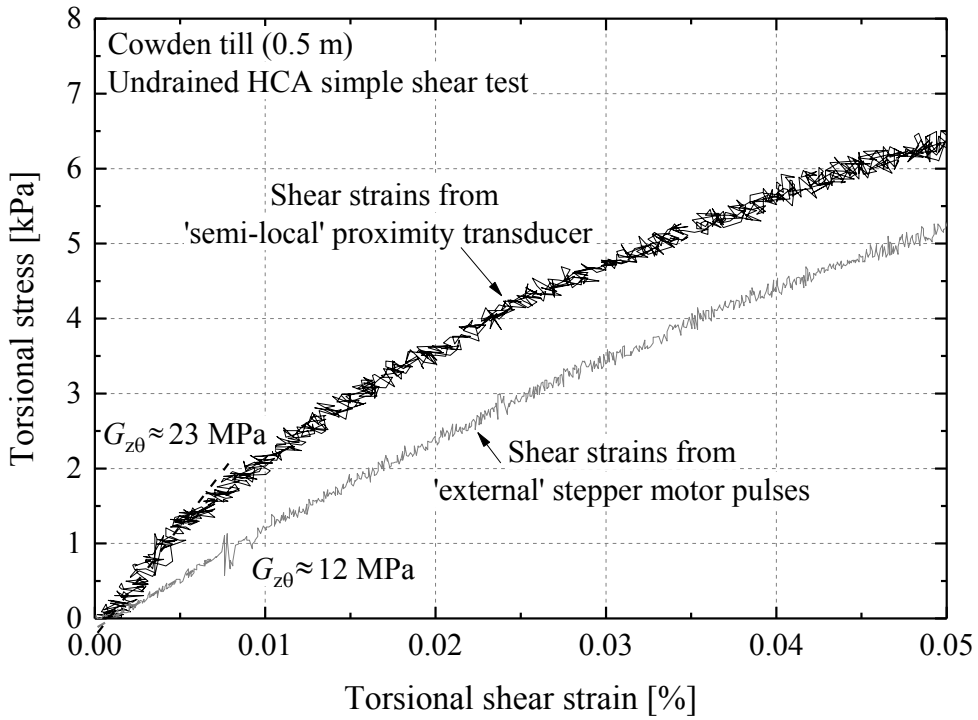

Figure 2-17 Illustrative torsional shear stress-strain and stiffness determined from ‘external’ and ‘semi-local’ strain measurements

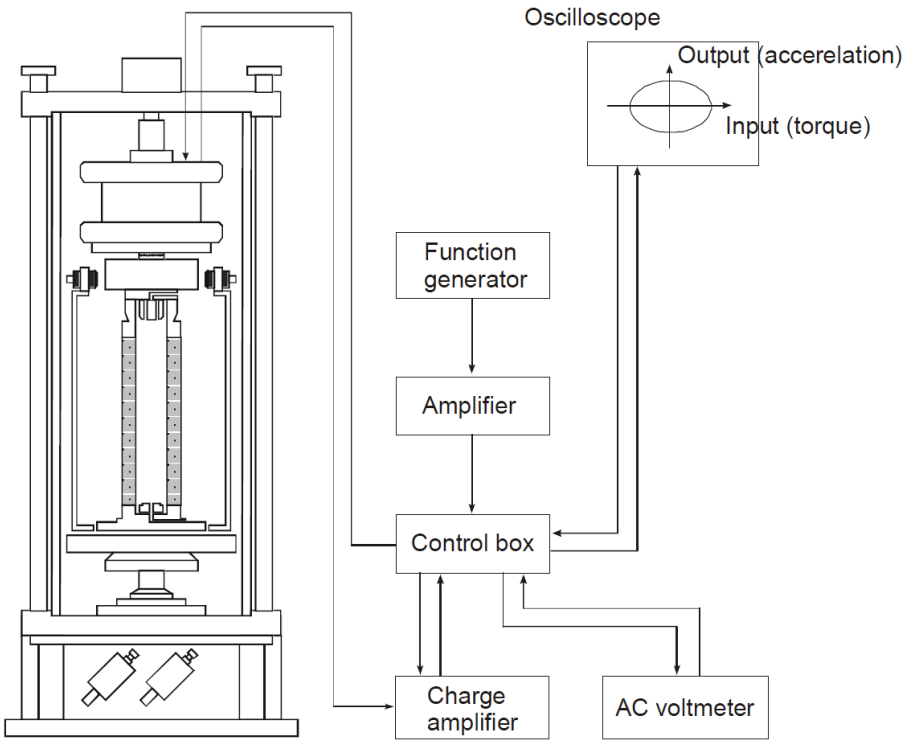

Figure 2-18 Set-up and electrical connections for resonant column testing in the ICRCHCA (Nishimura, 2006)

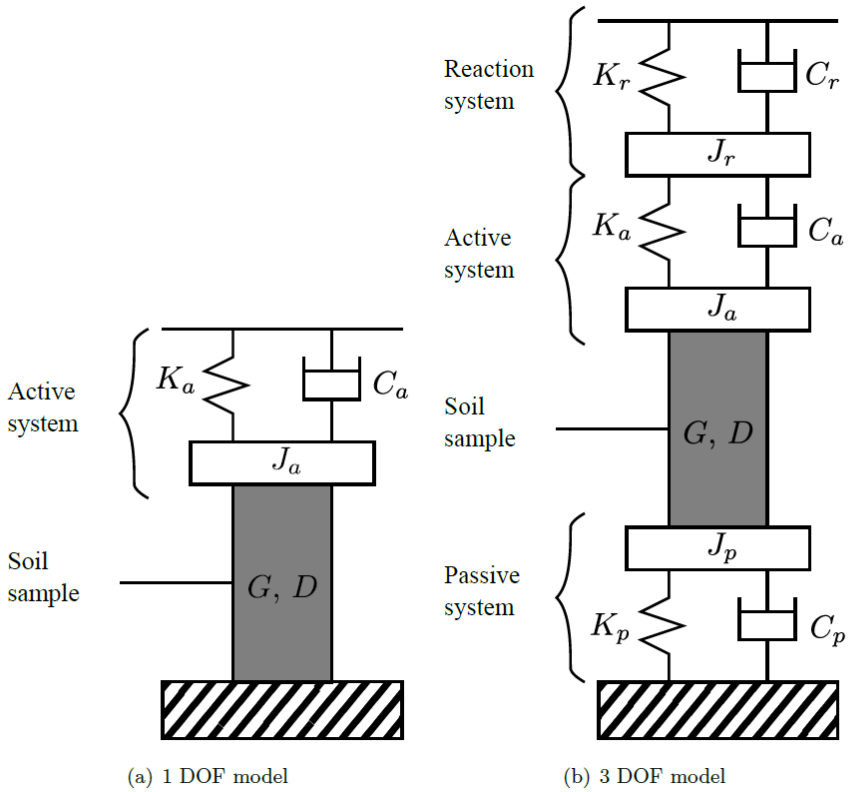

(a) 1 DOF model (b) 3 DOF model

Figure 2-19 Models of different degrees of freedom (DOF) for interpreting resonant column tests in the ICRCHCA (Brosse, 2012)

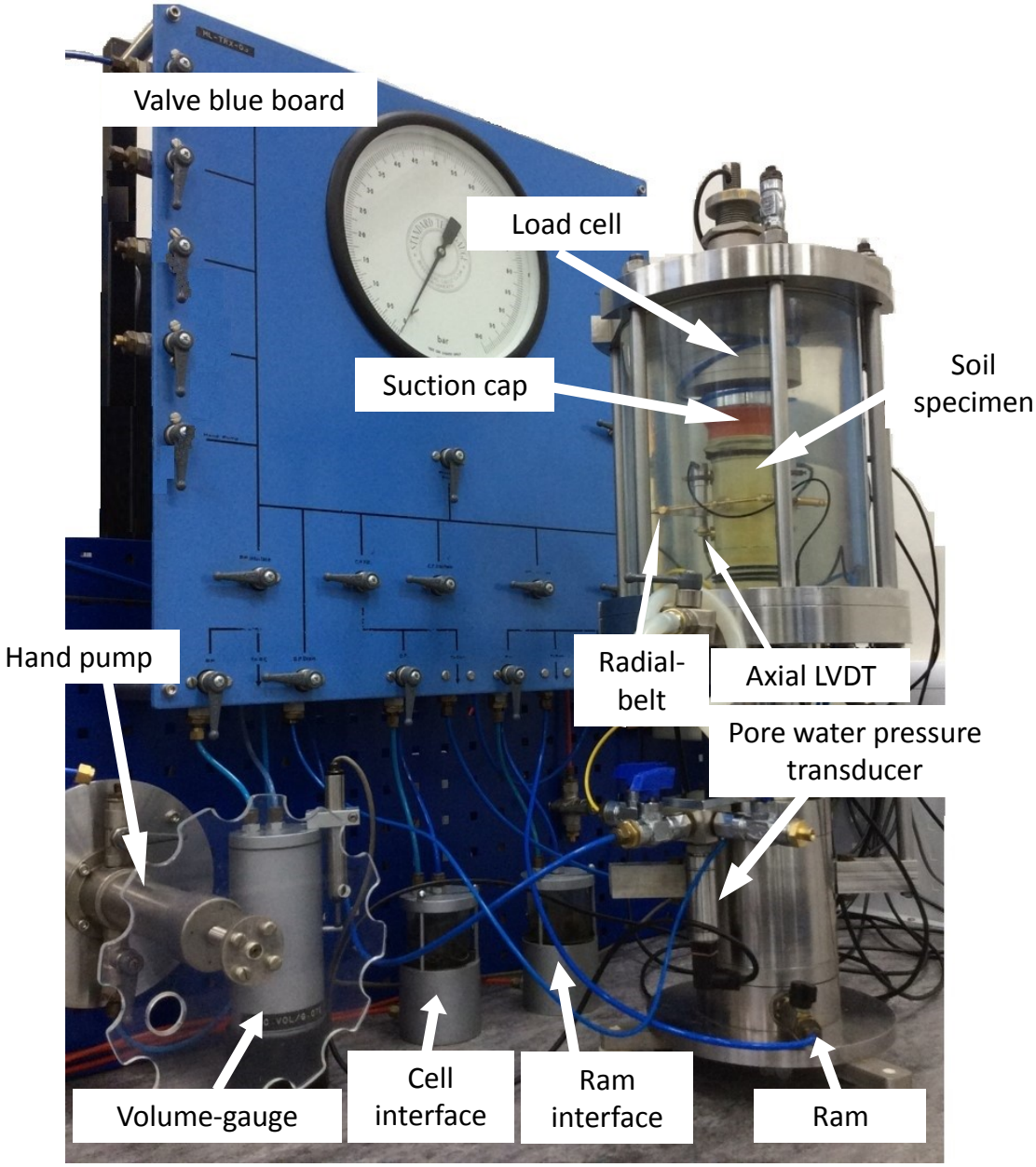

Figure 2-20 General configuration of the Bishop-Wesley automated stress-path triaxial apparatus for testing 38 mm diameter soil specimens

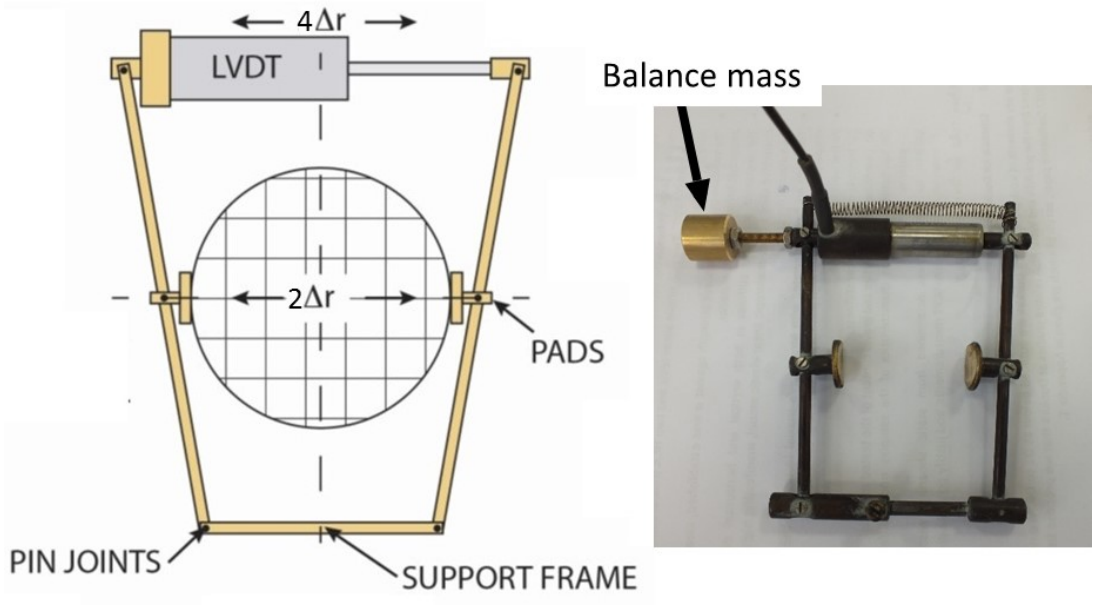

Figure 2-21 Schematic diagram of the radial-belt used in the '38 mm' triaxial apparatus (modified from Schutt (2015)) and the modification implemented

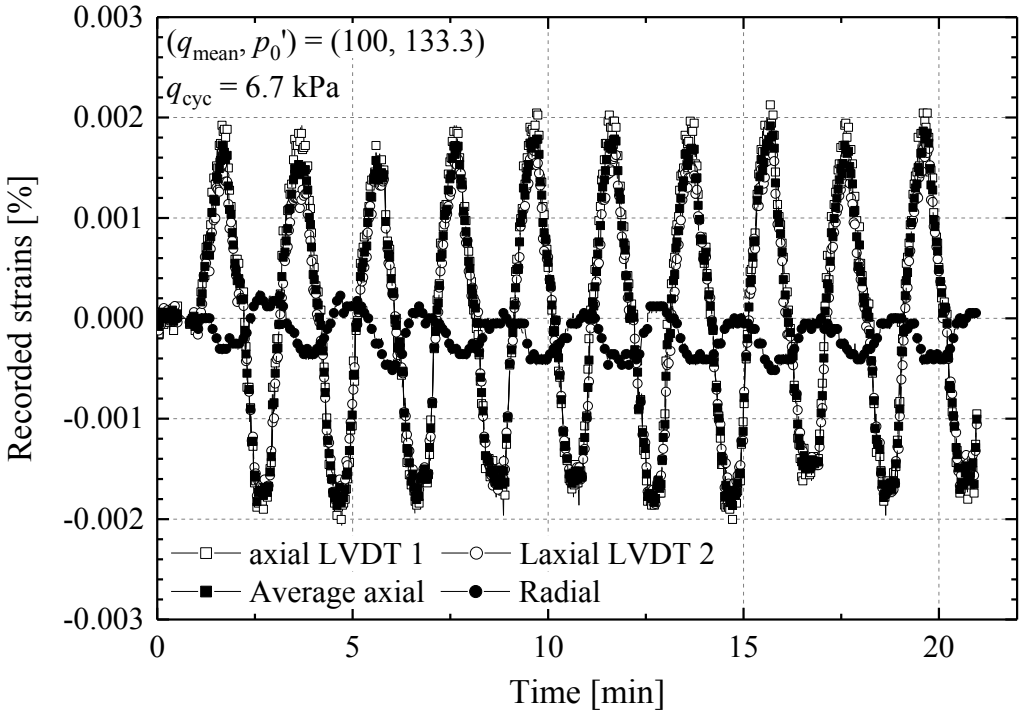

Figure 2-22 Records of local axial and radial (made with the modified radial-belt) strains in a drained cyclic test (q_{cyc} = 6.7 kPa) on Dunkirk sand

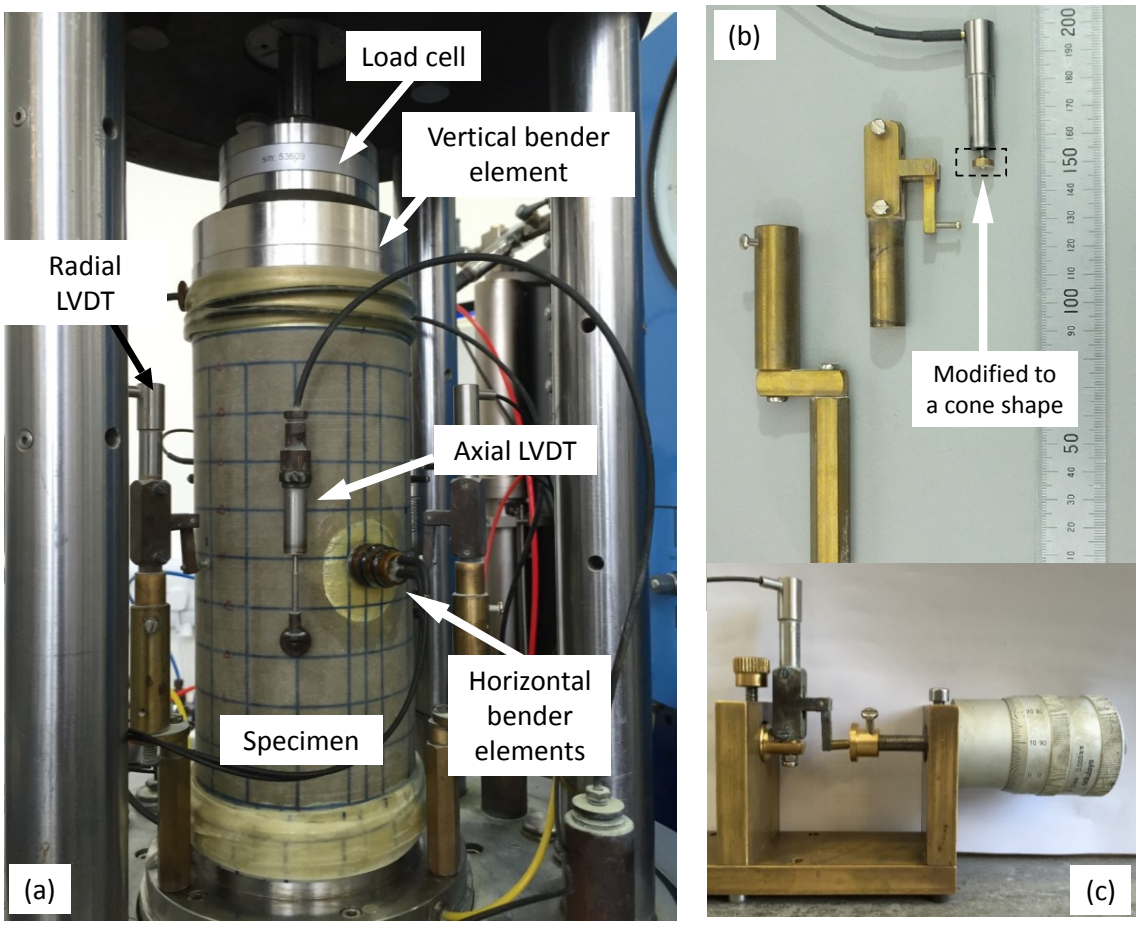

Figure 2-23 (a) Local instruments deployed in the '100 mm' triaxial apparatus; (b) Components of the new radial strain measuring system developed by Ackerley *et al.* (2016); (c) Set-up for calibrating the radial strain sensor with a micrometer

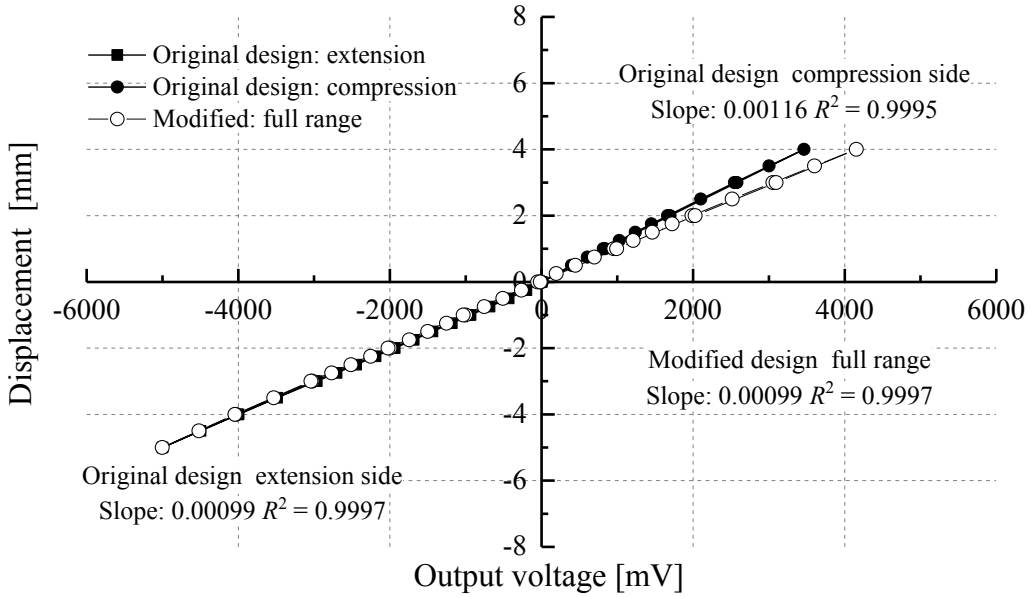

Figure 2-24 Mismatched calibration coefficients in the compression and extension side and the improvement made by modifying the base of the LVDT core

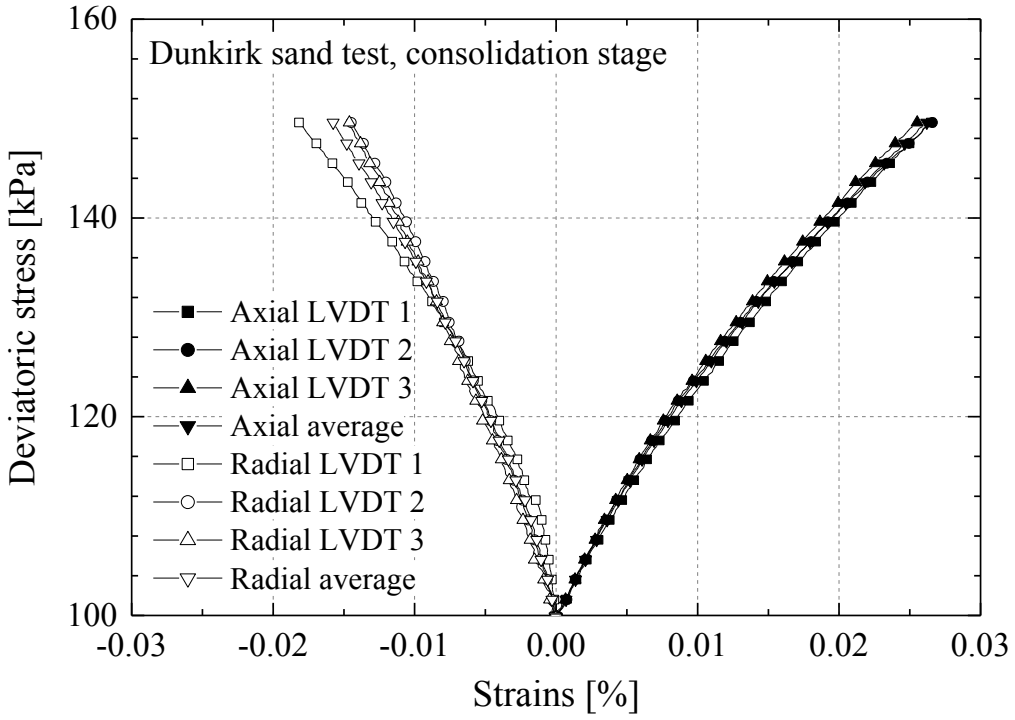

Figure 2-25 Strains recorded in a consolidation stage of a test on Dunkirk sand from the full set of local axial and radial strain instruments in the '100 mm' triaxial apparatus

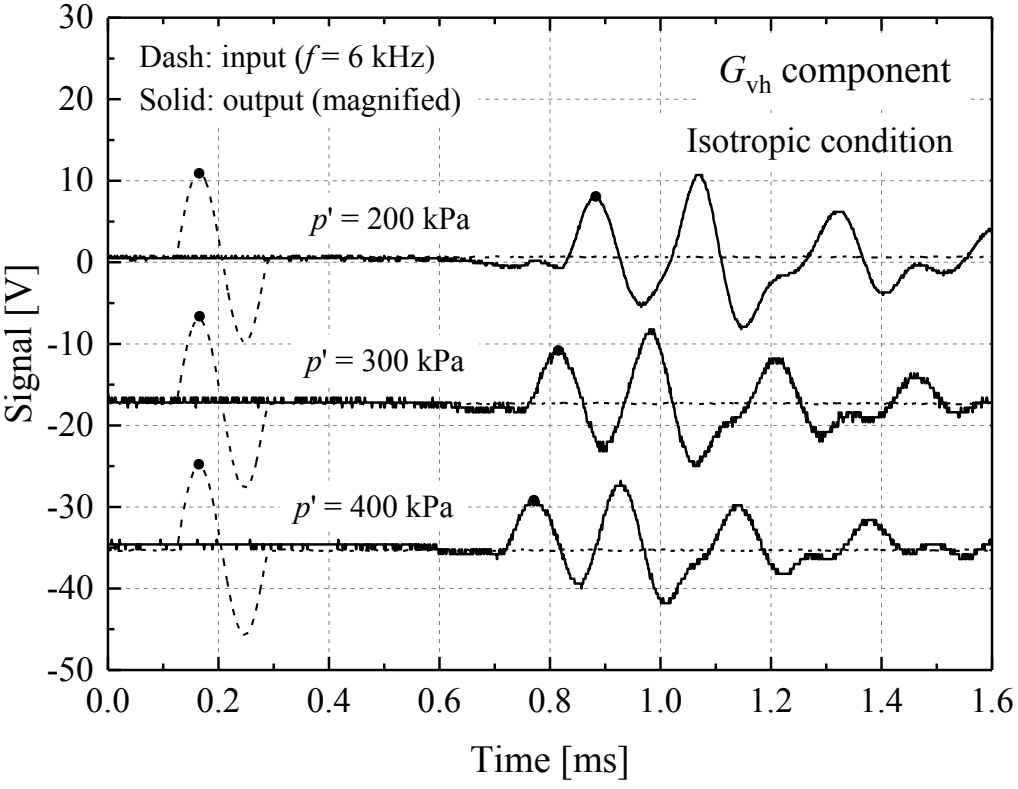

Figure 2-26 Typical bender element signal and the identified first-arrival peaks in time domain

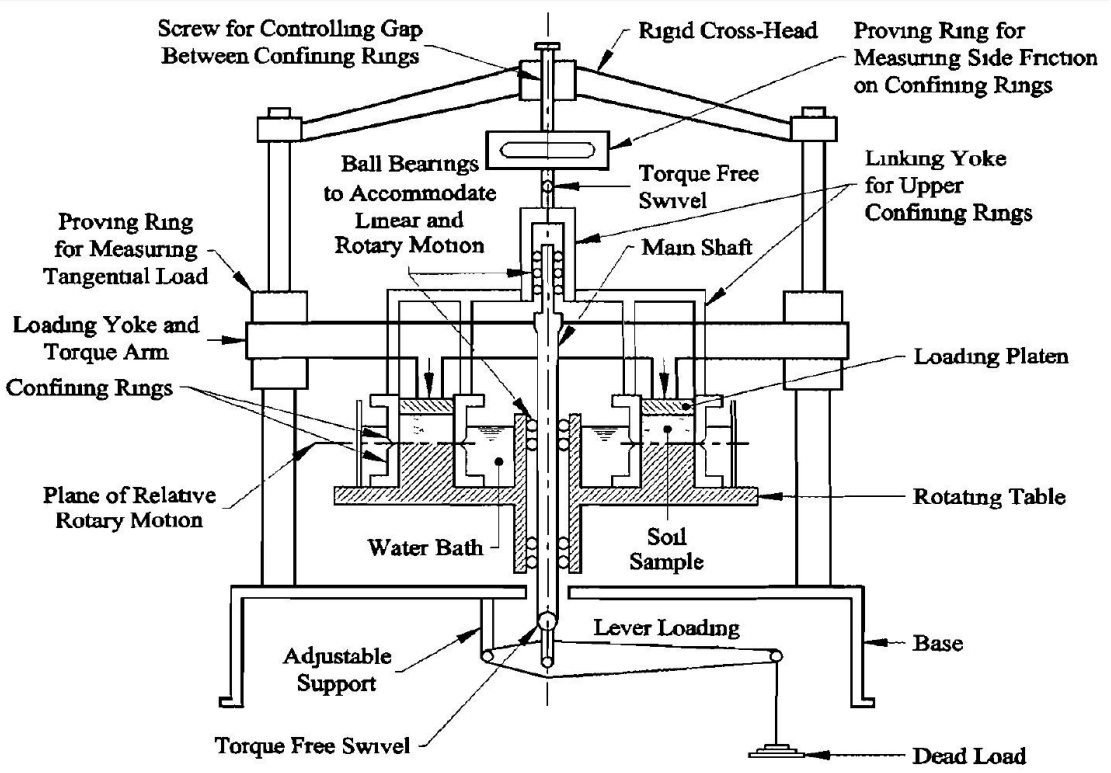

Figure 2-27 Schematic diagram of the Bishop type ring shear apparatus for soil-soil and soil-interface testing (Bishop *et al.* (1971), redrawn by Ramsey *et al.* (1998))

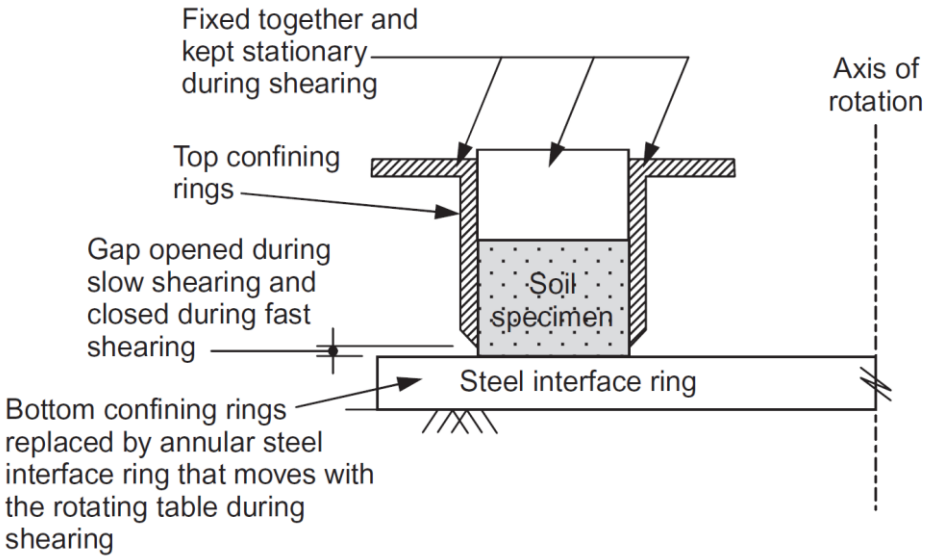

Figure 2-28 Configuration of lower interface arrangement of soil-interface ring shear testing (Ho *et al.*, 2011)

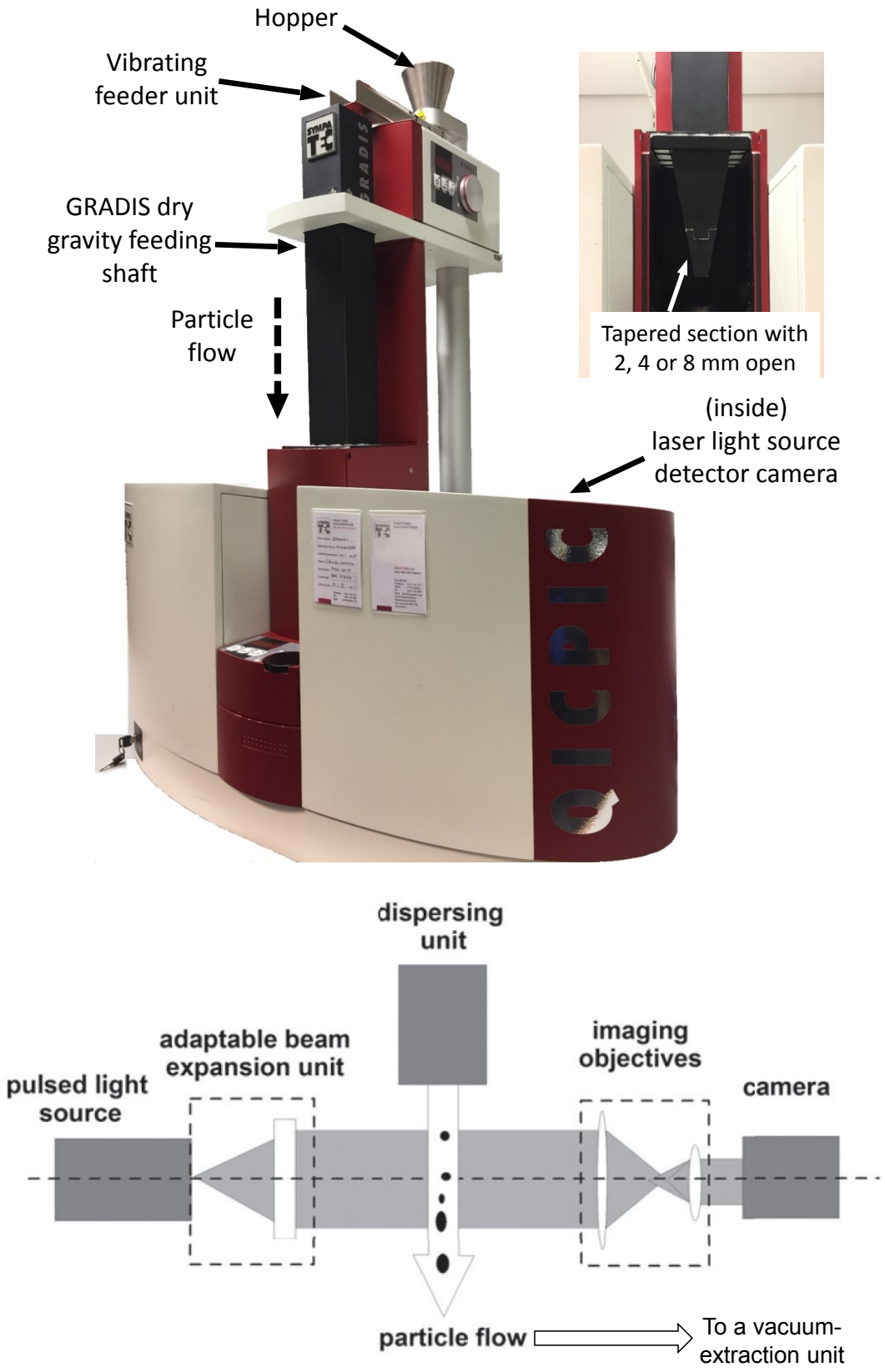

Figure 2-29 Overview of the QicPic set-up with the GRADIS dry gravity feeding system (top) and schematic diagram of the laser imaging unit (Altuhafi *et al.*, 2013) (bottom)

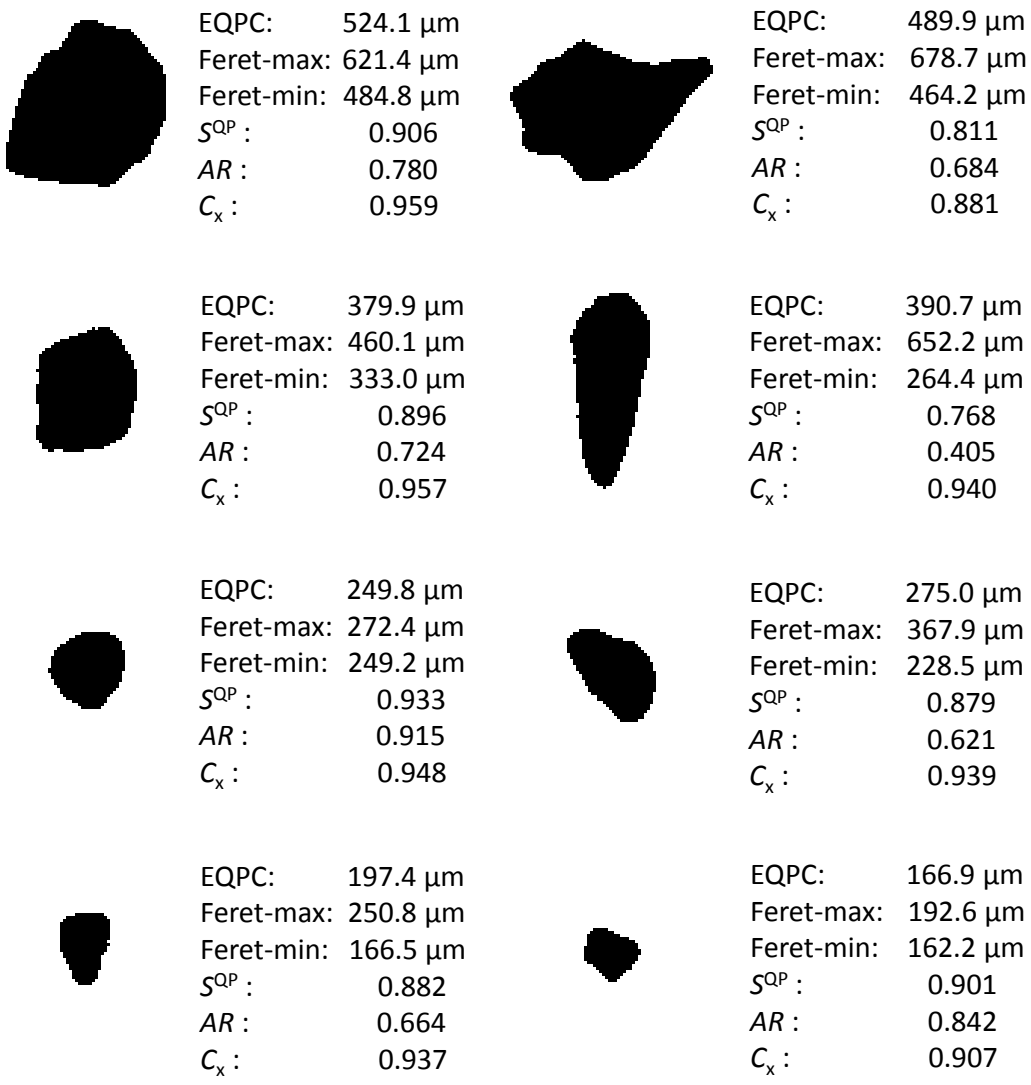

Figure 2-30 Binary images of Batch 2 Dunkirk sand particles from QicPic measurements and the determined size and shape parameters

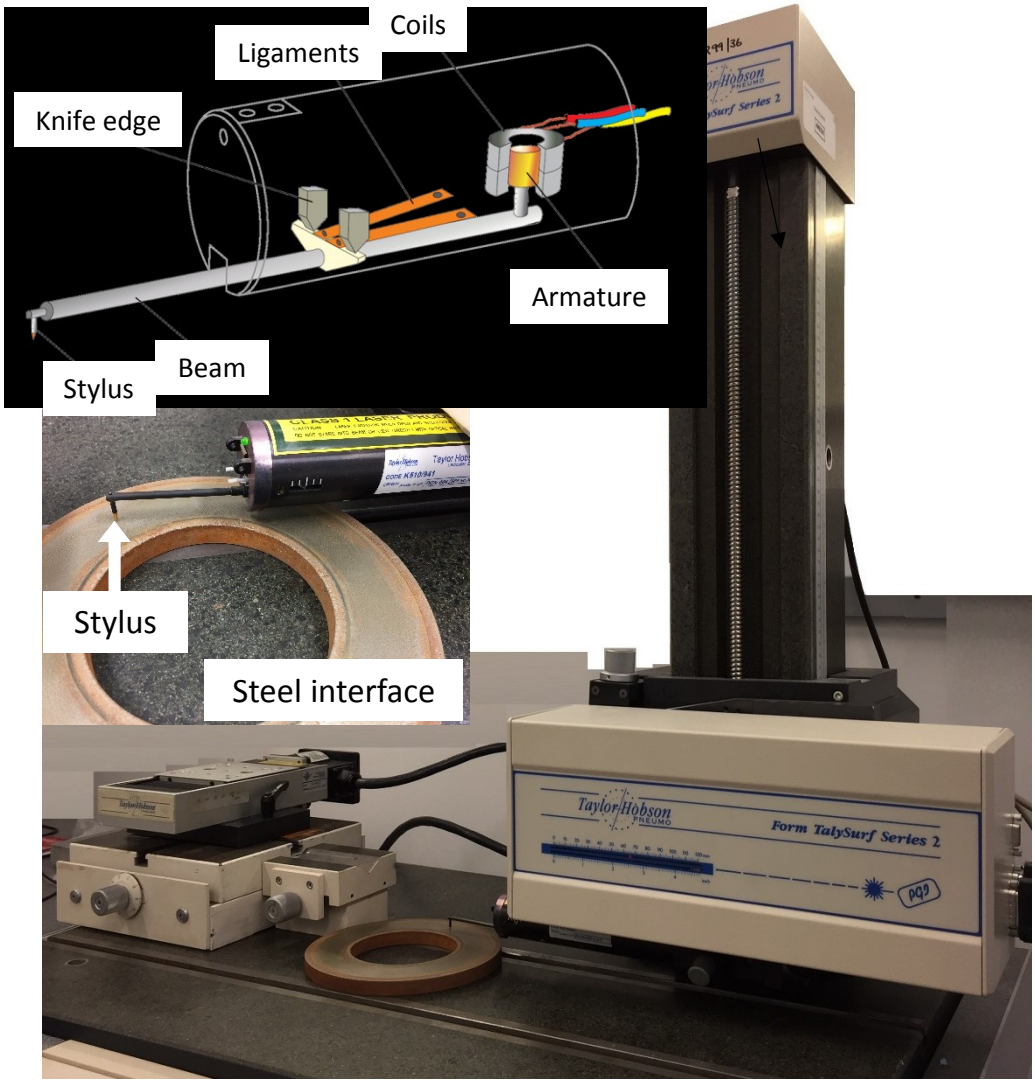

Figure 2-31 The Taylor Hobson Talysurf profilometer for measuring steel roughnessness

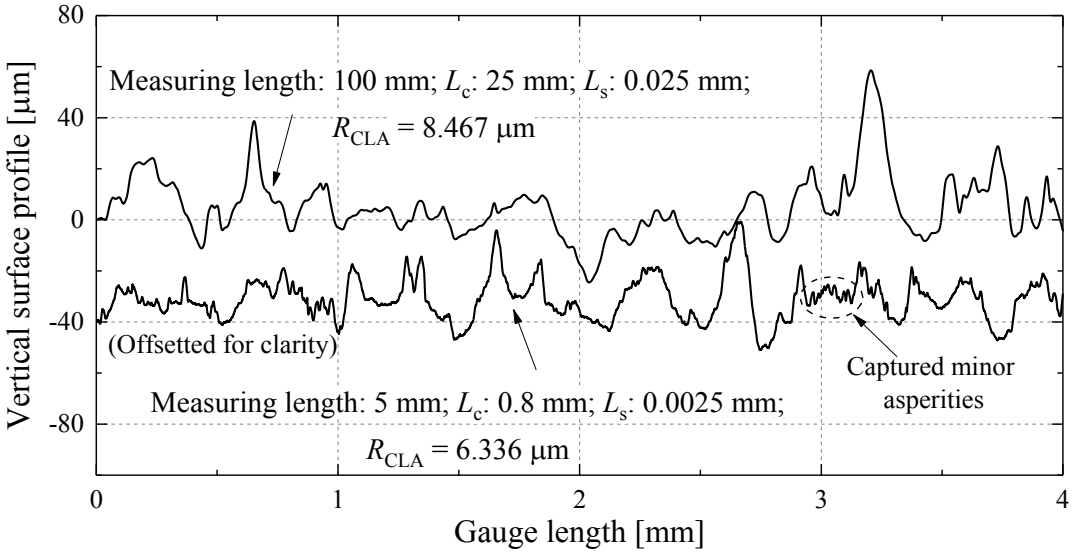

Figure 2-32 Vertical surface profiles and R_{CLA} values determined with different measuring lengths and cut-off values (L_s and L_c)

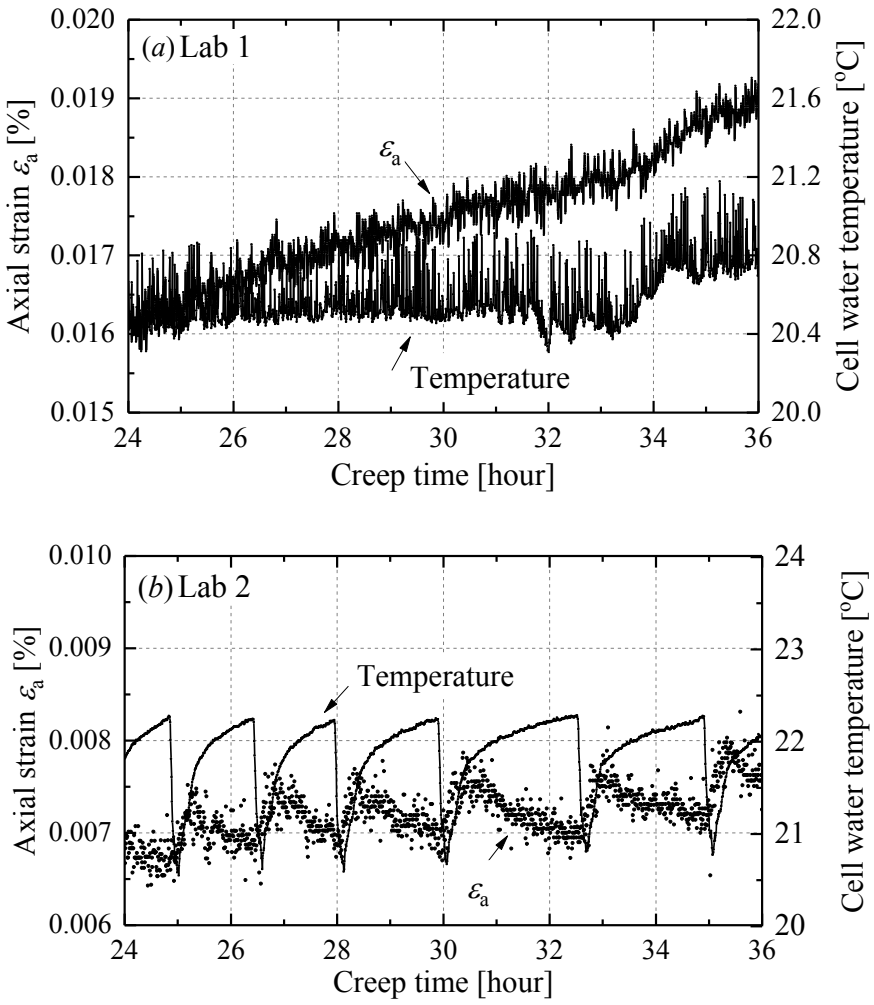

Figure 2-33 Effects of environment temperature fluctuation on the monitoring of creep strains

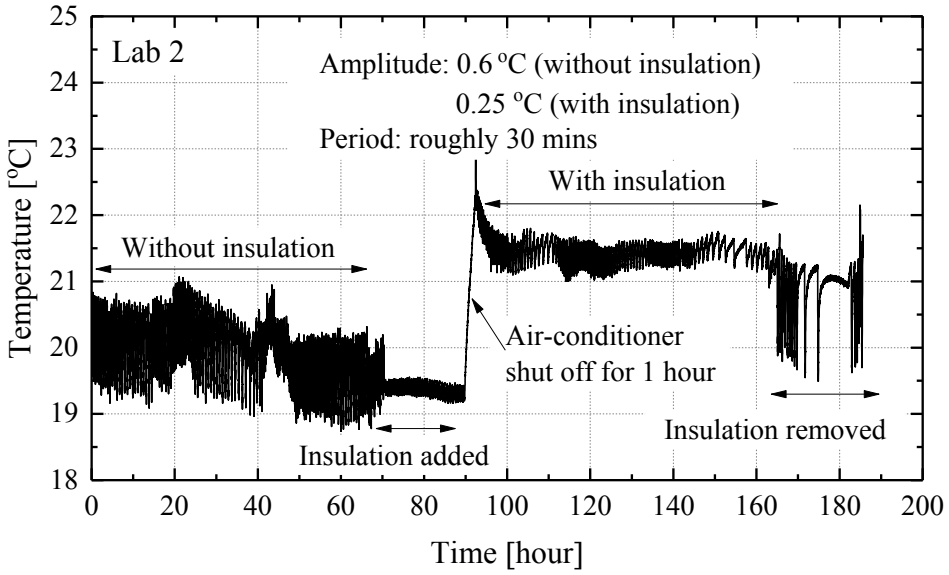

Figure 2-34 Countermeasure undertaken to alleviate cell water temperature fluctuation in a lab equipped with less capable air-conditioning system

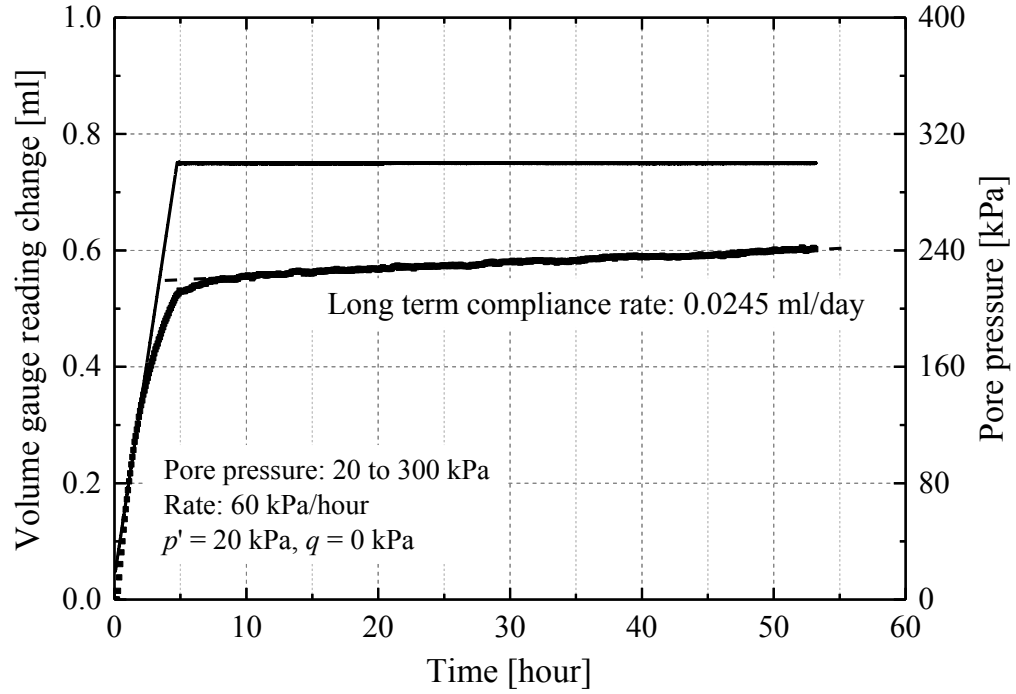

Figure 2-35 Trends of external volume-gauge reading during "saturation" of a dummy sample and porous stone, also indicating the long-term compliance rate of the pore water pressure system under 300 kPa pressure

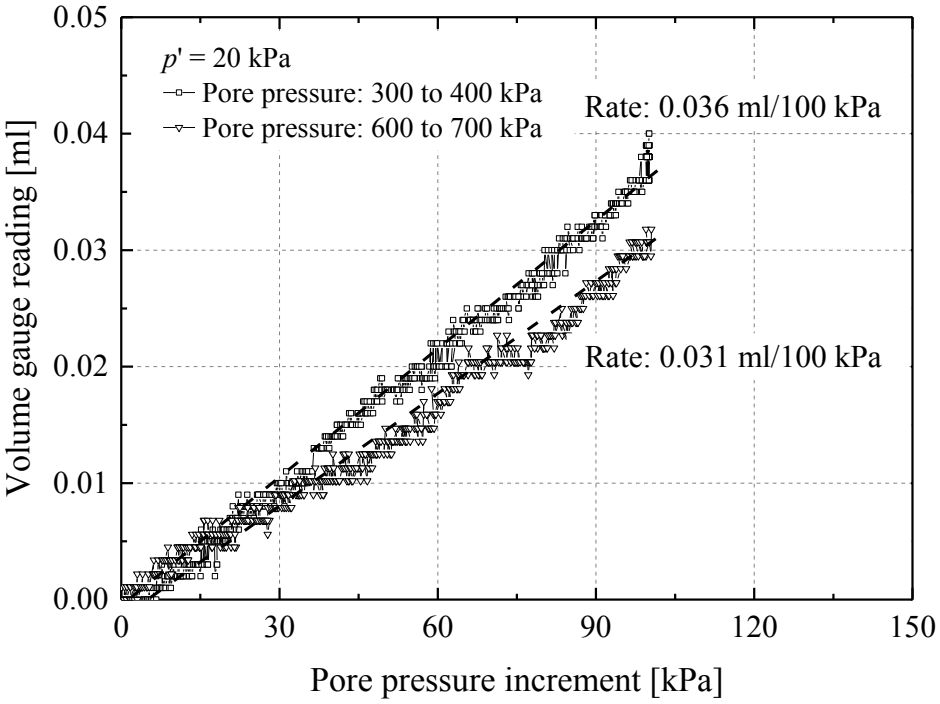

Figure 2-36 Determination of short-term compliance rate of the pore water pressure system under two pressure levels

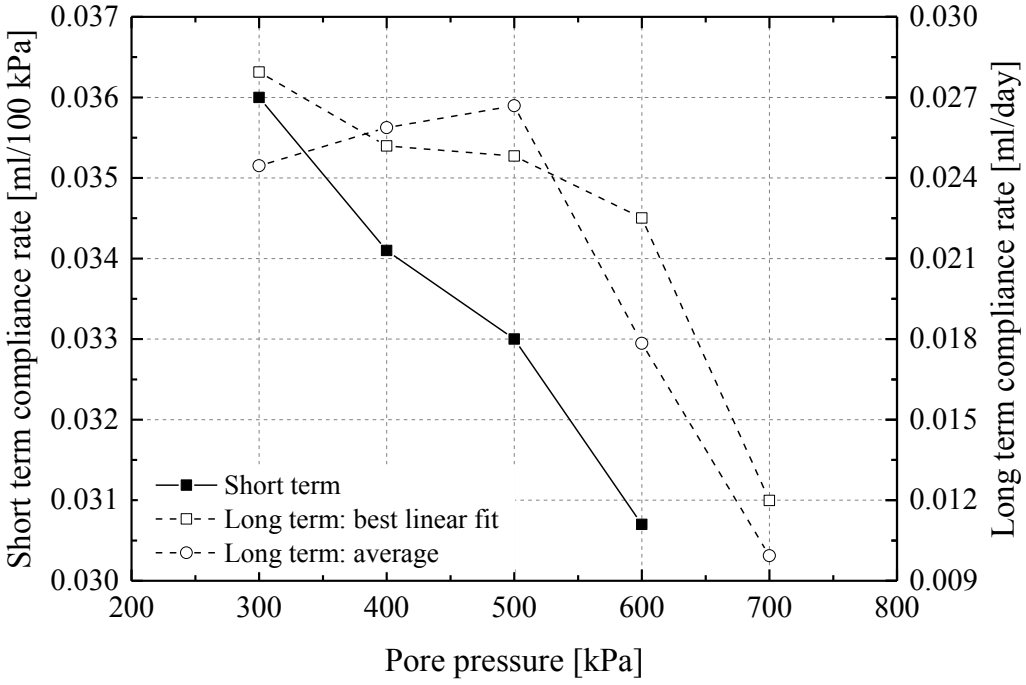

Figure 2-37 Summary of the rates of short-term compliance (mL/100 kPa) and long-term compliance (mL/day) of the pore water pressure system in a '38 mm' triaxial apparatus

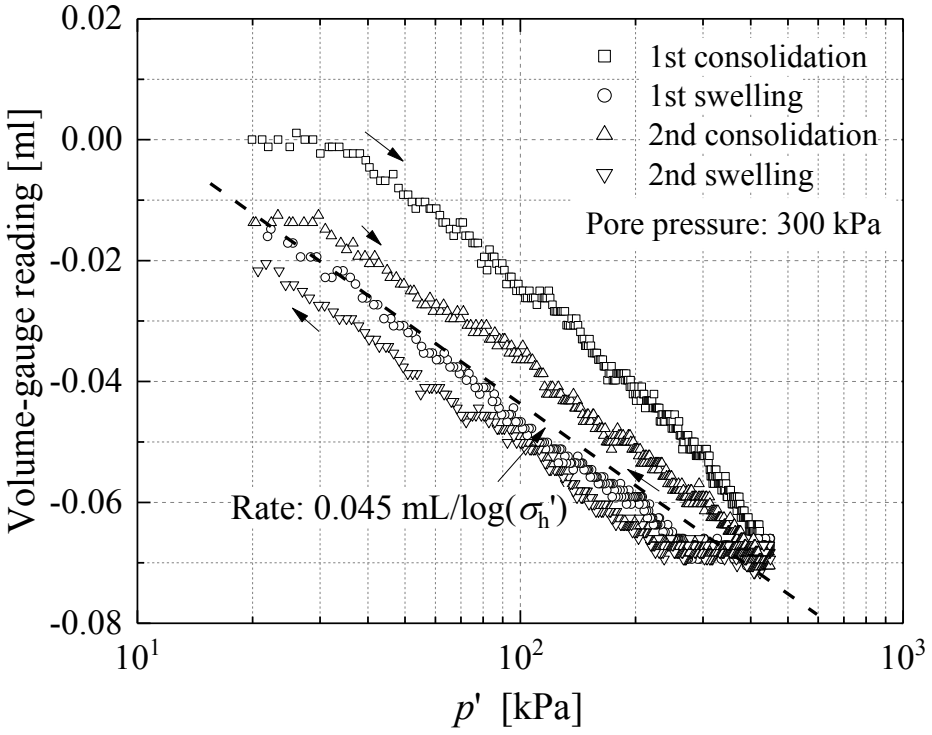

Figure 2-38 Volume-gauge reading against mean effective stress level in cycles of "consolidating" and "swelling" of a dummy sample and porous stone, maintaining 300 kPa pore water pressure

2.4 Summary

This chapter sets out the background to the Author's laboratory-based research programme, including introducing the PISA test sites, their sampling campaigns, the principles of the laboratory apparatuses employed and their performance.

Historical and recent site investigations and laboratory testing provided a base-line characterisation of the ground conditions and soil properties at the Cowden and Dunkirk PISA test sites. New rotary core and block sampling campaigns at Cowden provided material for further comprehensive laboratory characterisation, but the unsuccessful rotatory core sampling at Dunkirk led to the Author's laboratory study on the sands relying principally on reconstituted samples prepared with materials collected from shallow pits.

The initial stages of laboratory studies on Cowden till and Dunkirk sand completed by Ushev (2018) and the Author provided inputs to the PISA finite element simulations, which were undertaken with advanced soil constitutive models.

The later stages of the Author's research programme employed more advanced testing equipment, including hollow cylinder apparatus (HCA) that could provide control over and measurements of the four-dimensional stress and strain tensors. This equipment allowed an exploration of the Cowden till's anisotropic mechanical behaviour over the fully non-linear range. It is acknowledged that HCA tests suffer from non-uniform stress and strain conditions, which were explored in this chapter.

The Bishop-Wesley type stress-path triaxial apparatuses employed in the Author's research offered high resolution stress and strain measurements which were upgraded with recently enhanced radial strain measuring systems. These systems, along with bender element and resonant column measurements enriched the information available regarding the Cowden till's and Dunkirk sands' stiffness anisotropy at small strains. Bishop-Wesley type cells were also employed in the Author's study of the cyclic behaviour of Dunkirk sand under drained triaxial testing conditions.

CHAPTER 3
Anisotropic stiffness and undrained shear strength behaviour of Cowden till

3.1 Introduction

Stiffness and shear strength anisotropy, which is common in soils, is significant conceptually and important practically. Anisotropy can be critical in assessing ground deformations and failure conditions in a wide range of geotechnical engineering problems: see for example by Addenbrooke *et al.* (1997), Zdravković *et al.* (2002) and Jardine (2002).

This chapter presents a laboratory testing programme that investigates the stiffness and undrained shear strength anisotropy of Cowden till, employing a hybrid hollow cylinder apparatus (HCA) and triaxial apparatus equipped with full set of local strain instruments and multi-directional bender elements. First, a review is presented on the anisotropic stiffness and strength behaviour of clay dominated geo-materials, focusing principally on stiff clay studies employing similar testing methodologies to the current study. The testing procedures and programme completed are described, before reviewing the Cowden till's index properties and the sampling quality of the tested specimens. The main outcomes regarding stiffness and strength anisotropy of the material are presented and discussed, before adding additional information from small strain (drained and undrained) triaxial probing experiments.

The Author's contribution adds to the laboratory characterisation of Cowden till conducted for the PISA project by Ushev (2018). His research focused on the material's undrained monotonic and cyclic shearing behaviour under triaxial compression and extension conditions, oedometer compression behaviour and critical state behaviour, as well as interface shearing properties.

The three main hypotheses tested in this chapter are that:

#1. The Cowden till exhibits anisotropy in its mechanical behaviour from small to large strains.

#2. The patterns of anisotropy imparted by the apparently over-consolidated till's glacial deposition may vary from those seen in mechanically over-consolidated and aged marine sediments (such as the London, Gault, Kimmeridge or Oxford clays).

#3. Any mechanical anisotropy shown by advanced laboratory tests is comparable to that revealed by in-situ dynamic stiffness measurements.

3.2 Review: laboratory investigation of anisotropic stiffness and strength of geo-materials

The stiffness and shear strength behaviours of naturally deposited soils are often assumed to be cross-anisotropic. Extensive laboratory research has been carried out to investigate the anisotropic properties from initial linear elastic zone over the wide non-linear range up to failure. A literature review is present in this section to summarise the current understanding of anisotropic behaviour of clay materials. It is noted that although the review primarily quotes research on clay materials, the interpretive framework and testing methodologies introduced are equally applicable to coarser materials, as demonstrated for example by Kuwano & Jardine (2002b).

3.2.1 Cross-anisotropic elasticity and laboratory investigation approaches

For an element of a continuous material, six stress components (three normal stresses and three shear stresses) are required to fully describe its stress state. However, at present no experimental device exists with the capability to control and measure independently the six degrees of freedom of stress and strain and fully determine the material's anisotropic properties under general stress conditions.

However, as many naturally formed sediments are deposited under gravity and experience initially mainly vertical loading, unloading and water level changes while experiencing relatively minor lateral straining, it is often assumed that the initial structure and properties of the material are symmetrical with regard to the vertical axis. Such conditions are termed transversely isotropic (or cross-anisotropic) and this special

condition reduces the number of independent parameters required to describe the anisotropic stiffness or shear strength properties (Lings, 2001).

However, more complex stress regimes and anisotropies may apply to natural sediments deposited on sloping ground or those that experience asymmetric geological actions, such as tectonic activity, basal shear loading from glaciers or tumultuous ground movement. Their sedimentary and post-sedimentary structures may be altered and anisotropy can be developed in the horizontal plane. Meanwhile, as noted by Zdravković & Jardine (2001), certain natural deposition settings or construction activities (such as the construction of multiple stage embankments on soft ground or tailings deposited on sloping ground) rotate the axis of principal stresses during consolidation and give conditions that cannot be simplified adequately as being cross-anisotropic. The Cowden till deposit studied by the Author is thought to have been subjected to directionally oriented glacial shearing. However, in the absence of any clear evidence regarding its detailed glacial stress history, the assumption of cross-anisotropic behaviour will be retained in this chapter.

Cross-anisotropic elasticity model and parameters

Considering first soils' drained elastic stiffnesses within the initial linear elastic range, the effective compliance equation for a cross-anisotropic elastic material can be written as:

$$\begin{Bmatrix} \delta\varepsilon_{xx} \\ \delta\varepsilon_{yy} \\ \delta\varepsilon_{zz} \\ \delta\gamma_{yz} \\ \delta\gamma_{zx} \\ \delta\gamma_{xy} \end{Bmatrix} = \begin{bmatrix} \frac{1}{E'_h} & -\frac{\nu'_{hh}}{E'_h} & -\frac{\nu'_{vh}}{E'_v} & 0 & 0 & 0 \\ -\frac{\nu'_{hh}}{E'_h} & \frac{1}{E'_h} & -\frac{\nu'_{vh}}{E'_v} & 0 & 0 & 0 \\ -\frac{\nu'_{hv}}{E'_h} & -\frac{\nu'_{hv}}{E'_h} & \frac{1}{E'_v} & 0 & 0 & 0 \\ 0 & 0 & 0 & \frac{1}{G_{hv}} & 0 & 0 \\ 0 & 0 & 0 & 0 & \frac{1}{G_{vh}} & 0 \\ 0 & 0 & 0 & 0 & 0 & \frac{1}{G_{hh}} \end{bmatrix} \times \begin{Bmatrix} \delta\sigma'_{xx} \\ \delta\sigma'_{yy} \\ \delta\sigma'_{zz} \\ \delta\tau_{yz} \\ \delta\tau_{zx} \\ \delta\tau_{xy} \end{Bmatrix} \qquad (3.1)$$

where the stress and strain increments are referred to rectangular Cartesian axes, with *x*- and *y*- axes denoting respectively the horizontal (h′) plane and *z*-axis vertical (v′).

The following constraints also apply.

$$G_{vh} = G_{hv} \tag{3.2}$$

$$\frac{\nu'_{hv}}{E'_h} = \frac{\nu'_{vh}}{E'_v} \tag{3.3}$$

$$G_{hh} = \frac{E'_h}{2(1+\nu'_{hh})} \tag{3.4}$$

The symbols E_v' and E_h' represent the Young's moduli in the vertical and horizontal directions respectively. ν_{hh}' and ν_{vh}' are the drained Poisson's ratios for horizontal normal strain caused by an imposed horizontal and vertical strain respectively, and ν_{hv}' is the drained Poisson's ratio for vertical normal strain due to an imposed horizontal strain. G_{hh} is the shear modulus in the horizontal plane, and G_{vh} and G_{hv} denote the shear moduli in the vertical plane, which are assumed to be equal, as seen in Equation (3.2), Combining Equations (3.1) to (3.4), five independent parameters are required to fully characterise the cross-anisotropic properties under drained condition.

Under undrained conditions, the generic form of drained cross-anisotropic elasticity model and constraining equations still apply, only with the superscript '′' in the above equations changing to 'u' to denote undrained conditions while the shear moduli G remained unchanged. The following additional restrictions are applied to meet the assumption of constant volume (Gibson, 1974).

$$\nu^u_{vh} = \frac{1}{2} \tag{3.5}$$

$$\nu^u_{hh} = 1 - \nu^u_{hv} = 1 - \frac{1}{2}\frac{E^u_h}{E^u_v} \tag{3.6}$$

Therefore, the number of independent parameters required to characterise undrained cross-anisotropic condition further reduces to three (E_v^u, E_h^u, G_{vh}). The undrained Young's moduli E_v^u and E_h^u can be derived from the above set of drained parameters with the following relationships, but the reverse is not achievable (Lings, 2001, Brosse *et al.*, 2016).

$$E_{\mathrm{v}}^{\mathrm{u}} = \frac{E_{\mathrm{v}}^{'}[2(1-\nu_{\mathrm{hh}}^{'})E_{\mathrm{v}}^{'} + (1-4\nu_{\mathrm{vh}}^{'})E_{\mathrm{h}}^{'}]}{2(1-\nu_{\mathrm{hh}}^{'})E_{\mathrm{v}}^{'} - 4(\nu_{\mathrm{vh}}^{'})^2 E_{\mathrm{h}}^{'}} \tag{3.7}$$

$$E_{\mathrm{h}}^{\mathrm{u}} = \frac{E_{\mathrm{h}}^{'}[2(1-\nu_{\mathrm{hh}}^{'})(E_{\mathrm{v}}^{'})^2 + (1-4\nu_{\mathrm{vh}}^{'})E_{\mathrm{v}}^{'}E_{\mathrm{h}}^{'}]}{[1-(\nu_{\mathrm{hh}}^{'})^2](E_{\mathrm{v}}^{'})^2 + (1-2\nu_{\mathrm{vh}}^{'} - 2\nu_{\mathrm{vh}}^{'}\nu_{\mathrm{hh}}^{'})E_{\mathrm{v}}^{'}E_{\mathrm{h}}^{'} - (\nu_{\mathrm{vh}}^{'})^2(E_{\mathrm{h}}^{'})^2} \tag{3.8}$$

Additionally, for both drained and undrained conditions, Pickering (1970) pointed out the following relationships are required to meet thermodynamic requirements. These restrictions, however, are rarely invoked under common laboratory testing conditions.

$$-1 \le \nu_{\mathrm{hh}} \le 1 \tag{3.9}$$

$$\frac{E_{\mathrm{v}}}{E_{\mathrm{h}}}(1-\nu_{\mathrm{hh}}) - 2(\nu_{\mathrm{hh}})^2 \ge 0 \tag{3.10}$$

In principle, static triaxial testing allows only three independent drained cross-anisotropic elasticity parameters to be determined. Any complete assessment of the five independent parameters has to introduce additional assumptions, for example, the assumed relationship between Young's moduli and shear stiffness $E_{\mathrm{h}}'/E_{\mathrm{v}}' = (G_{\mathrm{hh}}/G_{\mathrm{vh}})^2$ proposed by Graham & Houlsby (1983). However, as argued by Lings (2001) and recently by Nishimura (2014b), these additional correlations are not physically binding, and in some cases may deviate from experimental observations. Conventional triaxial testing is also commonly constrained by the quality and accuracy of stress strain control and measurement, and usually lacks of the means to determine even E_{v}' effectively.

Advanced laboratory characterisation of cross-anisotropic elasticity parameters

Advances in soil testing techniques and developments of hybrid triaxial cells and hollow cylinder apparatus (HCA) equipped with high resolution local strain sensors and versatile shear stiffness measuring techniques have improved the accuracy and reliability in determining cross-anisotropic parameters significantly. This section sets out the assumptions and methodologies employed by the Author to determine the cross-anisotropic parameters using these apparatuses.

Stress probing tests in hybrid triaxial cells

Hybrid triaxial tests may be performed that combine multi-directional bender element (or shear plate) measurements of shear stiffness components (G_{vh}, G_{vh}, G_{hh}) with stress or strain controlled probing tests that apply small stress increments in the vertical (axial) or horizontal (radial) direction (Kuwano & Jardine, 2002b, Gasparre *et al.*, 2007b, Nishimura, 2014b). The basic assumption required in the interpretation is that the soil behaviour is elastic and rate-independent over a definable (small-strain) range, and the elastic moduli determined from dynamic (involving a shear strain rate of 10 to 10^3%/min, Kuwano *et al.* (2000)) and static (where the shear strain rate may be far lower at 0.0003% - 0.0006%/hour in drained tests on clays, Gasparre *et al.* (2007b)) approaches are compatible and inter-changeable. In other words, they assume strain-rate independent behaviour.

For triaxial conditions, the effective stress-strain relationship in the compliance Equation (3.1) can be simplified as:

$$\begin{Bmatrix} \delta\varepsilon_v \\ \delta\varepsilon_h \end{Bmatrix} = \begin{bmatrix} \frac{1}{E'_v} & -\frac{2\nu'_{hv}}{E'_h} \\ -\frac{\nu'_{vh}}{E'_v} & \frac{1-\nu'_{hh}}{E'_h} \end{bmatrix} \times \begin{Bmatrix} \delta\sigma'_v \\ \delta\sigma'_h \end{Bmatrix} \tag{3.11}$$

Where $\delta\varepsilon_v$ and $\delta\varepsilon_h$ are vertical and horizontal strain increments; $\delta\sigma_v'$ and $\delta\sigma_h'$ are vertical and horizontal effective stress increments. The Young's moduli and Poisson's ratios are determined through the following vertical and horizontal stress probing and bender element measurements.

In drained vertical probes, the sample is loaded axially with a $\delta\sigma_v'$ increment while maintaining constant radial effective stress ($\delta\sigma_h' = 0$), and Equation (3.11) simplifies to

$$\delta\varepsilon_v = \frac{1}{E'_v}\delta\sigma'_v \tag{3.12}$$

$$\delta\varepsilon_h = -\frac{\nu'_{vh}}{E'_v}\delta\sigma'_v \tag{3.13}$$

With corresponding axial and radial strain measurements, E_v' and ν_{vh}' can be derived. Further, with horizontal probes performed under constant vertical effective stress ($\delta\sigma_v' = 0$) while applying horizontal stress increment $\delta\sigma_h'$, Equation (3.11) reduces to

$$\delta\varepsilon_{\mathrm{v}} = -\frac{2\nu_{\mathrm{hv}}^{'}}{E_{\mathrm{h}}^{'}}\delta\sigma_{\mathrm{h}}^{'} \tag{3.14}$$

$$\delta\varepsilon_{\mathrm{h}} = -\frac{1-\nu_{\mathrm{hh}}^{'}}{E_{\mathrm{h}}^{'}}\delta\sigma_{\mathrm{h}}^{'} \tag{3.15}$$

Meanwhile, the G_{vh}, G_{vh} and G_{hh} shear stiffness components can be directly determined from bender element measurements. We assume material property is isotropic in horizontal planes, leading to the following relation between shear stiffness and Young's modulus.

$$G_{\mathrm{hh}} = \frac{E_{\mathrm{h}}^{'}}{2(1+\nu_{\mathrm{hh}}^{'})} \tag{3.16}$$

Combining Equations (3.15) and (3.16) leads to the determination of parameters in the horizontal plane.

$$E_{\mathrm{h}}^{'} = \frac{4AG_{\mathrm{hh}}}{A+2G_{\mathrm{hh}}} \tag{3.17}$$

$$\nu_{\mathrm{hh}}^{'} = \frac{A-2G_{\mathrm{hh}}}{A+2G_{\mathrm{hh}}} \tag{3.18}$$

Where $A = \delta\sigma_{\mathrm{h}}'/\delta\varepsilon_{\mathrm{h}}$, as measured from radial probing tests. With E_{h}' and ν_{hh}' determined, Poisson's ratio ν_{hv}' can be derived directly from Equation (3.14) which only uses vertical strain measurement in the horizontal probing, or by combining Equations (3.14) and (3.15), leading to the following two equations respectively.

$$\nu_{\mathrm{hv}}^{'} = -\frac{E_{\mathrm{h}}^{'}}{2}\frac{\delta\varepsilon_{\mathrm{v}}}{\delta\sigma_{\mathrm{h}}^{'}} \tag{3.19}$$

$$\nu_{\mathrm{hv}}^{'} = -\frac{\delta\varepsilon_{\mathrm{v}}}{\delta\varepsilon_{\mathrm{h}}}\frac{(1-\nu_{\mathrm{hh}}^{'})}{2} \tag{3.20}$$

The above two equations should give very close ν_{hv}' values due to the fact that the radial strain has been applied uniformly to determine E_{h}' and ν_{hh}', as seen in Equations (3.17) and (3.18). Alternatively, ν_{hv}' can also be derived from the matrix symmetry Equation (3.3), knowing E_{v}' and ν_{vh}' from drained vertical probing and E_{h}' from

drained horizontal probing. However, as presented by Gasparre *et al.* (2007b) and Nishimura (2014a), v_{hv}' values determined from these two approaches may deviate from each other, and discrepancies can also be noted when comparing with direct measurement of v_{hv}' (or $v_{\theta z}'$) from drained HCA uniaxial σ_θ' probing (as explained below). These inconsistencies might be due to errors in bender element and/or local strain measurements. These errors tend to accumulate and sometimes amplify when substituted into Equations (3.1)-(3.20), and approaches for deriving the parameters have to be optimised.

The above methodologies for measuring and deriving cross-anisotropic parameters through drained stress probing tests were revisited by Nishimura (2014a), who approached E_h' determination without relying on radial strain measurements, but employed an additional undrained axial probing test stage to determine E_v^u, as shown in Figure 3-1. This approach effectively reduces the reliance on the often more scattered radial strain measurements and offers alternative cross checks on the results obtained from different approaches. Under undrained conditions, constant volume can be assumed ($v_{vh}^u = 0.5$), and Equation (3.7) can be transformed to derive E_h' using the following expression.

$$E_h' = \frac{4G_{hh}(E_v^u - E_v')}{E_v^u + 4a^2 E_v^u E_v' G_{hh} + (1 - 4aE_v')G_{hh} - E_v'} \tag{3.21}$$

Where $a = v_{hv}'/ E_h' = - \delta\varepsilon_v/(2\delta\sigma_h')$, as seen in Equation (3.19).

Stress probing tests in hybrid Hollow Cylinder Apparatus (HCA)

Behaviour can only be studied in triaxial equipment with the principal stress direction either in vertical or horizontal and intermediate stress factor b either 0 or 1. When adding information from bender element tests, full compatibility between the static and dynamic stiffness measurements has to be assumed.

Hybrid Hollow Cylinder Apparatus (HCA) equipped with full sets of local instruments (for example Hight *et al.* (1983), Jardine (1996), Minh (2006), HongNam & Koseki (2005), Ibraim *et al.* (2011)) and/or dynamic shear stiffness measurement (for example resonant column system, Porovic (1995)) offers more degrees of stress and strain freedom and allows stiffness anisotropy to be characterised from the linear elastic domain up to failure in four dimensional stress space (Zdravkovic, 1996,

Zdravkovic & Jardine, 1997).

In hollow cylinder tests, it is more convenient to describe stress and strain vectors using cylindrical coordinates, as shown in Figure 3-2. The *r*-θ plane in HCA tests is equivalent to the horizontal plane in triaxial tests, thus $E_h = E_r = E_\theta$ and $\nu_{hh} = \nu_{rr} = \nu_{\theta\theta} = \nu_{r\theta}$. Without the aid of radially orientated dynamic measurements, only one shear stiffness component ($G_{z\theta}$) can be directly measured and the drained cross-anisotropic compliance Equation (3.1) can be rewritten as following.

$$\begin{Bmatrix} \delta\varepsilon_z \\ \delta\varepsilon_r \\ \delta\varepsilon_\theta \\ \delta\gamma_{z\theta} \end{Bmatrix} = \begin{bmatrix} \frac{1}{E'_z} & -\frac{\nu'_{rz}}{E'_r} & -\frac{\nu'_{\theta z}}{E'_\theta} & 0 \\ -\frac{\nu'_{zr}}{E'_z} & \frac{1}{E'_r} & -\frac{\nu'_{\theta r}}{E'_\theta} & 0 \\ -\frac{\nu'_{z\theta}}{E'_z} & -\frac{\nu'_{r\theta}}{E'_r} & \frac{1}{E'_\theta} & 0 \\ 0 & 0 & 0 & \frac{1}{G_{z\theta}} \end{bmatrix} \times \begin{Bmatrix} \delta\sigma'_z \\ \delta\sigma'_r \\ \delta\sigma'_\theta \\ \delta\tau_{z\theta} \end{Bmatrix} \tag{3.22}$$

The Young's moduli and Poisson's ratios in the equation can be determined through suites of uniaxial drained probes in which a single small stress increment is imposed in one direction at a time with the others maintained constant (Zdravkovic & Jardine, 1997, Minh, 2006).

In a drained vertical probe, a small vertical stress increment $\delta\sigma_z'$ is applied while $\delta\sigma_r' = \delta\sigma_\theta' = \delta\tau_{z\theta} = 0$, giving:

$$E'_z = \frac{\delta\sigma'_z}{\delta\varepsilon_z},\ \nu'_{zr} = -\frac{\delta\varepsilon_r}{\delta\varepsilon_z},\ \nu'_{z\theta} = -\frac{\delta\varepsilon_\theta}{\delta\varepsilon_z} \tag{3.23}$$

In a drained circumferential probe, a small circumferential stress increment $\delta\sigma_\theta'$ is imposed while keeping $\delta\sigma_z' = \delta\sigma_r' = \delta\tau_{z\theta} = 0$, resulting in:

$$E'_\theta = \frac{\delta\sigma'_\theta}{\delta\varepsilon_\theta},\ \nu'_{\theta z} = -\frac{\delta\varepsilon_z}{\delta\varepsilon_\theta},\ \nu'_{\theta r} = -\frac{\delta\varepsilon_r}{\delta\varepsilon_\theta} \tag{3.24}$$

A drained radial probe test, through which E_r', ν_{rz}', and $\nu_{r\theta}'$ can be derived, can also be performed using the similar approach. In drained torsional probing, a small torsional stress increment $\delta\tau_{z\theta}$ is introduced with the normal stresses remaining constant, deriving:

$$G_{z\theta} = \frac{\delta\tau_{z\theta}}{\delta\gamma_{z\theta}} \tag{3.25}$$

The obtained $G_{z\theta}$ can be integrated with data obtained from other HCA torsional shear modes (for example simple shear), resonant column measurement, triaxial bender element measurement (G_{vh}, G_{hv}), or in-situ down-hole wave velocity measurements made by Seismic CPT (SCPT) or Seismic Dilatometer Marchetti test (SDMT), as demonstrated by Brosse *et al.* (2016).

Undrained HCA stress probes can also be carried out to produce directly undrained Poisson's ratios (ν_{hv}', ν_{hh}'), undrained vertical and horizontal Young's moduli (E_v^u , E_h^u) and shear stiffnesses components (G_{vh}, G_{hh}). Brosse (2012) has demonstrated how this can be achieved using the following equations, with the aid of the two additional Equations (3.5) and (3.6).

$$E_v^u = \frac{2\delta\sigma_z - \delta\sigma_r - \delta\sigma_\theta}{2\delta\varepsilon_z} \tag{3.26}$$

$$E_{hr}^u = \frac{\delta\sigma_r(\delta\sigma_r - 2\delta\sigma_z) - \delta\sigma_\theta(\delta\sigma_\theta - 2\delta\sigma_z)}{\delta\varepsilon_r(\delta\sigma_r + \delta\sigma_\theta - 2\delta\sigma_z) + \delta\varepsilon_z(\delta\sigma_\theta - \delta\sigma_z)} \tag{3.27}$$

$$E_{h\theta}^u = \frac{\delta\sigma_r(\delta\sigma_r - 2\delta\sigma_z) - \delta\sigma_\theta(\delta\sigma_\theta - 2\delta\sigma_z)}{\delta\varepsilon_\theta(\delta\sigma_r + \delta\sigma_\theta - 2\delta\sigma_z) + \delta\varepsilon_z(\delta\sigma_r - \delta\sigma_z)} \tag{3.28}$$

$$G_{vh} = \frac{\delta\tau_{z\theta}}{\delta\gamma_{z\theta}} \tag{3.29}$$

Brosse *et al.* (2016) concluded that the more direct determination of E_h^u using Equations (3.27) and (3.28) generated more representative results than those indirectly derived from drained parameters, using Equation (3.8), although the reliability of the former approach may be reduced when high quality local strain measurements are not available. The above interpretation may be applied over the full extent of undrained shear tests to failure, so allowing both shear strength and stiffness anisotropy to be evaluated from the same suite of tests on nominally identical samples.

The undrained stiffness components that can be measured in a single HCA test depend on the number of total stress increments and strain components involved during

shearing. For example, in an undrained hollow cylinder 'triaxial' test with $\sigma_r = \sigma_\theta$ maintained constant and only an σ_z increment applied, only E_v^u can be determined, while in an hollow cylinder simple shear test with the three normal strains restraint ($\delta\varepsilon_z = \delta\varepsilon_r = \delta\varepsilon_\theta = 0$) and only the torsional strain ($\delta\gamma_{z\theta}$) allowed (see Nishimura (2006)), only the shear stiffness component G_{vh} can be measured. Employing a shearing path that controls the major principal stress increment directions while maintaining p and b, allows the Young's moduli components (E_v^u, E_{hr}^u, $E_{h\theta}^u$) to be obtained when no torsional stress is applied, provided it is assumed that the stiffness parameters are stress-path independent, even if anisotropic. Keeping the same assumption, all four components can be obtained simultaneously if a torsional stress is also applied.

Low loading rates (for example 0.3-0.5 kPa/hour stress increment rate corresponding to 0.0003-0.0006 %/hour strain rate in probing tests on London clay samples, see Gasparre *et al.* (2007b)) are required to ensure drained conditions in drained probing tests on clay-dominated materials. Undrained tests interpreted using the above approach provide a less time-consuming and more convenient method of determining undrained moduli and Poisson's ratios over both the linear and non-linear ranges. However, the undrained approach requires that the HCA's multiple pressure/stress controlling loops can be controlled precisely and simultaneously. Full optimisation of the measuring and testing systems is necessary to accomplish such tests successfully.

3.2.2 Shear stiffness anisotropy over non-linear range

Most soils only manifest linear elastic behaviour within a small kinematic (Y_1) yield surface and exhibit non-linear stress-strain behaviour once Y_1 is engaged (Jardine, 1992). The non-linear stiffness trends depend critically on stress path and effective stress level, loading rate and direction, principal stress axes direction, and other factors (Jardine *et al.*, 2004).

Jardine *et al.* (1986), Burland (1989), Mair (1993) and Clayton (2011) among others demonstrated that characterisation of non-linear stiffness is crucial to a range of geotechnical engineering problems and stiffness degradation trends need to be assessed over the wide range of strains. Engineering problems, such as the laterally loaded monopiles investigated in the PISA project, require both serviceability and fatigue

analyses covering the response from very small strain range through to the ultimate capacity conditions achieved after large deformations. Soil constitutive models and numerical methods applied to simulate such problems have to be able to capture and reproduce soil stiffness characteristics over full strain ranges (Potts & Zdravković, 2001).

Advanced soil testing apparatus equipped with body wave measurements and high resolution local instruments are able to capture the non-linear and anisotropic stiffness-strain degradation trends of geo-materials, provided the technical specifications are optimised to attain reliable and representative stiffness data, as demonstrated by Gasparre *et al.* (2014) and Brosse *et al.* (2015).

3.2.3 Shear strength anisotropy of soils

The significance of shear strength anisotropy in soils has long been recognised. Zdravković *et al.* (2001) and Zdravković *et al.* (2002) simulated both offshore suction caisson foundations and a full-scale embankment test adopting the anisotropic MIT-E3 constitutive model based on laboratory test results, including HCA tests. Considering the Saint-Alban embankment case, the undrained shear strength value S_u varied along the failure surface ranging from the highest values under near plane strain vertical compression strength (where the slip surface first entered the clay layer) to the lowest value under near plane strain extension condition at the toe, as shown in Figure 3-3. Capturing these trends allowed accurate failure predictions, whereas simulations adopting an isotropic model based solely on triaxial compression data overestimated the collapse height by 25%.

As further pointed out by Jardine *et al.* (2004) and Brosse *et al.* (2017), the patterns of anisotropy vary with soil type and over-consolidation ratio. Any rules of thumb relating averaged operational strength to index S_u values (triaxial compression or extension, field measurements) could depend critically on soil types and loading conditions and therefore have to be case specific.

Compared to soft soils, relatively few studies of shear strength anisotropy have been made with over-consolidated medium-to-high plasticity stiff sedimentary clays or lower plasticity tills. So the impact of their potential shear strength anisotropy remains unclear for a wide range of geotechnical engineering problems. The mechanical

behaviour of natural stiff plastic clays is often markedly brittle, and presents progressive failure mechanisms (Vaughan *et al.*, 1975, Burland, 1990, Jardine *et al.*, 2004, Kovacevic *et al.*, 2007). These characteristics, together with other factors, such as soil structure (laminations, fissures, and joints) and the impact of sampling disturbance, encumber the understanding of the anisotropic behaviour of such natural geo-materials.

Laboratory characterisation of strength anisotropy

Laboratory characterisation of shear strength anisotropy in the vertical plane usually requires control over and measurement of two factors: the major principal stress axis direction (α) within the vertical plane and the intermediate stress factor b. These requirements can be partly or fully met by testing apparatuses such as direct simple shear (DSS), true triaxial apparatus (TTA), hollow cylinder apparatus (HCA), and directional shear cell (DSC). Porovic (1995) provided a comprehensive review of the capabilities of those apparatus in studying strength anisotropy in terms of α and b.

HCA and DSC apparatus are two types of devices that are able to provide continuous control and measurement of both the rotation of the principal stress axis and the intermediate stress factor. However, a DSC requires relatively large specimen widths to minimise stress non-uniformity at the edges, and thus less favourable for testing intact low permeability clays. The apparatus's arrangements also make strain measurements difficult to achieve reliably.

However, the HCA specimens can be formed from high quality tube, rotary core or block samples and drainage through the specimens' relatively thin annular sections can be facilitated through filter paper drainage channels attached to the outer and inner walls of the specimens. As detailed by Nishimura (2006), hollow cylinder apparatus can also be arranged to perform simple shear tests which record α and b variations fully during shearing, rendering great advantages over conventional simple shear tests. High quality strain measurements can be more readily achieved in HCA apparatus, especially when local strain sensors are deployed.

In addition to those apparatus, triaxial apparatus can determine shear strengths under compression ((α, b) = (0˚, 0)) and extension ((α, b) = (90˚, 1)) conditions, which may indicate the potential scope of shear strength anisotropy and, together with direct shear tests, can provide useful datasets to help calibrate models for numerical analysis

and practical design. Laboratory determination of strength anisotropy has been attempted through triaxial testing on vertically, diagonally, and horizontally prepared clayed specimens (Bishop, 1966, Agarwal, 1968) and reconstituted sand specimens (Arthur & Menzies, 1972, Oda *et al.*, 1978). However, it has been recognised that, particularly for natural clay testing, such diagonally-formed specimens are subject to several aspects of inherent limitations, particularly the infeasibility of applying equivalent in-situ K_o stress conditions and the generation of bending moments under load (Saada, 1970, Molenkamp, 1998).

Extensive research programmes have been carried out at Imperial College since the 1980s to establish undrained shear strength anisotropy of reconstituted low *OCR* sand or artificial sand-clay-silt mixed soils using HCAs, as in the PhD studies by Symes (1983), Shibuya (1985), Menkiti (1995), Porovic (1995) and Zdravkovic (1996). The established trends of undrained shear strength S_u varying against α of K_o consolidated samples are shown in Figure 3-4, indicating overall pattern of decreasing S_u against α in a monotonic fashion. Similar trends have been observed with soft low *OCR* clays. For example, Lade & Kirkgard (2000) reported torsional HCA tests on natural San Francisco Bay Mud. Figure 3-5 displays the trend of effective friction angle against b and α values. In addition to HCA tests, directional shear cells (DSC) tests were also used to assess strength anisotropy of soft soils, for example Boston Blue Clay (BBC), as reported by Whittle *et al.* (1994).

The separate effects of intermediate stress factor b on shear strength are more conveniently investigated through true triaxial apparatus (TTA) due to its capability of continuous imposition of b from 0 to 1 during shearing. Kirkgard & Lade (1993) and Lade & Kirkgard (2000) reported TTA tests on soft normally consolidated natural San Francisco Bay Mud and demonstrated that the undrained shear strength varied substantially with b values and deviated from the failure envelopes predicted for an isotropic material, as shown in Figure 3-6.

3.2.4 Anisotropic behaviour of natural stiff clays and the effects of structure

Moving to studies of natural stiff high *OCR* clays, Hight & Jardine (1993) highlighted the importance of: (*a*) high quality sampling; (*b*) addressing natural structure from micro to macro level; (*c*) reproducing in-situ stress states and applying appropriate

effective stress paths during testing. Other aspects, such as specimen size, creep, loading rate and direction can also play important roles.

The anisotropic stiffness and strength characteristics of four Jurassic to Eocene high plasticity heavily over-consolidated stiff plastic clays (the London, Gault, Kimmeridge, and Oxford clays) have been comprehensively characterised at Imperial College London through extensive triaxial and HCA testing programmes (Gasparre, 2005, Nishimura, 2006, Minh, 2006, Hosseini Kamal, 2012, Brosse, 2012). Systematic laboratory triaxial studies on the cross-anisotropic linear elastic stiffnesses of six sedimentary clays from Japan were also reported by Nishimura (2014a, 2014b). These studies have highlighted the dependency of the natural clays' mechanical behaviour and anisotropic stiffness and shear strength characteristics on their structures, including those at the micro level (particle orientation, micro-shell or fossil inclusions) and at the meso level (fissures, laminations, partings or discontinuities). The potential effects of other variables were also investigated, including geological age, burial depth, sedimentary environment (marine, lacustrine, etc.), sampling technique and testing specimen size, as well as the possibly interacting effects between the micro- and meso-structures under varied stress paths and strain levels. Some of the key findings generated from the above studies are reviewed as follows.

Characteristics of stiffness anisotropy and effects of soil structures

The intrinsic microstructure of clays has been recognised as one of the dominant factors affecting their stiffness characteristics. Hosseini Kamal *et al.* (2014) and Brosse *et al.* (2016) reported that their Oxford clay particles exhibited a strong preferred fabric orientation in the horizontal direction and the samples also contained intensive horizontal-oriented shell beds, whereas the London clay presented moderate horizontal particle orientation but featured more intensive visible fissures, leading to the clays' varied degrees of anisotropy.

Considering London clay samples from different units (depths), Gasparre *et al.* (2007a) noted more packed and orientated clay structures in the samples from deeper strata (27 m), while those from shallow units exhibited more open and disturbed fabrics, indicating an increasing trend of anisotropy with depth. Figure 3-7 summarises the normalised bender element shear stiffnesses (G_{vh}, G_{hv} and G_{hh}) of intact London clay samples of different units at their estimated in-situ stresses (K_o = 1.8), and it is

evident that the intact samples of all the units exhibited significantly higher stiffness in the horizontal plane than in the vertical plane ($G_{hh} \approx 2G_{vh}$). The obtained $G/f(e)$-p' relationships also indicated the samples from deeper units possessed more packed structure, and possibly more advanced lithification as they exhibited clearly higher normalised shear stiffnesses (and slightly higher anisotropy G_{hh}/G_{vh}) than those of the shallow units, which is not simply an effective stress level effect.

Nishimura (2014b) also reported consistent trends for horizontal stiffnesses to be higher than those in the vertical plane in his tests on sedimentary clays of varied geological age, under both intact and reconstituted conditions, as shown in Figure 3-8. The inherent stiffness anisotropy was believed to be derived mostly from the clay particles' intrinsic nature (such as shape and inter-particle actions) and their consolidation histories. The study also revealed no clear dependency of the magnitude of shear stiffnesses nor their degrees of anisotropy on the clays' age and burial depth. Similar findings were also made by Brosse *et al.* (2016) for the four stiff clays with varied burial depth, as shown in Figure 3-9.

The effects of meso-structure on intact clays' shear stiffness was also highlighted by Brosse *et al.* (2016) in comparing with those of isotropically consolidated reconstituted samples. Depending on the meso-structure features (such as the intensity and orientation of discontinuities) as well as the effective stress levels, the effects could be 'positive', 'negative' or 'neutral', indicating that the intact soil structure does not necessarily lead to enhanced bender element stiffnesses.

Characteristics of shear strength anisotropy and effects of soil structures

The above HCA and triaxial studies have also characterised the stiff clays' anisotropic shear strength properties, also highlighting the effects of soil structures.

Nishimura *et al.* (2007) and Gasparre *et al.* (2007a) reported how S_u varied with α (while maintaining $b = 0.5$) with London clay samples taken at 5.2 m and 10.5 m bgl at the Heathrow T5 site, as shown in Figure 3-10. The overall trends for the plastic, high *OCR*, natural and geologically aged clays are significantly different from those seen in low-OCR *K*o-reconstituted soils (see Figure 3-4). The London clay from 10.5 m exhibited its minimum undrained shear strength at intermediate α values and maximum strength under $\alpha = 90^{\circ}$, whereas the strengths of the samples from 5.2 m covered a wider range, depending critically on the intensity and orientation of fissures .

Comparable hierarchies in undrained shear strength were observed for the other three stiff clays, as summarised by Brosse *et al.* (2017). As shown in Figure 3-11, the clays generally manifested their lowest strengths when α fell between 10˚ and 45˚, which was largely attributed to the presence of pre-existing horizontal or sub-horizontal fissures or discontinuities that provide weak features, while the highest strengths were met at α = 90˚. The four clays showed variable degrees of strength anisotropy, mainly due to their different micro- and macro-fabrics.

Gasparre *et al.* (2007a) reported triaxial peak shear strength envelopes for intact and reconstituted London clay samples, as presented in Figure 3-12. The peak states of the Eocene origin intact samples plot significantly higher than the intrinsic state boundary surface (SBS^*) for the reconstituted samples, clearly reflecting the natural clay's structured feature induced by its depositional history and long geological ageing. Meanwhile, the sub-set of samples that failed along pre-existing fissures manifested clearly lower strengths, and the circumstances that promoted such failure occurred more often in extension than in compression tests, indicating the directional dependency of fissure orientation on shear strength.

Hosseini Kamal *et al.* (2014) further demonstrated that, similar to the intact London clay samples, Oxford clay also manifested remarkable effects of structure. Its intact boundary surface extended far above the intrinsic local (isotropic) boundary surface (SBS^*). However, these 'positive' structural effects on peak strengths were not observed in the Kimmeridge and Gault clays which presented intact boundary surfaces that remained inside their SBS^* surfaces, primarily due to their closer spaced systems of fissures.

3.2.5 Figures

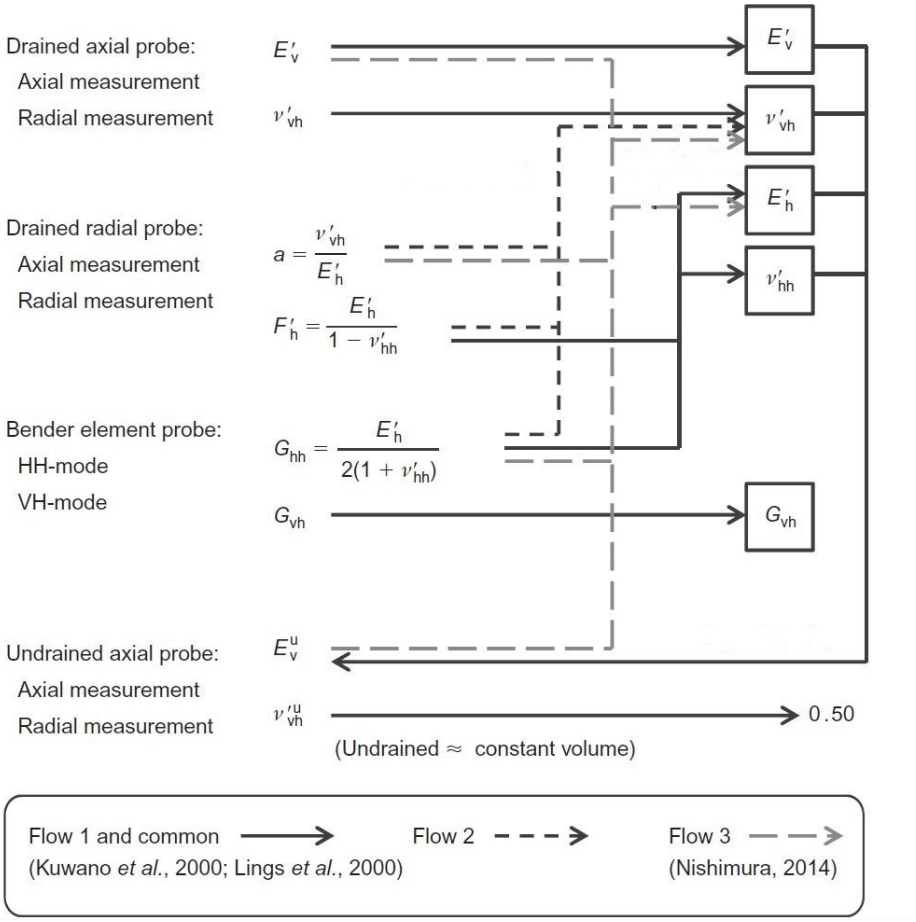

Figure 3-1 Probing test approaches for determining cross-anisotropic linear elastic parameters employing hybrid triaxial cells (Nishimura, 2014a)

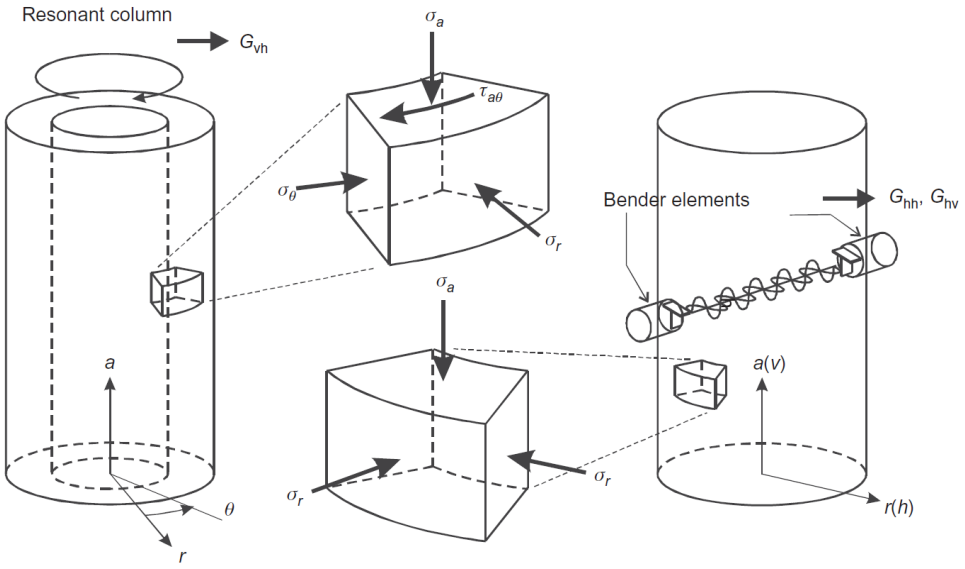

Figure 3-2 Coordinate systems in hollow cylinder (left) and triaxial tests (right) on cylindrical specimens (Gasparre *et al.*, 2007b)

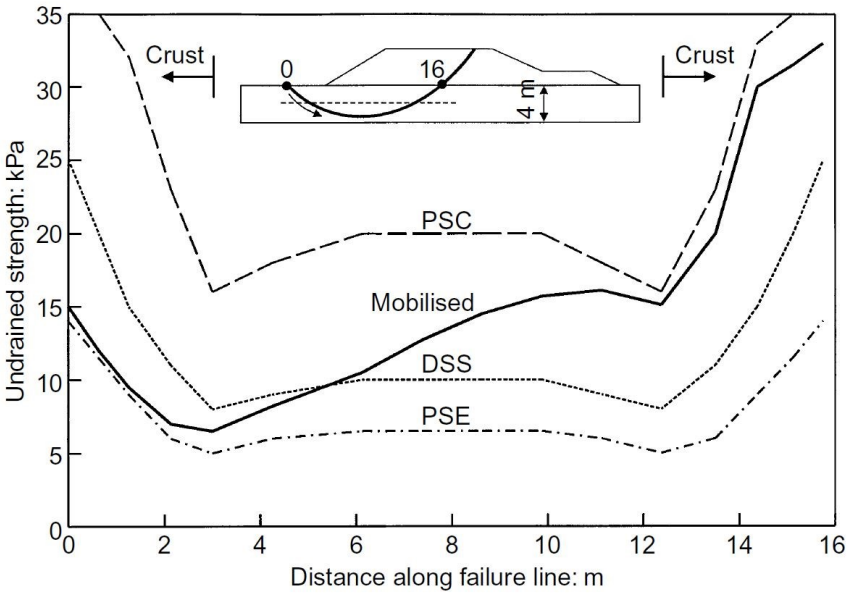

Figure 3-3 Mobilised undrained shear strength (S_u) values along failure surface compared with S_u profiles determined through plane strain compression (PSC), plane strain extension (PSE), and direct simple shear (DSS) (Zdravković *et al.*, 2002)

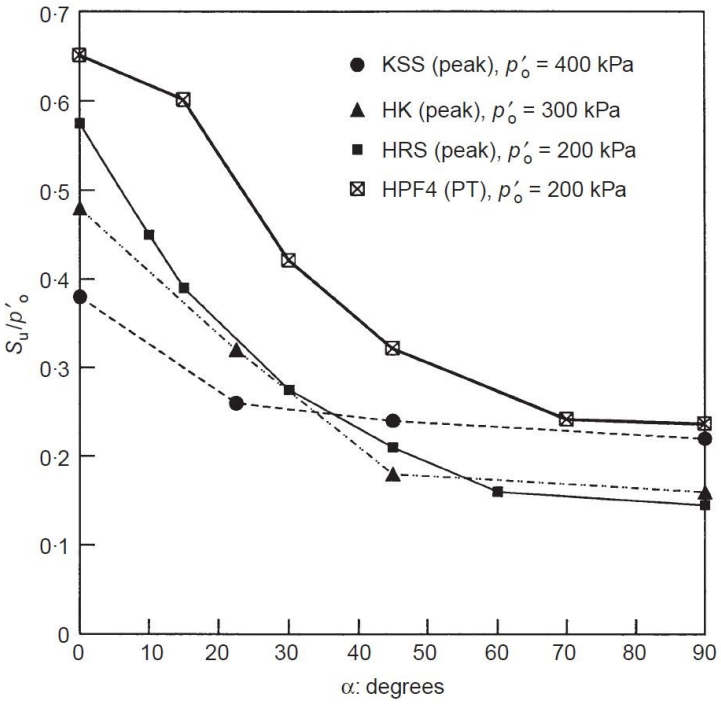

Figure 3-4 Study of undrained shear strength anisotropy at Imperial College for four K_o-consolidated materials at OCR = 1 (Zdravković & Jardine, 2001)

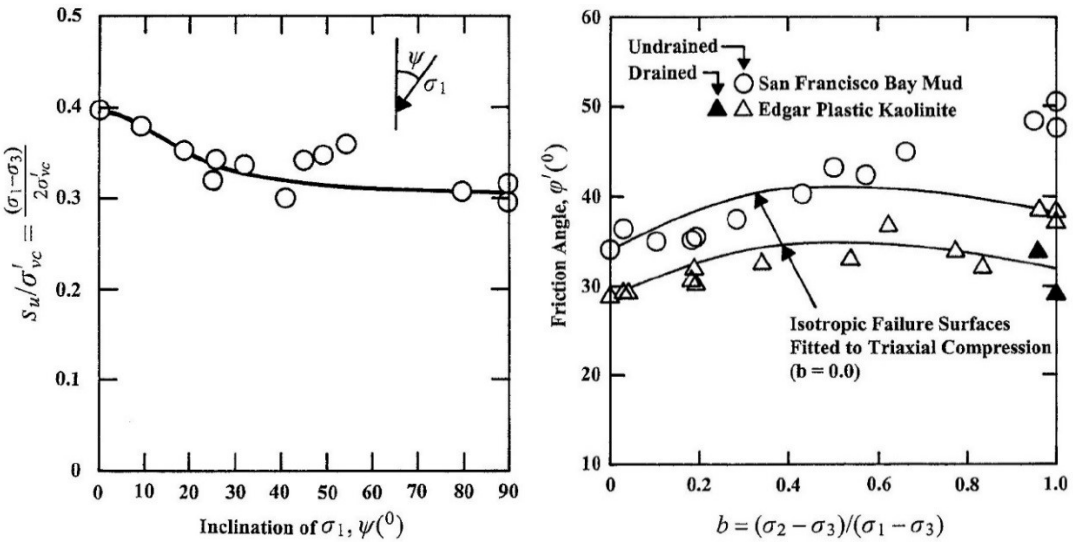

Figure 3-5 Variation of undrained shear strength and friction angle against α and b of natural low *OCR* San Francisco Bay Mud established through torsional HCA tests
(Lade & Kirkgard, 2000)

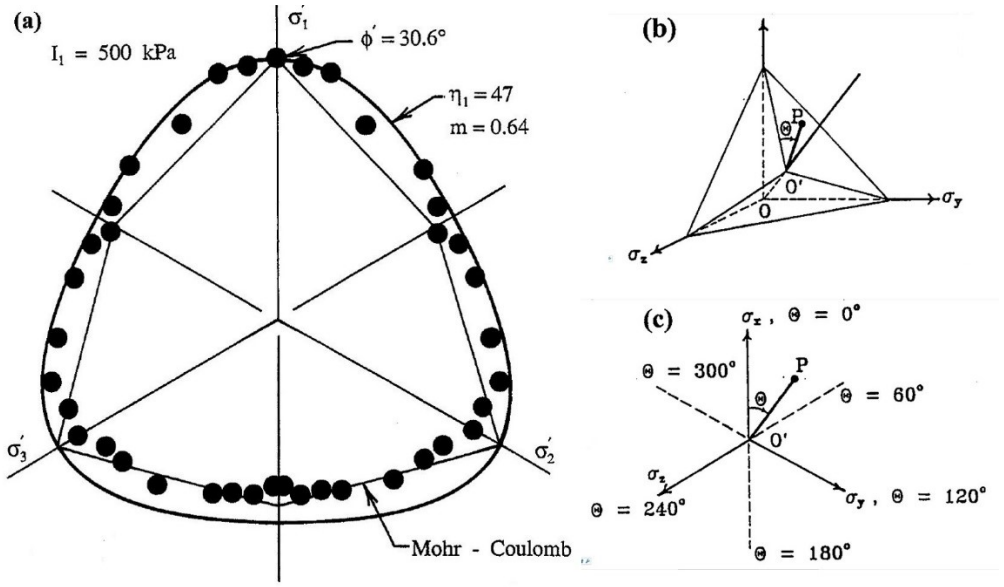

Figure 3-6 (a) Cross-anisotropic failure surfaces of natural San Francisco Bay Mud established through TTA tests; (b) principal stress space; (c) octahedral plane
(Kirkgard & Lade, 1993, Lade & Kirkgard, 2000)

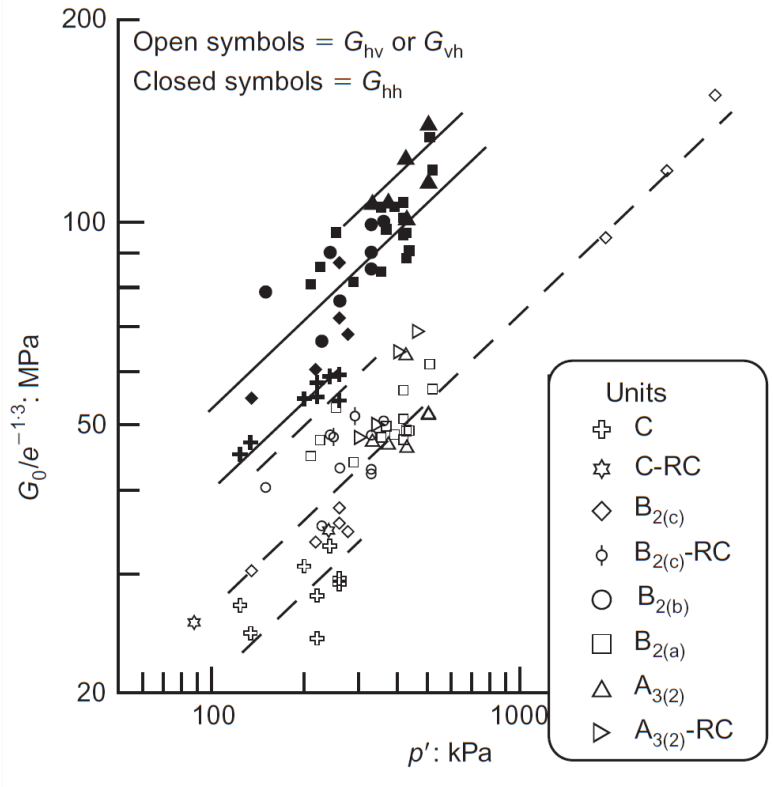

Figure 3-7 Anisotropic elastic shear stiffness of intact London clay samples from different units (Gasparre *et al.*, 2007a)

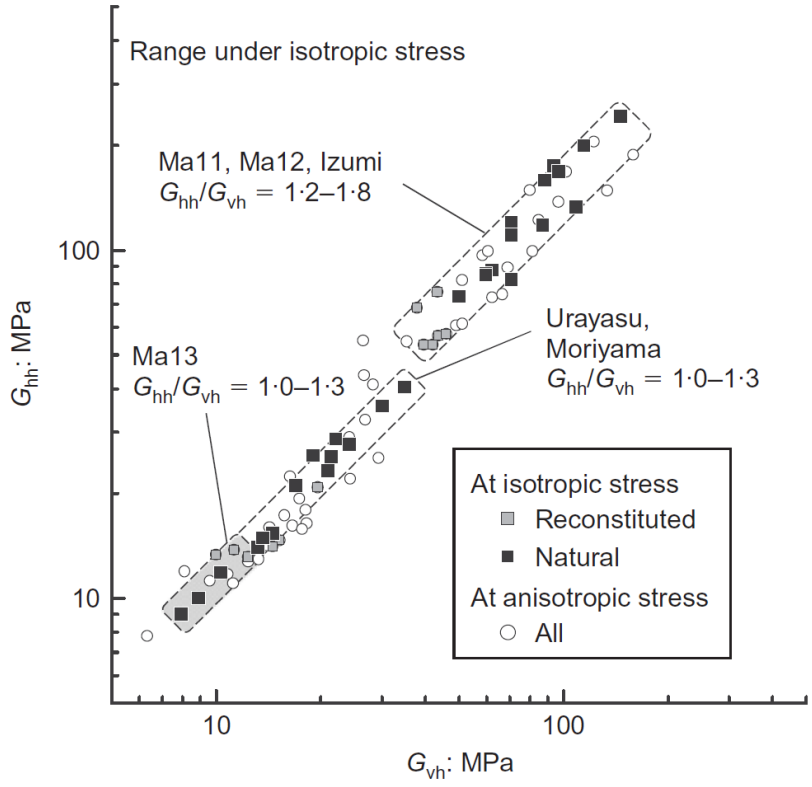

Figure 3-8 Drained elastic Young's moduli of natural sedimentary clays (Nishimura, 2014b)

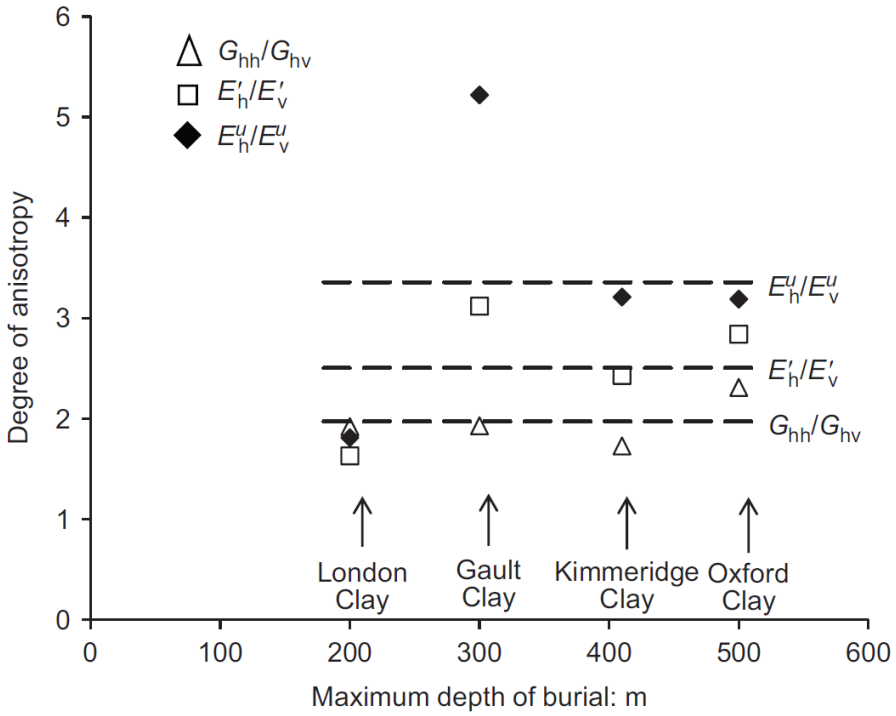

Figure 3-9 Degrees of elastic shear stiffness anisotropy of four natural sedimentary clays, in relation to their maximum burial depth (Brosse *et al.*, 2016)

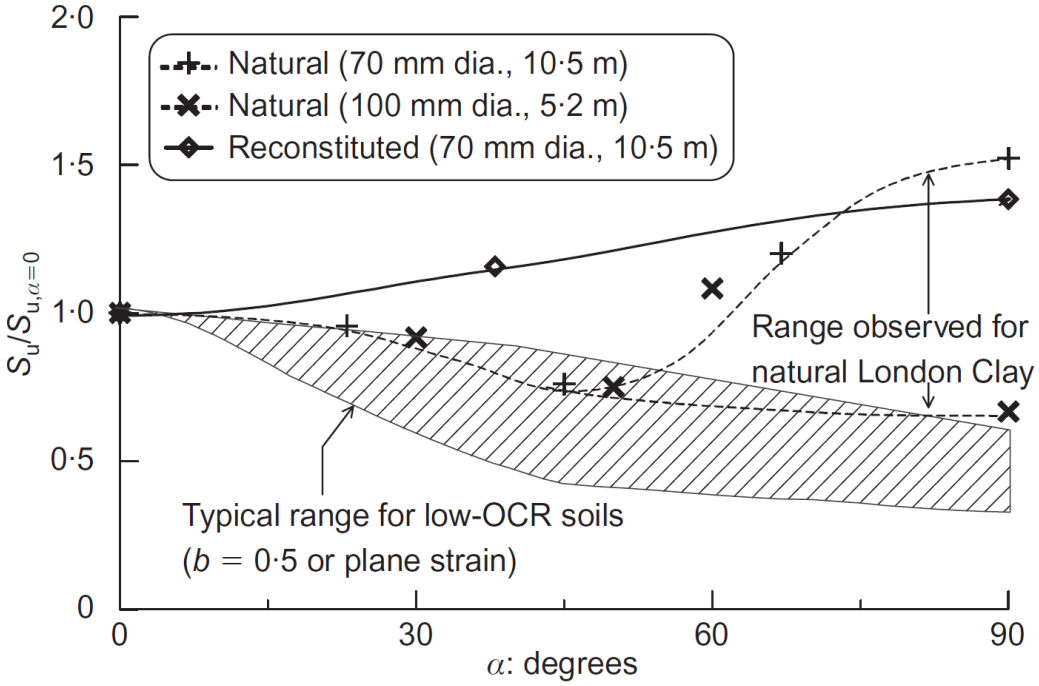

Figure 3-10 Variation range of S_u with α for London clay and low-OCR K_o-reconstituted soils (Gasparre *et al.*, 2007a)

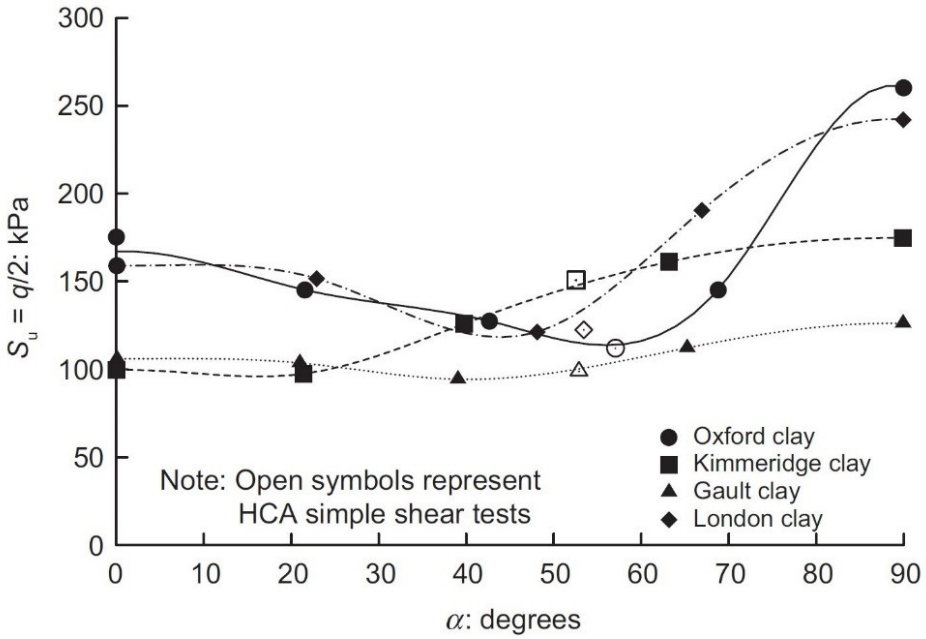

Figure 3-11 Undrained peak strength (S_u) of four Jurassic to Eocene stiff clays varying against α_f characterised through HCA tests (Brosse *et al.*, 2017)

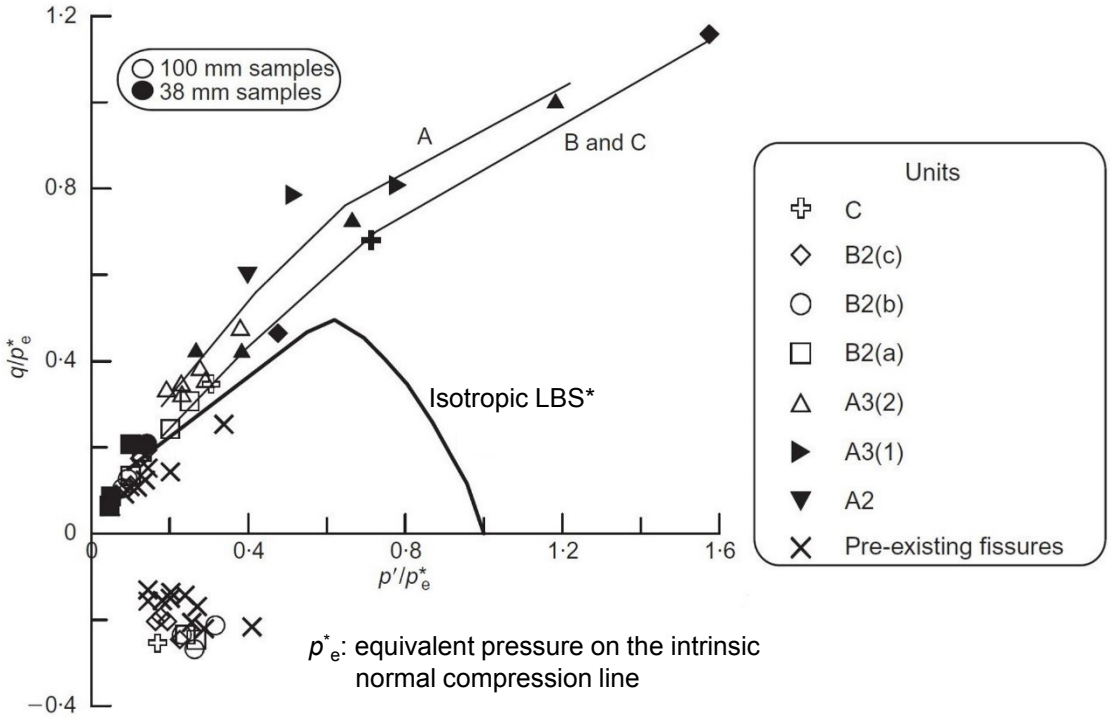

Figure 3-12 Peak strength envelopes of intact and reconstituted London clay, distinguishing samples that failed on fissures or other discontinuities (Gasparre *et al.*, 2007a)

3.3 Cowden till testing methodology and programme

This section sets out the testing methodology and programme for Cowden till, starting with detailed descriptions of specimen conditions, the challenges encountered and the corresponding countermeasures. Detailed information regarding the site profile (soil strata, ground water, K_o, etc.) and the sampling campaigns were set out in Section 2.2.1.

3.3.1 Challenges in forming Cowden till HCA specimens

The sandy, low plasticity, Cowden clay till contains frequent erratic rock inclusions and occasional fissured zones that developed as a result of its glacial deposition and subsequent weathering (Powell & Butcher, 2003). Previous investigations reported that the particles greater than 2 mm (gravel) are mainly composed of relatively soft chalk, with the rest mainly being harder flint, siltstone, limestone and shale. However, relatively hard often igneous rock inclusions were noted frequently at all stages of HCA specimen preparation, with some firmly embedded in the clay till matrix while others were concentrated in heavily fissured or weathered zones. Examples of these features are demonstrated in Figure 3-13. The inclusions led to severe drilling difficulties and low recovery rates in the Geobor-S sampling campaigns undertaken for the PISA project. In the retrieved block samples, igneous cobbles with dimensions of 10-15 cm were found in some extreme cases.

Another important feature of the macro-structure of the Cowden till is the presence of fissures, which are likely to weaken substantially the mass shear strength of the till and reduce the probability of forming testable hollow cylindrical samples. One example of the highly fissured zones containing large gravel particles and decayed roots encountered in Block D2 (2.5 m depth) is shown in Figure 3-14. The fissured till was also affected by weathering, with some areas presenting modified clay with a grey/blue colour compared to the light brown surrounding soil. It was also noted that most fissures were vertical or sub-vertical, and so hampered any form of trimming or drilling. Additionally, the presence of decayed roots frequently resulted in complete block splitting and collapse of the soil matrix in all directions. Unfortunately, the "Layer D" layer block samples were found to include more intensive fissuring than other layers and more than ten of the Author's attempts to form specimens from this layer resulted in failure. The fissuring suggested that Layer D could represent a

boundary or transition layer formed during the till's initial deposition.

The stony and fissured nature of the Cowden till posed great difficulties when attempting to form good quality solid cylindrical specimens, and the process of drilling through the specimens to form the inner hollow cavity posed further problems. Figure 3-15 presents an example of prematurely terminated sample preparation due to an unforeseen large gravel fragment appearing in the centre part of the specimen. Two examples of cylindrical specimens that failed during the drilling of the inner cylinder are illustrated in Figure 3-16.

The difficulties encountered led to gradual improvement and optimisation of the sample preparation methods taken to reduce operational mishaps. Great effort was taken to identify soil blocks with minimal gravel content that would facilitate specimen formation and drilling. This involved both visual inspection and X-ray CT scanning of the block samples at the beginning of the programme. However, it was recognised that avoiding samples that contained gravel fragments inevitably led to a bias in which the HCA specimens had higher fines and lower coarse fractions than are typical in the till. The potential effects of the sampling bias are discussed latter.

3.3.2 Trial X-ray CT Scanning of the block samples

X-ray computerised tomography (CT) scanning techniques have been used extensively in many areas of research and practical application that exploit their capabilities in providing three-dimensional non-destructive visualisation of X-ray attenuation within objects, which can be related to many physiochemical properties of the objects (Ketcham & Carlson, 2001). In geotechnical research, great interest has arisen in applying this technique to investigate micro-level particle morphology and fabric (see examples by Fonseca (2011)), and soil-fluid coupling phenomenon (Taylor, 2016). This technique has also been employed for clay materials to map the density profiles of small cored marine sediment samples (Orsi & Anderson, 1999) and large Sherbrooke-type (25 cm or more in diameter and 30-35 cm in height) block samples (Sau *et al.*, 2015).

Rotary core samples with cylindrical shape and modest dimensions (commonly 100 mm diameter) are naturally suitable for all-around X-ray scanning. However, the Cowden block samples had initial dimensions of 460 mm (L)×440 mm (W)×400 mm

(W) and weighed around 110 kg each, which made them laborious to handle and infeasible to scan directly, even with a medical-level X-ray scanner with a large (450 mm diameter) effective view field. Therefore, block sample pre-cutting had to be performed. This process, as shown schematically in Figure 3-17, included two cuts along a top horizontal line and a middle vertical line. The ultimate block size could fit into the maximum field view of the X-ray scanner.

The pre-cut and resealed blocks were then set up for CT scanning, which was performed in a Universal Systems, Inc., HD-350E X-ray CT scanner. The normal set-up for scanning cylindrical samples and the modified arrangement for the large block samples is shown Figure 3-18. The obtained X-ray attenuation data can be further manipulated and interpreted to produce 2-D or 3-D views of the blocks, with the aid of self-developed algorithms.

The above X-ray scanning procedures were performed on several block samples. An example that located gravel particles and cavities from reconstructed X-ray images is illustrated in Figure 3-19. Gravel particles with variable sizes and shapes are seen randomly distributed in one of the cross-sections of Cowden block C3 (1.5 m bgl). Inspection along two lines revealed abrupt changes of X-ray attenuation in the areas containing stones or cavities. 3-D images can be constructed with those cross-section profiles for each scanned block and complete views of the size, shape, and location of large gravel particles encased in the blocks can be attained.

The obtained 3-D distribution of gravel particles inside the block samples provided useful information to assess gravel contents and locate less stony soil volume, which, in some cases, were successfully applied to guide sample trimming and eventually led to specimens free of large gravel inclusions. However, the X-ray scanning technique itself is subjected to a range of artefacts and limitations (see examples by Ketcham & Carlson (2001) among others), especially when applied to large cuboid objects, although the process can be improved to some extent through deliberately object-specific calibration of the scanner, optimised scanning procedures, or enhanced image post-processing techniques. Scanning of relatively slender or ideally cylindrical block samples is preferable, but this involves undesired pre-cutting of the soil blocks. The large block size also restricts the scanning resolution. Gravel fragments with dimensions less than 4 mm could not be resolved clearly. The limited scanning resolution also made it impossible to generate reliable information regarding the

location and intensity of fissured zones in the block samples, which was found to be critical to successful specimen preparation.

The X-ray scanning results and the observations made in pre-cutting the soil blocks from all six depths led to the judgement that, unlike fissures, which seemed to be heavily concentrated in the block D (2.5 m bgl) layer, there was essentially no clear trend of gravel content variation with depth or direction. Large volumes of stone-free till could not be assured. This judgement was supported by wet-sieving results which showed comparable gravel contents (6.3% to 8.2%) in rotary core samples from depths between 0.74 m to 10.2 m bgl.

The research aim was to investigate strength and stiffness anisotropy of Cowden till through multiple tests on nominal identical specimens from the same (or at least close) depth. This requirement could not be met with single specimens taken from a range of depths that might be identified as apparently less stony by X-ray scanning. Therefore, it was decided that the specimens for the main HCA testing programme would be formed from just two 110 kg blocks available from the E layer (3.0 m bgl). This target was eventually achieved through optimised specimen trimming, drilling and setting up procedures, as detailed below.

3.3.3 HCA specimen preparation and setting-up procedures

Preparation procedures for hollow cylinder specimens mainly consisted of cutting, trimming, drilling and in some cases forming radial grooves. These procedures were well documented by previous researchers working on stiff mudrocks (see examples by Porovic (1995), Nishimura (2006), Minh (2006) and Brosse (2012)), and are briefly described below. The main focus below is on the techniques developed to obtain HCA specimens from the stony till blocks. Specimen preparation and setting-up procedures for the Author's triaxial testing were largely the same as described by Ushev (2018).

Block cutting

The first stage of specimen preparation involved forming prisms of appropriate 90 mm × 90 mm × 200 mm dimension from the large soil blocks. Use of mechanical band saws or chain saws turned out to be infeasible due to the stone content and plastic nature of the soil matrix. Several attempts with a band saw ended up with blunt and distorted blades and severely disturbed soil zones where large gravel particles were

pushed along cutting lines and dragged aside into surrounding soil volume. Frequently, the blades tended to become jammed and the cutting became difficult to advance when soil started to clog and accumulate between blade teeth, even with regular cleaning of the blade. After trials and failures, it was decided that a large hand saw with a toughened blade (of thickness around 2 mm) and hardened teeth was the most appropriate and safe tool for the cutting purpose, although the process was time-consuming and physically laborious. However, the solution was found encouragingly suitable for Cowden till considering its shear strength and ductile nature, compared to the stiffer and more brittle mudrocks. The soil can be readily smeared and remoulded along cutting lines without inducing clogging or tensile cracks.

An electrical circular saw was used first to cut the wooden boxes along pre-drawn lines, and a hand saw was then used to gradually cut through the block from different edges until two split blocks were formed. It was noted that the gap formed in between the two blocks during cutting tended to expand, and quite often the soil in the centre part would crack and fall apart in tension. This problem was resolved by anchoring several wooden bars on the two split blocks to reduce any relative displacements during cutting. In the case where large gravel particles were met, cutting was attempted from all around the gravel inclusion until the block split around the gravel areas without inducing excessive disturbance.

Throughout the cutting process, the soil blocks were retained firmly by protective plywood boxes or boards. Once cutting edges were formed, several layers of cling film and wax were immediately applied to seal the exposed edges, followed by plywood boards that resealed the box.

Specimen external trimming

The trimming procedure was essentially the same for the hollow cylinder specimen and Ø100 mm triaxial specimen. The soil prisms were uncovered from the protective plywood boxes and then fitted into a soil lathe where they were gradually trimmed and shaped into the targeted cylinder dimensions. Similar to the tool kit used by Brosse (2012), a set of hand tools was used for the trimming purpose, including knives, wire saw, flat bar knife, and rigid bar, as shown in Figure 3-20. The knives were regularly sharpened to facilitate the trimming process. Trimmings from the ends and edges of the specimens were collected for moisture content measurements. Sample diameters were

measured regularly and trimming continued until diameters of 71±0.5 mm were achieved along the specimen lengths.

Trimming had to be slowed down when encountering any gravel inclusions or fissured areas to minimise disturbance, and if possible, gravel particles were carefully removed with tweezers as trimming progressed and the remaining cavities refilled with remoulded till matrix material. However, in the cases where the soil was heavily fissured or the central part was occupied by large gravels, the specimen had to be abandoned and trimming restarted with another soil block.

Specimen internal drilling

Successfully trimmed cylindrical specimens were then prepared for drilling using a metal working lathe. The specimen was wrapped in layers of cling film and placed in a split aluminium mould that was clamped to encase the sample. Thin layers of latex membrane were routinely placed on the surface of the specimen to provide an adequate frictional grip during the high-speed drilling.

A set of drilling and reaming tools was used to bore the specimen and form the inner cylindrical cavity. A small diameter drill (Ø11.1 mm) was advanced first from one end of the specimen through its whole length, and then replaced by larger diameter drills to gradually ream the cavity until the desired final inner diameter (Ø38 mm) was achieved. Soil material trapped in the grooves of drills was collected for additional moisture content measurements. Meanwhile, as used by previous researchers, for the final stage of drilling, the larger-diameter drill (Ø32.5 mm) was replaced by a specialised boring bar, which imposed uniform point-edge reaming and thus minimised the generation of tensile forces. During boring, a compressed air line was used to continuously blow air through the inner cavity to flush out drilling debris and thus avoid clogging at the cutting edges, although this also induced undesirable specimen drying.

Not surprisingly, the drilling procedures were frequently interrupted, and in many cases prematurely terminated, when gravel inclusions were encountered in the specimens. Although some relatively soft inclusions, such as chalk or sandstone fragments could easily be cut in-place by the drills without inducing major disturbance, harder inclusions remained unbroken and tended to be dragged forward and pushed aside into surrounding soil mass, rupturing the specimen and causing great disturbance.

Some counter-measures were developed. When the drills encountered gravel particles, the operation was stopped and careful inspection made inside the cavity to check the feasibility of removing the obstruction. If this turned out to be impractical, the specimen was inverted and drilling was attempted from the opposite end. These procedures were performed iteratively and some specimens were successful rescued in this way, although the overall drilling time was greatly extended.

Successfully drilled specimens were prepared for any torsional shear applications by forming six radial grooves (4 mm deep) using a saw at the two ends while the main part was retained in the split mould. The grooves were made to accommodate the vanes of the porous stone and assured sufficient coupling for torque. This procedure was only applied to the specimens subject to torsional forces in the later testing stages, with the purposes of saving time and avoiding unnecessary disturbances to the sample ends.

The specimens that completed all preparation stages successfully were ready to be setup and tested in the hollow cylinder apparatus. After many trials and errors, the probability of successfully trimming solid cylindrical samples from the two “Layer E” blocks grew from less than 10% to around 40%, and that of obtaining qualified hollow cylinder specimens from drilling these cylinders to near 50%, resulting an overall final successful rate of around 20%. The failure in trimming of four out of five specimens imposed a major restriction on the number of tests that could eventually be completed. Around 6-7 hours were needed to successfully shape a cylindrical sample from the soil blocks and prepare for subsequent drilling, while another 1-2 hours were required to drill the inner cylindrical cavity under normal circumstances.

Setting-up procedures for HCA tests

Specimen setup commenced immediately after the completion of the trimming stages. The sample weight and dimensions (outer/inner diameter, height) were recorded, together with water contents determined from the trimmings. The dimensions of the specimen were measured at multiple locations and averaged to account for any irregularities.

All the HCA parts and accessories were properly cleaned, saturated or greased (if needed) and water tubes were flushed beforehand. Grids were pre-drawn on the outer membrane to help depict sample deformation patterns. The inner membrane was first installed and sealed at the base of the cell chamber. The specimen was then installed on

the base porous stone and the inner membrane was passed through the inner cylinder. Several damp filter papers (around 10 mm width) were then placed vertically and evenly on the outer surface of the specimen to facilitate drainage. The top cap was then placed on the specimen and the outer and inner membranes were then fitted and sealed with O-rings. The proximity transducer cage was placed and adjusted to give close readings at the best resolution range. The positions of the cables and tubes and the height of the proximity transducer were adjusted and optimised according to the test scheme, aiming to reach the maximum available travel of the apparatus.

After the specimen was sealed and isolated, a suction (around 20 kPa) was applied to the base of the specimen to remove air entrapped in between the specimen and membranes. The valve to the suction supply was then switched off and the pore pressure was monitored to check any leakage through membranes or tubes. After the air-tightness of the specimen was verified, the cell chamber was closed, and the inner cell and half of the outer cell chamber were filled with water. As recommended by Brosse (2012), before pressurising the specimen, a small amount of water was circulated from the volume-gauge through the bottom porous stone and connecting tubes to eliminate any air entrapped in the system.

With careful planning and preparation, the overall setting-up procedure could be completed in around five hours. However, the process had to be extended if any mishaps occurred, such as leaking through membranes.

3.3.4 Appraisal of specimen preparation and setting-up procedures

Specimen preparation and setting-up involved a series of complex and time-consuming steps which naturally raised concerns regarding their potential impact on the mechanical response of the material. Three areas of potential impact were identified as: mechanical disturbance; sample drying and swelling; and sampling bias. These issues and the corresponding countermeasures are addressed below.

Mechanical disturbance

Mechanical disturbance could occur at several stages of the preparation and setting-up process. Although unlikely to be avoided completely, disturbance was largely alleviated when versatile (although inefficient) hand tools were used for cutting or trimming that effectively avoided dragging or pushing gravel particles as well as

disturbing fissured soil zones. The disturbance was further reduced as the soil blocks diminished in size (and became easier to handle) and when the Author's dexterity increased through practice. The soil blocks were maintained sealed and protected with careful attention given to avoiding any tensile crack opening.

Disturbance during specimen drilling was most likely to occur when the drill hit gravel during high-speed rotation. The impact was reduced by carefully removing gravel with tweezers wherever possible and by advancing the drilling from both ends of the specimen. Although time-consuming, these counter-measures were found to be effective and increased the rate of successful specimen formation.

It was fortunate that mechanical disturbance was also partly restricted by the ductile nature of the material, which enabled the specimens to accommodate a certain level of local deformation without inducing rupture or major tensile cracks. This feature contrasts with brittle high plasticity stiff clays that are more susceptible to mechanical disturbance, particularly tensile fracturing.

Sample drying and swelling

Soil drying commenced from the trial pit sampling stage on site when soil blocks were exposed in air before being sealed. Further drying occurred in the preparation stage in which specimens were trimmed or drilled without being fully sealed for periods of 6-7 hours. The frequently encountered gravel fragments and fissures slowed down the trimming and drilling process severely and extended the exposure time. It was also noted that the fissured zone tended to desiccate more quickly than the intact soil matrix.

A series of counter-measures was developed to alleviate soil drying. The main stages of specimen preparation were carried out in a non-airconditioned preparation room with relatively high humidity which helped maintaining soil moisture. During cutting, the soil blocks were enclosed over all their edges and once formed, the cut edges were immediately sealed. Whenever cut surfaces or specimens were exposed to air, fine water spraying was applied frequently to increase the humidity of the environment. After the specimens were enclosed by latex membranes, water mist was continuously sprayed on the outer membrane until the cell chamber was filled.

Further processes led to inadvertent soil swelling in the Author's testing, although some took place on specimen set up through imbibing water from the saturated porous

stones and leakage through the membranes. Excessive water was wiped from the porous stones with paper tissue to reduce swelling at the ends. In the cases where the porous stones equipped with vanes, the specimens were essentially supported by the vanes and a gap was left between the specimen ends and the porous stone, which effectively avoided end swelling. Leakage through membranes was largely eliminated by carefully checking (by eye) before testing to identify any imperfections (such as bubbles or unusual thin spots) in the membranes.

To assess soil drying and swelling, the initial suction values of all tested specimens were recorded and integrated with those obtained from triaxial tests performed on both rotary core and block samples. The long specimen preparation times were not the only factors attributing to specimen drying. Other factors, such as the presence of gravel particles or fissures, and also the shrinkage properties of the matrix material, also played important roles. Those aspects were further investigated through filter paper tests on a group of intact and reconstituted samples, as further discussed in Section 3.4.1.

3.3.5 Gravel contents and appraisal of sampling bias

Noting the long preparation times and other factors involved in preparing HCA specimens, concern was raised whether the eventually tested specimens could be representative of the behaviour applying under undisturbed in-situ conditions. The potential issue of sampling bias on sample composition was addressed by checking the gravel contents of the untested intact soil blocks, specimens that failed at different preparation stages, and the successfully tested HCA specimens. These investigations showed that the HCA specimens had systematically lower gravel contents than applied, on average, to the soil mass in-situ. Further assessments were made between the HCA stiffnesses or strengths and those from other sources, such as triaxial and in-situ measurements. These aspects are considered below, before moving on to report the detailed HCA testing programme that was eventually achieved.

Gravel contents

Initial gravel content checks were performed on a range of soil blocks and the tested specimens using wet sieving tests, determining the soil mass percentages retaining on 2 mm aperture standard sieves. The results are presented in Table 3-1 and Figure 3-21.

Four groups were categorised for comparison, based on the intensity of gravel inclusions and the stage of specimen formation. Group A represents two cases where 10±2% gravel contents were noted in heavily fissured and weathered stony block samples that offered little scope for forming testable HCA specimens. As noted earlier, cobbles of up to 150 mm diameter were encountered in the soil block samples. Geobor-S sampling was found to be impossible in such Group A layers. Group B is populated by rotary core samples from five depths at the site, and represents the limiting level of gravel intensity at which Geobor-S samples could be successfully drilled and recovered on site with 6.3 to 7.9% gravel contents.

Group C includes soil blocks and putative HCA specimen cylinders where trimming was attempted but failed. This group showed a wider range of gravel contents (3-7%), and indicates the level of gravel inclusions that triggered failure in sample trimming or HCA internal cavity drilling. The gravel fragments collected from this group were markedly smaller (no greater than 4 mm in diameter) than those from Group A or B. Finally, Group D covers the ranges applying to hollow cylinder specimens that were successfully prepared and tested. This group manifested notably lower gravel contents (2-4%) and minimum particle size.

The above results confirm that hollow cylinder specimen formation was only possible in soil volumes with gravel contents below 4%. The preparation process effectively eliminated all specimens with higher gravel contents. The sampling process was unintentionally selective and the tested specimens were more matrix dominated than is typical in-situ.

Appraisal of sampling bias

Checks were also made to assess the degree to which the imposed biased sampling and HCA specimen preparation processes affected the shear stiffnesses and shear strengths of the Cowden till.

Considering first the dynamic shear stiffnesses determined from different approaches ($G_{z\theta}^{RC}$, G_{vh}^{BE} and G_{vh}^{SCPT}), it was found that the HCA resonant column $G_{z\theta}^{RC}$ of the 3.0 m depth specimens were around 45% lower than the laboratory bender element G_{vh}^{BE} measurements on similar depth specimens, while the G_{vh}^{BE} data showed a close match with in-situ SCPT G_{vh}^{SCPT}. The HCA specimens tested under undrained 'triaxial' conditions with equal inner and outer cell pressure (HCATXC tests) also

exhibited small-strain compression Young's moduli E_{vu0}^{HCA} (as later included in Table 3-7) that were 38% lower than the triaxial linear-elastic secant Young's moduli E_{vu0}^{TXC} reported by Ushev (2018) from locally instrumented tests on rotary core samples from similar depths. However, this may reflect the HCA tests' lack of local axial strain measurement system and their poorer ability to capture precisely the initial linear elastic stiffnesses that applied at axial strains less than 0.002% due to potential end bedding effects and the limit of the HCA instruments' resolutions.

The till's shear strength characteristics were also seen to be affected. As later shown in Figure 3-43, the shear strengths of the HCA TXC specimens (S_u^{HCATC}) were lower by an average of around 25% than those of the standard triaxial tests (S_u^{TXC}) on samples from similar depths.

However, a further factor to consider is a small error made by the Author in assessing the site's ground water profile. This led to a marginal underestimation of the σ_v' and p_0' values applying to the '2.93 m' HCA specimens by 7.3 kPa and 8.8 kPa, respectively, giving values that were 16% and 14.5% lower than those applied to Ushev (2018) triaxial tests. The lower effective stresses applied could partly explain the above clearly lower HCA $G_{z\theta}^{RC}$ and E_{vu0}^{HCA}. The $G_{z\theta}$-p' correlation established from resonant column tests later reported in Figure 3-30 indicated a 2% correction to the G_{vh}^{RC} values, indicating still 25-35% lower than in-situ G_{vh}^{SCPT} and 30-40% lower than the bender element G_{vh}^{BE}.

The differences in gravel contents offers one explanatory factor. As mentioned, HCA testing on the stony Cowden till was only possible with soil volume of low (2-4%) gravel content. The larger triaxial specimens (100 mm diameter) in which the bender element shear stiffness G_{vh}^{BE} measurements were made, could include gravel contents of around 8%, which were clearly higher than those of the HCA specimens but were comparable with those of the in-situ undisturbed soils.

The low values of HCA $G_{z\theta}^{RC}$, E_{vu0}^{HCA} and S_u^{HCATC} may also reflect the influences of mechanical disturbance involved in the cutting, trimming and drilling stages of specimen formation despite the various counter-measures implemented. Potential effects of sample size and geometry may also play a role. Ushev (2018) reported that on average his triaxial tests with 100 mm diameter specimens gave 30% higher elastic vertical Young's moduli (E_{vu0}^{100mm}) than those with 38 mm diameter samples

(E_{vu0}^{38mm}). He attributed these variations to the larger specimens' more representative element volumes and potentially higher gravel contents as well as their lower susceptibility to mechanical disturbance on trimming. The HCA specimens, on the other hand, featured relatively thin walls with nominal thickness of only 16.5 mm that made them susceptible to mechanical disturbance, although the specimens' soil volume fell between that of the 38 mm and 100 mm diameter solid cylindrical triaxial specimens.

The different shear modes and frequencies generated in resonant column and bender element tests might also contribute to the differences seen between $G_{z\theta}^{RC}$ and G_{vh}^{BE}. Shear waves generated from the bender elements transmit through specimens' central volume that was normally less affected by mechanical disturbance. The resonant column tests, on the other hand, measure global stiffness across the vertical planes that were more likely to incorporate 'softening' effects from any disturbed zone included in the HCA specimens. The resonant column tests also applied far slower wave frequencies (always less than 150 Hz) than the bender element systems which often operated in the frequency range of 3-12 kHz.

The key aim of the HCA programme was to investigate the potentially anisotropic behaviour of Cowden till. The sampling bias, although undesirable, did not necessarily distort the degree of stiffness anisotropy. Indeed, as shown later in Section 3.8.2, comparisons with triaxial probing tests revealed the HCA and triaxial samples' similar degrees of stiffness anisotropy at small strains. This finding encourages the view that the sampling bias and disturbance did not alter too greatly the Cowden till's mechanical anisotropy.

Table 3-1 Gravel contents of Cowden till soil blocks and tested specimens

Group	Description	Gravel content range [%]	PSD test No.	Dry mass [g]	Gravel content [%]	Depth [m]
A	Heavily fissured and weathered stony soil zones identified in the block samples; no cutting or trimming attempted	8-12	1	2093.5	12.2	2.9
			2	2667	8.5	2.9
B	Successfully rotary cored samples recovered from Cowden Borehole 01; gravel content measured on samples from varied depths	6-8	1	2000(1)	7.1	0.74
			2		6.5	3.5
			3		8.2	5.93
			4		7.9	7.3
			5		6.3	10.2
C	Soil prisms or solid/hollow cylinder specimens that failed in the attempts to form hollow cylinder specimens; No.1-3: soil blocks with or without trimming attempts; No.4-6: cylindrical samples, trimming terminated due to gravels or fissures; No.7-9: hollow cylinder specimens failed during drilling	3-7	1	1515	4.9	2.9
			2	2533.5	4.4	2.9
			3	2688	4.3	2.9
			4	1490	5.4	2.9
			5	1638.5	4.8	2.9
			6	1394	5.3	2.9
			7	1038	4.8	2.9
			8	1075.5	6.6	2.9
			9	1015.5	3.3	2.9
D	Successfully prepared and tested hollow cylinder specimens	2-4	1	891.5	2.75	0.5
			2	972.5	3.8	2.9
			3	1104.5	4.1	2.9
			4	1051	4.1	2.9
	Typical specimens triaxial tests (Ø100 mm, H 200 mm)			3000 (2)	-	-
	Typical specimens triaxial tests (Ø38 mm, H 76 mm)			165 (2)	-	-

Note:

(1) Initial dry mass data not available; shown data (2000 g) indicates minimum mass requirements for wet sieving tests on materials with gravel inclusions (BS 1377-2: 1990).

(2) Assuming bulk density: 2.2 Mg/m^3, water content: 15%.

3.3.6 HCA testing programme and procedures

The research programme aimed to characterise potentially anisotropic undrained strength and stiffness behaviour of the Cowden till. Ideally, multiple combinations of (b, α) values would be covered in four dimensional stress space so that the net effects of both principal stress axis direction (α) rotation and relative intermediate principal stress level (b) could be fully investigated, as has been explored previously for example by Zdravkovic (1996) or Nishimura (2006).

However, this was not achievable in the current testing due to the challenges imposed by specimen preparation and the limitations of sample availability. Therefore, the main programme was performed on specimens from a single depth (2.9 m bgl.) and concentrated on a b value of 0.5 while covering a range of α values from 0 to 90˚, supported by HCA 'triaxial' and 'simple shear' tests. The Author also performed tests in triaxial equipment with bender elements and undertook a small-stress probing programme to investigate anisotropic stiffness behaviour in triaxial stress space over a wider depth range, adding these tests to the earlier experiments by Ushev (2018).

HCA Testing programme

The main testing programme and the corresponding test conditions are summarised in Table 3-2, featuring the HCA tests on Cowden till samples from 2.9 m depth, supplemented by bender element and probing tests using the fully-instrumented 100 mm specimen diameter triaxial apparatuses. Prior to shearing, all the samples were re-consolidated to their estimated in-situ K_o effective stresses.

Two alternative schemes shown in Figure 3-22, as employed by Nishimura *et al.* (2007) for the study of London clay using hollow cylinder apparatuses, were considered for the current study. The first scheme, which was employed by previous researchers (including Menkiti (1995), Zdravkovic (1996) and Rolo (2004) among others), featured undrained shearing with constant α, b and p values proceeded by stages of consolidation to target stress states and principal stress rotation to desired α values. However, Nishimura (2006) and Brosse (2012) argued that the α-rotation stage may induce undesirable excessive strains to the samples, which potentially might result in failure, particularly with brittle materials under high initial deviatoric stresses. The second scheme involves consolidation to the target stress states and b values before the samples were sheared at a constant orientation of principal stress increment $\alpha_{d\sigma}$ up to

failure, without involving any α-rotation stage prior to final shearing. The second scheme was adopted for the Cowden till tests.

As noted already, the mechanical response of Cowden till is primarily ductile. Bringing the samples to failure at target α values might necessitate large shear strains (> 20%) and involve continuous rotation of α up to large ultimate failure strains. HCA experiments are not well suited to large strain testing. As explained later, steps were required to allow for the possibility that failure had not developed fully before the HCA tests were terminated. However, the initially estimated in-situ deviatoric stress (q or σ_z-σ_θ) for the specimens from 2.9 m depth was relatively low ((σ_z-σ_θ)/2 = -9.5 kPa), in comparison with the final undrained shear strength (≈ 130 kPa) in triaxial compression. In fact, the constant $\alpha_{d\sigma}$ shearing stress paths largely coincided with the alternative constant α shearing path at large shear strains. Nevertheless, adopting this shearing scheme made the current programme compatible with the stiff brittle clay studies by Nishimura (2006) and Brosse (2012), and so facilitated the comparisons between the behaviours of these different types of clay.

The single b value of 0.5 adopted for the main test programme is often thought to represent approximately plane strain conditions. The HCA tests covered α values from 0 to 90˚ and avoided the 'no-go' zones of HCA testing set out by Symes (1983). As noted in Table 3-2, HCA simple shear tests on the till culminated with b values close to 0.5 and α values slightly greater than 45˚, allowing these tests to be broadly compatible with the $\alpha_{d\sigma}$ controlled type test controlled under b = 0.5 and α_f = 45˚.

HCA testing procedures

The HCA tests involved seven main stages which are outlined below.

Initial p' stage In this stage, the sample was isotropically pressurised under undrained conditions, with the inner and outer cell pressures simultaneously increasing by a rate of 30 kPa/hour up to usually 300 kPa. The specimen were left overnight for pore pressures to stabilise. The final stable pore pressure was recorded and the difference between the cell pressures and recorded pore pressure was then taken as the sample's initial suction (p').

Saturation stage The specimens should ideally reach their target degree of specimen saturation before consolidating the samples to target stress states. Saturation is usually checked by aiming for the Skempton parameter B ($\Delta u/\Delta p$) ≥ 0.95. This can

often be achieved by elevating back pore pressure up to 300-350 kPa over extended periods while maintaining constant p_0'.

However, it turned out to be difficult to reach the target B value by simply raising the back pressures. Most specimens started with relatively high initial suction (p_0') values (around 250 kPa) and the safe limit of outer cell pressure was around 630 kPa. Therefore, the highest pore pressure available to saturate specimens while maintaining the initial p' was less than 400 kPa.

Several counter-measures were applied to increase specimen initial saturation. Before the initial p' stage, a stage of water circulation was performed to remove air entrapped in the bottom porous stone and water tubes. Additionally, water in the volume-gauge was also regularly replaced with fresh deaired water.

Nevertheless, the target B value of 0.95 could not be reached before starting re-consolidation in several tests. In those cases, a two-stage consolidation scheme (as detailed below) had to be implemented to ensure the target B value could be achieved by the end of re-consolidation.

Anisotropic re-consolidation No attempt was made to reproduce the probably complex glacial depositional stress history of the till or any subsequent geological processes. Instead, a simplified one-step stress-path controlled consolidation scheme was applied to re-consolidate the specimens from the isotropic initial p' states to the estimated K_o in-situ stresses. For the specimens that had reached their target B value in the saturation stage, the re-consolidation stage usually induced swelling by decreasing the cell pressures by a rate of -2 kPa/hour while maintaining constant pore water pressure. Regular shear stiffness ($G_{z\theta}$) measurements were made using the resonant column (RC) system while progressing along the re-consolidation path.

A two-stage consolidation strategy was applied for the specimens that could not reach the target B value in their saturation stages. In the first stage, the cell pressures were kept constant and the pore pressure was elevated by 100-150 kPa at a rate of 2 kPa/hour, followed by a second stage of consolidation in which the pore pressure was held constant and the cell pressures were reducing at a rate of -2 kPa/hour until the in-situ stress state was reached. B checks performed either at the end of the first or second consolidation stage confirmed that the target B value was finally reached in all cases. This approach ensured that sufficient specimen saturation was achieved in the

end of consolidation, but may potentially led to errors in the strains recorded during consolidation. However, the errors are believed be minimal compared to overall consolidation strains, considering the large stress changes imposed during the re-consolidation (see Table 3-2).

Typically, re-consolidation to in-situ stresses required 3-4 days. The specimens were left to creep under constant effective stresses until the strain rates decreased to less than 1/100 of the nominal shearing rate that was to be applied in the subsequent shearing stage. The adopted limiting creep rate of 0.0005%/hour was usually reached within further 3-4 days. Resonant column measurements were regularly taken during the creep stages, and the resonant frequency variations decreased to less than 0.5 Hz per day as the creep criterion was approached. The cell chamber water was changed on a 24-hour basis during the re-consolidation and creep stage, following the same scheme as Nishimura (2006) and Brosse (2012).

Undrained *b*-change stage As discussed, a single b value of 0.5 was adopted for the undrained $\alpha_{d\sigma}$ -controlled shearing. Since the in-situ stresses corresponded to a state of $b = 1$, $\alpha = 90^{\circ}$, stages of b-change from 1 to 0.5 were required. The stages were performed under undrained conditions, and the b value was slowly reduced from 1 to 0.5 at a rate of -0.1/hour while maintaining constant p, q and α. The sample was then left for 24 hours to creep before the subsequent shearing was applied. This creep period was found sufficient and only minimal strains were developed during these stages.

Undrained $\alpha_{d\sigma}$ -controlled shearing The main testing programme consisted of undrained $\alpha_{d\sigma}$-controlled shearing and simple shear tests. The key variables of the $\alpha_{d\sigma}$ tests (axial force, outer and inner cell pressures and torque) were controlled to keep constant values of p and b. In the tests with $\alpha_f = 0^{\circ}$ and 90°, the shearing was initiated by imposing constant rate of axial strain. In other tests, the samples were sheared under constant rates of torsional shear strain. In both cases, the shearing strain rate applied was based on a deviatoric strain rate of around 0.15%/hour.

Resonant column measurements were performed frequently throughout the shearing stage to trace the variations of dynamic shear stiffness. No de-aired water changes were made for the outer cell chamber until shear strains exceeded 10% to avoid any disturbance at the early stage of shearing. Regular water changes were resumed afterwards.

Undrained HCA simple shear Undrained simple shear HCA tests were undertaken on two samples from their in-situ stresses, without undertaking any undrained *b* change stage. The testing configurations adopted were largely the same as employed by Nishimura (2006), Brosse (2012) and Aghakouchak (2015). Sample volume change was prevented by applying undrained conditions, while the radial and circumferential strains were repressed by maintaining a constant inner cavity volume. The vertical (axial) displacement was restrained mechanically through a rigid bar that blocked axial movement of the shaft, and additional constraint was imposed by a feed-back algorithm implemented in TRIAX to compensate compliance and limit axial strain below 0.002%. In such a way, the vertical, radial, and circumferential straining of the samples was restrained, allowing only torsional shear strains. Nishimura (2006) presented detailed descriptions of the above procedures and offered comparisons between HCA simple shear and conventional simple shear tests.

Post-test recording and processing Shearing was terminated when the maximum available apparatus displacement limits were reached, or when the sample had deformed too severely to make any sensible measurements. After each test, the sample deformation pattern was recorded and visual observations performed to identify any rupture or shear band, with the aid of the grids pre-drawn on the outer membrane. The water contents and dry masses of the specimens were measured to back analyse sample initial conditions (water content, initial void ratio, saturation degree, etc.).

Table 3-2 Summary of the tests performed on Cowden till specimens and the corresponding testing conditions

Apparatus	Test code	Sample	Depth [m]	Type	In-situ stress[kPa]				α at peak	b_0[2]	b_u[2]
					p_0'	q_0	$\sigma_{v'}$	$\sigma_{h'}$	q[1] [°]		
ICRCHCA	CA0005	Block E2	2.93	Constant $\alpha_{d\sigma}$	51.6	19.4	38.7	58.1	0	0.5	0.5
	CA2305	Block E2	2.93	Constant $\alpha_{d\sigma}$	51.6	19.4	38.7	58.1	23	0.5	0.5
	CA6705	Block E1	2.87	Constant $\alpha_{d\sigma}$	50.6	18.9	38.0	56.9	67	0.5	0.5
	CA9005	Block E2	2.93	Constant $\alpha_{d\sigma}$	51.6	19.4	38.7	58.1	90	0.5	0.5
	CASS	Block E2	2.93	Simple shear	51.6	19.4	38.7	58.1	48.2	1.0	0.47
	CATC	Block E1	2.87	HCA TXC	50.6	18.9	38.0	56.9	0	1.0	0
	CATC2	Block E1	2.87	HCA TXC	50.6	18.9	38.0	56.9	0	1.0	0
	CTSS	Block A2	0.50	Simple shear	19.3	7.3	14.5	21.8	46.7	1.0	0.49
Triaxial (100 mm OD)	CTX1	Core BH3	5.1	BE, PB, TXC[3]	93.2	35	69.9	104.9	0	1.0	0
	CTX2	Core BH3	12.5	BE, PB, TXC[3]	216	5.7	212.3	218	0	1.0	0

Notes:

[1]. $q = \sigma_1 - \sigma_3$.

[2]. b_0 and b_u are b values at beginning of undrained shearing and at ultimate state.

[3]. BE: bender element tests; PB: drained and undrained triaxial probing tests; TXC: triaxial compression shearing.

3.3.7 Figures

Figure 3-13 Examples of large hard inclusions encountered in Cowden till block samples

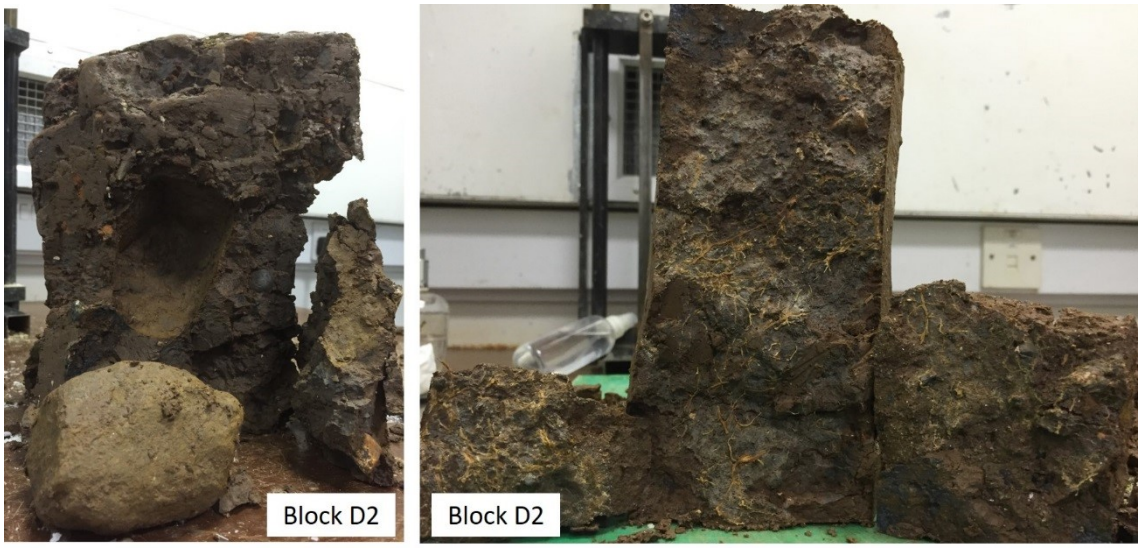

Figure 3-14 Extreme cases of highly fissured zones with excessive gravel particles or decayed roots noted in Cowden Block D2 (2.5 m bgl.)

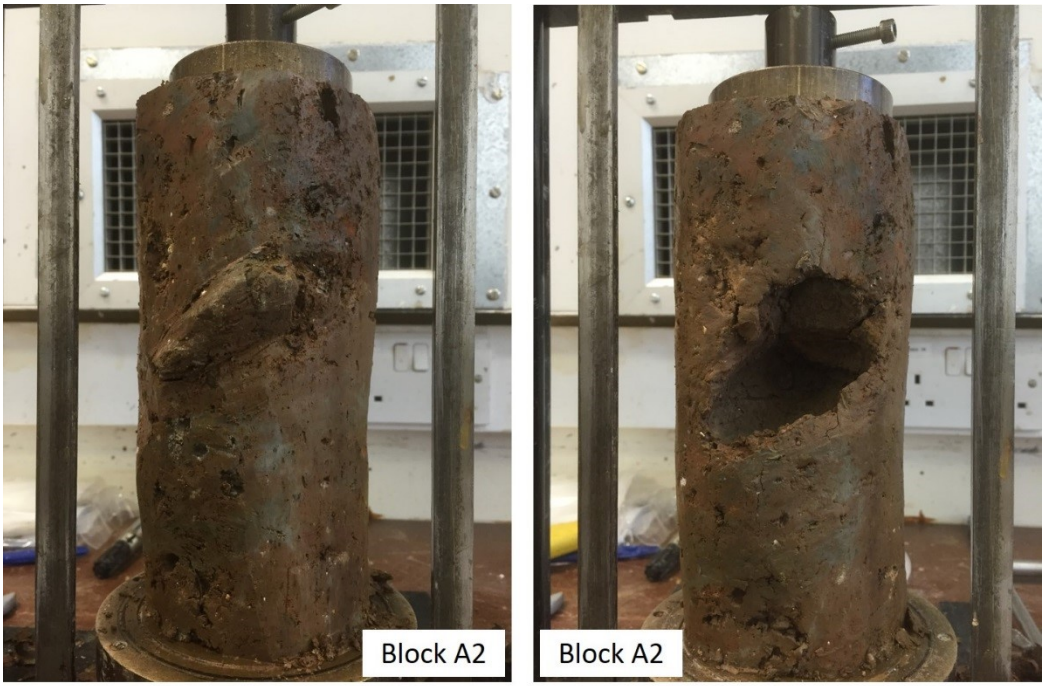

Figure 3-15 Failure of specimen preparation due to unforeseen large gravel inclusion (longest dimension > 70 mm)

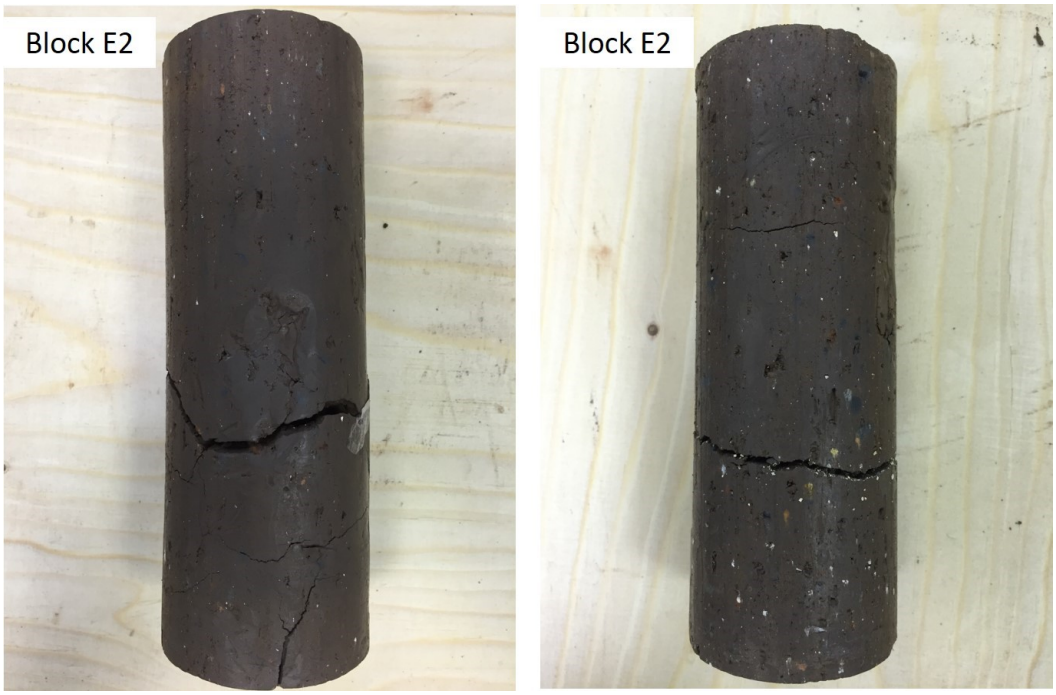

Figure 3-16 Loss of two promising specimens from Block E2 due to extended cracks induced by drilling of inner cylinder cavity

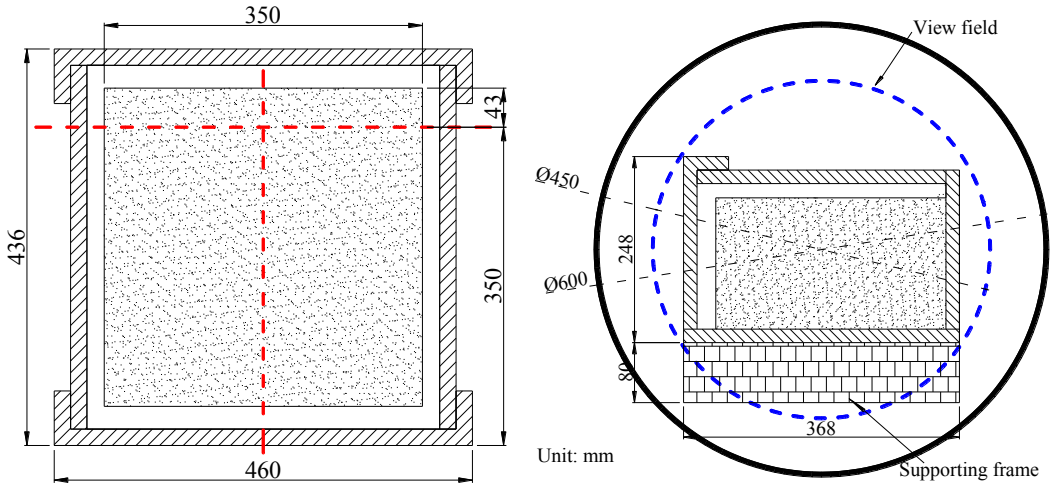

Figure 3-17 Pre-cutting of Cowden block samples to fit into the maximum field of view (Ø450 mm) of a X-ray CT scanner

Figure 3-18 Scanning of block C3 in a medical level X-ray scanner: normal set-up for small cylindrical samples (left) and modified set-up for large soil blocks (right)

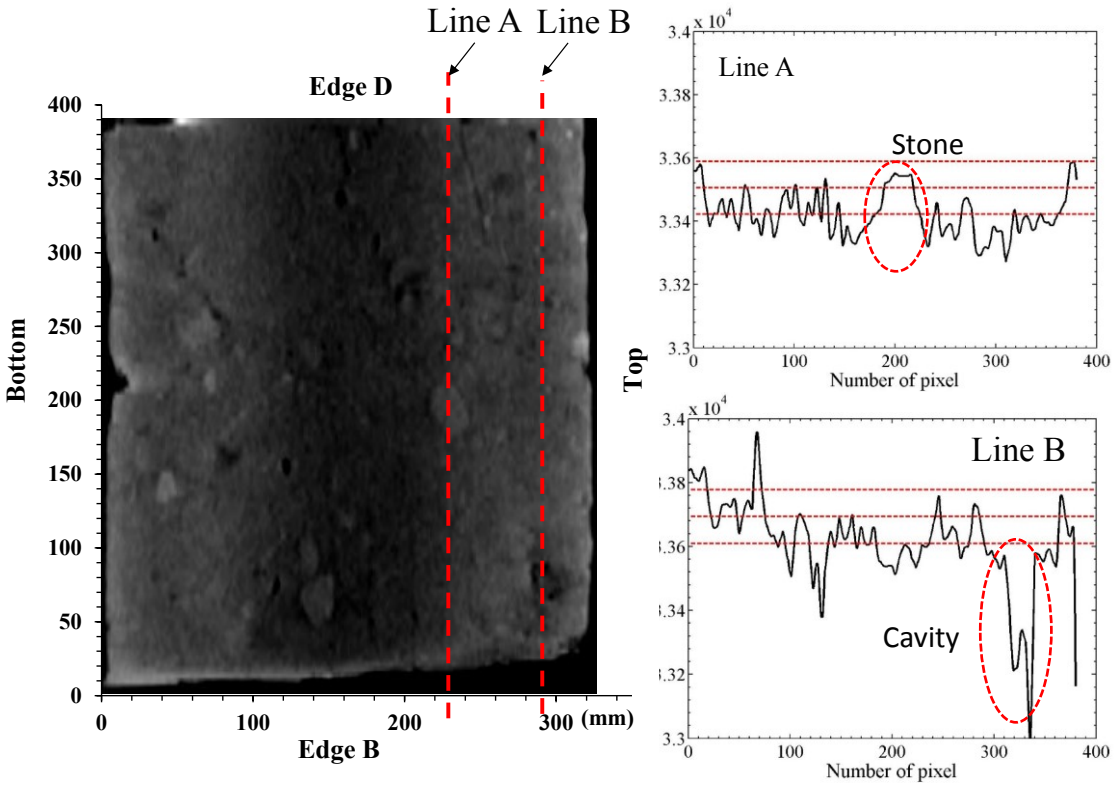

Figure 3-19 Results of X-ray CT scanning on Cowden block C3: re-constructed cross section showing locations and dimensions of gravels or cavities (left); abrupt change of grey values along two lines at locations where stone and cavity could be located (right)

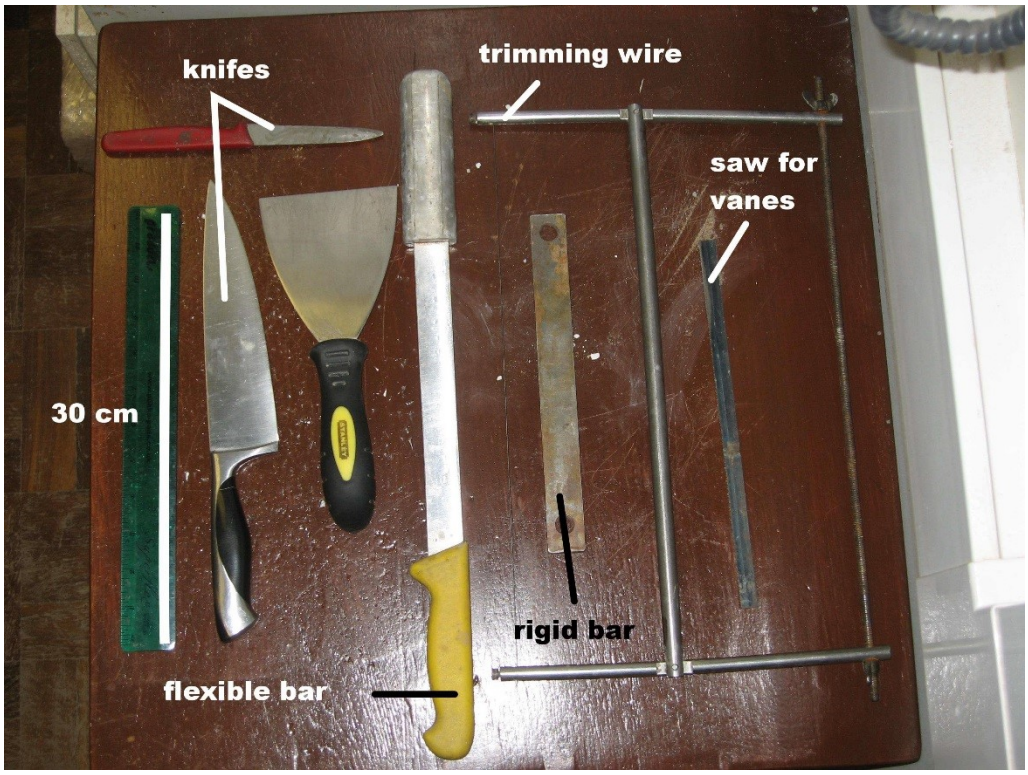

Figure 3-20 Collection of tools for trimming and forming soil specimens (Brosse, 2012)

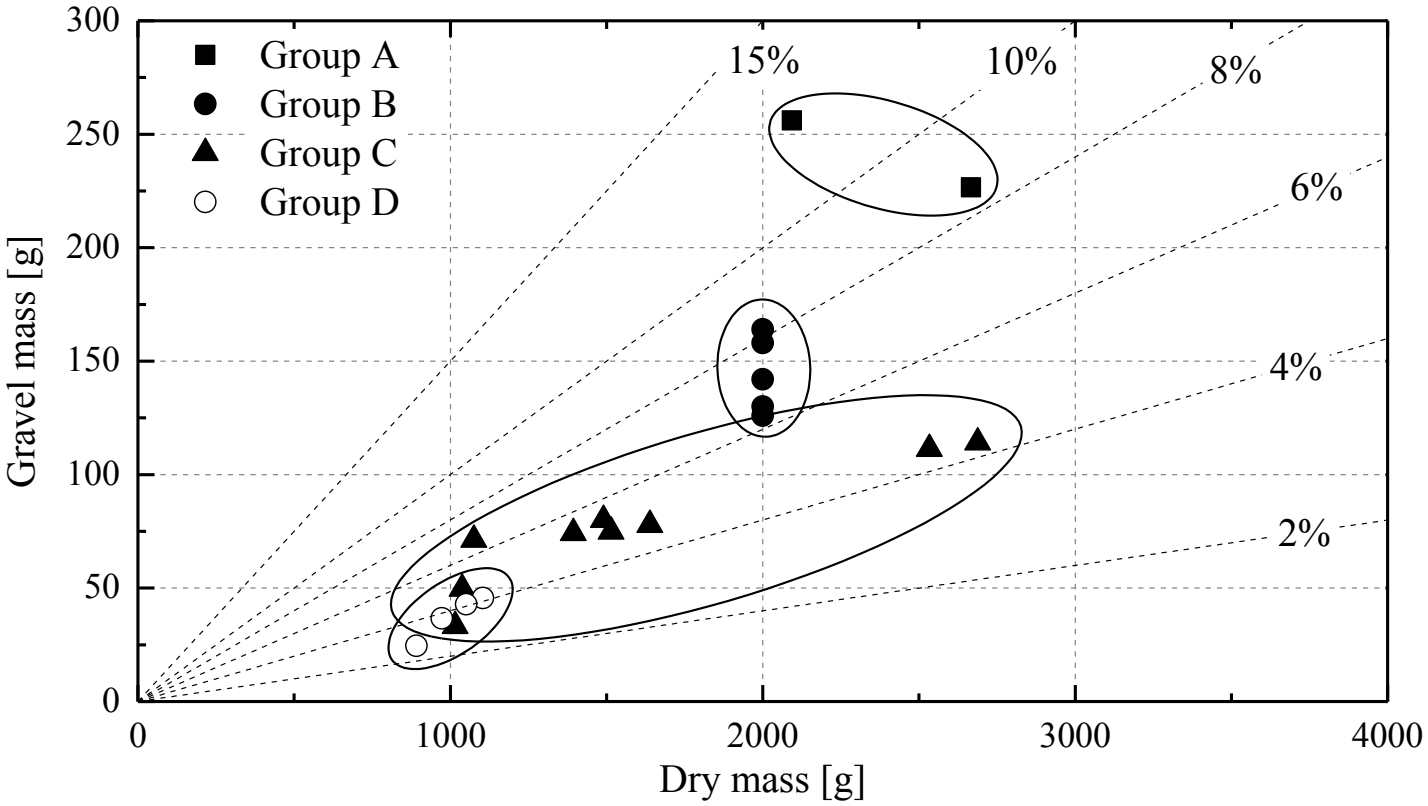

Group A: Heavily fissured stony soil blocks
Group B: Successfully rotary cored samples by Geobor-S system
Group C: Failed soil prisms or cylinders in trimming or drilling stage
Group D: Successfully tested hollow cylinder specimens

Figure 3-21 Gravel contents of four groups of Cowden till samples

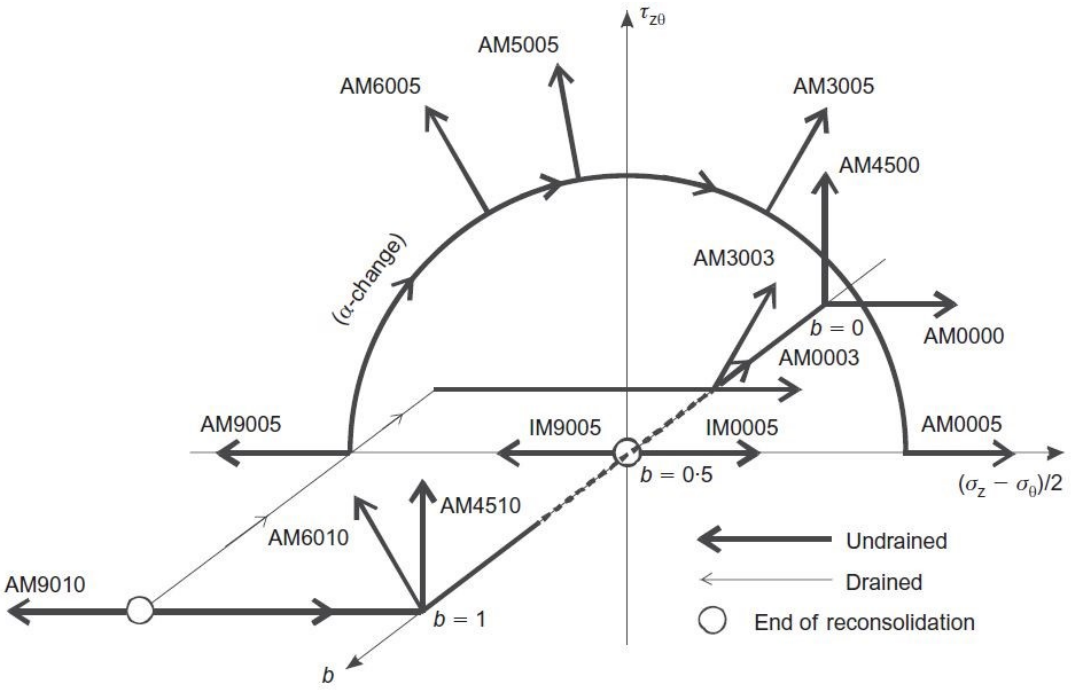

(*a*)

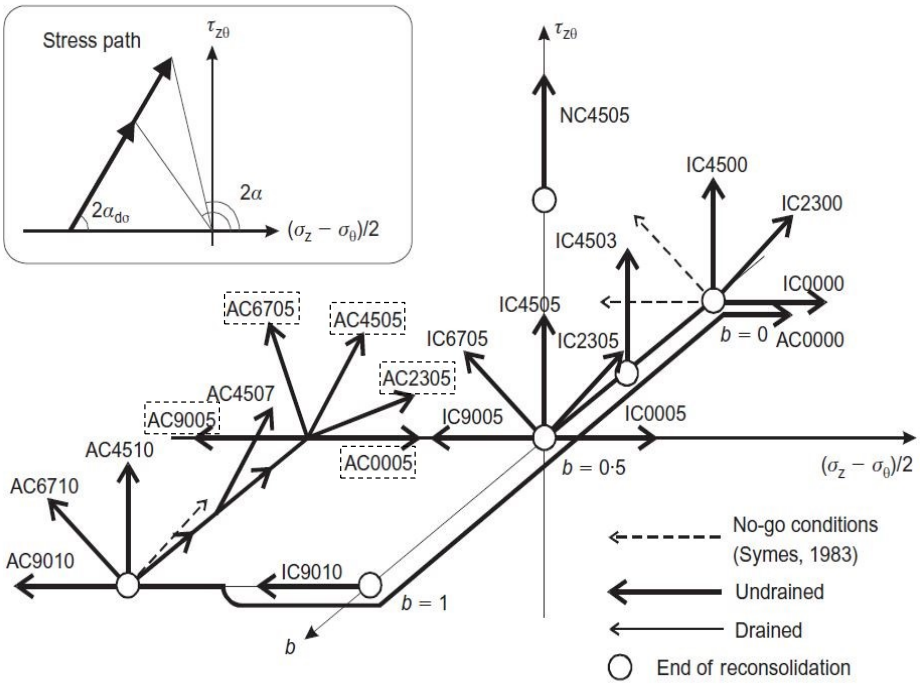

(*b*)

Figure 3-22 Two testing schemes adopted by Nishimura *et al.* (2007) for the study of shear strength anisotropy of London clay: (*a*) undrained shearing with constant α proceeded by an α rotation stage; (*b*) undrained shearing with constant orientation of principal stress increment $\alpha_{d\sigma}$. Test codes outlined by a square box indicate the HCA tests performed in the current study

3.4 Index properties, consolidation behaviour and sample quality

This section summarises the Cowden till's index properties (bulk density, initial suctions and shrinkage behaviour), consolidation responses and dynamic shear stiffness. The data obtained is integrated with in-situ test measurements made at the PISA Cowden test site and laboratory research programme reported by Ushev (2018).

3.4.1 Index properties and initial suctions

Bulk density and water content

The bulk densities of the HCA specimens are listed in Table 3-3, and compared with those from the triaxial specimens tested by Ushev (2018), as shown in Figure 3-23. The triaxial specimens prepared from the rotary cores exhibited a uniform bulk density below 2 m, with an average of 2.2 Mg/m^3. No clear differences of bulk density could be observed between specimens prepared from rotary coring and block samples at 3.5 m. The bulk densities of HCA specimens, however, plotted at the lower bound of bulk density profile and exhibited an average of 2.15 Mg/m^3. These results reflect the unintended bias that eliminated heavier gravel inclusions through the sample preparation procedures.

The water contents and Atterberg limits of the HCA specimens are summarised in Table 3-3. The initial states of the tested specimens showed a consistent pattern that fits with the range of existing data. The Atterberg limits of the Cowden till from this depth classify it as low to medium plasticity material. Only slight variations of initial water content were noted between specimens, indicating good uniformity of the initial states. Meanwhile, a possible trend of radial distribution of water content inside the specimens can be observed as the water contents of the HCA inner cavity material were consistently 0.6% higher than those of the outer edges, presumably due to drying.

Table 3-3 Bulk density and water content of the Cowden till HCA and triaxial specimens

Test reference	Bulk density [Mg/m^3]	Water content [%]	Outer WC [%]	Inner WC [%]	Plastic limit [%]	Liquid limit [%]	Plasticity index [%]
CA0005	2.15	14.42	14.01	14.67	17	35	18
CA2305	2.19	13.78	12.97	14.04	-	-	-
CA6705	2.14	13.88	13.70	14.06			
CA9005	2.14	14.44	14.04	14.60	-	-	-
CATC	2.13	14.16	13.58	14.42			
CATC2	2.16	13.48	13.41	13.52			
CASS	2.14	14.64	14.33	14.89	-	-	-
Average	2.15	14.11	13.72	14.31	-	-	-
Std. dev.	0.019	0.387	0.420	0.435	-	-	-
COV [%]	0.86	2.74	3.06	3.04	-	-	-
CTSS	2.02	18.40	-	18.40			
CTX1	2.17	15.57	-	-	-	-	-
CTX2	2.20	15.60					

Note: COV - coefficient of variation;

Table 3-4 Initial conditions of the Cowden till HCA and triaxial specimens

Test reference	e_0	Dry density [Mg/m^3]	S_r [%]	Initial p' [kPa]
CA0005	0.440	1.87	88.5	254.8
CA2305	0.405	1.92	93.7	265.5
CA6705	0.440	1.88	85.2	278.0
CA9005	0.441	1.87	88.4	248.2
CATC	0.449	1.86	85.1	261.2
CATC2	0.417	1.91	87.5	265.5
CASS	0.447	1.87	88.5	188.8
Average	0.437	1.88	88.2	262.2
Std. dev.	0.015	0.02	2.83	9.34
COV [%]	3.371	1.04	3.21	3.56
CTSS	0.532	1.70	90.3	185
CTX1	0.441	1.87	95.3	85
CTX2	0.421	1.90	99.9	113.7

Notes:

(1) e_0 and S_r represent the specimens' pre-test void ratio and degree of saturation calculated from their initial dimensions and wet weight, soil water content (from trimmings) and specific gravity (taken as 2.72 from Ushev (2018)).

(2) Calculation of average and standard deviation of the initial p' excluding the test CASS.

Sample initial suction (p′)

The initial void ratios, degrees of saturation and suctions (p') of the specimens are summarised in Table 3-4. The initial suction (p') values from the HCA specimens are further combined with those of triaxial specimens tested by Ushev (2018), as summarised in Figure 3-24. A profile of mean effective stress (p') estimated from in-situ stress conditions and pore water pressure profile is also included for comparison.

Generally, the triaxial specimens prepared from block samples manifested substantially higher initial suctions than those from the rotary cores, which had had access to drilling fluids during sampling as well avoiding the significant soil drying associated with in-situ block sampling in the low plasticity, high bulk stiffness Cowden till. The initial suctions of most of specimens retrieved from above 4 m depth were higher than the in-situ p' values estimated as applying at the same depth. The suctions determined from rotary core specimens from below 7 m fell below the estimated in-situ p' trend, indicating the scope for drilling fluids to have affected their initial states.

The HCA specimens prepared from blocks taken from 3.0 m bgl exhibited around 25% higher initial suction than the triaxial specimens formed from adjacent blocks sampled at 3.5 m bgl. As noted earlier, longer preparation times were normally required for the HCA specimens and soil drying was further promoted through the annular HCA samples' inner walls, which did not occur with triaxial specimens.

Shrinkage limit

The shrinkage limit (w_s) is a useful index property for clay materials, and is defined as the water content below which clay shrinking ceases on drying and the overall sample volume becomes relatively unaffected by any further loss of water. With initially fully saturated soils, the shrinkage limit represents a transitional state where nearly saturated conditions cannot be maintained and after which any further loss of water markedly decreases the degree of saturation (Marinho, 1994, Al-Haj & Standing, 2016). The difference between the initial water content at its initial nearly saturated state and the shrinkage limit (w_s) represents the soil's ability to retain water while maintaining a high degree of saturation.

Filter paper tests, as described by Chandler & Gutierrez (1986) were performed on sets of intact and reconstituted Cowden till samples to characterise their shrinkage behaviour and gain insights regarding suction development trends during drying.

Typical test results are summarised in Figures 3-25 and 3-26. Figure 3-25 plots the specimens' shrinkage trends during drying, indicating an initially nearly saturated stage, a transition stage and a desaturation stage. The shrinkage limit (w_s) was defined as 14.2%. Figure 3-26 shows the corresponding variation of saturation degree against water content, and indicates that the specimens experienced sharp reductions in the degree of saturation after their water contents fell below this limit.

The initial water contents of the intact Cowden samples (w_c = 14.1%, noted in Table 3-3) were essentially close to the shrinkage limit as determined above, indicating that sharp desaturation and suction increase could develop in the specimens if exposed to even slight further drying. Unlike reconstituted specimens which were readily to form smooth surfaces and edges during drying, minor crack channels, cavities and other imperfections were often observed on the surfaces of the intact specimens, potentially facilitating the desaturation process and helping to explain the initially high suction values seen in Table 3-4.

3.4.2 Consolidation behaviour and dynamic properties

Anisotropic consolidation behaviour

Given the samples' high initial suctions, anisotropic re-consolidation led to (negative) swelling axial (ε_z), radial (ε_r) and circumferential (ε_θ) strains. An example of the straining developed as p' reduced is shown in Figure 3-27. Marked creep strains were noted at the end of re-consolidation. The re-consolidation strains developed in all tests and the corresponding void ratio changes are summarised in Table 3-5.

In most cases, the radial strains (ε_r) developed were greater than the circumferential strains (ε_θ). This trend was not anticipated since identical radial and circumferential stress changes were applied throughout the re-consolidation. Noting the possible errors in the external strain measurements, these discrepancies could also suggest stress and strain non-uniformity and a deviation from the assumption that the HCA specimens retain a right cylindrical shape during re-consolidation.

The development of volumetric strain ($\Delta\varepsilon_{vol}$) against the average triaxial shear strain $\Delta(\varepsilon_z - \varepsilon_h)$ along the re-consolidation path is shown in Figure 3-28. No attempts were made to predict the $\Delta\varepsilon_{vol}$-$[\Delta(\varepsilon_z - \varepsilon_h)]$ relationship based on cross-anisotropic stress-strain analysis, as was made by Nishimura (2006) for example, partly because of the

discrepancies noted in the elastic moduli determined from triaxial and HCA tests, which are discussed in the next section. The shear stress ratio-shear strain relationships, [(σ_z - σ_θ)/(2p')]-[Δ(ε_z - ε_h)] followed during reconsolidation, are presented in Figure 3-29. Although the in-situ stresses of the samples were similar, the (σ_z - σ_θ)/(2p') stress paths followed were not identical due to the wide range of initial p' states. The strain responses of individual samples showed a spread of values.

Table 3-5 Strains development during the re-consolidation and creep stages

Test reference	ε_z [%]	ε_r [%]	ε_θ [%]	ε_{vol} [%]	e	$(e - e_0)/e_0$ [%]
CA0005	-0.691	-0.421	-0.326	-1.433	0.461	4.69
CA2305	-0.732	-0.393	-0.470	-1.60	0.428	5.56
CA6705	-0.691	-0.546	-0.346	-1.591	0.463	5.21
CA9005	-0.649	-0.467	-0.371	-1.49	0.463	4.99
CATC	-0.672	-0.493	-0.342	-1.518	0.471	4.90
CATC2	-0.753	-0.625	-0.370	-1.757	0.441	5.98
CASS	-0.539	-0.436	-0.254	-1.234	0.460	2.87
CTSS	-0.917	-1.137	-0.599	-2.673	0.573	7.71

Dynamic shear stiffness and damping properties during re-consolidation and creep

Resonant column measurements were performed frequently during the re-consolidation and creep stages to trace the evolution of dynamic shear stiffness ($G_{z\theta}$) and damping ratio.

Figures 3-30 to 3-32 plot the trends of dynamic shear stiffness ($G_{z\theta}$) and damping ratio against p' in the consolidation and creep stage of four HCA tests. The $G_{z\theta}$-p' trends can be broadly fitted by power functions, reflecting the material's stress-dependent stiffness behaviour. A void ratio function $f(e) = e^{-1.3}$ (Jamiolkowski *et al.*, 1991) was employed to account for specimen void ratio variations and normalise the resonant column shear stiffnessess, as shown in Figure 3-31, indicating overall good uniformity with R-square approaching 0.98. As the specimens possessed much higher initial suctions (262.2 kPa on average) than their estimated effective stresses (shown in Table 3-2), the re-consolidation stress paths approached near isotropic swelling patterns. The derived fitting coefficients (M and N) of resonant column $G_{z\theta}$ were close to those from

Ushev's (2018) bender element tests on specimens tested under nominally K_o = 1 conditions, but differed significantly from those found with his specimens tested with K_o = 1.5.

The damping ratio characteristics of Cowden till also varied with p' during swelling, rising from around 5% under initial p' conditions to give ratios of 7-8% after approaching the in-situ stresses, which matched the range reported by Ushev (2018) from his low-amplitude undrained cyclic triaxial tests on specimens sampled from comparable depths.

The resonant column tests made while travelling on the re-consolidation paths may not represent those expected in fully stable states in which all pore pressure equalisation had occurred and creep strains have had settled. Additional measurements made during the 3-4 day creep stages revealed around a 2 MPa (4%) decrease in $G_{z\theta}$ and an ≈ 0.15% decrease in damping ratio over this period, indicating a marginal impact of creep straining and final pore pressure equalisation on the dynamic properties at the effective stress levels considered.

3.4.3 Sample uniformity and quality assessment

As shown earlier, the tested HCA specimens demonstrated a narrow range of index properties. Their gravel contents fell between 2-4%, while their initial bulk densities, water contents and void ratios exhibited low degrees of variation, as noted in the values of standard deviation and coefficients of variation (COV) given in Tables 3-3 and 3-4. The final in-situ shear stiffnesses determined from resonant column tests also presented good consistency, with a standard deviation of 1.43 MPa and coefficient of variation 2.73%. The consistencies of the specimens were assured as far as possible by following optimised preparation procedures and taking specimens from the same depth.

Adopting the approach used by Brosse (2012), the quality of the tested specimens can be assessed based on two criteria: volumetric strain (ε_{vol}) developed or void ratio change ($\Delta e/e_0$) during consolidation, as shown in Table 3-6. Referring to Table 3-5, the quality of the specimens can be ranked as "good" based on the volumetric strain (ε_{vol}) criterion, while using the void ratio change ($\Delta e/e_0$) criterion, the quality could only be graded as "Fair" or "Poor".

Such differences reflect a certain degree of inconsistency between the criteria

adopted. As demonstrated by Brosse (2012), significant deviations were seen in the determination of samples' initial void ratio adopting different approaches. However, it is important to note that the void ratio criteria were not developed to cope with high *OCR* low plasticity over-consolidated tills that possess low initial void ratios. They are also unavoidably subject to errors from several aspects, including measurements of specimen dimensions (particularly the inner diameter), representing specimen water content using trimmings, adopting specific gravity (G_s) of the silt and clay fraction to represent the overall soil mass with different components of varied densities. In contrast, the re-consolidation strains were measured directly from displacement transducers and volume-gauges that are less subject to operational errors or bias, and therefore could be taken as a more reliable measure in assessing specimen quality.

Table 3-6 Criteria adopted to assess specimen quality based on volumetric strain (ε_{vol}) or void ratio change ($\Delta e/e_0$) during reconsolidation (Brosse, 2012)

Reference	Index	Very good to excellent	Good	Fair	Poor	Very poor
Andresen & Kolstad (1979)	ε_{vol} [%]	≤1	1-2	2-4	4-10	>10
Lunne *et al.* (1997)	$\Delta e/e_0$ [%]	≤3		3-5	5-10	>10

3.4.4 Figures

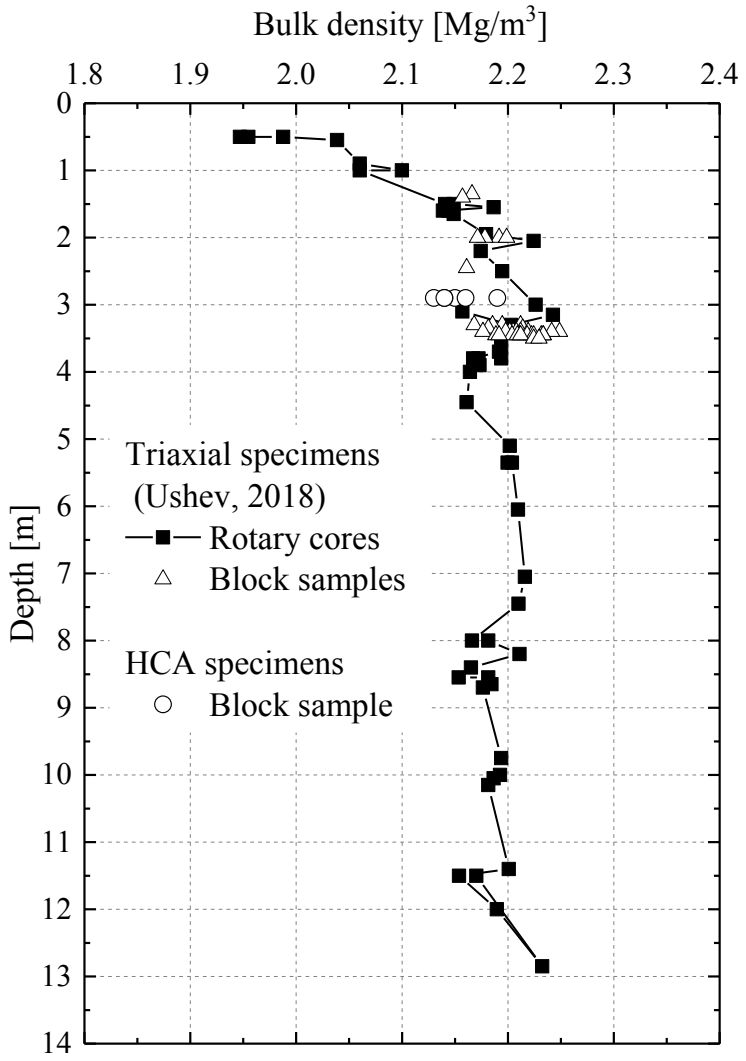

Figure 3-23 Bulk densities of Cowden till triaxial and HCA specimens

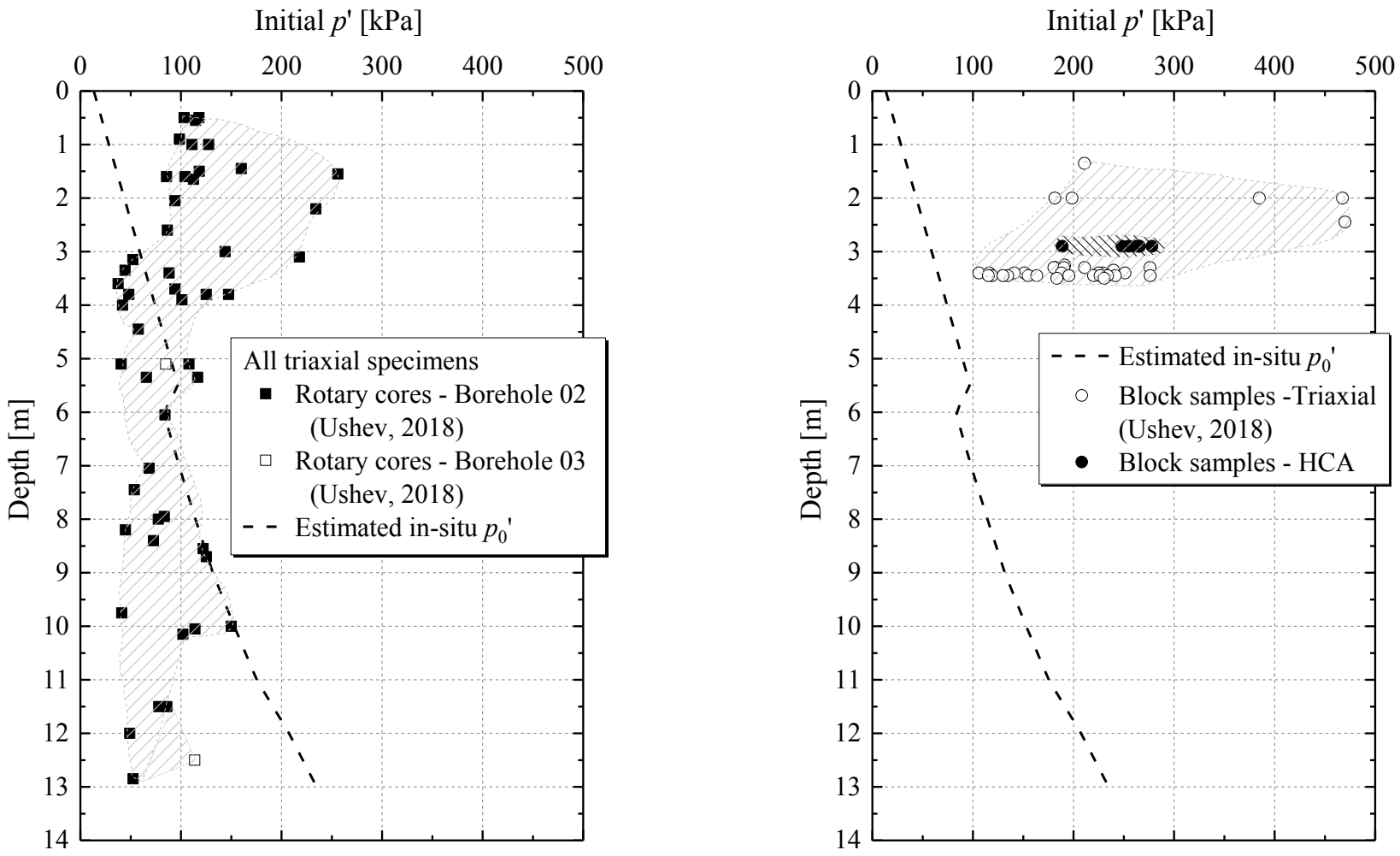

Figure 3-24 Initial suctions of Cowden till triaxial and HCA specimens prepared from rotary cores and block samples

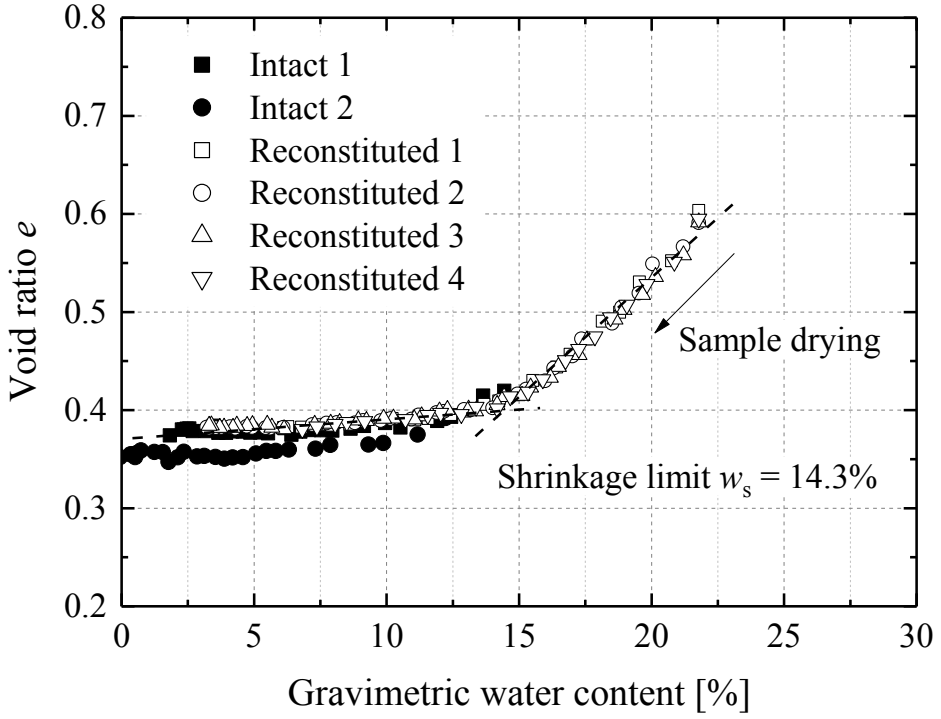

Figure 3-25 Determination of shrinkage limit of intact and reconstituted Cowden till samples

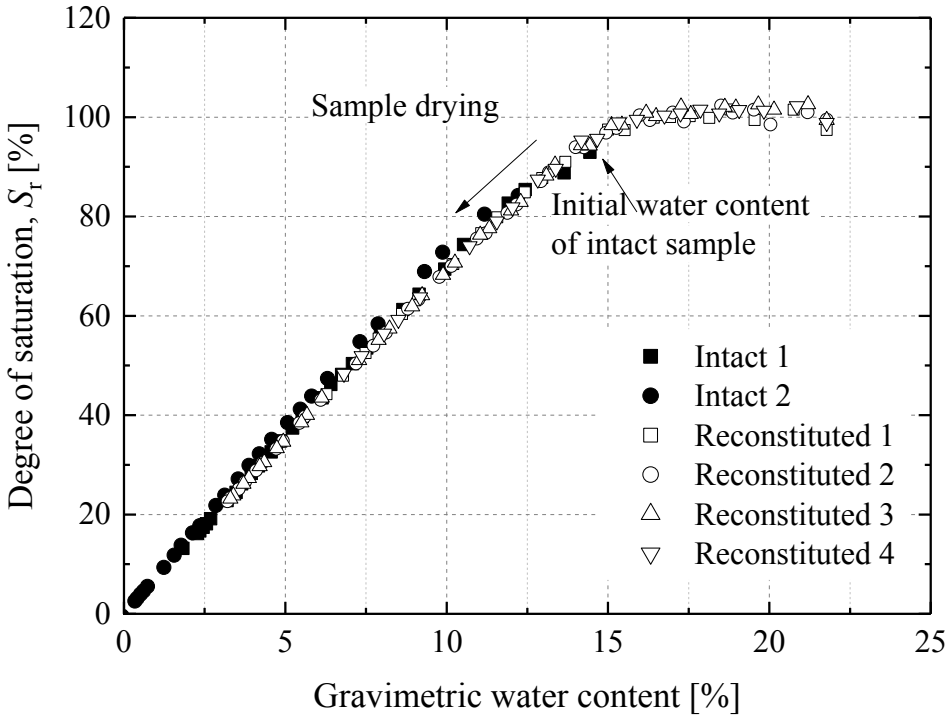

Figure 3-26 Variation of saturation degree against gravimetric water content during drying of intact and reconstituted Cowden till samples

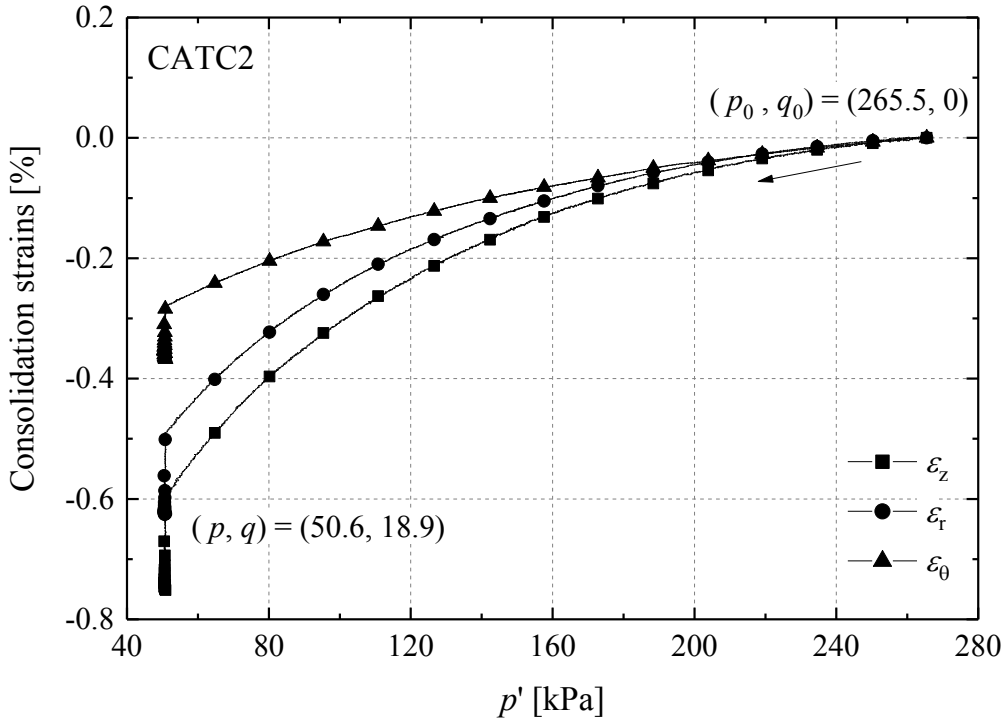

Figure 3-27 Trends for strain components developed in re-consolidation from initial p' to the estimated in-situ stress state and subsequent creep stage

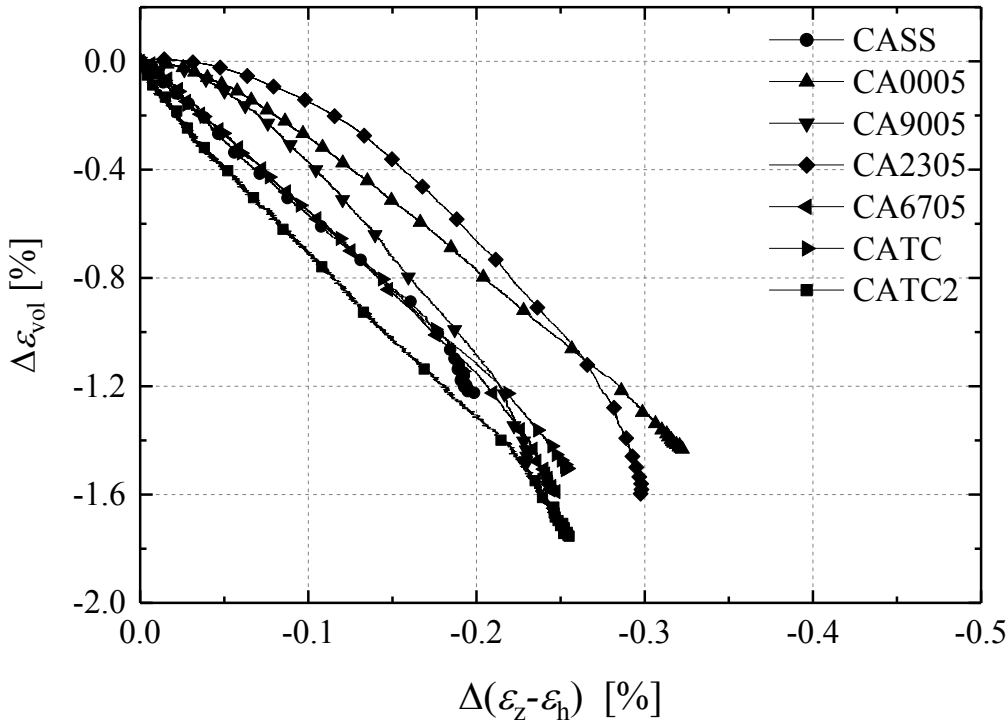

Figure 3-28 Development of volumetric strains along re-consolidation paths from initial p' to in-situ stress states ($\Delta\varepsilon_h = (\Delta\varepsilon_r + \Delta\varepsilon_\theta)/2$)

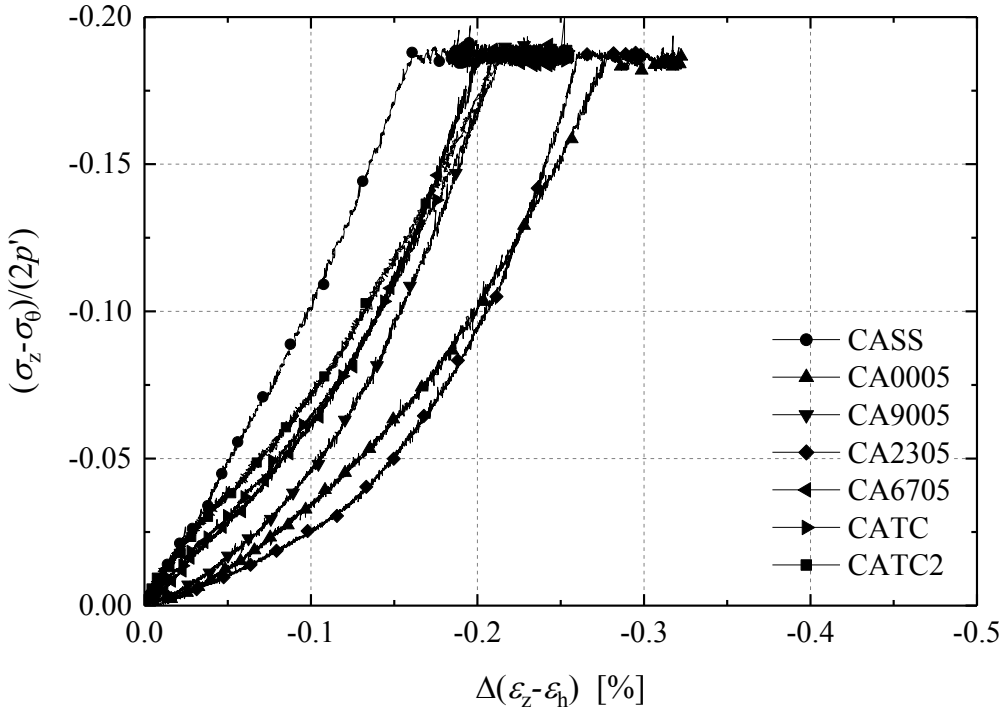

Figure 3-29 Shear stress-strain relationships along consolidation paths from initial p' to in-situ stress states ($\Delta\varepsilon_h = (\Delta\varepsilon_r + \Delta\varepsilon_\theta)/2$)

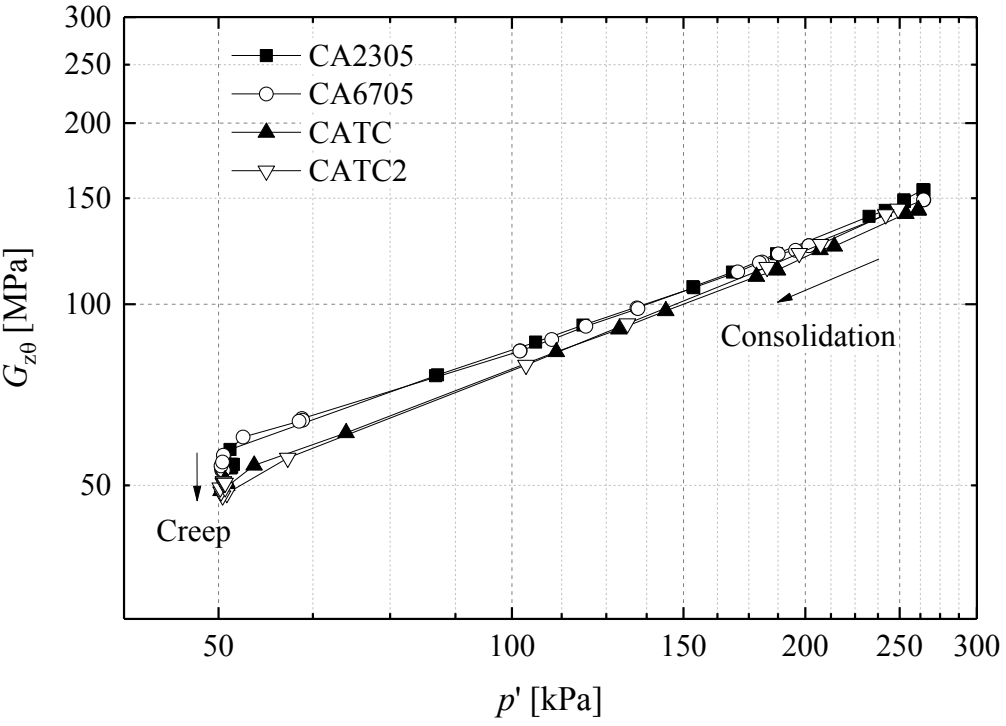

Figure 3-30 Evolution of shear stiffness $G_{z\theta}$ against p' in consolidation and creep stages

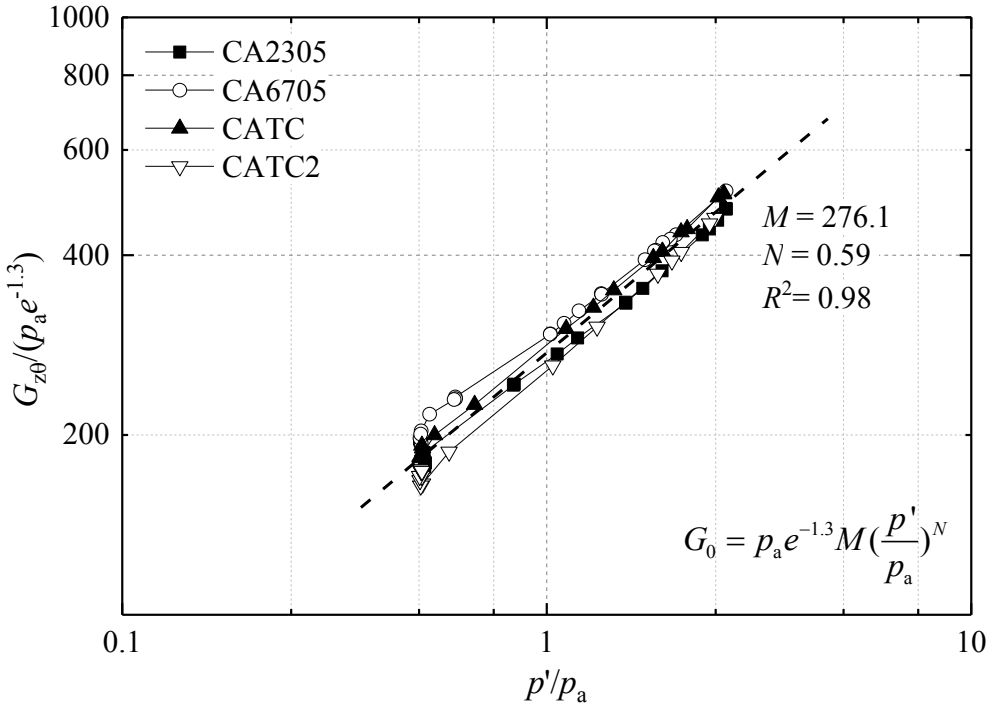

Figure 3-31 Normalised elastic shear stiffness $G_{z\theta}$ and the fitting trend made by HCA resonant column measurements

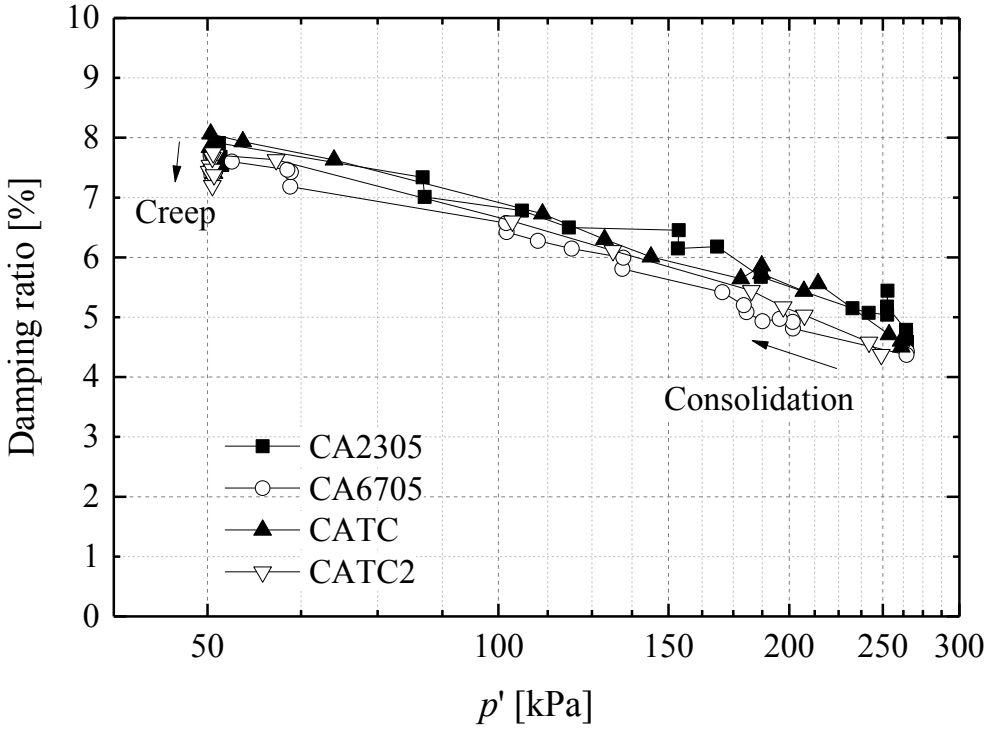

Figure 3-32 Evolution of damping ratio against p' in consolidation and creep stages

3.5 Response to undrained *b*-change and final shearing behaviour

The paragraphs below describe first the mechanical response of the Cowden till samples observed as they underwent their undrained *b*-change stages, before proceeding to discuss the subsequent undrained shearing tests to failure.

3.5.1 Undrained *b*-change response

As detailed in Table 3-2, undrained *b*-change stages were imposed following the consolidation and creep stages on four samples to change the *b* value from 1.0 to 0.5 while maintaining constant p, q and α. Their strain development and effective stress variations were continuously monitored and are discussed below.

Figures 3-33 to 3-36 present how the strain components developed as *b* changed. Linear regressions were applied to derive ratios between the strain components, as annotated in the plots. Although the stress increments imposed were small (of the order of a few kPa), the strain response is clearly non-linear, particularly for the radial strain component, and creep straining is observed for all the strain components. In the *b*-change stage, the stress increments of the three normal stresses ($\Delta\sigma_z$: $\Delta\sigma_r$: $\Delta\sigma_\theta$) entailed constant ratios of 1: -2 : 1. For an isotropic linear elastic material, these stress increments should result in an identical strain development ratio, namely $\Delta\varepsilon_z$: $\Delta\varepsilon_r$: $\Delta\varepsilon_\theta$ = 1: -2 : 1. Although subject to slight variations, the average strain component ratios for $\Delta\varepsilon_z$: $\Delta\varepsilon_r$: $\Delta\varepsilon_\theta$ were 1: -1.69 : 0.66, and diverged from the isotropic elastic values.

The trends of mean effective stress p' during the *b*-change stage are plotted in Figure 3-37. The trends clearly deviate from those anticipated for isotropic linear elastic materials, which would not generate any change in p' under undrained stress path with constant p and q. Small increases (around 3 kPa) of p' were noted in all the tests, and the stress paths generally followed linear trends in the b-p' space with an average db/dp' ratio of -0.167 /kPa. The trends of strain development and effective stress path provide preliminary evidence of the material's anisotropic and non-linear stiffness characteristics.

3.5.2 Undrained shearing to failure and ultimate deformation modes

The shear stress-strain behaviour seen in the undrained HCA tests sheared to failure are presented below in terms of both total stress (q or S_u) and effective stress (t/s' or q/p').

Discussion is then given on of the material's anisotropic shear strength characteristics.

Generally, large shear strains are required for the Cowden till to mobilise stable ultimate shear strengths. However, the maximum strains, particularly the axial strain, achieved in the current HCA tests were constrained by the configuration of the proximity transducer cage and the resonant column system in the ICRCHCA, as seen in Figure 2-13. The axial strains were limited to around 15% in most cases.

The interpretation of the stress and strain components at large shear strains is also hampered by strain non-uniformity in the HCA samples, especially that due to bulging, necking, torsional straining or the development of shear planes. Reliable and consistent approaches are generally not available to correct for such non-uniformities and produce more representative stresses and strengths. No strain uniformity corrections were attempted in the study and the discussions presented below focus on the recorded datasets, as interpreted with the "apparent" average stress and strain measurements.

Ultimate deformation modes

As mentioned in Section 3.3.1, during the setting up stage, grids were pre-drawn on the surface of the outer membranes to facilitate visually inspecting and locating any fissures, ruptures or shear bands. Visual inspection was aided by optical magnification through the cell water and the transparent perspex wall of the cell chamber. The approach was implemented and the shearing deformation and failure modes of the HCA specimens under different straining patterns were recorded, although pre-existing fissures or fractures were rarely encountered and strain localisation was not expected to be a major concern for the ductile Cowden till.

Figure 3-38 presents photographs taken at the end of each HCA test, while also indicating the ultimate maximum shear strain (ε_1-ε_3) achieved. The aim was to shear the samples to their ultimate stable strength states, with tests only halting after substantial deformation and straining to the point where severe stress non-uniformities were anticipated. Bugling and necking deformations were observed in the tests imposing axial (CA0005) and horizontal compression (CA9005), respectively. Continuous torsional straining was superimposed on the axial strains in the cases of CA2305, CASS and CA6705.

In some cases (in particular, tests CATC and CATC2), concentrated shear zones or bands were noted in the specimens that were not observed in the triaxial compression

tests on solid cylindrical specimens conducted by Ushev (2018). However, no clear evidence was found that these mechanisms involved pre-existing macro- or meso-fabric features and the non-uniform deformation was attributed to excessive straining and/or unobserved weak zones formed from sample preparation stage or non-uniformity due to gravel inclusions. The thin HCA wall thicknesses (around 16.5 mm) and the non-homogeneity of the specimens encouraged non-uniform straining after large deformations. The specimens were prone to their greatest geometrical difficulties under paths that involved large vertical compression strains and resulted in greater strain localisation in the HCA "triaxial" compression tests than in Ushev's (2018) tests in stress path triaxial cells.

While the grids and photographs provided records of sample deformation and the failure modes under different stress paths, no attempt was made to use the information to modify the calculation of average stresses, strains or anisotropic shear strength properties of the material. The till exhibits no systematic pattern of micro- and meso-structure and the presence of gravel fragments or locally weak zones in the specimens appeared too random to be assessed consistently. The deformation records confirmed duly that the horizontal planes of the material are not particularly weak while under torsional shear.

3.5.3 Development of strain components

Figures 3-39 to 3-41 show how the individual strain components (ε_z, ε_r, ε_θ and $\gamma_{z\theta}$) developed during shearing by plotting these against the largest shear strain (ε_1-ε_3) and considering two shear strain ranges (0-0.05% and 0-5%) for the four $\alpha_{d\sigma}$-controlled shearing tests and the two HCA "triaxial" compression tests.

The intermediate principal strain ε_2 (or ε_r) remained relatively low, compared with the other strain components in the four (b = 0.5) $\alpha_{d\sigma}$-controlled shearing tests. This was expected as the b = 0.5 stress condition was intended to provide approximately plane strain conditions and indeed generated low radial strains.

Naturally, no such trend was observed in the two HCA "triaxial" compression tests which started with b = 1 followed by an abrupt change to 0. However, the undrained HCA "triaxial" compression tests generated greater (negative) radial than circumferential strains and the difference between the two appeared greater over the

initial small strain range. The discrepancy between the two horizontal strain components may reflect the annular specimen's geometry and the additional boundary condition constraints in the circumferential direction under axial compression condition with equal inner and outer cell pressure.

The strain evolution trends indicate apparently linear relationships between the strain components that alter slightly between the small (0.05%) and medium (5%) strain range and indicate relatively stable patterns of anisotropy between the E_v^u, E_h^u and G_{vh} stiffness components over the non-linear strain range.

3.5.4 Shear stress-strain behaviour over large strains

The shear strengths developed at failure were considered in terms of three failure criteria, namely the Tresca undrained shear strength S_u (= q/2), Mohr Coulomb stress ratio t/s' and the critical state ratio q/p'. These measures were appropriate to characterise the anisotropic shear strength properties of the Cowden till.

As pointed out by Nishimura *et al.* (2007) and Brosse *et al.* (2017), these parameters essentially represent alternative models of idealised isotropic materials: a Tresca material where shear strength is quantified in terms of total stress (independent of effective stress level), a purely frictional material that possesses no true cohesion (c') component or potential failure envelope curvature and conforms to either hexagonal or radial shapes in the deviatoric plane. Deviations from these patterns can be employed to quantify any anisotropy in the till's shear strength. Since the main test series were performed with b fixed at 0.5, the chosen parameters S_u (= q/2) and t, s', q, p' can be linked simply to the Cauchy stress invariants, with $p' = s'$ and $q = 2t$, as set out by Brosse *et al.* (2017).

Figure 3-42 presents overall trends of deviatoric stress (q = σ_1-σ_3) against shear strain (ε_1-ε_3) for the seven HCA tests. In most cases, the shear stress-strain responses were predominantly ductile without showing clear peaks up to (ε_1-ε_3) =20%, whereas the two high α_f tests (CA6705 and CA9005) manifested peak strengths at around 8-9% shear strain, followed by slight reductions before the tests terminated. A 'residual' strength plateau was reached in test CA6705. For the lower α_f tests, the stresses were still slowly climbing at the end of the tests and fully stable ultimate strengths could not be reached within the travel limits of the apparatus. Strain localisations or ruptures were

rarely observed, and the recorded stress-strain responses were treated as representing broadly continuous element behaviour, rather than locally non-uniform rupture responses.

The results reveal the material's anisotropic strength characteristics. The 'extension' test (CA9005) with $\alpha_f = 90^\circ$ showed clearly higher undrained shear strength ($S_u = q_{max}/2$) than the other shearing modes, while the sample that underwent ($b = 0.5$) compression (CA0005) exhibited the lowest strength. The undrained shear strengths of the tests involving the torsional shearing mode (CA2305, CASS, and CA6705) and intermediate α_f values spanned between the bounds of the compression and extension tests. Meanwhile, the two tests that involved primarily torsional shearing (CA2305 and CASS) showed relatively steep final stress-strain curves as the specimens underwent continuous shearing without experiencing strain localisation. It is also interesting to note that the two HCA "triaxial" compression tests developed apparently higher strength than the 'plane-strain' $\alpha_{d\sigma}$-controlled test CA0005.

The shear stress-strain trends for the two HCA 'triaxial' compression specimens are plotted together with those from standard triaxial compression (TXC) tests on specimens from 2.0-3.5 m, as shown in Figure 3-43. The shear strengths of the HCA TC specimens (S_u^{HCATC}) were lower by around 25% (on average) than those of the standard triaxial tests (S_u^{TXC}). The difference reflects the impact of sampling bias and mechanical disturbance occurred to the HCA specimens, as previously discussed in Section 3.3.5. It is also important to note that the HCA 'triaxial' tests could develop non-uniform radial and circumferential strains (with radial strain being higher, see Figure 3-41) during compression and lead to buckling failure across the specimens' thin wall (16.5 mm) (as seen in Figure 3-38), potentially leading to lower strength compared to those of solid cylindrical specimens which invariably exhibited bulging deformation when sheared to large strains.

The evolving trends of effective stress ratio (or effective stress obliquity) t/s' (= $q/(2p')$) against shear strain for the HCA tests are plotted in Figure 3-44, also indicating the corresponding equivalent mobilised shear resistance angle ϕ_{mob}'. As in the total stress 'Tresca' analyses above, the highest t/s' (= $q/(2p')$ at $b = 0.5$) was noted with $\alpha_f = 90^\circ$ and lowest $\alpha_f = 0^\circ$, with the tests with intermediate α_f values lying in between the two (excluding the HCA 'triaxial' compression tests). The high α_f tests (48.2°, 67°, 90°) showed relatively stable and 'dilatant' trends of t/s', while marked peaks were observed

in the two lower $\alpha_f = 0^\circ$ and $\alpha_f = 23^\circ$ tests (CA0005, CA2305). These differences were reflected in the effective stress paths plotted in Figure 3-48, where the q-p' paths curve to the right after following initially contractant patterns.

Considering the Mohr-Coulomb failure criterion, Figure 3-44 shows the ϕ_{mob}' values developed in the $b = 0.5$ HCA tests were markedly higher than the triaxial compression mode. It is reassuring that the HCA 'triaxial' compression tests reached ultimate mobilised ϕ' angles of around 27°, which matched well with the critical state shear resistance angle of intact weathered Cowden till established through standard triaxial compression tests by Ushev (2018).

3.5.5 Undrained shear strength anisotropy

Projections of shearing stress paths

The shear strength anisotropy revealed from the above stress-strain traces is investigated further by projecting the stress paths in the q-p', $[(\sigma_z-\sigma_\theta)/2]$-$p'$ and $\tau_{z\theta}$-$[(\sigma_z-\sigma_\theta)/2]$ plane, as shown in Figures 3-45 to 3-49.

The trends of p' for the four $\alpha_{d\sigma}$-controlled tests under constant total mean stress p during shearing directly indicates the generation of both positive and negative excess pore pressures and hence the contraction/dilation characteristics. As presented in Figure 3-48, an overall trend of 'dilative' behaviour was noted for the extension loading ($\alpha_{d\sigma} > 45^\circ$), whereas for the compression loading ($\alpha_{d\sigma} < 45^\circ$), the response commenced with an initial limited contraction, followed by extended dilative period up to ultimate states. Nishimura *et al.* (2007) and Brosse *et al.* (2017) argued that the pre-failure contraction/dilation response contributed significantly to shear strength (S_u and t/s') anisotropy of their brittle stiff clays which could not dilate significantly without developing shear bands that truncated their effective stress paths. This feature appears to be practically insignificant with the ductile Cowden till. Considering the undrained HCA simple shear (HCASS) test, its test path was characterised by minimal variations in the total normal stresses (σ_z, σ_r, σ_θ) in comparison with the applied torsional shear stress ($\tau_{z\theta}$). These features are discussed further in Section 3.5.6.

Figure 3-49 presents the projections of the stress paths in the $\tau_{z\theta}$-$[(\sigma_z-\sigma_\theta)/2]$ plane, annotating the envelopes at the 10% shear strain and maximum shear strain (ultimate) states. If considered as a purely cohesive material (Tresca criterion), the undrained shear

strength of the Cowden till is represented by the radial distance between the failure stress path point projected in the $\tau_{z\theta}$-[(σ_z-σ_θ)/2] plane and the (0, 0) origin. For an isotropic material following this criterion, the shear strength envelope should form a half circle centred on the origin. However the envelopes depicted in Figure 3-49 extend latterly to the left and are skewed on the right hand side.

Variation of shear strength against major principal stress direction

The variation of undrained shear strength S_u with major principal stress orientation α at both the 10% shear strain and last recorded states are plotted in Figure 3-50. By both measures, the till exhibited its lowest and highest undrained shear strengths at α_f = 0˚ and α_f = 90˚, respectively, with a range of values being noted at the intermediate α_f values. Considering the peak points, the ratio of the maximum to minimum S_u values is 1.37, reflecting significant but relatively mild anisotropy.

Anisotropic undrained shear strengths were also observed in the standard triaxial compression (α_f = 0˚, b = 0) and extension (α_f = 90˚, b = 1) tests, but the pattern revealed was different from that seen in the $\alpha_{d\sigma}$-controlled HCA tests discussed here. Ushev (2018) reported higher average triaxial compression strength (S_u^{TXC} = 150 kPa) than extension strength (S_u^{TXE} = 125 kPa) for the materials sampled from 2.0-3.5 m, leading to a strength ratio (S_u^{TXC}/ S_u^{TXE}) of 1.25. However, Ushev (2018) found that his triaxial extension tests all underwent necking failures with strain localisation, leading to premature failures before any global critical state could be achieved in extension. It is also important to note the difference in the b value, the effects of which on shear strength anisotropy cannot be isolated in triaxial testing. The triaxial extension tests failed with α = 90˚ and b = 1, while the HCA tests failed with b = 0.5.

The Cowden till's undrained shear strength anisotropy is different to that observed in the heavily over-consolidated high plasticity sedimentary stiff clays that were summarised in Figure 3-11. The high plasticity stiff clays' more distinct micro- and meso-structures (with horizontal beddings and sub-horizontal and sub-vertical fissures) were best exploited during torsional shearing and led to S_u minima over the 10˚ to 45˚ α range. However, the over-consolidated glacially deposited, low plasticity, Cowden till did not show any clear weakness on horizontal planes, although it manifested its highest strengths under high α_f passive loading. These features appear to have been imparted by the till's glacial deposition and subsequent geological history.

The till's anisotropic strength characteristics are also assessed in terms of stress ratio t/s' and mobilised shear resistance angle (ϕ_{mob}') at 10% shear strain, peak and ultimate states, as shown in Figure 3-51. As with the S_u traces, for all the strain levels considered, the t/s' minima develop at $\alpha_f = 0^\circ$, while the maxima are noted at $\alpha_f = 90^\circ$, giving a relatively mild ratio of 1.19 between the two extreme values. Intermediate t/s' values are found between the limits. Note that the anisotropy in S_u follows a similar but more accented pattern than that for t/s', indicating that both fabric anisotropy and a tendency for the till's dilatancy to vary with α contribute to the overall directional dependency of undrained shear strength.

As shown in Figures 3-50 and 3-51, the simple shear strengths, which are often prescribed in practical design as offering intermediate values between triaxial compression and extension, also fell in this case between the compression and extension strength. Further comments on these tests are given below.

3.5.6 Undrained HCA simple shear (HCASS) behaviour

Assessing simple shear behaviour is practically important, particularly in geotechnical analyses that involve high degree of kinematic straining, as in axial pile loading, and in earthquake engineering analyses of ground motion amplification. One of the advantageous features of HCA equipment is its ability to perform simple shear tests in which all four dimensions of the stress tensor can be measured, revealing full information regarding intermediate stress level and principal stress axis angles during shearing, which cannot be achieved in routine simple shear tests.

Adopting an analogue with cyclic axial pile shaft loading, Aghakouchak (2015) carried out extensive undrained cyclic HCA SS tests on Dunkirk and NE34 sands and demonstrated that how his laboratory element tests could be applied to interpret cyclic behaviour of offshore piles and guide practical design. Near simple shear conditions might also be expected in the problem of large diameter laterally loaded monopiles under the pile base and in shaft shear zones. Jeanjean *et al.* (2017) employed laboratory direct simple shear (DSS) testing as one of the primary tools for deriving monotonic and cyclic *p-y* curves for laterally loaded pile design.

The procedures for performing undrained HCA simple shear (HCA SS) tests were briefly described in Section 3.3.6. Two HCA SS tests were performed on specimens

taken from 0.5 m and 2.93 m depth, and while same results were presented in earlier plots, further interpretation is presented blow.

Shear stress-strain behaviour

The shear stress-strain responses q-(ε_1-ε_3) of the two HCA SS tests are summarised in Figure 3-52, also plotting the results from one of the HCA 'triaxial' tests (CATC2). The shear stress-strain traces indicate ductile behaviour. Both HCA SS tests terminated at shear strains of around 16%, before the peak $\tau_{z\theta}$ had developed fully. The stress-strain curves were extrapolated, denoted as dashed lines, to estimate ultimate stable torsional stresses $\tau_{z\theta\_max}$.

The trends for normalised torsional shear stress ($\tau_{z\theta}/\tau_{z\theta\_max}$) against torsional strain are shown in Figure 3-53 on a linear scale, while Figure 3-54 replots the results in a semi-logarithmic scale to aid scaling at small strains. The paired tests on specimens from 2.93 m indicate HCA simple shear peak strength $\tau_{z\theta}$ and HCA 'triaxial' compression peak S_u values were closely comparable: peak $\tau_{z\theta}^{SS} \approx$ peak S_u^{HCATXC}.

Stress evolution and principal stress rotation

The undrained HCA simple shear effective stress paths are plotted on the $\tau_{z\theta}$-[(σ_z-σ_θ)/2] plane normalised by mean effective stress p', as shown in Figure 3-55. The normal stress components (σ_z, σ_θ) developed only minor changes in response to loading to failure under torsional shear.

Figure 3-56 presents the variation trends of the major principal stress direction, intermediate stress level, and deviatoric stress in a b-q-α space, also indicating the ultimate values of b and α reached in the two tests. Rapid rotation from 90˚ of the major principal stress direction took place after the onset of shearing, and the ultimate α values fell between 45˚ to 50˚.

Meanwhile, the intermediate stress factor b decreased from 1.0 to an ultimate value of around 0.45 under imposed plane strain conditions. The dashed line denotes the relationship of $b = \sin^2(\alpha)$, which applies when the inner and outer cell pressures are identical. While this condition was not imposed, the test paths plotted only slightly below this curve, following the relationship at relatively small shearing strains and then moving downwards, implying slight decreases in the inner cell pressures. The fact that the inner and outer cell pressures usually stay close in undrained HCA SS tests is a

favourable factor that alleviates stress non-uniformity in HCA specimens, and offers further advantages over the widely recognised stress non-uniformity that is implicit in conventional DSS testing (see for example by Airey & Wood (1987) among others).

3.5.7 Figures

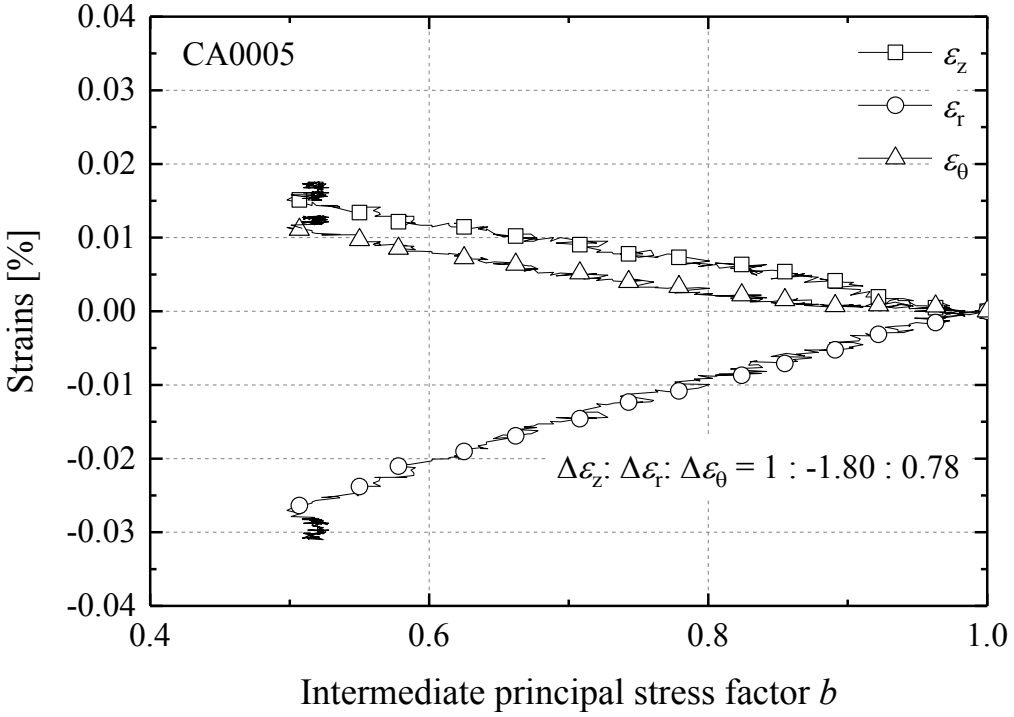

Figure 3-33 Strain development in the undrained b-change stage of test CA0005

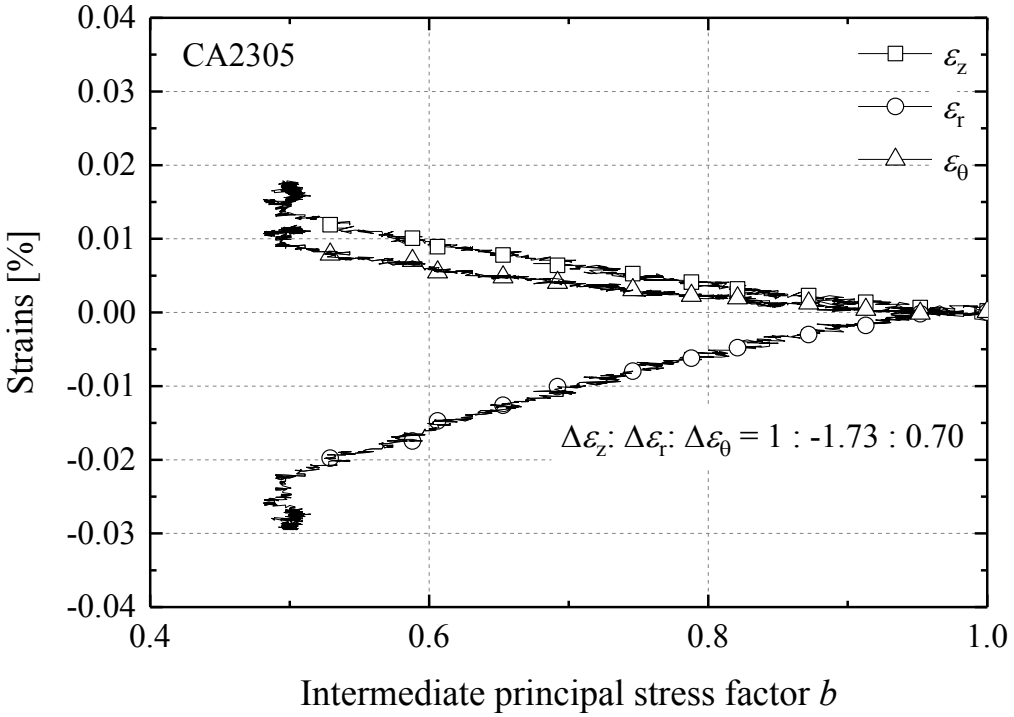

Figure 3-34 Strain development in the undrained b-change stage of test CA2305

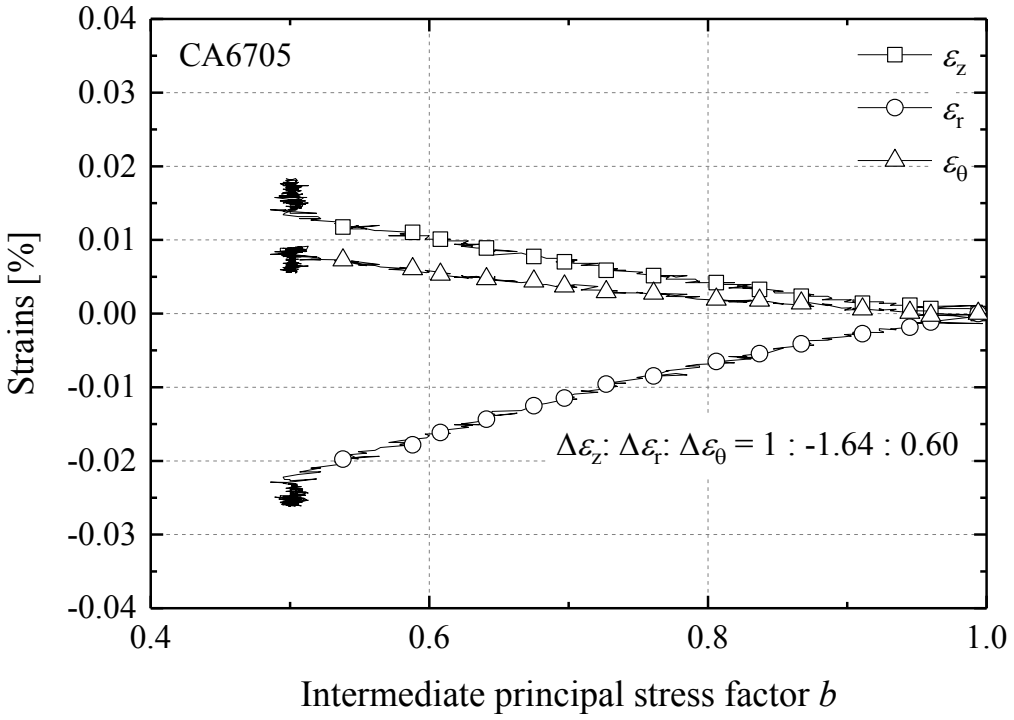

Figure 3-35 Strain development in the undrained *b*-change stage of test CA6705

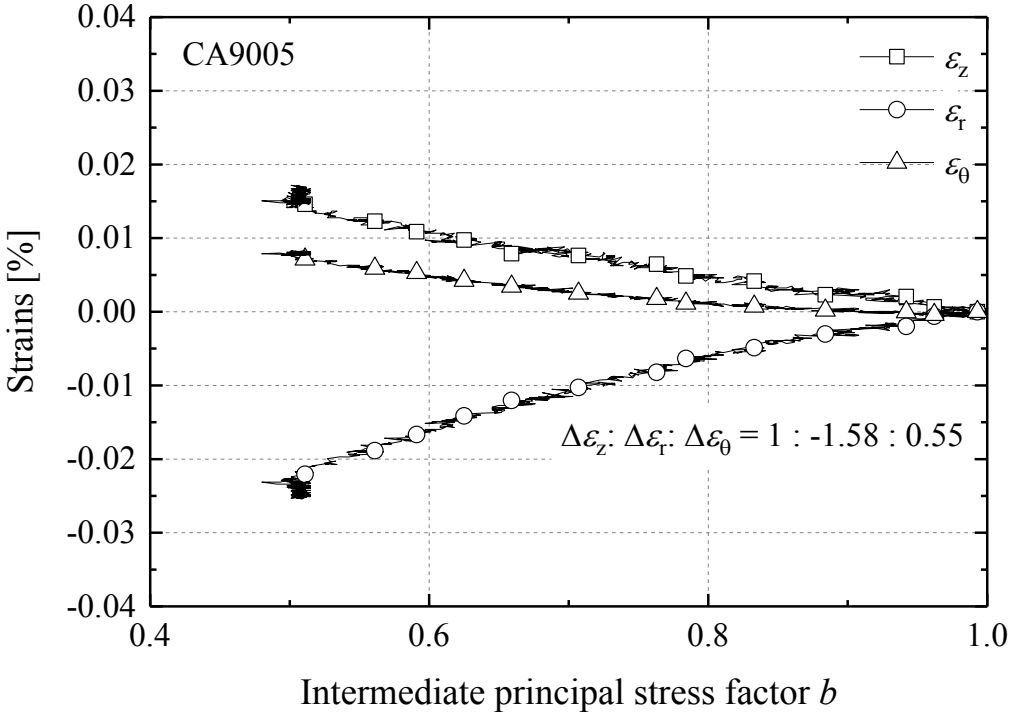

Figure 3-36 Strain development in the undrained *b*-change stage of test CA9005

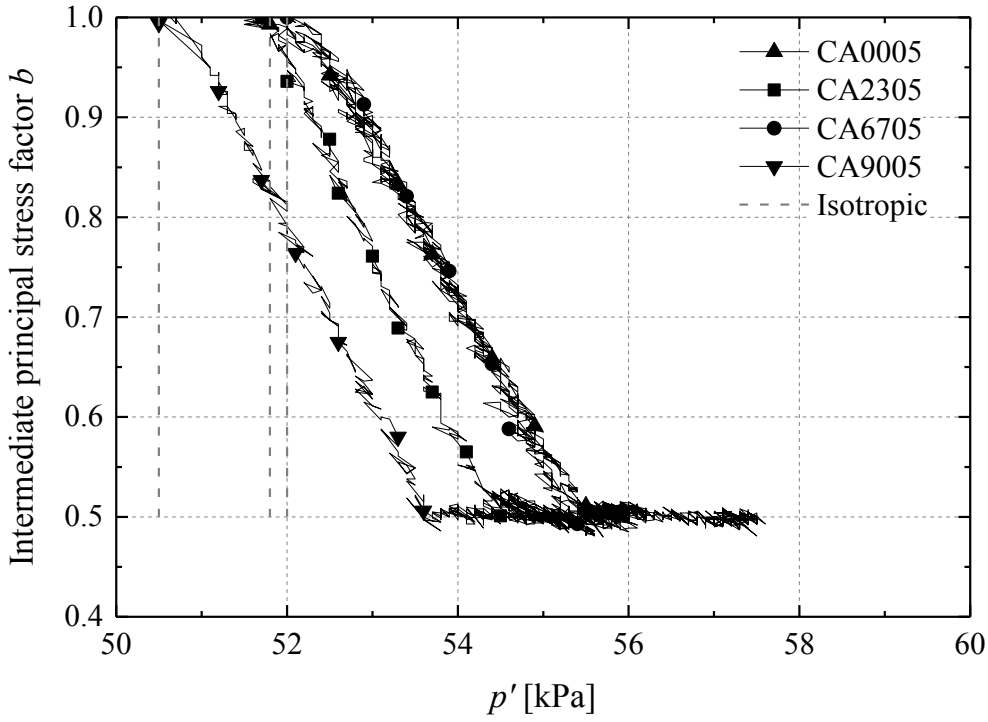

Figure 3-37 Effective stress paths during the undrained *b*-change stage

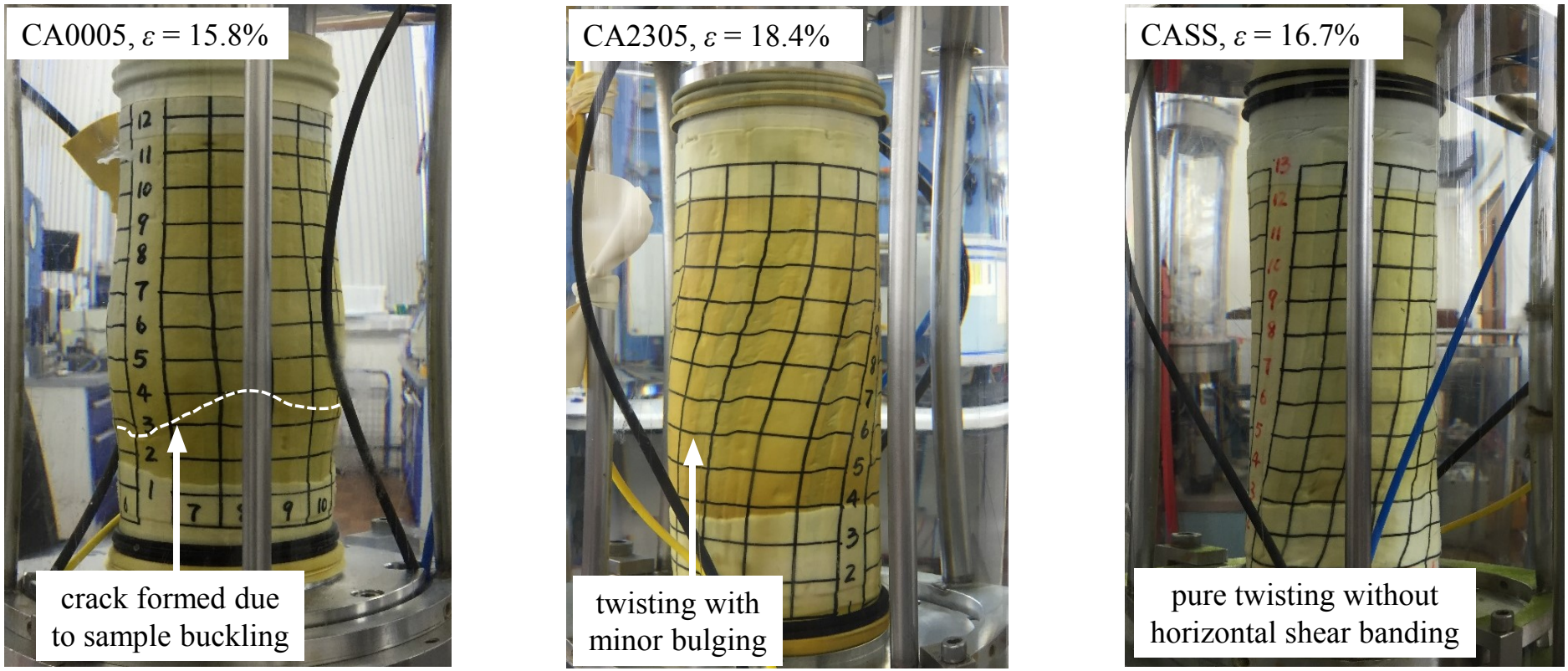

Figure 3-38 Deformation pattern and failure mode of the HCA samples at ultimate shearing strains ε (= ε_1-ε_3)

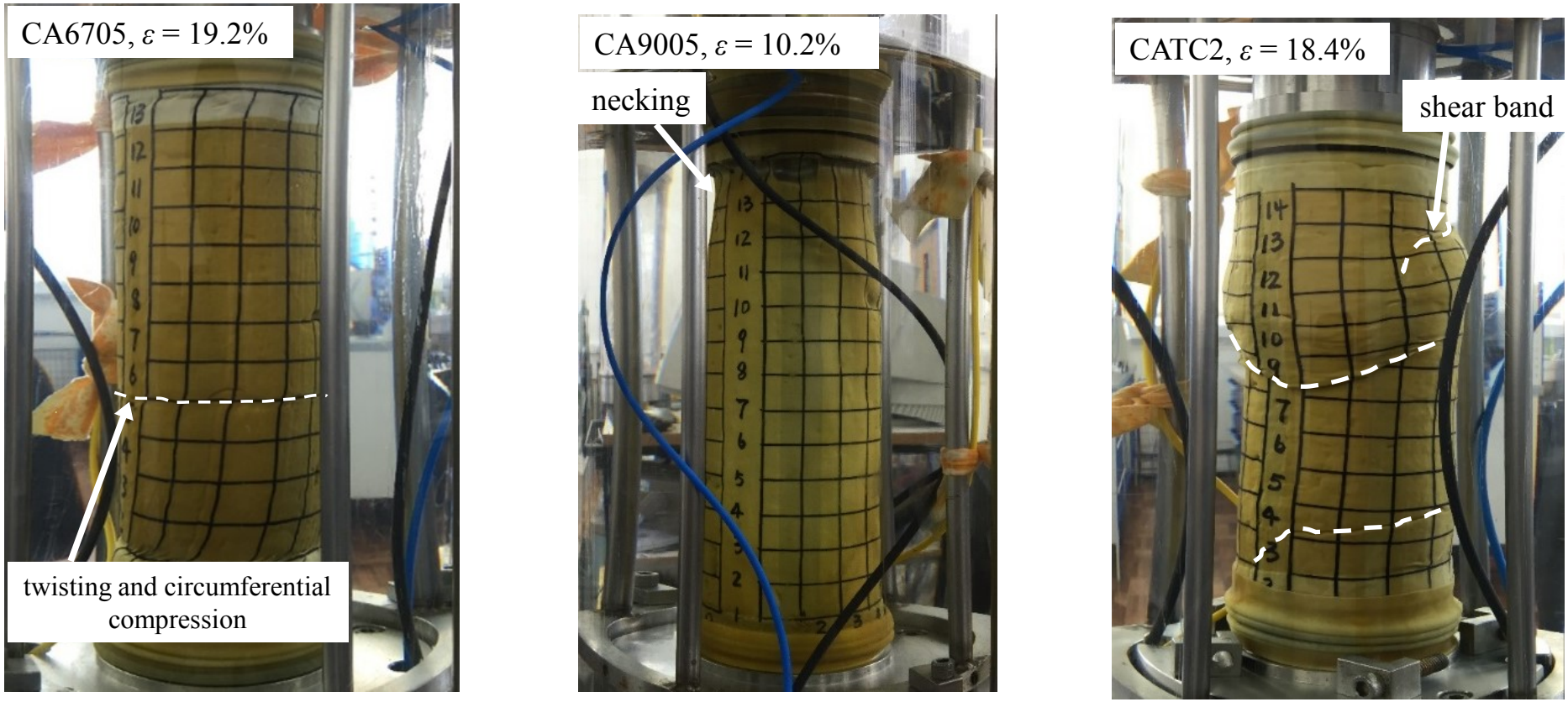

Continued Figure 3-38 Deformation pattern and failure mode of the HCA samples at ultimate shearing strains ε (= ε_1-ε_3)

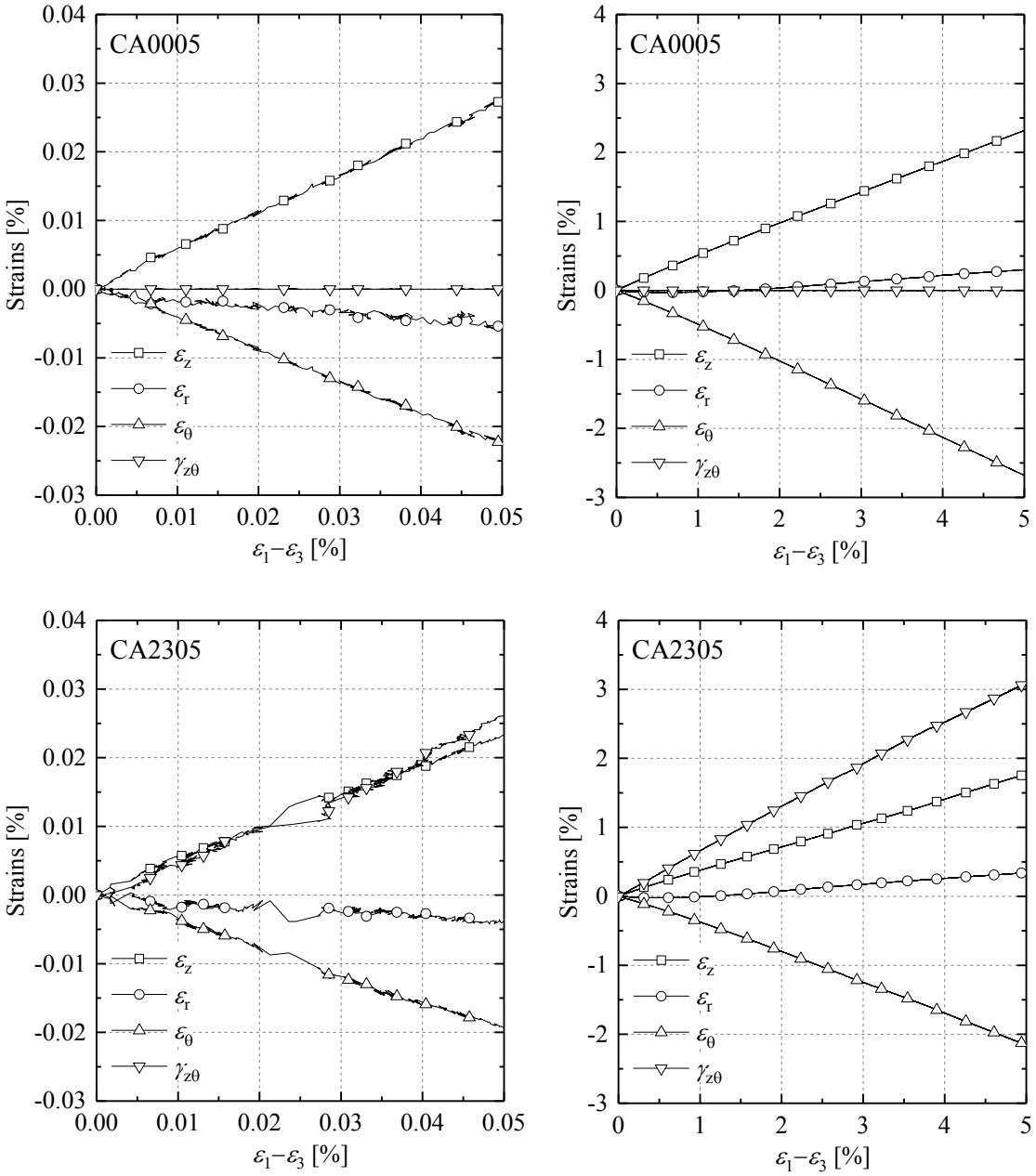

Figure 3-39 Strain component development trends during undrained constant $\alpha_{d\sigma}$ shearing stage at small strain range (left) and large strain range (right) for tests CA0005 and CA2305

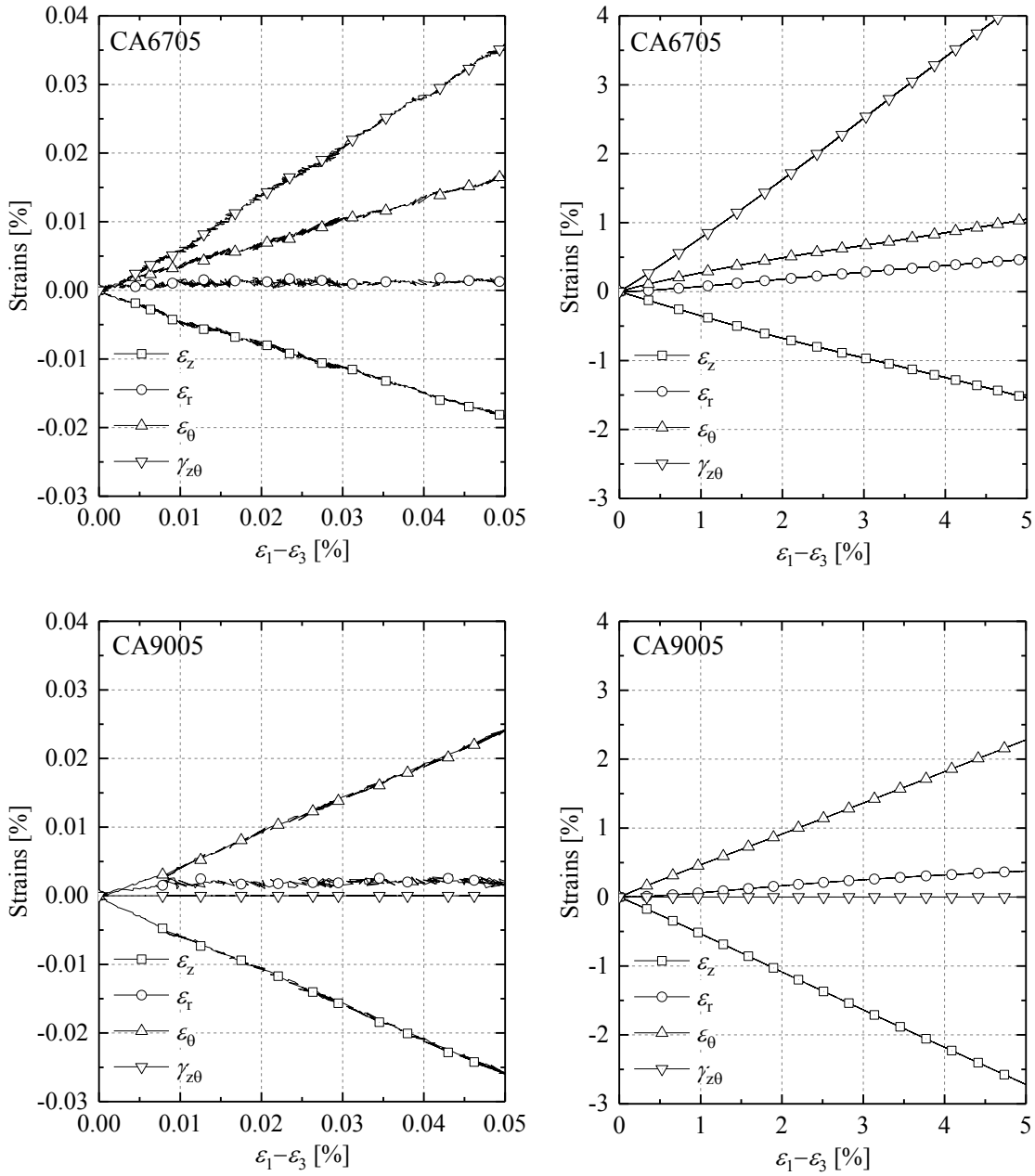

Figure 3-40 Strain component development trends during undrained constant $\alpha_{d\sigma}$ shearing stage at small strain range (left) and large strain range (right) for tests CA6705 and CA9005

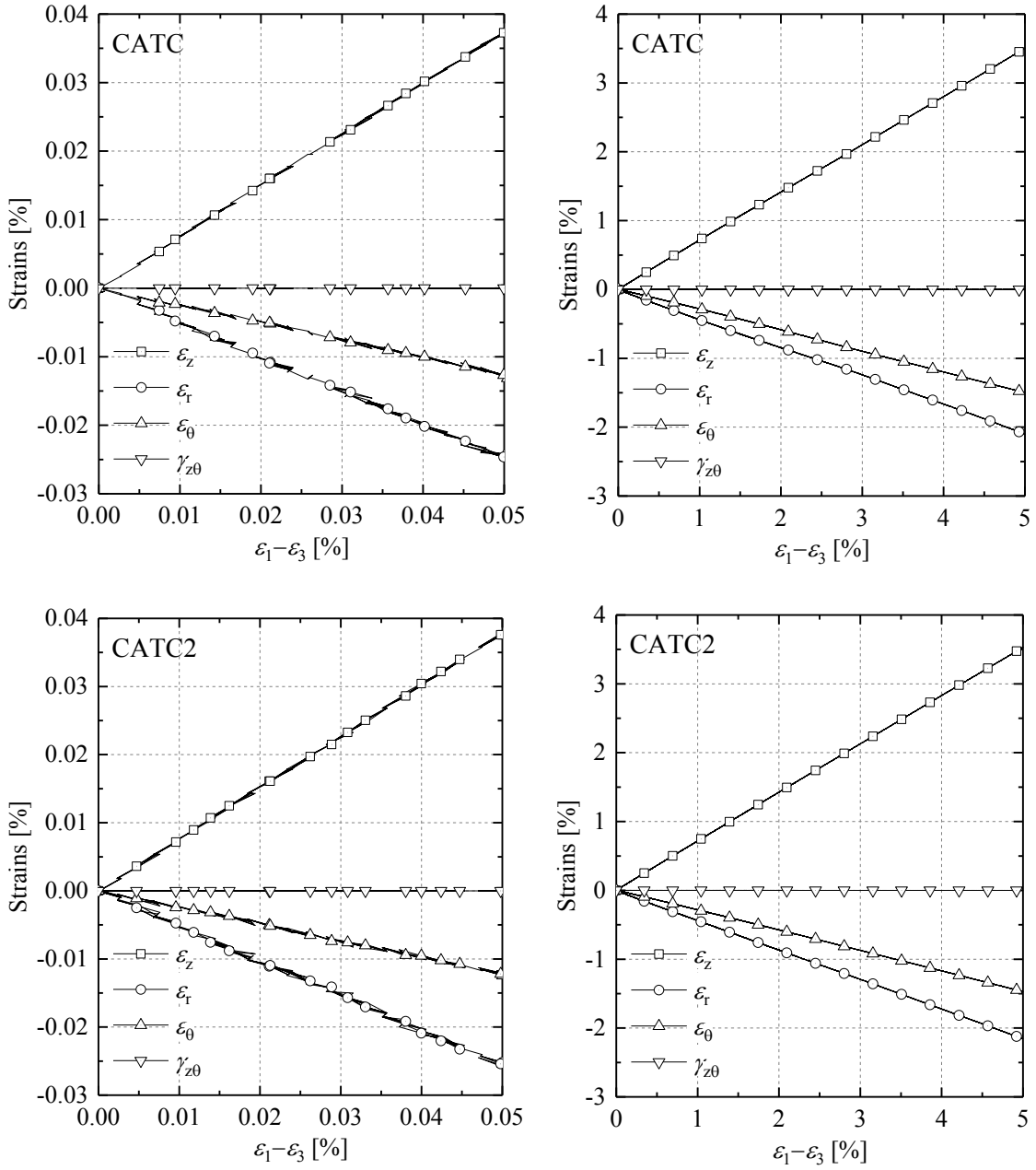

Figure 3-41 Strain component development trends during undrained shearing stage at small and large strain range for the HCA ‘triaxial’ compression tests CATC and CATC2

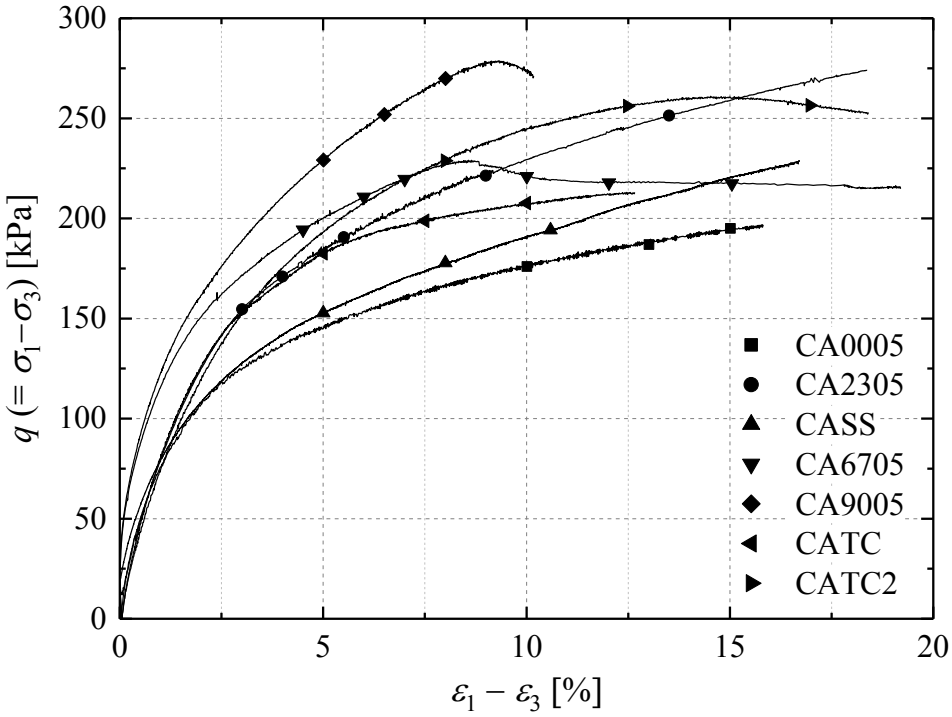

Figure 3-42 Deviatoric shear stress-strain trends q-(ε_1-ε_3) in the undrained HCA shearing tests

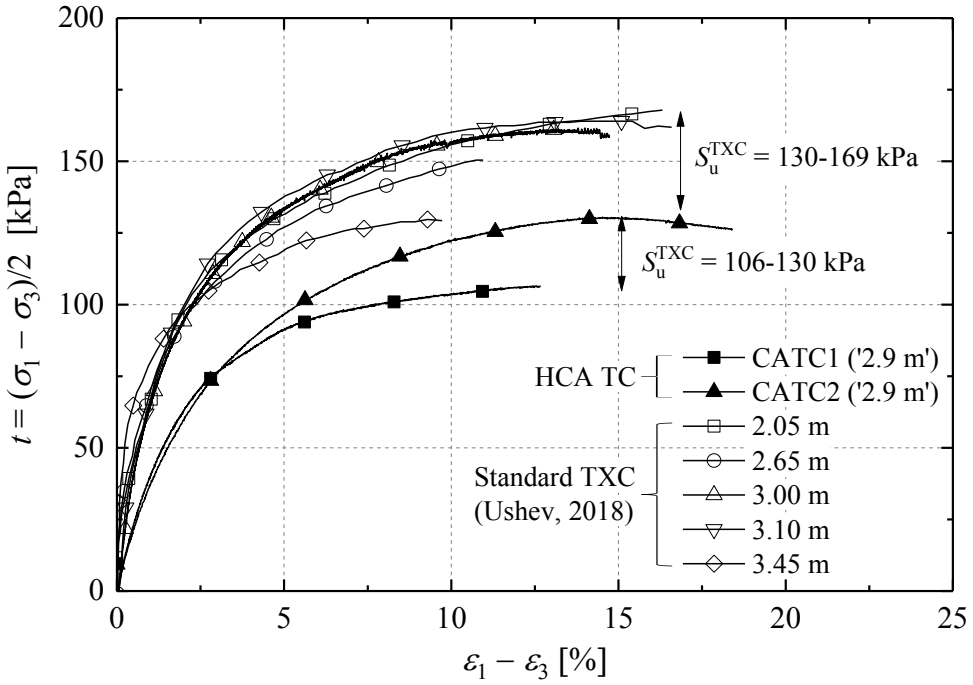

Figure 3-43 Stress-strain trends and shear strength of the HCA 'triaxial' compression tests and standard triaxial compression tests (Ushev, 2018) on samples from close depths

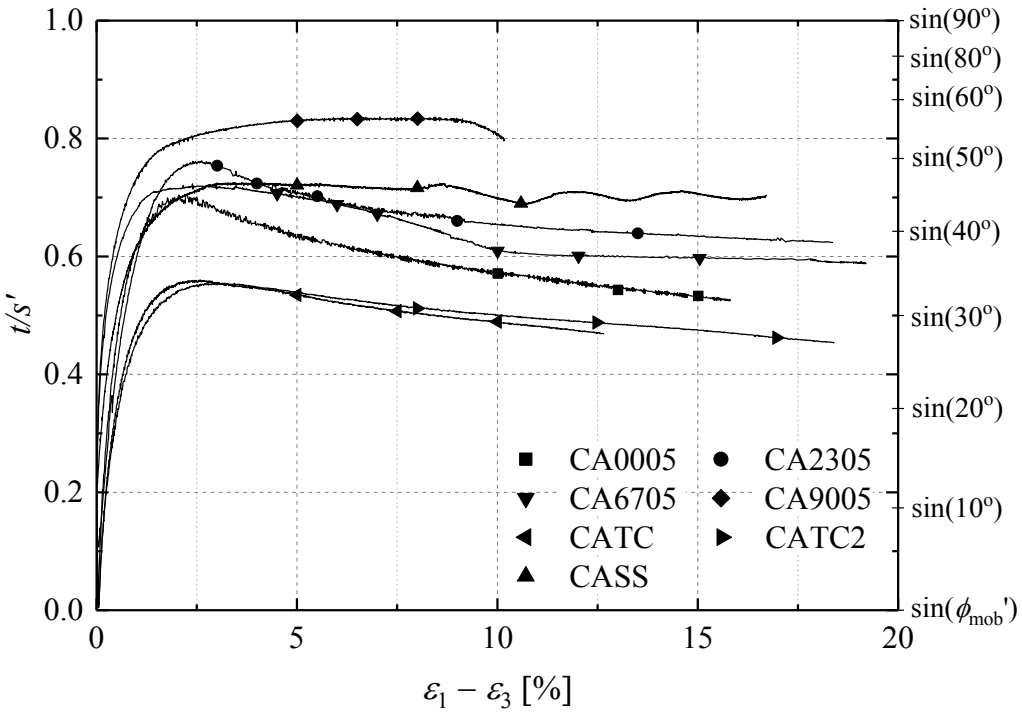

Figure 3-44 Stress ratio-strain trends t/s'-(ε_1-ε_3) in the undrained HCA shearing tests

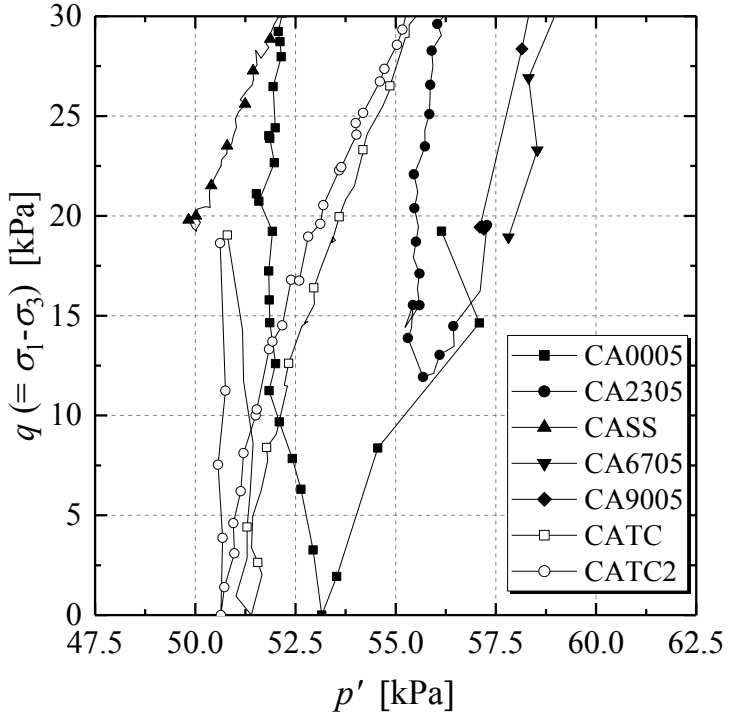

Figure 3-45 Effective stress paths of the HCA tests in q-p' plane ($q = \sigma_1$-σ_3) over initial small stress increment range

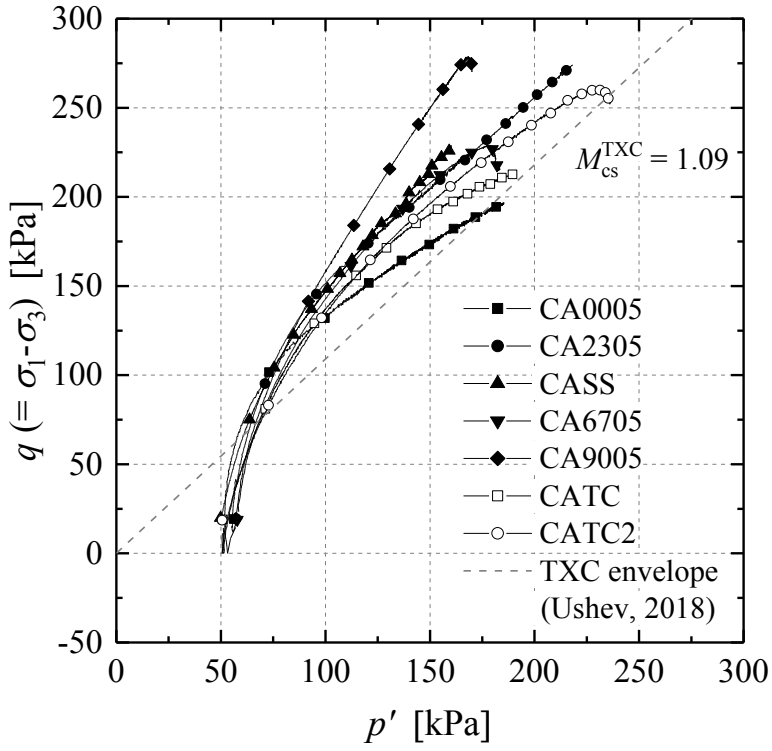

Figure 3-46 Overall effective stress paths of the HCA tests in q-p' plane ($q = \sigma_1$-σ_3)

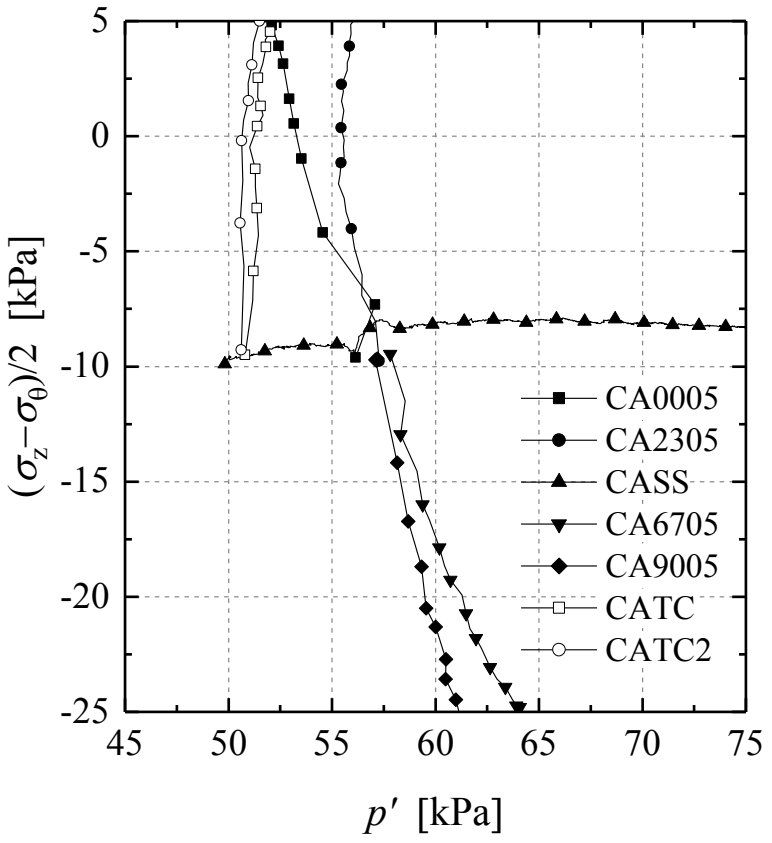

Figure 3-47 Projection of effective stress paths in the [(σ_z-σ_θ)/2]-p' plane over initial small stress increment range

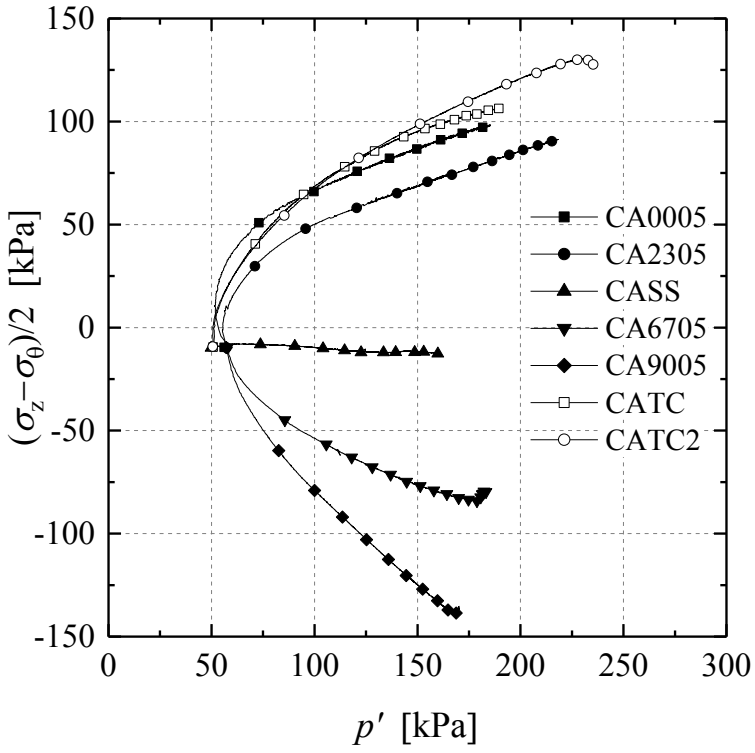

Figure 3-48 Projection of effective stress paths on the $[(\sigma_z-\sigma_\theta)/2]$-$p'$ plane

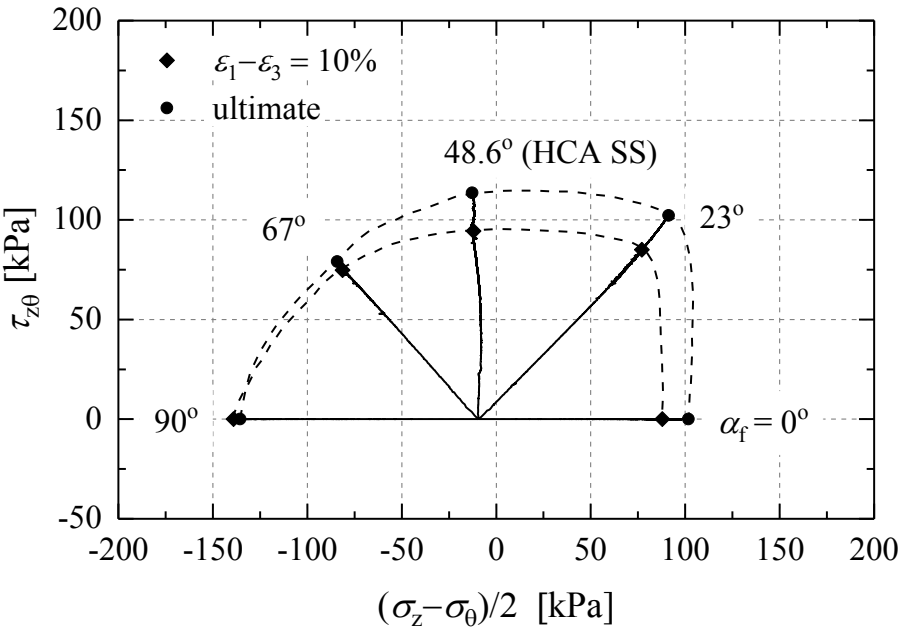

Figure 3-49 Projection of the stress paths on the $\tau_{z\theta}$-$[(\sigma_z-\sigma_\theta)/2]$ plane

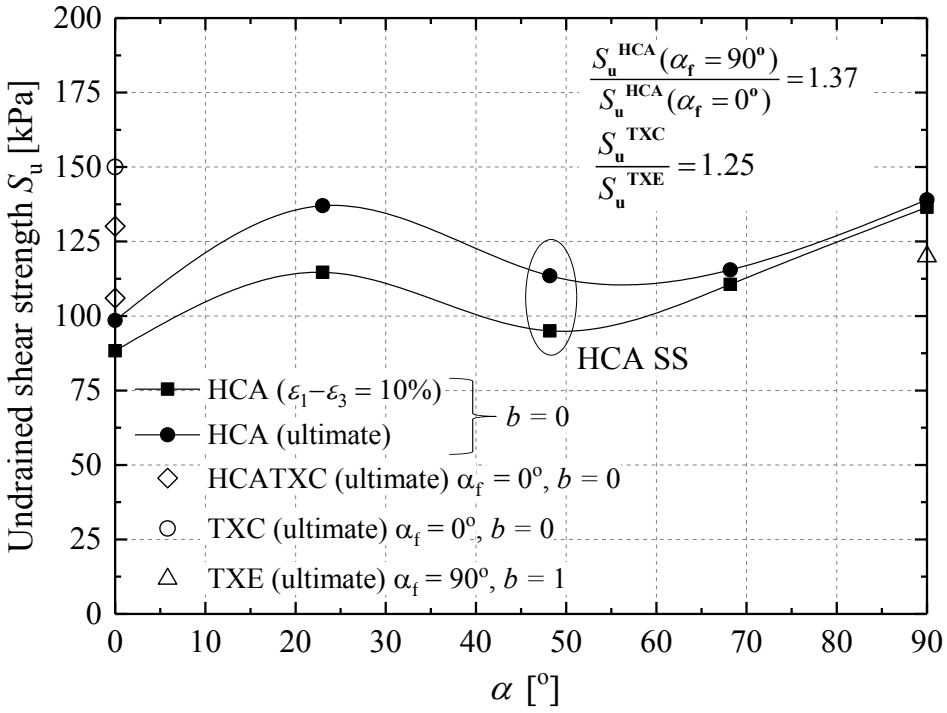

Figure 3-50 Variations of undrained shear strength S_u with the orientation of major principal stress (α) at varied shear strain levels

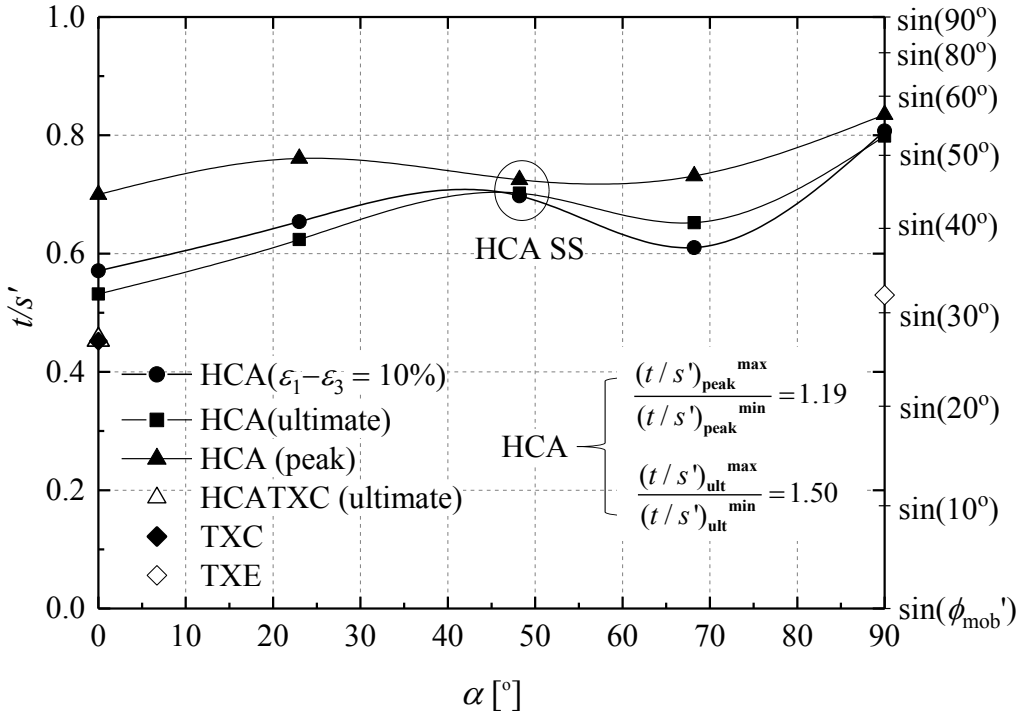

Figure 3-51 Variations in stress ratio t/s' with the orientation of major principal stress

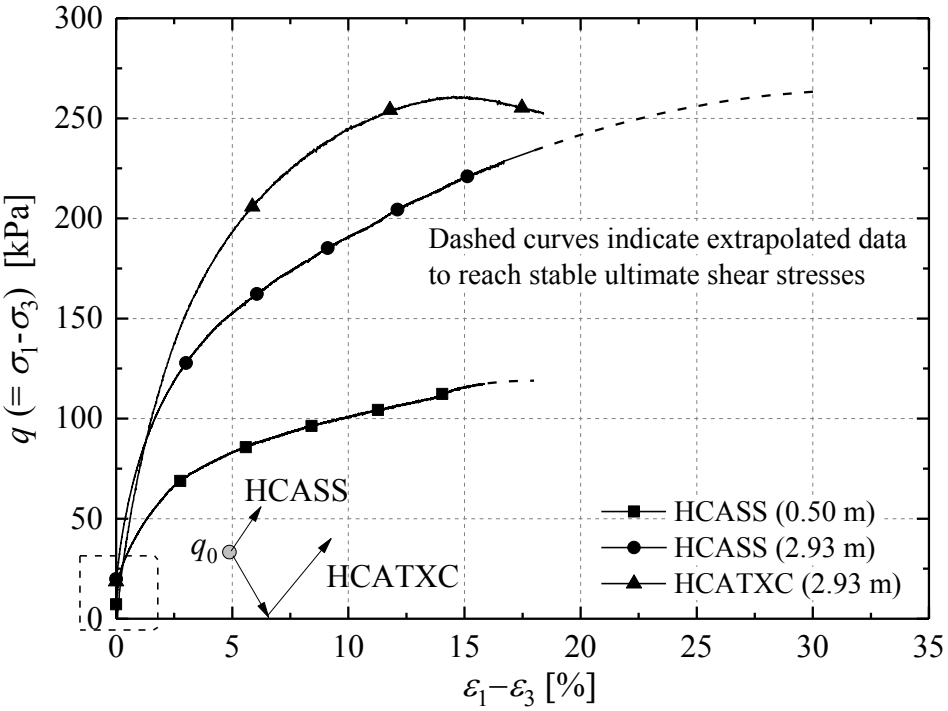

Figure 3-52 Shear stress strain curves of the two HCA simple shear tests on Cowden till samples from 0.50 m and 2.93 m bgl., in comparison with the HCA 'triaxial' compression test

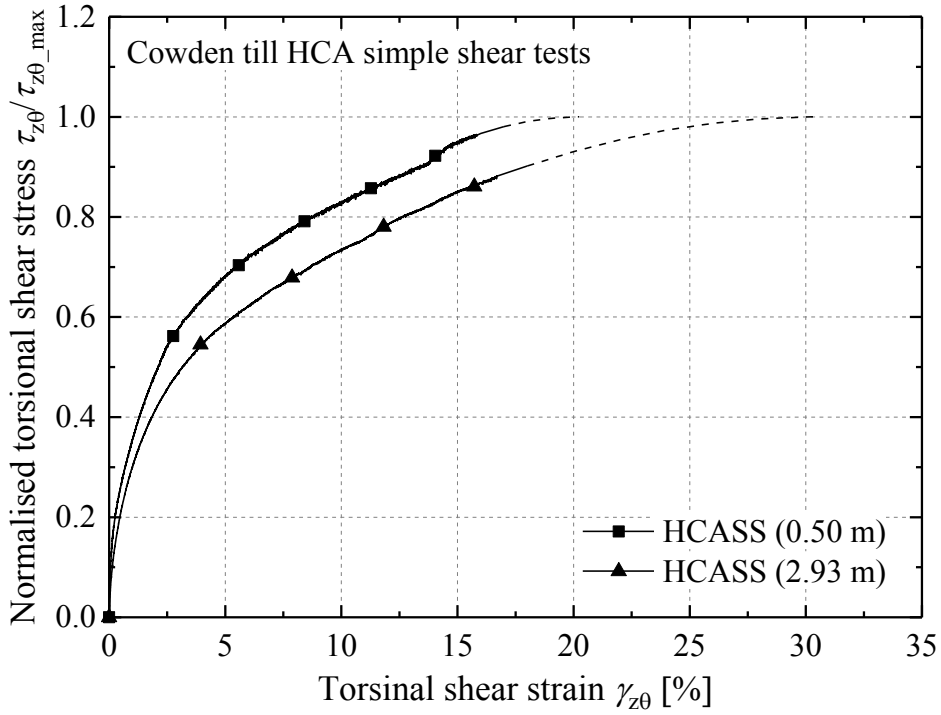

Figure 3-53 Normalised torsional shear stress-strain responses in undrained HCA simple shear (in linear scale)

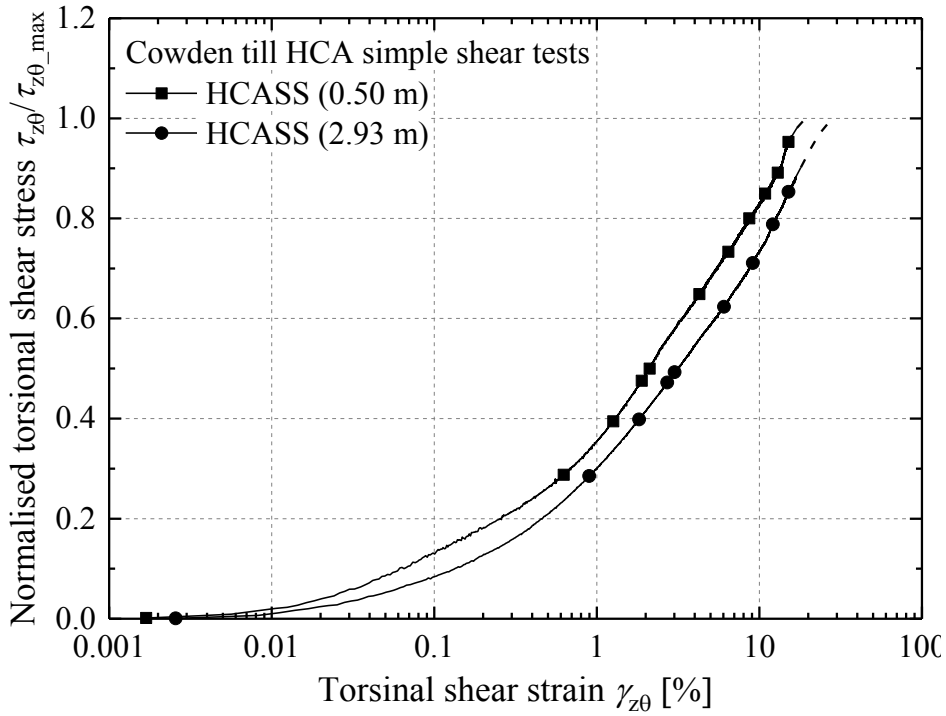

Figure 3-54 Normalised torsional shear stress-strain responses in undrained HCA simple shear (in semi-logarithmic scale)

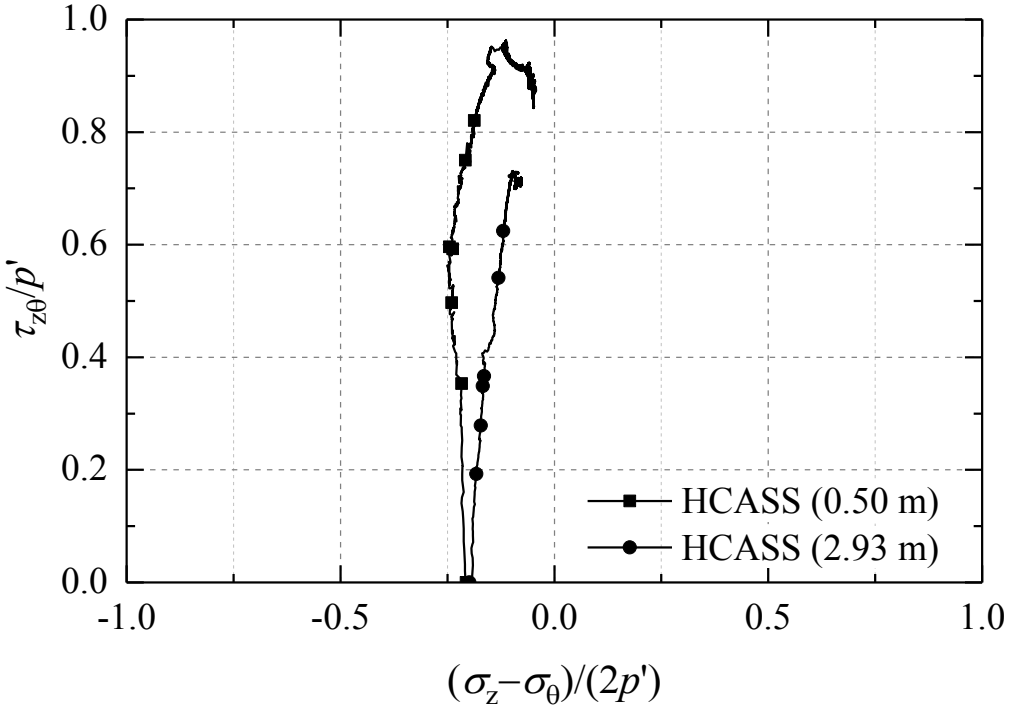

Figure 3-55 Projection of the undrained HCA simple shear stress paths on the $\tau_{z\theta}$-[(σ_z-σ_θ)/2] plane normalised by mean effective stress p'

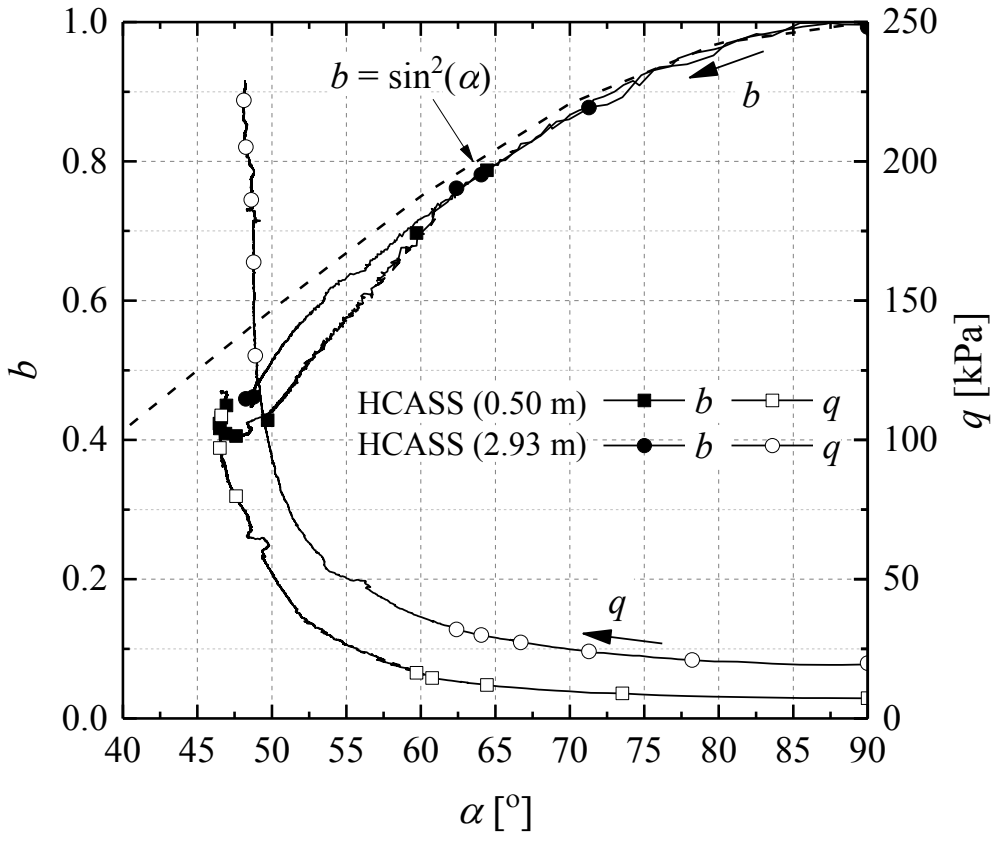

Figure 3-56 Variation trends of the major principal stress direction α and intermediate principal stress factor b during undrained HCA simple shear

3.6 Pre-failure behaviour and stiffness anisotropy

As described in Section 3.2.1, the undrained shearing stages of the HCA tests may be analysed to deduce the Cowden till's anisotropic stiffness characteristics over the full non-linear range. This section first discusses the stiffness characteristics seen under $\alpha_{d\sigma}$ undrained shearing from small up to medium strain levels, with a particular focus on degradation trends with strain of the anisotropic stiffness components.

Section 3.7 goes on to report and interpret the triaxial small-stress probing programme carried out to investigate the material's anisotropic linear elastic stiffnesses. Finally, the anisotropic stiffness profiles of the Cowden site are depicted and discussed in Section 3.8.

Interpretation and data processing approach

Under undrained conditions, the number of parameters required to fully describe a linear elastic cross-anisotropic model reduces to three, and can be measured and defined using a hollow cylinder apparatus. Equations (3.26) and (3.29) were adopted to derive the undrained vertical and horizontal Young's moduli (E_v^u, E_h^u) and shear stiffness (G_{vh} or $G_{z\theta}$). Least square linear regressions were applied over the strain up to 0.005% to determine best fit values of E_{v0}^u, E_{h0}^u and G_{vh0}.

Initial comparison between the raw stiffness data obtained from the current testing and those reported by Brosse (2012) revealed that the Cowden till dataset was subject to less instrument scatter, despite the fact that the hardware of the employed testing apparatus ICRCHCA remained largely unchanged. This apparent improvement is considered to be mainly due to three factors. Firstly, the tested Cowden till being from shallower depth and substantially softer than the deeper and stiffer strata tested by Brosse (2012), leading to system compliance effects being less significant. The second aspect that may attribute to the difference is that the current testing employed an upgraded controlling software programme (TRIAX) (Toll, 2002) which provided better servo-control of the multiple actuator variables involved. Finally, the temperature control systems employed in the Bishop Laboratory have been improved greatly since Brosse's (2012) studies, leading to less scattered readings of the instruments.

3.6.1 Undrained Young's moduli and shear stiffness

The elastic-plastic degradation trends of undrained equivalent vertical and horizontal Young's moduli (E_v^u and E_h^u) and torsional shear stiffness G_{vh} were derived by adopting the vertical strain ε_z, averaged horizontal strain $(\varepsilon_r + \varepsilon_\theta)/2$ and torsional shear strain $\gamma_{z\theta}$ as the key strain variables, respectively. The degradation trends of the tested specimens are plotted in Figures 3-57 to 3-59, while Table 3-7 summarises the initial cross-anisotropic parameters derived from linear regression over the strain range up to 0.005%.

Despite the scatter over the initial small strain range, the undrained Young's moduli exhibit clearly defined and consistent degradation trends. The curves for each component tend to converge after reaching a strain level of around 0.08%, suggesting that their stiffness evolutions are not markedly dependent on the shearing stress path followed. The CA6705 test presents slightly higher values of E_v^u below 0.01% vertical strain than the other tests, and a better defined plateau seems to be reached over strain range up to 0.003%. The stiffer E_v^u response noted in this test may have been due to the specimen's slightly higher gravel content or less mechanical disturbance being imposed during the preparation, and correlates with the sample's higher shear stiffness values: see in Table 3-7 and Figure 3-57. The two HCA triaxial tests (CATC and CATC2) which had initial b values of 1.0 prior to shearing presented encouragingly close correspondence and overlapping E_v^u trends that fell below the b = 0.5 tests (except CA2305), which may be due to the imposed b-change stage resulting in higher vertical total and effective stress, as reflected in Figure 3-37.

Figure 3-58 summarises the degradation trends of E_h^u against average horizontal strain $(\varepsilon_r + \varepsilon_\theta)/2$. The curves show a slightly higher degree of scatter than the E_v^u trends, which can be expected as the derivation of E_h^u involves all the three normal strains while the determination of E_v^u only requires vertical strains, as seen in Equations (3.26) and (3.29), making it less prone to the impact of measurement errors. Nevertheless, the E_h^u data depict well-defined trends of undrained horizontal Young's moduli during shearing, which clearly exceed the corresponding E_v^u values shown in Figure 3-57.

The degradation trends for monotonic shear stiffness G_{vh} ($G_{z\theta}$) are presented in Figure 3-59. Also plotted are the corresponding resonant column measurements taken at around 20 stages in each shear test. Scatter is evident at small strains, although the three

tests show clearer degradation trends once $\gamma_{z\theta} > 0.01\%$.

The resonant column stiffnesses show far less degradation and remain situated well above the monotonic trends. The resonant column G_{vh} values were found to be around 20-25% higher than the initial values determined over the small strain range of the monotonic shearing trend. Such discrepancies were also noted by Nishimura (2006) and Brosse (2012) who identified several possible reasons, including the influences of resonant column model adopted and calibration approach, stress-strain non-uniformities in the HCA specimens, potential strain rates effects, and accuracy limitations of the external and semi-local strain measurements. Several improvements, such as more extensive compliance checks in the torsional shear system or deployment of high resolution local strain instruments, may help to enhance stiffness data and possibly alleviate the discrepancies. However, such improvements could not be accomplished in the current study.

It is also observed that the resonant column shear stiffness trends appear to increase at large torsional strains (>0.4%). However, as pointed out by Gasparre *et al.* (2007b), the dynamic measuring techniques, such as resonant column and bender element, generally do not trace the current tangent elastic-plastic shear stiffness degradation as applying during monotonic loading but show how stiffness develops within the till's moving Y_1 kinematic yield surface (see descriptions in Section 5.2.2), as could be checked by applying small static unload-reload loops. The characterisation of non-linear tangent shear stiffness degradation may only be achieved through monotonic shearing.

3.6.2 Stiffness anisotropy and further discussion

The attained HCA results revealed significant stiffness anisotropy in the Cowden till, both over the initial, presumably elastic range and the non-linear range. The initial cross-anisotropy of the initial (small strain) stiffness was assessed through a regression approach, as summarised in Table 3-7. The average ratio of horizontal and vertical Young's moduli (E_{h0}^{u}/E_{vo}^{u}) is 1.74, while the ratio of horizontal to vertical shear stiffness (G_{hh0}/G_{vh0}) is 1.64, indicating overall stiffer behaviour in horizontal planes. The derived undrained Poisson's ratios (μ_{hh0}, μ_{hv0}) are also included in Table 3-7, giving average $\mu_{hh0}^{u} = 0.111$ and $\mu_{hv0}^{u} = 0.889$ which clearly deviate from the value of 0.5 expected for isotropic elastic materials.

The degradation trends shown in Figures 3-57 and 3-58 were reprocessed over the non-linear range to obtain ratios of undrained Young's moduli (E_h^u/E_v^u) that varied with vertical strain ε_z, as presented in Figure 3-60. It is clear that the soil presents higher horizontal stiffness over the strain range up to 0.4%. The shearing path undertaken affected the non-linear stiffness anisotropy trends. The two tests undergoing primarily vertical compression (α_f = 0˚, 23˚) presented much slower degradation of E_h^u/E_v^u with shear strain than the two horizontally loaded tests (α_f = 67˚, 90˚), which exhibited much steeper E_h^u/E_v^u decay over the small to medium strain range and increased at larger strains. A similar dependency of the degree of anisotropy on test paths was noted in the previous research on stiff mudrocks, see Brosse *et al.* (2015).

Table 3-7 Initial cross-anisotropic parameters derived from linear regression over small strain range and the resonant column measurements

Test	E_{v0}^u [MPa]	E_{hr0}^u [MPa]	$E_{h\theta 0}^u$ [MPa]	E_{h0}^u [MPa]	E_{h0}^u/E_{v0}^U	G_{vh0} [MPa]	G_{hh0} [MPa]	μ_{hh0}^u [-]	μ_{hv0}^u [-]	$G_{z\theta}^{RC(2)}$ [MPa]
CA0005	86.3	137.8	160.1	149.0	1.73	-	65.6	0.135	0.865	56.3
CA2305	78.8	121.6	154.5	138.1	1.75	40.0	61.4	0.125	0.875	56.5
CA6705	100.1	214.0	141.0	177.5	1.77	46.7	81.0	0.095	0.905	59.3
CA9005	86.4	145.8	148.0	146.9	1.70		74.5	0.090	0.910	53.1
CATC	82.0									50.1
CATC2	76.8									50.5
CASS						43.3				51.0
CTSS						26.0				
Average	85.1	154.8	150.9	152.9	1.74	43.3(1)	70.63	0.111	0.889	53.8
Std. dev	7.75	34.9	8.03	14.76	0.04	3.87(1)	7.65	0.019	0.019	3.31

Note: (1) Average and standard deviation of G_{vh0} excluding the test CTSS;

(2) Resonant column measurements prior to shearing (after the *b*-change stage if applied).

3.6.3 Figures

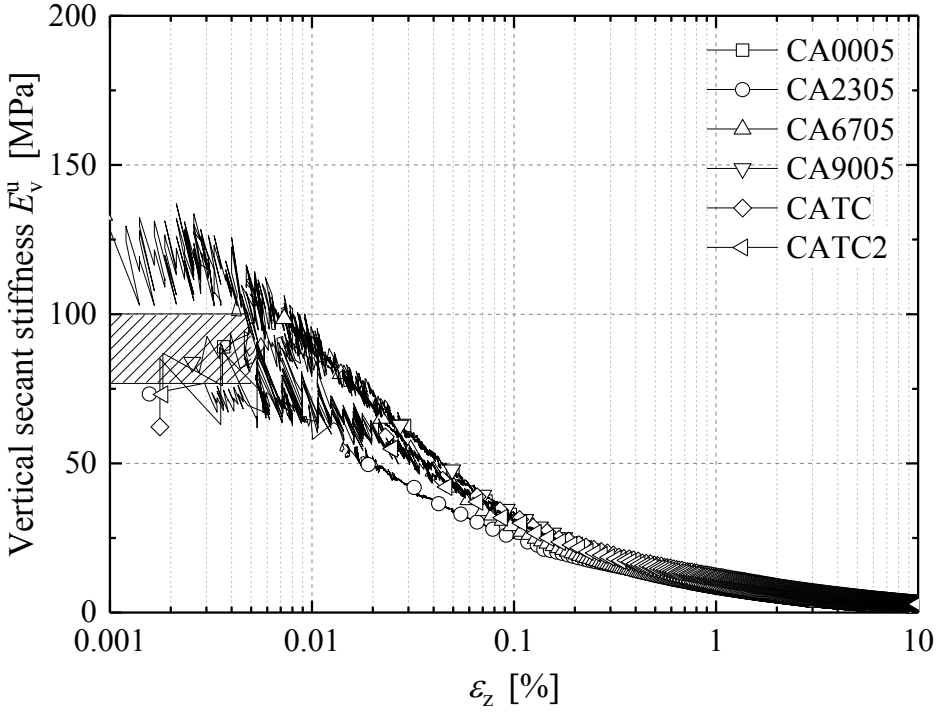

Figure 3-57 Degradation of undrained vertical Young's Moduli E_v^u against vertical strain

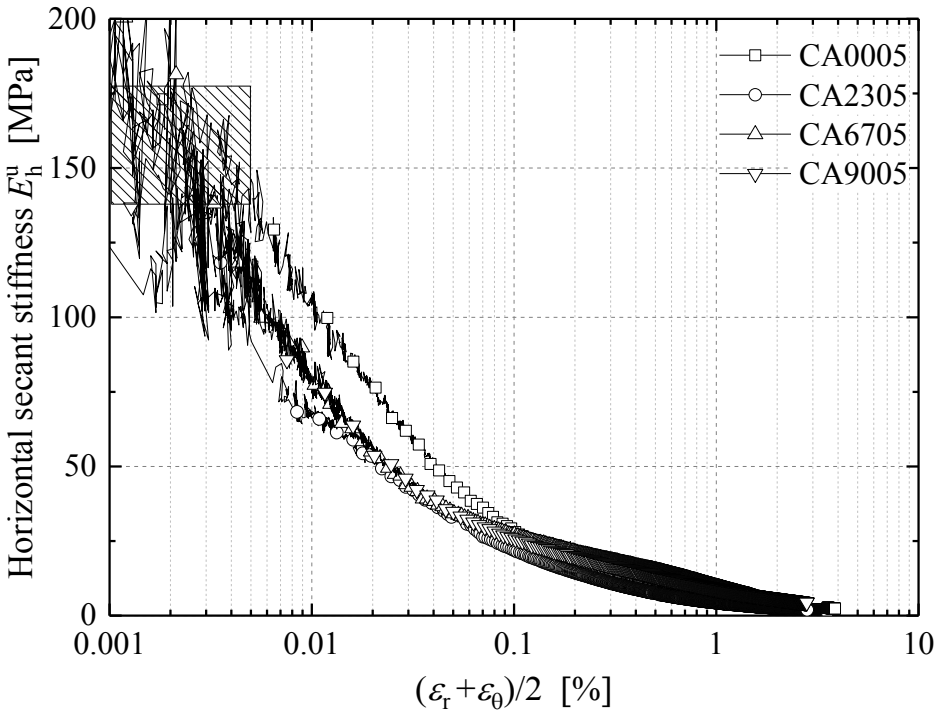

Figure 3-58 Degradation of undrained horizontal Young's Moduli E_h^u against horizontal strain

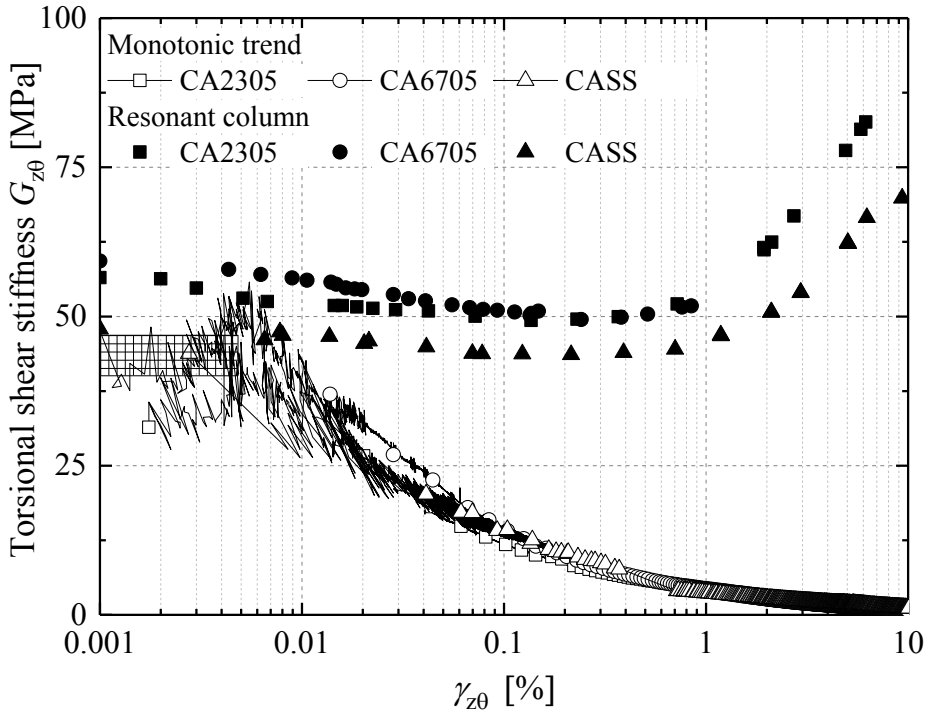

Figure 3-59 Degradation of torsional shear stiffness $G_{z\theta}$ against torsional shear strain

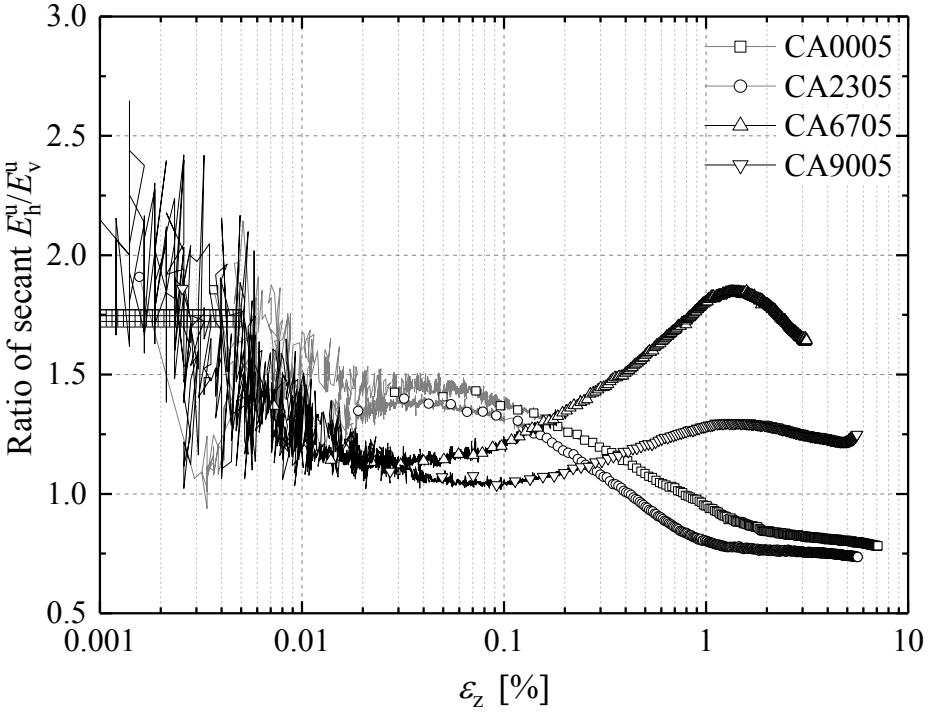

Figure 3-60 Variation of Young's moduli ratio E_h^u/E_v^u against axial strain during $\alpha_{d\sigma}$ shearing

3.7 Cross-anisotropic stiffness parameters from triaxial probing tests

The above HCA testing enabled characterisation over the full strain range of the till's equivalent undrained Young's moduli (E_v^u and E_h^u) and shear stiffness ($G_{z\theta}$). Additional stress-controlled probing tests were performed using the '100 mm' fully instrumented triaxial apparatuses to characterise the material's stiffnesses over the initial linear elastic (Y_1) range accurately and determine the five effective-stress cross-anisotropic compliance parameters described in Section 3.2.1.

It would have been ideal to perform the probing tests on block samples from a similar depth (3.0 m) to the HCA specimens. However, this could not be achieved due to sample availability limits. Instead, two tests were performed on rotary core samples (from Cowden borehole 3) taken at 5.1 m and 12.5 m, respectively. Their test conditions and estimated in-situ stresses are given in Table 3-2 (CTX1 and CTX2). Similar probing tests were reported by Ushev (2018) on samples from 2.0 m and 12.0 m. It should be noted that the sample from 12.5 m (text CTX2) was initially re-consolidated to its 'true' in-situ stress at (σ_v', σ_h') = (230.6, 230.6) and K = 1. However, the stress state slowly drifted to nearby stresses with (σ_v', σ_h') = (212.3, 218) after a malfunction of the laboratory's central air compressor. Time limitations led to its probing tests being performed at the latter effective stresses.

3.7.1 Test scheme and procedures

Although broadly similar to the processes for preparing HCA specimens (see Section 3.3.1), the formation of solid triaxial specimens from rotary cores was more straightforward. The index properties and initial suctions (listed in Tables 3-3 and 3-4) of the two prepared specimens (CTX1 and CTX2) were consistent with those reported by Ushev (2018) for samples from similar depths.

The employed '100 mm' apparatuses allowed double drainage from both ends, which was further facilitated by vertical side filter paper drains attached evenly to the specimen's circumference. A mid-height probe was deployed in the middle of the specimen to track water pressure in the central soil zone. Lubrication disks consisting of layers of latex membrane and high-vacuum grease were implemented at both specimen ends to alleviate friction constraints.

The testing stages of initial p', saturation (and B value check) and consolidation

were similar to those of the HCA testing, as described in Section 3.3.6. The specimens were less desiccated than the shallower HCA samples and B values > 0.97 were reached readily with 350-400 kPa back pore water pressures.

Similar re-consolidation stages were imposed to consolidate the specimens to their estimated in-situ stress at a rate of around 2 kPa/hour. Extended waiting periods (> 3 weeks) were required for the specimens to creep until the axial and radial strain increment rates decreased to less than 0.0002%/day. These low residual strain rates were required to ensure that strains in the subsequent probing tests were not affected by any residual creep straining. Figure 3-61 plots the secant strain rates of local axial and radial strains developed in the long-term creep stage of the test at the 5.1 m depth specimen (CTX1). The re-consolidation path, which took the specimen from (σ_v', σ_h') = (80, 80) to (σ_v', σ_h') = (69.9, 104.9) led to higher creep strain rates in the radial direction. The required creep strain criterion was only approached after an approximately 3 week long pauses of 520 hours. The creep rates over the final period fluctuated slightly, probably induced by the 0.2-0.3 ˚C temperature fluctuations recorded in the cell water.

Figure 3-61 also denotes the limiting creep strain criteria adopted to decide whether shearing could start in the triaxial and HCA testing on Cowden till; these are re-summarised in Table 3-8. Also listed are the shearing rates employed for the different types of tests and the corresponding shearing/creep strain ratios. It was observed in the testing case of CTX1, the strain rate criterion (0.01%/day) for undrained triaxial compression or extension shearing was reached after initial around 50 hours of creep, over which period the creep strains accumulated represented around half of those that would have developed if the specimen had been allowed to creep further to 520 hours, as with other causes.

Long term creep may have allowed the ductile, fissured and stony till to saturate any residual air trapped in the soil matrix, close more voids and develop more compacted structure, manifesting as the evident residual strains. These features may also lead to ageing effects that could exhibit as enhanced stiffnesses in the 3-week aged specimens compared to those from tests involving shorter creep stages. Further comparisons are presented in the next section.

The triaxial cell chamber was wrapped in a thick temperature buffer layer consisting of bubble wrap and aluminium foil throughout the testing. The maximum temperature

fluctuation recorded in the cell water was 0.5 ˚C, while most fluctuations fell below 0.2 ˚C over individual 10-12 hour probing stages. Differences of around 1 kPa were seen between the pore water pressures measured at the base and the specimen mid-height over the consolidation stage. However, the differences decreased significantly to below 0.2 kPa as creep evolved and remained negligible over the subsequent probing stages. Pore water pressures from the mid-height probe were adopted in the analysis of probing tests.

Table 3-8 Creep strain criteria and shearing rates adopted in the Cowden till study

Test type	Strain rates [%/day]		
	Creep (≤)	Shearing	Ratio
Triaxial undrained shearing Ushev (2018)	0.005-0.01	5	500-1000
Triaxial drained & undrained probing	0.0002	0.007-0.014	35-70
HCA undrained shearing	0.012	3.6	300

Bender element measurements

Bender element tests were performed regularly throughout the triaxial tests. Clear input and output signals were attained in most cases of the Author's tests, which could be interpreted readily with the time-domain first arrival peak method. Examples of the recorded signals are given in Figure 3-62. As has been noted by previous studies (see for example Yamashita *et al.* (2009)), the interpreted bender element stiffnesses were dependent on the input signal frequencies. The interpretation below quotes average shear stiffness values based on measurements made with input frequency range of 3-10 kHz.

3.7.2 Stress-controlled probing tests

Suites of drained and undrained stress-controlled probing tests were performed on each specimen. Ideally, these would each be conducted on separate identical specimens. However, the stress probing increments were kept to very low levels (< 2 kPa) so that the probing tests could be regarded as being non-destructive and multiple tests could be performed on single specimens without affecting the results. The probing tests imposed a stress change rate of 0.2 kPa/hour and the specimen was left for at least 24 hours after

each probing test to allow for the stabilisation of any residual strains.

The small probing stress increments ($\Delta\sigma_v'$, $\Delta\sigma_h'$ and Δq) were applied using both 'half-cycle' and 'full-cycle' configurations. The former consisted of (axially or radially) loading or unloading in one direction and then returning to the initial stress states, designated as +v′, -v′, +h′, -h′, +q and -q, whereas the latter included full stress cycles that extended to both loading and unloading directions, representing as ±v′, ±h′ and ±q. In both methods, stress changes were imposed in one direction (either axial or radial) while the stress in the other direction was maintained constant. Both methods require the stress increments to be sufficiently small to maintain the specimen within its linear elastic zone (Y_1) and the derived Young's moduli (E_v', E_h' and E_v^u) should ideally be identical, regardless of the methods used and the stress increment direction (loading or unloading). The 'full-cycle' method, however, could be preferred in some cases. Assuming that the Y_1 region was initially centred on the current effective stress, this method involved less risk of exceeding the linear zone in one direction while it covered a larger strain range and so enhanced the representativeness of the attained data.

The specimens were further sheared to failure after the stress probing tests under drained conditions at an axial loading rate of 0.2 kPa/hour while maintaining constant σ_h'.

3.7.3 Test outcomes and discussions

Two approaches (as shown in Figure 3-1) were employed to derive the cross-anisotropic stiffness parameters and Poisson's ratios, namely the Kuwano (1999) approach which utilises both axial and radial strain measurements from drained axial and radial probes, and the Nishimura (2014a, 2014b) approach which employs only axial strain measurements from drained axial and radial probes plus an additional undrained (axial) probe. Table 3-9 summarises the stress probes performed and the results, and Table 3-10 lists all the measured and derived stiffness parameters and Poisson's ratios using the above approaches.

Starting from the 'half-cycle' probing tests on the 5.1 m specimen (test CATC1), Figure 3-63 demonstrates the trend of the axial ($\Delta\varepsilon_a$) and radial ($\Delta\varepsilon_r$) strain increments in two drained axial loading (+v′) and unloading (-v′) probing tests, while Figure 3-64 plots the corresponding $\Delta\varepsilon_r$ -$\Delta\varepsilon_a$ trends, from which the Poisson's ratio (ν_{vh}') can be

directly determined. The results indicate linear elastic stress-strain response over the small stress range and the strain components were found to be fully reversible. The vertical drained Young' moduli (E_v') were closely comparable in the two tests, independent of the sign of the load increment. The radial strain components and the corresponding Poisson's ratio ν_{vh}' showed slightly more scatter, reflecting the generally greater difficulties in making local radial strain measurements, as noted by previous researchers for example Nishimura (2014a) and Ackerley *et al.* (2016).

Figure 3-65 plots axial ($\Delta\varepsilon_a$) and radial ($\Delta\varepsilon_r$) strain responses against the horizontal effective stress increments ($\Delta\sigma_h'$) for the two drained horizontal loading (+h′) and unloading (-h′) probes. Also denoted are the determined linear elastic stress-strain ratios ($\Delta\sigma_h'/\Delta\varepsilon_a$ and $\Delta\sigma_h'/\Delta\varepsilon_r$ (or F_h')). Again, generally good much was seen between the two loading and unloading probes. The outcomes from the above two sets of 'half-cycle' drained axial and radial probes, together with bender element measurements (G_{vh} and G_{hh}), allowed full determination of five effective-stress cross-anisotropic stiffness parameters, as summarised in Table 3-10.

Figures 3-66 and 3-67 show 'full-cycle' stress-axial strain responses ($\Delta\sigma_v'$-$\Delta\varepsilon_a$, $\Delta\sigma_h'$-$\Delta\varepsilon_a$, Δq-$\Delta\varepsilon_a$) recorded in the drained axial (±v′) and radial (±h′) as well as undrained axial (±q) probes. The ±v′ and ±h′ probing tests gave results close to those seen in the 'half-cycle' probes. The additional ±q probe enabled the Nishimura (2014a, 2014b) approach to be applied, and the derived parameters are compared with those from the Kuwano (1999) in Table 3-10.

Similar suites of results are shown in Figures 3-68 and 3-69 for the 12.5 m depth specimen (test CATC2). The radial strain measurements in this test were less reliable, particularly in the drained axial probing tests (+v′) where the radial strains were particularly low in proportion to the already small axial strains. Nevertheless, the stiffnesses derived from the loading and/or unloading probes were consistent, as summarised in Table 3-9.

As shown in Table 3-10, the undrained Young's moduli E_v^u and E_h^u determined from drained parameters using Equations (3.7) and (3.8) gave E_v^u values that were close to those from the undrained probes, and E_h^u values that were consistent between the two approaches, with average deviations of 4% from their mean values.

However, more significantly different E_h' values were found between from the

Kuwano (1999) and Nishimura (2014) approaches, particularly for the CTX1 test which gave a markedly higher E_h' from the Nishimura (2014) approach. The Nishimura (2014) approach is highly sensitive to small variations in the E_v^u determined from undrained probing. It is likely that, as previously noted by Zdravkovic & Jardine (1997) in the testing with a far larger HCA, local volume change and pore water pressure non-uniformity can take place in undrained tests primarily due to end restraint, system compliance (as discussed in Section 2.3.7) and possible sample inhomogeneity. Further investigation is required to assess possible errors and optimise the measuring procedures.

Overall, the results in Table 3-10 confirm that Cowden till manifests stiffer behaviour in the horizontal planes than the vertical planes, with the stiffness ratios (G_{hh}/G_{vh}, E_h'/E_v' and E_h^u/E_v^u) invariably greater than unity. Further data integration is presented in the following section, in which the HCA test outcomes are combined with triaxial stress path probing tests on specimens from different depths as well data from site investigation. Integrating these data allows anisotropic stiffness profiles to be proposed for the Cowden till site.

Table 3-9 Summary of the triaxial probing tests performed on Cowden till

Test	Stresses [kPa]		Drained axial				Drained radial				Undrained axial		
	σ_v'	σ_h'	Type	$\Delta\sigma_v'$	E_v' [MPa]	ν_{vh}'	Type	$\Delta\sigma_h'$	a [MPa^{-1}]	F_h' [MPa]	Type	Δq	E_v^u [MPa]
CTX1 (5.1 m)	69.9	104.9	±	0.7	120.2	-	±	0.7	0.00393	102.8	±	1.4	132.1
			-	1.3	124.4		+	2.2	0.00269	92.8			
			+	2.2	111.6	0.36	-	2	0.00350	110.5			
			Average		**120.0**	**0.36**			**0.00336**	**102.0**			**132.1**
CTX2 (12.5 m)	212.3	218	±	1.8	**204.5**	**1.09***	±	1.8	**0.00181**	**274.3**	±	1.8	**212.0**
			+	2.7	219.1	1.06*	±	1.8	0.00209	344.0			

Notes:

1. $a = \nu_{hv}'/E_h' = -1/2\times\Delta\varepsilon_a/\Delta\sigma_h'$; $F_h' = E_h'/(1-\nu_{hh}') = \Delta\sigma_h'/\Delta\varepsilon_r$; see Equations (3.14) and (3.15).
2. Numbers in bold represent the values adopted for parameter derivation.
3. Poisson's ratios with '*' superscript subjected to errors from residual radial straining.

Table 3-10 Summary of the derived cross-anisotropy stiffness parameters and Poisson's ratios

Test	Method	G_{vh} [MPa]	G_{hh} [MPa]	E_v' [MPa]	E_h' [MPa]	ν_{hh}'	ν_{vh}' (1)	ν_{hv}' (1)	ν_{hv}' (2)	ν_{vh}' (2)	E_v^u [MPa]	E_h^u [MPa]	ν_{hh}^u	ν_{hv}^u
CTX1 (5.1 m)	Kuwano (1999)	125	161	120.2	155.0	-0.52	0.36	0.46	0.52	0.40	122.7	278.5	-0.14	1.14
	Nishimura (2014)	125	161	120.2	271.7	-0.16			0.91	0.40	132.1	290.3	-0.10	1.10
CTX2 (12.5 m)	Kuwano (1999)		119	204.5	254.9	0.07	1.08	1.36	0.46	0.37	219.1	308.5	0.30	0.70
	Nishimura (2014)		119	204.5	199.5	-0.16			0.36	0.37	212	304.9	0.28	0.72

Notes:

1. The drained Poisson's ratios were derived with flow (1) and (2) methods (see Figure 3-1) and denoted as ν_{vh}' (1) or ν_{vh}' (2);
2. The undrained Young's moduli were calculated with Poisson's ratios calculated from the flow (2), i.e. ν_{vh}' (2) and ν_{hv}' (2);
3. Underlined numbers represent variables from direct measurements while the others from derivation.

3.7.4 Figures

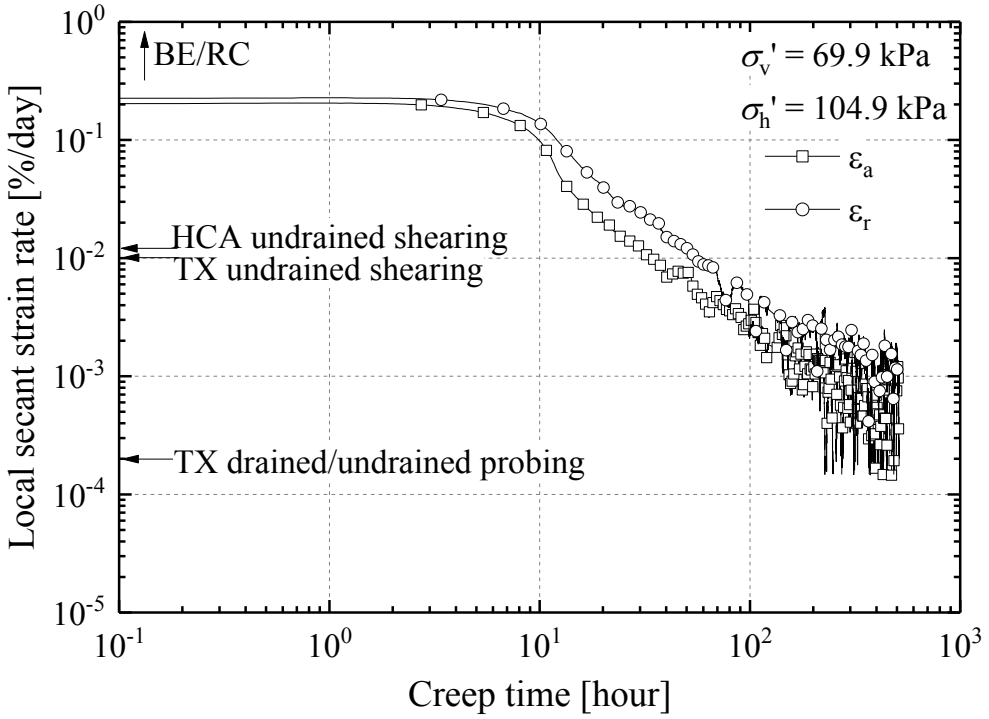

Figure 3-61 Trends of local axial and radial secant strain rates (absolute values) against creep time for test CTX1, also denoting the creep strain rate criteria adopted for initiating shearing Cowden till samples in different tests

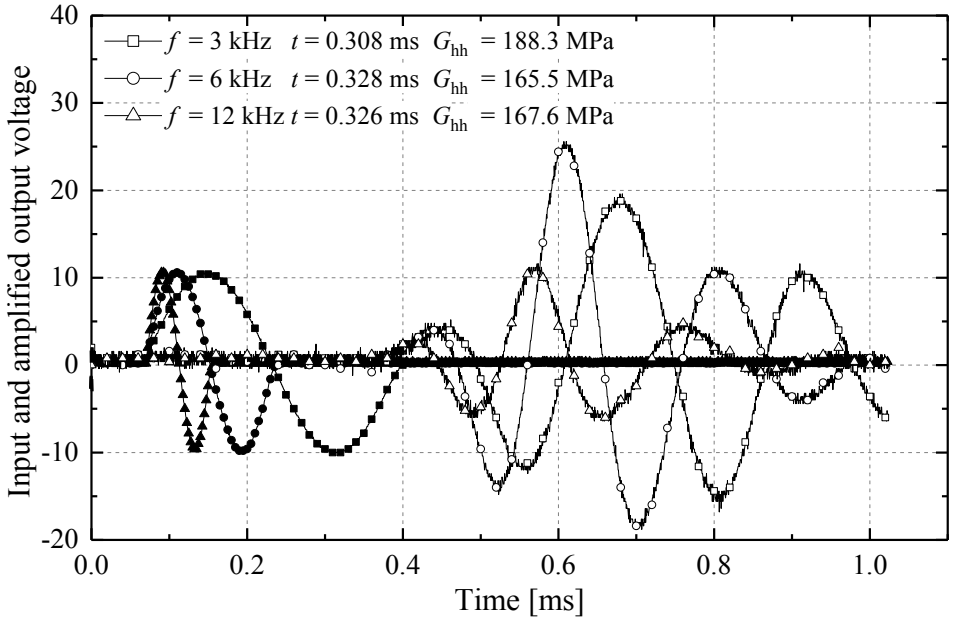

Figure 3-62 Input and amplified output bender element signal, also indicating the interpreted travel time and G_{hh} based on first arrival peak method at three input frequencies

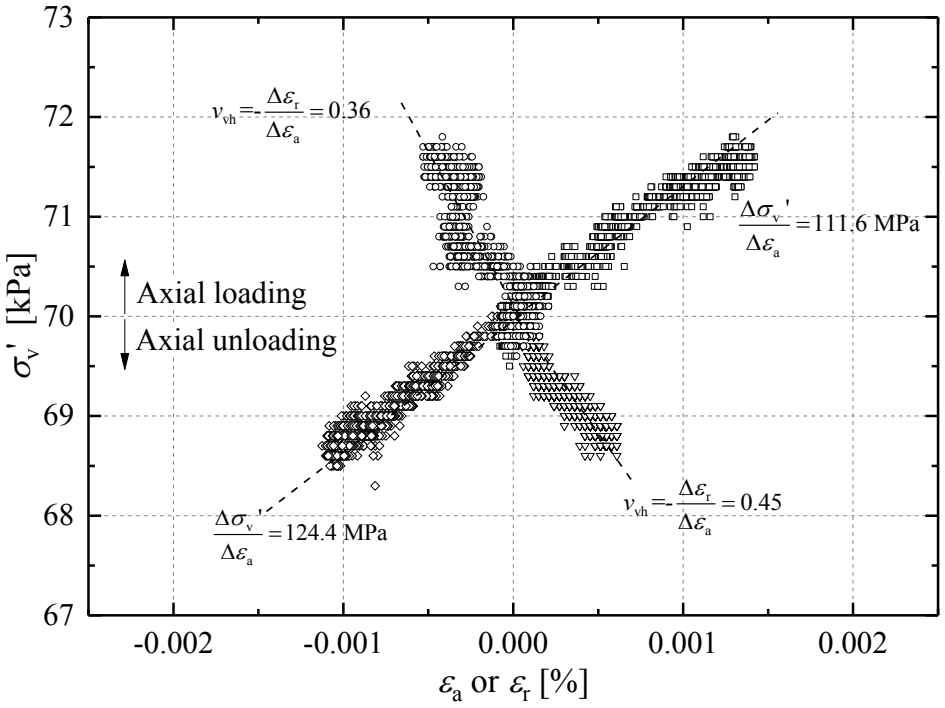

Figure 3-63 Stress-strain increments in the drained axial loading (+v′) and unloading (-v′) probes on the 5.1 m depth specimen (test CTX1)

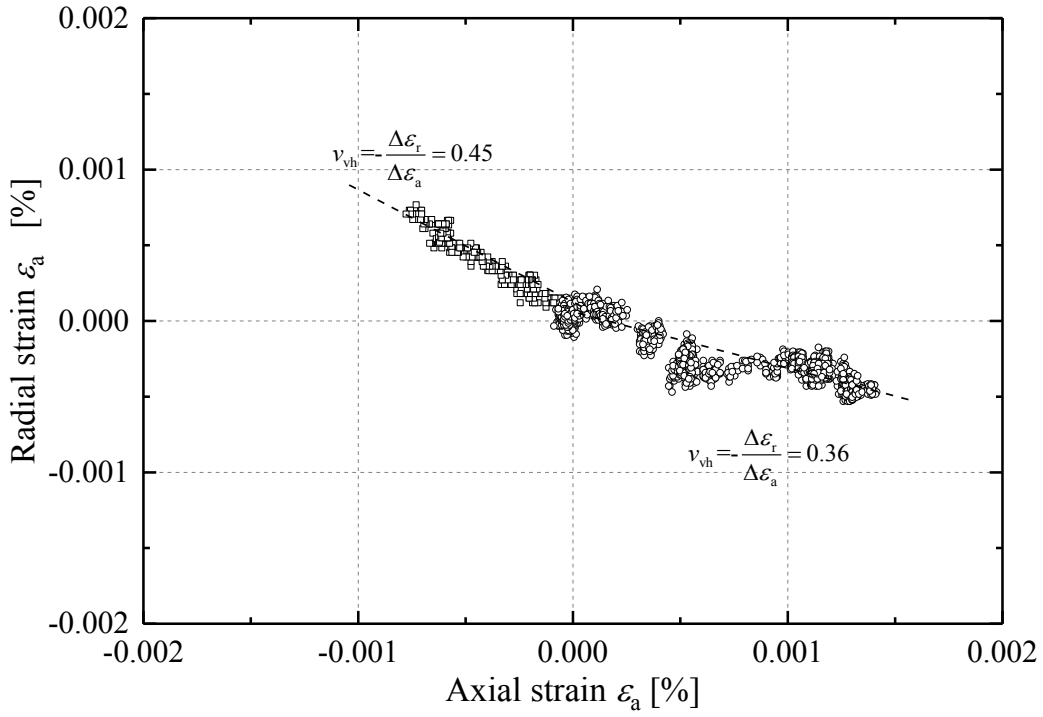

Figure 3-64 Poisson's ratio (v_{vh}′) determined in the drained axial loading (+v′) and unloading (-v′) probes on the 5.1 m depth specimen (test CTX1)

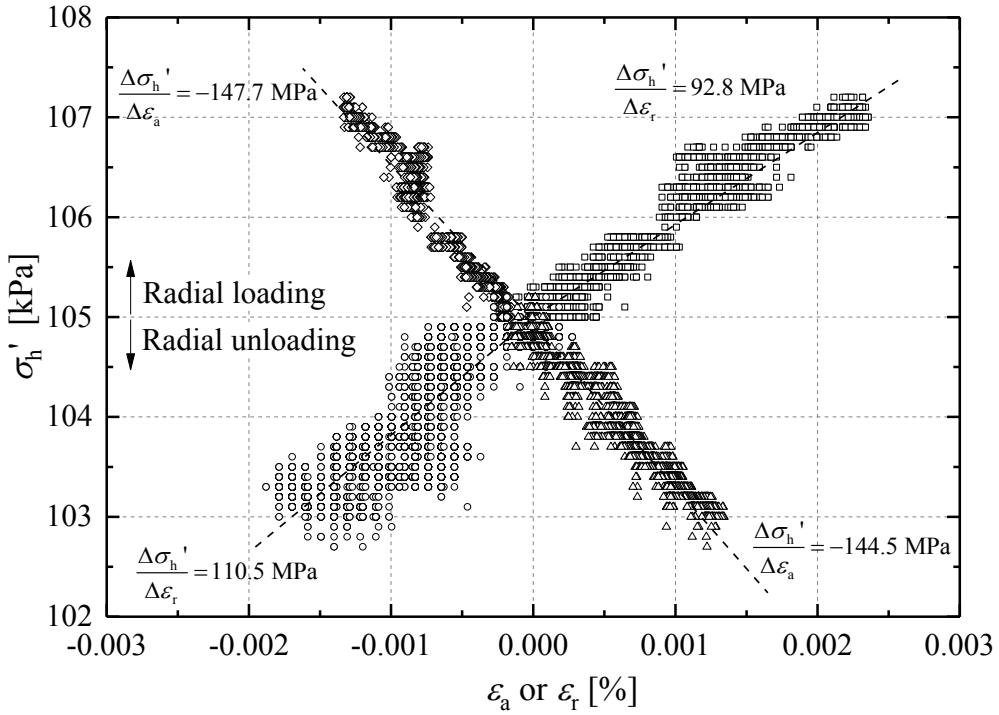

Figure 3-65 Stress-strain increments in the drained radial loading (+h′) and unloading (-h′) probes on the 5.1 m depth specimen (test CTX1)

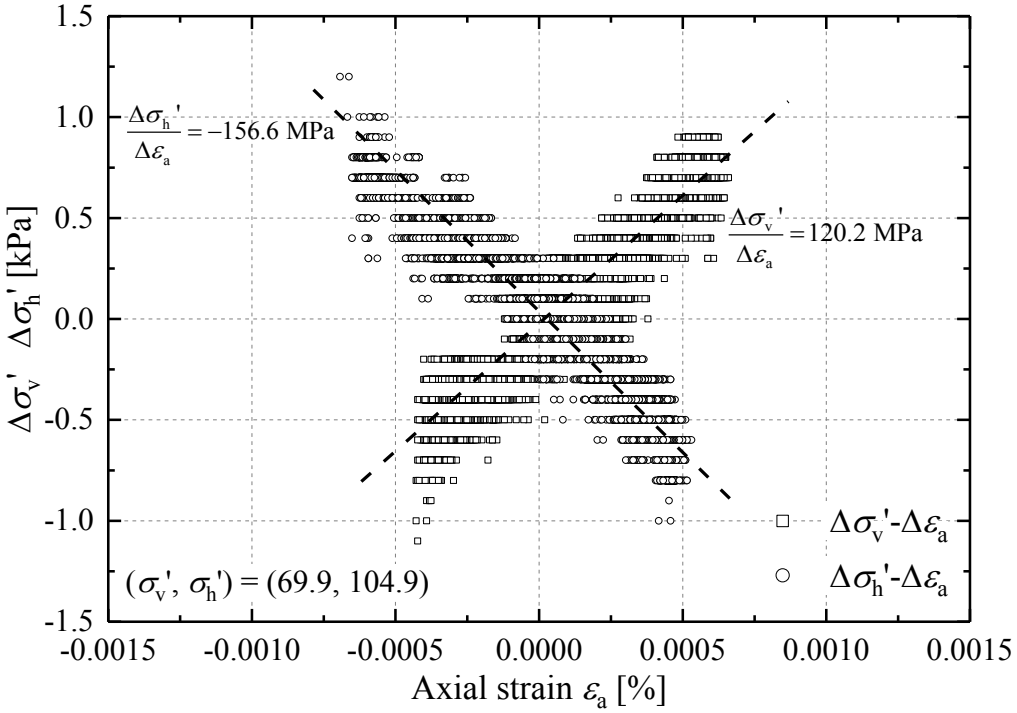

Figure 3-66 Stress increment-axial strain responses in drained axial (±v′) and radial (±h′) stress probes on the 5.1 m depth specimen (test CTX1)

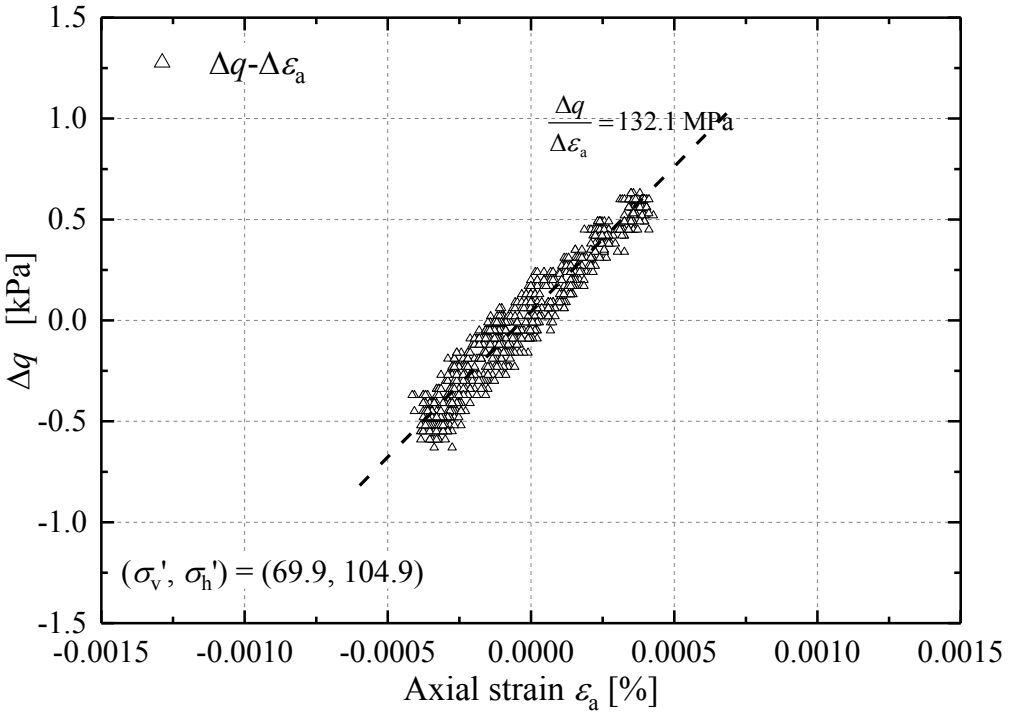

Figure 3-67 Stress increment-axial strain response in undrained axial (±q) stress probes on the 5.1 m depth specimen (test CTX1)

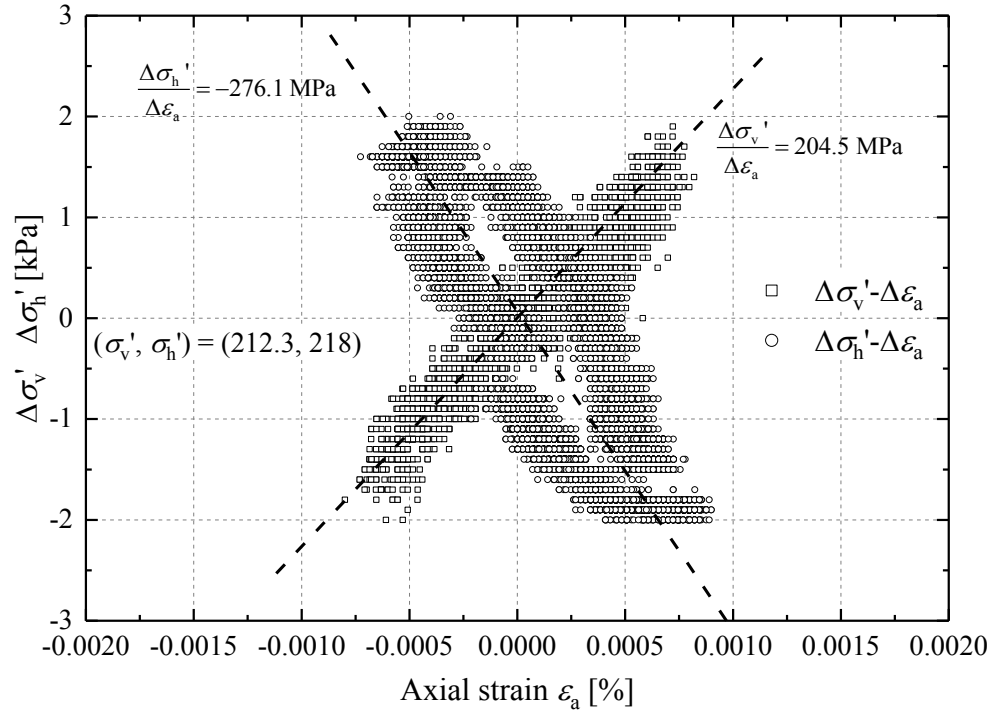

Figure 3-68 Stress increment-axial strain responses in drained axial (±v′) and radial (±h′) stress probes on the 12.5 m depth specimen (test CTX2)

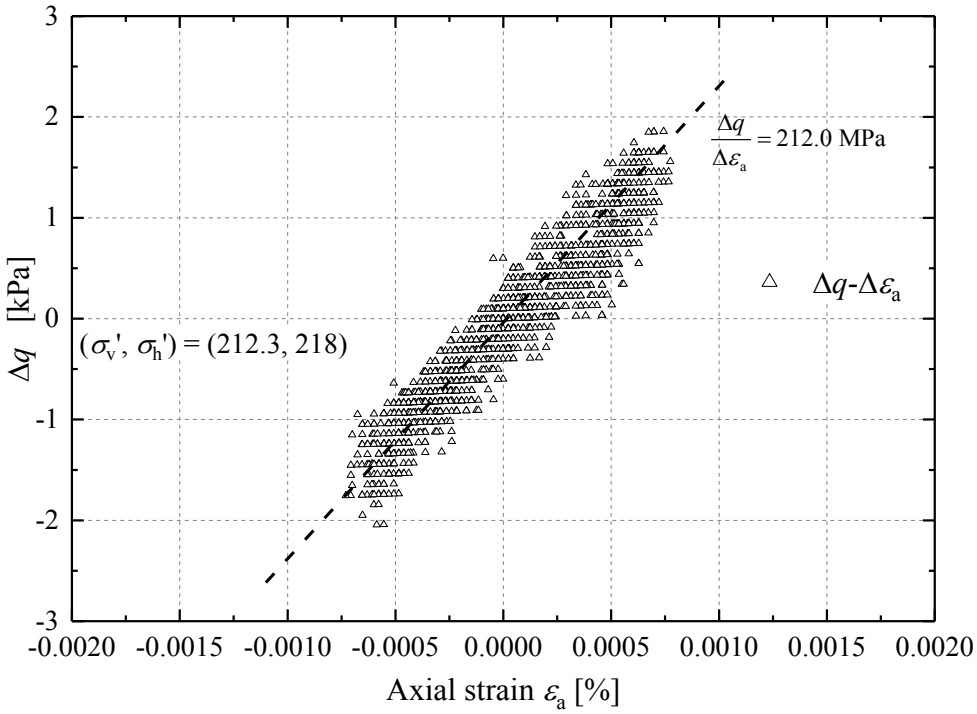

Figure 3-69 Stress increment-axial strain response in undrained axial (±q) stress probes on the 12.5 m depth specimen (test CTX2)

3.8 Integration of laboratory and in-situ stiffness measurements

Further integration is presented below of the stiffness data from various laboratory apparatuses and approaches (Triaxial, HCA, 'static' shearing and dynamic wave velocity measurements from bender element and resonant column) as well as from in-situ site measurements reported by Powell & Butcher (2003) and the PISA project. Potential variations induced by sampling techniques (rotary coring or block sampling), spatial variations, specimen size effects are discussed. Finally, an anisotropic stiffness profile of the Cowden till site is depicted, and the practical implications particularly for analysing laterally loaded monopiles are indicated.

3.8.1 Shear stiffnesses from different approaches

The triaxial and HCA tests involved re-consolidating the specimens to their estimated in-situ effective stresses, at which dynamic shear stiffnesses were measured with bender element (BE) and resonant column (RC) equipment, providing laboratory data that could be compared directly with in-situ seismic cone tests (SCPT), as summarised in Figures 3-70 to 3-72. As noted earlier, the period for which specimens were aged prior to BE testing could influence the results greatly. It is therefore important to differentiate the BE measurements made on the triaxial specimens (TX) left for 'standard' creep times (following the criteria set in Table 3-8) and those on triaxial probing (TX-PB) specimens which were tested after ten times longer creep periods.

As shown in Figure 3-70, Ushev (2018) found that his laboratory bender element G_{vh}^{BE} measurements on rotary core samples agreed well with in-situ seismic cone G_{vh}^{SCPT} tests which were carried out at locations close to (within 5 m) the rotary core boreholes, although relatively low G_{vh}^{BE} were noted in the deeper horizons (below 8 m), which may reflect the effects of rotary drilling disturbance. Although not by a marked degree, the bender element G_{vh}^{BE} trend is generally located above that of the G_{hh}^{BE} component over the upper 5 m deposit.

However, Ushev's tests on block samples from 2.0 m and 3.45 m depth exhibited higher G_{vh}^{BE} values than his rotary core samples or the field seismic cone penetration (SCPT) tests, as shown in Figure 3-71. Ushev (2018) attributed this trend to irreversible effects of drying of the block samples during field sampling and trimming, although it is also possible that the field SCPT testing affected soil stiffness due to its invasive penetration process and other sources of uncertainty. Recalling that the till

sampled between 1.5 m and 3.0 m was severely desiccated and variable (as noted from the suction profile in Figure 3-24), the discrepancies noted above might also reflect spatial variations, as the rotary coring and block sampling locations were spaced around 60 m apart.

Figure 3-72 further demonstrates that the shear stiffnesses of the shallower specimens (2.0 m and 5.1 m) determined in the triaxial probing tests were significantly higher than those in the standard triaxial tests, regardless of the possible effects of the sampling techniques employed. The 2.0 m depth probing specimen was prepared from a soil block whereas the 5.1 m specimen was from a rotary core. It appears that BE stiffness measurements grew considerably over the 3-4 week creep/ageing stages, which may reflect the formation of more compacted structure in the fissured shallower specimens. As mentioned above, the block samples from 2.0 m were severely desiccated, and any residual free air trapped may have been further saturated during long-term creep, even though high B values (> 0.97) had been achieved before re-consolidating these specimens.

The stiffness gains were more significant in the G_{hh}^{BE} direction than the G_{vh}^{BE}, particularly for the 5.1 m specimen. This may reflect the fact that the radial creep strain rates were consistently higher than those in the axial direction, as shown in Figure 3-61.

Any stiffness gains through ageing were, however, less prominent with the ≈ 12.0 m deep specimens, as shown in Figure 3-72. The deeper rotary core specimens were much less fissured and desiccated, and showed significantly lower initial suctions (≈70 kPa) and higher initial degrees of saturation (close to 1). Their imposed re-consolidation stress paths followed purely isotropic consolidation. The ageing mechanisms postulated for the shallower specimens did not apply.

3.8.2 Anisotropic stiffness profile of the Cowden till site

The triaxial probing results for the samples from 5.1 and 12.5 m depth, together with similar tests reported by Ushev (2018) and the HCA tests on samples from 3.0 m, indicated the anisotropic stiffness ratios G_{hh}/G_{vh}, E_h'/E_v' and E_h^u/E_v^u, as summarised in Table 3-11. The data are replotted in Figure 3-73, together with shear modulus ratios (G_{hh}/G_{vh} and G_{hh}/G_{hv}) determined from in-situ down-hole and cross-hole shear velocity tests reported by Powell & Butcher (2003).

The combined available dataset confirms that the Cowden site manifests clearly higher stiffnesses in the horizontal plane than in the vertical plane, particularly in the top 7 m of the till in which the PISA piles were primarily embedded.

The PISA lateral pile testing took place over a matter of hours each and applied principally undrained horizontal loading in the "passive" region in front of the pile, in combination with horizontal unloading in the "active" region behind the pile and shear straining in horizontal planes around the two flanking areas of the piles, as shown in Figure 1-5. The E_h^u and G_{hh} stiffnesses are more representative of the field response to loading than those from triaxial compression (E_v^u) tests.

Table 3-11 Ratios between horizontal and vertical Young's moduli and shear stiffnesses along the Cowden site profile

Test/depth	Stress [kPa]		G_{hh}/G_{vh}	E_h'/E_v'	E_h^u/E_v^u	Method
	σ_v'	σ_h'				
2.0 m (Ushev, 2018)	33.0	49.5	1.17	1.13	2.44	Kuwano (1999)
				1.91	2.29	Nishimura (2014)
2.9 m (HCA tests)	38.4	57.6	1.63[(a)] (1.31)[(b)]	-	1.74	Brosse (2012)
CTX1 (5.1 m)	69.9	104.9	1.29	1.29	2.27	Kuwano (1999)
				2.26	2.20	Nishimura (2014)
12.0 m (Ushev, 2018)	223.8	223.8	0.97	0.84	1.36	Kuwano (1999)
				0.89	1.35	Nishimura (2014)
CTX2 (12.5 m)	212.3	218	-	1.25	1.41	Kuwano (1999)
				0.98	1.49	Nishimura (2014)

Notes:

(a) Shear stiffness from monotonic shearing;

(b) Shear stiffness from resonant column measurements, see Table 3-7.

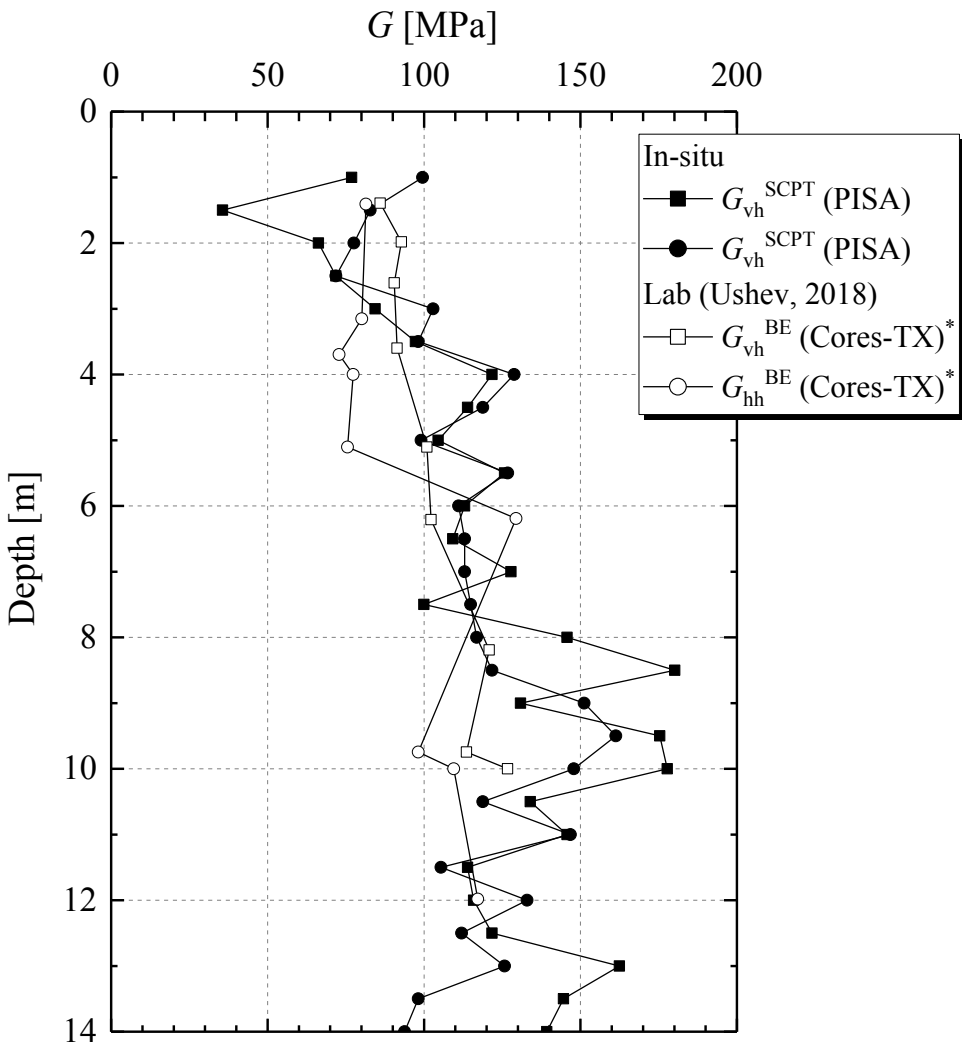

Figure 3-70 Stiffness profile: SCPT vs. triaxial BE (rotary core samples)

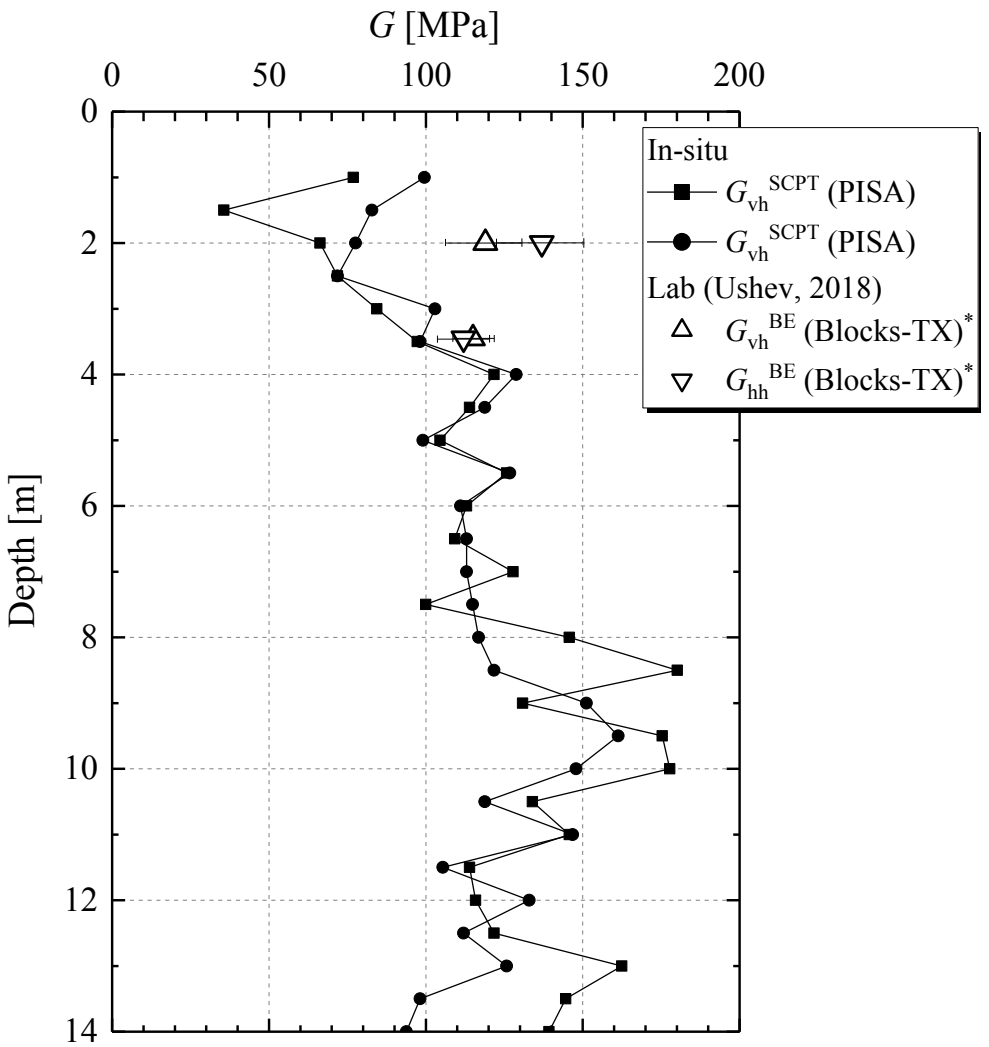

Figure 3-71 Stiffness profile: SCPT vs. triaxial BE (block samples)

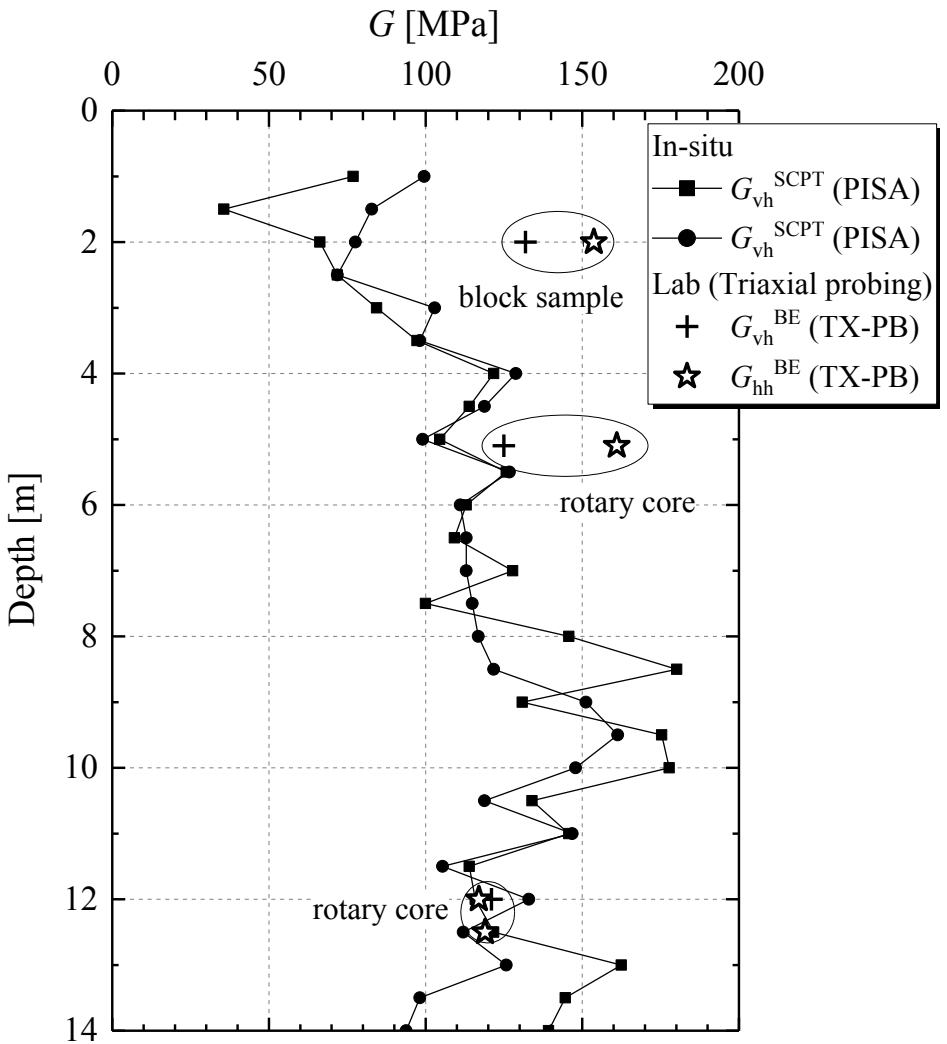

Figure 3-72 Stiffness profile: SCPT vs. triaxial probing BE

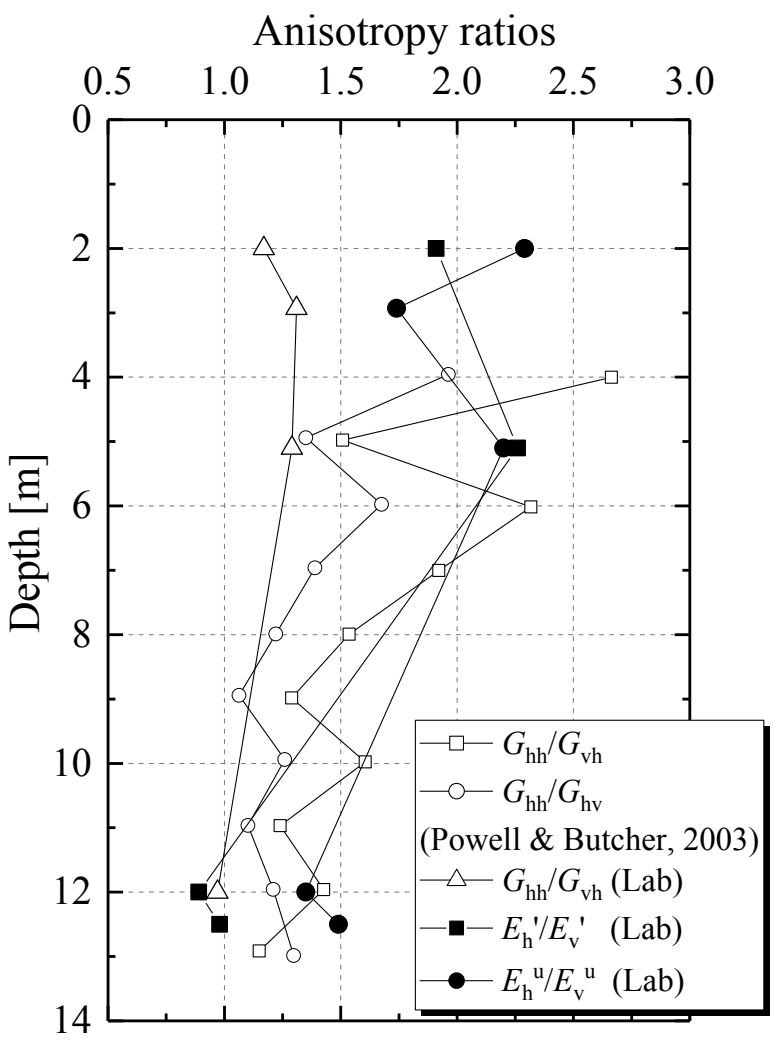

Figure 3-73 Anisotropic stiffness profile of the Cowden till site

3.9 Summary and conclusions

This chapter presented a laboratory investigation of the anisotropic stiffness and undrained shear strength behaviour of the over-consolidated low plasticity stiff Cowden till. It was shown how challenges imposed by the stony and fissured nature of the material were overcome to form hollow cylinder specimens that were tested successfully on samples from around 3.0 depth, supplemented by triaxial probing tests on rotary core samples from 5.1 m and 12.5 m depth. Index properties and suction measurements were also undertaken and integrated with triaxial tests by Ushev (2018) and other in-situ test data. The HCA programme investigated undrained behaviour in tests conducted with b = 0.5 and major principal stress axis directions α set at angles from 0˚ to 90˚ in the vertical plane, supplemented by triaxial and simple shear tests conducted in the HCA. The main conclusions drawn from the study are as follows.

1. The optimised specimen preparation procedures developed in the programme ensured tolerably good quality and uniformity of the tested specimens. However, specimen preparation was only possible with samples that presented relatively low (2-4%) gravel contents, which represented only the least gravel rich section of the in-situ profile, within which the gravel fractions ranged from 2 to 10%.

2. This bias in sampling, combined with possible specimen formation disturbance and HCA test non-uniformity factually led to the HCA tests giving triaxial shear strengths around 25% below Ushev's (2018) stress-path triaxial tests and resonant column G_{vh} values around 30% below those from in-situ SCPT tests.

3. Nevertheless, the HCA tests on Cowden till exhibited clearly trend of anisotropic stiffness characteristics. The undrained Young's moduli in the horizontal direction were 70% higher than those in vertical direction (i.e. E_h^u/E_v^u = 1.7) over the initial linear elastic range. The Young's moduli and shear stiffness components showed clear trends of decaying against shear strain over non-linear range regardless the shearing stress paths followed, and the horizontal undrained Young's moduli remained higher than the vertical up to 0.4% vertical strain range.

4. The markedly ductile Cowden till exhibited a mildly anisotropic shear strength patterns that were different from those of brittle stiff clays. Quantified in both total stress measure (S_u) and effective stress measure (t/s'), the minimum shear strength was noted in α = 0˚ and the maximum developed at α = 90˚. The torsional shear

mode was not particularly weak and manifested shear strengths in between the active (vertical) and passive (lateral) compression modes.

5. Simple shear tests performed in the HCA, which allows the principal stress axis direction and intermediate stress factor to be characterised fully while generating less severe non-uniformities than conventional simple shear apparatuses, offered key insights into the till's behaviour under simple shear conditions.

6. The triaxial probing tests that involved multi-directional bender element measurements and small loading-unloading stress cycles confirmed the till's linear cross-anisotropic stiffness behaviour within the linear elastic zone. Drained and undrained cross-anisotropic Young's moluli and Poisson's ratios were interpreted using both the Kuwano (1999) and Nishimura (2014a, 2014b) approach that gave generally consistent results, and the horizontal to vertical linear elastic stiffness ratios (G_{hh}/G_{vh}, E_h'/E_v' and E_h^u/E_v^u) were found to be invariably greater than unity.

7. The results from the HCA tests and triaxial probing tests by the Author and Ushev (2018) outlined the Cowden till site's anisotropic stiffness profile that indicated stiffer behaviour in horizontal than vertical planes. The E_h^u and G_{hh} stiffnesses are more representative than those from triaxial compression (E_v^u) tests in the analyses of large diameter monopiles under predominantly horizontal loading.

8. The small-strain stiffness ratios found in the HCA tests were generally compatible with those from triaxial probing tests, indicating insignificant effects of the HCA sampling bias on the established anisotropic stiffness trends.

9. Integration of in-situ dynamic shear stiffnesses from various laboratory and field techniques revealed clearly higher block sample G_{vh}^{BE} and G_{hh}^{BE} than those found with rotary core samples. BE stiffnesses found from triaxial samples from 2 and 5.1 m depth after being subjected to 3-week creep/ageing were markedly higher than those of specimens tested after shorter ageing, regardless of the sampling techniques, probably due to the formation of more compacted structures through ageing in the fissured and initially desiccated specimens.

10. Returning to the three main hypotheses posed in the Section 3.1 Introduction, the experiments reported above proved that: (i) the Cowden till does have significant anisotropy in its mechanical behaviour from small to large strains; (ii) it manifests broadly similar patterns of anisotropy to the aged and over-consolidated marine

stiff clays, although sharing important differences in its detailed behaviour; and (iii) the pattern of behaviour seen in the laboratory tests are also broadly compatible with those seen in in-situ tests.

CHAPTER 4
Oedometer compression and interface shearing behaviour of sands

4.1 Introduction

The compression and yielding behaviours of granular materials are fundmental features of their mechanical response. Improved understanding of these aspects and also of behaviour in interface shear provides significant insights that help elucidate applications in soil-structure engineering problems.

From the micro-mechanical perspective, uniaxial compression is dominated by grain strength, particle force chain collapse and variations in packing efficiency, whereas interface shearing reflects the combined effects of tangential grain-grain/interface shearing and normal compression. Significant insights into the micromechanical characteristics of particle crushing and grain damage modes have been gained from advanced laboratory techniques. Important advances have also been made in characterising the interface shearing behaviour of granular materials in contact with a wide range of interface materials under varied shearing paths and boundary conditions.

This chapter presents laboratory studies aimed to characterise the compression, yielding and interface shearing behaviour of four silica dominated sands on which extensive research has already been conducted mainly to advance understanding of how driven piles respond under complex loading: Dunkirk sand (in France), Blessington sand (in Ireland), Larvik sand (in Norway) and Fontainebleau NE34 sand (from France). A brief review is presented of the key factors dominating macro-scale compression and interface shearing responses, also addressing the underlying micro-mechanical behaviour.

Detailed descriptions of the Author's experimental schemes and methodologies are

presented. Research outcomes from stress-controlled high-pressure oedometer tests, small-displacement direct shear and large-displacement ring shear interface tests are summarised and discussed, highlighting the materials' distinct stress- and time-dependent compression and interface shearing behaviours.

Three main hypotheses are proposed at this stage which are investigated through the Author's experiments in the later sections of this Chapter. The hypotheses are:

#1. Sand particles' minerology, size, shape and uniformity characteristics are fundamental aspects that dominate sands' non-linear and time-dependent compression, yielding and crushing behaviour, as well as their response to interface shearing;

#2. Sand-steel interfaces experienced large shear displacement pre-conditioning develop interface shear resistances that are critically dependent on the imposed normal stress levels, despite the grade of interfaces' steel and their surface roughnesses;

#3. Physiochemical reaction associated with corrosion-active mild steel interfaces is central to the time-dependent ageing gains of interface shear resistances and dilation.

4.2 Review: oedometer compression and interface shearing behaviour of sands

This section reviews recent developments regarding the one-dimensional compression and interface shearing characteristics of granular materials, highlighting micro-mechanical understandings of grain-grain and grain-interface interactions and grain failure mechanisms. An appraisal of the varied experimental devices and methodologies for characterising interface shearing behaviour is provided. Key factors dominating small- and large- displacement interface shearing behaviour of sand-steel interfaces are reviewed.

4.2.1 Oedometer compression and yielding behaviour of granular materials

Granular aggregates are composed of particles that may present uniform or mixed compositions, comprising ranges of sizes, shapes, morphological and mineralogical

properties. The aggregates' overall compression and yielding characteristics are inherently linked to the compression behaviour, frictional behaviour and strength of individual grains and are affected by the fabric and efficiency of grain packing. Novel experimental techniques, such as high-resolution micro-CT, high-speed microscopic photography and acoustic emission (AE) tools have been developed in recent decades to monitor and visualise grain-scale yielding, crushing and failure modes, as well as their associated energy emission phenomena.

Experimental investigation of grain-scale yielding and failure modes

Fundamental insights into the compression and yielding behaviour of single grains has been gained from uniaxial inter-platen single- or multiple-grain compression tests. A schematic setup for such tests is shown in Figure 4-1. The tests are usually performed in a displacement-controlled manner to capture the grains' often dramatically rapid brittle response. A typical trend of recorded force-displacement response and the corresponding particle deforming and crushing pattern is illustrated in Figure 4-2.

Antonyuk *et al.* (2005) and Cavarretta *et al.* (2017) identified four stages of pre- and post-failure mechanical response under uniaxial compression and demonstrated that the pre-failure load-deformation response is invariably non-linear due to the non-conformity of the surfaces. Grain failure was found to originate from the zone of contact, accompanied by modifications of the contact topology. For relatively rigid, irregular silica sand particles, Cavarretta & O'Sullivan (2012) identified five stages of micro-mechanical response, including initial rotation of the particle as a rigid body, chipping or yielding of the asperities, the elastic response of the rigid body, fragmentation as the grain fails and loses parts of its bulk, followed by catastrophic crushing.

Extensive research has demonstrated that single grain compression and crushing characteristics and the corresponding deformation and failure modes are affected by a range of factors, including grain size (average diameter $\bar{d}$), grain shape and geometry (quantified by aspect ratio, sphericity, roundness, etc.), contact morphology (roughness, local roundness, etc.), mechanical properties (hardness, Young's modulus) and test environment (dry conditions or immersed in water, humidity, atmospheric air pressure or under suction). Earlier laboratory studies revealed significant size-dependency of single grain strength and the average diameter $\bar{d}$ of grains has been taken as the

primary descriptor of grain strength in the Weibull statistical fracture framework for particle tensile failure (Lee, 1992, Nakata *et al.*, 2001).

Advances in single and multiple grain compression tests, in conjunction with novel nano- and micro-scale observation techniques, have enabled close monitoring of the initiation and propagation of breakages within grains and their ultimate failure modes.

Wang & Coop (2016) employed a high-speed microscopic camera to capture the rapid brittle breakage process of grains under inter-platen compression tests. Visual inspection of the violence of grain failure and the formation and number of fragments created led to the identification of four failure modes: splitting, explosive, chipping and a mixed mode. The initiation and propagation of cracks and the ultimate occurrences of these failure modes were found to be largely affected by the mineralogical composition and morphologies of the sand particles, including local roundness, particle size and other geometric properties. It was demonstrated that grains with higher local roundness (flatter contact surfaces) were prone to fail in an explosive mode, whereas those with lower local roundness tended to split.

Todisco *et al.* (2017) performed inter-platen multiple-grain compression tests with a controlled number of grain-grain contacts (or coordination number) and found a general trend for failure stresses to increase with contact number. The experimental evidence from their high-speed camera images identified the role of material hardness. Hard contacts tended to preserve their morphology during compression, leading to more severe stress concentrations and brittle failure in the local contact zone, whereas soft contacts allowed particle moulding relative to accommodate neighbouring particles that could withstand relatively high compressive strains, so the whole particle was involved in the subsequent deformation and crushing.

The fracture patterns of quasi-brittle single grains under uniaxial compression were explored by Zhao *et al.* (2015) using a mini single-particle loading apparatus fitted in a nano-focus X-ray CT apparatus. Figure 4-3 presents a typical fracture pattern of a Leighton Buzzard sand (LBS) grain under compression, revealing grain fracturing planes that were parallel to the imposed compression direction. The morphology of crushed fragments computed from X-ray scanning followed a fractal distribution, conforming to previous laboratory and theoretical studies (see for example by Nakata *et al.* (2001)).

Compression and yielding behaviours have also been studied through associated elastic energy emissions, which can be captured and interpreted with the acoustic emission (AE) technique (Koerner *et al.*, 1976, Hardy, 2005). The characteristics of emitted acoustic signals have been found to correlate with multi-scale physical processes ranging from soil grain level to geological scale and can be adopted as a non-destructive detecting technique (Dixon & Spriggs, 2007, Michlmayr *et al.*, 2012). Luo *et al.* (2016) and Ibraim *et al.* (2017) reported the attempts to correlate the recorded amplitude and accumulated average signal level (ASL) with the processes of compressing single silica grains and chalk particles, and revealed clear connections between the obtained signal characteristics and ongoing crushing events. The AE technique has also been applied in other research of granular materials, including for example, oedometer tests (Fernandes *et al.*, 2010, Zhu, 2016), ring-shear friction tests (Jiang *et al.*, 2017), and force chain characterisation for compressed materials (Hidalgo *et al.*, 2002).

Single grain tensile strength and failure criteria

Early research revealed that particles' global failure under compression is controlled by their tensile strength. Despite the irregular and highly variable nature of grains, a simplified failure criterion proposed by Lee (1992) is commonly used. The particles' nominal tensile strength (σ_f) (with units of stress) is linked to their average diameter $\bar{d}$ through the following correlation.

$$\sigma_f = \frac{N_f}{\bar{d}^2} \tag{4.1}$$

Compression experiments reported by Lee (1992) and Nakata *et al.* (2001) demonstrated decreasing nominal strength σ_f with increasing grain diameter $\bar{d}$. The trend can be depicted as linear relation in a double-logarithmic scale, i.e.:

$$\log(\sigma_f) = a + b\log(\bar{d}) \tag{4.2}$$

Statistical approaches have been employed to assess the tensile strength of brittle materials and quantify the particles' probability of "surviving" under a certain stress level. McDowell & Bolton (1998) adopted the concept of Weibull statistics of fracture and developed the following expression (plotted in Figure 4-4) to quantify the survival probability $P_s(V)$ of a given particle volume V ($\propto d^3$) under a tensile stress σ.

$$P_s(V) = \exp\left[-\frac{V}{V_0}\left(\frac{\sigma}{\sigma_0} \right)^m \right] \tag{4.3}$$

Where σ_0 is a characteristic stress under which 37% of the compressed particles would survive, and m is Weibull modulus, which indicates the variability of tensile strength of the tested particles. McDowell & Bolton (1998) reported that a range of $5<m<10$ is commonly expected for soils. As seen in Figure 4-4, as m decreases, particle strengths span over a wider stress range, indicating greater variability and the onset of breakage at relatively lower stresses.

The above probability-based framework provides useful measures for single grain strengths. However, due to the highly variable and irregular nature of soil grains, it has been recognised that their tensile failure may not be adequately represented using the nominal strengths σ_f that correlate solely with their global diameters. Cavarretta *et al.* (2017) correlated the failure strength of particles to their geometrical and mechanical properties and proposed a particle failure criterion based on a plastic flow ratio p_f, defined as:

$$p_f = \frac{\sqrt{4N_c / \pi H}}{2(3N_c R^* / 4E^*)^{1/3}} = \frac{N_c^{1/6}}{\sqrt{\pi H}} \left(\frac{4E^*}{3R^*} \right)^{1/3} \tag{4.4}$$

Where N_c is the crushing load; H is the Vickers hardness of the bulk, describing particle's resistance to indented load. R^* represents the contact geometry with $1/R^*$ being the relative curvature of the contact. E^* is the equivalent Young's modulus. R^* and E^* are parameters incorporating geometries and mechanical properties at the particle-particle contacts and their detailed formulations are referred to Cavarretta *et al.* (2017). As implied in Equation (4.4), the plastic flow ratio p_f is not size dependent and only contains the particles' mechanical properties and shape parameters at the contacts.

Compression and yielding behaviour of granular aggregates

Uniaxial compression tests can be performed readily in oedometer apparatuses under stress- or strain-control (Yamamuro *et al.*, 1996, Mesri & Vardhanabhuti, 2009). The evolving trends of specimen void ratio (e) and vertical stress (σ_v) are often presented in e-log(σ_v) plots, as shown in Figure 4-5.

From the micro-mechanics perspective, the typical e-log(σ_v) trends can be divided

into three regions (McDowell *et al.*, 1996), as denoted in Figure 4-5. Region 1 is the initial compression range associated with particle rearrangement and net locking and the void ratio change is a function of particles' elastic modulus and inter-particle friction coefficient. Region 2 corresponds to a 'clastic' yielding range with the initiation of particle fracture, followed by significant compression and catastrophic crushing. The yield stress depends critically on strengths of individual particles. As compression stress increases, the behaviour moves towards a plastic hardening range (termed as Region 3) where successive fracturing and generation of fine particles continues. The aggregates trend towards more efficient packing with substantial increasing of particle contacts and the response converges towards an approximately straight line in linear-log plots.

An additional Region 4 can be included to depict the responses over a still higher stress range (McDowell & Bolton, 1998), within which the smaller particles reach comminution limits and further fracturing becomes unlikely, while the larger particles are also stabilised by increasing numbers of contacts with surrounding particles.

The existence of the Region 4 implies that the uniaxial compression and particle breakage cannot be a never-ending process. Under sufficiently high stresses, the aggregates should reach a limit breakage and an eventually constant grading would emerge. The limit grading was found to satisfy a fractal distribution of particle sizes with a fractal dimension in the range of 2.5-2.6 (McDowell *et al.*, 1996, McDowell, 2002). Similar observations were reported by Coop *et al.* (2004) from interface shearing tests on Dog's Bay sand (DBS). They found that after very large shearing strains, the grains reached their breakage limits and constant gradings could be attained.

The compression e-log(σ_v) responses and the amount of relative breakage depend critically on particles' mineralogy and the samples' initial density (void ratio) and grading. Altuhafi & Coop (2011) concluded that, for uniformly graded materials, the variations of the samples' initial void ratios were erased at high stresses and the e-log(σ_v) plots trended towards a unique normal compression line (NCL), as shown in Figure 4-5. Less uniformly graded samples failed to converge in the same way and showed a much less identifiable Region 2. A transitional compression behaviour was seen in those well graded samples, of which the e-log(σ_v) trends started different initial void ratios did not converge and the compression regions cannot be clearly

distinguished.

The samples' initial void ratio and grading significantly affect the fracturing mechanism and the amount of particle breakage, as depicted in Figure 4-6. For the poorly graded samples (with smaller D_{90}/D_{10} ratios), considerable breakage commences at the onset of yielding until a breakage limit has been reached. Both the amount of breakage and the inclination of the NCL (if there is one) reduce significantly with increasing of D_{90}/D_{10}, as the soils become better graded. In the cases where transitional behaviour dominates, the degree of breakage becomes minimal and the granular aggregate densifies principally through particle rearrangement.

The distinct compression behaviours of uniformly graded and transitional soils can be explained from a micro-mechanics perspective. It has been recognised that the stress distributions within the particle assemblies of uniformly graded soils are extremely heterogeneous, with external compression stresses being transmitted through strong force chains (McDowell, 2002). The non-uniform and anisotropic systems of particle contacts impose severe stress concentrations that make the aggregates more susceptible to particle fracturing. As compression loads rise, the force chains break, reconstruct and evolve until the comminution limit of the grains is reached and ultimately stable fabrics and particle contacts are achieved. However, transitional soils tend to develop more homogeneous and robust initial fabrics, which could survive during loading, resulting in non-converging compression responses. Todisco *et al.* (2018) recently carried out laboratory and statistical studies on transitional soils and reported isotropic elastic stiffness ($G_{hv} \approx G_{hh}$) from their bender element measurements, which they took as inferring uniform and isotropic fabrics.

Apart from the above laboratory studies, micro-scale studies employing discrete element modelling (DEM) methods have also been employed to investigate the uniaxial compression behaviour. For example, McDowell & De Bono (2013) developed DEM analyses considering the effects of different particle strength characteristics, hardening laws and fracture mechanisms, and reproduced many features seen in previous experimental studies. Insights gained from element-scale compression studies have led to developments in modelling complex engineering scale boundary-value problems, such as cone penetration in sands, see for example by Ciantia *et al.* (2016).

Progressive and time-dependent compression and crushing behaviour

Over the low stress ranges, the secondary compression (quantified by index $C_\alpha = \Delta e/\Delta\log(t)$) of granular materials is often considered insignificant, even though creep settlements are known to be important beneath foundations placed on sand layers in the field: Jardine *et al.* (2004). However, creep becomes impossible to ignore when the particles start to undergo significant yielding and fracturing. Other compression responses, including particle rearrangement through inter-particle slip and rotation, are also expected to be time-dependent. Mesri & Vardhanabhuti (2009) reviewed extensive compression test data and reported linear correlations between compression index and secondary compression index in a double-logarithmic scale, as shown in Figure 4-7.

The time-dependency of compression behaviour is dependent on particle strength. Tapias *et al.* (2016) reported oedometer tests on low strength, highly-crushable, sugar cubes in ordered and disordered piling arrangements as analogues of coarse crushable aggregates (gravels and rockfill) in different arrangements. As shown in Figure 4-8, the results revealed significant time-dependent behaviour with clear evolving trends of particle size distributions with time under constant compression stresses.

In particle assemblies with high strengths, particle crushing can lead to straining developing as a progressive series of abrupt events, as were captured by Ciantia *et al.* (2017) using the acoustic emission (AE) technique, as described above. The AE monitoring results revealed an avalanche pattern of crushing where successive crushing events were triggered within the assembly by the failure of a few particles.

Summary of the micro-mechanical behaviour of 1D compression

As can be summarised from the above review, the uniaxial compression of granular aggregates is dominated by particle strengths (as functions of particle mineralogy, size, shape and their variations) and packing conditions, resulting in distinct characteristics of compressibility and stress- and time-dependent responses. Particle characteristics and soil grading evolves with compression stress and time and could reach ultimately stable states as the granular aggregates reach their comminution limits.

The micro-mechanical behaviour of grain-interface shearing and grain failure mechanisms is further complicated by the role of predominantly tangential grain-interface/grain shearing. Interface shearing behaviour at both the micro- and macro-scale is affected by a wide range of factors, as discussed below.

4.2.2 Sand-steel interface shearing behaviour

Interface shearing is a complex physical process incorporating normal compression and tangential shearing, accompanied by continuing modifications to the characteristics (size, shape, topology, etc.) of both the particles and interfaces. Particles are subject to combined splitting failure (induced by tensile stresses) and comminution failure from inter-particle shearing and particle-interface abrasion. These features of micro-mechanical behaviour differ significantly from those under uniaxial compression.

From the perspective of practical engineering, interface shearing behaviour is critical in a range of soil-structure interaction and geotechnical design problems. For example, pile shaft resistance can be dominated by the response at the pile-soil interface. Site-specific interface shear tests that reproduce pile installation processes are required to design driven piles in the ICP-05 procedures set out by Jardine *et al.* (2005). For large-diameter laterally loaded piles, it has been recognised that shearing components developed over the piles' shaft and base can contribute significantly to the piles' initial horizontal stiffness and lateral ultimate capacity (Byrne *et al.*, 2015b, Zdravković *et al.*, 2015), and thus affect both the serviceability and capacity design.

Experimental characterisation of interface shearing: apparatus and methodologies

In interface shearing, the ratio of the variation in the normal stress ($\Delta\sigma_n$) developed during shearing under any given system of boundary condition to the variation in the normal displacement (Δv) is often defined as the interface shearing boundary normal stiffness K, i.e. $K = \Delta\sigma_n/\Delta v$. Fakharian & Evgin (1997) identified three types of boundary conditions that are often applied in interface shear tests.

Type I: Constant Normal stress or Load (CNL), $\Delta\sigma_n = 0$, $\Delta v \neq 0$, $K = 0$;

Type II: Constant Volume (CNV), $\Delta\sigma_n \neq 0$, $\Delta v = 0$, $K = \infty$;

Type III: Constant Normal Stiffness (CNS), $\Delta\sigma_n \neq 0$, $\Delta v \neq 0$, K = constant.

Interface shear tests performed with representative boundary conditions may be able to provide analogies for practical cases and enable case-specific assessment of interface shear resistance. For example, the changes in radial effective stress ($\Delta\sigma_n$) and soil radial deformation ($\Delta\sigma_r$) developed close to the shaft of a pile installed in a linear elastic soil can be related to shear stiffness of the soil (G) and pile radius R using

elastic cylindrical cavity expanding theory as:

$$\frac{\Delta\sigma_r'}{\Delta r} = \frac{2G}{R} = K_{\mathrm{CNS}} \tag{4.5}$$

Airey *et al.* (1992) and Dejong *et al.* (2003), for example, recommended monotonic and cyclic constant normal load (CNL) and constant normal stiffness (CNS) interface direct shear tests as useful approaches in assessing pile shaft resistance under monotonic and cyclic loading.

Soil-structure interface testing apparatuses can be broadly categorised as direct, simple and torsional shear devices. These apparatuses have significantly different test configurations and boundary conditions and a detailed summary of their main features and limitations is presented in Table 4-1.

Table 4-1 General features of laboratory devices and applied boundary conditions for soil-structure interface shearing

Type	Examples and boundary conditions	Shearing motion	Main features & advantages	Major limitations
Direct shear	Lemos (1986) (CNL); Airey et al. (1992) (CNS); Dejong *et al.* (2003) and DeJong & Westgate (2009) (CNL, CNS); Ghionna & Mortara (2002) and Mortara *et al.* (2007) (CNL, CNS); Zhang & Zhang (2006), Zhang *et al.* (2018) (CNS, CNV, CNL) Chen (2017b) (CNS)	Monotonic, cyclic or multi-directional cyclic shearing	1. Relatively simple system configuration and testing procedures; 2. Suitable for testing a range of intact and remoulded fine to gravelly materials; 3. Suitable for applying different normal boundary conditions; 4. Commercially available; 5. Local shear behaviour can be observed in specific equipment, e.g. Dejong *et al.* (2003); 6. Readily be extended for controlled temperature testing	1. Non-uniform stress within the sample; 2. Usually limited shearing distance, and not suitable for applying large displacement pre-conditioning and shearing; 3. May not be able to fully mobilise residual strength; 4. Unable to separate sliding displacement and the displacements due to material deformation (Kishida & Uesugi, 1987)
Simple shear	Uesugi & Kishida (1986), Uesugi *et al.* (1989), Uesugi *et al.* (1990) (CNL); Fakharian & Evgin (1996, 1997) (CNS); Oumarou & Evgin (2005) (CNL) Zhang & Zhang (2009) (CNL, CNV, CNS)	Monotonic, cyclic or multi-directional cyclic shearing	1. Relatively simple system configuration and testing procedures; 2. Suitable for testing a wide range of intact or remoulded soils; 3. Suitable for applying different normal boundary conditions; 4. Measure separate displacement factors with special arrangement (Kishida & Uesugi, 1987); 5. Commercially available	1. Usually limited shearing distance, and not suitable for applying large displacement pre-conditioning and shearing; 2. May not be able to fully mobilise residual strength; 3. Stress concentration at ends

Notes: CNL: constant normal stress/load; CNV: constant volume; CNS: constant normal stiffness.

Continued Table 4-1 General features of laboratory devices and applied boundary conditions for soil-structure interface shearing

Type	Examples and boundary conditions	Shearing motion	Main features & advantages	Major disadvantages
Torsional shear	GDS interface shear tester for solid cylindrical specimens (GDS, Ziogos *et al.*, 2017) (CNL, CNV)	Continuously monotonic or cyclic shearing	1. Suitable for testing intact or remoulded soils or rocks; 2. Apply un-limited torsional shearing; 3. Commercially available	Non-uniform shear stress at the interface
	Bromhead (1979) type ring shear: Stark & Vettel (1992) and Stark *et al.* (1996) (CNL) Tan *et al.* (1998) (CNL) Garga & Infante Sedano (2002) (CNV)	Continuously monotonic or cyclic shearing	1. Relatively simple system configuration and testing procedures; 2. Generally suitable for reconstituted clay and fine sands; 3. Un-limited torsional shear; 4. Uniform shear stress; 5. Commercially available	1. Limited specimen thickness, not suitable for testing coarse materials; 2. Not suitable for testing intact soils or rocks; 3. Cannot account for side wall friction; 4. Not applicable for soil-soil shearing
	Bishop *et al.* (1971) type ring shear: Lupini *et al.* (1981), Ramsey *et al.* (1998), Coop *et al.* (2004), Yang *et al.* (2010), Barmpopoulos *et al.* (2010), Ho *et al.* (2011), Chen (2017a), Quinteros *et al.* (2017)	Continuously monotonic or cyclic shearing	1. Nominally endless shear distance; 2. Obtain both peak and residual strength or shearing angle; 3. Able to impose large displacement pre-conditioning; 4. Sidewall friction can be directly measured and compensated; 5. Uniform torsional shear stress; 6. Applicable for large displacement soil-soil shearing	1. More complicated system configuration and time-consuming set-up; 2. Limited availability; 3. Difficult for testing intact soils or rocks; 4. Originally designed solely for constant normal stress testing
	Other ring shear apparatus, Yoshimi & Kishida (1981), Vaid & Rinne (1995), Kelly *et al.* (2003), Airey & Kelly (2010), Sassa *et al.* (2004), Sadrekarimi & Olson (2010)	Monotonic or cyclic shearing	Designed with specific features and testing purposes	1. May require complicated control and measurement system; 2. Usually limited availability
Others	Tilt-table interface test, e.g. Najjar *et al.* (2007) (CNL)	Monotonic shearing	Specific testing for remoulded marine soils under low effective stress	Not suitable for sandy or coarse materials
	Specialised axisymmetric interface shear device testing with friction sleeve by DeJong & Frost (2002) and Martinez *et al.* (2015)	Monotonic or cyclic shearing in axial & torsional directions	1. Uniform shear stress distribution; 2. Well-controlled stress and drainage boundary condition	Require a relatively complex set-up of pressure chamber to perform

Factors dominating interface shearing behaviour

Pioneering studies by Potyondy (1961) on soil-interface shearing resistance identified a wide range of factors potentially affecting soil-structure interface shearing behaviour, which are summarised in an expanded form in Table 4-2. Some of the dominant aspects concerned in silt/sand-interface shearing behaviour are discussed below.

Table 4-2 Influential factors affecting silt/sand-structure interface shearing behaviour

Variables		Details and references
Soil	grading	quantified by D_{10}, D_{50}, D_{90} or coefficients (C_u, C_c)
	particle minerology, hardness, roughness	siliceous origin, biogenic origin or other
	particle shape	quantified by aspect ratio and others (see Section 2.3.6); see for example DeJong & Westgate (2009) and Sadrekarimi & Olson (2010)
	chemical properties	pH, carbonate content, etc.; possible physiochemical reaction with fluid or interface material
	specimen preparation method/inherent fabric	pluviation, moisture tapping and others; significant impacts of initial bedding plane direction on δ'_{peak}, see for example by Farhadi & Lashkari (2017)
	specimen density	significant impacts on δ'_{peak}, much less marked on δ'
	fines content and properties (plastic or non-plastic)	trends not yet established; see the attempt by Quinteros *et al.* (2017)
	sample condition	under dry, saturated, or partially saturated condition
Interface	type	mild/stainless steel with variable grades, concrete, PVC, geomembrane, geotextile, etc.
	surface finish/roughness	roughness quantified by R_{CLA} or R_{max}; varied surface textures from manufacturing
	surface hardness	quantified by for example Brinell hardness number
Test set-up	apparatus	direct shear, simple shear, ring shear and many others
	interface configuration	upper, middle or lower interface set-up, see Sadrekarimi & Olson (2010) and Ho *et al.* (2011)
	normal boundary condition	constant normal load (CNL), constant volume (CNV), constant normal stiffness (CNS)
	drainage boundary	drained or undrained, e.g. Martinez & Frost (2018)
Test condition	stress level	normal stress from a few kPa up to several MPa
	shearing rate	varied with soil properties, drainage, etc.
	shearing distance	a few millimetre to meters (Yang *et al.*, 2010)
	consolidation time/ageing	see for example by Chow (1997)
	temperature	see for example by Chen (2017b) on cooled and heated sand-PVC interface tests
Shearing motion	monotonic/ mono- or multi-directional cyclic	see for examples by Uesugi *et al.* (1989), Uesugi *et al.* (1990), Fakharian & Evgin (1996)
Test procedure	pre-shearing	fast shearing with or without pulses to model pile installation process (Jardine *et al.*, 2005)

It is widely established that interface shearing resistances (usually represented by peak and constant volume interface friction angles, δ'_{peak} and δ'_{cv}) are dominated by interface surface roughness. Roughness reflects smallest-scale surface topography and is commonly quantified by R_{CLA} (central-line average roughness) or R_{max} (maximum height difference along a surface profile). Earlier studies by Uesugi & Kishida (1986), Kishida & Uesugi (1987), Jardine *et al.* (1992) and Lings & Dietz (2005) demonstrated that $\tan\delta'_{peak}$ increases approximately linearly with the increase of surface roughness until an upper limit is reached after a critical roughness, as shown in Figure 4-9. The upper limit of the peak interface friction angle δ'_{peak} could either be the peak or constant volume soil-to-soil shearing angle (ϕ'_{peak} and ϕ'_{cv}, respectively), depending on whether the tested soil is deposited on the interface (lower interface set-up) or placed beneath the interface (upper interface set-up) (Rao *et al.*, 1996).

The effects of specimen density have also been clearly established. Similar to soil-soil shearing, peak shear strength increases with increasing specimen density, accompanied by enhanced dilation. However, the impact of stress level on peak shear resistance is dependent on interface type and roughness. In their sand-steel direct shear interface tests, Lings & Dietz (2005) observed δ'_{peak} trends to increase with increasing of normal stress applied in tests with rough interfaces, while the reverse trend was noted in tests on polished smooth interfaces. They attributed this trend to ploughing effects at high stresses. Dove & Frost (1999) reported sand-smooth geomembrane direct shear interface tests and argued that a critical normal stress existed that differentiated the shearing behaviour in two ranges. Below the critical stress, the shearing mechanism was dominated by sliding and δ'_{peak} decreased with the increase of normal stress, while above the critical value, particle motion involved both sliding and ploughing and δ'_{peak} increased with normal stress level.

The above studies demonstrate that the effects of stress level on interface shearing behaviour may not be as clearly identified as in soil-soil shearing. Another important factor that may add to the complexity is particle crushing, which usually commences at much lower normal stress levels in interface shearing than in oedometer compression or soil-soil shearing. These aspects are addressed further in the Author's testing programme.

Although peak shearing resistance has been the main focus in many laboratory studies, the selection of friction angles has to be based on the physical settings

concerned. Gaining insights from instrumented field pile tests, Jardine *et al.* (1992) emphasised that the operational friction angle for assessing shaft capacity of piles driven in sands should be those at constant volume (or critical state), rather than peak conditions. Their laboratory direct shear tests further proved that although the specimens' relative density affected peak friction angle δ'_{peak} strongly, the ultimate value δ'_{cv} remained largely unchanged. Their test results led to the generation of δ'_{cv}-(R_{CLA}/D_{50}) correlations that have been used widely in the preliminary selection of interface shearing angles.

Ho *et al.* (2011) reported a series of large displacement ring shear tests using stainless steel interface and established trends of δ'_{cv} varying against D_{50} as shown in Figure 4-10. Significant differences were noted between the upper interface configuration (interface placed above the deposited material) and the lower interface configuration (interface placed beneath the material) as the former set-up led to much lower δ'_{cv} value particularly with larger (higher D_{50}) particles. This difference was thought to be due to the escape of crushed material from the interface and fines migration downwards into the soil mass when using the upper interface set-up for testing coarse materials. Meanwhile, for coarser materials with $D_{50} > 0.1$ mm, tests performed under 800 kPa normal stress presented higher δ'_{cv} than those under 100 kPa, while the trend was reversed for finer materials.

The above reported trends provide useful guidance when making a preliminary selection for design friction angles. However, the trends were based on limited number of soil, interface and stress level combinations. As emphasised by Jardine *et al.* (1992) and Jardine *et al.* (2005), it is important to carry out site-specific interface testing to address potential variations and produce representative interface friction angles for practical design purposes.

4.2.3 Figures

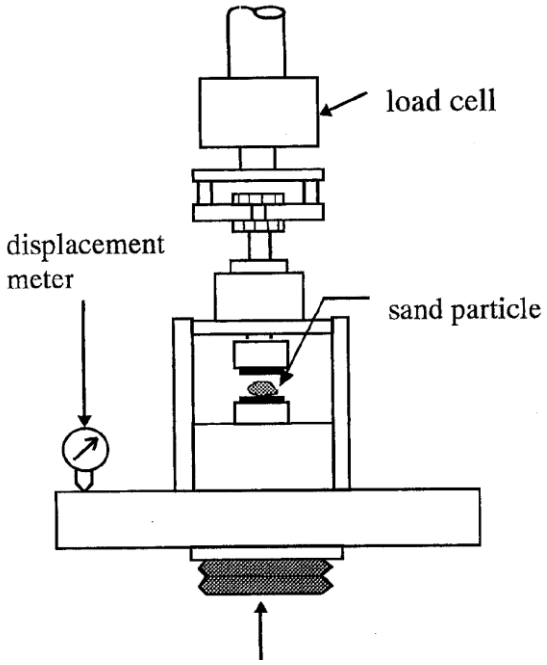

Figure 4-1 Schematic diagram of typical inter-platen compression apparatus for single grain compression and crushing test (Nakata *et al.*, 2001)

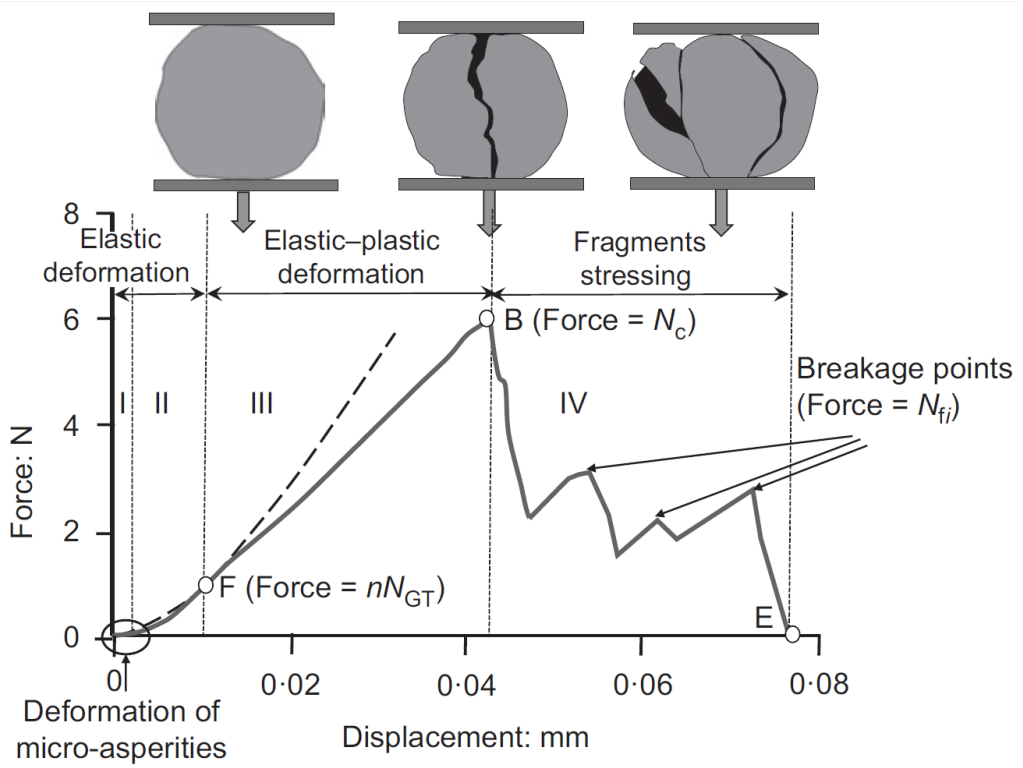

Figure 4-2 Four-stage compression and crushing behaviour of single grains characterised from displacement-controlled inter-platen compression tests

(Antonyuk *et al.*, 2005, Cavarretta *et al.*, 2017)

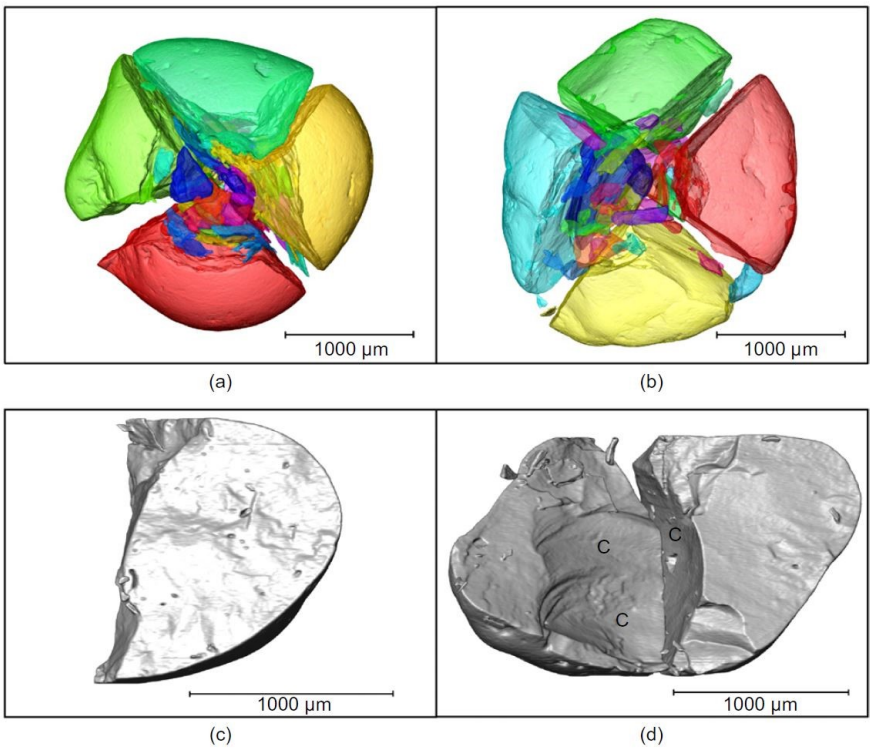

Figure 4-3 Typical fracture pattern of a Leighton Buzzard sand grain under inter-platen uniaxial compression captured by laboratory nano-focus X-ray CT scan (Zhao *et al.*, 2015)

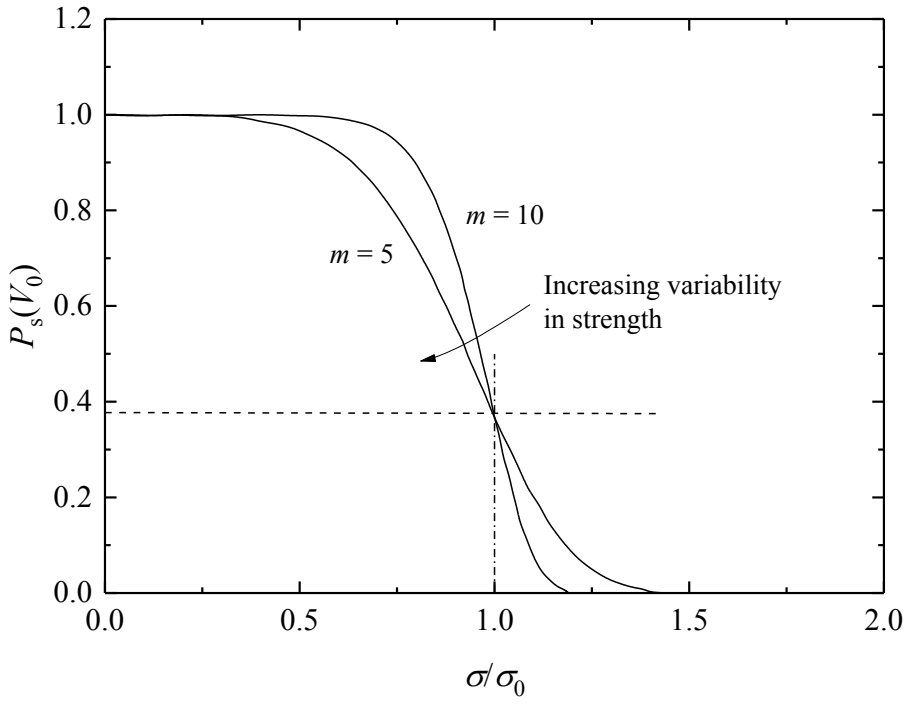

Figure 4-4 Weibull distribution of single grain compression strength (McDowell & Bolton, 1998)

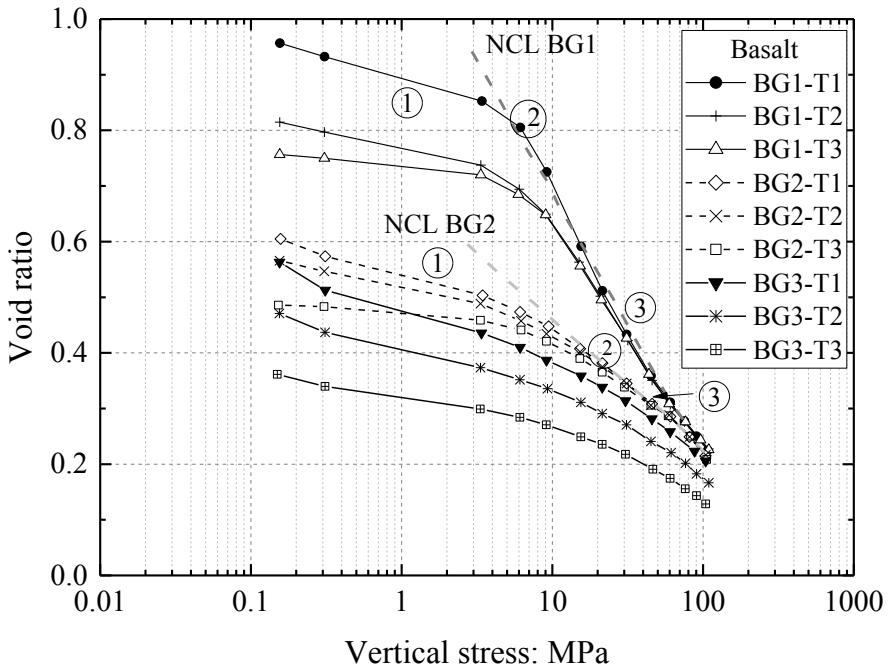

Figure 4-5 1D compression and yielding behaviour of Langjokull glacial sediments with varied initial gradings and void ratios (reproduced after Altuhafi & Coop (2011))

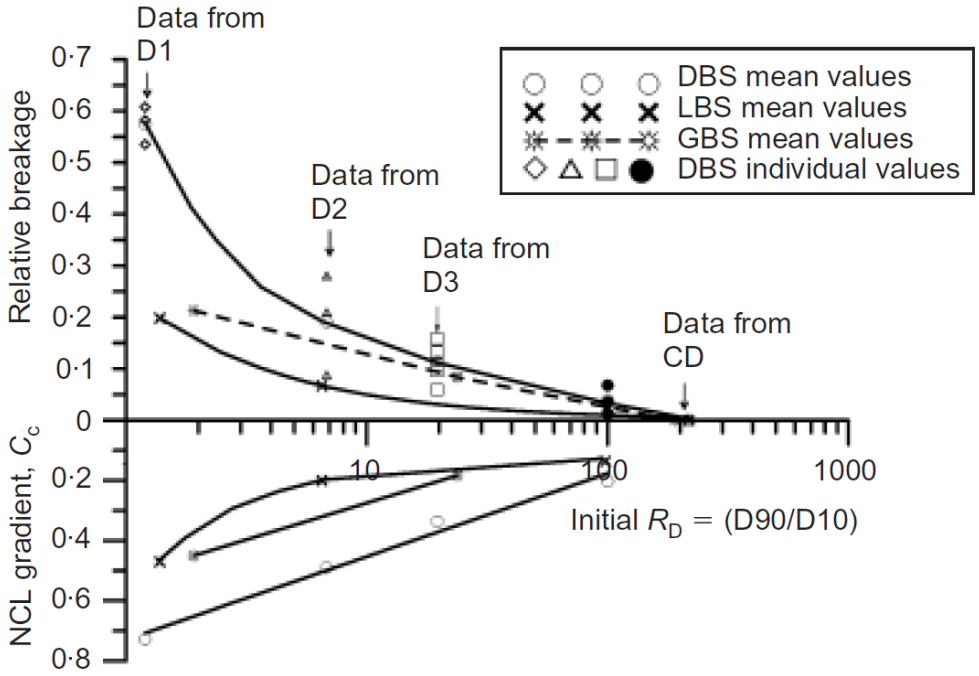

Figure 4-6 Dependency of relative breakage and normal compression line slopes on the mineralogy and initial grading of sands (Altuhafi & Coop, 2011)

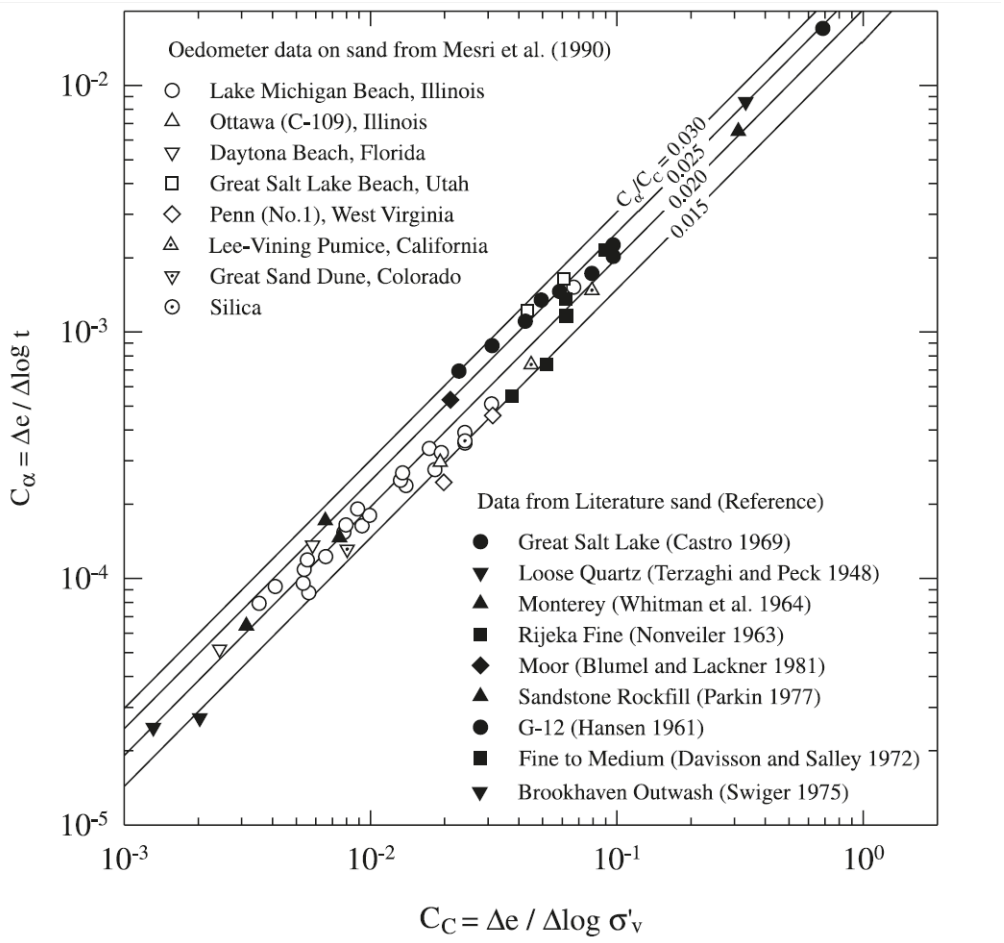

Figure 4-7 Correlations between compression index and secondary compression index of granular materials (Mesri & Vardhanabhuti, 2009)

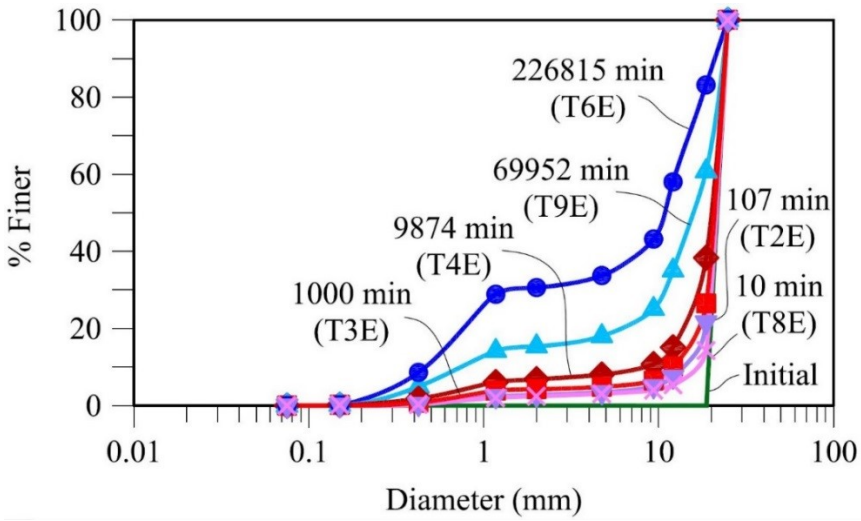

Figure 4-8 Evolution of sugar cube grading with creep time under constant 240 kPa vertical stress (Tapias *et al.*, 2016)

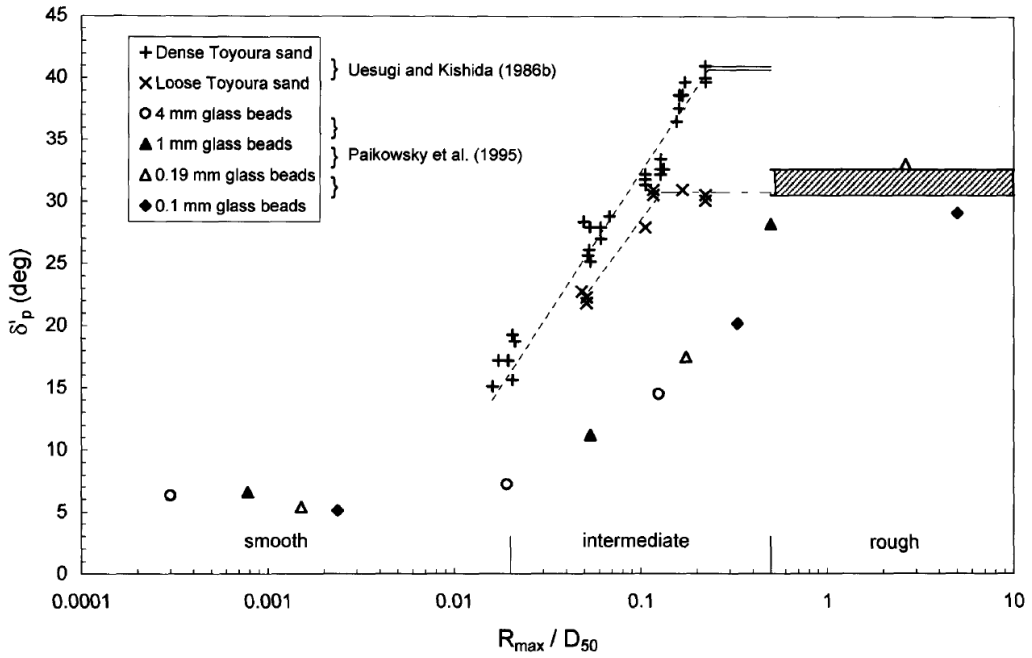

Figure 4-9 Trends of peak interface shearing angle against normalised interface surface roughness (Lings & Dietz, 2005)

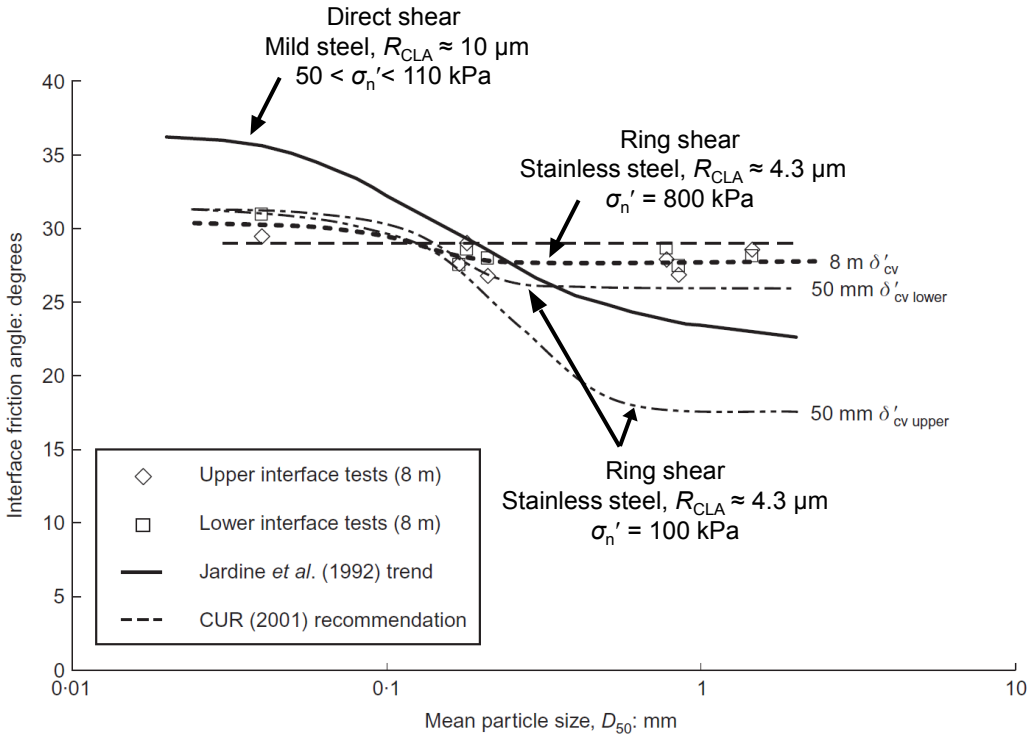

Figure 4-10 Trends of ultimate friction angle against mean particle size from direct shear and ring shear interface tests (Ho *et al.*, 2011)

4.3 Research motivation and programme

Sand calibration chamber experiments conducted jointly by Imperial College and Grenoble University (France) with displacement piles have been reported by Yang *et al.* (2010), Jardine *et al.* (2013a, 2013b) and others. These studies demonstrated how the effective stress components and sand states developed as pile tips advanced during installation and passed through instrumented horizons in pluviated and pressurised sand masses. Very high stresses built up and then relaxed, resulting in intensive particle breakage and micro-morphological modifications to the sand materials positioned beneath the pile tips and adjacent to their shafts. The crushing and interface shearing regimes identified are demonstrated in Figure 4-11. It is thought possible that the properties of the severely mutated materials affected the piles' subsequent time-dependent behaviour (ageing) as well as their load-carrying responses under monotonic and cyclic loads (Rimoy *et al.*, 2015).

Axial shaft capacity gains have been noted over time with piles in sands. Trends established from field studies at Dunkirk, Blessington and Larvik sites were summarised by Rimoy *et al.* (2015), as shown in Figure 1-3. Chow *et al.* (1998) were the first to suggest that the main causes of the ageing effects are: (1) physio-chemical process around the pile shaft; (2) radial stress redistribution; (3) enhanced dilation at the sand-shaft interface under axial loading. These hypotheses have been examined in studies that covered an extended range of pile materials and geometries, see for example by Rimoy *et al.* (2015) and Carroll *et al.* (2017).

Insights gained from the above field and model pile research led to the design of the Author's research programme. The aims were set to further investigate the behaviour of granular materials undergoing high pressure compression and interface shearing and examine some of the above hypotheses of pile ageing mechanisms. The experimental programme involved high pressure oedometer tests, Bishop ring shear and direct shear interface tests, combined with grain-scale optical microscopy and QicPic laser imaging analyses. This section sets out the methodology, materials and testing programmes employed for the research.

4.3.1 High pressure oedometer tests: materials and programme

Testing apparatus and set-up

Hi-loader dead-weight oedometer apparatus was employed by the Author to compress sand samples under a maximum hanger load of 300 kg and lever arm ratio of 11.03. The oedometer ring employed had a height of 19 mm, inner diameter of 20 mm and wall thickness of 10 mm, allowing a maximum compression stress of 100 MPa. A guiding ring with identical inner diameter and wall thickness, but shorter height was also fabricated to guide the compression of the piston bar to facilitate the loading alignment. The oedometer ring, guidance ring and loading piston were made of heat treated stainless steel with yield stress greater than 1500 MPa to minimise compression compliance and eliminate surface scoring or scratching. The compliance of the system was determined based on prescribed loading steps and corrections were made to the vertical displacement measurements.

In this study, the oedometer ring was configured in a fixed ring manner. Although floating ring set-ups minimise the effects of ring side-wall friction (Altuhafi & Coop, 2011), trial tests performed by the Author indicated that fine materials generated during crushing tended to escape from the bottom edges of the ring, particularly in the cases where even slight initial misalignments or inclinations of the loading parts occurred, leading to significant errors in determining specimen void ratios. In the fixed ring set-up, side wall friction was reduced by regularly polishing inner side wall surface roughness (R_{CLA}) down to less than 0.1 μm. Meanwhile, as recommended by Yamamuro *et al.* (1996) and others, the inner side of the compression ring was lubricated using a thin layer of high vacuum grease, even although the grease affected some edge grains and caused inconvenience in post-test particle size and shape analysis.

Tested materials

The main materials studied were Batch 2 Dunkirk sand and Fontainebleau NE34 sand. Additional tests performed by Vinck (2016) on Batch 3 Dunkirk sand (see Section 2.2.2) were also included to complement the discussion.

Mineralogy analyses on Dunkirk sand reported by Chow (1997) identified an average composition of 84% SiO_2 quartz, 8% feldspar and 8% calcium carbonate fragments. The sand's mixed composition and variable crushability offered an

opportunity to compare its compression and interface shearing behaviour with both pure silica sands (such as NE34) and mainly carbonate sands, such as Dog's Bay sand (88%-94% carbonate content), which has been investigated extensively by Coop (1990), Coop *et al.* (2004) and Altuhafi & Coop (2011).

Fontainebleau NE34 sand is a pure silica sand. Laboratory research programme reported by Aghakouchak (2015) and Altuhafi *et al.* (2017) characterised the material's mechanical properties and critical state behaviour over low-to-high (up to 10 MPa) mean effective stress levels. Ciantia *et al.* (2018) recently reported their simulations of the material's critical state plane (e-logp'-I_G) through discrete element modelling (DEM), establishing the correlation between breakage-induced grading evolution (I_G) and the critical state line location in the e-logp' plane. The DEM model adopted was calibrated and validated against experimental results that were partly produced through the Author's testing.

Testing procedures

All the oedometer tests were performed under dry conditions to maintain consistency with previous calibration chamber tests. Although beyond the scope of the current study, silica granular materials may present lower particle strengths under saturated condition than when dry due to the stress corrosion mechanism identified by Atkinson (1979) and Michalske & Freiman (1982) or intra-particle suction (Coop & Lee, 1995).

All the specimens were prepared to achieve an initial void ratio of 0.64 using the air pluviation method. The void ratio was adopted to be consistent with the previous calibration chamber model pile tests and laboratory studies. Choosing this single void ratio also facilitated direct comparison of relative breakage while eliminating the effects of variable initial density noted by Altuhafi & Coop (2011).

Stress-controlled loading and unloading steps were imposed with axial strain rates being monitored and extended for creep. The low stress level creep period was typically extended for a few hours or overnight, whereas at high stress levels the specimens had to be left for a few days before the residual axial strain rates diminished to negligible values (less than 0.002%/day). The creep time applied in the unloading steps were markedly shorter.

The particle gradings were determined after testing through both dry sieving and the QicPic technique, while particle shape characteristics were studied using an optical

microscope and the QicPic images.

Testing programme completed

The Author's testing programme is summarised in Table 4-3. Several similar tests on other materials reported in the literature are quoted for comparison and interpretation.

Table 4-3 Summary of high pressure oedometer tests programme and dataset referred from literature (all tests performed under dry condition)

Material	Test code	e_0	$\sigma_{v,\,max}$ [MPa]	Source
Dunkirk sand Batch 2	OED-DKB2-8	0.64	7.9	Current programme
	OED-DKB2-25	0.64	25.1	
	OED-DKB2-25(2)	0.64	25.1	
	OED-DKB2-50	0.64	50.2	
	OED-DKB2-75	0.64	75.4	
	OED-DKB2-91	0.64	91.1	
	OED-DKB2-101	0.64	101.0	
Fontainebleau NE34	OED-NE34-8	0.64	7.9	Current programme
	OED-NE34-25	0.64	25.1	
	OED-NE34-50	0.64	50.2	
	OED-NE34-75	0.64	75.4	
	OED-NE34-101	0.64	101.0	
		0.64	50.0	Yang *et al*. (2010)
Dunkirk sand Batch 3	OED-DKB3-25	0.64	25.9	Vinck (2016)
	OED-DKB3-103	0.66	103.4	

Notes:

1. All tests performed under dry condition;
2. Tests OED-DKB2-8 and OED-NE34-8 performed by the Author were also reported in Aghakouchak (2015);

4.3.2 Large-displacement Bishop ring shear sand-steel interface tests

The Author's Bishop ring shear testing programme was designed to: (1) reproduce the heavily mutated soil states encountered during pile installation; (2) apply long post-installation ageing periods to examine the time-dependency of interface shearing behaviour; (3) assess the potential effects of other variables, including interface type and surface characteristics, soil fines content and chemical composition. The outcomes were compared and integrated with small-displacement direct interface shear tests.

Testing apparatus, set-up configuration and procedures

As noted in Table 4-1, the Bishop ring shear type interface apparatus is capable of providing an analogue for soil-steel interaction at pile shafts. The testing procedures employed herein generally followed those recommended by Jardine *et al.* (2005). Figure 4-12 illustrates some of the key steps in setting up and dismantling as well as visual observations made in the process of sub-sampling.

Varying from the oedometer tests described above, the interface shear tests were performed under saturated conditions to represent the practical settings of offshore piled foundations. The lower interface configuration (as shown in Figure 2-28) was adopted throughout the testing. This set-up bears the benefits of immersing the interfaces at the bottom of the water bath, rather than requiring a set-up with an elevated enclosed water bath to soak the interface from the top. The thickness of the specimen accommodated in this set-up (around 12 mm) was believed to be sufficient, even accounting for soil loss during testing.

Throughout the testing, the water bath was open to the atmosphere, leaving the immersed steel interfaces in a humid environment to allow corrosion. While mild steel interfaces tended to corrode rapidly, little corrosion or rusting was observed in the stainless steel confining moulds. This ensured that corrosion or other physiochemical processes were occurring solely at the sand-mild steel interfaces and not in the confining moulds. Distilled water was used to saturate the sand specimens and no attempt was made to adopt site-specific salt or other solute concentrations during saturating and testing. The use of distilled water provided a more repeatable and convenient approach for testing.

A post-test sub-sampling procedure was applied to divide the wet specimens into

three to five sub-layers and collect each layer separately. A specialised soil 'scraper' enabling flexible and continuous height adjustment was designed and fabricated for this purpose so that uniform soil layers could be scraped off evenly from the top to bottom of the specimen. In most cases, the sheared "basal" zone could be differentiated easily from the parent soils by its distinct colour and often the presence of bonding or cementation close to the interfaces. The retrieved soils were oven-dried and preserved for further analyses.

The surface roughness of the steel interfaces was determined before and after interface shearing tests using a Rank Taylor Hobson Talysurf profilometer, considering three or four measuring locations on the interface each with a sampling length of 100 mm. Examples of measured roughness profiles are given in Figure 4-14. Multiple surface roughness measurements covering sufficiently long circumferential shearing distances offered the opportunity to check the roughness uniformity of the air-abraded steel interfaces.

Tested soils and interfaces

The test programme considered sands from three sites, Blessington (eastern Ireland), Dunkirk (northern France) and Larvik (south-eastern Norway). These sites have been intensively employed for testing industrial scale driven piles (Chow, 1997, Jardine *et al.*, 2006, Gavin *et al.*, 2013, Karlsrud *et al.*, 2014, Gavin *et al.*, 2015) and 'micro' scale small diameter piles with outer diameters in the range of 50-60 mm (Carroll *et al.*, 2017). The initial part of the interface testing programme was carried out by Chen (2017a) as part of his MSc research project in conjunction with the Author, who subsequently extended the work.

Under in-situ conditions, the normally consolidated Larvik sand is substantially looser than the heavily over-consolidated Blessington and normally consolidated Dunkirk sands (Carroll *et al.*, 2017). The ring shear testing, however, did not attempt to reproduce in-situ density conditions, and the specimens were installed at common dry densities in the range of 1500-1600 kg/m^3. However, the specimen density of each tested soil was maintained consistent (as noted in Tables 4-4 to 4-6) to eliminate its potential effects on interface shearing behaviour. Dry pluviation was adopted to form the initially dry Dunkirk sand specimens, and moist tamping to prepare the Blessington and Larvik specimens from their initial moisture contents.

Two types of interfaces, mild steel and stainless steel, were adopted for testing. The standard "rough" mild steel and stainless steel interfaces were air-abraded to reach roughnesses (quantified by centre-line average roughness, R_{CLA}) of 10-15 μm, which fall within the range of surface roughness of industrial piles. Some interfaces with lower roughness were also considered so as to expand the roughness range. Smoother stainless interfaces were also machined to reach $R_{CLA} \approx 1$ μm to represent the surface characteristics of standard CPT friction sleeve as well as the stainless and galvanised piles tested by Carroll *et al.* (2017). The sand-steel interface shear tests performed previously by Yang *et al.* (2010), Barmpopoulos *et al.* (2010) and Ho *et al.* (2011) on dry materials concentrated on steel interfaces with roughness in the range of 3-5 μm which matched the mini-ICP piles employed for the Grenoble calibration chamber tests.

Testing design and programme completed

Initial, fast, "conditioning" shearing was applied to 5 m at a rate of 400 mm/min. Ten minute pauses were imposed in between every 200 mm of fast shearing. Slow shearing was applied at a rate of 0.016 mm/min to reach shearing distances of 50-250 mm. The gap between the confining moulds and the interface was closed in the fast shearing stage but was kept opened for around 0.1 mm over the slow shearing stage. In most cases, stable friction angle trends were reached after 10 mm of slow shearing, although the dilation trends were truncated in some cases due to material losses at the interface.

Time-dependent interface shearing behaviour was examined by leaving a group of specimens for ageing periods between 0.5 day and 30 days, while maintaining constant normal stresses. The soil specimen and steel interface remained immersed in the water bath which was topped up regularly throughout the testing. Tables 4-4 to 4-6 summarise the stress levels, pre-shearing ageing time, interface materials, pre- and post-testing roughnesses for all the tests performed.

In some tests, a second consolidation stage was imposed after terminating the slow shearing stage while maintaining constant normal stress, followed by a slow re-shearing stage at the same rate. The additional re-shearing stage enabled further characterisation of interface shearing behaviour that could be correlated to practical scenarios such as tests that involve re-loading or re-striking piles after their first-time loading to failure.

Table 4-4 Testing conditions of the large-displacement Bishop ring shear sand-steel interface tests on Batch 2 Dunkirk sand

Test code	Steel interface			σ_v [kPa]	"Consolidation" & ageing time [day]	Slow shearing distance [mm]	Number of sub-layers
	Type	R_{CLA}[μm]					
DKSS100S	SS	S	0.53±0.06	100	0.5 0.5	135 70	3
DKSS200S				200	0.5	45	3
DKSS200S-2				200	0.5	45	3
DKSS200S-3				200 200	0.5 30	120 50	3
DKSS400S				400	0.5 0.5	120 185	3
DKSS100R	SS	R	-	100	0.5 0.5	120 185	3
DKSS200R			11.8±1.13	200	0.5	45	3
DKSS400R			12.5±0.79	400 400	0.5 0.5	135 70	3
DKMS200R	MS	R	15.1±0.72	200	0.5	50	3
DKMS200R-aged			12.9±0.85	200	26	50	3
DKMS400R			13.5±1.11	400	0.5	45	3
DKMS400R-aged				400	26	95	5
DKMS600R			12.9±0.85	600	0.5	45	3
DKMS600R-aged				600	30 0.5	95 185	4 4
DKMS800R			12.9±0.85	800	0.5	75	3
DKMS1200R			12.9±0.85	1200 1200	0.5 30	115 50	4
DKMS400M	MS	M	6.17±0.66	400	0.5	70	4

Notes:

1. Specimens were formed by dry pluviation method to an initial dry density of 1610 kg/m^3;
2. Interface type, *SS*: stainless steel, *MS*: mild steel; Interface roughness, *S*: smooth, *M*: medium rough, *R*: rough;
3. Interface roughness is denoted in a format of $A\pm B$, with A and B being respectively the mean and standard deviation of the four roughness measurements made on each interface;
4. Number of sub-layers denotes the sub-layer number divided in post-test sub-sampling process.

Table 4-5 Testing conditions of the large-displacement Bishop ring shear sand-steel interface tests on Blessington sand

Test code	Steel interface			σ_v [kPa]	"Consolidation" and ageing time [day]	Slow shearing distance [mm]	Number of sub-layers
	Type	R_{CLA}[μm]					
BLMS100R	MS	R	8.03±0.32	100	0.5	50	3
BLMS200R			8.03±0.32	200	0.5	45	3
BLMS200R-2			12.7±0.88	200	0.5	50	3
BLMS200R-aged			12.9±0.85	200	30	210	4
				200	0.5	250	
BLMS400R			12.7±0.88	400	0.5	70	3
BLMS400R-aged				400	30	95	4
BLSS200S	SS	S	0.53±0.06	200	0.5	60	3

Note:

Specimens were formed by moist tamping method at the material's initial water content to an initial dry density of 1510 kg/m^3.

Table 4-6 Testing conditions of the large-displacement Bishop ring shear sand-steel interface tests on Larvik sand

Test code	Steel interface			σ_v [kPa]	"Consolidation" and ageing time [day]	Slow shearing distance [mm]	Number of sub-layers
	Type	R_{CLA}[μm]					
LVSS200S	SS	S	0.53±0.06	200	0.5	115	3
LVMS200R	MS	R	12.9±0.85	200	0.5	115	3
LVMS200R-aged			12.9±0.85	200	30	210	3
					0.5	250	
LVMS400R			12.9±0.85	400	0.5	70	4
LVMS400R-aged				400	30	95	4
					0.5	185	

Notes:

Specimens were formed by moist tamping method at the material's initial water content to an initial bulk density of 1550 kg/m^3.

4.3.3 Small-displacement direct shear sand-steel interface tests

Small-displacement direct shear sand-steel interface tests were performed on Dunkirk sand to supplement the ring shear tests. A lower interface set-up (materials deposited over the interface) was used and the friction between the mould and interface was measured beforehand and applied to correct the measured shear forces. The preparation method and testing procedures were maintained consistent with the ring shear tests described above. The sand specimens were immersed in a water bath throughout the testing. No pre-conditioning states were applied to the specimen, and shearing was initiated with a rate of 0.1 mm/min after the specimens were consolidated and aged for the prescribed periods. A similar sub-sampling approach was applied after testing.

Details of the tests performed, including initial void ratio, stress level, interface material and roughness are summarised in Table 4-7. Photographic records of the different steel interfaces used are presented in Figure 4-13, and their typical surface profiles are demonstrated in Figure 4-14. The testing outcomes are further integrated with those from similar interface tests on non-aged and aged (Batch 1) Dunkirk sand specimens shearing against stainless steel interfaces reported by Chow (1997).

Table 4-7 Summary of the small-displacement direct shear sand-steel interface tests on Batch 2 Dunkirk sand

Test code	Steel interface			e_0	σ_v' [kPa]	"Consolidation" and ageing time [day]	Shearing distance [mm]
	Type	R_{CLA} [μm]					
DS-MS200R	MS	R	14.3±1.67	0.64	200	0.1	7
DS-MS200R-26day			12.9±0.71	0.64	200	26	7
DS-MS200R-180day			12.7±0.88	0.64	200	180	8.5
DS-MS200R-Den			12.3±1.51	0.60	200	0.1	7
DS-MS400R			14.3±1.67	0.64	400	0.1	7
DS-MS200M		M	4.61	0.64	200	0.1	7
DS-SS200R	SS	R	13.2±0.33	0.64	200	0.1	7
DS-SS200S		S	1.19±0.19	0.64	200	0.1	7

Note:
Interface type, *SS*: stainless steel, *MS*: mild steel; Interface roughness, *S*: smooth, *M*: medium rough, *R*: rough.

4.3.4 Figures

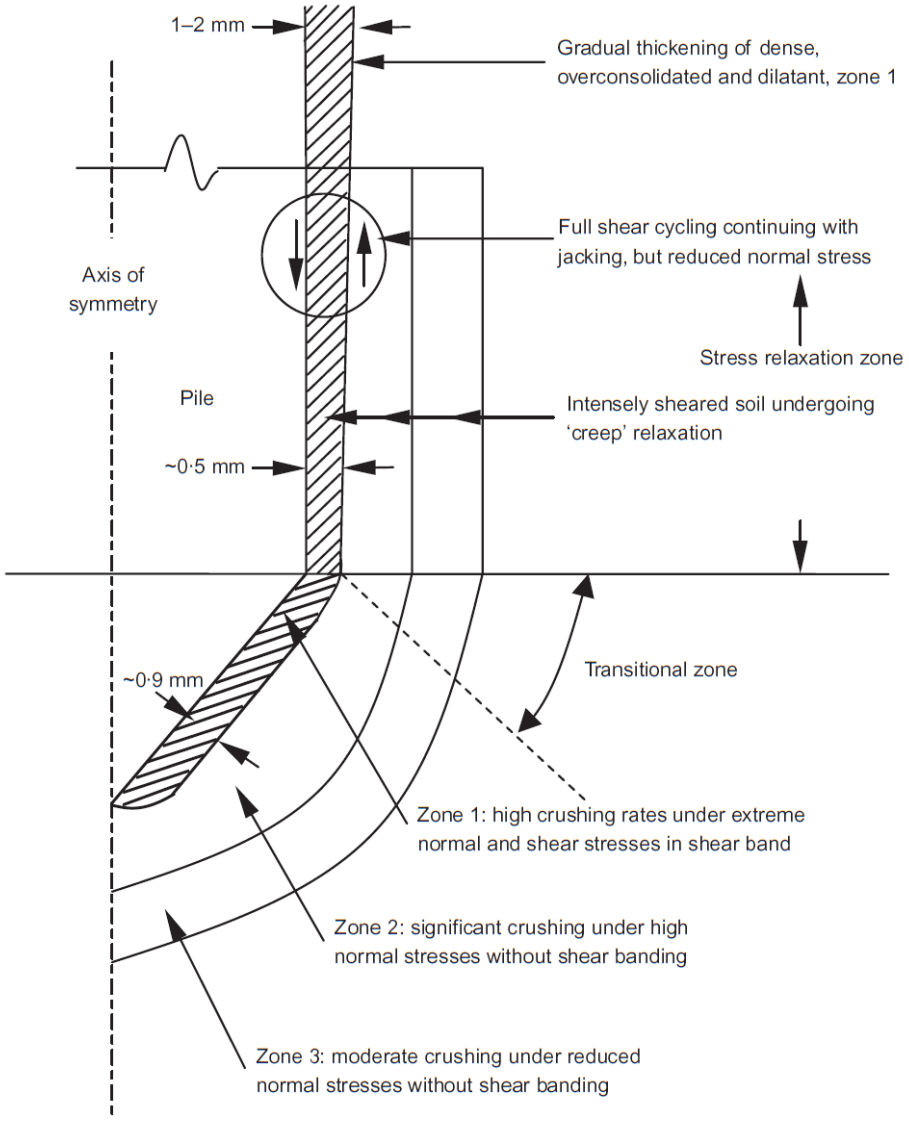

Figure 4-11 Schematic development of crushing and interface shearing regimes around laboratory instrumented model piles (Yang *et al.*, 2010)

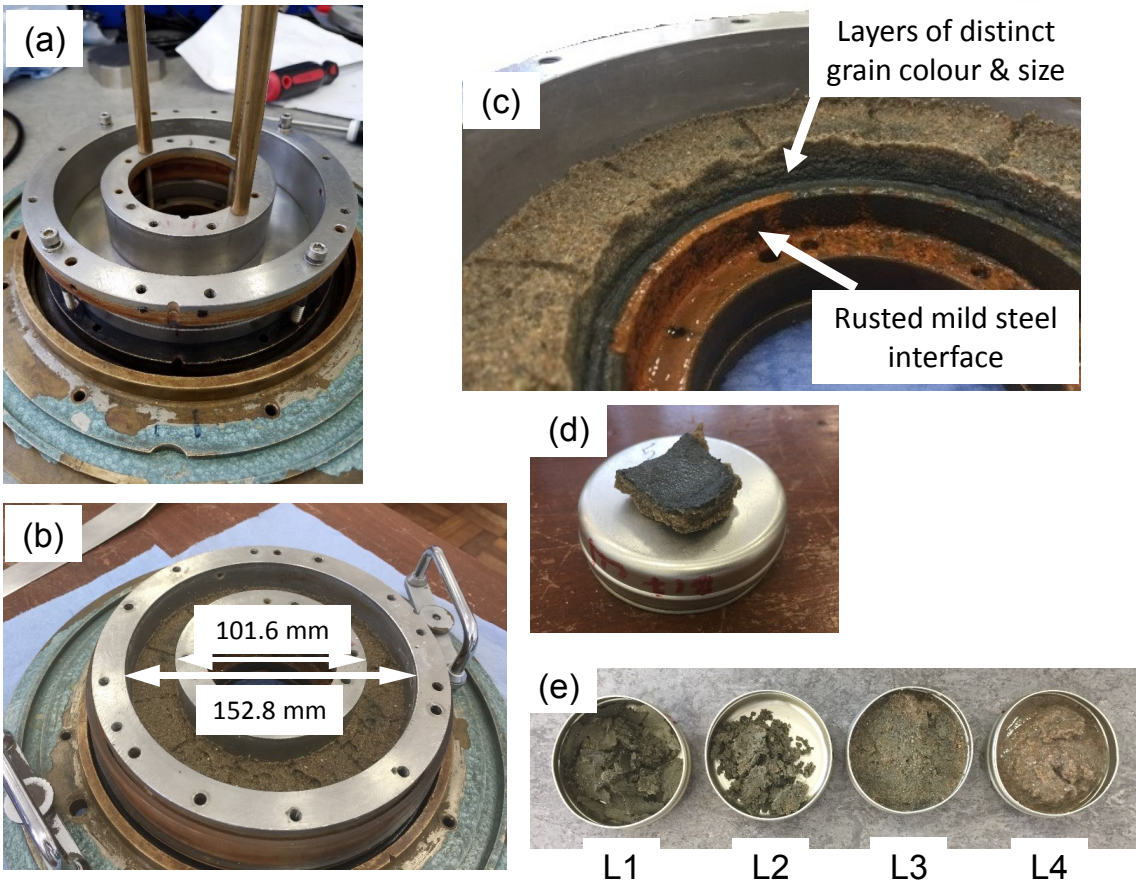

Figure 4-12 Bishop ring shear interface testing, (a) set-up of the confining moulds and steel interface; (b) post-testing specimen condition; (c) soil and interface condition after shearing, noting clear corrosion to the mild steel interface and changes to soil colour; (d) soil state at the localised sheared zone; (e) soil conditions of the different sub-sampled layers

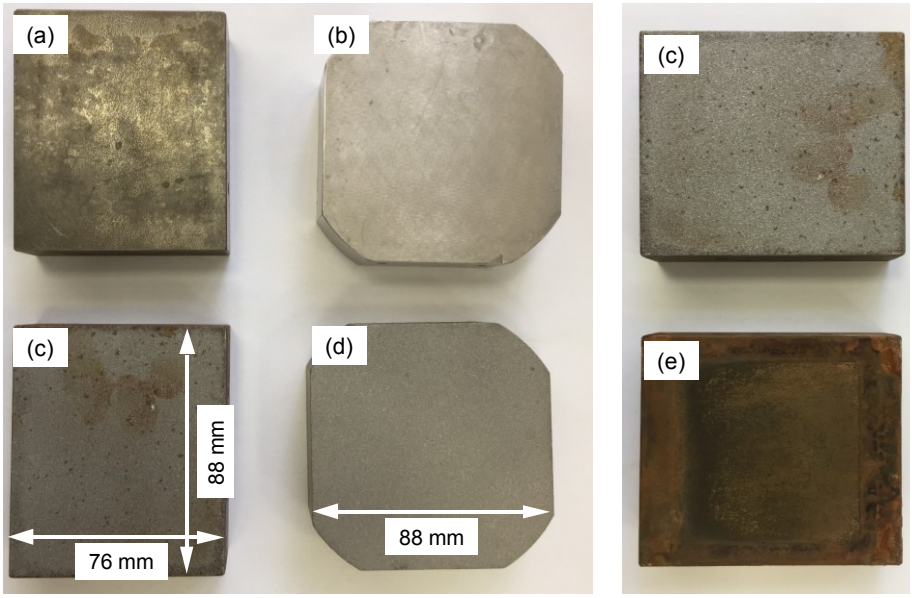

Figure 4-13 Steel interfaces for direct shear interface testing: (a) smooth mild steel; (b) smooth stainless steel; (c) rough mild steel; (d) rough stainless steel; (e) tested rough mild steel

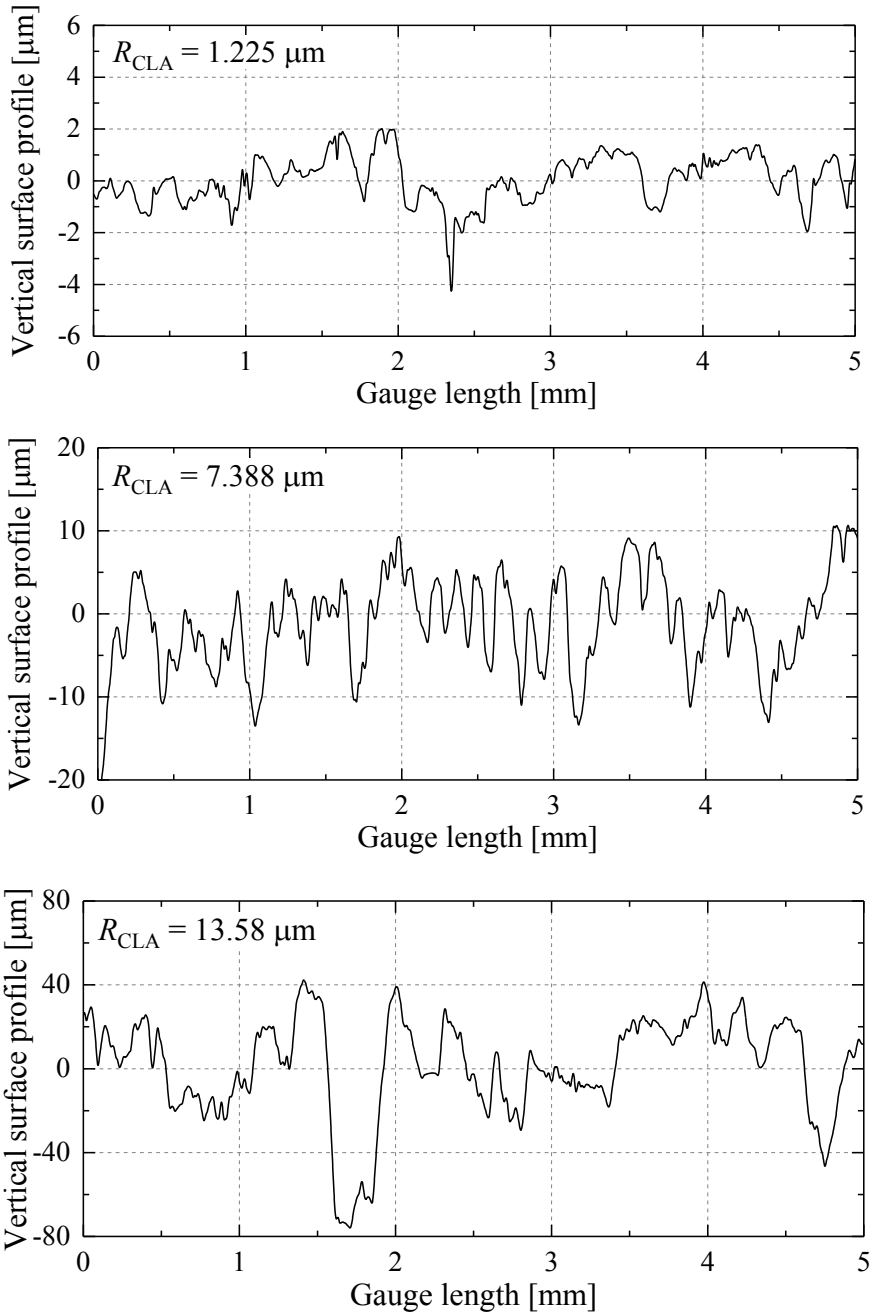

Figure 4-14 Surface roughness profiles of typical smooth, medium and rough steel interfaces

4.4 High pressure compression behaviour

This section presents the main outcomes from the Author's high pressure oedometer tests. Discussion is focused on the sands' yielding and time-dependent compression behaviour at high stresses.

4.4.1 Index properties and shape factors of the tested materials

***Particle size distribution* (*PSD*)**

The sands' grading curves were determined through standard dry sieving (referred to BS 1377-2:1990) and the laser-based imaging QicPic technique, as described in Section 2.3.6. The Feret-min mode measurements given by QicPic are adopted for comparison, since this mode generates grading results closest to those from conventional sieving.

Figure 4-15 presents grading curves of Dunkirk sand Batch 2 and Batch 3, confirming their similar gradings. The QicPic Feret-min mode curves fall to the right hand side of those from dry sieving method, as reported by Yang *et al.* (2010) and Altuhafi *et al.* (2013) among others. Grading curves of Fontainebleau NE34 sand are shown in Figure 4-16, along with results reported by previous researchers which show closely comparable results. The dry sieving method is subjected to greater discrepancies by factors such as number of sieves used, input sieving energy and other operational inconsistencies, whereas the QicPic outcomes are concentrated in a narrower band that give statistically a more stable grading characterisation.

Checks were also made to cover cases where only a few grams of soil that might be available from, for example, the sheared near interfaces zone. Although more difficult to perform and more susceptible to experimental errors, the Author's small-mass sieving tests were able to produce comparable grading curves through optimised sieving and measuring procedures. As shown by results from two tests on small mass (4 g) fresh samples of NE34 sand included in Figure 4-16, the small-mass sieving tests are encouragingly consistent and only marginally finer than those from standard sieving with 200-250 g sand. This optimised approach was employed to determine gradings for samples collected from the oedometer and ring shear tests.

An overall comparison of particle size distribution for the tested materials is shown in Figure 4-17, and their index properties, characteristic diameter and grading

coefficients are summarised in Table 4-8. The Dunkirk sand Batch 2 and Batch 3 are slightly coarser than the NE34 sand, while the latter is more uniform. Recalling the size dependency of particle strength (see section 4.2.1), the differences imply that the Dunkirk sands have greater variations of particle strength, corresponding to a lower Weibull modulus (see Figure 4-4).

From Figure 4-17, it is interesting to note that the Dunkirk sands exhibit greater 'deviation' between the gradings determined from the dry sieving and QicPic methods than the NE34 sand, indicating a more varied level of shape irregularities. For perfectly spherical particles with homogeneous density, the grading determined from the sieving and all QicPic modes should converge to a single curve. The implied variations in particle morphology and shape parameters are examined below, employing optical microscope observations and QicPic measurements.

Table 4-8 Summary of the index properties of the fresh soil materials

Material	Method	Characteristic diameter [μm]				Coefficients			Notes
		D_{10}	D_{50}	D_{60}	D_{90}	C_u	C_c	R_D	
Dunkirk Batch 2	dry sieving	174.2	240.9	261.9	401.5	1.50	0.99	2.31	m = 250 g
	QicPic	189.3	277.1	299.7	476.6	1.58	0.98	2.52	Feret-min
Dunkirk Batch 3	dry sieving	163.6	240.9	257.8	391.2	1.58	1.04	2.39	m = 250 g
	QicPic	180.6	265.8	292.0	471.7	1.62	0.98	2.61	Feret-min
Fontain-ebleau NE34	dry sieving	161.1	221.1	233.9	288.4	1.45	1.03	1.79	m = 250 g
	dry sieving	150.0	203.8	214.5	279.7	1.43	1.04	1.87	m = 4 g
	dry sieving	144.7	199.7	211.2	276.9	1.46	1.09	1.91	m = 4 g
	QicPic	177.5	236.3	246.2	305.1	1.39	1.02	1.72	Feret-min

Notes:

1. R_D relative distribution factor defined as ratio between D_{90} and D_{10} (Altuhafi & Coop, 2011);
2. m = 250 g and m = 4 g indicate the initial soil mass used for dry sieving analysis;
3. Feret-min: characteristic particle diameter defined as the minimum distance between two tangents on opposite sides of the particle, see Altuhafi *et al.* (2013).

Grain morphology: micro- and macro-observation

While Table 4-8 summarises the materials' particle size characteristics, Figures 4-18 to 4-20 show optical microscope images of dry Dunkirk sand Batch 2, Batch 3 and NE34

sand, as obtained from a Zeiss Axioskop 40 instrument with an AxioCam MRc 5 camera. The images of the Dunkirk sand Batch 2 may reflect the shallow sea origin of this material, reflected by the presence of shell fragments, feldspar, and other mixed mineralogy with presumably varied particle strengths. The images also show significant variations in the grains' size, shape, colour and densities. The siliceous grains are mostly transparent and clean, and with rounded and sub-rounded shapes. Similar to Batch 2, the images of Dunkirk sand Batch 3 clearly indicate mixed grains with varied compositions. However, Batch 3 seems to contain less elongated and flaky shell fragments. Also the silica grains appear to be less clean and reflective, probably due to the inclusion of fines or dirt adhering to their surfaces. Clearly different from the Dunkirk sands, as shown in Figure 4-20, the NE34 sand represents high purity silica grains with clean and reflective surfaces. The grain shapes concentrate in the rounded and sub-rounded range and the variation of grain size is much less remarkable, compared with the Dunkirk batches.

The micro-scale observations were also apparent in visual inspections of the materials in their dry or saturated states. The NE34 sand typically showed light colour, with only minimal material dispersing on water pluviation. The Dunkirk sands, however, tended to exhibit much darker colour after saturating and more fine materials could be observed clearly dispersing in sand-water mixtures. Although the sands present comparable gradings (see Figure 4-17), the micro- and macro-features contribute to the sands' non-identical behaviour in compression, monotonic and cyclic shearing that has been noted by Aghakouchak (2015) in his extensive testing on the Dunkirk sand Batch 2 and NE34 sand, and by Vinck (2016) and the Author in tests on the Dunkirk sand Batches 2 and Batch 3.

Statistical distribution of grain shape

As introduced in Section 2.3.6, particle shape is quantified in QicPic using aspect ratio, sphericity, convexity and other parameters. Statistical analysis can be made to assess the accumulation and density distribution of particles' shape.

Figures 4-21 and 4-22 plot probability density distributions for sphericity and aspect ratio for the three studied materials, indicating broadly similar patterns. Particle sphericity reaches its peak at 0.89 while the peak aspect ratio covers in the range of 0.74-0.8. The distribution trends of the NE34 sand concentrate in narrower ranges and

the peak density values reached are higher than those of the Dunkirk sands. As with the particle size distribution, NE34 is more uniform also in terms of particle shape.

4.4.2 Yielding and crushing behaviour under uniaxial compression

As discussed in section 4.2.1, particle characteristics of size, shape and mineralogy composition are likely to control the uniaxial yielding and crushing behaviour of granular materials. The high pressure oedometer tests specified in Table 4-3 examined how these features applied to the Author's test sands.

1D compression responses

The e-σ_v compression and yielding responses observed under various maximum vertical stresses are plotted in Figures 4-23 and 4-24, and are further compared in Figure 4-25. The evolving trends of void ratio against vertical stresses exhibit the three-region compression response commonly seen in uniform granular materials. Each sand developed overlapping e-σ_v curves over its low-to-medium stress range.

Compared to those of NE34 sand, the curves of Dunkirk sands showed more scatter, reflecting their greater variabilities and more mixed mineralogy composition. The Dunkirk sand tests shown in Figure 4-23 exhibited a "Region 4" response (as defined in Section 4.2.1) in which $\Delta e/\Delta\log(\sigma_v')$ reduced slightly over the 91.1 to 101 MPa range. No such curvature reduction was noted in the NE34 sand tests. Although not converging perfectly, the compression curves of Dunkirk sand Batches 2 and 3 were broadly parallel, indicating slight variations in mineralogical compositions and grain surface characteristics that became less pronounced at high stresses where the compression responses were dominated by the fracturing of the silica particles.

As demonstrated in Figure 4-25, grain crushing was delayed until higher yield stresses with the more uniform and finer NE34 sand. Once started, the crushing was more abrupt and followed a steeper normal compression line. NE34 sand could not reach the same final void ratio as the Batch 2 Dunkirk sand. These characteristics highlight the dependency of crushing on particle size and strength, as the initial void ratios of the tested specimens were all nominally identical. However, the Dunkirk Batch 3 specimen was formed with slightly higher initial void ratio (0.66 in comparison with 0.64 of those Batch 2 specimens) and its compressibility appeared to be higher, leading to a lower final void ratio than the Batch 2 sand. Finally, the

unloading responses appear insensitive to the differences in material properties and initial density, as the unloading (e-σ_v) curves are approximately parallel to each other.

Compared with the Author's dataset, the test on NE34 reported by Yang *et al.* (2010) (included in Figure 4-24) showed higher compressibility up to 25 MPa but slightly lower compressibility over the last stress increment to 50 MPa. The differences may reflect the differences in oedometer configuration, since a floating ring oedometer was adopted in Yang *et al.* (2010)'s test, whereas a polished and lubricated fix ring was used in the current study. The small "kink" noted in Yang *et al.* (2010)'s curve at the initial loading might be induced by unwanted misalignment or material loss, which was also experienced in the Author's and Vinck (2016)'s initial tests.

Compressibility characteristics

The above compression characteristics were further interpreted from the perspective of semi-logarithmic compressibility ($C_c = \Delta e/\Delta\log(\sigma_v)$), as summarised in Figures 4-26 and 4-27 for the three soils investigated. The sands' C_c trends gradually increased over low to medium stress level, followed by steep increasing stages after exceeding yield stress point. On approaching the maximum available stresses, the increasing C_c trends started to slow down or reverse, as in the case of the Dunkirk sands. The soils' log-linear compressibility remained broadly constant on unloading.

The compression characteristics can also be interpreted using the linear compressibility index ($C_{LC} = \Delta e/\Delta\sigma_v$), as summarised in Figure 4-28 for Dunkirk Batch 2 and NE34 specimens with identical $e_0 = 0.64$. The linear compressibility of Dunkirk Batch 2 sand decreased rapidly in the initial loading steps up to 7.8 MPa, after which the trend stayed stable and decreased slightly while approaching the maximum compression stresses. The linear compressibility of NE34 sand fell below those of Dunkirk sand over the initial 50 MPa compression, while afterwards the trends stepped up and stayed above those of Dunkirk Batch 2 sand.

An overall comparison is presented in Figure 4-29. Also included are the reinterpreted trends from two oedometer tests on Dog's Bay sand reported by Altuhafi & Coop (2011). As introduced in Section 4.3.1, the three materials have distinct features of mineralogy composition and particle strengths, which are reflected in their compressibility trends. The NE34 sand exhibits lower compressibility over its low stress range, followed by abruptly increasing semi-logarithmic compressibility trends

accompanied by catastrophic grain crushing. On the other hand, the Dog's Bay sand developed much higher compressibility under low stress range and its peak compressibility was reached at a far lower stress level. Both the peak compressibility and the corresponding stress level depended on the specimens' initial void ratios. The impact of initial void ratio, however, reduces at higher stresses when the crushing process slows as the grains gradually reach their comminution limit. The Dunkirk sands exhibited compressibility features that trended to diverge from that of NE34 sand and shift towards those of the Dog's Bay sand.

4.4.3 Progressive compression behaviour at elevated stresses

Stress-controlled dead-weight oedometers provide very stable stress conditions for monitoring creep deformation. As mentioned, after each loading stage, the specimens were left until the axial strain rates decayed to a negligible level of 0.002%/day.

Figures 4-30 and 4-31 present traces of axial strain increments against logarithmic time for the loading and creep stages of two tests on Dunkirk sand Batch 2 and NE34 specimen compressed up to 101 MPa. Also plotted are similar records for three unloading stages. It is clear that for both materials, creep strains were substantial and were dependent on both stress level and particle strength. At relatively low stresses (<12.5 MPa), creep deformation is interpreted as being mainly due to particle rearrangement, accompanied with grain surface abrasion and breakage of weak asperities or grains, allowing a gradually enhanced micro-fabric. At higher stresses, grain fracture propagated until sufficient particle contacts had developed and the distributed stresses had moderated below the level required to induce further fracturing. From a micro-mechanics perspective, the creep straining indicates continuous process of force chains collapsing and rebuilding, accompanied by the propagation of grain crushing.

The axial strain traces with time indicate that, compared with NE34 sand, the compression and crushing response of the Dunkirk sand is more progressive, developing less well-defined sharp increases related to the onset of crushing. The creep trends for $t > 0.05$ hours can be broadly fitted with linear lines in a semi-logarithmic scale, as shown in Figures 4-30 and 4-31. The slopes of the fitting lines depict the rate of creep strain accumulating with time and is defined here as a creep strain ratio C_ε (=

$\Delta\varepsilon_a/\Delta\log(t)$), which is similar to secondary compression ratio C_α (=$\Delta e/\Delta\log(t)$) but is based on only axial strains under K_o conditions.

The rate of creep strain accumulation is clearly dependent on stress level, as presented as creep strain ratio against vertical stress shown in Figure 4-32. The trends of creep strain ratio exhibit broadly similar patterns to those of compressibility shown in Figure 4-29. The Dunkirk sands presented greater creep straining from relatively lower vertical stresses, and peak creep strain ratios were reached at in the vertical stress range of 50-75 MPa. The NE34 sand, which is much less compressible, shows lower creep strain ratio over low vertical stress range, followed by a dramatic increase after the onset of yielding and crushing and high values of creep strain ratio were noted in the stress range of 75-91 MPa. This abrupt pattern of creep strain accumulation with delayed peak values at higher stress levels is compatible with the trends of compressibility.

The above results indicate that, in practical scenarios where significant particle crushing is encountered, for example in pile installation, a marked tendency to develop substantial creep straining should be expected to follow each major compression event. Creep strain accumulation is highly dependent on stress level and material strength. The overall effects could attribute to the differences between the end of driving and subsequent (set-up) capacities of driven piles.

Given the link between creep and grain crushing as well as the potential dependency of particle strength on the presence of water (mechanisms see in Section 4.3.1), it is possible that fully saturated sands will show higher compressibility and greater rate of creep straining than dry samples. In that sense, in practical scenarios, it may be important to consider groundwater level and soil deposit conditions (dry, partially or fully saturated) and assess their potential effects, as in the field pile studies summarised by Rimoy *et al.* (2015) and Carroll *et al.* (2017).

4.4.4 Figures

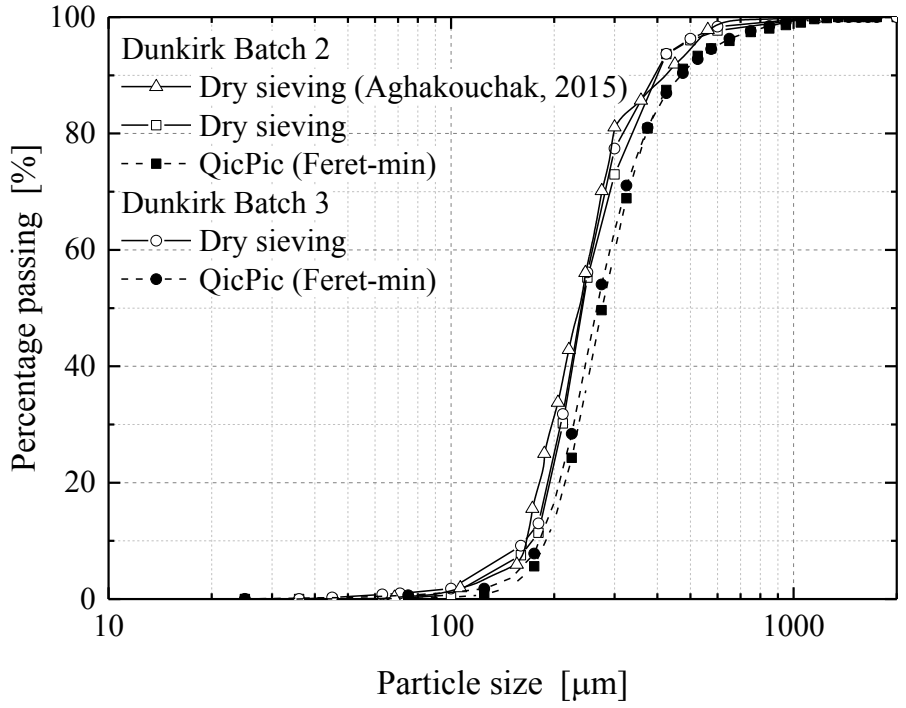

Figure 4-15 Grading of Dunkirk sand Batches 2 and 3 from dry sieving (soil mass: 200-250 g) and QicPic Feret-min mode

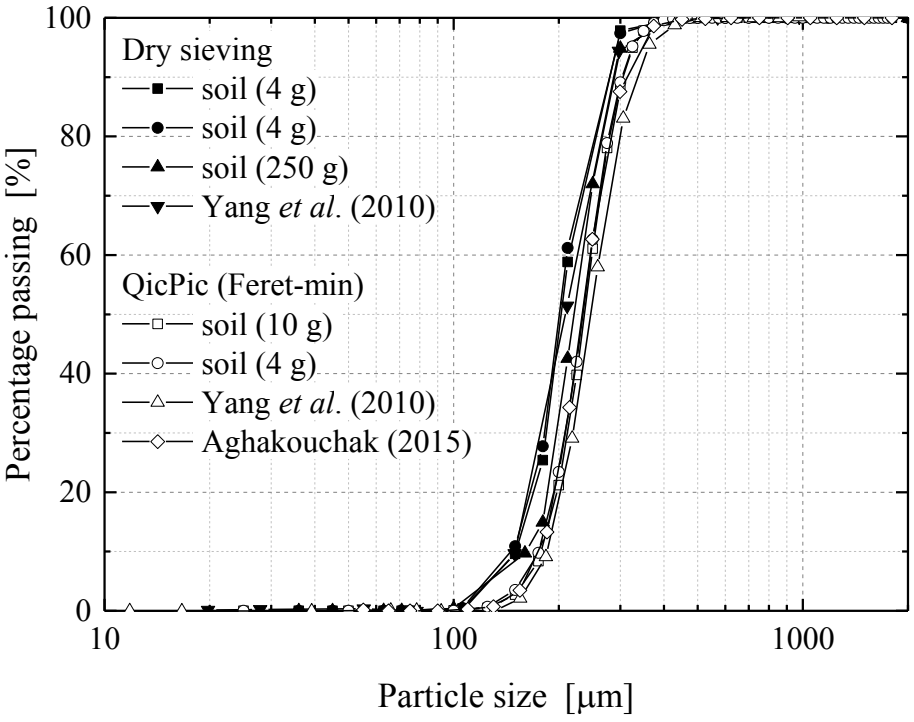

Figure 4-16 Grading of Fontainebleau NE34 sand from dry sieving (soil mass: 4 g or 250 g) and QicPic Feret-min mode

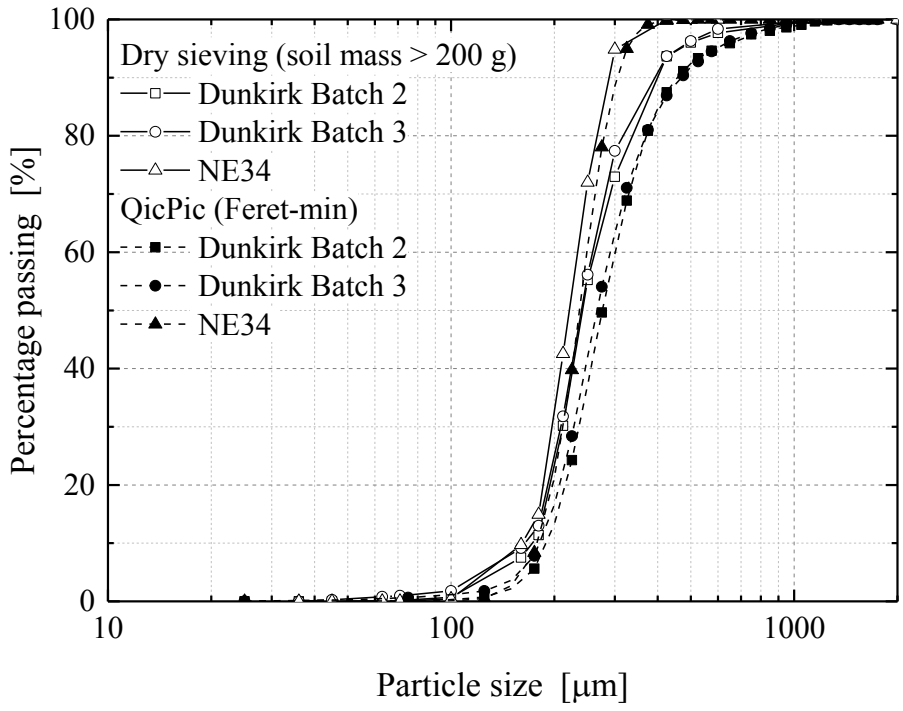

Figure 4-17 Grading curves of the materials employed in high pressure oedometer tests

Figure 4-18 Optical microscope images of dry Dunkirk sand Batch 2, featured with elongated shell fragments and grains of varied shape, size and colour

Figure 4-19 Optical microscope images of dry Dunkirk sand Batch 3, identifying mixed grains of varied origins and less reflective grains surfaces compared to the Batch 2

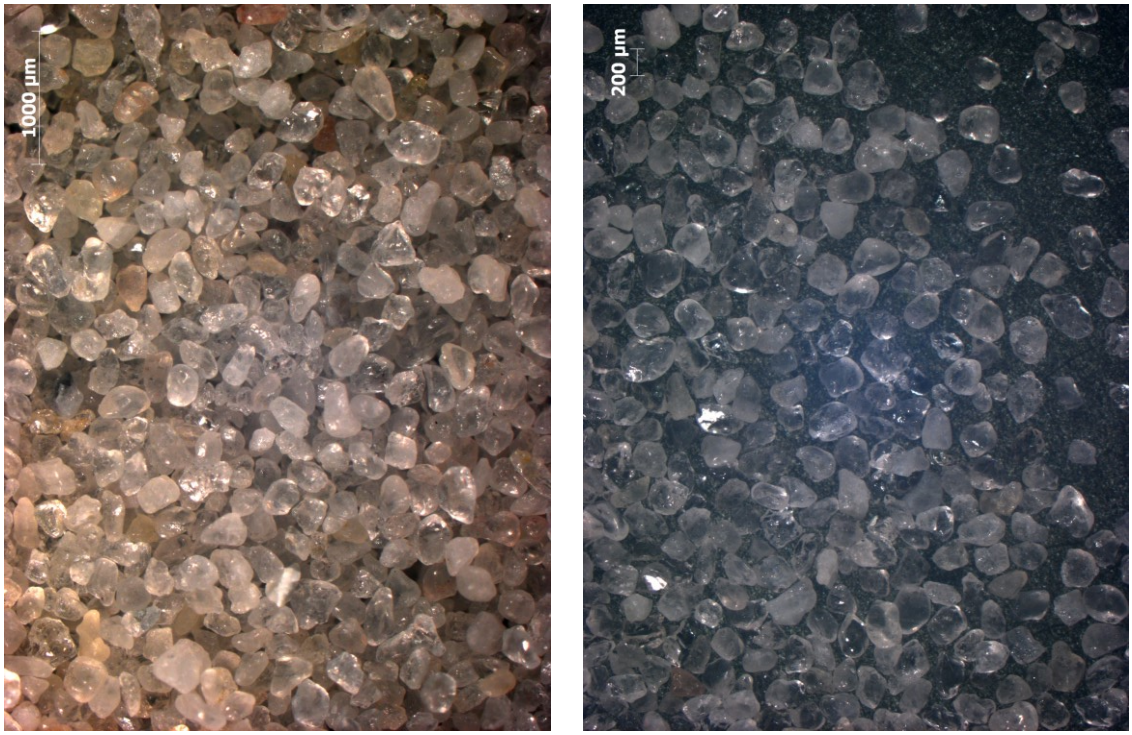

Figure 4-20 Optical microscope images of dry Fontainebleau NE34 sand, consisting of clean rounded to sub-rounded high purity silica grains with reflective grain surfaces

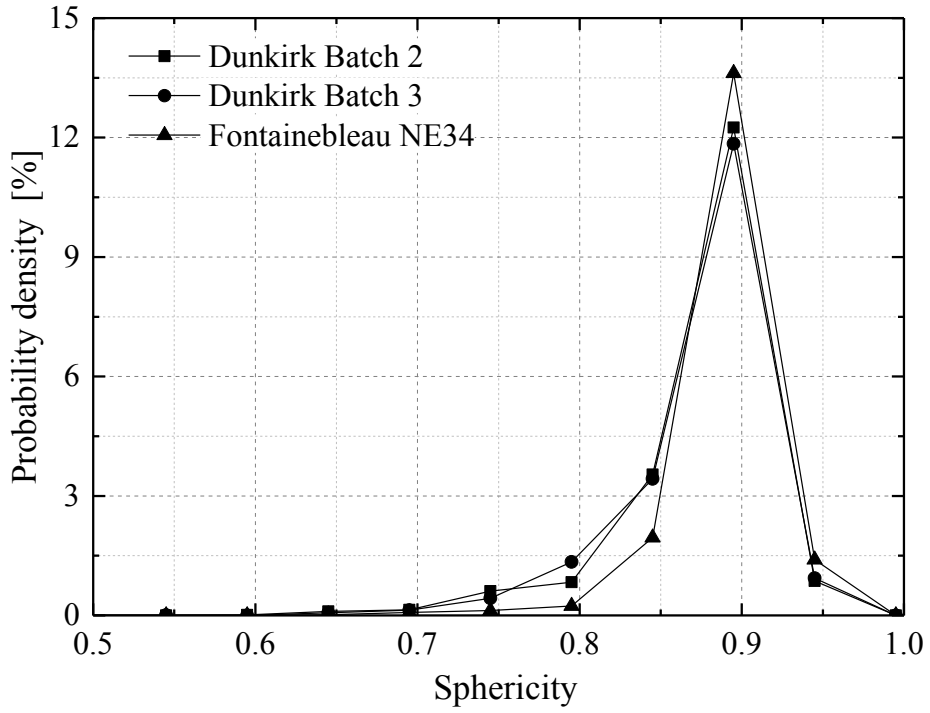

Figure 4-21 Density distribution of QicPic grain sphericity of the tested materials

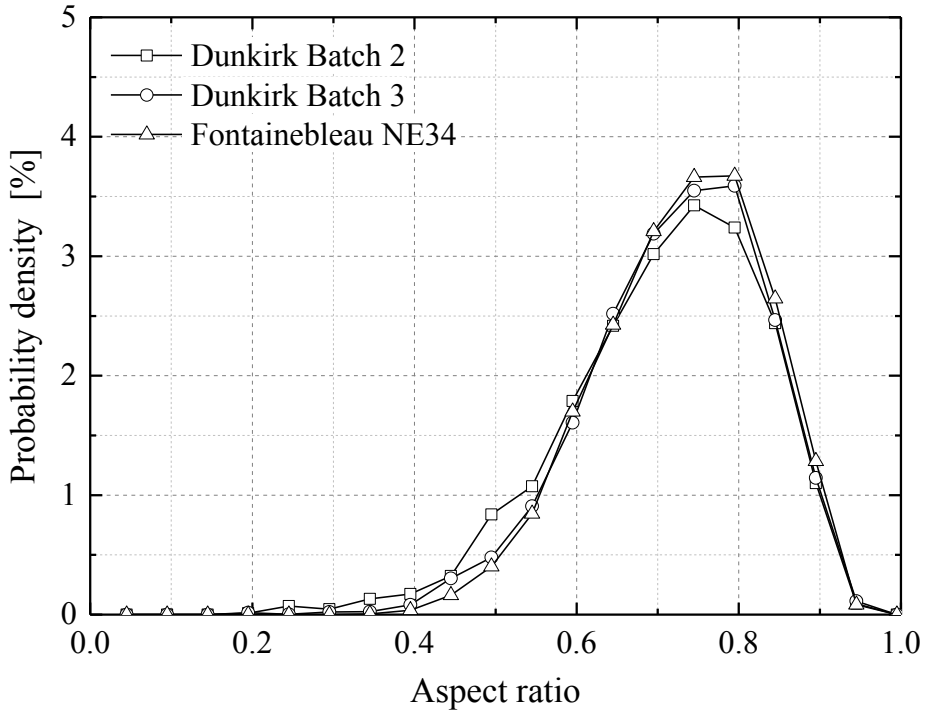

Figure 4-22 Density distribution of QicPic grain aspect ratio of the tested materials

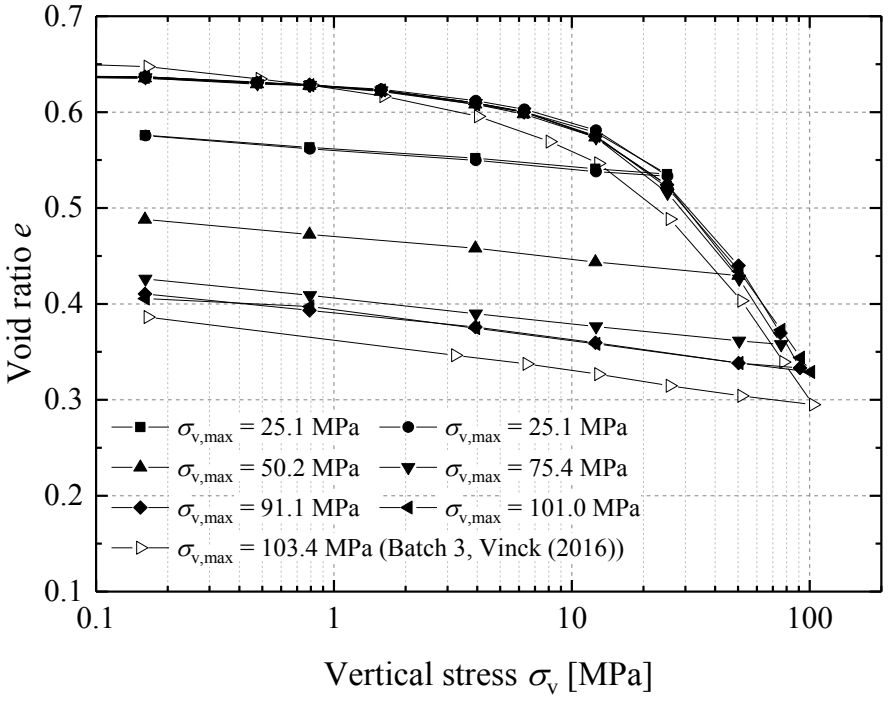

Figure 4-23 Compression and yielding response of the Dunkirk sands

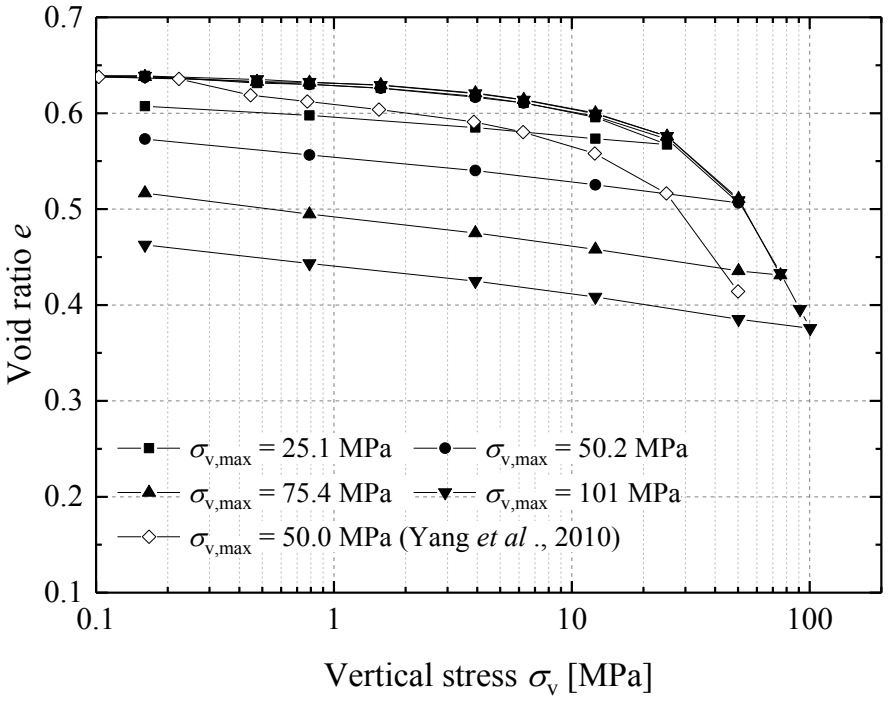

Figure 4-24 Compression and yielding response of Fontainebleau NE34 sand

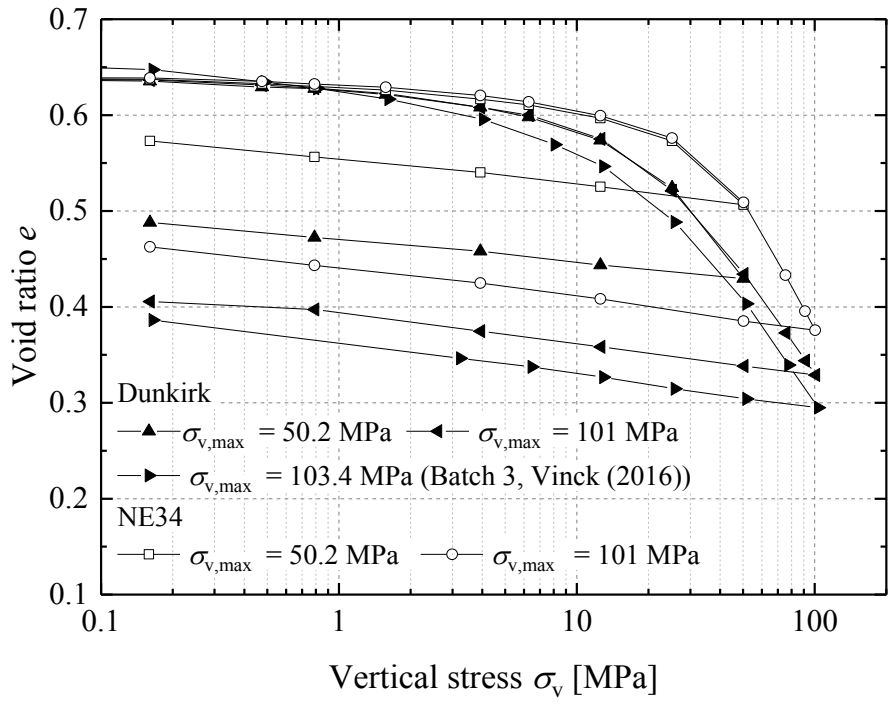

Figure 4-25 Overall comparison of yielding and crushing response of the three studied materials (excluding Yang *et al.* (2010)'s test on NE34)

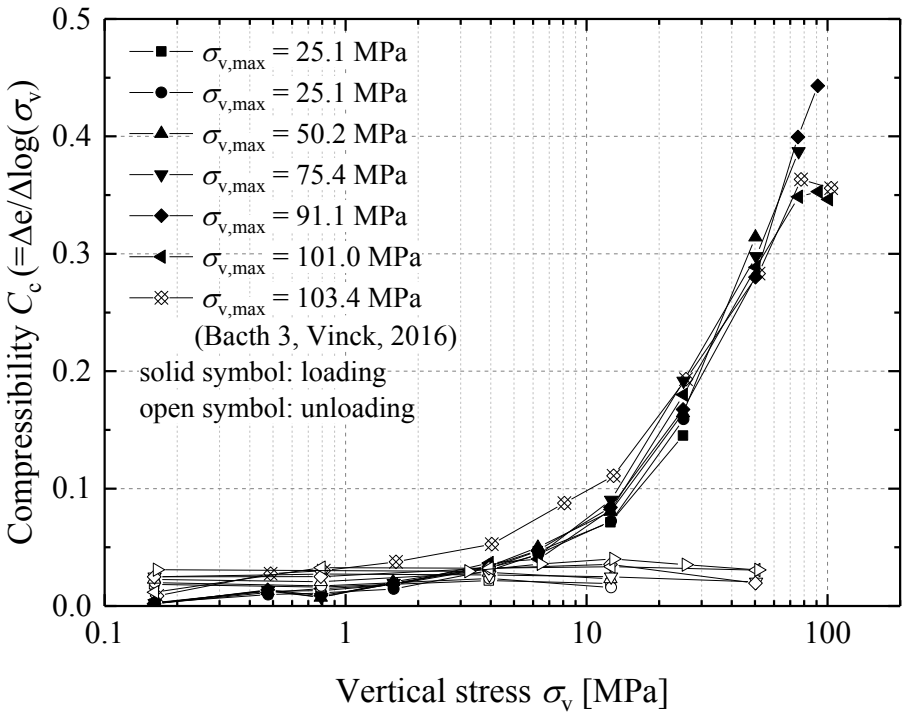

Figure 4-26 Compressibility trends of the Dunkirk sands against vertical stress level

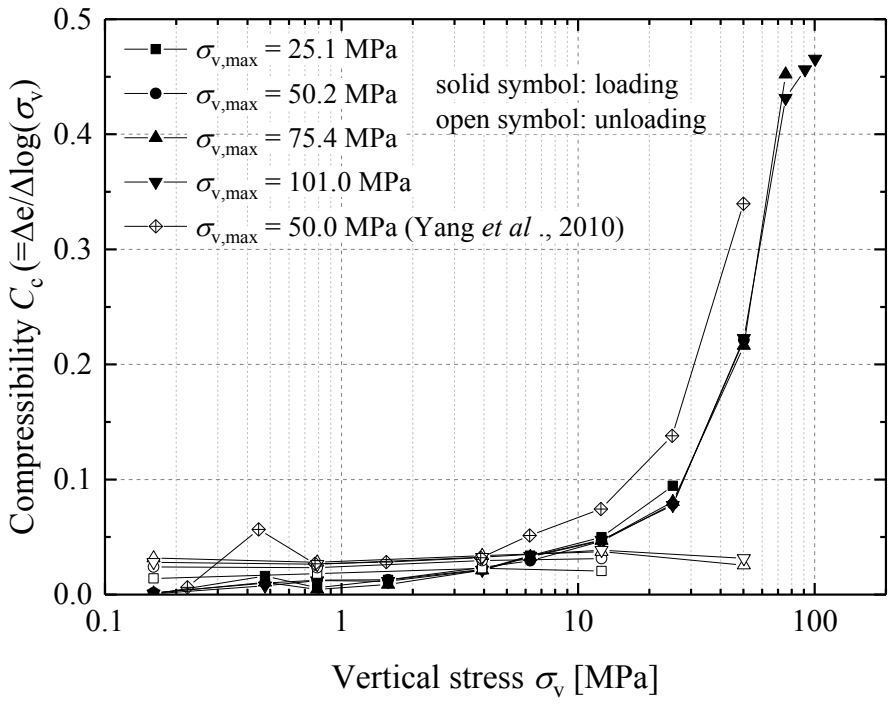

Figure 4-27 Compressibility trends of the Fontainebleau NE34 sand against vertical stresses

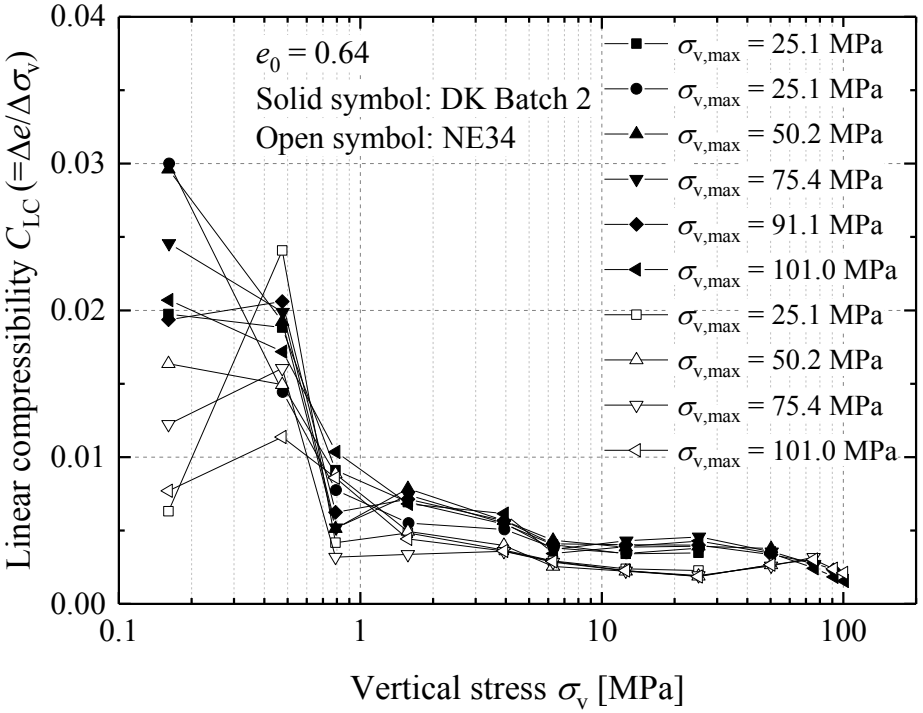

Figure 4-28 Trends of linear compressibility C_{LC} (=$\Delta e/\Delta\sigma_v$) against compression stress of Dunkirk sand Batch 2 and NE34 sand specimens (e_0 = 0.64)

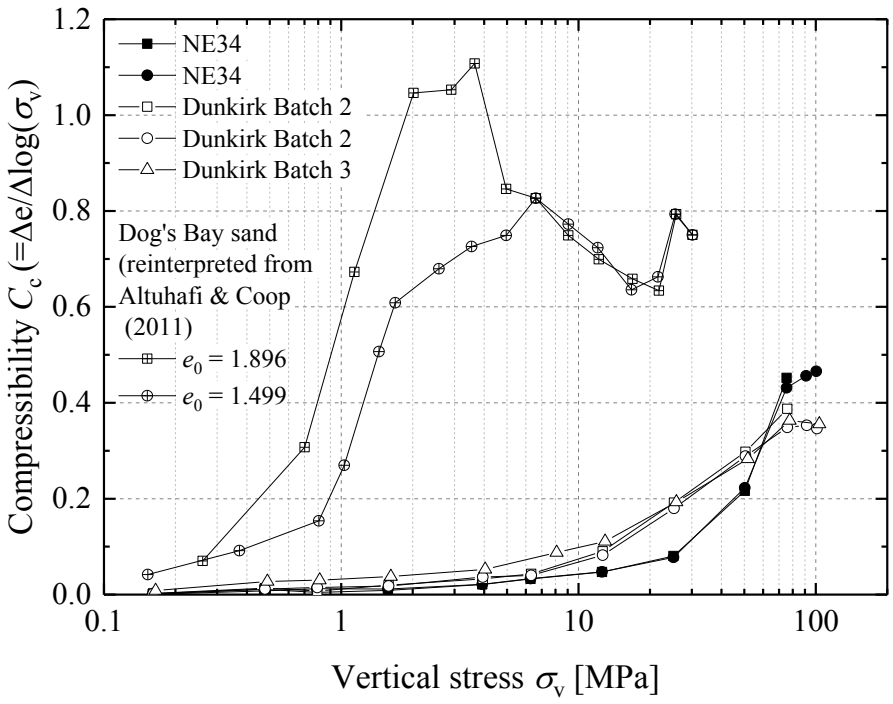

Figure 4-29 Overall compressibility of the studied materials, also included are reinterpreted oedometer tests on high carbonate content Dog's Bay sand reported by Altuhafi & Coop (2011)

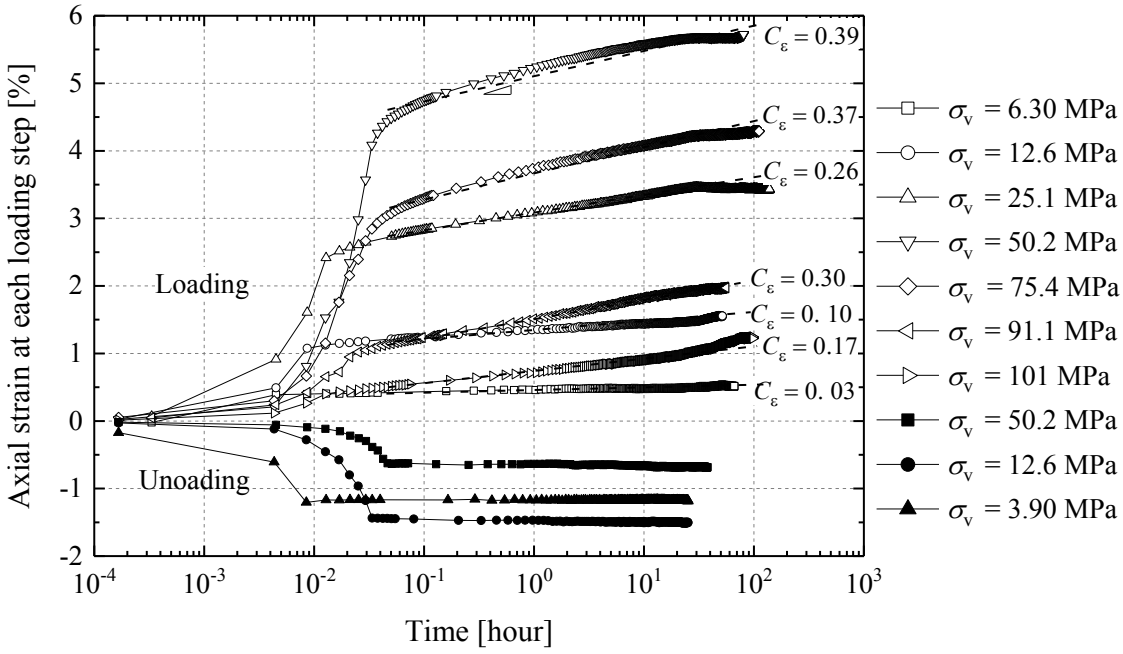

Figure 4-30 Axial strain development of the Dunkirk sand Batch 2 test with $\sigma_{v,max}$ = 101 MPa, also indicating creep strain ratio C_ε (= $\Delta\varepsilon_a/\Delta\log(t)$) for each creep stage

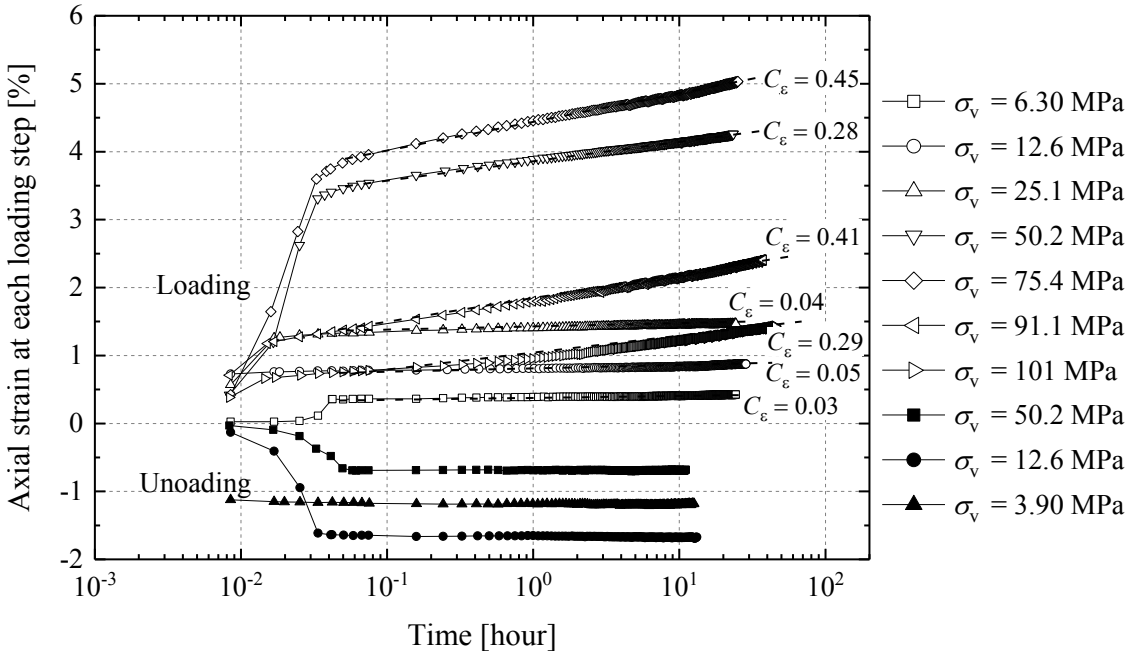

Figure 4-31 Axial strain development of the NE34 sand test with $\sigma_{v,max}$ = 101 MPa, also indicating creep strain ratio C_ε (= $\Delta\varepsilon_a/\Delta\log(t)$) for each creep stage

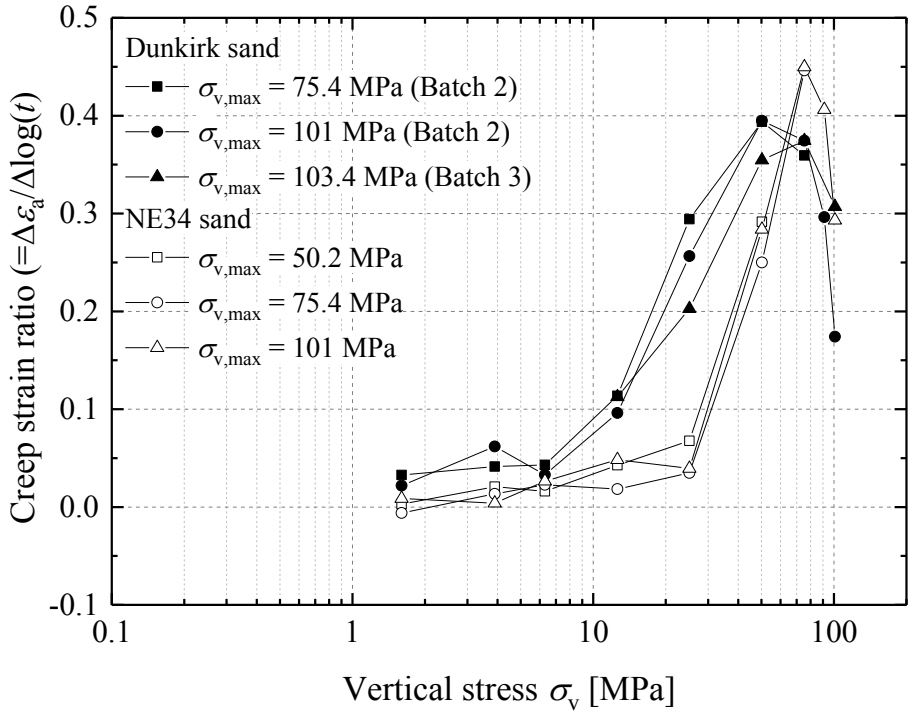

Figure 4-32 Creep strain ratio ($\Delta\varepsilon_a/\log(t)$) against vertical stress level of oedometer tests on Dunkirk sands and NE34 sand

4.5 Sand-steel interface shearing behaviour

This section of the chapter summarises the main outcomes from the small- and large-displacement sand-steel interface shearing experiments. The index properties, chemical and mineralogical compositions of the studied soils are described, followed by detailed characterisation of the sand-steel interface shearing behaviour. The effects of material property, interface type and surface roughness are discussed and the stress- and time-dependency of interface shearing behaviour is highlighted.

4.5.1 Characterisation of index and chemical properties

The grading curves of the studied materials are shown in Figures 4-33 and 4-34, differentiating "initial" grading and "as-tested" gradings, as summarised also in Table 4-9. Blessington and Larvik sands have similar fines contents and are finer and better graded than the Dunkirk sand. The initial "as sampled" states were determined from wet or dry sieving tests on 'in-situ' materials, whereas the 'installed' states represented gradings of soils tested in the apparatuses after pre-sieving through a 2 mm aperture standard sieve. This pre-treatment step was essential to remove excessive shell or gravel fragments.

Table 4-10 summarises the materials' chemical index properties and mineralogical composition from tests reported by Carroll *et al.* (2017). The Larvik sand exhibits a significantly high sulphate content with pH in the acidic range (< 7), reflecting its volcanic rock origin and possibly industrial contamination. The Blessington and Dunkirk sand fall in the alkaline range and contain medium-to-low carbonate content (20.5% and 9.5% respectively) with similar chemical compositions, featuring the limestone origins of the glacial Blessington sand and the nearshore origin of the Dunkirk sand. Meanwhile, the Dunkirk sand, as tested, has lower carbonate content compared to its sampled state, due to the manual removing or sieving of coarse shell fragments.

Table 4-9 Index properties of the studied materials at their "as-sampled" and "as-tested" states

Material	State	Characteristic diameter [μm]				Coefficient		Fines content [%]
		D_{10}	D_{50}	D_{60}	D_{90}	C_u	C_c	
Blessington sand	as-sampled	80.8	207.5	237.9	526.2	2.95	0.99	4.3
	as-tested	79.8	204.8	235.7	480.9	2.95	0.99	3.8
Dunkirk sand Batch 2	as-sampled [(1)]	165.7	253.1	280.6	401.8	1.69	0.84	0.2
	as-tested	172.9	242.6	264.0	400.3	1.53	0.97	0.1
	as-tested	181.0	244.1	270.9	419.0	1.50	0.90	0.1
Larvik sand	as-sampled	74.7	159.9	181.0	291.0	2.42	1.12	6.0
	as-sampled[(2)]	68.2	154.8	177.5	318.8	2.60	1.10	7.0
	as-tested	74.5	157.7	179.8	284.3	2.41	1.13	6.3

Notes:

1. Sampling depth: Dunkirk sand Batch 2, shallow depth (< 0.5 m); Larvik sand, 3.95 m; Blessington sand, unavailable;
2. Grading curves were determined using dry sieving method, excluding Larvik as-sampled[(2)], which was from wet sieving performed at NGI;
3. Fines content defined as percentage passing 63 μm aperture standard sieve.

Table 4-10 Chemical properties and composition of the tested materials

Material	State	Chemical properties[(1)]					Chemical composition
		pH [-]	Sulphate [mg/kg]	Carbonate [%]	Inorganic carbon [%]	Conductivity [mS/m]	
Blessing-ton sand	as-sampled	8.0	<1000	20.5	4.1	8.6	Highly angular quartz, calcite feldspar, muscovite mica[(2)]
Dunkirk sand Batch 2	as-sampled	8.6	1000	9.5	1.9	8.3	84% SiO_2 quatrz, 8% feldspar, 8% calcium carbonate fragments[(3)]
	as-tested	8.1	2200	1.7	0.3	10.5	Similar to above, lower carbonate content due to manual removal of shell spar or fragments
Larvik sand	as-sampled	3.5	11900	0.1	0.02	67.7	25% quartz, 37% feldspars and 38% plagioclase, no clay mineral[(1)]

Notes:

[(1)] Data courtesy of Dr. R. Carroll at NGI;

[(2)] Reported by Doherty *et al.* (2012) from optical petrography analysis;

[(3)] Reported by Chow (1997) based on X-ray diffusion (XRD) analysis.

4.5.2 Large-displacement sand-steel interface shearing behaviour

The mechanical factors and physicochemical processes that could affect sand-steel interface shearing behaviour include interface material, surface roughness, chemical and mineralogical nature of the soil and water, stress level and time. Referring to the test schemes set out in Tables 4-4 to 4-6, this section focuses on the non-aged first-time interface shearing behaviour of the three materials. The re-shearing behaviour in some of the tests are reported in the subsequent Section 4.5.6, and the responses of the aged specimens are presented and analysed in Section 4.5.7.

Dunkirk sand shearing against rough mild steel interfaces

Figure 4-35 summarises the evolving trends of interface friction angle for Dunkirk sand shearing against mild steel interfaces under normal stresses of 200 to 1200 kPa. The data presented were taken from slow shearing stages after fast pre-shearing, but without prolonged ageing.

A clear trend of increasing friction angles with elevated stress levels can be observed. The peak friction angles were reached within 0.5 mm slow shearing, followed by a shearing 'softening' range. As shearing continued, most tests reached stable residual states within 20 to 40 mm while some slowly climbed to reach higher ultimate states. One exception was the σ_v = 1200 kPa test which gave a quasi-stable friction angle of 32.1˚ after 40 mm shearing distance, followed by a slowly increasing trend. A stable residual shearing angle of 36.6˚ appeared to be reached after 5 days and a 115 mm displacement. On post-test dismantling, a layer of heavily sheared material was found attached firmly to the steel interface, and it appears likely to the Author that shearing had extended from the interface deep into the soil mass and involved a significant degree of grain crushing in the soil mass.

Stress-dependency was also observed in the accompanying dilation trends, as seen in Figure 4-36. The ring shear test procedure calls for the gap between the confining rings and interface to be opened during slow shearing. This improves stress measurements but induces errors in determining the degree of vertical dilation. Nevertheless, the observed trends indicate dilation reducing with increasing normal stress level, as expected for soil-soil shearing, although the 600 kPa test was clearly affected by soil loss through the gap at displacements greater than 10 mm. Also indicated in the figure is the range of peak-to-trough roughness (twice the centre-line

average roughness, R_{CLA}) as an approximate measure of the amount of soil radial dilation (Δr) experienced at pile shaft during loading to failure (over typically less than 10 mm pile head displacement), as recommended by Jardine *et al.* (2005). The observed dilative movements for shear distance up to 10 mm are 18 to 50 μm, while $2R_{CLA}$ range is 16 to 30 μm, indicating a similar range, but not a precise match.

Dunkirk sand shearing against stainless steel interfaces

Parallel tests were undertaken with rough and polished stainless steel interfaces with R_{CLA} values around 12 μm and 0.5 μm respectively. The machined smooth surfaces became marginally rougher after multiple tests, with R_{CLA} increasing to 1 μm. The tests discussed here applied the 'short-term' consolidation period of 0.5 days, without experiencing prolonged ageing.

Figure 4-37 summarises the friction angle trends for Dunkirk sand shearing against rough stainless steel interfaces at three stress levels. Also plotted is the response seen in two re-shearing tests. The peak and residual interface friction angles showed clear stress dependency and stable residual states were achieved in most cases. The stainless steel interface tests seem to exhibit more stable post-peak softening responses, compared with those seen in mild steel interface tests. This is further supported by the re-shearing responses which matched well with those from first time shearing.

Considering the tests with polished interfaces, Figure 4-38 summarises the friction angle trends under three stress levels. The results diverge from those expected in small displacement direct shear interface tests as the smooth interfaces give angles that are comparable to, or even higher than, those shearing against rough interfaces. As shown by Ho *et al.* (2011), pre-shearing to large displacements (5 m) affects the subsequent slow shear responses markedly. A further comparison is shown in Figure 4-39 where the smooth and rough interface coincide at σ_v = 100 kPa, but under higher stresses, the smooth interfaces' δ values show a surprising trend of exceeding those of the rough interfaces by 2-3˚. The difference between peak and residual friction angles is generally more pronounced in the rough interface tests than the equivalent smooth interface tests.

The tests at σ_v = 200 kPa on smooth interfaces were repeated by three researchers using two apparatuses, and the attained residual angles all fell within a narrow range of 27.9˚ to 28.2˚, providing confidence that the "anomalous" smooth interface tests do not

reflect experimental scatter or errors. A recent database study of Bishop ring shear tests reported by Quinteros *et al.* (2017) also indicated a weak dependency of the residual friction angles on the interface roughnesses in tests on offshore North Sea silica sands that present low fines fractions.

Comparison of the dilation trends in the rough and smooth interface tests are presented in Figures 4-40 and 4-41, respectively. Despite the effects of material loss, it can be observed the smooth interface tests slowly developed dilation as shearing evolved and dilation peaks were reached after about 60 mm shearing, whereas with rough interfaces, peak dilation occurred in the early stage of shearing. Nevertheless, the peak dilations reached with the rough and smooth interfaces were essentially comparable, despite the considerable differences in their initial roughness (12 μm and 0.5 μm).

Contrary to the common expectation that soil dilation will reduce at the interface as the normal stress level increases (as in Figure 4-36), the above two figures demonstrate that in the tests with rough and smooth stainless steel interfaces, greater vertical dilation was generated in the tests under higher normal stress (400 kPa). A tentative explanation for the non-intuitive dilation and friction angle trends is offered below.

Discussion on the "non-intuitive" ring shear tests with stainless steel interface

When attempting to compare and integrate ring shear and conventional direct shear (see Section 4.5.3) interface testing data, it is important to acknowledge the consequences of the fast pre-shearing stage and the inherent differences of these two types of interface tests. These two aspects appear to justify the above "anomalous" test results with stainless steel interfaces, as discussed below.

In the course of long run (5 m) fast pre-shearing stage imposed in ring shear tests, both the soil and interface are heavily mutated. Initially rough interfaces experience roughness reduction with the surface material being abraded and mixed into the soil, whereas slight roughness increases may occur to smooth interfaces as they are scratched by hard grains. On the other hand, the soils experience volume change, grain crushing and possibly cementation, the extent of which depends critically on stress level, soil property, interface type and roughness. Although less prominent with stainless steel interfaces, post shearing cementation appeared to be common with saturated mild steel interfaces as localised basal shear zones developed that appeared to

be more adhesive silty soils when retrieved in post-test dismantling. Grain crushing and cementation is expected to grow as the normal stress increases, resulting in lower vertical dilation in the subsequent slow shearing, as seen in Figure 4-36.

In the tests with stainless steel interfaces, volume change and grain crushing may dominate during the fast pre-shearing stage. Although the confining moulds were pushed against the interface under high normal load, material loss through the gap in between could not be eliminated and had to be accounted as part of specimen volume change. Figure 4-42 plots fast shearing vertical displacement trends of the tests with stainless steel interfaces. Also indicated are the increases in overall friction ($\Delta f = f_{end} - f_{start}$) acting on the soil specimen, which was simply taken as the decrease of the normal ring load in the beginning and end of fast shearing. The positive sign of the friction indicates the specimen's tendency of deforming downwards (contraction).

Figure 4-42 demonstrates that, after taking into account soil loss and grain crushing, all the tests experienced nominal contraction (densification) during fast-shearing. The amount of densification increased with normal stress level, resulting in denser specimens in the high stress tests, which may explain the relatively high dilation trends observed in the high stress tests seen in Figures 4-40 and 4-41. Compared with the smooth stainless steel interfaces, the tests with rough interfaces exhibited dilation at the beginning of fast shearing, which, however, trended towards global contraction due to the initiation of grain crushing close to the rough interface. Crushing-induced specimen densification also manifested as the larger increments of friction noted in the tests with rough interfaces at equivalent normal stress levels.

The second aspect concerns the inherent differences of these two types of interface tests particularly in terms of confining boundary conditions and the formation of localised sheared zone. In direct shear interface tests, the relative shearing motion between the soil and interface is constrained by the rigid end walls. Highly localised soil zones are formed adjacent to the interface regardless of its surface roughness (see PIV observations reported by DeJong & Westgate (2009)). However, the annular ring shear specimens are confined only in the radial direction, and relative soil-soil and soil-interface shear motion are not restricted in the shearing (circumferential) direction. The formation of localised shear zones may be encouraged by rough interfaces when grain crushing and roughness reduction is often significant. However, as often observed in post-test dismantling, only minor grain crushing was noted in the tests with

smooth interfaces and local sheared zone was often not well developed. As the torsional "twisting" shear motion is not restricted in the ring shear test arrangement, significant soil-soil inter-particle shearing is expected in the interface tests with smooth interfaces, leading to the delayed dilation trends noted in Figure 4-41 and the higher "interface" friction angles noted in Figure 4-39.

Although beyond the scope of the current study, it is believed that the different mechanisms of direct shear and ring shear interface shearing behaviour in conjunction with grain crushing and interface mutation phenomena require further investigation from the perspective of particulate soil mechanics through discrete element modelling (DEM) approaches, which may provide further insights into the "non-intuitive" interface shearing behaviour discussed above.

Blessington sand interface shearing

Referring to Table 4-5, the Blessington sand study was focused on mild steel interfaces with surface roughness in the range of 8-13 μm. Figure 4-43 summarises the interface shearing angle trends of the specimens tested after 0.5 day ageing periods. Also indicated is the soil-soil shearing angle at critical state determined from triaxial testing. Stable residual shearing angles were reached in all cases. Despite differences in the initial surface roughness (8.0 μm and 12.7 μm) of the interfaces used in the two σ_v = 200 kPa tests, their friction angles converged closely.

Striking stress-dependency was seen again, with at least 8˚ higher residual friction angle noted under 400 kPa than under 100 kPa normal stress. The vertical dilation displacement lay in the 0.005-0.018 mm range for all tests, significantly below those seen with the comparable tests on Dunkirk sand. Blessington sand's surprisingly high interface friction angles did not correlate with any exceptional dilation trends. Other factors, such as grain size, fines content, and mineralogical composition may be significant, as discussed further in Sections 4.5.4 and 4.5.5.

Larvik sand interface shearing

Referring to Table 4-6, ring shear tests were performed on Larvik sand with smooth and rough interfaces. The three non-aged tests are discussed here and the results are summarised in Figure 4-44.

Considering first the rough mild steel results, the two tests confirmed the expected

ultimate range (27.8 to 30˚) and the positive stress level dependency seen with Dunkirk and Blessington sands. However, in this case, the smooth interface gave a markedly lower δ'. The vertical dilation in the rough interface (with R_{CLA} = 12.9 μm) tests was 0.02-0.03 mm, which is close to the $2R_{CLA}$ prediction but below that seen with Dunkirk sand.

The smooth interface test σ_v = 200 kPa showed its mobilised friction angle increasing gradually and reaching 25˚ after around 100 mm of shearing displacement. The vertical dilation recorded (0.005 mm) was significantly lower than seen with the rough interfaces. Sliding appeared to dominate in the localised shear zone adjacent to the interface. Referring to the index properties summarised in Table 4-9, the Larvik sand has relatively small grain sizes and a higher fines content, generally leading to a less dilative response.

4.5.3 Small-displacement sand-steel interface shearing behaviour

A set of non-aged (0.1 day) and aged direct shear type interface shear tests was performed on Batch 2 Dunkirk sand with rough and smooth steel interfaces to supplement the above ring shear testing programme. The outcome is also integrated with previously reported results by Chow (1997).

Figure 4-45 summarises the friction angle trends from direct shear tests against mild steel interfaces with surface roughness in the 12-14 μm range. Peak friction angles were developed within 1 to 2 mm and stable residual angles are reached in most cases after several millimetres of shear displacement. The two tests with identical initial density, but with normal stresses of 200 kPa and 400 kPa, presented slightly higher angles at the lower stress level, but the traces tended to converge towards similar values. The post-test grading tests and roughness measurements showed that the lack of any fast pre-shearing stage led to minimal changes in sand grading and interface roughness.

As reported previously, interface shearing is affected significantly by surface roughness, as shown in Figure 4-46. In the two cases with smooth interfaces, no peak friction angle was observed and the ultimate friction angles reached values around 25˚, clearly lower than those found with rougher interfaces. It is also interesting to note that the residual angle from the rough stainless steel interface test was clearly lower than

that of using mild steel interface, despite the fact that the two tests had similar sand densities and roughnesses.

The above factors also impact the dilation trends during shearing, as plotted together in Figure 4-47. The tests with smooth interfaces clearly developed much less dilation compared to those of rougher interfaces. The dilation trends seemed to fit reasonably well with the $2R_{CLA}$ prediction for both the rough and smooth interfaces, with one exception being the denser case, which generated significantly higher dilation.

4.5.4 Effects of soil properties and interface surface roughness

The results presented above indicate a significant dependency of interface shearing behaviour on interface surface roughness as well as the sands' physical and chemical properties. The discussions below focus on ultimate interface shearing angle (δ'_{cv}) from the non-aged ring shear and direct shear tests.

Trends of friction angle against normalised roughness

Figure 4-48 presents $\tan\delta_{cv}'$ against the pre-test normalised surface roughness (R_{CLA}/D_{50}) from all the non-aged tests. Data reported by Chow (1997) on direct shear interface tests are also included. The attained data are plotted against the $\tan\delta'_{cv}$-R_{CLA}/D_{50} trend reported by Jardine *et al.* (1992) established from dry sand direct shear interface tests on mild steel interfaces with roughness around 10 μm, conducted principally under a single normal stress of 100 kPa.

The results indicate a relatively wide pre-test R_{CLA}/D_{50} range. The trend for $\tan\delta'_{cv}$-R_{CLA}/D_{50} from the tests performed with normal stresses below 400 kPa fits well with the published trend. However, larger deviations are noted for the tests performed under higher normal stresses, particularly in the case of Blessington sand. It should be noted that the upper plateau of the Jardine *et al.* (1992) trend corresponded to constant-volume friction angle of sand-sand shearing (ϕ'_{cs}), which is around 32.1˚ for Dunkirk sand and 35.2˚ for Blessington and Larvik sands.

In the tests with smooth interfaces, a good match was observed between the established trend and the results obtained from the direct shear interface tests conducted on Dunkirk sand at two stress levels. However, in the ring shear tests, a

good match was only found at the σ_v = 100 kPa stress level and the δ'_{cv} values clearly increased with rising stress level and approached the upper plateau of ϕ'_{cs} = 32.1˚.

Effects of soil grading and other properties

Figure 4-49 summarises the materials' "young" (non-aged) interface friction angles against rough steel interfaces at various stress levels. Also plotted are the trend lines reported from direct shear (Jardine *et al.*, 1992) and ring shear (Ho *et al.*, 2011) interface testing. The fixed value of δ'_{cv} = 29˚ recommended by CUR (2001) for use with steel piles and sands is also included for comparison. The reported correlations generally indicate that interface friction angle decreases as sandy soils become coarser.

The results on the three materials fit reasonably into the reported trends, while the deviations seen may reflect individual effects of varying material properties, stress level, interface type, roughness and test conditions. As seen in Figure 4-49, in most cases, the attained friction angles are located above Ho *et al.* (2011)'s 8 m shear displacement trend, which was established with dry silica dominated soils against medium rough ($R_{CLA} \approx$ 4.3 μm) stainless steel interfaces under a normal stress of 800 kPa, as denoted in Figure 4-10. Exceptional cases were noted with the low stress level (σ_v = 100 kPa) Blessington sand test (BLMS100R) and the two tests on Dunkirk sand with rough stainless steel interfaces (DKSS100R and DKSS200R).

In the tests with high normal stresses, the ring shear interface friction angles exceeded the direct shear trend reported by Jardine *et al.* (1992), reflecting the combined effects of normal stress and the applied large displacement pre-shearing in the ring shear tests. The effects of stress level are further discussed in the following section.

As summarised in Table 4-10, the natural Blessington, Dunkirk and Larvik sands studied here possess physical (grading, fines content) and chemical (pH, carbonate content, etc.) properties representing their natural origins, which differ significantly from the washed-clean silica dominated soils investigated by Ho *et al.* (2011). Meanwhile, the mild steel interfaces used in the Author's study were air-abraded to reach initial roughness (R_{CLA}) in the range of 8-15 μm, which were significantly rougher than the stainless steel interfaces used by Ho *et al.* (2011). The mild steel interfaces were also expected to experience physio-chemical reactions under water saturated condition, with some steel corrosion taking place even in short term tests. As

often noted in post-test sub-sampling process, cementation and plastic corrosion products were found both at the interface and within the soil mass, potentially resulting in interface shearing responses that were distinct from those developed under dry testing condition and with stainless steel interfaces.

The Blessington sand provides a special case which exhibited higher friction angles (both δ'_{peak} and δ'_{cv}) than the Dunkirk and Larvik sands under equivalent stress levels and interface roughness. The Blessington sand has an intermediate D_{50} and its fines content is close to that of Larvik sand (see Table 4-9). As discussed in Section 4.5.2, Blessington sand showed remarkable stress-dependency, whereas the amount of dilation it generated on interface shear was significantly lower than expected for silica sands.

These features are believed to be associated with the material's distinct physical and chemical properties and its inclusion of both highly angular quartz and high carbonate content limestone grains, both of which might be expected to result in relatively low grain strength, increased compressibility and susceptibility to particle breakage, as discussed in Section 4.4.2. This feature facilitated the formation of a localised sheared zone compacted of crushed grains with reduced sizes, resulting to lower dilation upon shearing, but higher friction angles which potentially increased further with stress level. More importantly, the presence of carbonate radicals may enhance soil cementation in the context of soil-water-steel physiochemical interactions, leading to the more distinct time-dependency of its interface shearing characteristics, as discussed later.

4.5.5 Stress-dependency of interface shearing behaviour

Significant stress-dependency has been identified in the ring shear tests. Figures 4-50 and 4-51 present the interface friction angles of Dunkirk sand against normal stress level, while Figure 4-52 presents the results for Blessington and Larvik sands. All indicate an overall trend for increasing friction angles with stress level, which was less prominent in earlier studies of interface shearing.

As previously mentioned, the tests with mild steel interfaces and Blessington sand exhibited the most significant stress-dependency. An increase of 5.7° was noted in δ'_{cv} as normal stress increased from 200 kPa to 400 kPa, whereas the increase were 1.7°

and 1.4˚ respectively for Dunkirk sand and Larvik sand under the equivalent stress range. For Dunkirk sand, the ultimate friction angle δ'_{cv} increased from 27.5˚ to 32.5˚ as normal stress increased from 200 kPa up to 1200 kPa. Similarly increasing trends were noted in the tests with stainless steel interfaces, as in Figure 4-50, and perhaps surprisingly the increments were greater than those seen with mild steel interfaces.

The remarkable stress-dependency of friction angles reflects the significant changes made to the interfaces and mutation of the sand during the pre-shearing stages. Earlier studies by Yang *et al.* (2010) and Ho *et al.* (2011) on silica sands with stainless steel interfaces reported much less pronounced stress dependency, partly because the interface roughnesses (R_{CLA} between 3 to 4 μm) were significantly lower than of those used in the current study. In interface shearing, higher surface roughnesses were often associated with greater reductions in particle size (ΔD_{50}) due to grain crushing and interface roughness (ΔR_{CLA}) due to abrasion of surface asperities. These mutations of the steel interface and soil, together with the potential development of soil cementation, are clearly dependent on stress level, and the overall effects may manifest as the stress-dependency of friction angles seen here, recalling the trend of δ'_{cv} dependency of normalised roughness (R_{CLA}/D_{50}) shown in Figure 4-48.

Changes to interface roughness or soil grading are generally much less significant in direct shear type interface tests conducted without pre-shearing, and the dependency of ultimate friction angles on stress level is less pronounced, as seen in Figure 4-45.

Correlation between stress level and change of interface roughness

The reductions related to pre-shearing of interface roughness, normalised by soil initial mean particle size ($\Delta R_{CLA}/D_{50}$), are summarised in Figure 4-53. The experimental points found for each soil are fitted with a linear trend line. Dunkirk sand interface tests showed only marginal decrease of surface roughness (ΔR_{CLA}<0.5 μm) at relatively low stresses (100 kPa and 200 kPa), but the reduction increased significantly with increasing normal stress. A maximum reduction of 9.38 μm was noted in the σ_v = 1200 kPa test.

The Blessington sand represents a special case where significant reductions of interface roughness were manifested at all the stress levels considered, reflecting a conjunct outcome of surface abrasion from the highly angular quartz and potential steel softening induced by corrosion. Figure 4-53 also includes the data points from the

ageing tests, as discussed below.

4.5.6 Interface shear response during re-shearing

Referring to Tables 4-4 to 4-7, a re-shearing stage was imposed to part of the specimens that had experienced a "standard" or prolonged consolidation period and a slow shearing stage. In most cases, these specimens were left for a further 0.5 day before the re-shearing was initiated.

The re-shearing responses of the tests with stainless steel interfaces are included in Figure 4-37 (initially rough interface) and Figure 4-38 (initially smooth interface). In the tests with initially rough interfaces, the responses of the initial shearing and re-shearing virtually overlapped each other, although the vertical dilations occurred in the re-shearing were slightly less. Greater differences emerged in the tests with initially smooth interfaces where the re-shearing stage exhibited consistently lower shearing resistance, particularly in the tests under higher normal stress (σ_v = 400 kPa). Vertical dilations seen in the re-shearing stage were distinctly less than those in the initial shearing.

Re-shearing tests were also performed on previously aged and sheared specimens. Taking the test DKMS600R-aged from Table 4-4 as an example, as plotted in Figure 4-54, it seems that any ageing gain or "memory" was eliminated during the re-shearing, and the specimen responded as a "fresh" specimen, exhibiting shearing responses that were very close to the non-aged specimen under identical conditions. Similar re-shearing responses were also found in the Blessington and Larvik tests. Important features of the aged sand specimens during first-time shearing are discussed below.

4.5.7 Time-dependency of interface shearing behaviour

As summarised in Tables 4-4 to 4-7, some ring shear specimens were left to age for 26-30 days under constant normal stresses, and one set of Dunkirk sand direct shear specimens was aged for up to 180 days under σ_v = 200 kPa. The interface shearing responses of these aged specimens are integrated with those of subjected to "standard" consolidation period, and the mechanisms of ageing effects are discussed based on the experimental evidences.

Ageing effects on large displacement interface shearing of Dunkirk sand

Starting with ring shear interface tests, Figure 4-55 summarises the trends of interface friction angle against shearing distance for the "young" non-aged and aged Dunkirk specimens. The peak friction angles and those mobilised after 20 mm shear displacement are further plotted against ageing time, as shown in Figure 4-56.

Adding to the stress-dependency behaviour discussed above, the results in Figure 4-55 show clear increases in interface friction angles with ageing time under the four stress levels considered. The ageing gain was most pronounced over the initial few millimetres of shear displacement where friction angles reached their peaks. Compared to those of non-aged specimens, the shearing response of the aged specimens were less stable and showed greater variations with shear displacement. The ageing benefits appeared to be displacement-dependent and generally decreased if shearing continued to relatively large displacements. It is interesting to also note that, as indicated in Figure 4-56, gains of shear resistance through ageing seen at relatively larger displacement ($\delta'_{20\ mm}$) appeared to be only marginally dependent of stress level, as similar amounts of increase (around 1 to 1.4˚) in $\delta'_{20\ mm}$ were noted under all the tested normal stresses.

The enhanced interface shear resistances of the aged specimens were found to be accompanied by a growth of 0.02-0.03 mm in the vertical dilation.

Much less significant ageing effects, however, were noted in the tests with smooth stainless steel interface. As shown in Figure 4-57 results from the aged (30 days) and re-sheared test, despite a small increase (0.7˚) in the δ'_{peak}, hardly any increase of δ'_{cv} can be observed, and the post-peak shearing responses (as shown in Figure 4-38) of the non-aged and aged tests were essentially overlapping, together with the similar dilations (0.03 mm) observed in both tests. Similar ring shear ageing test results were found in stainless steel interface tests performed by Yang *et al.* (2010), who reported essentially identical ultimate friction angles for a 20-day aged dry NE34 sand specimen under 800 kPa normal stress and a non-aged test. Similarly, Carroll *et al.* (2017) reported insignificant capacity gain with time with their stainless and galvanised steel 'micro-piles' driven at all the same three test sites (Dunkirk, Blessington and Larvik), contrasting significantly with those of rough mild steel piles. The laboratory and field studies both indicate that ageing gains are dependent on the interface material.

Ageing effects on small displacement interface shearing of Dunkirk sand

Moving to direct shear ageing tests, Figure 4-58 highlighted detailed post-test visual inspections of the specimen (sub-divided into five layers along the 20 mm specimen height) and mild steel interface after dismantling the 26-day and 180-day ageing tests. The mild steel interfaces became coated with a rusted layer of dark green (when fresh and damp after testing) or deep brown (after oven drying) corrosion product, indicating the occurrence of redox reactions over long-term ageing. The processes of forming the iron oxides or hydroxides were most active at the steel surface but also extended into the sand mass, as seen from the consistent trend of increasing darkness of the sub-sampled soils with reducing distance from the steel interface.

Figure 4-59 plots the trends of interface friction angle and vertical dilation of the three specimens aged for different periods (0.1 day, 26 days and 180 days). Significant differences were noted with both the peak and residual friction angles that consistently increased with ageing time. The aged specimens also manifested clear post-peak softening and stable trends for ultimate friction angles after large shear displacements. The 180-day aged Dunkirk sand specimen showed surprisingly high friction angles ($\delta'_{peak} = 50^{\circ}$, $\delta'_{res} = 45^{\circ}$).

Results from ageing direct shear tests reported by Chow (1997) on Dunkirk sand Batch 1 are replotted in Figure 4-60. The specimens were subjected to 300 kPa normal stress and left for ageing for varied periods (0 day, 7 days, 15 days and 63 days). The interfaces used were made of stainless steel air-abraded to $R_{CLA} = 9.8$ μm. The results indicate slightly higher friction angles in the test with longer ageing period. However, the overall differences were not significant and the shear responses trended towards a narrow band. The results conform to earlier observations in the stainless steel ring shear tests that exhibited very little gain of ultimate friction angle with time.

The above two direct shear datasets are integrated as shown in Figure 4-61, highlighting again the interface material dependency of how ageing affects interface shearing behaviour.

Increasing vertical dilation was observed in the ageing tests employing both the mild steel and stainless steel interfaces, as shown in Figures 4-59 and 4-60. Vertical dilation increased remarkably after prolonged ageing periods in the tests with mild steel interfaces. However, relatively less significant increases were noted in Chow's

(1997) ageing tests with stainless steel interfaces and the ageing dilation gains appeared to have reached an upper limit after 15 days; continuing ageing to 63 days showed only marginal further dilation increase.

Ageing effects on interface shearing of Blessington and Larvik sand

Figures 4-62 and 4-63 summarise the friction angles trends for the non-aged and aged Blessington and Larvik sands under 200 kPa and 400 kPa normal stress. The friction angle trends against ageing time are plotted in Figure 4-64, with only the 20 mm displacement angles ($\delta'_{20\text{ mm}}$) are presented for clarity.

Blessington sand showed remarkable ageing effects, particularly over the initial 40 mm of shearing. Less stable shearing responses were observed with the aged specimens, and the ageing gains tended to reduce or even turn negative as interface shearing continued to very large displacements. As shown in Figure 4-63, Larvik sand presented the least "age-enhanced" shear resistances among the three materials studied, with only marginal increase of friction angles (0.5-1˚) over the initial 20 mm displacement.

It appears that the magnitude of ageing induced shear resistance enhancement correlates well with increments in dilation. Blessington specimens showed the most significant dilation increases, from the non-aged specimens' range of 0.0075-0.0175 mm up to 0.04-0.09 mm of the one month aged specimens. The non-aged and aged Larvik specimens, however, showed closely comparable dilation (in the range of 0.03-0.04 mm).

Discussion of ageing mechanisms in interface shearing

The mechanisms and influential factors applying to time-dependent interface shearing behaviour are summarised and discussed as follows.

- Long-term densification appears to contribute to the ageing effects. As discussed in 4.4.3, compression of grain aggregates is time-dependent. Sand creep and densification is expected to continue even under moderate compression stresses, particularly in the cases of less uniformly graded soils. The densification leads on its own to the enhanced dilation trends noted in Chow's (1997) direct shear tests with stainless steel interfaces.
- The significant changes to the colours and by inference chemical compositions of

the sand and interfaces after long-term ageing shown in Figure 4-58, give evidence of physiochemical reactions in the soil-water-steel system, which leads to soil cementation and steel interface corrosion and softening. The latter is supported by the roughness changes shown in Figure 4-53, with greater interface roughness reductions after one month ageing than after short-term consolidation.

- Ageing-induced soil cementation or "bonding" may explain the "unstable" and displacement-dependent shearing responses noted in Figures 4-55 and 4-62. It is speculated that the enhanced cementation at the soil-steel interface, or within the soil mass, may be damaged as soil dilates, leading to the less stable and decreasing friction angle trends.

The development of cementation or the intensity of physiochemical reaction depends on the soils' physical properties and the chemical composition of the soil, ground water and interface. In earlier discussions, the remarkable stress-dependency interface shearing behaviour of Blessington sand was attributed to its high angularity grains and their carbonate content. These factors can also be applied to explain its significant time-dependent interface shearing behaviour. The Larvik sand, as described in Section 4.5.1, contains markedly high sulphate composition but least low carbonate content, along with highly acidic pH that may alter the formation of steel corrosion products and other physiochemical process. Meanwhile, as seen in Table 4-9, among the three materials studied, Larvik sand has the smallest particle sizes and highest fines contents, which, along with its low CPT q_c values, renders its far less susceptibility to grain breakage than the Dunkirk and Blessington sands.

It was also noted that ageing effects were more prominent in the direct shear type interface tests than in the ring shear interface tests, as seen in Figure 4-55 and Figure 4-59. This might be linked with the greater grain crushing, soil densification and interface abrasion developed during the fast shearing stage applied in the ring shear tests. In that sense, ageing effects are also dependent of testing apparatus and procedures. In addition, the laboratory shear tests had almost free access to air. It is worth noting that this condition does not apply beneath the water table, or indeed below the ocean floor.

Finally, since the many aspects of ageing mechanism are inherently linked with normal stress, it is envisaged that the ageing effects are also stress-dependent. However, it is difficult to establish clear trends from the available data. More research is required

to further explore this aspect.

Findings from the above sand-steel interface tests support the hypotheses made by Chow *et al.* (1998) on the gain of driven pile axial capacity over time. The ring shear tests with rough mild steel interfaces revealed an average increment of 3.1˚, 1.1˚ and 0.6˚ in δ'_{20mm} respectively in the one-month aged Blessington, Dunkirk and Larvik sand specimens. Interestingly, the sands' trend of increasing interface shear resistance conforms to the observations of field pile tests at the three sites by Karlsrud *et al.* (2014) and Gavin *et al.* (2015), who reported that steel piles tested at the Blessington site exhibited more pronounced increases of axial capacity than that were seen at Larvik. Normalised by 10-day capacity Q_0, the 20-month aged axial capacity Q of piles at Blessington, Dunkirk and Larvik were 2.5, 2.1 and 1.7, respectively.

The conditions of soils, groundwater or stresses are likely to be more variable under field conditions than in the Author's laboratory tests. Nevertheless, the laboratory study presented highlights the importance of an integrated consideration of the soils' and piles' physical, chemical and mineralogical properties. Case-specific ring shear interface tests incorporating "conditioning" and ageing stages remain the most useful way to assess soils' stress-dependent and time-dependent interface shearing behaviour, and aid in the interpretation and prediction of driven piles' axial capacity.

4.5.8 Figures

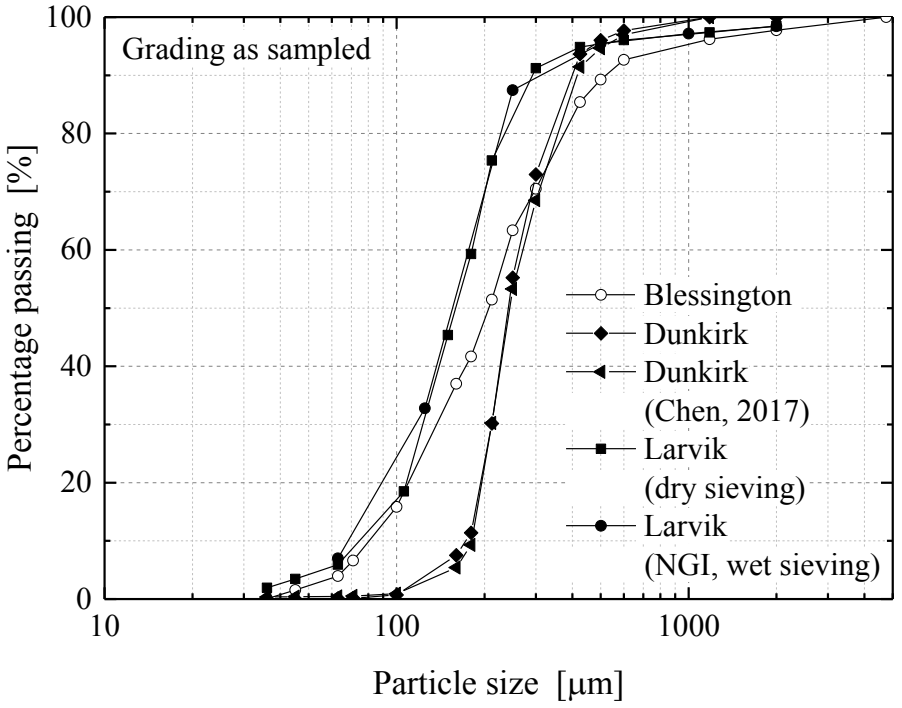

Figure 4-33 Particle size distribution of the materials studied at their in-situ states

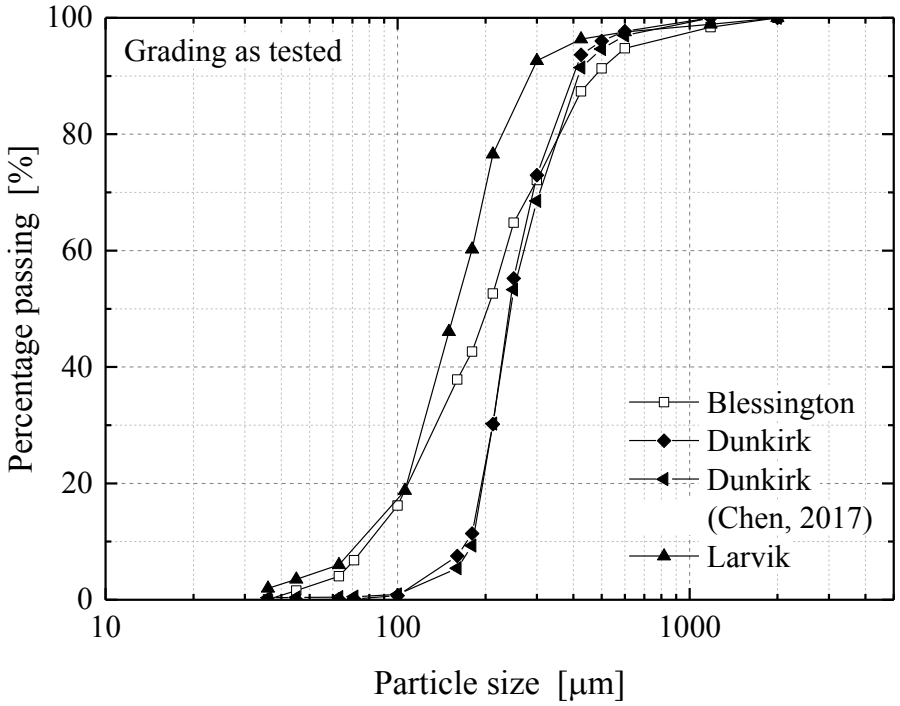

Figure 4-34 Particle size distribution of the materials studied at their testing states

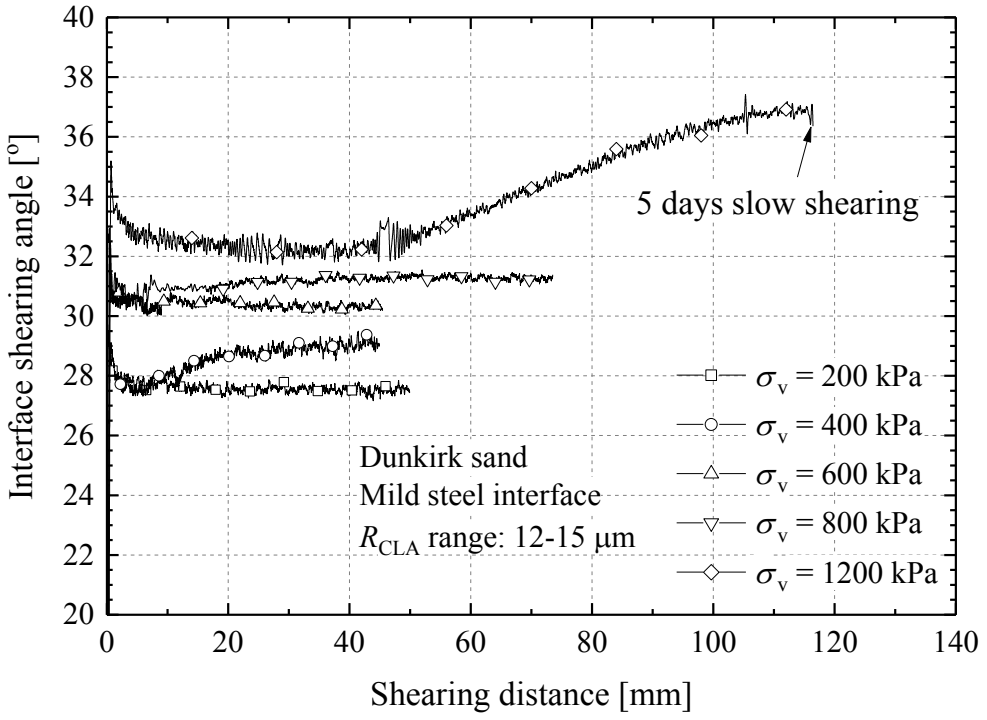

Figure 4-35 Interface friction angle evolution of Dunkirk sand Batch 2 shearing against rough mild steel interfaces at different vertical stress levels

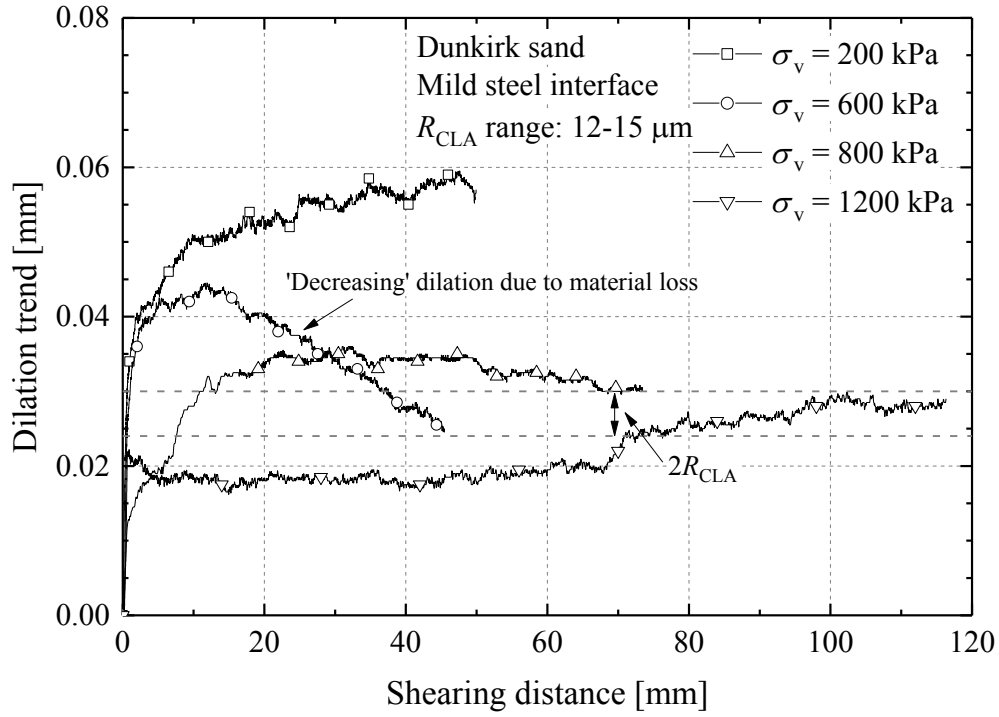

Figure 4-36 Dilation trend of Dunkirk sand Batch 2 shearing against rough mild steel interfaces (Dilation data of the σ_v = 400 kPa test discarded due to severe material loss)

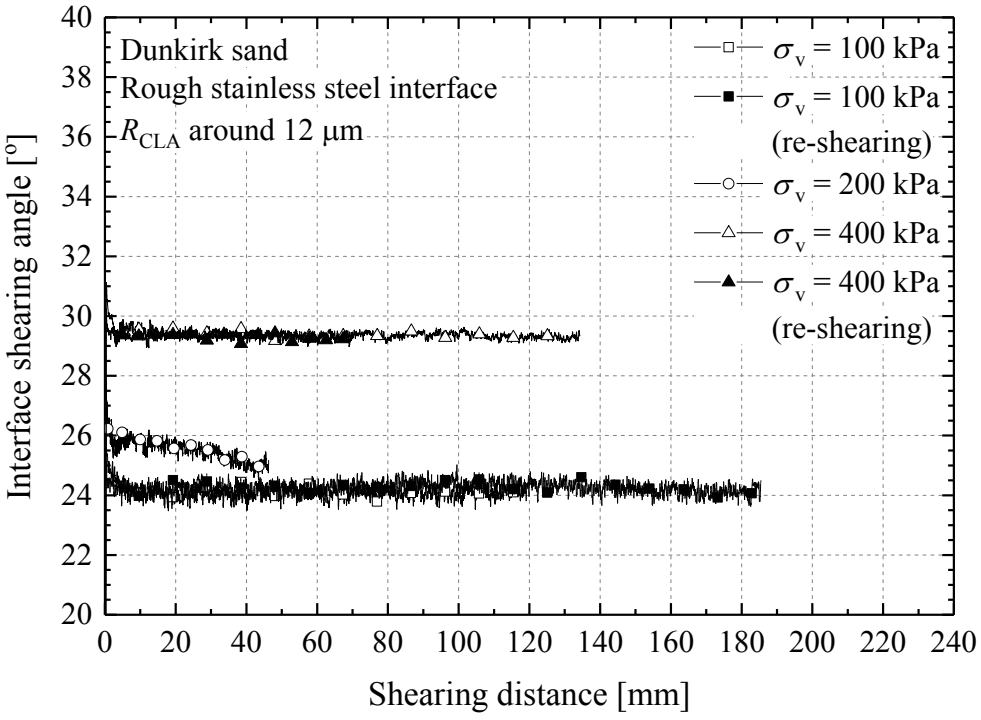

Figure 4-37 Interface friction angle evolution of Dunkirk sand Batch 2 against rough stainless steel interfaces

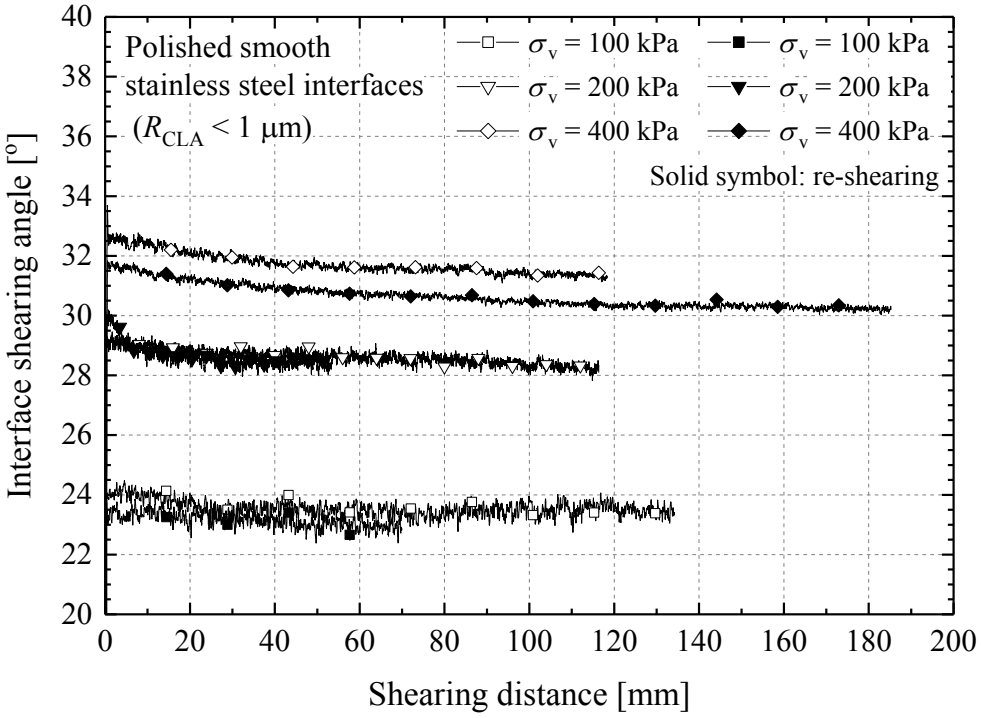

Figure 4-38 Interface friction angle evolution of Dunkirk sand Batch 2 against polished stainless steel interfaces

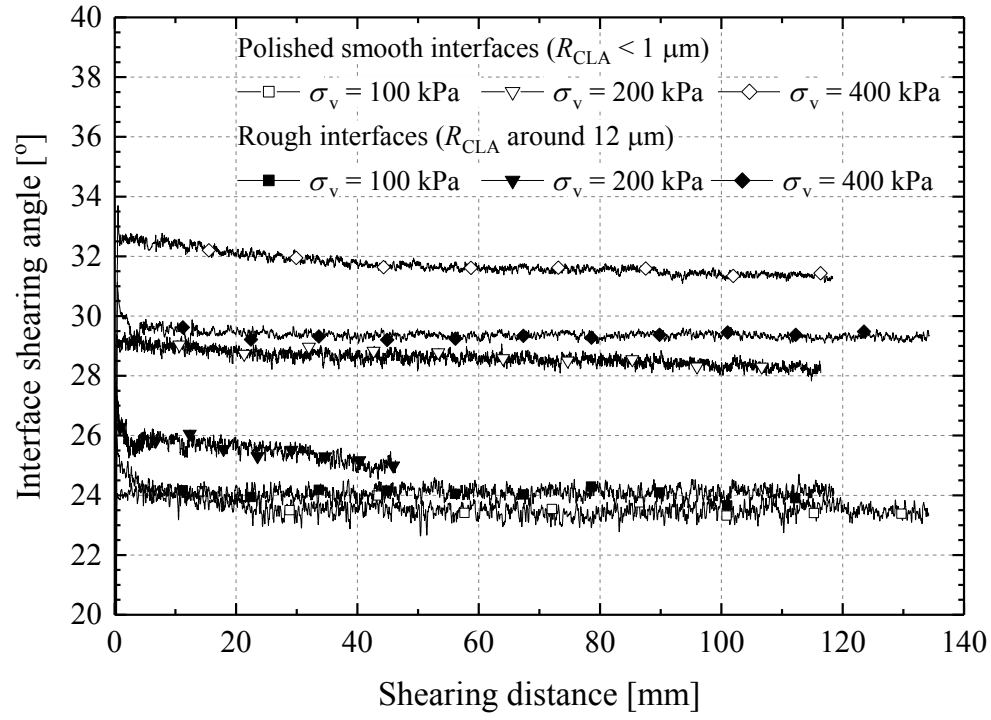

Figure 4-39 Comparison of interface friction responses of Dunkirk sand Batch 2 shearing against rough and polished smooth stainless steel interfaces

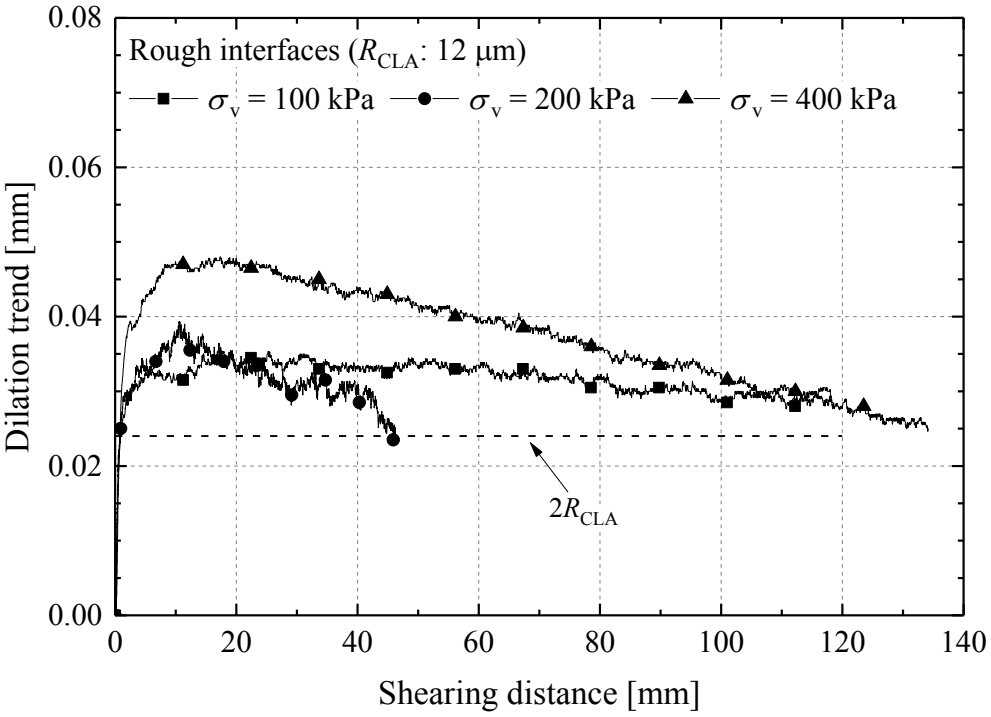

Figure 4-40 Dilation trends of Dunkirk sand Batch 2 shearing against rough stainless steel interface at three vertical stress levels

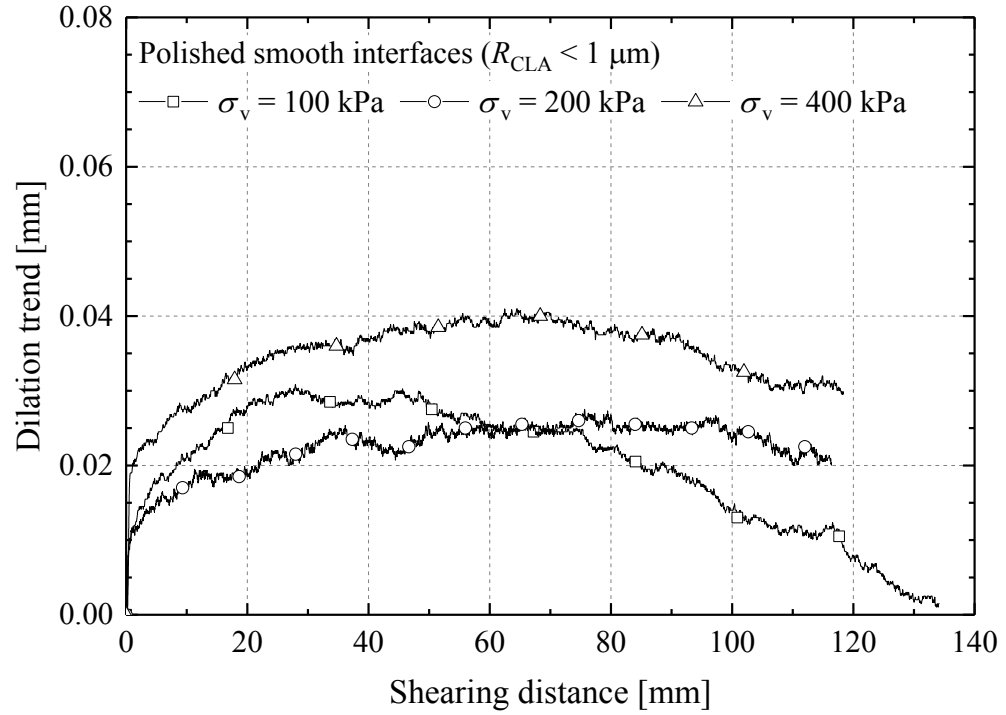

Figure 4-41 Dilation trends of Dunkirk sand Batch 2 shearing against smooth stainless steel interface at three vertical stress levels

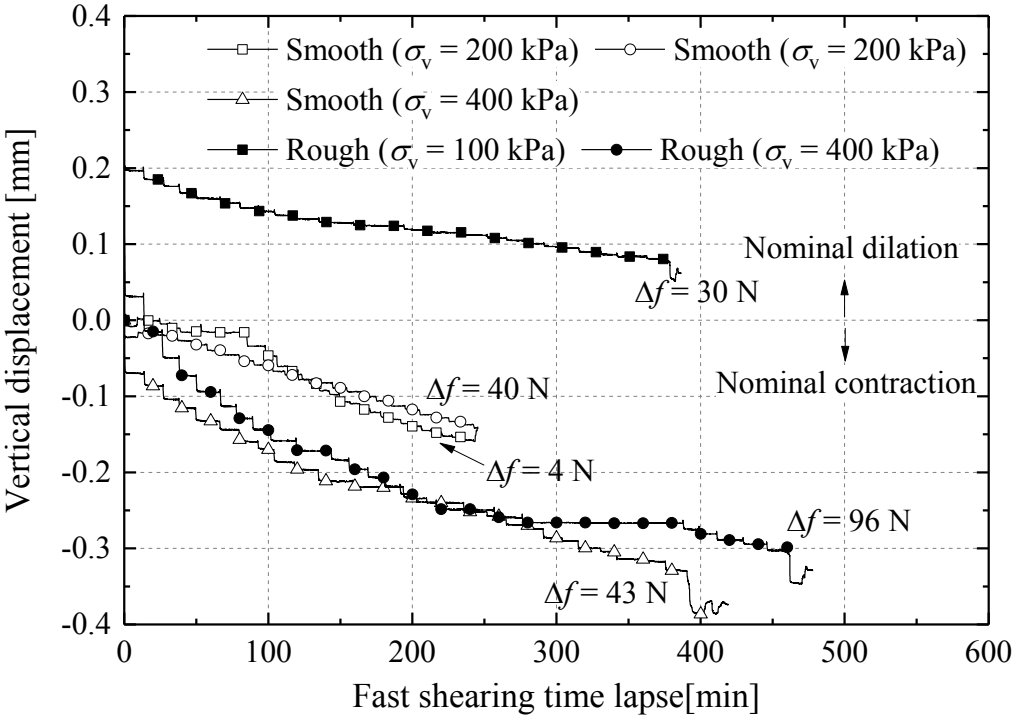

Figure 4-42 Fast-shearing vertical displacement trends on Dunkirk sand with stainless steel interfaces (Δf denoting changes of friction acting on the specimen, defined as f_{end}-f_{start}) (for clarity, only the tests performed with the same apparatus are included)

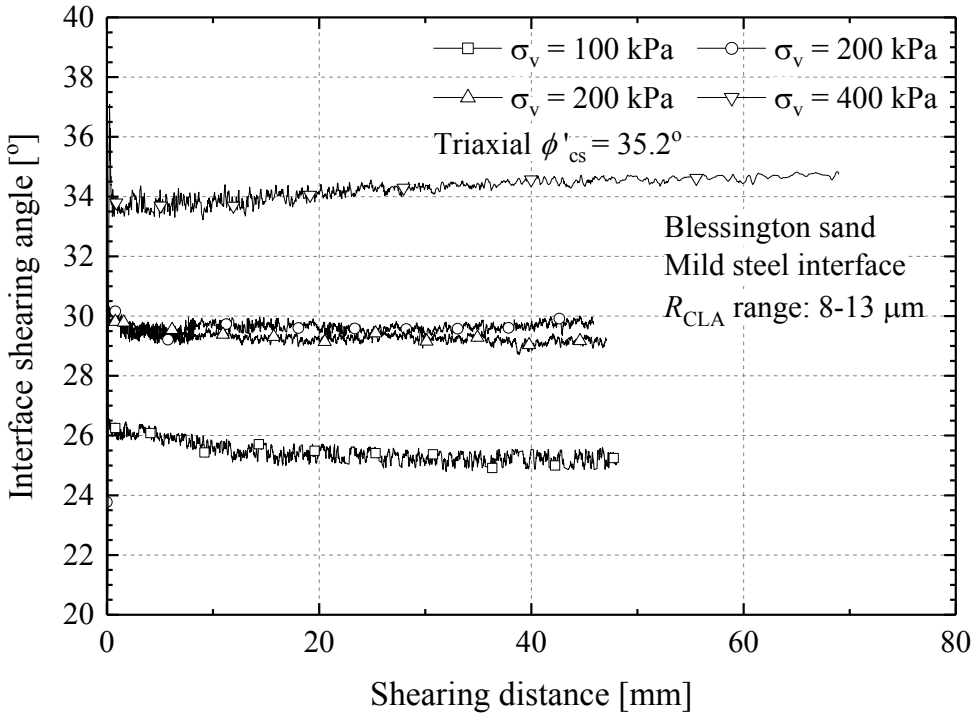

Figure 4-43 Interface friction angle evolution of Blessington sand shearing against rough mild steel interfaces at three vertical stress levels

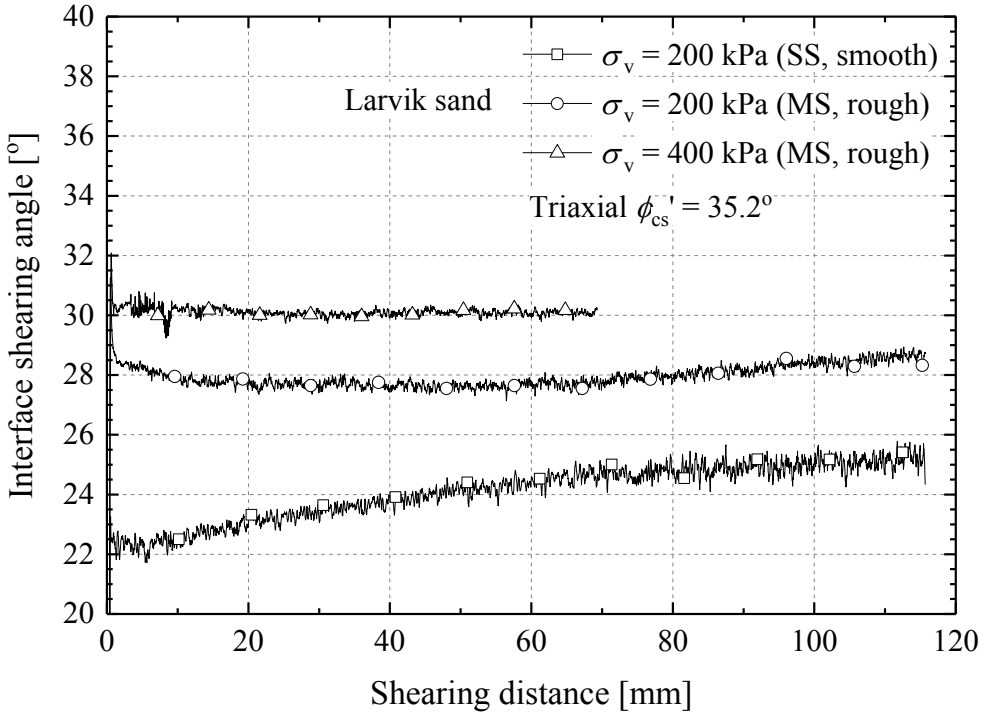

Figure 4-44 Interface friction angle evolution of non-aged Larvik sand shearing against rough and smooth steel interfaces

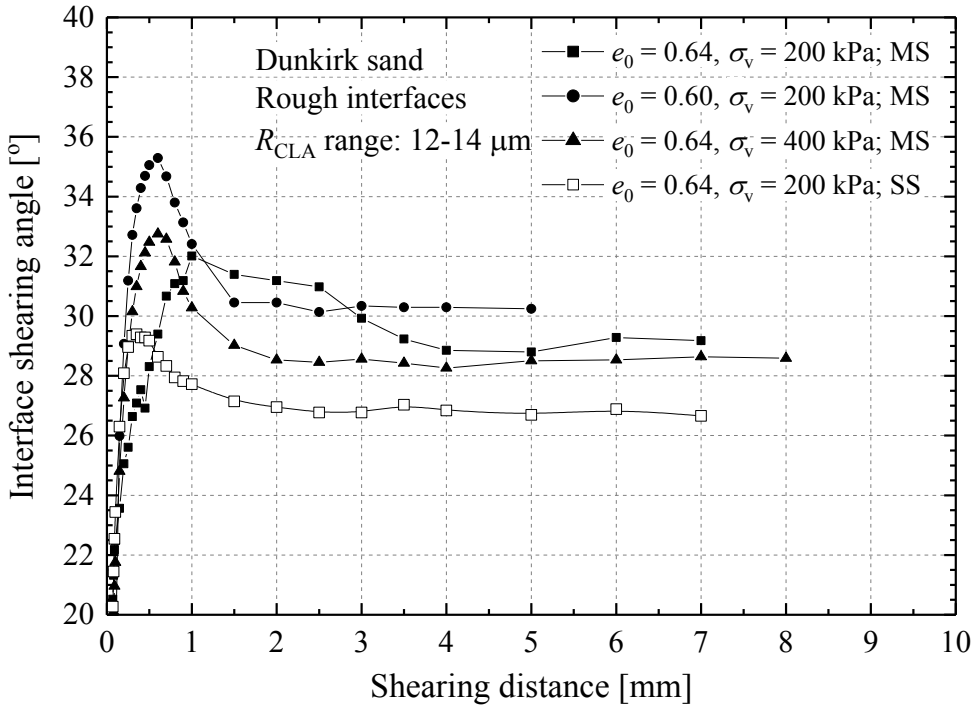

Figure 4-45 Friction angle trends of Dunkirk sand shearing against rough steel interfaces (0.1 day ageing time, 0.1 mm/min shearing rate)

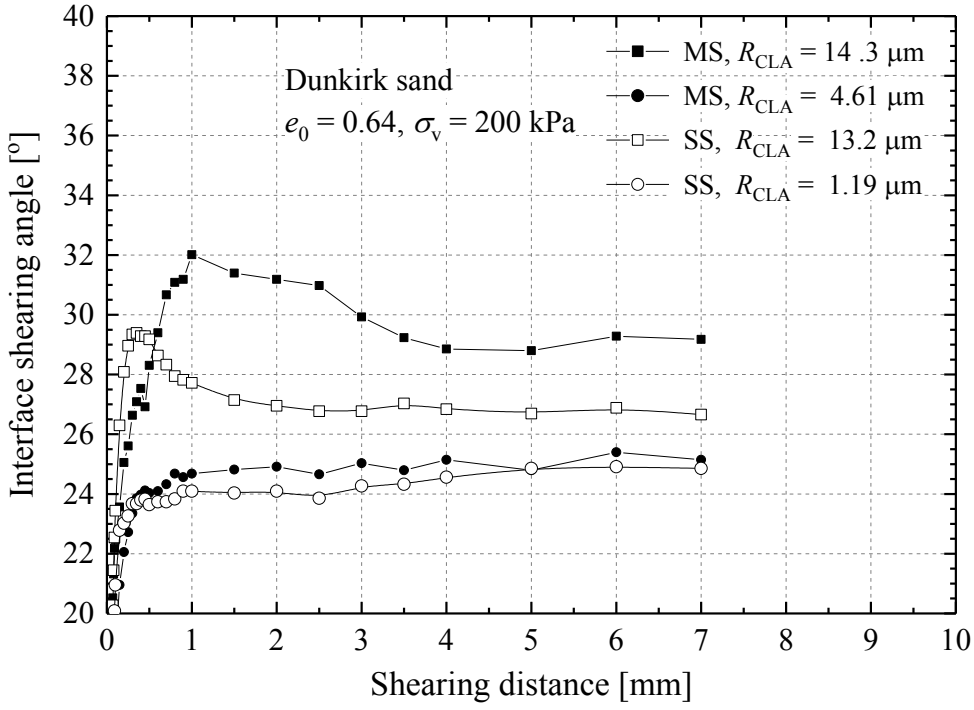

Figure 4-46 Comparison of friction angle trends of Dunkirk sand shearing against rough and smooth steel interfaces (0.1 day ageing time, 0.1 mm/min shearing rate)

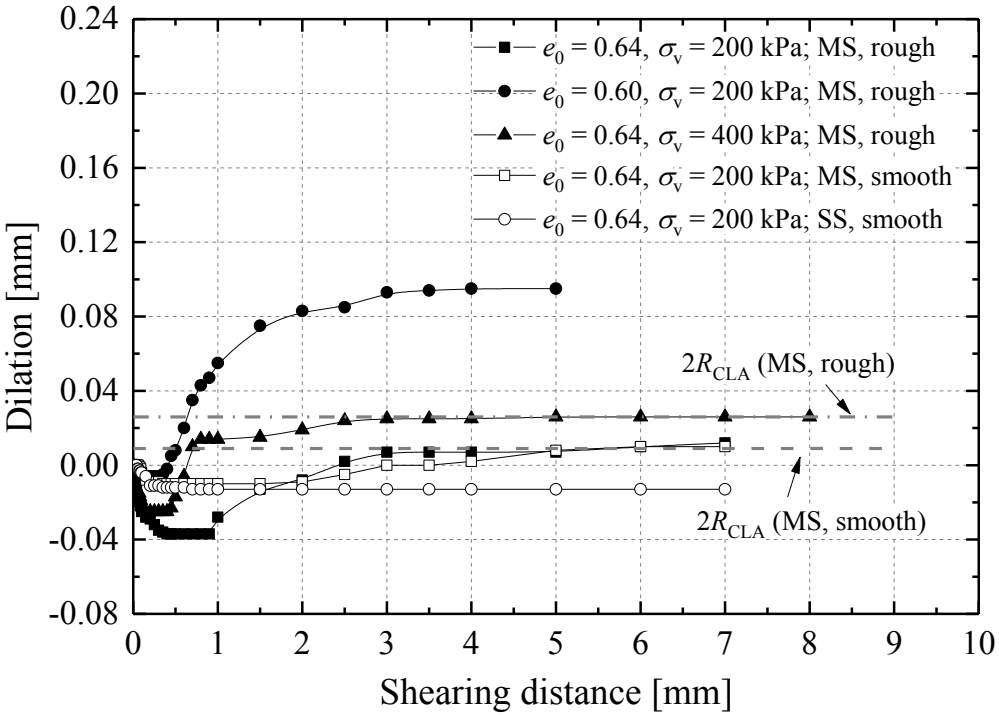

Figure 4-47 Dilation trends of Dunkirk sand shearing against rough and smooth steel interfaces (0.1 day ageing time, 0.1 mm/min shearing rate)

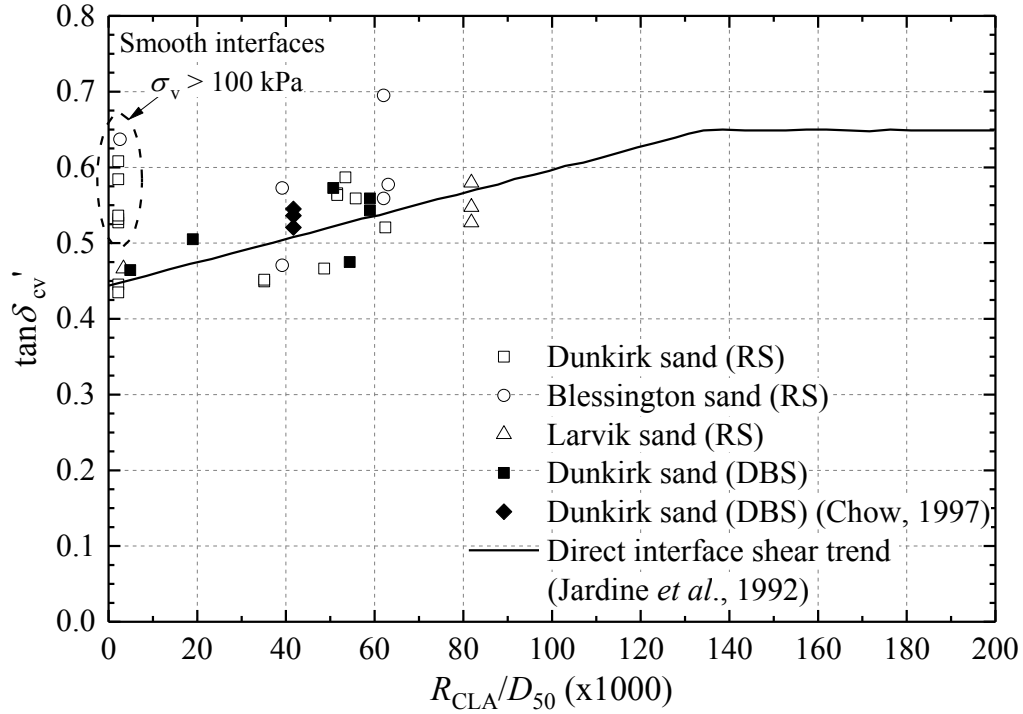

Figure 4-48 Correlation between $\tan\delta'_{cv}$ and pre-test normalised roughness (R_{CLA}/D_{50}) of all the non-aged ring shear and direct shear interface tests

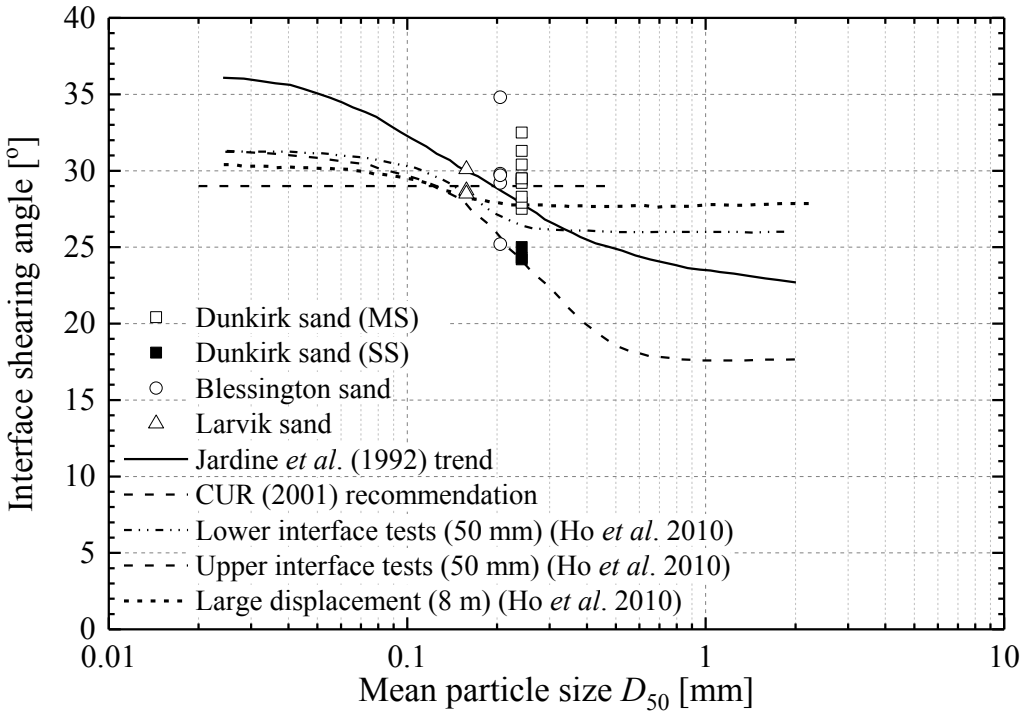

Figure 4-49 Comparison of non-aged ultimate friction angles of shearing against rough steel interfaces with published trends

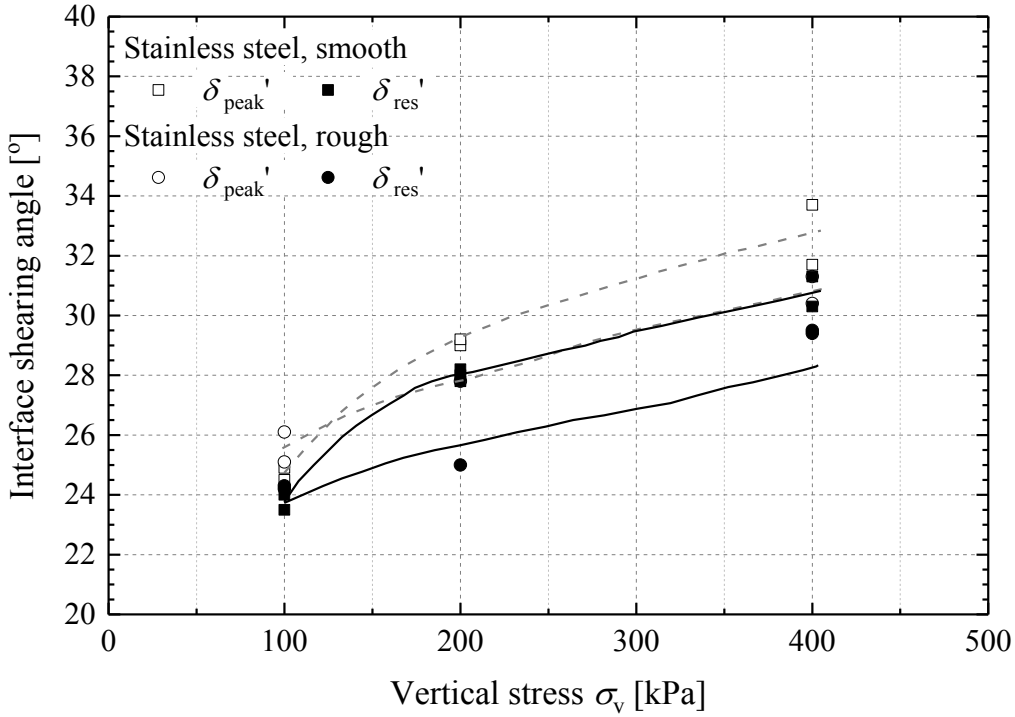

Figure 4-50 Effects of stress level on interface shearing angle of Dunkirk sand against smooth and rough stainless steel interfaces

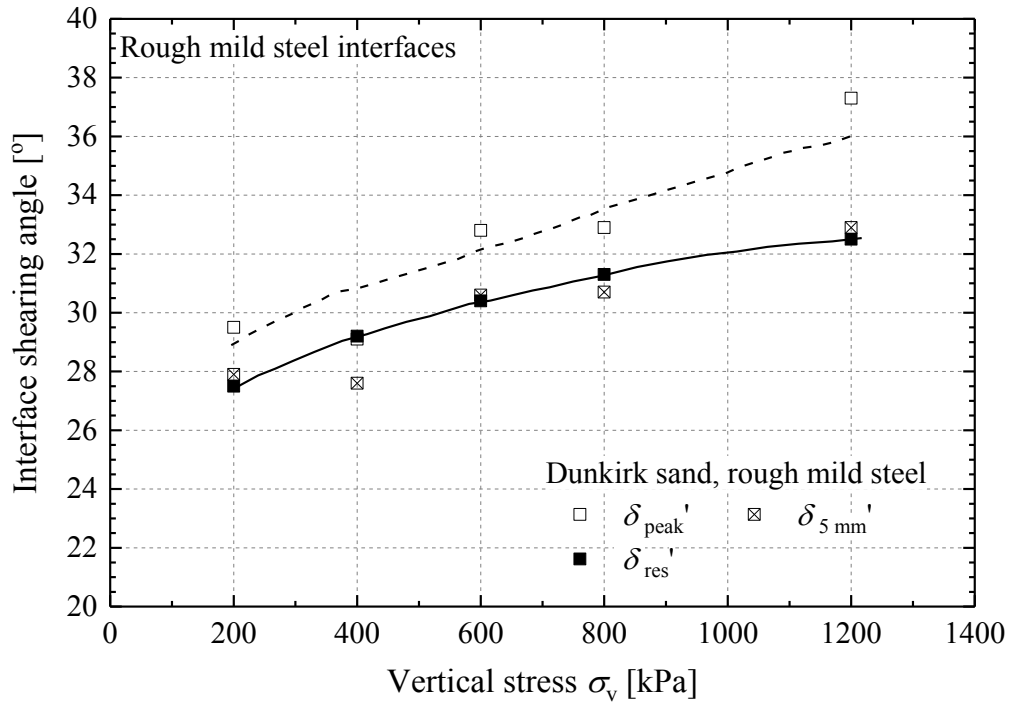

Figure 4-51 Effects of stress level on interface shearing angle of Dunkirk sand against rough mild steel interfaces

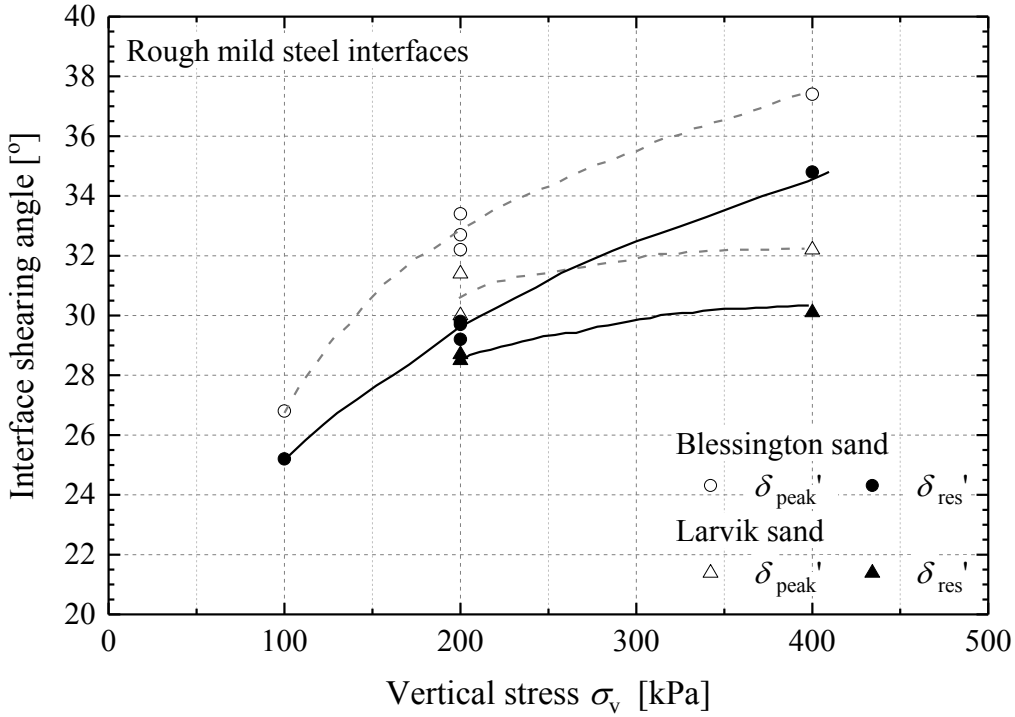

Figure 4-52 Effects of stress level on interface shearing angle of Blessington and Larvik sand against rough mild steel interfaces

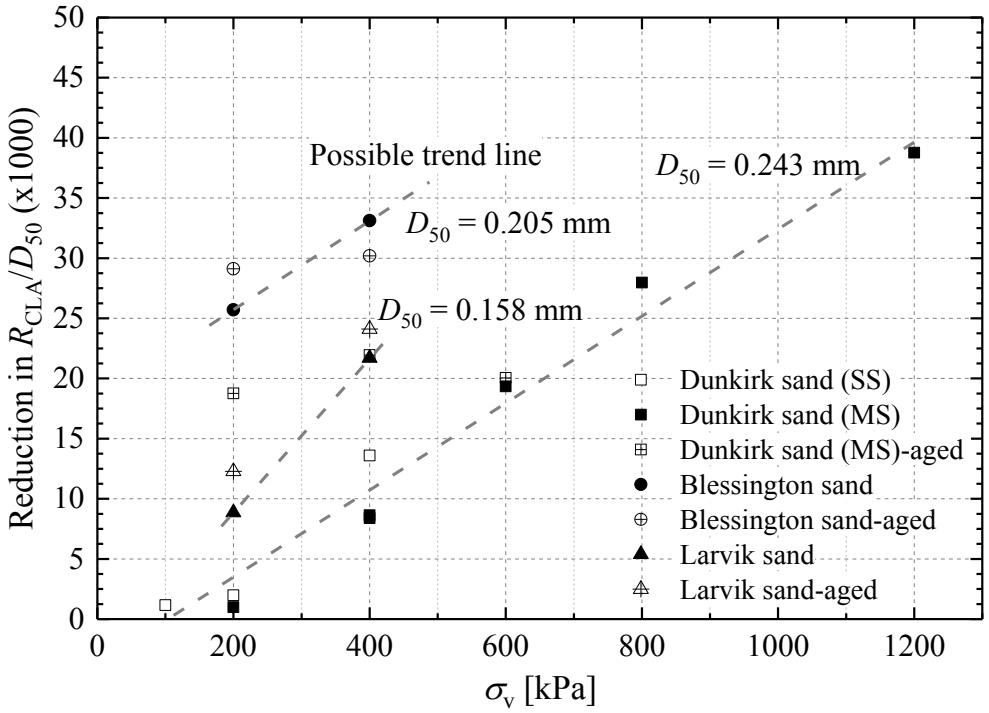

Figure 4-53 Correlation between vertical stresses with reduction in R_{CLA}/D_{50} in ring shear tests using rough steel interfaces

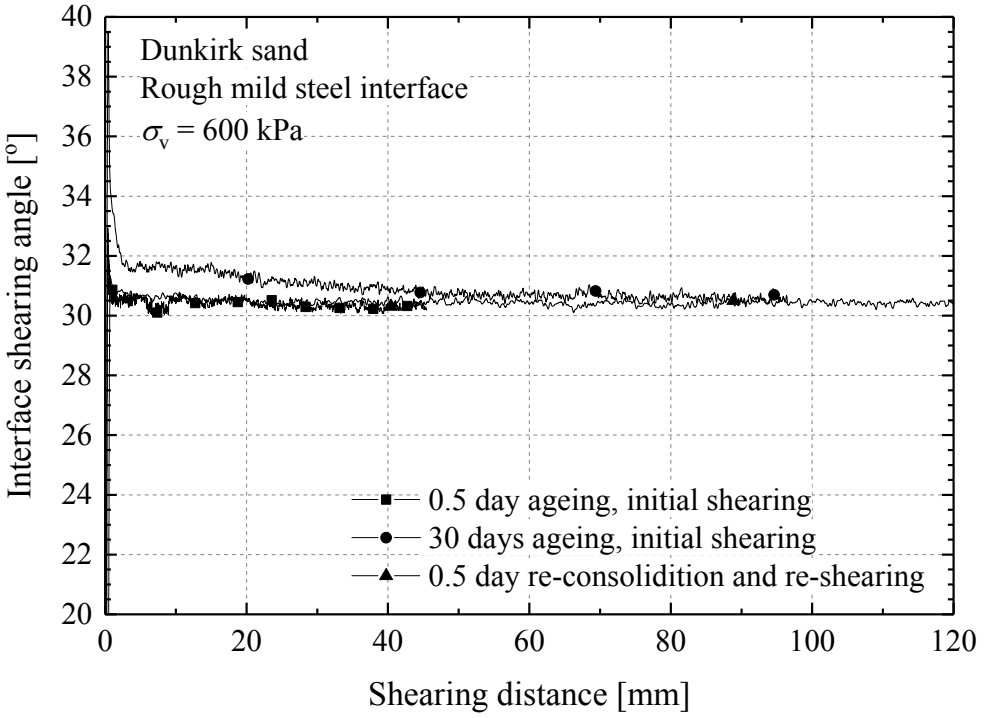

Figure 4-54 Initial shearing and re-shearing response of the test DKMS600R-aged, in comparison with the non-aged test DKMS600R

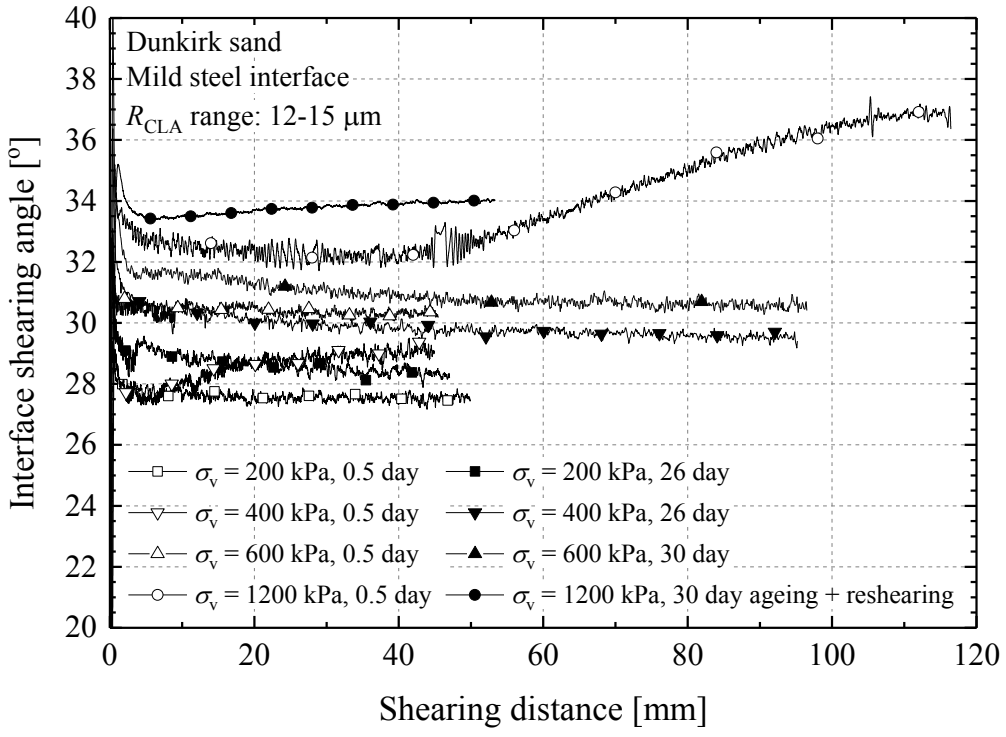

Figure 4-55 Effects of ageing on large-displacement interface shearing behaviour of Dunkirk sand against rough mild steel interfaces

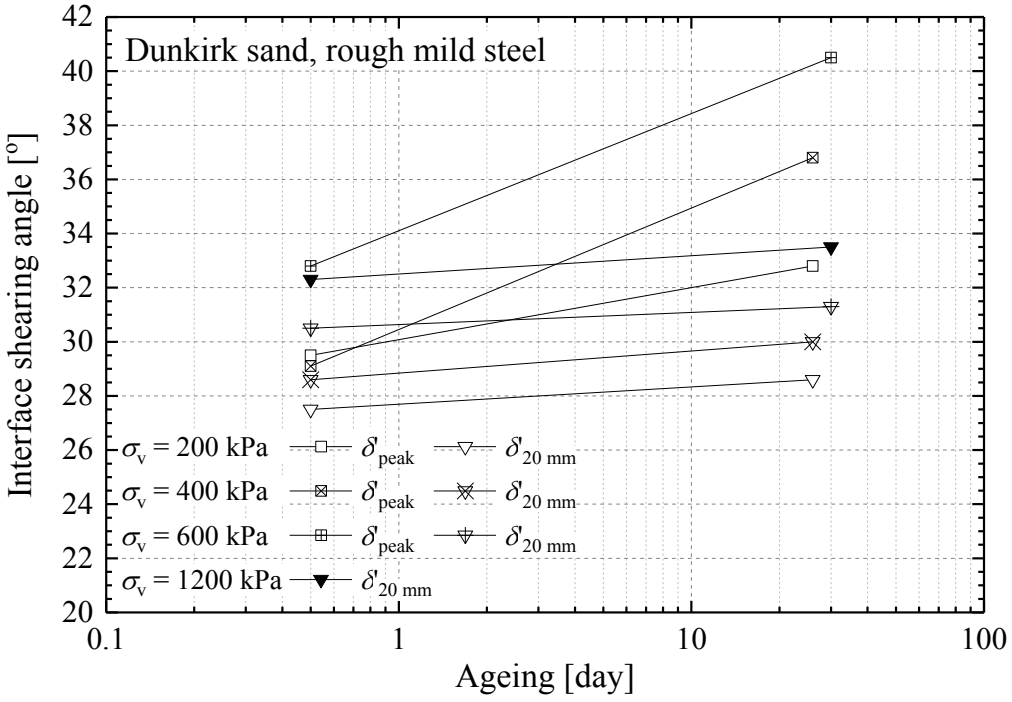

Figure 4-56 Interface shearing angles of non-aged and aged Dunkirk sand shearing against rough mild steel interfaces

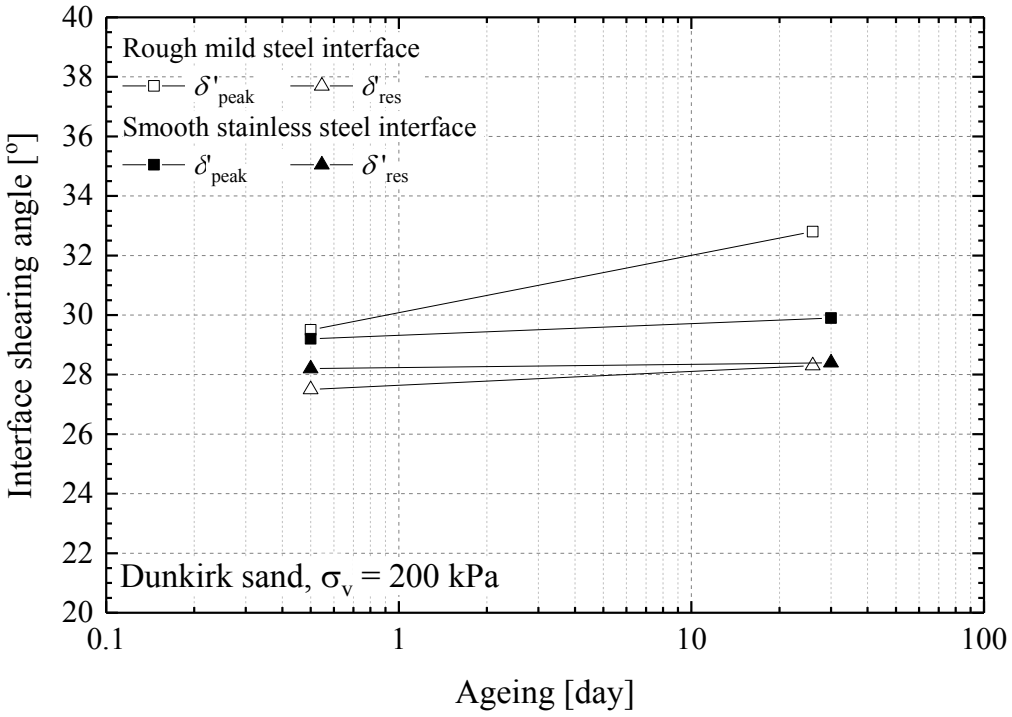

Figure 4-57 Comparison of aged and non-aged Dunkirk sand shearing against rough mild steel and smooth stainless steel interfaces under σ_v = 200 kPa

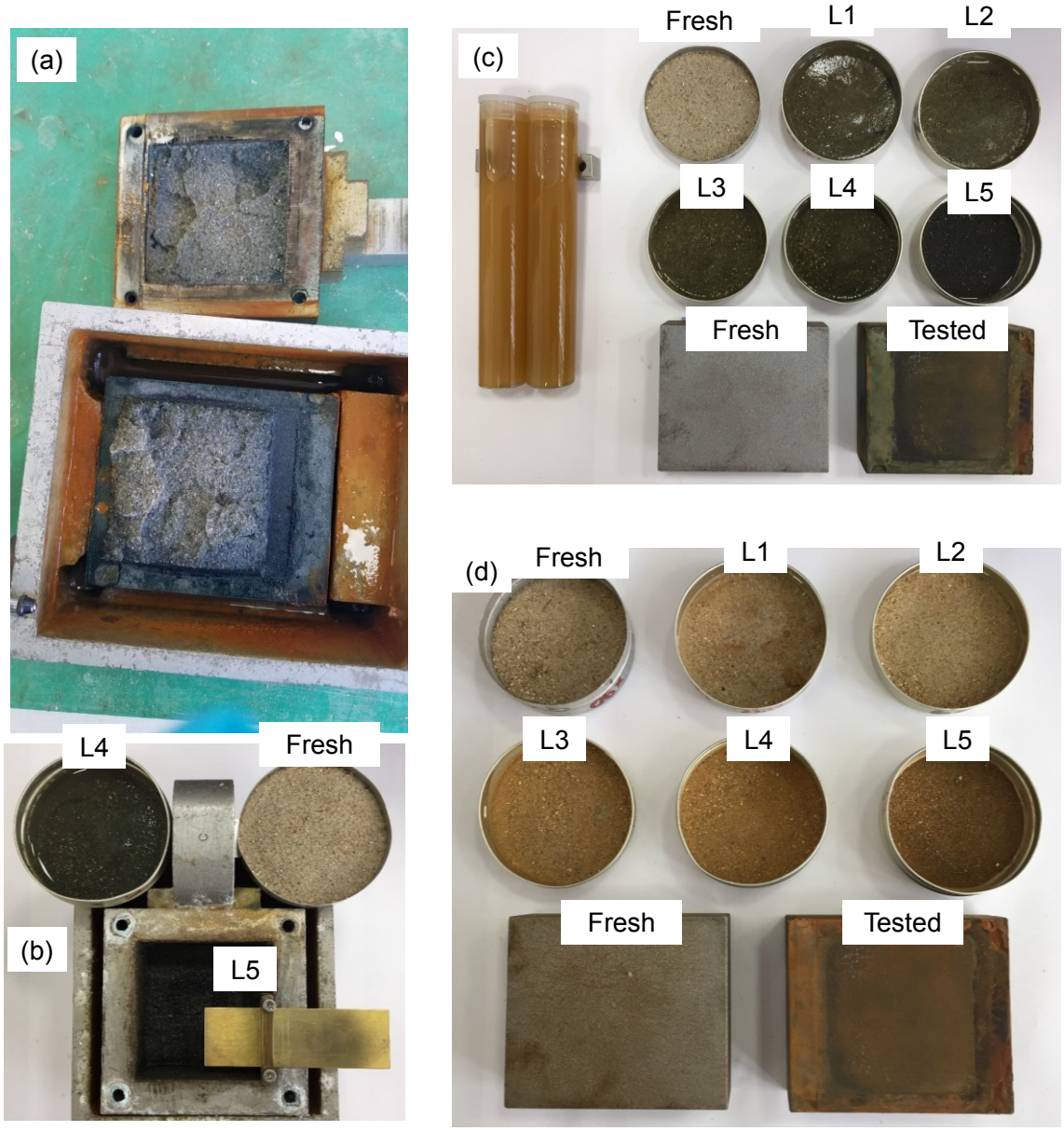

Figure 4-58 Post-test observations of aged Dunkirk specimens after direct shear interface testing, (a) significant colour changes to the sand and steel interface after 26 days ageing; (b) 180 days ageing test: sub-sampling procedure using a soil "scraper", differentiating soil states of different sampling layers compared to the material's initial fresh (dry) state; (c) 180 days ageing test: states of water bath solution, fresh and tested steel interface and sub-sampled soil layers (wet); (d) the same as (c) but after oven dried

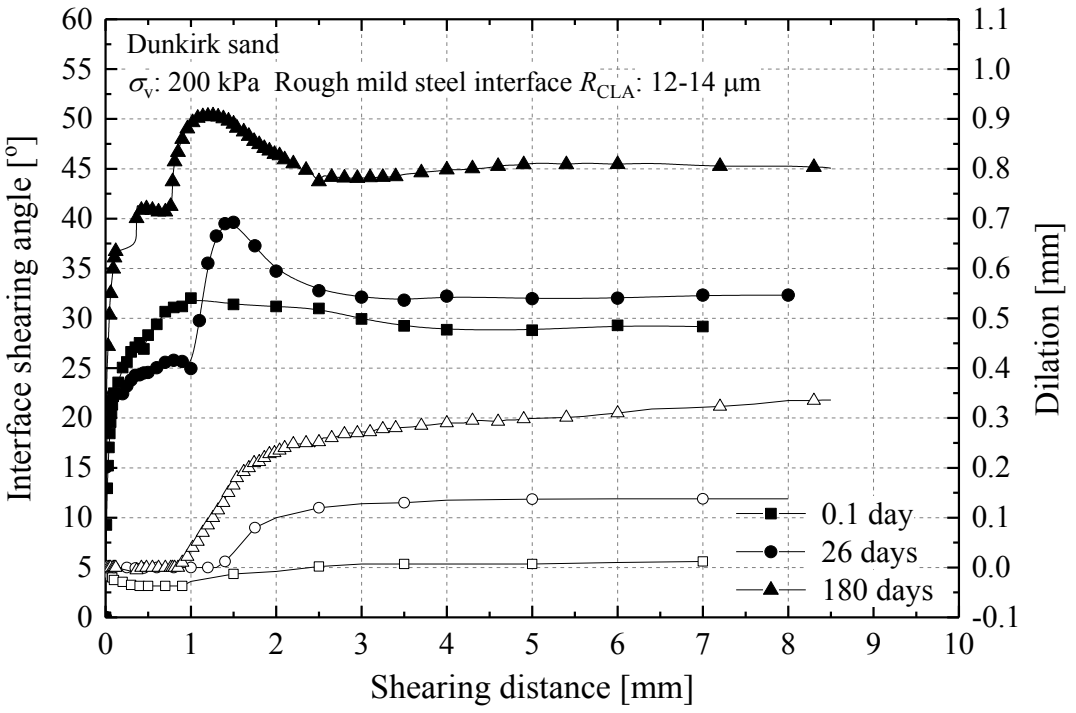

Figure 4-59 Effects of ageing on small-displacement interface shearing behaviour of Dunkirk sand against rough mild steel interfaces

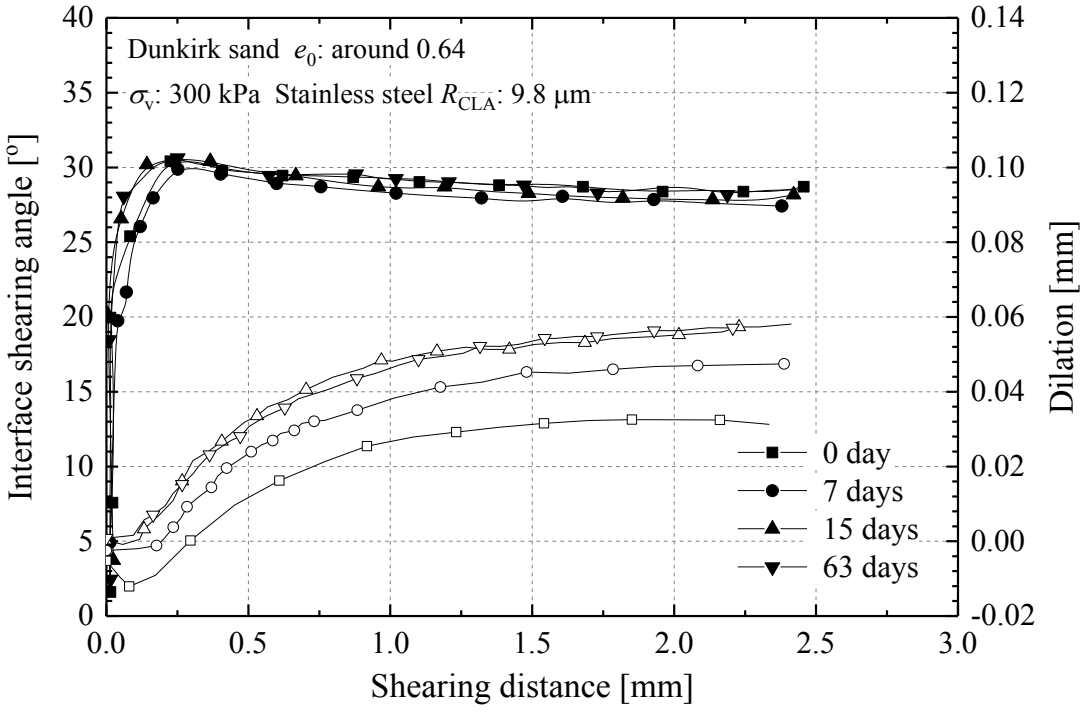

Figure 4-60 Effects of ageing on small-displacement interface shearing behaviour of Dunkirk sand against rough stainless steel interfaces (Chow, 1997)

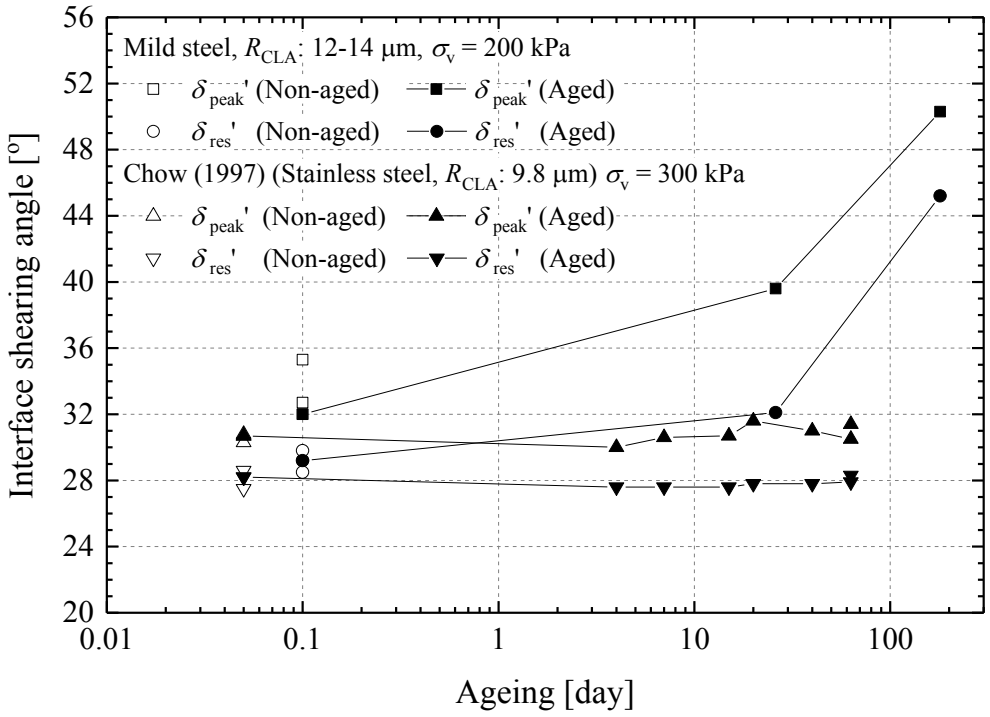

Figure 4-61 Peak and residual interface shearing angles of non-aged and aged Dunkirk sand against mild steel and stainless steel interfaces in direct shear interface tests

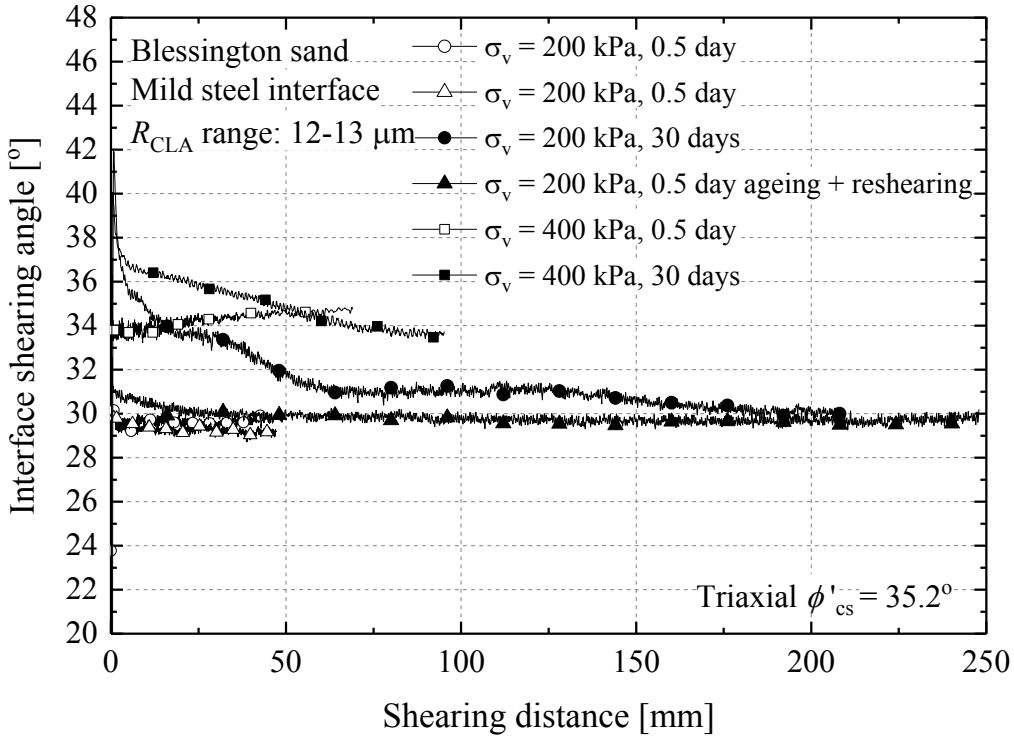

Figure 4-62 Effects of ageing on large-displacement interface shearing behaviour of Blessington sand against rough mild steel interfaces

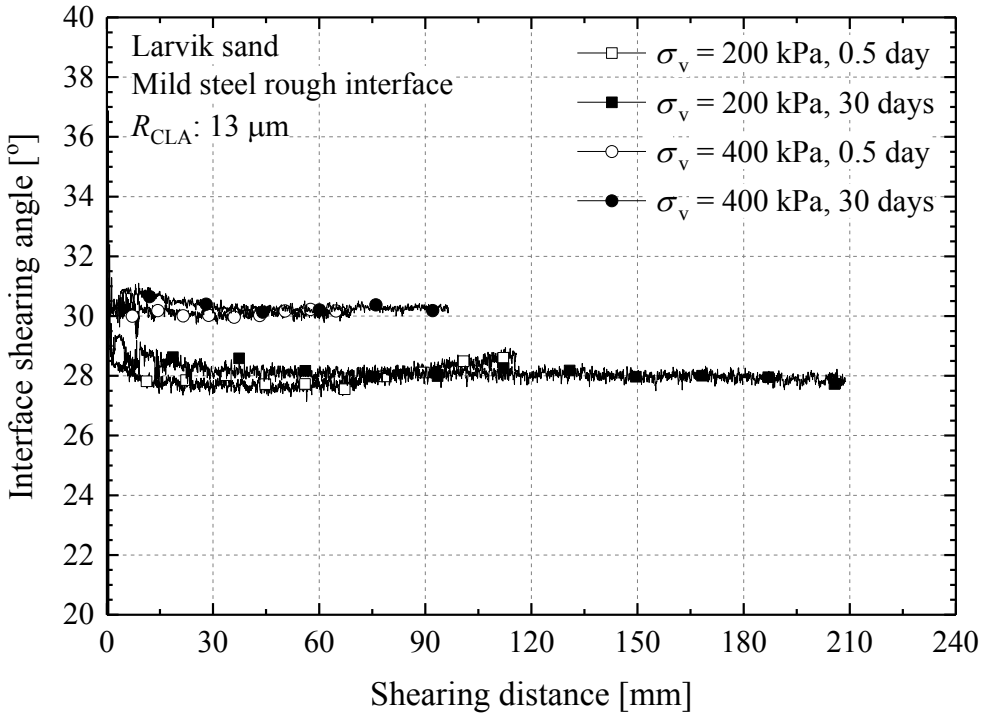

Figure 4-63 Effects of ageing on large-displacement interface shearing behaviour of Larvik sand against rough mild steel interfaces

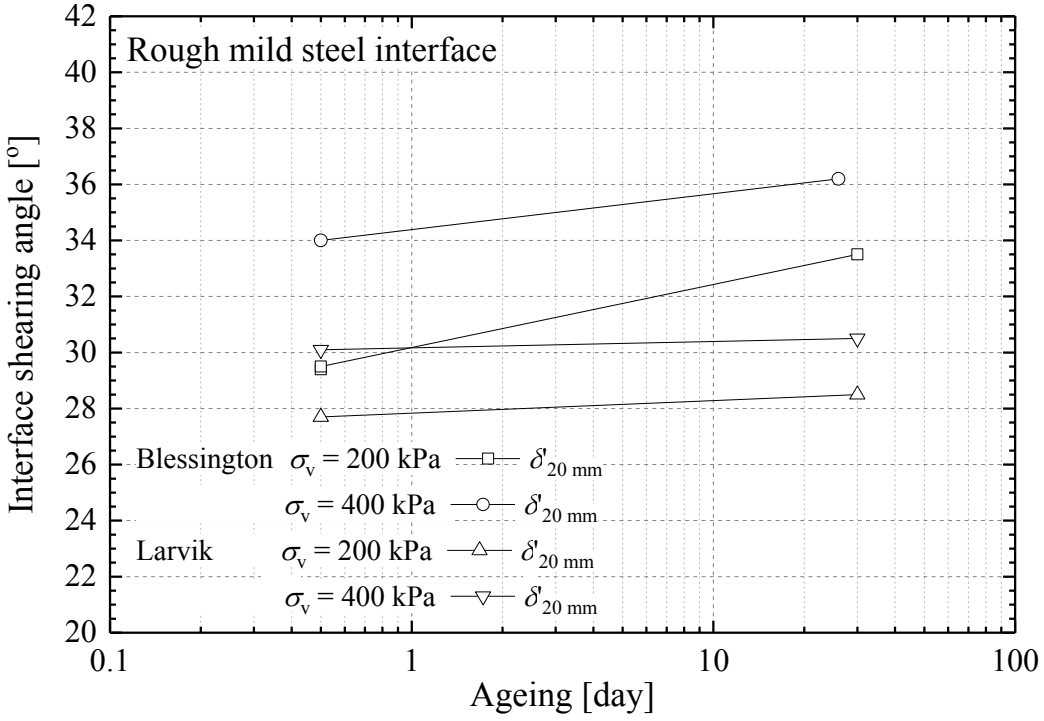

Figure 4-64 Interface shearing angles of non-aged and aged Blessington and Larvik sands shearing against rough mild steel interfaces

4.6 Summary and conclusions

This Chapter presented experimental studies on the compression, yielding and interface shearing behaviour of silica dominated sands, considering the soil states and stress conditions that might be expected under the base and near the shaft of driven piles during their installation, ageing and loading stages. The Author's studies were relevant to the earlier field pile studies at the Dunkirk, Blessington and Larvik sites and the calibration chamber pile tests performed with Fontainebleau NE34 sand.

The research programme, which was partly contributed by Vinck (2016) and Chen (2017a), consisted of 14 high pressure oedometer tests on Dunkirk sands and Fontainebleau NE34 sand, 29 large-displacement Bishop ring shear sand-steel interface tests on Dunkirk, Blessington and Larvik sands, as well as 9 small-displacement direct shear sand-steel interface tests on Dunkirk sand. Experimental evidence and interpretation was presented to support the hypotheses posed in Section 4.1. The main conclusions can be drawn as follows.

1. Index property testing and imaging analyses confirmed the Dunkirk sand's near-shore origin that led to its less uniform mineralogy composition, grain size and shape. The same features imparted its generally lower particle strength, higher compressibility and less clear yielding, in comparison with the high purity silica NE34 sand.

2. Compression deformation became more marked and time-dependent at elevated stresses, and the creep strain ratio ($C_\varepsilon = \Delta\varepsilon_a/\Delta\log(t)$) was dependent on the material properties and stress level.

3. The ring shear tests on non-aged sand specimens manifested clear stress-dependency in their interface shearing resistances. Increments of 1.7°, 5.7° and 1.4° were found in δ'_{cv} with the Dunkirk, Blessington and Larvik sand, respectively, in tests with rough mild steel interfaces when the normal stresses doubled from 200 kPa to 400 kPa. A further increase of 3.3° was obtained with Dunkirk sand when the normal stress was further tripled up to 1200 kPa. Similar shifts in δ'_{cv} were noted in the tests with rough and smooth stainless steel interfaces.

4. The stress-dependent characteristics noted in the ring shear tests are believed to relate to the imposed pre-shearing stages that induced significant mutations to the

soils and changes in the interfaces. Far less stress-dependency was seen in the direct shear interface tests which included no such conditioning stages.

5. The ring shear tests that involved ageing the three sands for one month against rough mild steel interfaces manifested clear increases in interface shearing resistance and vertical dilation. The ageing gain was most prominent over the initial shear stages (with displacement less than 30 mm) and gradually diminished as shearing progressed to larger displacements.

6. The ageing effects varied with sand type. Average increments of 1.1˚, 3.1˚ and 0.6˚ was noted in δ'_{20mm} in the one-month aged Dunkirk, Blessington and Larvik sands, respectively, compared with those non-aged specimens. Direct shear ageing tests on Dunkirk sand also revealed significant ageing gains that were more pronounced than were seen in ring shear tests.

7. The gains of shear resistance through ageing were only marginal in both the ring shear and direct shear tests with stainless steel interfaces, regardless their roughnesses.

8. Among the three materials studied, Blessington sand showed the most prominent stress- and time-dependency in its interface shear resistance, while Larvik sand showed the least. The differences were related to soil grading, chemical properties and mineral compositions.

9. Roughness reductions seen with the steel interfaces before and after testing became more marked with the increasing normal stress level and ageing period, considering otherwise equivalent test conditions.

10. Ring shear tests employing smooth interfaces (R_{CLA} < 1 μm) showed surprisingly high interface friction angles, and these 'non-intuitive' trends were related to the significant specimen densification that took place during pre-shearing and the different confining boundaries imposed in ring shear testing, compared to direct shear.

11. Case-specific interface testing involving appropriate soil media, water conditions, interface materials, stress levels, pre-conditioning stages, ages and displacement levels are required to derive representative interface friction angles for practical applications.

CHAPTER 5
Pre-failure stiffness behaviour of Dunkirk sands under monotonic loading

5.1 Introduction

Piles subjected to lateral and moment loading develop their reactions by mobilising stress changes and strains with large volumes of the soil layers into which they are driven. Together with the piles' structural properties, the soils' mechanical behaviour control the piles' stiffness and ultimate capacity characterisation, which must be addressed when considering both serviceability (fatigue) and capacity design. Any accurate modelling of the lateral and moment loading cases needs to capture and reproduce the soils' behaviours, from their very limited linear elastic ranges over their more extensive non-linear ranges up to and including ultimate shear failure.

Laboratory research into the monotonic shearing behaviour of Dunkirk sand was therefore a key part of the PISA project. The programme was developed first to provide the specific datasets required for calibrating the state parameter-based bounding surface plasticity model (Taborda *et al.*, 2014) employed to simulate the PISA pile tests at the Dunkirk site. The work was undertaken at an early stage of the project and the Authors' laboratory programme was extended subsequently to address further aspects of the sand's mechanical behaviour.

This chapter and Chapter 6 set out the Author's research programme into the monotonic loading behaviour of Dunkirk sand, which included the following four components.

(1) A first stage triaxial programme to support the calibration of PISA sand constitutive model, which consisted primarily of 15 tests on 38 mm diameter reconstituted Batch 2 Dunkirk samples from isotropic stress states (K = 1) under drained conditions. The testing employed standard (rough) end plattens and extended the earlier study by Aghakouchak (2015) who focused principally

on monotonic and cyclic loading behaviour of anisotropically (K_o) consolidated Batch 2 Dunkirk sand, working mostly with undrained test conditions;

(2) Conjunct triaxial testing with Mr. Ken Vinck as part of his MSc research project (Vinck, 2016) to investigate the mechanical behaviour of the Batch 3 Dunkirk sand as the secondary material employed for the Author's triaxial probing and drained cyclic triaxial testing programmes;

(3) An extended programme with Mr. Ken Vinck to study the effects of end restraint in triaxial testing on the pre-failure stiffness, large strain behaviour and critical state behaviour of Dunkirk sands;

(4) Triaxial probing tests on reconstituted Batch 3 Dunkirk sand samples using the fully instrumented '100 mm' triaxial appratuses equipped with upgraded local strain sensors and test control systems to investigate anisotropic linear elastic stiffnesses of Dunkirk sand, extending the earlier study by Kuwano (1999) on Batch 1 Dunkirk sand, which focused primarily on its anisotropic pre-failure behaviour over small strain ranges.

The current Chapter 5 sets out the overall research methodology and programmes, and summarises the findings regarding the sands' pre-failure stiffness behaviour (for PISA sand model calibration), anisotropic linear elastic stiffness and kinematic yielding characteristics. Chapter 6 follows by focusing on the sands' large strain behaviour. Discussion is offered in Chapters 5 and 6 on the possible differences in mechanical properties between the different batches of Dunkirk sand samples. The Author's cyclic triaxial programme and methodology is outlined in Chapter 7, presenting detailed studies on the sand's behaviour under long-term drained cyclic loading.

Focusing first on the study of pre-failure stiffnesses set out in this Chapter, the main questions the Author sough to investigate included:

#1. How the pre-failure stiffnesses of Dunkirk sands depends on its effective stress state, level and history as well as soil density and strain level;

#2. The effects of end restraint on pre-failure stiffness characteristics;

#3. Whether Dunkirk sands' anisotropic stiffnesses and pre-failure behaviour can be interpreted using the cross-anisotropic elasticity model and multiple kinematic yield surface approach as suggested by Jardine (1992) and Kuwano & Jardine (2007).

5.2 Review: Stiffness and yielding behaviour of granular materials

This section presents first a brief review of the effective stress-dependent and anisotropic stiffness characteristics of granular materials. The influence of the dominant factors are addressed, drawing outcomes from studies adopting advanced laboratory techniques and particulate modelling approaches.

This review refers to the frameworks of elastic cross-anisotropy (set out in Section 3.2.1) and the multiple kinematic yield surface (Y_1 to Y_4) model (Jardine, 1992, Kuwano & Jardine, 2007) which are both employed in the Author's interpretation of pre-failure behaviour of Dunkirk sands.

5.2.1 Stress-dependent and anisotropic stiffness characteristics

Early studies on elastic shear stiffness of granular materials by for example Roesler (1979) and Hardin & Blandford (1989) examined dependency of stiffness on effective stress level and state. Kuwano (1999) and Kuwano & Jardine (2002b) built on this within their extensive laboratory triaxial bender element and stress probing tests on sands (details of the apparatus and interpretive methods see Section 3.2.1), and adopted the following set of functions to correlate their soils' cross-anisotropic stiffnesses principally with the vertical and horizontal stress components (σ_v' and σ_h').

$$E_v' = f(e)C_v\left(\frac{\sigma_v'}{p_r}\right)^{a_v} \tag{5.1}$$

$$E_h' = f(e)C_h\left(\frac{\sigma_h'}{p_r}\right)^{b_h} \tag{5.2}$$

$$G_{vh} = f(e)C_{vh}\left(\frac{\sigma_v'}{p_r}\right)^{a_{vh}}\left(\frac{\sigma_h'}{p_r}\right)^{b_{vh}} \tag{5.3}$$

$$G_{hh} = f(e)C_{hh}\left(\frac{\sigma_v'}{p_r}\right)^{a_{hh}}\left(\frac{\sigma_h'}{p_r}\right)^{b_{hh}} \tag{5.4}$$

Where E_v', E_h', G_{vh} and G_{hh} are the elastic Young's moduli and shear stiffnesses in the triaxial vertical and horizontal planes. Note that Equations (5.1) and (5.2) assume purely uniaxial relationships and negligible dependency on the stress ratio (σ_v'/σ_h'). In this case, $f(e)$ is a void ratio function introduced to account for sample density effects, and is often adopted as $(2.17-e)^2/(1+e)$ for sands, as proposed by Hardin & Richart

(1963); p_r is a reference atmospheric pressure (= 101.3 kPa). C_v, C_h, C_{vh}, C_{hh} are material constants and the ratios C_h/C_v and C_{hh}/C_{vh} are commonly adopted as descriptors of stiffness anisotropy. a_v, b_h, a_{vh}, b_{vh}, a_{hh} and b_{hh} are exponents indicating the level of dependency of stiffness on each particular stress component.

The above set of correlations assume that the above elastic stiffness coefficients (or "constants") are independent of stress ratios. This assumption is examined by reference to Author's multiple constant stress ratio (σ_v'/σ_h') triaxial probing tests described in Section 5.9.

The above Equations (5.3) and (5.4) decouple the stresses in the shear waves' propagation and oscillation direction, and expresses their effects separately by introducing two parameters a_{vh} and b_{vh} to account for anisotropic stress states. Under isotropic stress conditions, a single exponent n is often used to express the overall effects of effective stress level through the following function.

$$G_0 = AF(e)\left(\frac{p'}{p_r}\right)^n \tag{5.5}$$

Where A is material constant, similar to the above C_{vh}. Although simple Hertzian particulate theory suggests that n = 1/3, many authors including Porovic (1995) and McDowell & Bolton (2001) reported n values closer to 0.5 were obtained in experimental studies on sands. However, as described later, both parameters n and A vary with soils' index and mineralogical properties as well as their particle-scale characteristics (shape, surface roughness, etc.). Other factors, for example stress history (OCR), creep and ageing, may also play a role.

Laboratory tests that can impose the three principal stresses independently, such as the special calibration chamber described by Bellotti *et al.* (1996) or the cubical cell apparatus (CCA) employed by O'Donovan (2014), enable correlations to be established between shear stiffness components and the normal stresses in the direction of shear wave propagation (σ_{prop}) and oscillation (σ_{osc}) as well as the remaining orthogonal stress (denoted as σ_{third}). The correlation is expressed as follows.

$$G_0 = C_p f(e)\left(\sigma_{prop}\right)^{n_{prop}}\left(\sigma_{osc}\right)^{n_{osc}}\left(\sigma_{third}\right)^{n_{third}} \tag{5.6}$$

The meanings of C_p and $f(e)$ are similar to those described above. In micromechanical analyses adopting DEM approaches, the above terms C_p $f(e)$ is often replaced by the

following expression to quantify separately the effects of several particle-scale properties (see for example by Nguyen *et al.* (2018)).

$$F(e) = C_{\mathrm{p}} f(e) = F\left(e, C_{\mathrm{N}}, \chi, \upsilon_{\mathrm{p}}, E_{\mathrm{p}}\right) \tag{5.7}$$

Where C_{N} is the average coordination number and χ is a measure of fabric orientation. υ_{p} and E_{p} denote particles' Poisson's ratio and Young's modulus, respectively.

Factors dominating elastic shear stiffness and recent developments

Extensive research employing various in-situ, laboratory and numerical approaches has identified a wide spectrum of factors affecting the elastic shear stiffness of granular materials or geo-materials in general. Some of the critical aspects and their potential effects are summarised below.

Sample preparation method Specimen reconstitution method is one of the key aspects that concerns inherent anisotropy (Oda, 1972, Yang *et al.*, 2008), liquefaction potential assessment (Tatsuoka *et al.*, 1986, Ishihara, 1993) as well as shear stiffness and anisotropic characteristics of granular materials. Schematic procedures of two commonly used methods, moist tamping and dry deposition, are demonstrated in Figure 5-1.

Employing a combined bender element (BE)-resonant column (RC)-torsional shear (TS) device, Gu *et al.* (2015) performed shear stiffness G_0 (G_{vh}) measurements on isotropically consolidated Toyoura sand specimens, and reported 17-21% higher BE G_0 and 6-7% higher RC and TS G_0 in their moist tamped specimens (relative density range 30-80%), than in those formed with 'gravity-reoriented' air pluviation or dry tamping methods under otherwise identical conditions.

Gu *et al.* (2015) attributed the higher stiffnesses seen in moist tamped specimens to the higher compaction energy required during tamping. However, in the Author's view, the differences could also be due to the fact that the horizontally preferred grain arrangement in the deposited specimens could be more susceptible to torsional shearing, compared to the moist tamped specimens possessing more uniformly distributed particle contacts in the horizontal plane. The differences of G_0 from BE, RC and TS may reflect the different measuring mechanisms involved, as the BE method gauges 'local' shear stiffness of the specimen's central soil column while the RC and TS represent the 'global' shear stiffness of the whole specimen, as discussed in Section

3.3.5.

Air and water pluviation approaches were applied in earlier research at Imperial College; see for example Porovic (1995) or Kuwano (1999). However, this approach can give difficulties in cases where significant fines are present. An in-mould slurry-based method (Carraro & Prezzi, 2008, Tastan & Carraro, 2013) for reconstituting triaxial and HCA specimens of sands or silty soils has recently been developed by Dominguez-Quintans *et al.* (2018). Further research is underway to explore shear stiffnesses and their anisotropic characteristics as well as dynamic behaviour of sand specimens formed with the new approaches.

Potential effects of particle size Yang & Gu (2013) reported extensive BE and RC tests on three batches of glass ballotini with similar uniformity but varied mean grain sizes (D_{50} = 0.195, 0.920 and 1.750 mm) and concluded that elastic stiffness was practically unaffected by particle size. However, as illustrated by Otsubo & O'Sullivan (2018), bender element testing of coarse grains may involve fabric disturbance and energy loss at the bender-grain interfaces, leading to local packing effects that could affect bender element signals. Further investigation may be required to quantify possible errors involved in assessing shear stiffness of coarse materials.

Effects of surface roughness While Altuhafi *et al.* (2016) found no clear correlation between surface roughness and the shear moduli of their natural and irregular sands, Otsubo & O'Sullivan (2018) reported a remarkable dependency of shear stiffness (from shear plate testing) on the surface roughness of coarse spherical glass ballotini (D_{50} = 1.2 mm). Particles prepared to higher roughness (quantified by root mean square roughness S_q) manifested clearly lower stiffness (low A values in Equation (5.5)) under equivalent void ratio and stress level conditions, but exhibited markedly greater stress-dependency (higher n values in Equation (5.5)) than specimens with lower roughness. The presence of asperities on the rougher grains moderated inter-particle stiffness and induced more energy dissipation as shear wave propagated, leading to lower A values. However, the differences tended to diminish when stress levels rose, as the asperities yielded and particle contacts became less asperity-dominated, with the G-p' curves of rough and smooth particle assemblies trending towards narrower ranges.

***OCR* effects** Over-consolidation appears to produce minor or slightly positive

effects independently of effective stress level on elastic shear moduli. Kuwano & Jardine (2002b), for example, reported no discernible effects of *OCR* and recent stress history on the elastic moduli of their specimens. It is also important to note that the degree of over-consolidation and recent stress history affects profoundly the elastic stress or strain range and the non-linear shear stiffness of sands, as well as the size and shape of their larger strain yielding loci, as demonstrated by Kuwano & Jardine (2007).

Finally, as laboratory studies of elastic shear stiffness often employ dynamic shear wave techniques (bender element, shear plate or resonant column), it is important to acknowledge the potential variations or discrepancies induced by the factors identified by Clayton (2011) as well as related issues such as frequency dependency and interpretive methods. Systematic studies and assessments of such factors are reported by for example Yamashita *et al.* (2009), Alvarado & Coop (2012), Yang & Gu (2013) and Otsubo (2017). No comparably comprehensive study, however, was feasible within the Author's research programme.

Characteristics of anisotropic shear stiffness

Triaxial tests capable of performing multi-directional bender element tests and small stress-strain probing tests enable the determination of elastic moduli under varied stress states, from which anisotropic stiffness characteristics can be depicted.

Referring to Equations (5.1) to (5.4), Kuwano (1999) and Kuwano & Jardine (2002b) reported ratios of C_h/C_v = 0.85 and C_{hh}/C_{vh} = 1.13 with their dry-pluviated Ham River sand (HRS) (C_u = 1.67, D_{50} = 0.27 mm), and C_h/C_v = 0.83 and C_{hh}/C_{vh} = 1.08 with air-pluviated specimens of spherical glass ballotini (C_u = 1.28, D_{50} = 0.27 mm), indicating clear inherent particle shape and 'gravity contact fabric' stiffness anisotropy. Both the sand and glass ballotini specimens were softer under horizontal normal stress changes but stiffer under horizontal shearing than when comparable stress perturbation were applied on vertical planes.

The above studies also revealed non-equal a_{vh} and b_{vh} exponents in the G_{vh} expression (see Equation (5.3)) for both materials, although their sums ($a_{vh} + b_{vh}$) were close to 0.5, indicating separate effects of the stress in the directions of shear wave propagation (σ_{prop}) and oscillation (σ_{osc}). Although triaxial testing cannot impose the three principal stress fully independently, the effects of the orthogonal stress (σ_{third} in Equation (5.6)) are implied in the G_{hh} correlation (Equation (5.4)) and relatively small

(but non-zero) coefficients of a_{hh} were noted in Kuwano' (1999) tests on Ham River sand and glass ballotini.

The degree of inherent anisotropy is likely to be affected by specimen preparation method. Escribano & Nash (2015) reported a lower G_{hh}/G_{hv} ratio of 1.04 with isotropically consolidated Hostun sand specimens formed by moist tamping method, compared with the ratios commonly noted in air-pluviated specimens. They attributed the difference to the sample reconstitution method used. Further study may be required to investigate the effects of particle size, shape and surface roughness separately on stiffness anisotropy.

Differences are commonly noted between the G_{hv} and G_{vh} components, which ideally should be identical for any homogeneous continuum. Kuwano & Jardine (2002b) attributed the differences to the material's particulate nature noting that different patterns of non-uniform fabric and particle contacts develop in different directions within specimens. DEM studies that also consider the orthogonal stress (σ_{third}) (such as those reported by Nguyen *et al.* (2018) can provide explanations from micromechanical perspectives. Other testing conditions, such as sample dimension and end constraints, may also explain the differences.

Considering anisotropic stress conditions, Kuwano & Jardine (2002b) demonstrated that the exponents a_{vh}, b_{vh} and other coefficients in Equations (5.1) to (5.4) could change when sufficiently high stress ratios (σ_h'/σ_v') are applied to cause the specimens to dilate significantly. Stiffness-stress correlations established from low σ_h'/σ_v' conditions may become invalid as significant unlocking and major changes in grain contacts commence after the onset of dilation.

5.2.2 Soil yielding and the multiple kinematic yield surface model

The yielding of soils was classically defined as the transition point from "elastic" behaviour to plastic behaviour after relatively large strains. However, advances in laboratory techniques proved that soils manifest highly non-linear stress-strain relationships before reaching the yielding point and linear elastic behaviour exists only in a very limited range (Daramola, 1978, Jardine *et al.*, 1984).

Soil yielding involves several progressive phases that are related to gross changes of stress-strain-stiffness behaviour. Progressive yielding behaviour has been modelled

mathematically by a range of approaches: see Mróz (1967), Simpson *et al.* (1979), Al-Tabbaa & Muir Wood (1989), Puzrin & Burland (1998) and Baudet & Stallebrass (2004). Experimental studies were also reported by Jardine (1985), Jardine (1992), Smith *et al.* (1992), Kuwano (1999), Chaudhary & Kuwano (2003) and Kuwano & Jardine (2007) to locate and depict the multiple yield surfaces and characterise key aspects of progressive yielding of both clays and sands.

Drawing on experimental observations, Jardine (1985, 1992) proposed that at least two kinematic surfaces (Y_1 and Y_2) existed inside the classical yielding surface (Y_3) when soil elements are perturbed from previously stable effective stress states. The yield surfaces have distinct features that are closely related to soils' shear stress-strain and stiffness behaviour and can be interpreted using a multiple kinematic yield model, as schemed in Figure 5-2. Important features of each yield surface are briefly summarised below.

Y_1 *yielding surface*

The Y_1 yield surface corresponds to the linear quasi-elastic boundary that defines an elastic region in the effective stress space within which soils manifest linear fully reversible stress-strain response. Jardine (1992) and Kuwano & Jardine (2007) speculated that stress changes that remain within this surface do not alter the arrangements of soil particles, which behave as a highly redundant elastic structure and relative movements between particles are negligible. Soil behaviour within this region may be cross-anisotropic that can be expressed by cross-anisotropy linear elasticity, see for example by Kuwano (1999), Gasparre (2005) and Brosse (2012).

Once engaged, the Y_1 yield surface is dragged around by the movement of the effective stress point with changes in its shape and size (Kuwano & Jardine, 2007). The Y_1 surface are located at the points at which the initially linear stress-strain trends commence to curve. Typical ranges of this surface are within the order of 10^{-3}% strain and can only be resolved using high-resolution local strain instruments.

Y_2 *yielding surface*

Soils commence to generate plastic strains once the Y_1 yield surface is engaged. However, the straining pattern is still dominated by reversible elastic strains and the unload-reload cycles appear to follow close hysteretic loops until the stress path

engages the Y_2 surface Jardine (1992). The Y_2 yield surface marks the stress states where the accumulation of plastic strains starts to accelerate, with markedly more energy being dissipated in loading cycles, and the stress-strain behaviour becomes both rate dependent and subject to creep (Kuwano & Jardine, 2007). For granular materials, Y_2 yielding indicates significant relative movements (rotation and slip) between the particle and some of the assemblies' strong force chains start buckling.

The limit of the Y_2 yield surface represents the points where abrupt changes in strain increment directions (denoted as $d\varepsilon_s/d\varepsilon_{vol}$) may occur in drained probing tests or the pore water pressure-deviator stress plots (Δu-Δq) deviate from linearity in undrained tests (Smith *et al.*, 1992, Kuwano & Jardine, 2007, Gasparre, 2005). In undrained cyclic tests, the Y_2 yield surface also indicates the limiting conditions at which hysteretic stress-strain loops fail to close and irrecoverable strains start to accumulate. Adopting this approach, Aghakouchak (2015), Guo *et al.* (2017) and Ushev (2018) identified the Y_2 yield surfaces for Dunkirk and Fontainebleau NE34 sand, low *OCR* soft Wenzhou clay and high *OCR* stiff glacial Cowden till respectively from undrained cyclic triaxial and HCA tests, as later reviewed in Section 7.2.2.

Y_3 *yield surface*

Y_3 yielding marks the onset of significant contraction, dilation or abrupt failure and corresponds to the conventional geotechnical definition of large scale yielding. Kuwano & Jardine (2007) demonstrated that the Y_3 yielding surface may be interpreted from: (i) sharp curvature in the stress-strain traces; (ii) plastic to total strain ratio $d\varepsilon^p/d\varepsilon^t$ reaching predefined limiting values (usually 0.85 or 0.95); (iii) effective stress path direction changes in undrained tests; (iv) abrupt changes in tangent stiffness. When plotted in normalised effective stress space, the Y_3 surface falls close to the local bounding surface (LBS) that is associated with prior consolidation stress history.

Y_4 *yield surface*

The onset of phase transformation is considered as a further Y_4 yield surface, and is located as the phase transformation point on the undrained shearing stress path or at the stress states when volumetric straining transforms from contraction to dilation in drained tests.

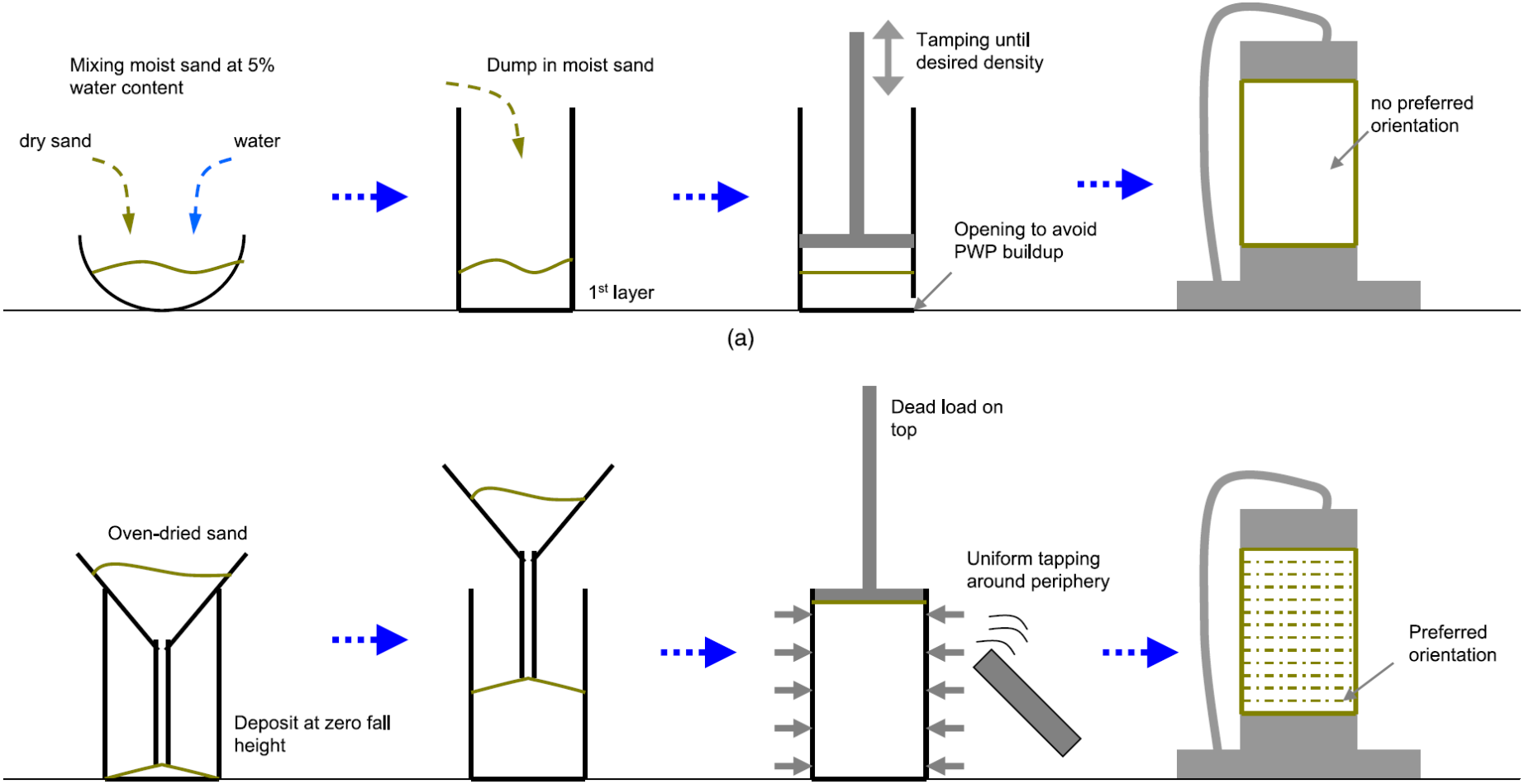

Figure 5-1 Schematic procedures for forming reconstituted specimens using moist tamping and dry-pluviation method (Sze & Yang, 2014)

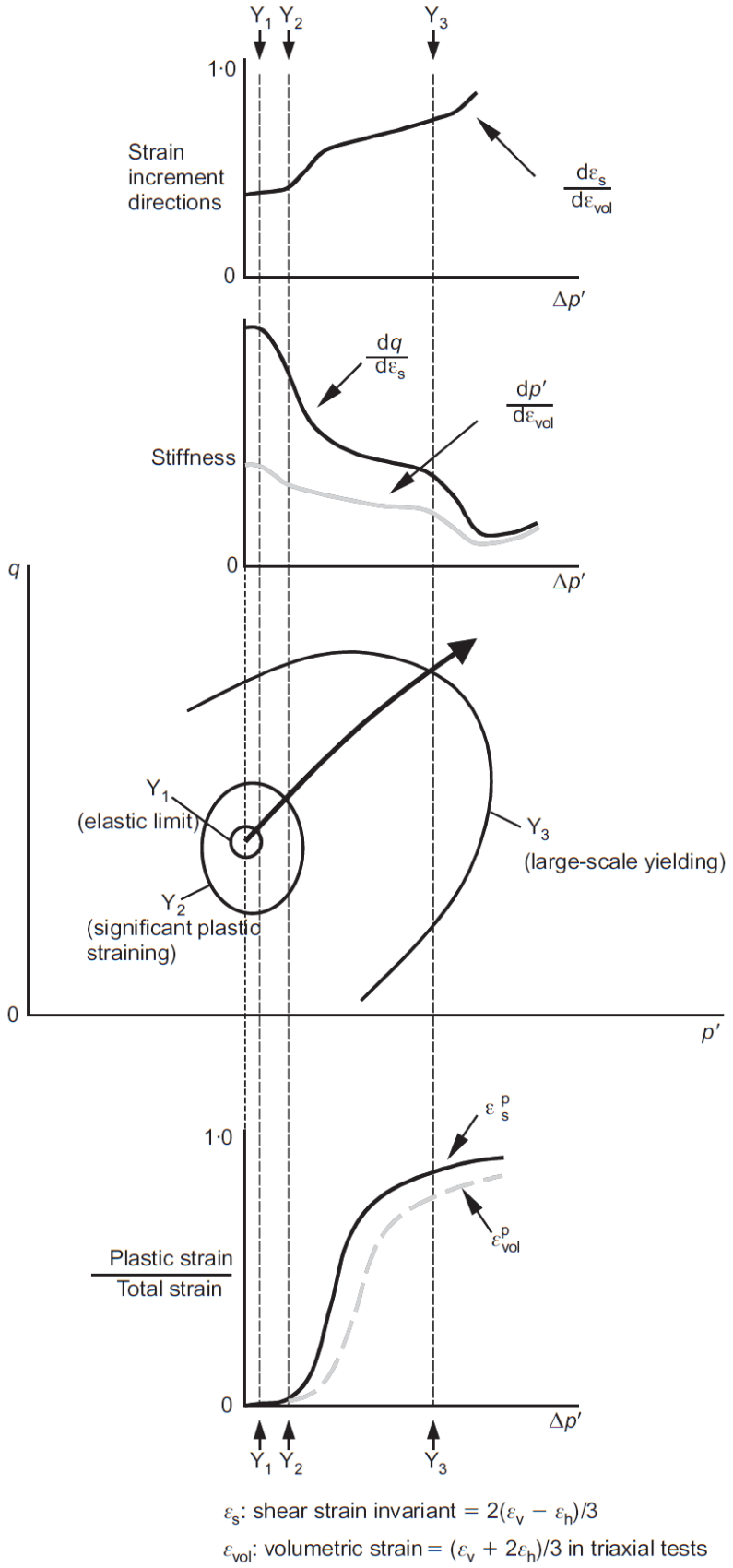

Figure 5-2 Multiple kinematic yield surface model (Jardine, 1992, Kuwano & Jardine, 2007)

5.3 Research programme and methodology

Accurate numerical modelling of boundary value problems such as laterally loaded piles, which apply a wide range of stress and strain changes in the surrounding soil mass, require advanced constitutive models that can capture and reproduce the soils' full-strain range behaviour. While site investigations using CPT or SCPT campaigns can produce important information on in-situ soil states and elastic shear stiffnesses, site-specific laboratory tests are also required to characterise soils' complex non-linear behaviour so allow constitutive models to be calibrated fully.

5.3.1 Research scope and aims

The initial scope (A) of the Author's programme conducted for the PISA project included:

A-1 Investigating the Batch 2 Dunkirk sand's highly non-linear and stress-dependent stiffness properties and exploring the effects of stress level, density and over-consolidation (in Chapter 5);

A-2 Depicting stiffness degradation trends over full strain range and characterising the sand's strain-dependent behaviour (in Chapter 5);

A-3 Establishing trends for (normalised) shear stress-strain responses, volumetric behaviour as well as stress-dilatancy relationships (in Chapter 6);

A-4 Investigating the sands' critical state behaviour and determining critical state line(s) (in Chapter 6);

A-5 Interpreting the test outcomes with the state parameter-based approach, in conjunction with the critical state framework (in Chapter 6).

The programme was extended subsequently to include the additional scope (B) elements:

B-1 Examining the potential differences of index properties and mechanical behaviour between the Batch 2 and Batch 3 Dunkirk sands (in Chapters 5 and 6);

B-2 Investigating the effects of end restraints on the stiffness, strength and critical state behaviour of sands in triaxial testing (in Chapters 5 and 6);

B-3 Characterising anisotropic linear elastic stiffnesses and deriving drained and undrained cross-anisotropic parameters (in Chapter 5);

B-4 Studying the sands' pre-failure yielding characteristics and depicted their kinematic yield surfaces (Y_1-Y_4) (in Chapter 5);

B-5 Exploring the long-term drained cyclic loading and post-cycling behaviour of Dunkirk sands (in Chapter 7).

5.3.2 Tested soils, index properties and methodology

Tested soils and gradings

As mentioned in Section 2.2.2, laboratory testing on Dunkirk sand had to focus on reconstituted materials collected from shallow pits (around 0.5 m) as the rotary coring attempted for the PISA Dunkirk site was unsuccessful. An additional post-PISA sampling campaign was proposed by the research team, but could not be accomplished within the project.

Nevertheless, Kuwano (1999) demonstrated that the index properties of the layers sampled in an earlier rotary drilling campaign showed only small variations within the range of 3.3-11.9 m depth. Differences in sand gradings appeared to be insignificant over the top 12 m deposit, as shown in Figures 2-8 and 2-9. Shallow samples collected at three locations and on different occasions also showed closely comparable gradings, suggesting relatively uniform sand composition across the site. It was suggested that soil properties and mechanical behaviours established from shallow samples could be extrapolated to represent the whole profile.

The above hypothesis was examined by parallel index property and triaxial tests on Batch 2 and Batch 3 samples by Vinck (2016) as part of his MSc research project, partly supported by the Author. Detailed comparisons are given in Sections 5.8 and 6.8 of the pre-failure stiffness, large strain behaviour and critical state lines associated with each batch.

Void ratio limits and relative densities

Table 5-1 summarises the limiting void ratios of the three batches of sands and the corresponding relative densities covered in the research programmes on Batch 1 by Kuwano (1999), Batch 2 by Aghakouchak (2015) and the Author, and Batch 3 by Vinck (2016) and the Author. All the triaxial tests reported involved samples reconstituted by air or water pluviation, and their relative densities covered the medium dense to very dense (R_d: 50-100%) ranges, regardless of the testing standards used to assess the sands' limiting void ratios.

Batch 2 samples were water pluviated to reach three levels of target void ratios: 0.587, 0.640 and 0.740, which correspond to relative densities of 95%, 79% and 50% respectively when the limiting void ratios (e_{max} and e_{min}) are determined as specified in BS 1337-4:1990.

The Batch 3 samples were prepared with two void ratios: 0.640 and 0.710, corresponding to relative densities of 92% and 73% respectively based on the e_{max} and e_{min} determined by Vinck (2016) following the JIS A1224 standard. Despite their similar grading curves, it is clear that quite different void ratio limits were observed for the Batch 2 and 3 sample.

Significant method-dependency exists when determining e_{max} and e_{min}, as has been widely recognised (see for example by Blaker *et al.* (2015)). A void ratio-controlled approach was adopted herein to ensure consistency and uniformity of the tested specimens.

Table 5-1 e_{max} and e_{min} of the three batches of Dunkirk sand and the typical relative densities of the tested specimens

Material	Batch 1[(1)]		Batch 2[(3)]				Batch 3[(3)]	
Method	BS		BS[(4)]		JIS A1224[(5)]		JIS A1224[(5)]	
Density	e	R_d [%]	e	R_d [%]	e	R_d [%]	e	R_d [%]
Minimum density (e_{max})	0.928[(2)]	0	0.910	0	0.918	0	0.980	0
Medium dense	0.686	60	0.740	50	0.740	52		
Dense			0.640	79	0.640	81	0.710	73
Very dense			0.587	95	0.587	96	0.640	92
Maximum density (e_{min})	0.528[(2)]	100	0.570	100	0.573	100	0.610	100

Notes:

[(1)]: Limit void ratio ranges for Batch 1 (3.30-11.9 m bgl.) material: e_{min}: 0.506-0.541; e_{max}: 0.881-0.942 (Kuwano, 1999);

[(2)]: Kuwano (1999)'s Batch 1 mixed C9 (5.85-6.2 m bgl.) + C15 (11.1-11.9 m bgl.) sand for triaxial probing tests;

[(3)]: Batches 2 and 3 collected from shallow pit (< 0.8 m);

[(4)]: Reported by Aghakouchak (2015);

[(5)]: Reported by Vinck (2016).

Research methodology

The main part of the testing programme was carried out with the '38 mm' Bishop-Wesley triaxial apparatus, while the triaxial probing tests were performed with the '100 mm' fully-instrumented apparatuses. Details of the apparatuses and their capabilities are given in Section 2.3.4. The suction cap and half-ball connection was employed throughout the Author's and Vinck (2016)'s '38 mm' triaxial tests for both compression and extension conditions, while platten types were varied for different testing purposes, as explained later.

Acknowledging the effects of specimen reconstitution method on sand behaviour, the water pluviation method was used throughout the programme on the Dunkirk Batch 2 and 3 sands to generate initial fabrics and structures that could represent the Dunkirk site's water bourne deposition environment (of hydraulic filling over marine sands). In the tests with the Batch 3 sand which included small proportions of (< 1%) fines and other particles that 'dissolved' in water and could not be fully transported to the mould, the water 'solution' was dried after setting-up and any left-over material was carefully collected and weighted. The results were used to re-calculate specimen initial void ratios.

5.3.3 Research programme completed

The research programme consisted primarily of suites of monotonic drained triaxial tests on 38 mm diameter reconstituted Dunkirk specimens that aimed to cover wide ranges of effective stress level, void ratio and over-consolidation ratio (*OCR*). The methodology and programme of the triaxial probing tests employing the '100 mm' apparatuses are detailed in a later Section 5.9.

The '38 mm' triaxial programme completed by the Author on Batch 2 Dunkirk sand was later extended comprehensively by Mr. Ken Vinck on Batch 3 material. Although the following interpretation and discussion is focused principally on the Author's Batch 2 tests in combination with earlier tests by Aghakouchak (2015), the tests on Batch 3 are also referred to for completeness.

Tables 5-2 and 5-4 provide detailed information regarding test code, void ratio (relative density), over-consolidation ratio (*OCR*), effective stress condition, shearing type, platten condition, apparatus used as well as test operator. Table 5-2 includes tests

on isotropically consolidated Batch 2 specimens completed by the Author, and Table 5-3 summarises anisotropically consolidated Batch 2 tests performed by both the Author and Aghakouchak (2015). The tests performed by Vinck (2016) and the Author on the Batch 3 material are summarised in Table 5-4. The main features of the testing programme and some of the key procedures are explained below.

Each test was named with a unique test code in the format of DKB2ICN25-79SR-DC or DKB2ICN25-79SR-DE, indicating the following meaning:

(a) DKB2 or DKB3, represent Dunkirk Batch 2 or Batch 3;
(b) The 5th and 6th letters, IC or KC, represent Isotropically Consolidation or anisotrpically (*K*) Consolidation;
(c) The 7th letters, N or O(m), signifies Normally consolidated or Over-consolidated specimens with an *OCR* of m;
(d) The following numbers, 25, 100 or 600, represents p' at the beginning of shearing;
(e) The followed numbers, -50, -79 or -95, represents specimens' initial relative density;
(f) The letters, SR, FR or OL, represent platten conditions of Semi-Rough, Fully-Rough or Over-sized fully Lubricated, respectively, as detailed below;
(g) The final set of letters, -DC, -UDC, -DC-dh or -DE, represent respectively shearing conditions of drained compression with increasing σ_v', undrained compression with increasing σ_v, drained compression with reducing σ_h', and drained extension with reducing σ_v'.

However, the codes for the tests reported by Aghakouchak (2015) were left as nominated in the latter's PhD thesis.

Determination of initial void ratio (e_0) and sample saturation

The initial void ratios were determined under 20 kPa suction (p' = 20 kPa) based on specimen dimensions (set of 9 diameter measurements and 3 height measurements at different locations). Also accounted for were the thicknesses of the membrane (with 20 measurements at different locations), lubrication disks (with sets of 4 measurements) as well as any material loss during set-up. The specific gravity of the materials were determined using the small pyknometer method (BS 1377-2:1990).

A constant p' of 20 kPa was maintained in the saturation stage. Desired *B* values of >

0.98 were readily achieved under 300 kPa back pressure, despite the possible inclusion of residual air bubbles in the nominally 'de-aired' water used.

Consolidation, creep and stress conditions

The fully saturated specimens were consolidated to target effective stress states in a stress-controlled manner at a rate of $\Delta\sigma_h'/\Delta t$ = 60 kPa/hour. Thereafter the specimens were left for a prolonged ageing period (usually 48 hours) over which the strain rates decreased to less than 0.002-0.01%/day, which were around 500-1000 times lower than the prescribed shearing rate of 5%/day. Specimen deformation was gauged from the local strain sensors over these stages.

A large proportion of specimens were isotropically consolidated to the target stress states that covered an effective stress range of 25-800 kPa. As shown later, the specimens sheared from isotropic stress conditions usually exhibited distinct contractive and dilative responses that allowed a more accurate calibration of the bounding surface plasticity model (Taborda *et al.*, 2014), although the tests conducted from isotropic stress states are less directly representative of the undisturbed in-situ conditions applying at the Dunkirk site, which has experienced normal consolidation under K_o conditions.

A constant axial strain rate of 5%/day was applied during shearing for all the tests performed. Most of the specimens were sheared under drained conditions while a small proportion were tested undrained. The high resolution axial local strain sensors deployed allowed the determination of axial stiffnesses (E_v' or E_v^u) and their degradation trends with high confidence. A single test, DKB2ICN100-50OL-DC-dh, was sheared in compression by decreasing σ_h' while maintaining constant σ_v'.

Impact of effective stress history and over-consolidation ratio

The impact of effective stress history was investigated by a set of specimens consolidated and swelled isotropically to give *OCR*s of 1, 4 or 12 and final mean effective stresses p_0' of 50, 100 and 150 kPa, as listed in Table 5-2. The potential effects of *OCR* on pre-failure stiffness behaviour are considered in this chapter. Later chapters report its influence on the large strain response (including failure) and on the response to drained cyclic loading.

The earlier tests identified in Table 5-2 were performed with rough plattens, while

other platten conditions were also investigated, as outlined below.

Effects of platten conditions

The effects of end constraints and platten configurations in triaxial testing have been highlighted in early studies by for examples Rowe & Barden (1964), Bishop & Green (1965) and Tatsuoka *et al.* (1984). However, most tests conducted for research or applied industrial projects employed rigid and rough plattens (typically with porous stones) to facilitate drainage. The potential effects of platten restraint, which varies with soil type, specimen size, test types and shearing conditions, are often overlooked. The Author's programme therefore investigated potential platten effects on the sands' full-strain behaviour.

Three types of platten configuration were implemented in the programme, including:

(a) A Semi-Rough (SR) configuration, which consisted of smooth perspex (R_{CLA} < 1 μm) cap mounted directly on the specimen top, and a standard rough porous stone (R_{CLA} around 10-15 μm) placed at the bottom. This non-symmetric configuration is commonly seen in triaxial tests involving one (usually bottom) drainage end. This configuration was adopted in the tests on dense and very dense (e_0 = 0.587, 0.640) specimens of both the Batch 2 and 3 sand.

(b) A Fully-Rough (FR) configuration, which was implemented by placing porous stones at both the top and bottom specimen ends, leading to symmetric, although aggravated, constraints at specimens' both ends. The set-up was only employed for the medium dense specimen (e_0 = 0.740, R_d = 50%) tests on the Batch 2 sand.

(c) An Over-sized fully Lubricated (OL) configuration. Both the specimens' top and bottom ends were lubricated by a lubrication disk consisting of two pieces of circular latex membrane sandwiched by thin layers of high vacuum grease. Rough porous stones were not used and drainage was allowed instead through a small (dimeter around 6 mm) polished brass porous stone positioned in the centre of the bottom platten. Both the smooth/polished base stainless platten and the smooth perspex top cap were made with enlarged diameters to accommodate around 13% radial strain before the specimen reached the platten edges. This configuration was employed for testing Batch 2 and Batch 3 specimens of all densities.

Local strain instruments are very important when quantifying the effects of end

configurations. The local strain sensors gauge the deformation of the specimen' central zone regardless of the platten conditions, and therefore provide strain that were representative of true soil behaviour. In the scenarios where the specimen height and volume could only be determined externally, significant material penetration into the lubricated latex membrane layers has to be considered and corrections made, as demonstrated by Kuwano (1999).

Testing apparatus and environment

Tables 5-2 and 5-3 list the apparatus used for each test, with ML1, ML2 and ML3 representing the three apparatuses located in the Main Laboratory and TL1 and TL2 indicating the two apparatuses in the Teaching Laboratory. The additional information is potentially useful when integrating test results from different labs and apparatuses, recalling the effects of temperature fluctuation discussed in Section 2.3.7. The test results from different apparatuses showed satisfactory consistency and most were believed to be only marginally affected by temperature variations. However, some tests carried out in the Teaching Laboratory exhibited inconsistent strain trends over certain periods when excessive temperature fluctuations occurred: these tests were discounted and repeated in the Main Laboratory.

Routine checks

Checks on the transducers, local strain sensors and temperature were carried out routinely to ensure suitably controlled conditions for the apparatuses and test environment. The axial LVDT sensors mounted at the diametrically opposite sides of the specimen served as good indicators of any imperfections that could occur during setting-up, load cell connection or subsequent testing, including specimen tilting or regularity, minor dislocation of the load cell, inclination of the top cap, unevenness of the porous stone or the lubricated disks.

In any case where uneven straining was proven, the test was repeated. Figure 5-3 demonstrates an example where significant disparities of local strain readings were seen with a specimen that experienced severe tilting. Also shown are the improved strain measurements from a re-test, representing stress-strain data that could be relied upon for the characterisation of the sand's small strain behaviour.

5.3.4 Summary tables

Table 5-2 Summary of the '38 mm' triaxial tests on isotropically consolidated Dunkirk sand Batch 2

Test code	Density			Stress condition/path			Shearing type	Platten condition	Device
	R_d [%]	e_0	e	(p_0, q_0) [kPa]	K	OCR			
DKB2ICN25-79SR-DC	79	0.635	0.635	(25, 0)	1	1	$+\sigma_v'$	SR	ML1
DKB2ICN50-79SR-DC	79	0.640	0.640	(50, 0)	1	1	$+\sigma_v'$	SR	TL1
DKB2ICO(4)50-79SR-DC		0.640	0.638			4			ML2
DKB2ICO(12)50-79SR-DC		0.642	0.639			12			ML1
DKB2ICN100-79SR-DC	79	0.641	0.639	(100, 0)	1	1	$+\sigma_v'$	SR	ML1
DKB2ICN100-79OL-DC		0.651	0.645					OL	ML2
DKB2ICN100-95SR-DC	95	0.584	0.584					SR	TL2
DKB2ICN100-95OL-DC		0.592	0.589					OL	ML1
DKB2ICN100-50FR-DC	50	0.734	0.730					FR	ML2
DKB2ICN100-50OL-DC		0.727	0.721					OL	ML1
DKB2ICN100-50OL-DC-dh	50	0.740	0.734				$-\sigma_h'$	OL	ML1
DKB2ICN100-79SR-DE	79	0.640	0.636				$-\sigma_v'$	SR	TL1
DKB2ICO100(4)-79SR-DC	79	0.636	0.630			4	$+\sigma_v'$	SR	TL2
DKB2ICO100(4)-95SR-DC	95	0.587	0.583					SR	TL2
DKB2ICO100(4)-50FR-DC	50	0.736	0.726					FR	ML2

Continued Table 5-2 Summary of the '38 mm' triaxial tests on isotropically consolidated Dunkirk sand Batch 2

Test code	Density			Stress condition/path			Shearing type	Platten condition	Device
	R_d [%]	e_0	e	(p_0, q_0) [kPa]	K	OCR			
DKB2ICN150-79SR-DC	79	0.641	0.637	(150, 0)	1	1	$+\sigma_v'$	SR	ML1
DKB2ICO(4)150-79SR-DC		0.640	0.632			4			
DKB2ICN200-50FR-DC	50	0.733	0.723	(200, 0)	1	1	$+\sigma_v'$	FR	ML1
DKB2ICN200-50OL-DC		0.736	0.729					OL	
DKB2ICN400-79SR-DC	79	0.642	0.633	(400, 0)	1	1	$+\sigma_v'$	SR	TL1
DKB2ICN400-79OL-DC		0.650	0.633					OL	ML2
DKB2ICN400-95SR-DC	95	0.585	0.576					SR	TL2
DKB2ICN400-95OL-DC		0.598	0.592					OL	ML1
DKB2ICN400-50FR-DC	50	0.728	0.714					FR	ML1
DKB2ICN400-50OL-DC		0.725	0.712					OL	ML1
DKB2ICN400-50FR-DE		0.740	0.723				$-\sigma_v'$	FR	TL1
DKB2ICN600-50FR-DC	50	0.731	0.707	(600, 0)	1	1	$+\sigma_v'$	FR	ML1
DKB2ICN600-50OL-DC		0.747	0.730					OL	

Table 5-3 Summary of the '38 mm' triaxial tests on anisotropically consolidated Dunkirk sand Batch 2

Test code	**Density**			**Stress condition/path**			**Shearing type**	**Platten condition**	**Device**	**Operator/ Source**
	R_d **[%]**	e_0	e	(p_0, q_0) **[kPa]**	K	OCR				
DKB2KCN75-79SR-DC	79	0.620	0.619	(75, 66)	0.45	1	$+\sigma_v'$	SR	TL2	Author
DK150C	79	≈0.640	-	(150, 138)	0.43	1	$+\sigma_v'$	SR	TL2	Aghakouchak (2015)
DK150E							$-\sigma_v'$			
DK300C				(300, 276)			$+\sigma_v'$			
DK300E							$-\sigma_v'$			
DK500C				(500, 460)			$+\sigma_v'$			
DK500E							$-\sigma_v'$			
DK-NC-CP	79	≈0.640	-	(506, 440)	0.45	1	$+\sigma_v$	SR	TL2	
DK-NC-ET							$-\sigma_v$			
DK-OC-CP				(167, 50)	0.75	4	$+\sigma_v$			
DK-OC-CP							$-\sigma_v$			

Table 5-4 Summary of the '38 mm' triaxial tests on Dunkirk sand Batch 3

Test code	Density			Stress condition/path			Shearing type	Platten condition	Device	Operator/ Source
	R_d [%]	e_0	e	(p_0, q_0) [kPa]	K	OCR				
DKB3ICN400-76SR-DC	76	0.698	0.682	(400, 0)	1	1	$+\sigma_v'$	OL	ML1	Author
DKB3KCN133-92OL-UDC	92	0.650	0.643	(133.3, 100)	0.5	1	$+\sigma_v$		ML2	
DKB3KCN133-76OL-DC	73	0.707	0.695	(133.3, 100)			$+\sigma_v'$		ML2	
DKB3KCN400-92OL-DC	92	0.651	0.638	(400, 300)			$+\sigma_v'$		ML1	
DKB3ICN25-69OL-DC	69	0.726	0.726	(25, 0)	1	1	$+\sigma_v'$	OL	TL2	Vinck (2016)
DKB3ICN50-84OL-DC	84	0.669	0.666	(50, 0)	1	1	$+\sigma_v'$	OL	TL2	
DKB3ICN50-65OL-DC	65	0.739	0.737						ML7	
DKB3ICN100-92SR-DC	92	0.633	0.628	(100, 0)	1	1	$+\sigma_v'$	SR	ML2	
DKB3ICN100-92OL-DC	92	0.636	0.632					OL	ML2	
DKB3ICN100-63OL-DC	63	0.746	0.742					OL	ML7	
DKB3ICN200-92SR-DC	92	0.640	0.633	(200, 0)	1	1	$+\sigma_v'$	SR	ML2	
DKB3ICN200-97OL-DC	97	0.623	0.612					OL	TL2	
DKB3ICN200-70OL-DC	70	0.722	0.710					OL	TL2	

Continued Table 5-4 Summary of the '38 mm' triaxial tests on Dunkirk sand Batch 3

Test code	Density			Stress condition/path			Shearing type	Platten condition	Device	Operator/ Source
	R_d [%]	e_0	e	(p_0, q_0) [kPa]	K	OCR				
DKB3ICN300-74OL-DC	74	0.708	0.688	(300, 0)	1	1	$+\sigma_v'$	OL	TL1	Vinck (2016)
DKB3ICN400-92SR-DC	92	0.638	0.620	(400, 0)	1	1	$+\sigma_v'$	SR	TL2	
DKB3ICN400-94OL-DC	94	0.631	0.619					OL	ML2	
DKB3ICN400-66OL-DC	66	0.737	0.715					OL	TL1	
DKB3ICN600-63OL-DC	63	0.747	0.722	(600, 0)	1	1	$+\sigma_v'$	OL	TL2	
DKB3ICN800-65OL-DC	65	0.741	0.709	(800, 0)	1	1	$+\sigma_v'$	OL	ML7	

Notes:

1. All specimens formed with the water pluviation method;
2. Relative density (R_d) determined based on the limiting void ratios listed in Table 5-1;
3. e_0: specimen void ratio after installation, determined under 20 kPa suction;
4. e: specimen void ratio after consolidated to target effective stresses;
5. Platten conditions:
   SR- standard size semi-rough platten
   FR- standard size fully-rough platten
   OL- over-sized fully lubricated platten
6. Device code:
   ML-Main Laboratory (three apparatuses: ML1, ML2, ML7)
   TL-Teaching Laboratory (two apparatuses: TL1, TL2).

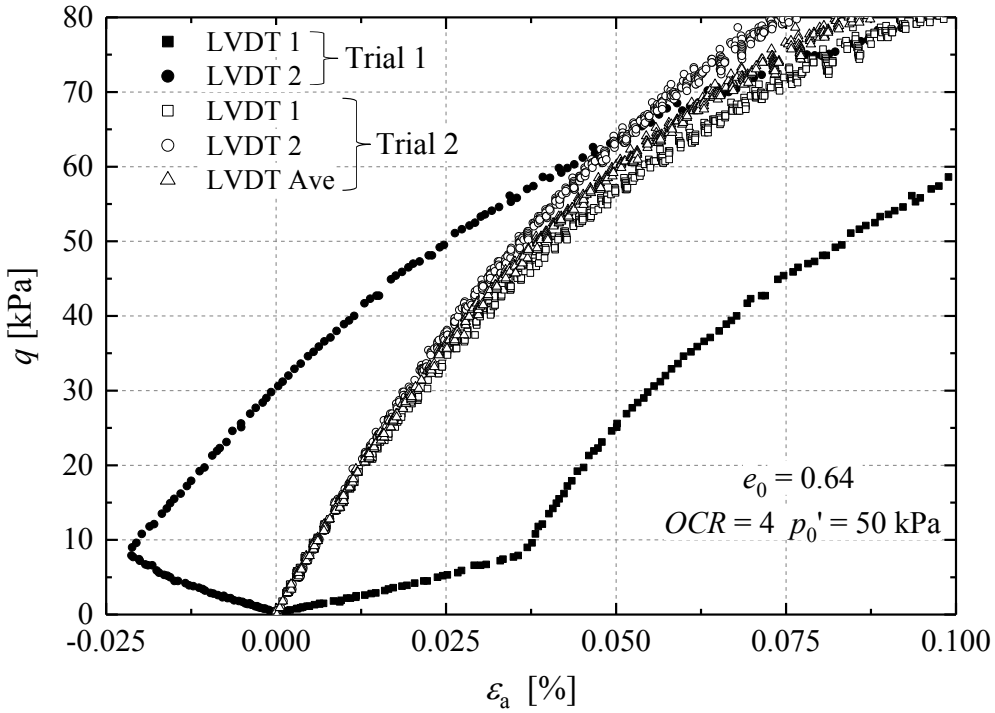

Figure 5-3 Significant disparities of local axial strain readings for a discounted test on a specimen experienced severe tilting, and the improved measurements obtained in a repeated test

5.4 Consolidation, swelling and creep characteristics

Following the above descriptions of the testing programme and methodology, this section presents results from the pre-shearing stages which comprise: consolidation, swelling and creep. The discussion focuses primarily on tests on Batch 2 Dunkirk sand performed after isotropic consolidation (K = 1) using the standard size non-lubricated plattens. Specimen deformation and volume changes were determined principally from local axial and radial strain sensors.

Specimen void ratio and compressibility

Figures 5-4 and 5-5 summarise the specific volume trends observed under isotropic consolidation for the medium dense specimens (target e_0 = 0.740) and the over-consolidated (OCR = 4 and 12) dense specimens formed with target initial void ratios of 0.640. The medium dense specimens showed greater variations in their initial void ratios as the target relative density (50%) approached the lower limit that can be achieved when reconstituting using the water-pluviation method. Nevertheless, the specimens showed satisfying uniformity and the (1+e)-p' trends to follow parallel curves. Volume changes continued to develop after each consolidation or swelling stage. The samples' creep trends are discussed in a later section.

The volume change characteristics were non-linear and stress-dependent. The log-linear compressibility indices λ and κ (defined as $\Delta v/\Delta\ln(p')$) observed under isotropic conditions for samples formed with three initial densities, are shown in Figure 5-6. The medium dense specimens (e_0 = 0.740) (unsurprisingly) showed higher compressibility, indicating more curved v-lnp' responses. As discussed in Section 4.2.1, far high pressures (around 10-30 MPa, see Coop & Lee (1993)'s triaxial tests on similar Ham River sand) are required to further cause the specimens to undergo particle breakage and converge towards any unified isotropic normal compression line (NCL),.

The local radial and axial strains developed along the isotropic consolidation stages are summarised in Figure 5-7. Isotropic stress increments led to compression strains that were clearly divergent from the equality (ε_r : ε_a = 1) expected for an isotropic material; the specimens developed radial strains that were around double the axial strains, regardless of the density and stress level. Recalling the discussion in Section 5.2.1, it is commonly reported that water or air pluviated specimens possess an inherently anisotropic structure, manifesting as lower post-consolidation horizontal than vertical

Young's moduli (E_v' and E_h'). The grains' preferred structure of horizontally layering and vertical stacking is more susceptible to horizontal compression, leading to greater radial strains and potentially more enhanced particle contacts and fabric in the horizontal plane, and higher shear stiffness G_{hh} than for the G_{vh} mode.

Accumulated creep strains

Previous studies by, for example, Kuwano & Jardine (2002a) have highlighted the factors that affect the rate and magnitude of residual creep straining of granular materials. The discussion below focuses on specimens that were isotropically consolidated at a constant rate of 60 kPa/hour, before sustaining at least 48 hours creep.

Figure 5-8 summarises the trends for accumulated axial and volumetric creep strains ($\varepsilon_{vol} = \varepsilon_a + 2\varepsilon_r$) developing in the medium dense (R_d = 50%) specimens. The ratio of radial to axial strains fell markedly to around unity or below during the creep stages. The residual axial strains appeared to be settled more rapidly and to be less dependent on effective stress level, whereas the volumetric strains (and therefore the radial strains) showed a trend to increase with stress levels. The ratio between the 48-hour radial and axial creep strain ($\Delta\varepsilon_r^{creep}/\Delta\varepsilon_a^{creep}$) was around 0.7 under p_0' = 100 kPa but increased to close to 1 under p_0' = 600 kPa. Figure 5-9 compares the volumetric creep strains for the medium dense and dense (R_d = 79%) specimens. Less remarkable, but broadly comparable stress-dependent creep strain trends were observed with the denser specimens.

The absolute magnitudes of 48-hour creep straining increased consistently with stress level. Figure 5-10 demonstrates the ratios between 48 hours accumulated axial creep strains (ε_a^{creep}) holding at a constant σ_v' to the consolidation axial strains (ε_a^{con}) generated as vertical effective stress raised from 20 kPa to σ_v'. Both the consolidation and creep axial strains increased with effective stress levels, leading to overall decreasing $\varepsilon_a^{creep}/\varepsilon_a^{con}$ trends. As expected, the medium dense specimens exhibited higher strain ratios than the denser specimens. The results also indicate the percentage of underestimation of long term axial strains that would have taken place if the specimens had been allowed for 48 hours creep. Such tests would have given significantly different stiffness, shear strength and cyclic shearing behaviours.

Creep strain rates

The creep strain trends (ε^{creep}-t) were fitted with high-order (> 6) polynomial functions, which were then differentiated by time to derive the tangent strain rates. Figure 5-11 demonstrates how the tangent axial creep strain rates reduced systematically with time after the end of isotropic loading, adopting double-logarithmic axes.

The trends exhibited relatively high creep strain rates over the early stages of creep (< 1 hour), after which the rates decayed and the $d\varepsilon^{creep}/dt$-t trends followed approximately power law functions.

The above trends demonstrate the dependency of creep strain rate on effective stress level and specimen density. Creep rates generally increased with the effective stress level and void ratio (decrease of density).

Effects of platten configuration

The above interpretation and discussion are based on the tests performed with non-lubricated plattens of standard size. The tests employing fully lubricated over-sized plattens and conducted under equivalent conditions revealed no clear difference of consolidation or creep characteristics that could be related to platten conditions. Deformations and volume changes determined from local strain measurements made over the specimens' central volumes, do not appear to have been constrained unduly under isotropic loading conditions by friction at the specimen ends.

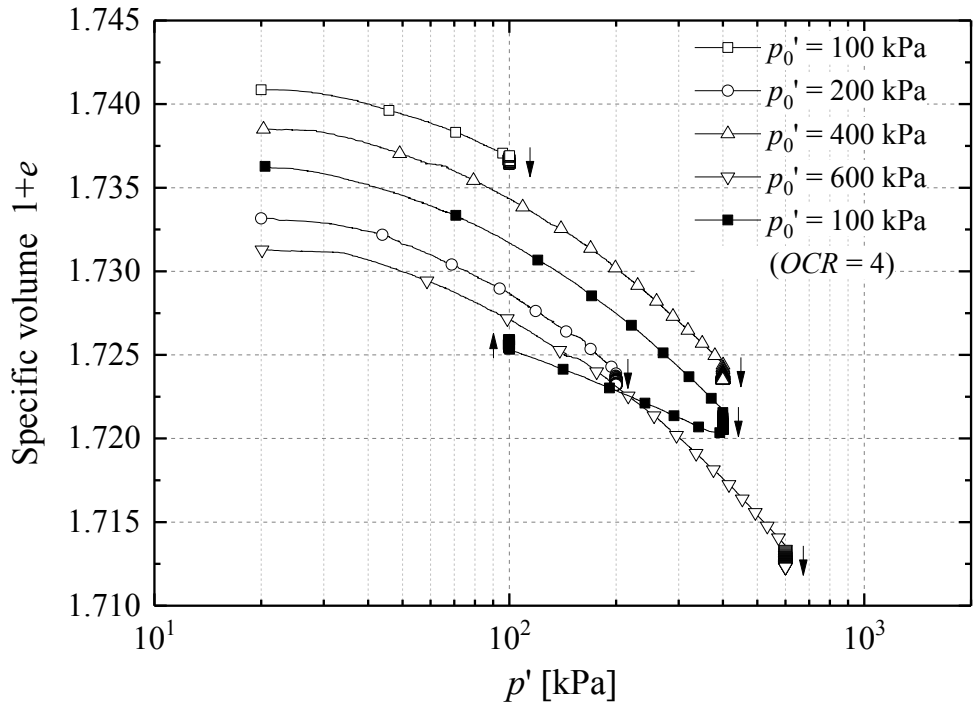

Figure 5-4 Specific volume change during isotropic compression and swelling of medium dense (R_d = 50%, e_0 = 0.740) Dunkirk sand Batch 2 specimens

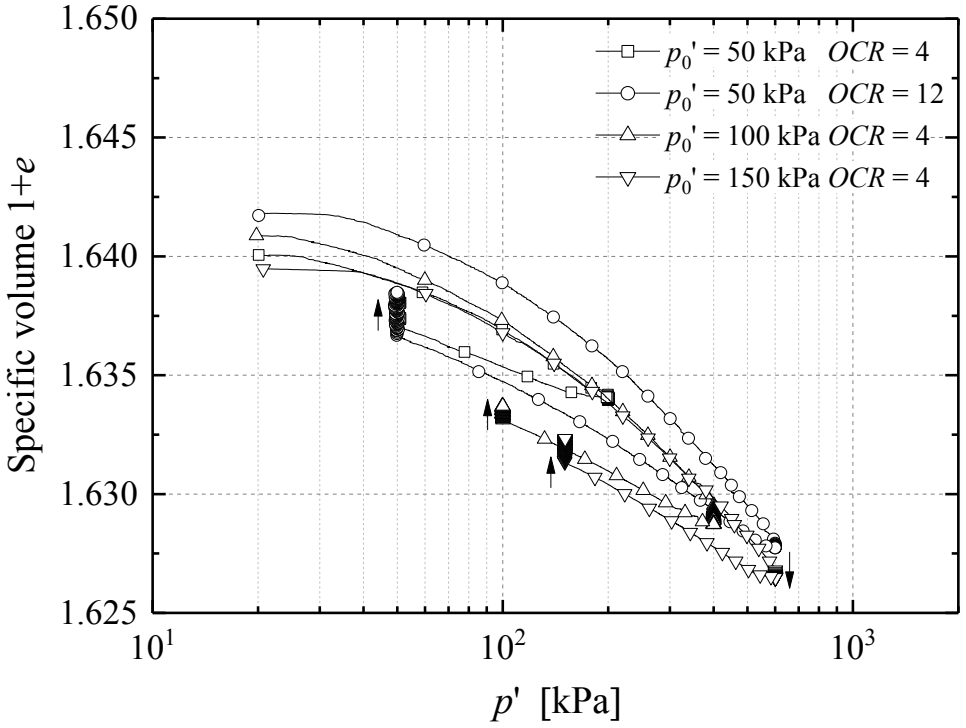

Figure 5-5 Specific volume change during isotropic compression and swelling of dense (R_d = 79%, e_0 = 0.640) Dunkirk sand Batch 2 specimens

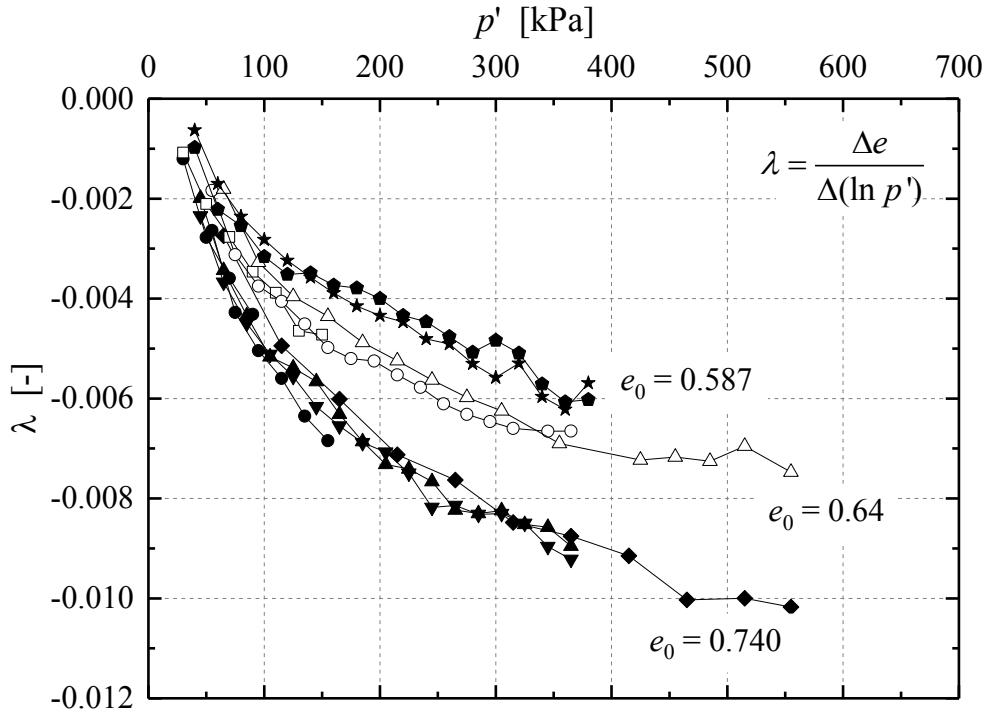

Figure 5-6 Compressibility change during isotropic compression of Dunkirk sand Batch 2 specimens of different initial densities

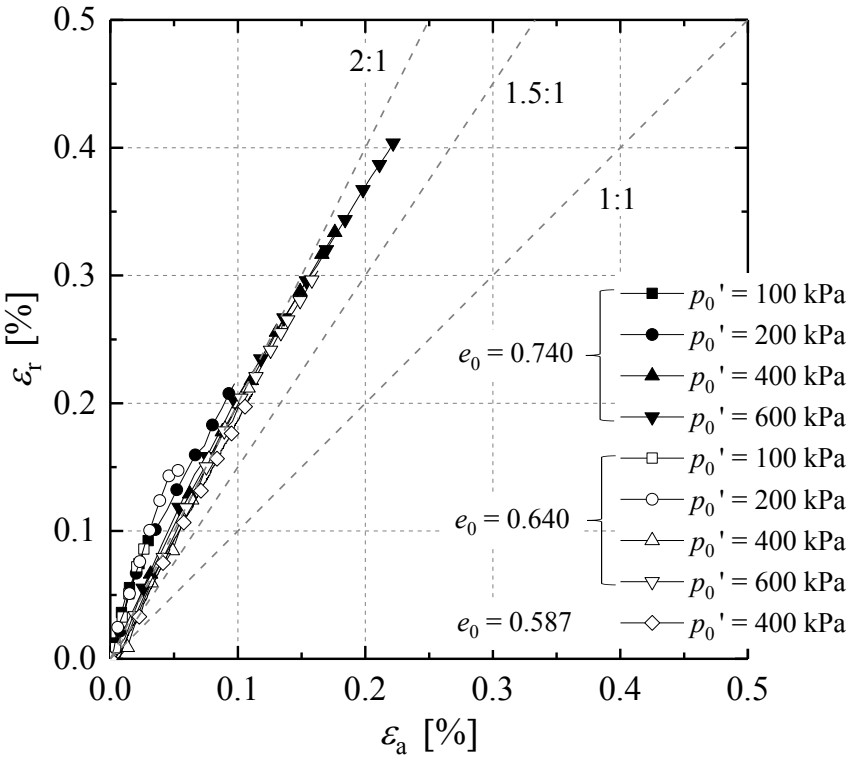

Figure 5-7 Local radial and axial strains developed during isotropic compression of water pluviated Dunkirk sand specimens

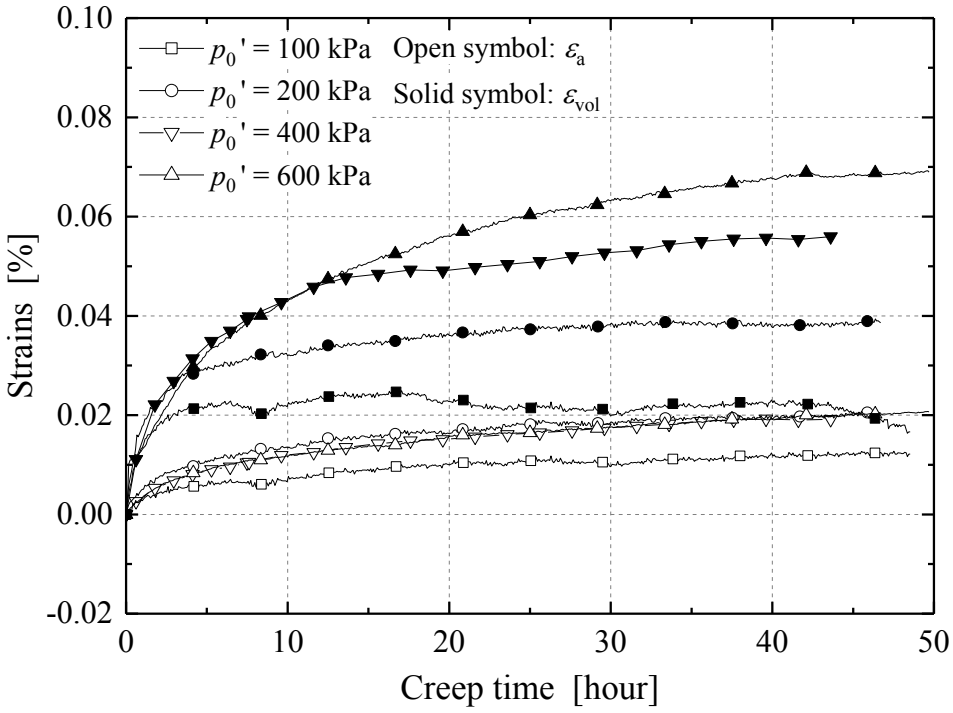

Figure 5-8 Development of accumulated axial and volumetric creep strains of the medium dense (R_d = 50%, e_0 = 0.740) Dunkirk specimens consolidated to different effective stress levels

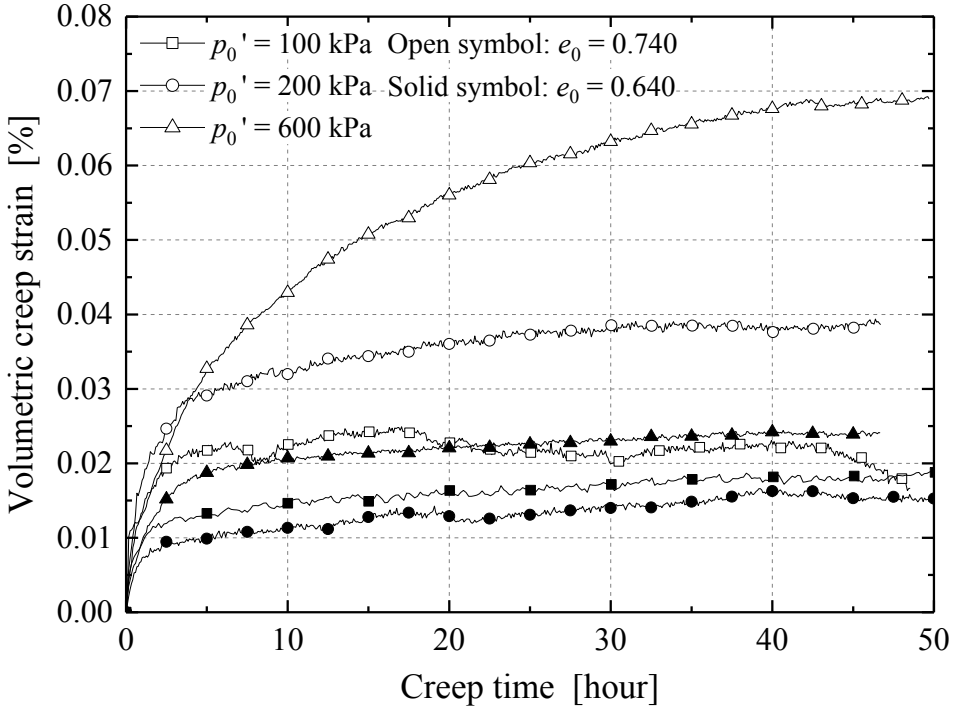

Figure 5-9 Effects of specimen density and effective stress level on the magnitude of accumulated volumetric strains

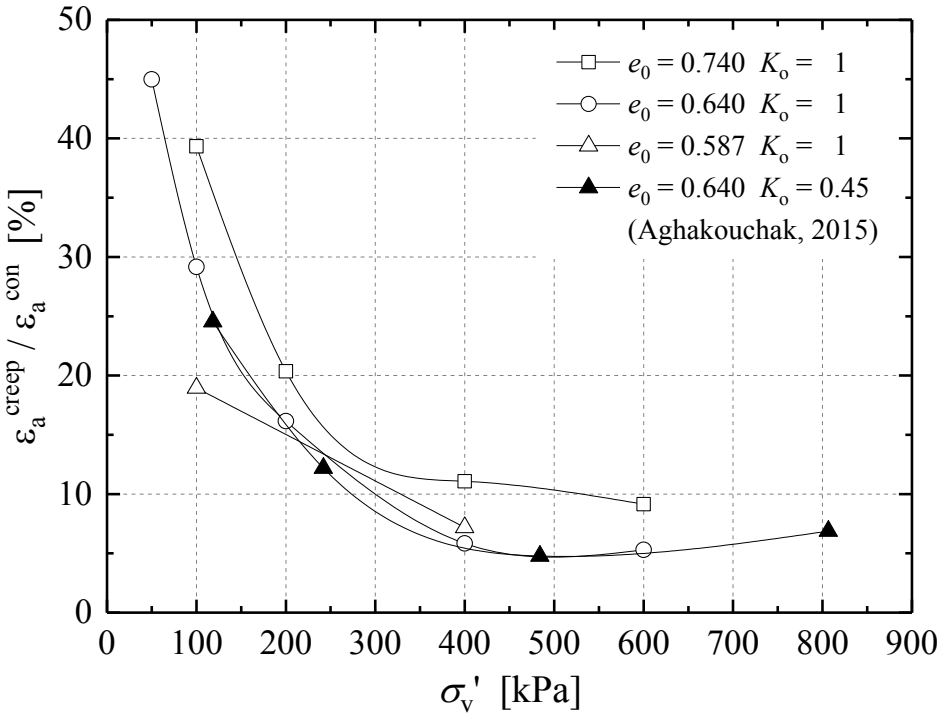

Figure 5-10 Ratios between 48 hours accumulated axial creep strains (ε_a^{creep}) holding at σ_v' to the consolidation axial strains (ε_a^{con}) generated as vertical effective stress raised from 20 kPa to σ_v'

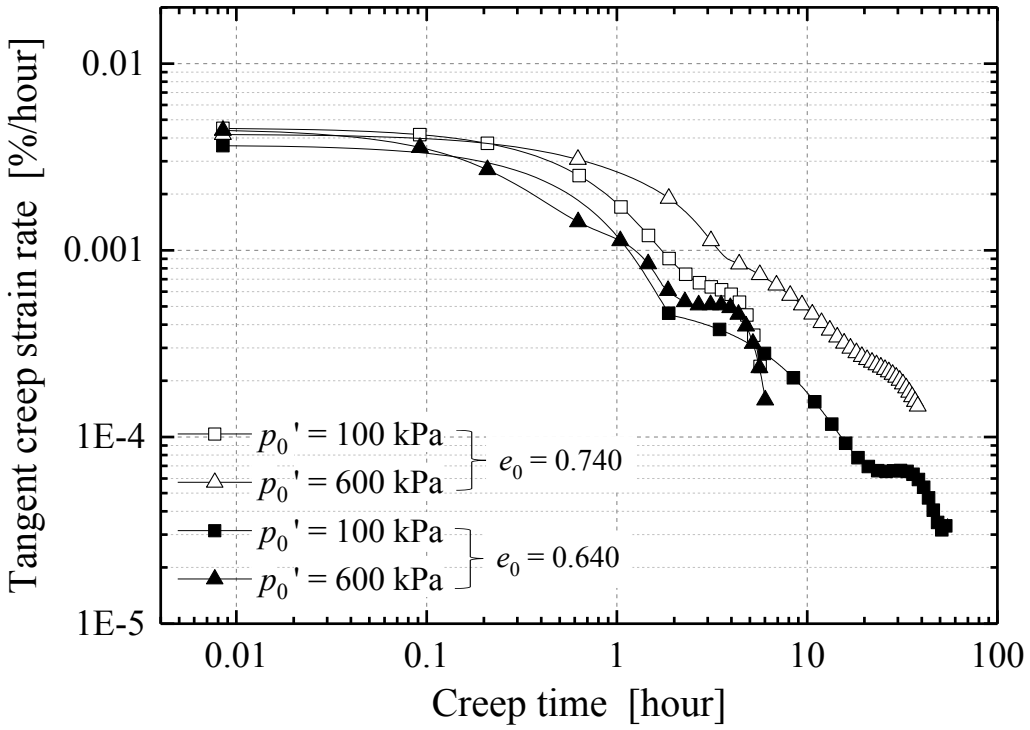

Figure 5-11 Degradation trends of tangent axial creep strain rate against time

5.5 Characteristics of pre-failure stiffness of Dunkirk sands

As shown in Tables 5-2 and 5-4, most of the Author's tests were sheared monotonically by applying only positive or negative axial stress changes, enabling the determination of uniaxial stiffnesses (Young's modulus, E_v' or E_v^u) with the aid of high resolution axial LVDTs. This section summarises the elastic response observed at very small strains and full-strain range axial stiffness degradation trends for the Batch 2 Dunkirk sand, followed by detailed discussion of its linear and non-linear stiffness characteristics.

The tests reported in this section were performed with standard size non-lubricated plattens, while the effects of platten configuration on small strain stiffness are further discussed in Section 5.6. The datasets presented formed the basis for calibrating elastic stiffness parameters and stiffness degradation trends in the bounding surface plasticity model applied to model the PISA test piles at Dunkirk (Taborda *et al.*, 2014, Taborda *et al.*, 2018). Further interpretation follows in Section 5.7 regarding the sand's kinematic yielding behaviour, also accounting for possible effects of end restraints.

5.5.1 Full-strain stiffness degradation trends

Derivation of vertical stiffness over small strain range

Tangent vertical Young's moduli ($E_{v,tan}'$ or $E_{v,tan}^u$) are employed below to represent the sand's axial stiffness under triaxial compression and extension.

The tangent Young's moduli, $E_{v,tan}$ (defined as $dq/d\varepsilon_a$) were determined with a combined approach of linear regression and multiple-section polynomial curve fitting. The initial section of q-ε_a data was plotted at a natural scale, and the quasi-elastic range was identified (by eye) as the point where the q-ε_a trend started to curve. Linear regression was then performed over the defined elastic range to derive the initial, linear, Young's modulus. The non-linear q-ε_a data were divided into several (usually 3-4) sections with certain lengths of overlap between consecutive sections. High order polynomial curve fitting was conducted for each section and the tangent Young's moduli were attained by differentiating the fitted functions. Trial and error checks were required to obtain smooth transitions between adjacent sections. In most cases, the derived stiffness degradation trends were found to be unaffected by the order (N) of the polynomial fitting curves employed once N exceeded 5.

The derived vertical Young's moduli variations with local axial strains (ε_a) represent

the sand's stiffness degradation. The axial strain component was chosen as the main strain parameter since: (i) it represents the "predominant" influential strain under axial stress changes and leads to clearest degradation trends of the vertical Young's moduli; (ii) other strain parameters, for example triaxial shear strain ε_s (= $2/3\times(\varepsilon_a - \varepsilon_r)$), involve the radial strain component, the measurements of which, however, were less reliable in some cases.

An average Poisson's ratio ν_{vh}' (= $-d\varepsilon_r/d\varepsilon_a$) of 0.18 was obtained from the Author's compression tests on medium dense and dense specimens over their initial elastic ranges up to the Y_2 yielding point (as later discussed in Section 5.7). The ratio is close to the value of 0.17 employed by Taborda *et al.* (2018) in the numerical modelling of PISA Dunkirk pile tests.

Effects of effective stress level

Starting with the normally consolidated specimens tested under a range of effective stress levels, Figures 5-12 and 5-13 plot the degradation trends for tangent vertical stiffness ($E_{v,tan}'$) up to 10% axial strain of the medium dense and dense specimens, respectively. The quasi-linear elastic range (Y_1) identified for each test is shown in the plots as the initial plateau section of each curve generally extended to 0.002-0.006% axial strains. Stiffness drops were often observed following the initial plateaux, which reflected sharp curvature of the q-ε_a trends and material yielding after exceeding the linear range.

The attained axial Young's moduli were clearly dependent on the effective stress level over both the linear and non-linear ranges. The linear elastic ranges extended slightly with increases in p_0' and specimen density. Further interpretation is included in Section 5.7 regarding the location and size of the elastic (Y_1) and larger strain yielding loci under various testing conditions.

The triaxial extension tests ($-\sigma_v'$) gave linear elastic axial Young's moduli that were close to those found in compression ($+\sigma_v'$) tests, but presented steeper non-linear stiffness degradation trends, reflecting the anisotropic behaviour of the Dunkirk sand at larger strains, which like most pluviated granular assemblies that give markedly earlier yielding under extensional loading (Kuwano & Jardine, 2007).

Effects of specimen density

The effects of specimen density on axial Young's moduli are evident in Figures 5-14 and 5-15, plotting stiffness degradation trends of the specimens of varied densities under p_0' = 100 kPa and 400 kPa, respectively.

The stiffnesses of the compression tests under p_0' = 100 kPa showed largely convergent trends after exceeding axial strains of around 0.01%. More widely spread stiffness trends were observed for the three tests with higher p_0' of 400 kPa and only the two relatively high density specimens exhibited convergent trends after 0.2% axial strain.

Effects of stress history and OCR

As listed in Table 5-2 the effects of over-consolidated stress history were examined at p_0' = 50, 100 and 150 kPa. Figures 5-16 and 5-17 summarise degradation trends of the tangent Young's moduli ($E_{v,tan}'$) normalised by a void ratio function $f(e)$ (= $(2.17-e)^2/(1+e)$) proposed by Hardin & Richart (1963).

Considering samples tested from equivalent stress conditions, the effects of over-consolidation on linear elastic stiffness appeared relatively minor, with over-consolidation giving initial $E_{v,tan}'$ values that differed by only 5%, which may be of a comparable range to the uncertainties involved in determining linear elastic stiffnesses under the conditions applied. However, over-consolidation extended the linear elastic range, giving longer initial tangent stiffness plateaux, particularly with the medium dense (R_d = 50%) specimens tested from low p_0' that led to markedly more gradual stiffness decay with strain.

It should be noted that the effects of *OCR* on axial stiffnesses cannot be explained by void ratio variations. As noted in Table 5-2, the void ratio variations between normally and over-consolidated specimens were minimal, and the above stiffness trends cannot be brought to convergent trends by applying any form of accepted void ratio function. The significant effects of *OCR* on the linear range and non-linear stiffness curves are linked to changes to contacts and micro-structures within the granular assemblies, which were accompanied by minimal volume changes.

Studies of site conditions that rely solely on linear elastic stiffness as assessed from in-situ tests or dynamic laboratory tests and then apply stiffness-strain degradation curves that are independent of stress history could not capture the potential effects of *OCR* on non-linear stiffness behaviour.

Interestingly, the heavily over-consolidated (OCR = 12) dense specimen with p_0' = 50 kPa showed stiffness trend that was located in between the OCR = 1 and 4 tests, which may be due to anisotropic axial and radial straining during the isotropic stages of consolidation, swelling and creep. Further laboratory or micro-mechanical numerical studies are required to further investigate the stiffness behaviour of heavily over-consolidated granular materials.

5.5.2 Stress-dependency of linear and non-linear stiffnesses

The characteristics of stress- and strain-dependent stiffness are further explored by correlating normalised vertical tangent Young's moduli ($E_{v,tan}'/f(e)$) with normalised vertical effective stress (σ_v') at four small axial strain levels (ε_a = 0.001%, 0.01%, 0.1% and 1%). As discussed in the introduction and implied by Equation (5.1), the E_v' moduli were considered independent of σ_h' under the conditions considered.

The $[E_{v,tan}'/f(e)]$-$[\sigma_v'/p_r]$ trends for the normally consolidated and over-consolidated tests are plotted in Figures 5-18 and 5-19, respectively. Also indicated in the plots are the coefficients C_v, a_v and R^2. The best fitting coefficient a_v for the over-consolidated tests were slightly higher than the normally consolidated specimens, reflecting the effects of stress history and OCR as previously discussed. The stiffness coefficients C_v (= 170.4 MPa) for the OCR = 1 tests were lower than those reported for air-pluviated Ham River sand (C_v = 204.0 MPa) and Batch 1 Dunkirk sand (C_v = 225 MPa) by Kuwano (1999) from triaxial probing tests, although the exponents a_v were close (≈0.52). Further interpretation and discussion on these aspects are presented in Section 5.9.

Similar approaches are adopted to interpret the tests on anisotropically consolidated (K = 0.45) specimens, as shown in Figure 5-20. Over the initial linear elastic ranges (ε_a = 0.001%), comparable but higher C_v coefficient was obtained for the K = 0.45 tests than that for the isotropoic (K = 1) tests, which suggests a moderate dependency of C_v on K, as further addressed in Section 5.9. Markedly lower C_v and higher a_v coefficients were observed in the larger strain range of the K = 0.45 tests, reflecting more abrupt non-linear stiffness degradation as the samples were sheared in compression from anisotropic initial effective stress states that were closer to the failure envelope.

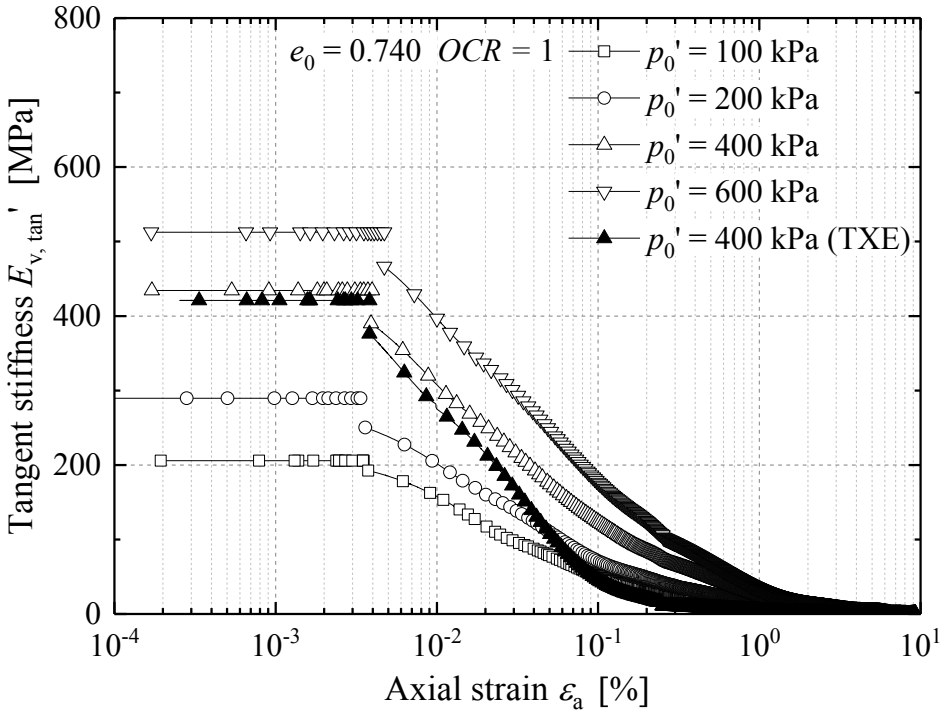

Figure 5-12 Tangent vertical stiffness ($E_{v,tan}'$) degradation trends for the normally consolidated medium dense (e_0 = 0.740, R_d = 50%) Batch 2 Dunkirk sand

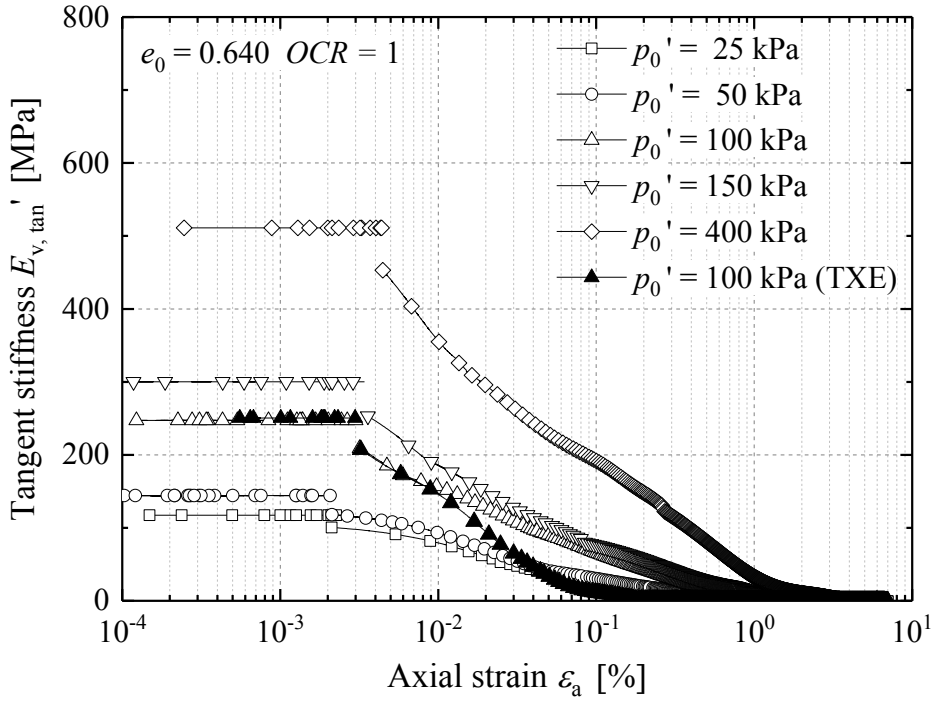

Figure 5-13 Tangent vertical stiffness ($E_{v,tan}'$) degradation trends for the normally consolidated dense (e_0 = 0.640, R_d = 79%) Batch 2 Dunkirk sand

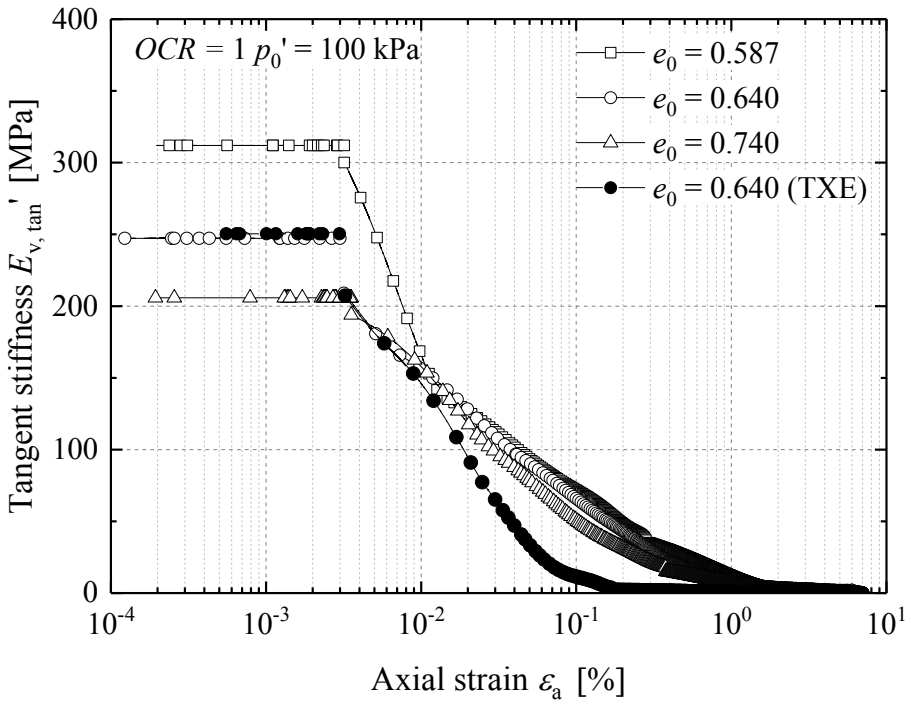

Figure 5-14 Tangent vertical stiffness ($E_{v,tan}'$) degradation trends for the normally consolidated Dunkirk sand Batch 2 specimens at three densities with p_0' = 100 kPa

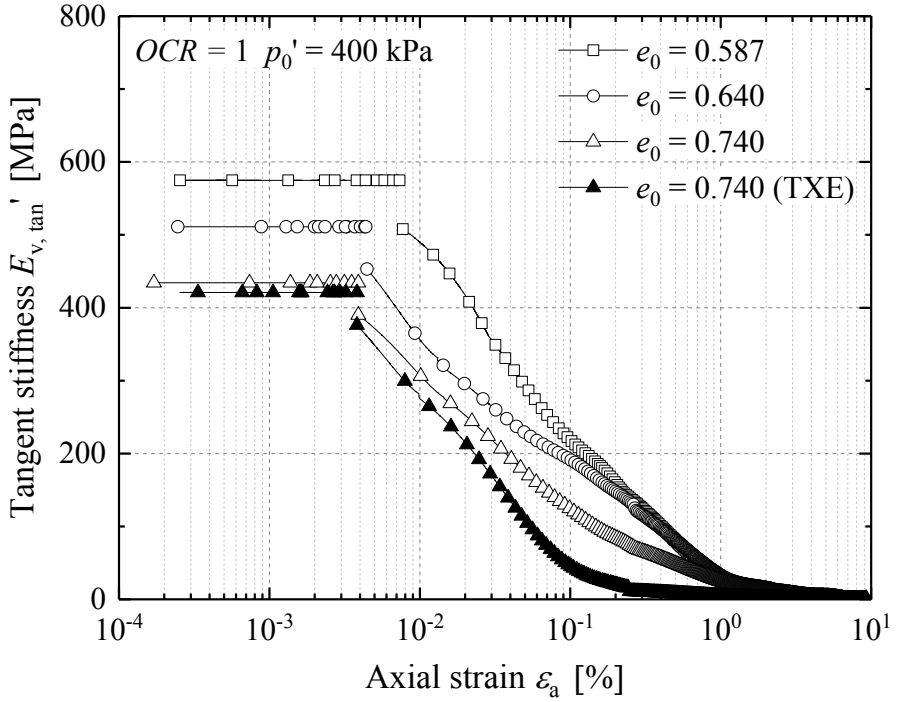

Figure 5-15 Tangent vertical stiffness ($E_{v,tan}'$) degradation trends for the normally consolidated Dunkirk sand Batch 2 specimens at three densities with p_0' = 400 kPa

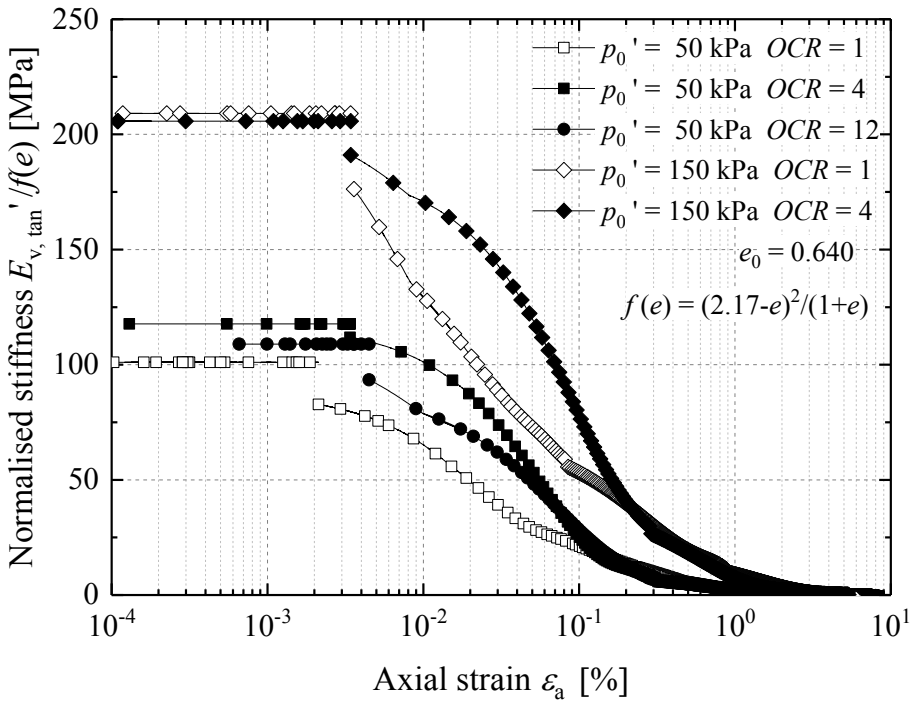

Figure 5-16 Normalised tangent vertical stiffness ($E_{v,\tan}'$) degradation trends for the Dunkirk sand Batch 2 specimens of varied *OCR*s (e_0 = 0.640, p_0' = 50 kPa and 150 kPa)

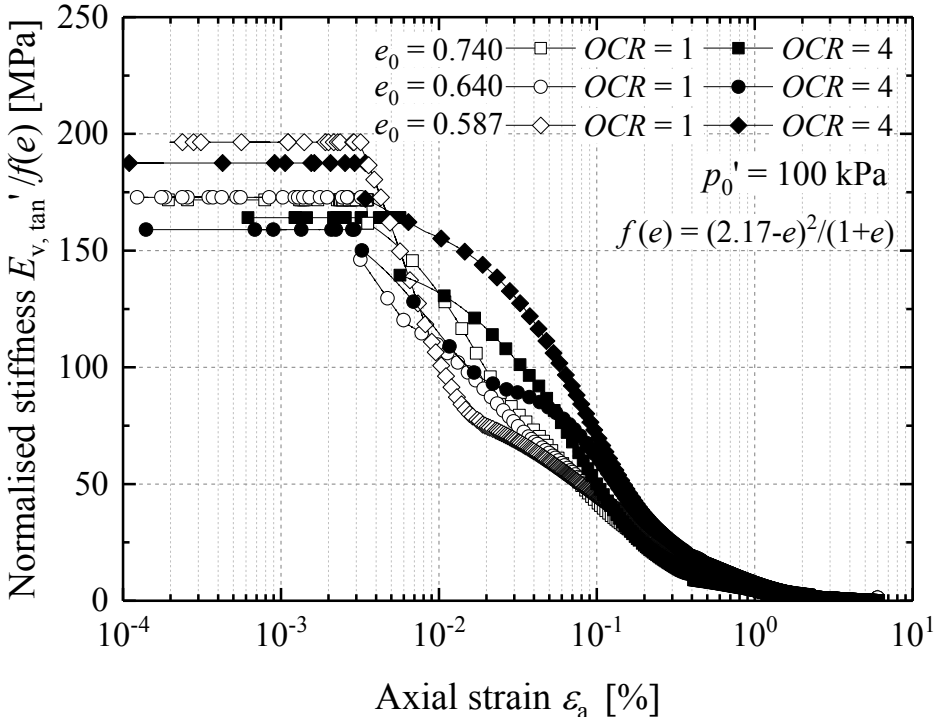

Figure 5-17 Normalised tangent vertical stiffness ($E_{v,\tan}'$) degradation trends for the Dunkirk sand Batch 2 specimens of varied densities and *OCR*s (p_0' = 100 kPa)

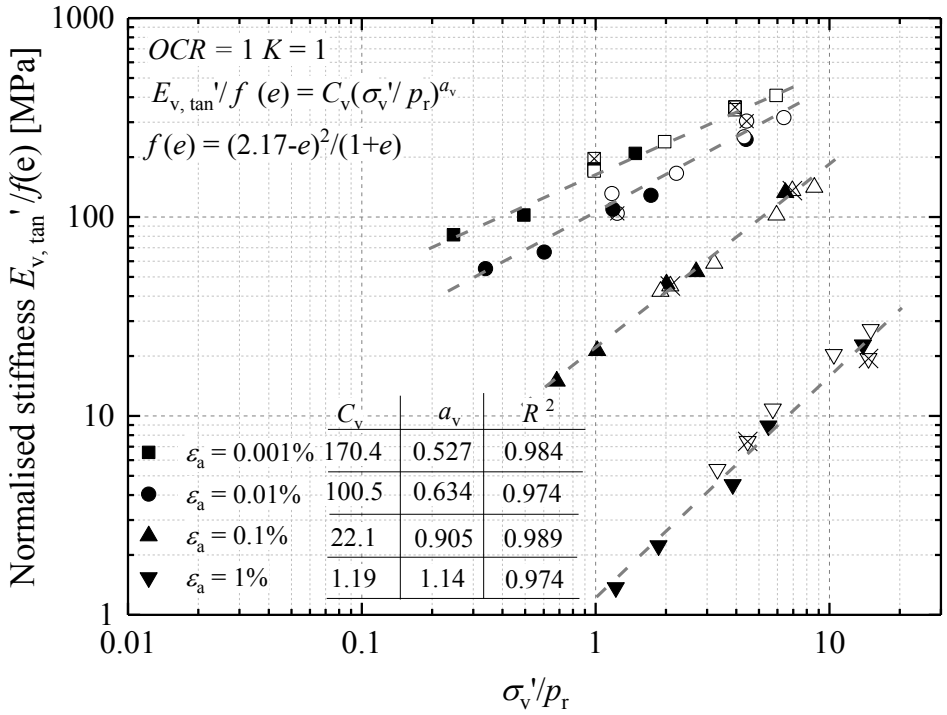

Figure 5-18 Normalised compression tangent stiffness $E_{v,tan}'/f(e)$ against normalised vertical effective stress σ_v'/p_r for the normally consolidated specimens

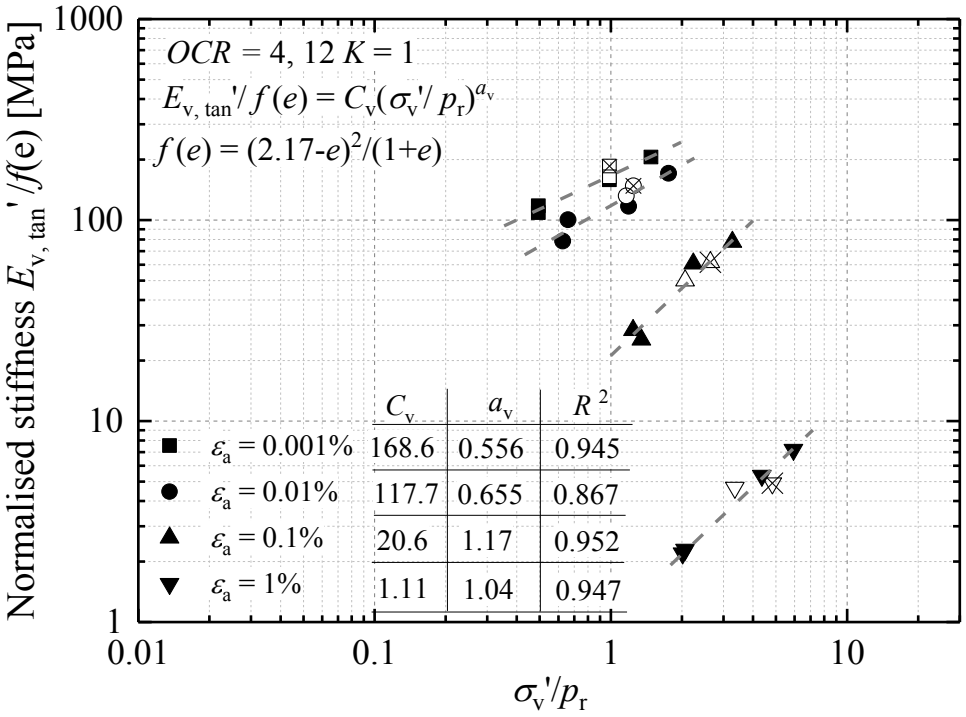

Figure 5-19 Normalised compression tangent stiffness $E_{v,tan}'/f(e)$ against normalised vertical effective stress σ_v'/p_r for the over-consolidated specimens

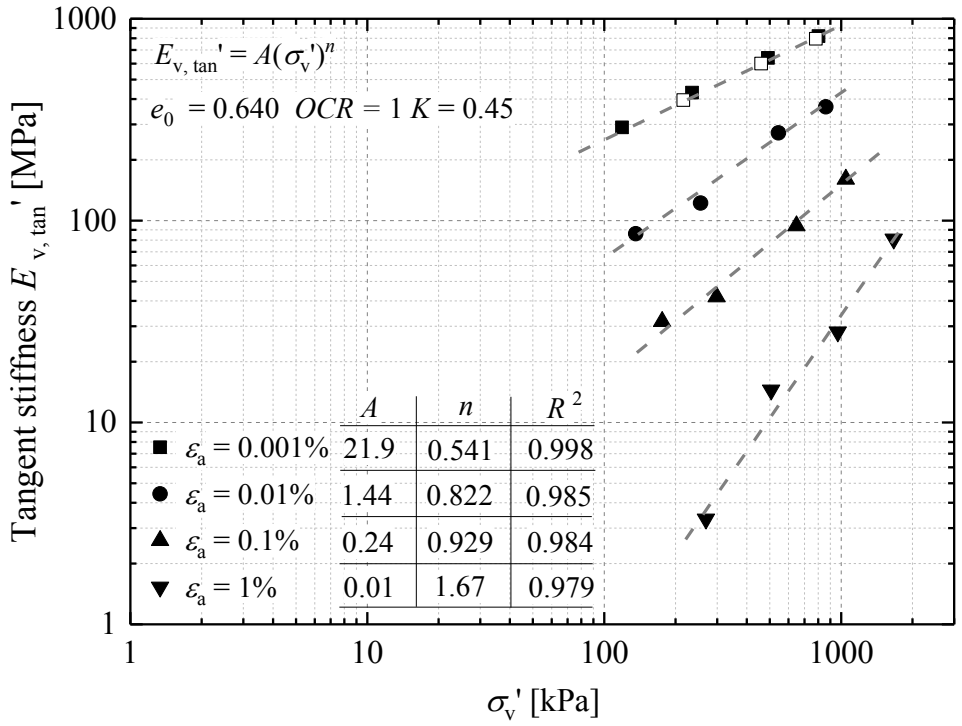

Figure 5-20 Normalised compression tangent stiffness $E_{v,\tan}'/f(e)$ against normalised vertical effective stress σ_v'/p_r for the anisotropically (K = 0.45) consolidated specimens (part of the test results reprocessed from Aghakouchak (2015))

5.6 Effects of platten configuration on pre-failure stiffnesses

As outlined in Table 5-2, parallel tests were performed using over-sized lubricated plattens to investigate the effects of platten constraint on full-strain stress-strain and stiffness behaviour.

Standard size fully-rough plattens with porous stones placed at both specimen base and top were employed in the tests on the medium dense (R_d = 50%) specimens, while the semi-rough plattens with rough porous stone at the base and relatively smoother perspex top cap were adopted for testing the dense (R_d = 79%) and very dense (R_d = 95%) samples. Parallel tests were performed using the over-sized fully lubricated plattens to check any dependency of end restraint on effective stress level and specimen density.

The trends for normalised tangent Young's moduli $E_{v,tan}'/f(e)$ of the medium dense specimens (e_0 = 0.74) testing with standard size fully-rough (porous stones placed at both base and top ends) and over-sized fully lubricated plattens are compared in Figure 5-21 at four strain levels. At strain level of 0.001%, the trend for the tests with rough platten (denoted as solid symbols in the figure) plots above the trend with lubricated plattens. Similar curve fitting exercises to that in Section 5.5.2 led to C_v = 172.8 MPa and a_v = 0.499 for the rough end trend, in comparison with C_v = 126.7 MPa and a_v = 0.551 for the lubricated end trend, suggesting end restraints resulted in surprisingly 36% higher elastic (ε_a = 0.001%) vertical stiffnesses under largely equivalent effective stresses and void ratios. However, the trends gradually converged as the axial strains increased, indicating strain-dependent end constraint effects.

Less significant effects were noted in the tests on very dense (e_0 = 0.587, R_d = 95%) and dense (e_0 = 0.640, R_d = 79%) specimens, as shown in Figure 5-22, and the influence of platten constraint appeared to be density dependent. However, the plattens employed in these tests were essentially semi-rough, it is likely more significant differences in stiffnesses could emerge if the tests were performed with the fully-rough plattens as used for the above tests on medium dense specimens.

Figure 5-23 plots overall normalised stiffness trends for the tests performed with lubricated ends, in contrast with those with (semi- or fully-) rough plattens as seen in Figure 5-18. The tests with rough plattens exhibited higher coefficients of C_v and slightly lower a_v values, particularly at the 0.001% and 0.01% strain levels.

The effects of the platten restraints could have been more prominent in low density states and under lower effective stress level because under these conditions, the sand grains possess more freedom to rotate and rearrange. Denser states and higher stresses may lead to grains being significantly constrained by neighbouring particles and so less prominently affected by platten roughness.

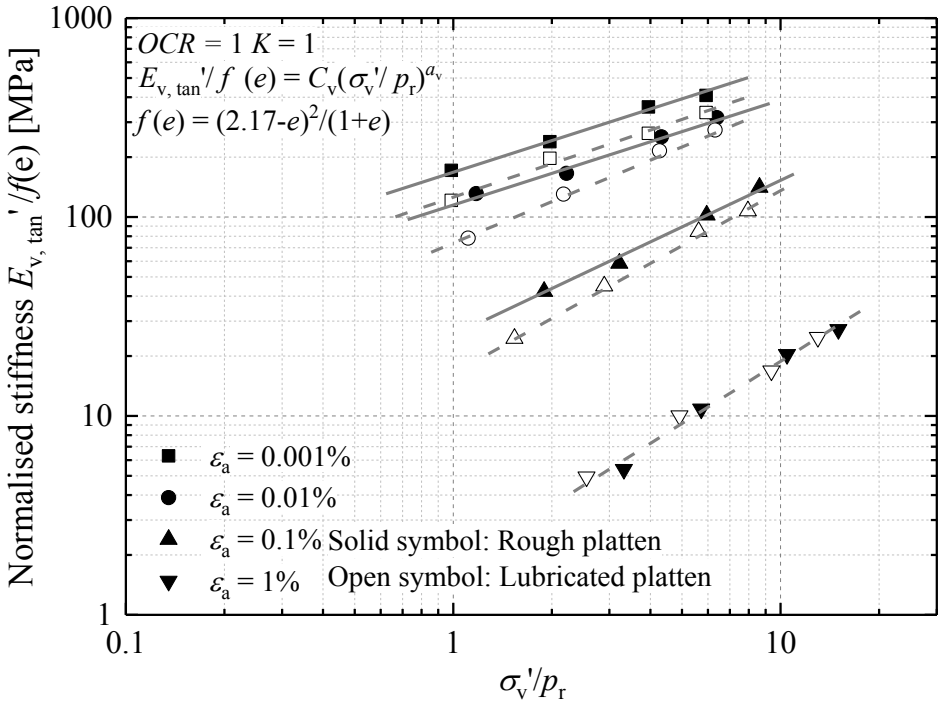

Figure 5-21 Comparison of normalised stiffness trends for medium dense (R_d = 50%) specimens employing fully-rough plattens and fully lubricated plattens

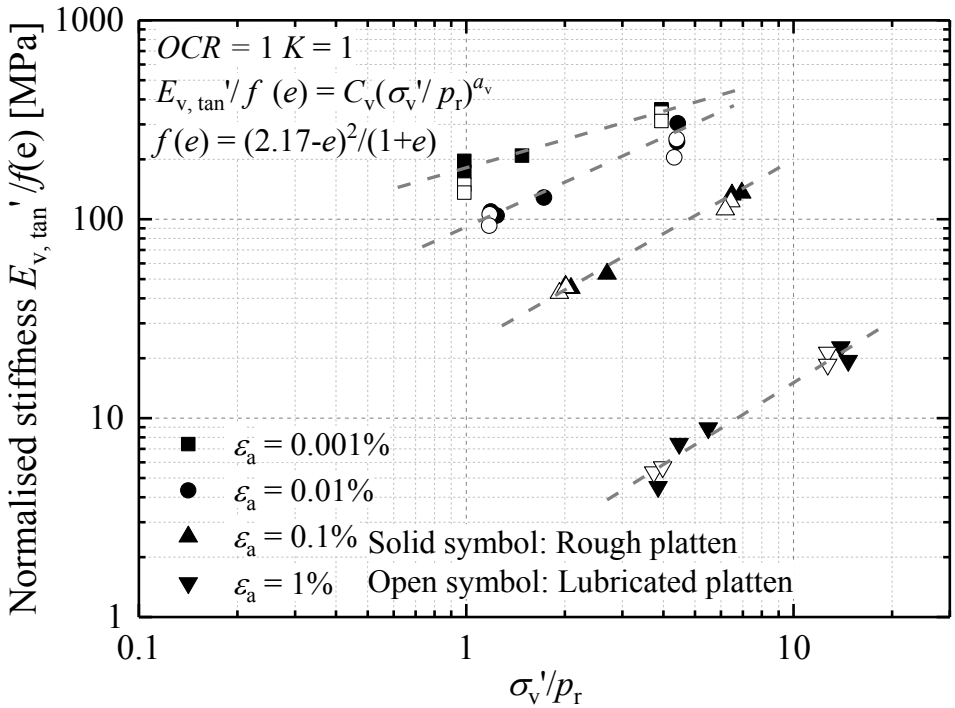

Figure 5-22 Comparison of normalised stiffness trends for dense (R_d = 79%) and very dense (R_d = 95%) specimens employing semi-rough plattens and fully lubricated plattens

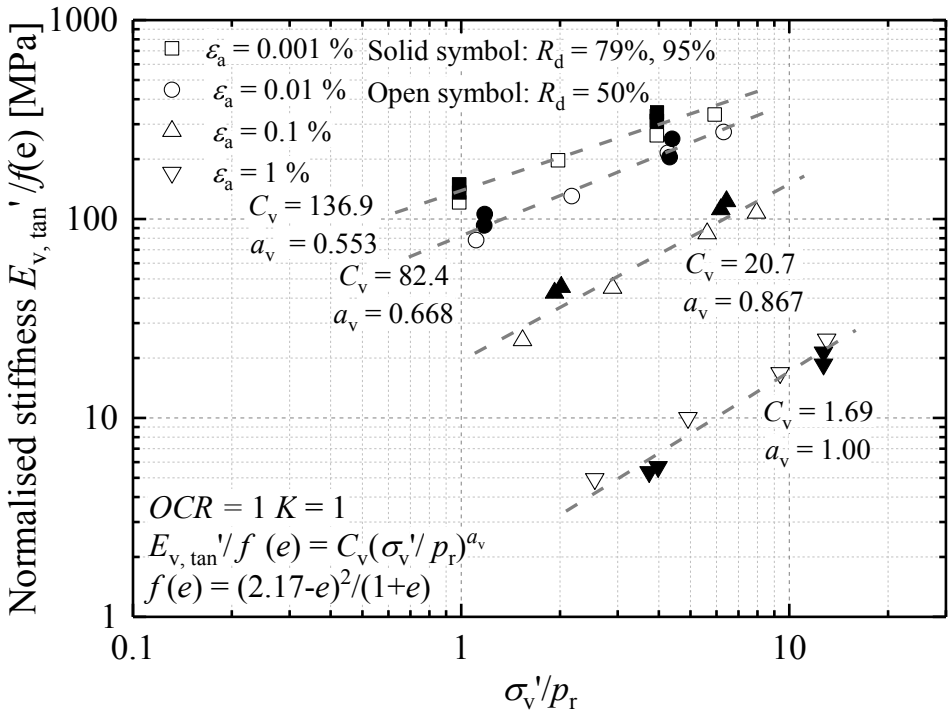

Figure 5-23 Overall trends for $E_{v,tan}'/f(e)$ against σ_v'/p_r for the tests performed with over-sized fully lubricated plattens

5.7 Pre-failure kinematic yielding of the Batch 2 Dunkirk sand

The Dunkirk sand's pre-failure stress-strain and stiffness behaviour are further interpreted below in relation to the multiple kinematic yield surface framework introduced in Section 5.2.2.

Y_1 yielding

The Y_1 yielding is defined as the point where the stress-strain (q-ε_a) curves commence to deviate from their initial quasi-linear trends and the tangent stiffnesses fall below their initial plateau values (see for example Figure 5-12). As demonstrated in 5.5.1, Y_1 yielding generally occurred when axial strains exceed limits of 0.002-0.006%, with the higher values being associated with increasing specimen density, higher effective stress levels (p_0') and *OCR* greater than unity.

Figure 5-24 depicts the sizes of the Y_1 yield surfaces in terms of the deviatoric stress changes (Δq_{Y1}, as developed along the imposed $\Delta q/\Delta p' = 3$ stress paths under constant σ_h'). Similar values were determined from both axial compression and extension tests on isotropically consolidated specimens performed at $OCR = 1$, employing both rough and lubricated plattens. Overall, the Y_1 "bubble" appears to have a vertical extent from its origin to the points indicated in Figure 5-24, that is around 3 to 4% of p_0' for the medium dense specimens ($R_d = 50\%$) and 5 to 6% of p_0' for the dense specimens ($R_d = 79\%$). Over-consolidated specimens developed larger Y_1 surfaces. The tests performed on dense specimens with rough plattens gave slightly higher Δq_{Y1}. The Y_1 limits applying for tests from $p_0' = 400$ kPa from specimens formed with three R_d values are indicated on Figure 5-25, in which the surfaces are shown as having a nominally circular shape in q-p' space. Further probing tests conducted on a wider range of stress paths are required to confirm the surface's shape.

The sizes of the surface do not scale exactly linearly with p', and the $\Delta q_{Y1}/p'$ ratios vary between 0.03 and 0.06 over the stress ranges considered, depending primarily on specimen density and, to a minor extent, end restraint conditions. The overall trends for Δq_{Y1} with p' trends are best fitted by power law functions ($\Delta q_{Y1} = A(p')^n$ with exponents n of around 0.8.

Y_2 yielding

Kuwano & Jardine (2007) suggested that a second type of Y_2 kinematic yielding may be

identified under drained monotonic shearing tests by considering the stages where the strain increment vector ($d\varepsilon_s/d\varepsilon_{vol}$; ε_s: shear strain, $2/3(\varepsilon_a-\varepsilon_r)$; ε_{vol}: volumetric strain, $\varepsilon_a+2\varepsilon_r$) developed while following stress paths of constant inclination, can start to curve away from their initial constant 'elastic' strain vector directions, given by $d\varepsilon_s/d\varepsilon_{vol}$.

Figure 5-26 plots the ε_s-ε_{vol} traces from six tests on dense (R_d = 79%) specimens employing rough plattens. One of the tests appeared to have experienced greater temperature variations than the others. However, the gradients developed over the initial stages of the five compression tests plotted all fell within the $1 < d\varepsilon_s/d\varepsilon_{vol} < 1.23$ range, with the extension test showing a more variable trend and an initial $d\varepsilon_s/d\varepsilon_{vol} = 1.44$. The Y_2 yielding points where the $d\varepsilon_s/d\varepsilon_{vol}$ traces deviated from each test's initial trend are indicated in Figure 5-26 as solid symbols. A clear trend can be noted for Y_2 yielding to be delayed in higher p_0' tests with the initial 'elastic' patterns being maintained until larger strains developed before curving upwards towards developing dilative behaviour.

Figure 5-27 indicates the size of Y_2 yielding surface in terms of Δq_{Y2}-p' for tests that started from the isotropic axis, noting that only the yielding stress points from the p_0' = 100 and 400 kPa tests are shown for clarity. The data points were fitted by power law functions that passed through the origin. The Y_2 yield surface, which is shown again as having a nominally circular shape in q-p' space, is not symmetric about the $q = 0$ axis as the extension tests manifested their Y_2 yielding after smaller changes of q. As shown later in Chapter 7, sand specimens subjected to two-way cycling centred at isotropic states engaged their Y_2 yielding first on the extension side.

The Y_1 and Y_2 surfaces are kinematic and are relocated by any stress path that engages their limits and moves to new positions in effective stress space. The surfaces adjust their sizes in scale with isotropic changes in p' and also change their shapes as q/p' varies.

Y_3 and Y_4 yielding

Y_3 yielding was identified by Kuwano & Jardine (2007) as applying at the effective stress states when plastic (axial) straining becomes dominant in triaxial tests on sands and the plastic strain ratio $d\varepsilon^p/d\varepsilon^t$ exceeds 0.85. The strain ratio for the axial strain component, $d\varepsilon_a^p/d\varepsilon_a^t$, is calculated as

$$\frac{d\varepsilon_a^p}{d\varepsilon_a^t} = 1 - \frac{d\varepsilon_a^e}{d\varepsilon_a^t} \tag{5.8}$$

Where the superscripts "t", "e" and "p" represent total, elastic and plastic strains, respectively. The elastic strains were determined based on the $[E_{v,tan}'/f(e)]$-$[\sigma_v'/p_r]$ trends established in Section 5.5.2, also distinguishing the different fitting coefficients for the test cases of rough and lubricated plattens shown in Figures 5-18 and 5-23. Most of the tested specimens showed initial contractive volume changes that transformed to dilation after certain amount of shearing. Assuming that no specimen underwent significant dilation before approaching the Y_3 yielding, the $[E_{v,tan}'/f(e)]$-$[\sigma_v'/p_r]$ fitting parameters established for isotropic conditions can be adopted for determining elastic stiffnesses under anisotropic stress conditions.

The final Y_4 form of yielding is characterised here as the state of phase transformation, which was identified readily from sample volume measurements as the points where $d\varepsilon_{vol}/d\varepsilon_s$ became zero before tending to negative gradients.

Figure 5-28 reports the plastic strain ratio trends shown by tests on two medium dense (R_d = 50%) samples under p_0' = 100 and 600 kPa. The identified Y_3 yielding strains are denoted, also noted are the strain states when Y_2 yielding was observed. It is clear the samples developed plastic strains once the Y_1 yield surface was engaged (at around 0.004% axial strain). The plastic strain ratio also grew to around 0.5 before Y_2 yielding occurred.

Figure 5-29 demonstrates the Y_3 and Y_4 yielding points identified for the medium dense (R_d = 50%, e_0 = 0.74) specimens in ε_s-ε_{vol} space, indicating the evolving trends seen for the strain vector as plastic straining became gradually more dominant.

Further discussion on Y_3 and Y_4 yielding

Most of the Author's tests were performed under constant σ_h' axial compression and extension conditions that commenced from isotropic stress states and allowed "contours" to be established in a triaxial q-p' stress space, as shown in Figure 5-30 for the stress states under which Y_3 and Y_4 yielding took place. Under low p_0' conditions (< 200 kPa), the Y_3 and Y_4 yielding points were closely aligned on a constant (q/p') axis that appeared to match the critical state stress ratio. As p_0' increased, the specimens underwent more significant contraction, and the Y_3 yielding took place at much lower

q/p' ratios than those under which volumetric straining transformed to dilation and Y_4 yielding occurred. Kuwano & Jardine (2007) argued that the Y_3 surface is likely to form a cap shape to the right of the diagram. However, higher pressure tests are required to explore this conjecture for Dunkirk sand.

The nominal kinematic yielding surfaces established above at two isotropic stress states (p_0' = 100 and 400 kPa) from constant σ_h' compression and extension tests are shown in triaxial q-p' space in Figure 5-31, along with the Y_3 and Y_4 yielding points. The sizes and locations of the yield surfaces (or "bubbles") evolved during shearing and were dependent on the specimens' initial stress states. The Y_3 and Y_4 yielding appeared to be approaching the critical state line on the compression and extension side in the p_0' = 100 kPa tests, while the specimens sheared from p_0' = 400 kPa developed Y_3 yielding well before undergoing Y_4 yielding or approaching critical state stress ratios.

The Y_2 yielding identified under monotonic loading is explored further with reference to the cyclic tests described in Chapter 7, where the same framework is applied in considering the points where significant permanent plastic straining and changes in stiffness occurred under drained cyclic loading.

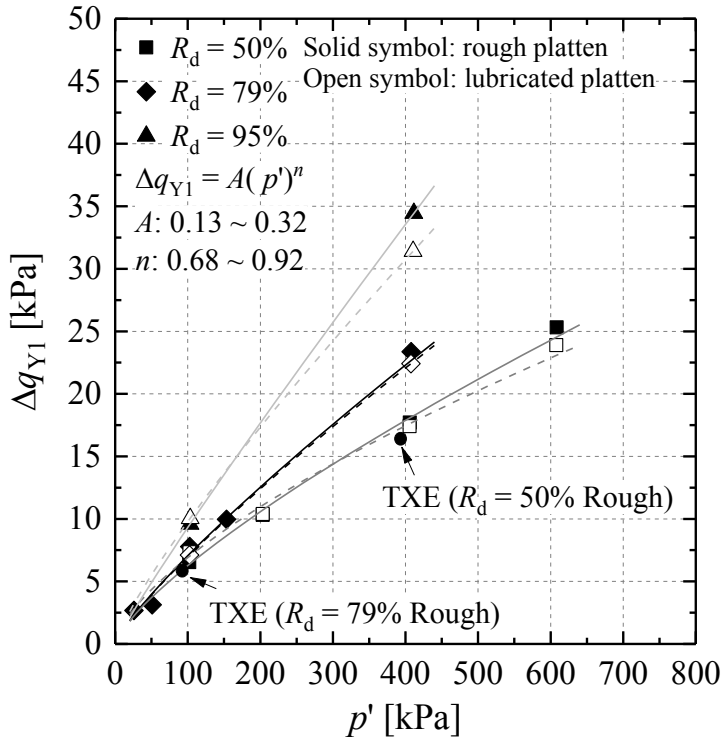

Figure 5-24 Sizes of the Y_1 yield surface for normally consolidated samples in terms of deviatoric stress change under $+\sigma_v'$ or $-\sigma_v'$ shearing from isotropic stress states

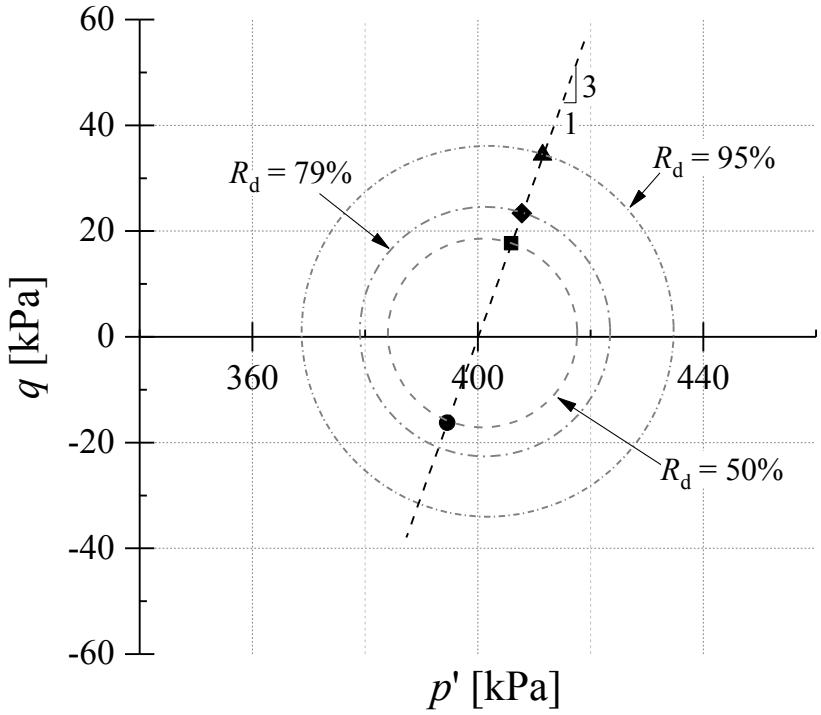

Figure 5-25 Y_1 yielding points for specimens sheared from isotropic p_0' = 400 kPa (all tests performed with rough plattens)

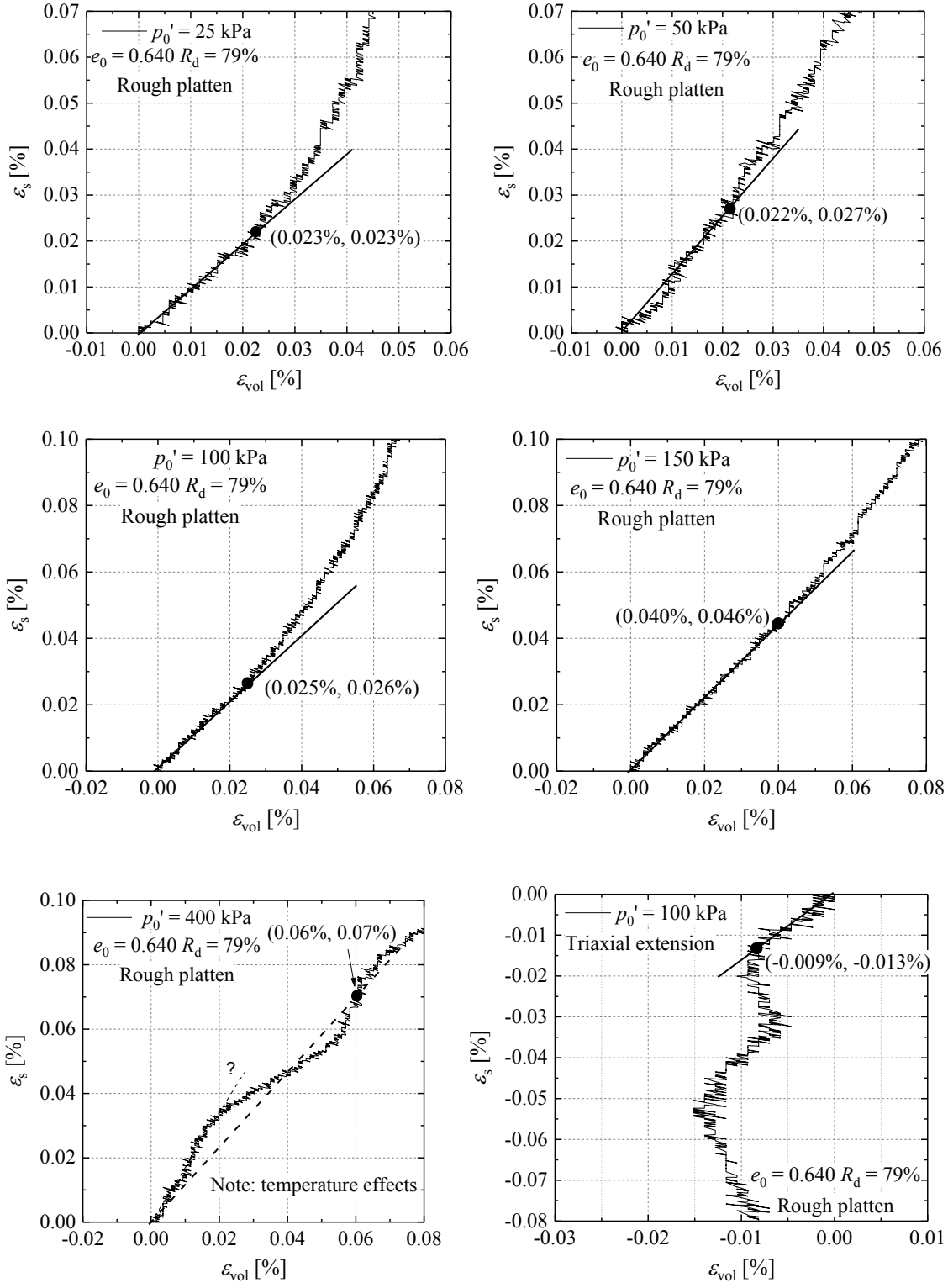

Figure 5-26 Initial ε_s-ε_{vol} response and determination of Y_2 yielding points for tests on dense specimens (R_d = 79%) with rough plattens

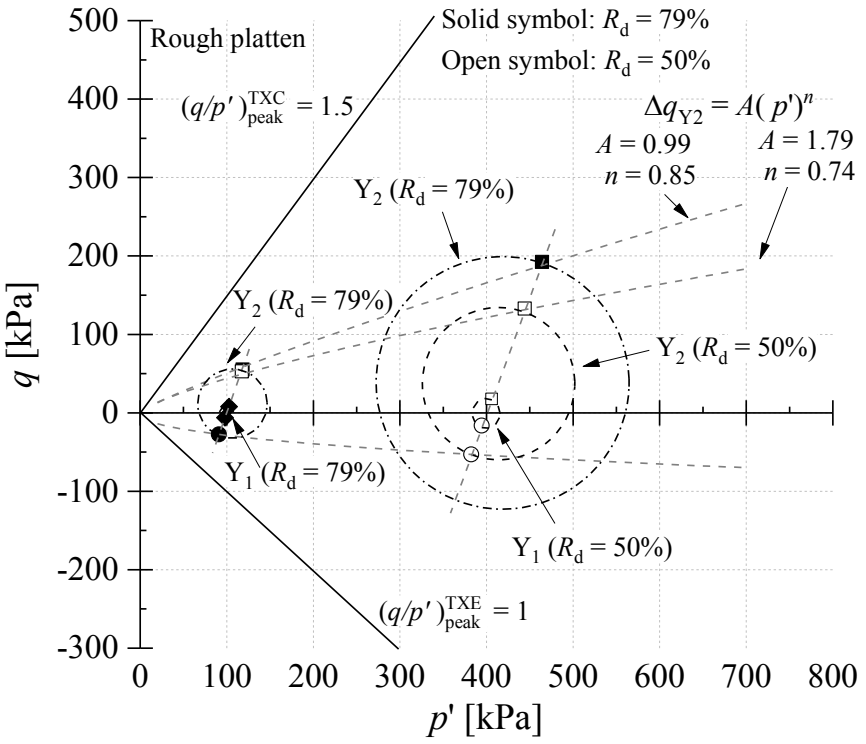

Figure 5-27 Size of Y_2 yielding surface identified for medium dense (R_d = 50%) and dense (R_d = 79%) specimens under constant σ_h' compression and extension

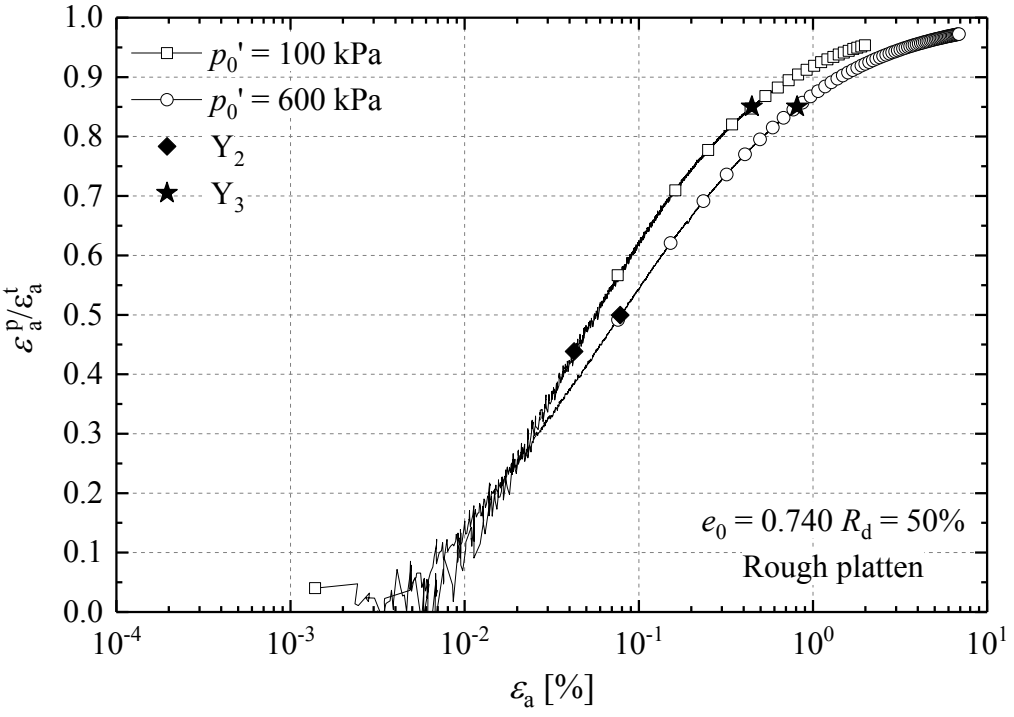

Figure 5-28 Evolution of plastic strain ratio against axial strains under $+\sigma_v'$ shearing, also indicating the Y_2 yielding point

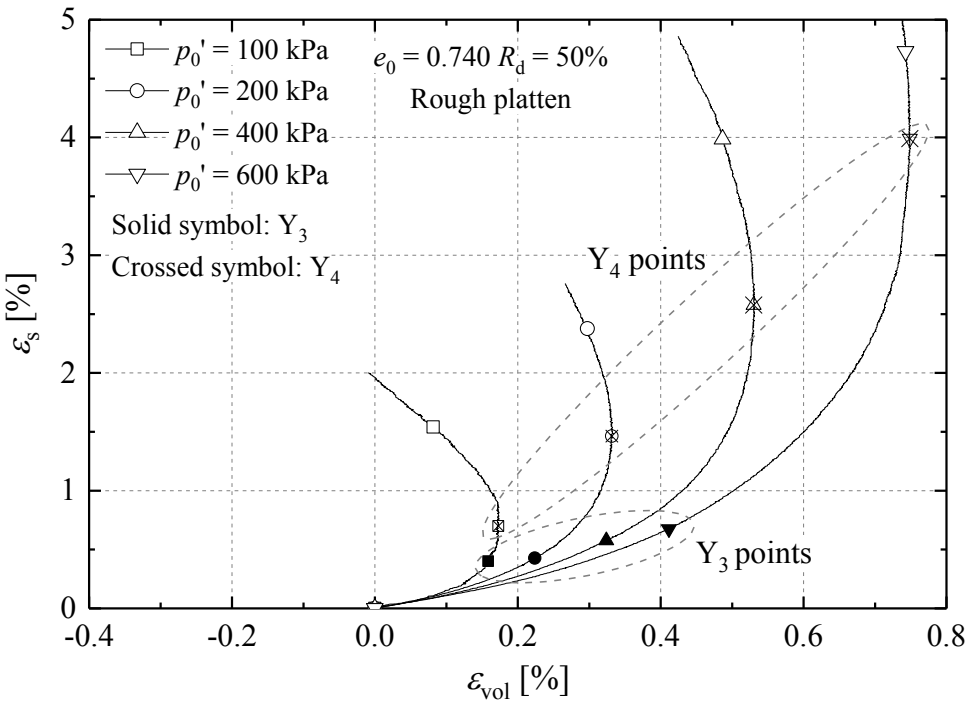

Figure 5-29 Characterisation of Y_3 and Y_4 yielding for the medium dense (R_d = 50%, e_0 = 0.74) specimens

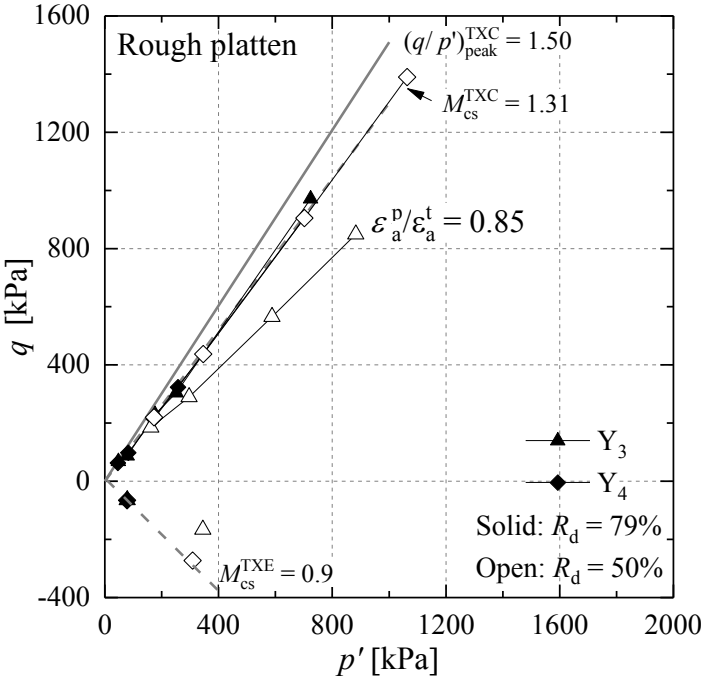

Figure 5-30 'Contours' linking Y_3 and Y_4 points found from constant σ_h' compression and extension tests from isotropic stress states

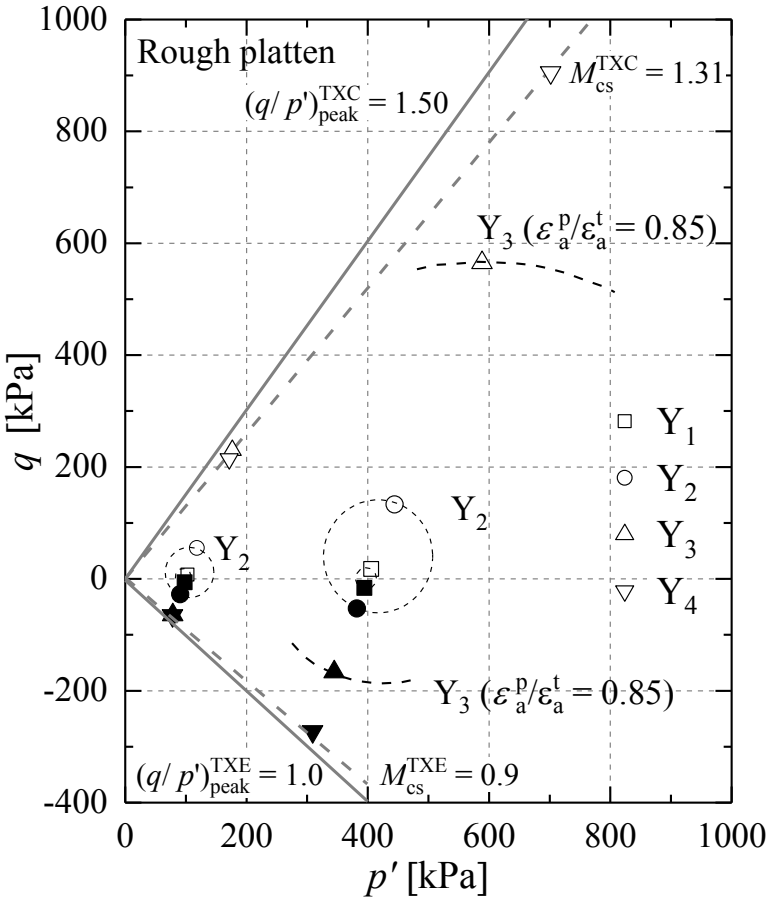

Figure 5-31 Yield surface bubbles defined from constant σ_h' compression and extension tests

5.8 Pre-failure stiffnesses of the Dunkirk Batch 2 and 3 sands

The investigations into the Dunkirk sand's pre-failure stiffnesses reported up to this point involved tests on Batch 2 samples, most of which were tested from isotropically consolidated conditions. These experiments almost exhausted the supply of fresh Batch 2 material and left little sand to extend the research to cover investigations into either stiffness anisotropy or long-term cyclic loading. These experiments that explored these facets of behaviour had to rely on the supply of Batch 3 material, which was also originated from bulk sampling undertaken near the PISA test site.

As set out below, some differences exist between the Batches' small-strain stiffnesses, which were identified through comparisons with tests on Batch 3 material performed by Vinck (2016). Comparisons between the grading and limiting void ratios of the Dunkirk Batches 2 and 3 sands were included in Sections 2.2.2 and 5.3.2. Their grain characteristics were broadly similar but the Batch 3 material exhibited notably higher limiting void ratios of e_{max} and e_{min}, as listed in Table 5-1.

The comparison of pre-failure stiffnesses presented below focuses on dense and very dense Batch 2 and Batch 3 samples on which the triaxial probing tests and cyclic triaxial tests were primarily performed. Figure 5-32 summarises the normalised small-strain stiffnesses $[E_{v,tan}'/f(e)]$-$[\sigma_v'/p_r]$ trends at four axial strain levels (ε_a = 0.001%, 0.01%, 0.1% and 1%) for Batch 2 and Batch 3 specimens tested with standard semi-rough plattens, and Figure 5-33 plots the corresponding trends for the tests performed with over-sized fully lubricated plattens, also denoting the fitting coefficients C_v and a_v derived for each strain level.

The general trend was for the Batch 3 Dunkirk sand to exhibit lower pre-failure stiffnesses than the Batch 2 sand. The differences in small-strain stiffnesses were also found to vary with the platten conditions employed. The Author's tests on Batch 2 performed with semi-rough plattens manifested the greatest divergence with those conducted with fully lubricated plattens at the four strain levels considered, while Vinck's (2016) tests on Batch 3 employing rough and lubricated plattens showed almost unperceivable differences in stiffnesses over the elastic range (ε_a = 0.001%), followed by more significant variations as strain levels increased. It is important to note that the Batch 3 samples prepared to similar void ratios as the Batch 2 samples had higher nominal relative densities when the index properties outlined in Table 5-1 are applied to

compare the two sand batches. The Batch 3 sand also showed lower shear strength at peak and a less dilative response, as presented later in Section 6.8.

It is interesting to note that the tests on Batch 2 and Batch 3 sands performed with fully lubricated plattens gave very consistent stiffnesses over the linear elastic range, within which the triaxial probing tests are primarily concerned. The cross-anisotropic linear elastic stiffness parameters characterised from the triaxial probing tests for the Batch 3 material are arguably equally applicable to both batches of Dunkirk sand.

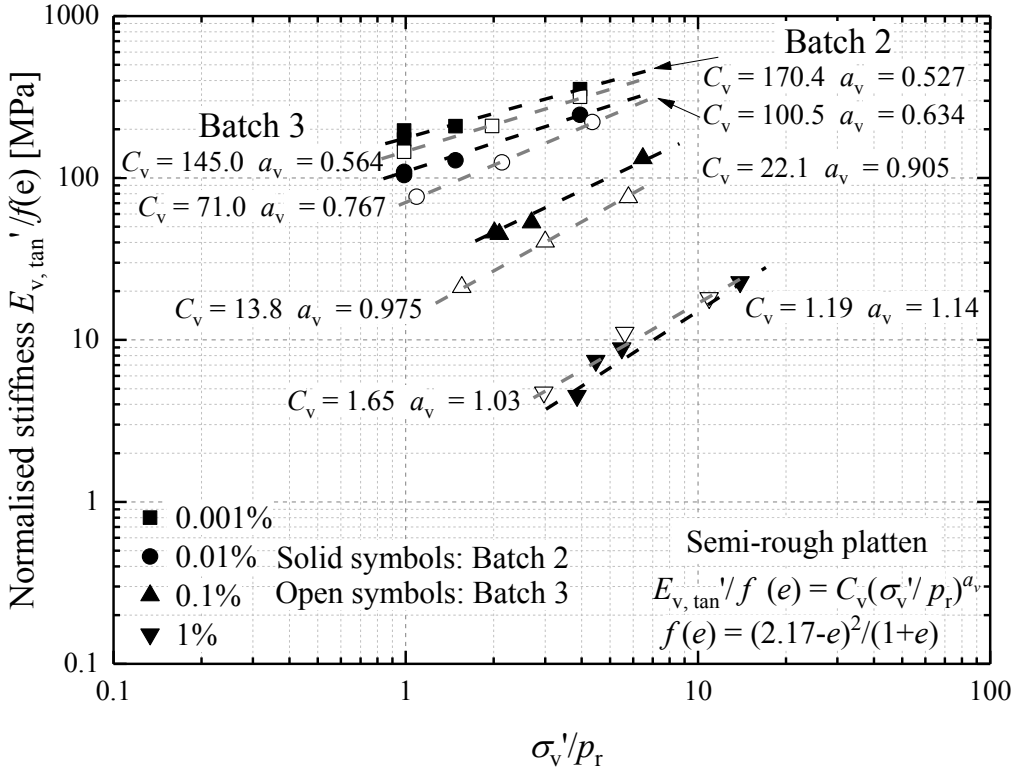

Figure 5-32 Normalised pre-failure stiffnesses of dense Batch 2 (R_d = 79%, 95%) and Batch 3 (R_d = 92%) Dunkirk sands (all tests performed with semi-rough plattens)

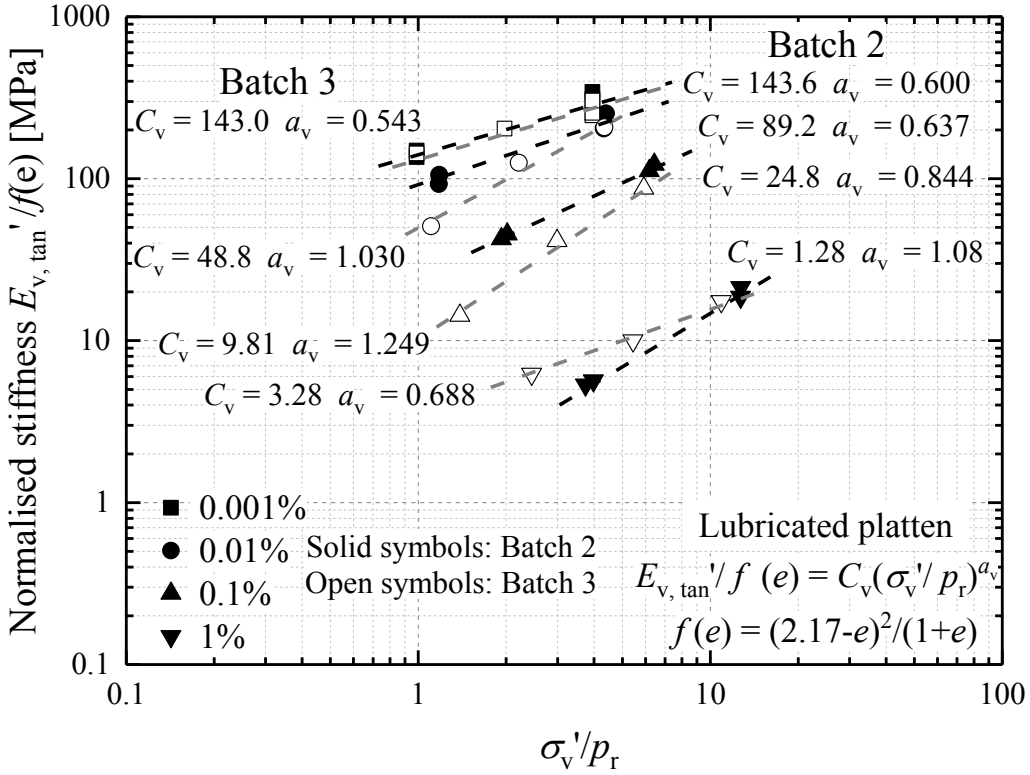

Figure 5-33 Normalised pre-failure stiffnesses of dense Batch 2 (R_d = 79%, 95%) and Batch 3 (R_d = 92%) Dunkirk sands (all tests performed with fully-lubricated plattens)

5.9 Characteristics of cross-anisotropic linear elastic stiffnesses

The previous sections discussed how the vertical equivalent Young's moduli (E_v') varied with p', e_0, K ratio and OCR over the linear and non-linear ranges. This last main section of the Chapter completes the discussion by considering the potential anisotropy of Dunkirk sand's stiffness behaviour within the small linear elastic (Y_1) range. Descriptions of the testing programme and methodology are given below, followed by detailed interpretation of the anisotropic stiffness parameters as well as integration with the outcomes from the '38 mm' triaxial tests and similar probing tests performed on the Batch 1 Dunkirk sand reported by Kuwano (1999). Aspects of the sand's anisotropy over the non-linear range were discussed on the basis of earlier research as described by Kuwano (1999) and Jardine (2013).

5.9.1 Testing programme and methodology

Test apparatus and material

The '100 mm' fully instrumented triaxial apparatuses equipped with upgraded radial strain measuring system were employed for the triaxial probing tests. Full details of the apparatuses, their capabilities and performance were given in Section 2.3.4. The same apparatuses were employed for both the Cowden till and Dunkirk sand triaxial probing test series, as discussed in Section 3.7.

Due to the specimens' substantial volume (D: 100 mm, H: 200 mm, around 2500 g dry mass) compared to the 38 mm diameter samples ($m_{dry} \approx 140$ g), the probing tests had to be performed with the Batch 3 Dunkirk sand. As shown in Section 5.8, the Batch 2 and Batch 3 sands appeared to exhibit comparable linear elastic stiffness component of E_v' in tests that employed lubricated plattens.

The triaxial probing '100 mm' specimens were formed by water-pluviation method to be consistent with the tests on the '38 mm' specimens. Figure 2-23 illustrates the general arrangements for specimen setting-up, after deploying the local strain sensors and dual-axis bender elements.

Probing programme and methodology

Stress-path probing tests were performed on five specimens formed initial void ratios around 0.64 (R_d = 92%). Individual specimens were consolidated and swelled along constant stress ratio (K) axes of 1, 0.67, 0.53, 0.5 and 0.4, corresponding to vertical to

horizontal effective stress ratios (σ_v'/σ_h') of 1, 1.5, 1.9, 2 and 2.5. Similar consolidation/swelling and probing schemes described below were applied to all the tests performed.

The discussion below focuses on the outcomes from two specimens whose characteristics were investigated under isotropic (K = 1) and quasi-K_o (=0.5) effective stress conditions, denoted respectively as DKB3PBIC and DKB3PBKC. Their stress states were comparable with those of the '38 mm' monotonic (in Chapters 5 and 6) and cyclic (in Chapter 7) triaxial experiments. The consolidation stress states were schemed with 50 kPa σ_h' measurements, increasing up to (σ_v', σ_h') = (550, 550) (kPa) and (σ_v', σ_h') = (1000, 500) (kPa) for DKB3PBIC for DKB3PBKC respectively, leading to around 20 effective stress states in total. Probing tests were initiated after 48-72 hours of creep to allow residual strain rates to decrease to negligible levels, less than 0.0005%/hour.

Sets of 10 stress-controlled probes were performed at each of the effective stress states. Referring to Section 3.7, the probes were applied in as full cycles, including: (i) ±v′, constant σ_h' and small axial loading-unloading cycle; (ii) ±h′, constant σ_v' and small radial loading-unloading cycle; (iii) ±p′, constant q and varying p′; (iv) ±q′, constant p′ and varying q; and (v) ±q, constant σ_h (undrained) and axial loading-unloading cycle. Each of the probes was repeated at least once, and sufficient time was allowed in between probes for any residual strains to settle. The stress probes were applied with stress change rates (in σ_v', σ_h' or σ_v) of 30 kPa/hour or less, which was similar to the rates applied by Kuwano (1999).

The above probing scheme enabled interpretation of the full set of drained and undrained cross-anisotropic stiffness parameters and Poisson's ratios, using both approaches of Kuwano (1999) and Nishimura (2014), as outlined in Section 3.2.1 and 3.7. The current interpretation focuses on stiffness parameters of E_v', E_h', E_v^u, G_{vh} (G_{hv}) and G_{hh} deriving from the Kuwano (1999) approach to facilitate direct comparisons with Kuwano's (1999) probing tests on air-pluviated Batch 1 Dunkirk sand.

Bender element measurements and interpretation

As with the Cowden till probing (tests described in Section 3.7), multiple-directional bender element tests were performed at each probing stress state to provide direct measures of shear stiffnesses, G_{vh} (G_{hv}) and G_{hh} based on time-domain, first arrival, peak-to-peak shear wave velocity interpretation. The G_{vh} and G_{hv} data points recorded at

each effective stress state were averaged to represent an overall G_{vh} component for stiffness analysis.

5.9.2 Test outcome and discussion

Illustrative stress-strain responses

Typical stress-strain responses recorded in full-cycle multi-directional stress probes (±v′, ±h′ and ±q) are illustrated in Figures 5-34 to 5-36, drawing on results from a set of probes performed on the DKB3PBKC specimen with e_0 = 0.64, R_d = 92% at (σ_v', σ_h') = (400, 200) (kPa) with stress increments of ±6 kPa, also denoting derived Young's moduli and Poisson's ratios.

It is evident that the soil remained within its linear elastic range (Y_1) under most of the imposed stress perturbations, with the stress-strain responses manifesting (in most cases) fully reversible linear elastic features that allowed the stiffnesses and Poisson's ratios to be determined with high confidence. The sample developed minor hysteric radial straining (-0.0025%) over the radial unloading (-h′) cycle while the response over the initial radial loading (+h′) cycle was largely reversible. The applied 6 kPa radial loading probe (+σ_h') kept the specimen within its Y_1 surface, which appeared to have been exceeded over the radial unloading probe (-σ_h'), indicating features of kinematic yielding. The yielding surfaces may not be centred at the initial stress state and the stress points' orientations relative to the surfaces are known to be highly dependent on recent stress and creeping history (Kuwano & Jardine, 2002b).

The stiffnesses all grew as the effective stress levels rose. Figures 5-37 and 5-38 demonstrates the relationships between the elastic stiffnesses and p' for the K = 1 and 0.5 specimens, respectively. Under isotropic stress conditions, the specimen developed higher stiffnesses in the horizontal planes (E_h' and G_{hh}) than in the vertical planes (E_v' and G_{vh}), reflecting inherent anisotropic features as discussed below. The opposite trend was observed under anisotropic K = 0.5 test conditions because the stiffness is governed by the vertical effective stress σ_v' component, which has a higher ratio σ_v'/p' under K = 0.5 condition.

Cross-anisotropic stiffness coefficients

The Dunkirk sand's stiffness anisotropy was investigated first by assessing the K = 1

and 0.5 conditions separately. A second approach similar to that employed by Kuwano (1999) and Kuwano & Jardine (2002b) was also attempted to derive a single set of cross-anisotropic stiffness material constants (referring to Equations (5.1) to (5.4)) to represent Dunkirk sand's overall anisotropic stiffness characteristics that were assumed to be largely independent of stress states.

Figures 5-39 and 5-40 demonstrate the established trends for normalised vertical and horizontal Young's moduli, respectively. Also indicated are the derived stiffness parameters, C_v, C_h, a_v and b_h, distinguishing $K = 1$ and 0.5 conditions.

Although not overly significant, the established trends indicated moderate dependency of the stiffness parameters on the stress conditions (or K), as the attained C_v and C_h from the $K = 0.5$ test were around 15% higher than those for the $K = 1$ condition, suggesting the Equations (5.1) to (5.4) were not fully verified. The latter led to (C_v, a_v) value of (149.5, 0.55) that were close to the value of (143.0, 0.54) (shown in Figure 5-40) obtained from the triaxial monotonic tests using the '38 mm' triaxial apparatus, bearing in mind that the two sets of tests were performed independently by two researchers and that the '100 mm' apparatuses generally offered better stress-strain measuring resolution and control performance.

The differences in stiffness parameters for $K = 1$ and 0.5 conditions indicated that the micro-fabrics developed within the specimens led to stiffness trends that could not be characterised precisely by the formulations given by Equations (5.1) to (5.4). Further experimental and numerical studies from the perspective of particulate soil mechanics are required to investigate these aspects.

Nevertheless, a set of stiffness parameters that represented overall anisotropic characteristics for both isotropic and K_o states were derived, leading to C_v and C_h values that were in between those found for $K = 1$ and 0.5 conditions, as denoted in Figures 5-39 and 5-40. It should be noted that double linear regression of shear stiffnesses (G_{vh} and G_{hh}) data from a single constant K (or σ_v'/σ_h' ratio) tests inevitably involved significant uncertainties. The derivation of parameters for the shear stiffness components were therefore only performed on the joint $K = 1$ and 0.5 dataset, and the outcomes are shown in Figure 5-41.

Regardless of the approach employed, the ratios between the horizontal to vertical stiffness parameters (or material "constants"), C_h/C_v, C_{hh}/C_{vh}, were found to be

invariably greater than unity, indicating that the water-pluviated Dunkirk sand has inherent anisotropy, which reflects the preferred horizontal orientation of the pluviated sand particles that was also evident in the isotropic consolidation stages discussed in Section 5.4. The obtained stiffness parameters for water pluviated Batch 3 sand also allowed direct comparison with those for air pluviated Batch 1 Dunkirk sand reported by Kuwano (1999).

Further discussion

The derived stiffness coefficients for water-pluviated and dense Batch 2 and 3 of the Dunkirk sands are compared with those reported by Kuwano's (1999) for her air-pluviated medium dense (R_d: 57-65%) Batch 1 Dunkirk sand, as shown in Table 5-5. The '38 mm' method represents vertical Young's moduli determined from monotonic shearing, while the '100 mm' method denotes stiffness parameters determined from stress probes.

The air pluviated Batch 1 specimens and the water pluviated Batch 3 specimens showed comparable degrees of inherent stiffness anisotropy. Gravitation-based pluviation methods led to similar particle preferential orientations, regardless of the pluviation environment. However, the Batch 2 and 3 sands exhibited consistently lower Young's moduli and shear stiffnesses than Batch 1 in terms of the material constants (C_v, C_h, C_{vh} and C_{hh}), which could not be simply attributed to their index properties that exhibited insignificant differences.

The differences may reflect direct consequences of the K-dependency of the stiffness parameters, as discussed above. Kuwano's (1999) triaxial stress probes on Batch 1 sand were performed primarily under anisotropic stress states with K ranging from 0.35 to 0.53, which arguably led to higher values of C_v, C_h, C_{vh} and C_{hh} than under isotropic condition.

The differences may also be attributed to sample preparation method employed. Although parallel tests using different reconstitution methods for Batches 2 and 3 sands were not possible within the Author's study, Table 5-6 summarises bender element shear stiffness correlations for isotropically consolidated sand specimens formed with moist tamping and air-pluviation methods, noting also the differences in the void ratio functions and reference pressures adopted. The shear stiffnesses corresponding to e_0 = 0.70 and p' = 100 kPa were listed for comparison, under which conditions the air

pluviated Batch 1 sand and water pluviated Batch 3 sand gave G_{vh} values of 88.3 MPa and 61.8 MPa, respectively. Table 5-6 indicated consistently higher (by 20-30%) shear stiffnesses of the specimens reconstituted by moist tamping than those formed with air pluviation method. Similar magnitudes of differences might apply between the water and air pluviation methods. The comparison sets out the scope for the potential effects of sample preparation method on sand stiffnesses, although other factors, such as particle size, shape, fines content, may also play important roles, as discussed in Section 5.2.1.

5.9.3 Anisotropic elastic stiffness profile of the Dunkirk site

The site's ground conditions were described in Section 2.2.2, based on earlier site investigation data reported by Chow (1997) and more recent PISA investigation (Zdravković *et al.*, 2015, Taborda *et al.*, 2018). The latter identified the phreatic level at 5.4 m, below which pore water pressure followed hydrostatic distribution. A suction profile was assumed to apply above the water table with a maximum suction of 13.5 kPa, as set out by Taborda *et al.* (2018) and supported to some degree by the suction developed in piezocone tests. Naturally these suctions and water table depths may change seasonally. The operational bulk unit weight γ was set as 17.1 kN/m^3 and 19.9 kN/m^3 for the sand layers above and below water table, respectively. The relative densities were characterised as 100% and 75% respectively for the top 3 m hydraulic fill and the underlying layers, and the corresponding void ratios were 0.57 and 0.628. The earth pressure coefficient K_o was determined as 0.40.

The above ground conditions, in conjunction with the elastic stiffness parameters established for the K_o-consolidated probing specimen (DKB3PBKC), led to profiles of the elastic stiffnesses (E_v', E_h', G_{vh} and G_{hh}), as shown in Figure 5-42. Naturally, the normally consolidated Dunkirk site exhibits consistently higher vertical stiffnesses (E_v') than those in the horizontal direction. Less significant differences, however, were observed between the shear stiffness components G_{vh} and G_{hh}.

However, it is important to note that the shear stiffness profile (G_{vh}) determined from laboratory bender element tests on the Author's water pluviated reconstituted specimens fell consistently below those found from the in-situ SCPT measurements, considering both the tests conducted for Chow's (1997) study and the measurements

made 20 years later. The divergence between the laboratory and field G_{vh} results are most pronounced above the water table in the unsaturated ground and reduce with depth below the water table. The laboratory E_v' and E_h' profiles show higher stiffness.

Potential reasons for the differences seen between the two sets of in-situ SCPT measurements were identified in Section 2.2.2 as: (i) spatial variations; (ii) long-term drainage; (iii) sand ageing with time, or a combination of these factors. The significant divergences between the laboratory and in-situ shear velocity measurements may be attributed to: (i) variations of sand index properties, as the samples collected from shallow pits (< 0.8 m) may not adequately represent the properties of those at greater depth; (ii) the laboratory tests on saturated specimens not representing adequately the unsaturated conditions applying above the water table; (iii) the reconstituted specimens not being fully representative of in-situ undisturbed conditions; (iv) in-situ stiffness gain due to ageing (over 40 years) and seasonal water table fluctuations which cannot be replicated by the short term (maximum 3 months) laboratory tests. It is also possible, of course, that the field shear wave velocity testing and its interpretation did not provide results that are fully representative of behaviour in-situ. The seismic CPT device raises the effective stress conditions in the soils around the probe as it penetrates through the ground and may lead to an over-recording of the in-situ shear wave velocities.

Figure 5-43 plots the G_0 and E_v' profiles based on the isotropic model ($\nu_{vh}' = 0.17$) that was employed in the PISA Dunkirk modelling. The G_0 trace, which corresponded to B value of 875 (see Equation (6.18)) manifested close match with the in-situ SCPT measurements. The derived E_v' trend was lower but generally compatible with that determined from the triaxial small strain probing test, bearing in mind the latter was performed on a specimen of constant $K = 0.5$ and the stiffness parameters (C_v and a_v) could lead to underestimated E_v' when applied to in-situ stress conditions of $K = 0.4$.

An integrated approach of combining high-quality site investigation, soil sampling and advanced laboratory element testing is required to enable accurate ground characterisation and derive representative parameters for field testing interpretation or numerical modelling. Case-specific numerical approaches, such as those set out by Taborda *et al.* (2018), may be applied to bridge field and laboratory outcomes and enable modelling of practical problems such as laterally loaded monopiles, which require the soils' full strain behaviour (from linear elastic range up to failure) to be characterised adequately.

Table 5-5 Comparison of stiffness parameters for Dunkirk sands

Material	Properties	R_d [%]	Method	Type	K	Stiffness parameters				
Batch 1 (C9 + C15: 5.85-11.9 bgl.)	e_{max}: 0.928 e_{min}: 0.528 D_{50}: 0.205-0.263 mm <0.1 mm: less than 2.5%	57-65	AP	'100 mm'	1, 0.53, 0.35	C_v: 225 a_v: 0.55	C_h: 228 a_h: 0.50	C_{vh}: 70 a_{vh}: 0.36 b_{vh}: 0.20	C_{hh}: 105 a_{hh}: 0.05 b_{hh}: 0.46	C_h/C_v: 1.01 C_{hh}/C_{vh}: 1.5
Batch 2 (0-0.8 m bgl.)	e_{max}: 0.910 (0.918) e_{min}: 0.570 (0.573) D_{50}: 0.240 mm <0.1 mm: less than 2.5%	79-95	WP	'38 mm'	1	C_v: 144 a_v: 0.60				
Batch 3 (0-0.8 m bgl.)	e_{max}: (0.980) e_{min}: (0.610) D_{50}: 0.240 mm <0.1 mm: less than 2.5%	(73-92)	WP	'38 mm'	1	C_v: 142 a_v: 0.54				
				'100 mm'	1, 0.5	C_v: 154 a_v: 0.51	C_h: 166 a_h: 0.50	C_{vh}: 49 a_{vh}: 0.30 b_{vh}: 0.19	C_{hh}: 63 a_{hh}: 0.10 b_{hh}: 0.42	C_h/C_v: 1.08 C_{hh}/C_{vh}: 1.29

Notes: (1). Limiting void ratios and relative density in brackets determined based on JIS standard, see Table 5-1; (2). AP-air pluviation; WP-water pluviation; (3). Stiffness parameters C_v, C_h, C_{vh} and C_{hv} with unit MPa; (4) All tests performed with lubricated plattens.

Table 5-6 Summary of bender element (BE) shear stiffnesses (G_{vh}) of sand specimens formed by different reconstitution methods

Source	Material	Properties	f(e)	Method	Shear stiffness (K = 1) [MPa]	$G^{(2)}$ [MPa]
Gu *et al*. (2015)	Toyoura sand	e_{max}: 0.98 e_{min}: 0.60 D_{50}: 0.17 m	$(2.17\text{-}e)^2/(1+e)$	Moist tamping (MT)	$G_{vh} = f(e)\times 104.6\times(p'/98)^{0.40}$	134.0
				Air pluviation (AP)	$G_{vh} = f(e)\times 86.5\times(p'/98)^{0.45}$	110.9
Escribano & Nash (2015)	Hostun sand	e_{max}: 1.00 e_{min}: 0.655 D_{50}: 0.35 mm	$e^{-1.10}$	Moist tamping (MT)	$G_{vh} = f(e)\times 77.6\times(p'/100)^{0.45}$	114.9
Azeiteiro *et al*. (2017)	Hostun sand	e_{max}: 1.00 e_{min}: 0.66 D_{50}: 0.33 mm	$(2.97\text{-}e)^2/(1+e)$	Air pluviation (AP)	$G_{vh} = f(e)\times 29.7\times(p'/101.3)^{0.49}$	89.5

Note: (1) All specimens isotropically (K = 1) consolidated; (2) Corresponding to p' = 100 kPa, e_0 = 0.70.

5.9.4 Figures

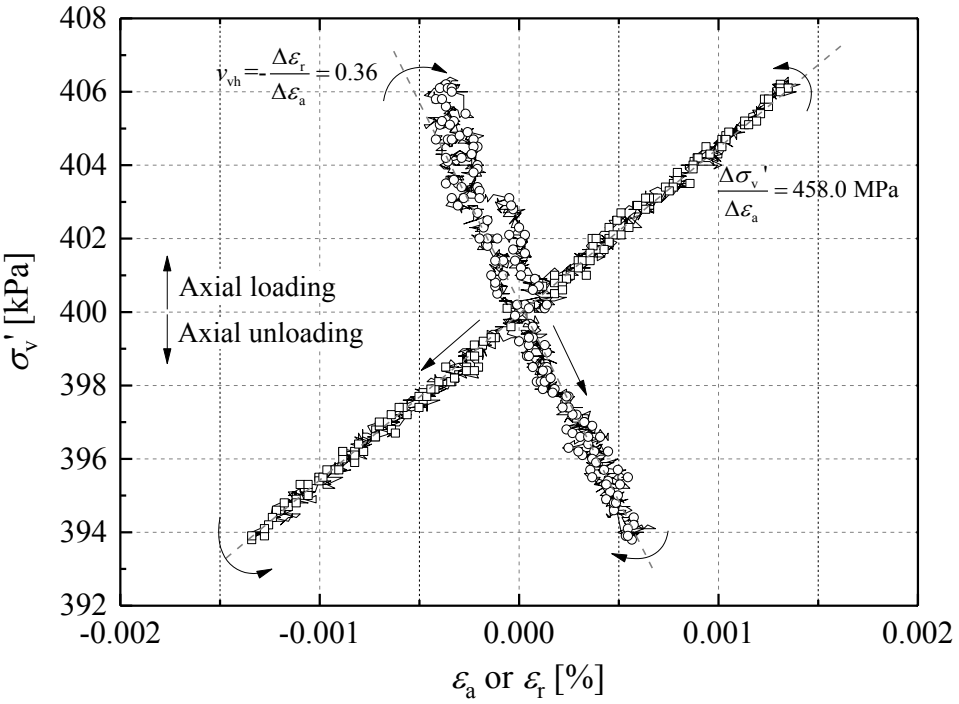

Figure 5-34 Stress-strain increments in a drained axial unloading-loading stress probe (±v′) at $(\sigma_v', \sigma_h') = (400, 200)$ (kPa)

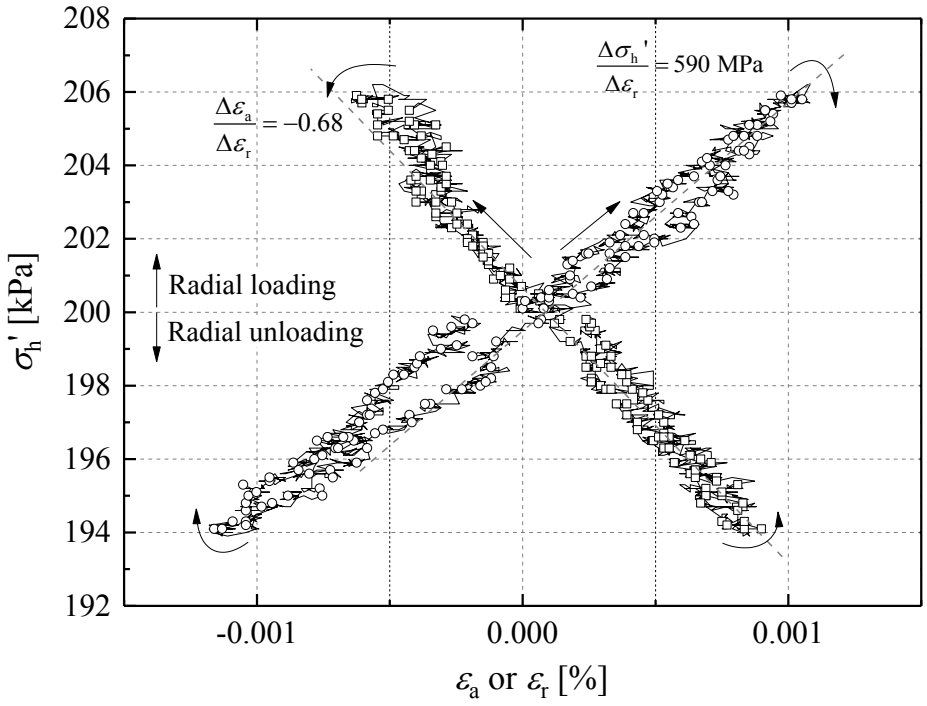

Figure 5-35 Stress-strain increments in a drained radial loading-unloading stress probe (±h′) at $(\sigma_v', \sigma_h') = (400, 200)$ (kPa)

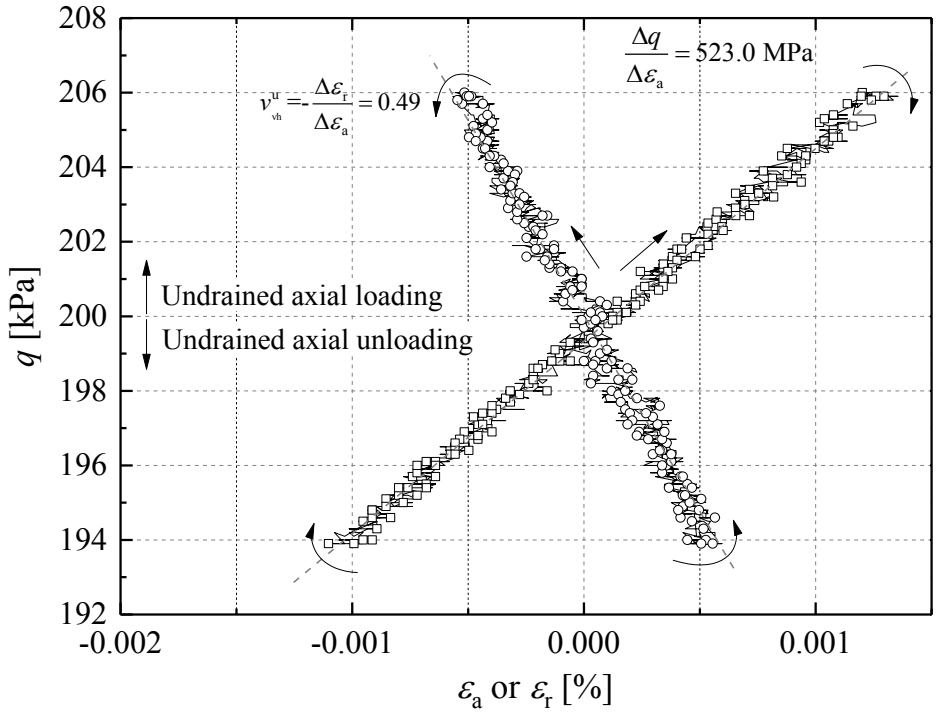

Figure 5-36 Stress-strain increments in an undrained axial loading-unloading stress probe (±q) at (σ_v', σ_h') = (400, 200) (kPa)

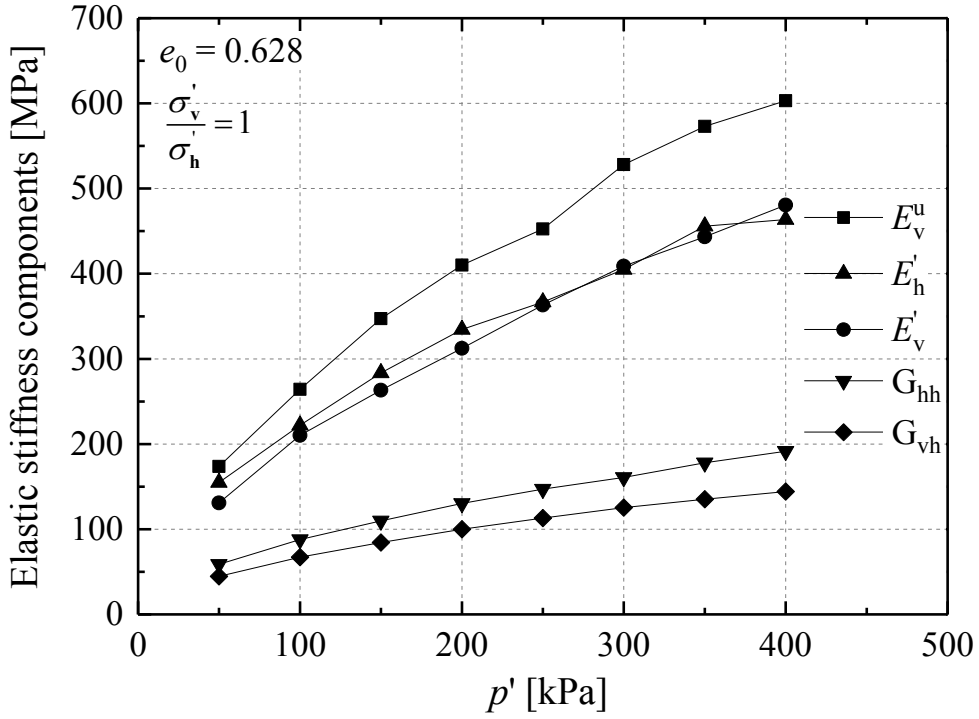

Figure 5-37 Variation trends of elastic stiffnesses against p' for the specimen DKB3PBIC with constant stress ratio K = 1

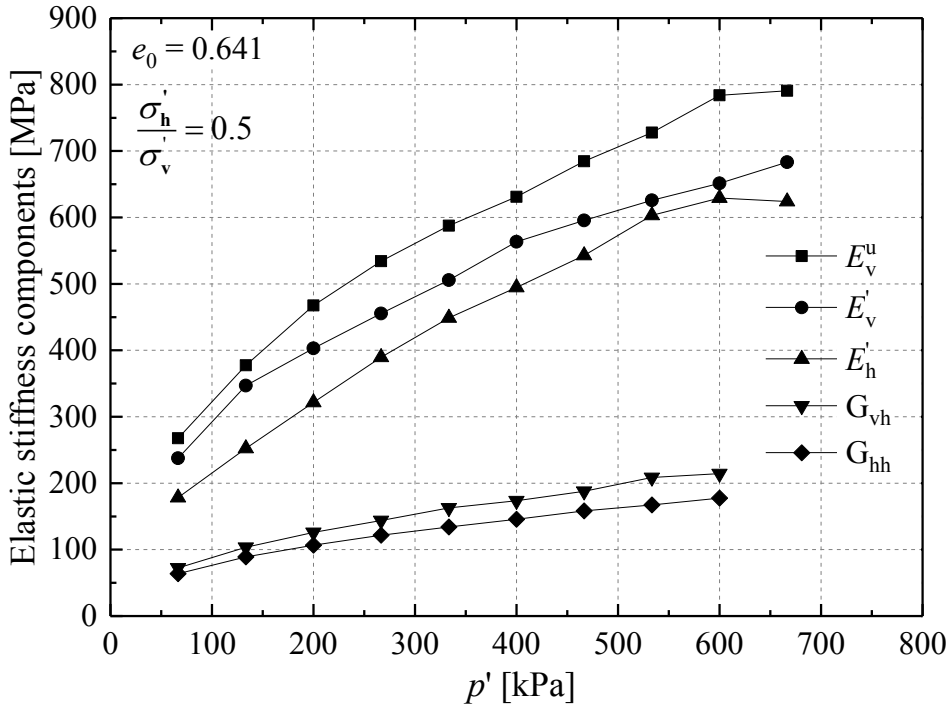

Figure 5-38 Variation trends of elastic stiffnesses against p' for the specimen DKB3PBKC with constant stress ratio $K = 0.5$

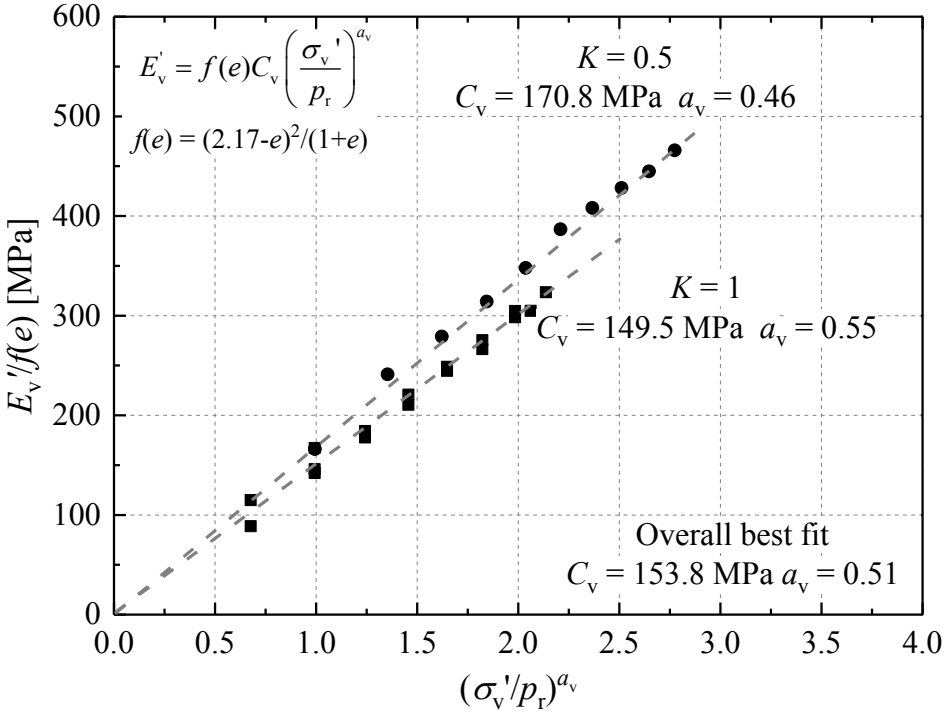

Figure 5-39 Correlations between $E_v'/f(e)$ and σ_v'/p_r and the derived stiffness parameters, C_v and a_v for the $K = 1$ and 0.5 tests

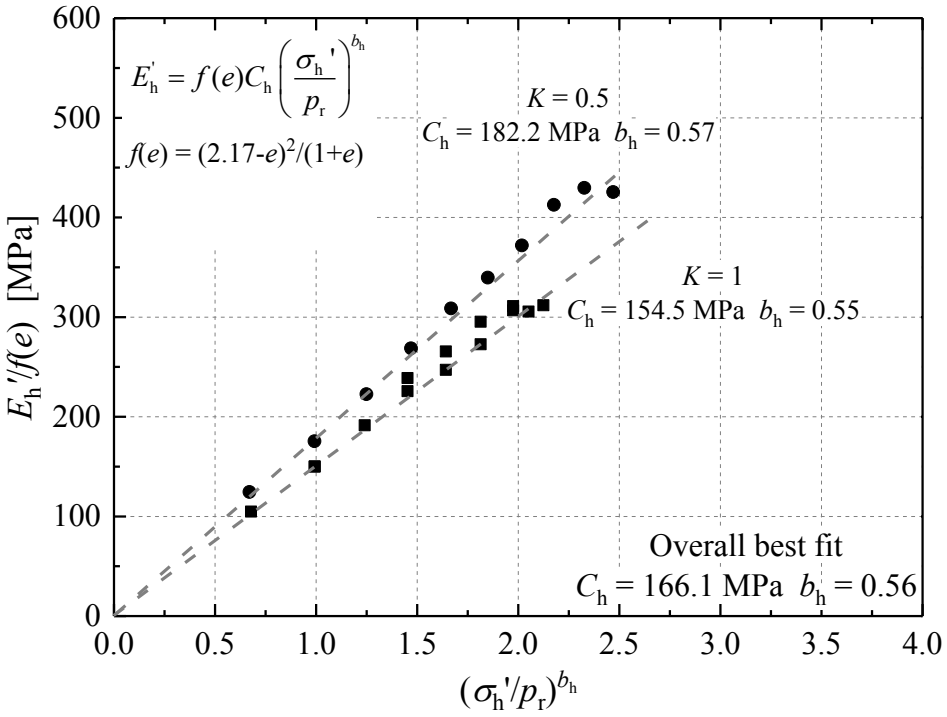

Figure 5-40 Correlations between $E_h'/f(e)$ and σ_h'/p_r and the derived stiffness parameters, C_h and b_h for the $K = 1$ and 0.5 tests

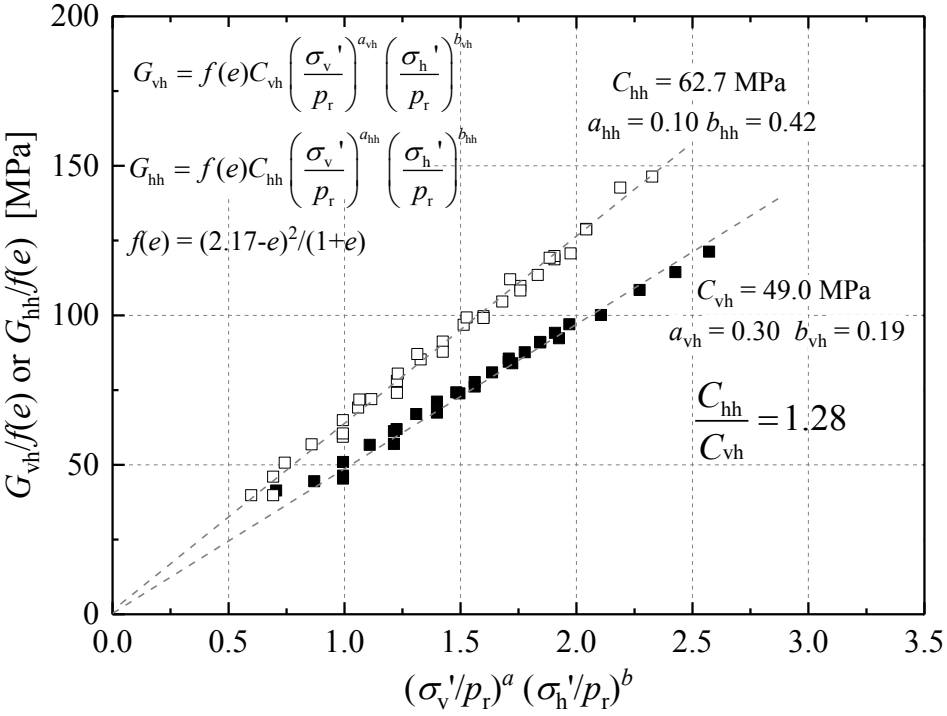

Figure 5-41 Correlations between normalised shear stiffnesses ($G_{vh}/f(e)$, $G_{hh}/f(e)$) and effective stresses components, also indicating the derived stiffness parameters

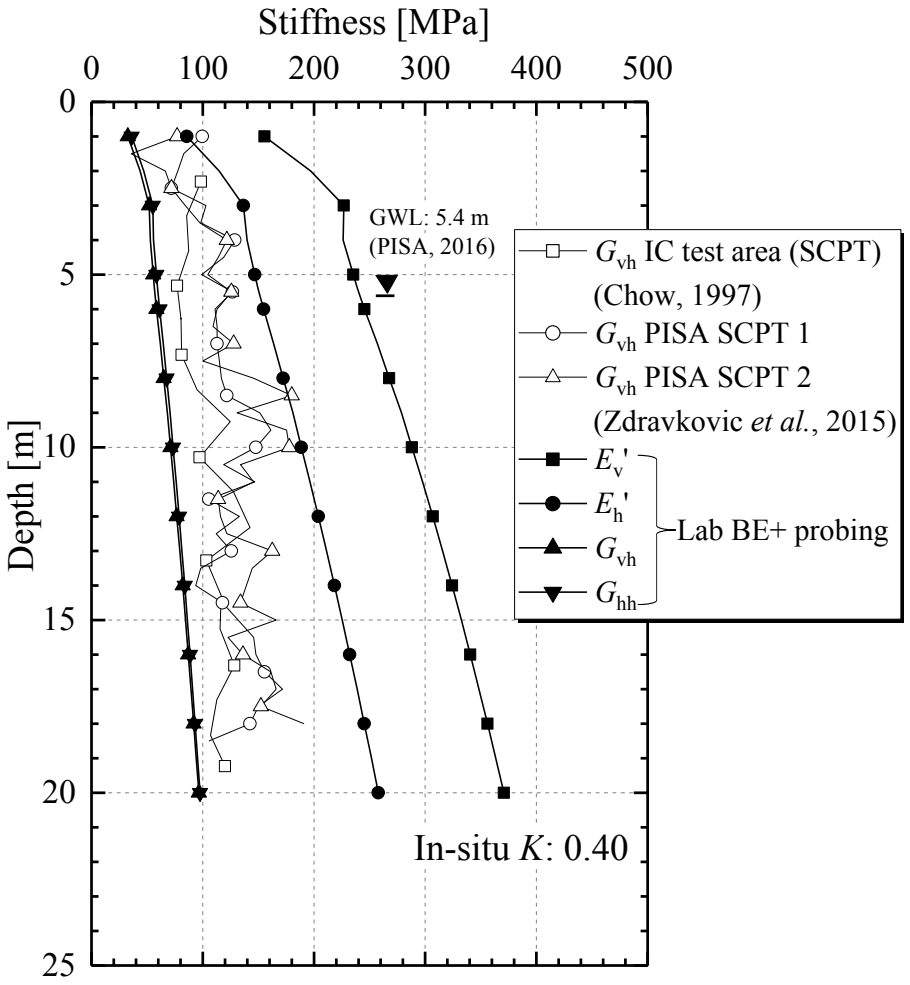

Figure 5-42 Dunkirk site stiffness profile determined from in-situ and laboratory shear velocity and triaxial probing tests

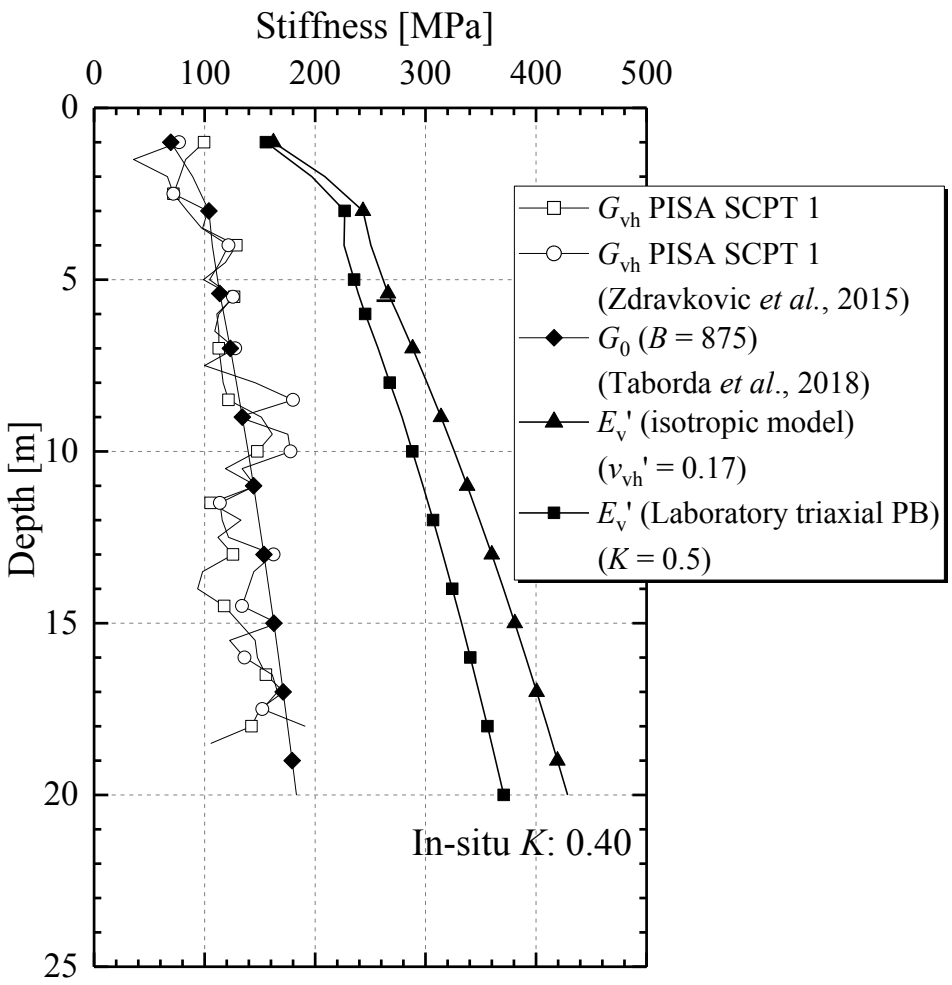

Figure 5-43 Profiles of G_{vh0} and E_v' based on isotropic model, in comparison with those from in-situ shear velocity (G_{vh}) and laboratory probing (E_v') measurements

5.10 **Summary and conclusions**

Characterisation of stiffness behaviour from the very small elastic range up to ultimate failure is crucial to the interpretation and modelling of geotechnical problems such as monopiles undergoing lateral and moment loading. This chapter summarises the outcomes of extensive triaxial testing programmes established to investigate the drained monotonic shearing behaviour of the Batch 2 and 3 bulk samples of Dunkirk sand.

The programme focused predominantly on isotropically consolidated specimens and consisted of 30 triaxial tests on Batch 2 Dunkirk sand performed by the Author, as well as 16 tests on Batch 3 carried out by Mr. Ken Vinck. Drained and undrained triaxial tests on anisotropically consolidated Batch 2 sand were reported earlier by Aghakouchak (2015), as were Kuwano's (1999) triaxial probing tests on Batch 1 sand. Bearing in mind the key hypotheses posed at the onset, the main conclusions can be drawn as follows.

1. Isotropic consolidation of water-pluviated specimens generated typically anisotropic patterns of local strains with $\Delta\varepsilon_r : \Delta\varepsilon_a \approx 2 : 1$, reflecting the sand particles' preferred orientation and anisotropic fabric that resulted from pluviation, which also contributed to the anisotropic stiffness characteristics observed after isotropic or K_o consolidation.
2. The degradation trends of vertical tangent Young's moduli ($E_{v,tan}'$) revealed the material's highly non-linear, stress- and strain-dependent pre-failure stiffness characteristics. Stiffness plateaux indicating the initial linear elastic zone were found that extended to axial strains of $(2\text{-}6)\times10^{-3}$%. Axial extension tests showed similar linear elastic $E_{v,tan}'$ values but followed more steeply non-linear stiffness degradation trends than equivalent compression tests.
3. Although the normally consolidated and over-consolidated specimens exhibited close (within 5%) elastic stiffnesses (E_{v0}') over their linear ranges, the over-consolidated specimens developed longer elastic plateaux and higher stiffnesses over their non-linear strain ranges. In-situ or laboratory geophysical measurements of elastic stiffness therefore provide incomplete information on the potential effects of effective stress history over the non-linear range. Site-specific monotonic laboratory tests are required to assess the full-strain range of stiffness

and strength characteristics.

4. The attained normalised vertical stiffness ($E_{v,tan}'/f(e)$) datasets correlated well with vertical effective stress (σ_v'/p_r) over a wide range of strain levels (ε_a = 0.001%, 0.01%, 0.1% and 1%) and can be satisfactorily represented by an hierarchy of power law functions ($E_{v,tan}'/f(e) = C_v(\sigma_v'/p_r)^{a_v}$) where C_v decreases with strain level while the exponents a_v increases. The anisotropically consolidated specimens (K = 0.45) exhibited lower C_v values over the non-linear range than the K = 1 specimens, reflecting the sand's anisotropic yielding characteristics when sheared in compression from anisotropic stress states that were closer to the yielding and failure envelopes.
5. The parallel tests performed with (semi- or fully-) rough plattens and over-sized lubricated plattens indicated that the apparent linear stiffnesses of the medium dense (R_d = 50%) specimens were raised, particularly under low effective stresses, by platten constraints that restricted grain movement and force chain buckling. The effects tended to diminish as the strain level increased and were less significant with denser specimens and under higher effective stress.
6. Two kinematic yielding surfaces, Y_1 and Y_2, were located and explained in detail for the isotropically consolidated specimens. The sizes of the surfaces in q-p' space varied with specimen density and effective stress level, and their vertical scales could be represented by power law functions of p'.
7. Parallel triaxial tests on Batches 2 and 3 Dunkirk sand revealed the latter to have generally lower pre-failure stiffnesses. However, the degree of difference depended on the platten conditions employed, and the tests adopting fully lubricated plattens gave close matches between the two batches' elastic Young' moduli.
8. Triaxial probing tests performed on water pluviated Batch 3 Dunkirk sand revealed its marked inherent anisotropy with the ratios of stiffness parameters, G_{hh}/G_{vh} and E_h'/E_v' being greater than unity. Moderate dependency on stress ratios (K) of the stiffness parameters C_v and C_h was noted as their values were higher for K = 0.5 condition than for K = 1.
9. The laboratory small strain stiffness measurements indicated trends for G_{vh} that resembled those measured in-situ by SCPT, but had distinctly lower values. However, the E_v' and E_h' laboratory measurements made at very small strains are more closely compatible with the field body wave stiffness trends.

CHAPTER 6
Large-strain behaviour of Dunkirk sands under monotonic loading

6.1 Introduction

Sand undergoing shearing to failure manifests highly non-linear stress-strain behaviour that is critically dependent on its "state", which comprises void ratio, stress conditions and fabric: Jefferies & Bean (2006). Unified approaches are required to interpret how the components of state affect sand behaviour so that appropriate relationships may be established that can be applied in realistic constitutive and numerical modelling of engineering problems, such as the monopile foundations considered in the PISA project.

Characterisation of Dunkirk sand's large strain behaviour, both experimentally and numerically, was essential to the accurate prediction of lateral capacity and load-displacement response of the PISA Dunkirk piles. The Author's research programme supplemented the previous laboratory studies by Kuwano (1999) and Aghakouchak (2015), and was schemed to support the calibration of the Taborda *et al.* (2014) bounding surface plasticity model employed in the PISA sand case analyses reported by Zdravković *et al.* (2015) and Taborda *et al.* (2018).

It is noted that, as described in Chapter 5, the Author's study focused on triaxial testing. While the testing was comprehensive, it generated only limited information on the sand's anisotropic shear strength and stress dilatancy properties that may apply under wider range of intermediate principal stress level (b) and major principal stress axis direction (α). Water bourne deposits such as Dunkirk sand are known to exhibit both significant inherent and stress-induced anisotropy. Experimental studies on these features of granular materials have been conducted earlier at Imperial College by for example Symes (1983), Porovic (1995) and Zdravkovic (1996), based on both HCA

and triaxial testing. Earlier studies have also shown that isotropically and K_o consolidated specimens can show quite different patterns of yielding, and markedly different behaviour under, for example, undrained shearing.

This Chapter focuses on the outcomes from the Author's triaxial tests on Batch 2 Dunkirk sand, reporting the experimental results that were input to the PISA numerical simulations described by Taborda *et al.* (2018). Detailed descriptions of the sand's index properties, and the Author's testing methodology and programme were given in Chapter 5. It was explained there that due to the limiting availability of the Batch 2 sand, the study of long-term cyclic and post-cycling behaviour of Dunkirk sand that is described in the following Chapter 7, had to be performed on Batch 3 material. Comparisons are therefore given in this chapter on possible differences between the two batches of materials in terms of their shear strength and volumetric behaviour.

A brief review is first presented of the critical state framework and state parameter approach for interpreting sand behaviour under monotonic loading. Testing outcomes and interpretation follow that focus on (normalised) shear stress-strain response, volumetric behaviour and critical state behaviour. The sand's phase transformation and peak stress ratio states are characterised based on the testing outcomes. Discussion is also give on the effects of triaxial sample end constraints on large shear strain behaviour.

The key hypotheses examined in this Chapter are as follows:

#1. The critical state of Dunkirk sand can be reasonably characterised under moderate stress ranges ($p' < 1$ MPa) through drained triaxial tests on reconstituted specimens prepared at states denser than critical;
#2. The critical state v-p' relationship can be described using power law functions;
#3. The phase transformation (PT), peak stress ratio (PSR) and critical states (CS) developed by Dunkirk sand under monotonic shearing can be depicted by linear correlations between the state parameter (ψ) and the triaxial stress ratio (q/p');
#4. Triaxial sample end constraints can affect the large shear strain behaviours developed in routine testing on sands.

6.2 Review: Critical state behaviour of granular materials and the state-parameter approach

The critical state framework has been widely employed for interpreting and modelling the multi-faceted behaviours of both clays (Schofield & Wroth, 1968, Wood, 1990) and sands (Been & Jefferies, 1985, Coop & Lee, 1993, Coop *et al.*, 2004). This section presents a brief review that focuses on the different descriptive approaches for the critical state behaviour of sands, as well as the state parameter-based framework for interpreting sand behaviour.

6.2.1 Description of the critical states

Several types of formulation have been introduced for describing the critical states of sands in a v:p' plane, where v is specific volume expressed as $1+e$. The classical formulation expresses the CSL as a straight line in the v:lnp' plane, which is assumed to be parallel to a log-linear triaxial normal compression line (NCL).

$$\upsilon = \Gamma - \lambda \ln p' \tag{6.1}$$

Where λ and Γ are parameters representing the slope of the critical state line in v:lnp' space and the intercept with the p' = 1 kPa axis. Adopting this formulation, Coop & Lee (1993) characterised critical state lines for a highly crushable Dogs Bay sand and quartzitic Ham River sand, as shown in Figure 6-1, noting that the critical states were accompanied by significant grain breakage for Dogs Bay sand from relatively low p' levels and Ham River sand under more elevated pressures.

Been *et al.* (1991) demonstrated that the critical state lines were curved in the v:lnp' plane with lower gradients λ applying over the engineering pressure range (< 1 MPa) than over the higher pressure ranges, where particle breakage develops. They proposed bilinear critical state lines to cover the full pressure range.

An alternative approach for describing the quasi-asymptotic trends over low pressures and the steeper trends noted under high pressures is to introduce power law expressions (Li & Wang, 1998) with the form of

$$e_{cs} = e_{cs\_ref} - \lambda \left(\frac{p'}{p_{ref}} \right)^{\xi} \tag{6.2}$$

Where e_{cs_ref} is a reference void ratio for p' = 0 kPa and is often considered to be close to the material's maximum void ratio (e_{max}). The λ and ξ parameters define the location

and curvature of the critical state line in the v:logp' plane. As shown in Figure 6-2, Taborda *et al.* (2014) demonstrated how a power law function led to comparable overall degree of fit to a set of experimental data as by the bilinear function.

However, as pointed out by Klotz & Coop (2002), it is difficult to determine critical states at relatively low stresses, primarily due to (i) the limited strains applied in commonly used triaxial apparatus; (ii) the development of strain localisations or barrelling deformations within the specimens that induce uncertainties in determining stress states and critical state volumes. Also the lowest densities that may be achieved by reconstituting specimens by air or water pluviation methods are often limited. In most cases, only data from tests on dilatant samples can be applied to investigate the critical state line over the typical engineering p' range of 0-1000 kPa.

Crushing induced relocation of CSL and its description

The critical state line curvature seen with silica sands at $p' > 1$ MPa is often associated with grain breakage. It has become recognised that the gradually mutating granular assemblies produced by grain breakage generate sets of critical state lines that are located beneath those of the 'parent unbroken' material in the e:logp' plane.

Altuhafi *et al.* (2017) reported how the critical state lines of Fontainebleau NE34 sand evolved under high pressure conditions, reporting the triaxial studies as shown in Figure 6-3. The specimens were pre-sheared to failure in compression with $p' = 10$ MPa, and were unloaded and swelled back to lower pressures (150-500 kPa), before being sheared again to failure. The new critical state line identified for the fractured materials fell substantially below that of the fresh specimens sheared at lower effective stress levels.

The fractured materials generate suites of critical state lines that vary with the evolving gradings. Muir Wood (2007) and Muir Wood & Maeda (2008) introduced a grading state index I_G, which is defined as the area ratio of the current grading to a limit grading, and they described the relocated critical state lines as

$$\upsilon = \Gamma(I_G) - \lambda(I_G) \ln p' \tag{6.3}$$

For any stable granulometry with a fixed I_G, the relocated critical state lines are practically parallel to the virgin critical state line in the e:lnp' space. Ciantia *et al.* (2018) considered evolving soil gradings in their discrete element models (DEM), and

introduced a critical state plane (CSP) in a 3-D e:p':I_G space that was expressed as

$$e = \alpha + \beta I_G + \delta \left(\frac{p'}{p_a} \right)^{0.7} \tag{6.4}$$

Where α, β and δ are fitting parameters.

The Author's study on Dunkirk sand focused on the stress range applying to field monopile lateral loading when p' is generally less than 1 MPa. Although significant grain crushing inevitably takes place beneath monopile tips, and immediately adjacent to the pile shafts, during pile driving (as discussed in Chapter 4), the effects were not deemed to be critical to modelling the PISA lateral loading cases, which mobilised large volumes of sand, much of which started from near undisturbed in-situ soil stresses.

6.2.2 State parameter approach and constitutive modelling

The states of soils represent the conditions under which they exist. A state parameter ψ is commonly used to determine the deviation between the soil's current state and the reference critical state in e:p space, and is defined by Been & Jefferies (1985) as

$$\psi = e - e_{cs} \tag{6.5}$$

Where e and e_{cs} represent the soils' current void ratio and the corresponding void ratio at critical state under equivalent p' level.

The state parameter concept has been widely employed in conjunction with the critical state framework in developing sand constitutive models that can reproduce multi-faceted soil behaviours under general monotonic and cyclic loading conditions, see for example by Wood & Belkheir (1994), Manzari & Dafalias (1997), Papadimitriou & Bouckovalas (2002) and Taborda (2011).

A two-phase plasticity model for sands was proposed by Manzari & Dafalias (1997) that employed linear state-dependent relationships between the three characteristic stress ratios (q/p'): critical state ratio (M_c or M_e, subscripts c for compression, e for extension), peak stress ratio (M_c^b, M_e^b) and dilatancy stress ratio (M_c^d, M_e^d), through the following formulations.

$$M_{\mathbf{c}}^{\mathbf{b}} = M_{\mathbf{c}} + k_{\mathbf{c}}^{\mathbf{b}}\langle -\psi \rangle$$
$$M_{\mathbf{e}}^{\mathbf{b}} = M_{\mathbf{e}} + k_{\mathbf{e}}^{\mathbf{b}}\langle -\psi \rangle \tag{6.6}$$

$$M_{\mathbf{c}}^{\mathbf{d}} = M_{\mathbf{c}} + k_{\mathbf{c}}^{\mathbf{d}}\psi$$
$$M_{\mathbf{e}}^{\mathbf{d}} = M_{\mathbf{e}} + k_{\mathbf{e}}^{\mathbf{d}}\psi \tag{6.7}$$

Where k_c^b and k_e^b are state parameter coefficients for correlating critical state and peak stress ratios, and k_c^d and k_e^d for correlating critical state and dilatancy stress ratios. The Macauley brackets $\langle\ \rangle$ make $\langle -\psi \rangle = -\psi$ if $-\psi > 0$ and $\langle -\psi \rangle = 0$ if $-\psi \leq 0$.

Soil dilation D is proportional to the difference between the dilatancy stress ratio $M_{c,e}^d$ and the current stress ratio η, and is linked using a dilatancy constant A_d as follows.

$$D = A_{\mathbf{d}}(M_{\mathbf{c,e}}^{\mathbf{d}} - \eta) \tag{6.8}$$

The above parameters, k_c^b, k_e^b, k_c^d, k_e^d and A_d can be calibrated using drained and undrained triaxial tests that cover a reasonable large range of soil densities. Azeiteiro *et al.* (2017) reported extensive laboratory triaxial tests on air-pluviated Hostun sand, and demonstrated how the test outcomes can be processed to determine these parameters.

The multiple bounding surface plasticity model (Taborda *et al.*, 2014) adopted for numerical modelling of the PISA pile tests at Dunkirk is an upgraded version of the bounding surface model initially proposed by Papadimitriou & Bouckovalas (2002) but with improved features in terms of the shape of the critical state line, the hardening modulus and the yield surface.

It should be noted that in the above models, as well as the initial proposition by Manzari & Dafalias (1997), both the elastic and plastic behaviour are formulated based on isotropic material behaviour assumptions without implementing anisotropic stiffness or hardening laws. The models can reflect the effects of variations in the relative magnitude of the intermediate principal stress (σ_2) (as expressed by parameter b or Lode angle θ), but do not incorporate any anisotropic features that may be observed by rotating the major principal stress axis direction (α). Lateral loading pile boundary value problems involve wide ranges of b and α conditions, and consideration needs to be given to their potential impact on field simulations when considering anisotropic media, such as Dunkirk sand.

The Author's triaxial testing programme was set up to generate the essential inputs for calibrating the isotropic bounding surface plasticity model. With this in mind, testing focused predominantly on isotropically consolidated specimens to facilitate the characterisation of the four distinctive bounding surfaces shown in Figure 6-4. Kuwano (1999) and Aghakouchak (2015) reported other experiments on K_o consolidated Dunkirk sand which provided evidence of the additional anisotropy in mechanical behaviour that develops under such test conditions.

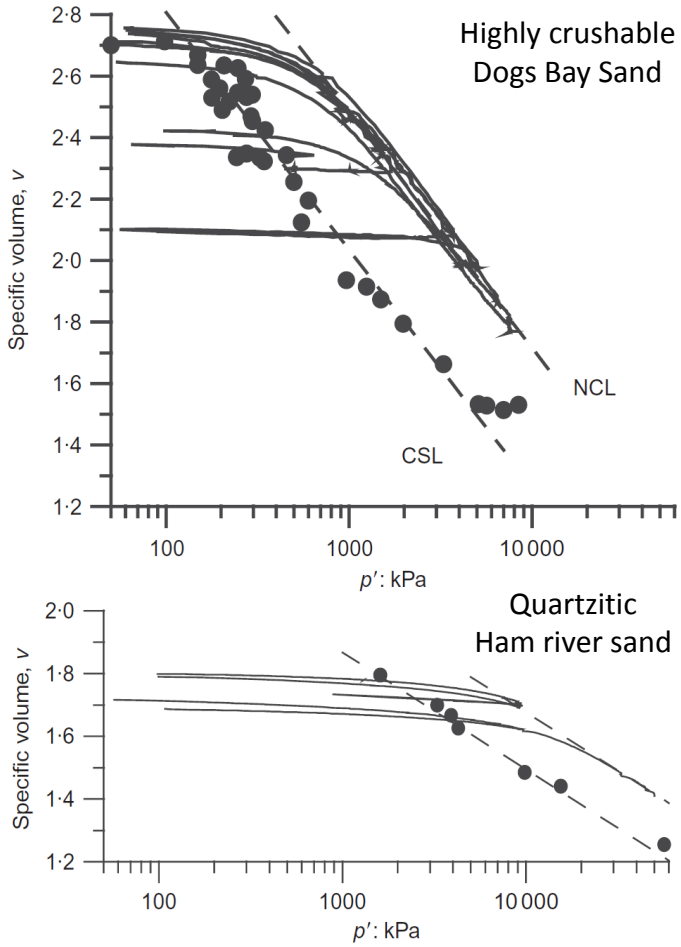

Figure 6-1 Representation of critical state behaviour of Dogs Bay sand and Ham River sand using linear v:lnp' critical state lines (Coop & Lee, 1993, López-Querol & Coop, 2012)

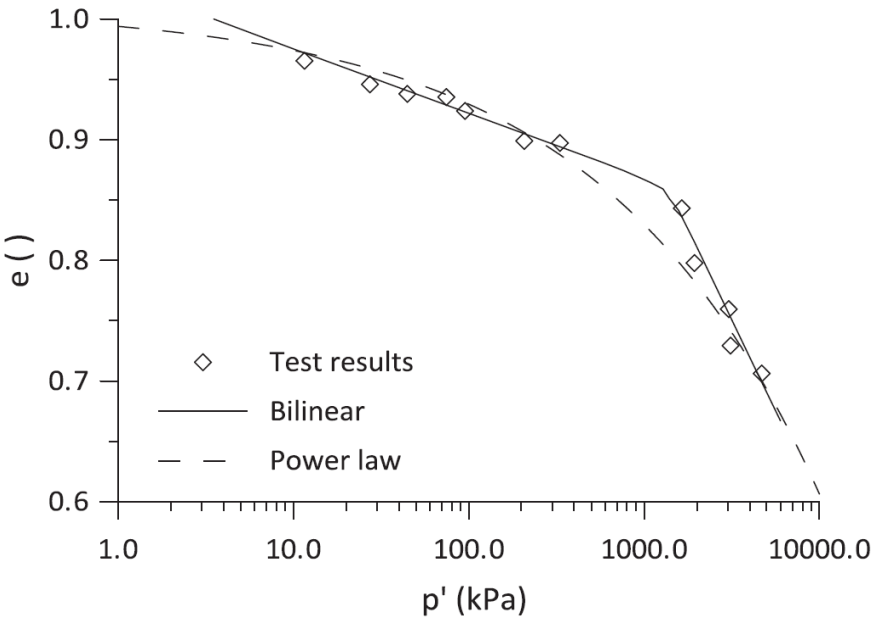

Figure 6-2 Alternative interpretation of critical state line using bilinear and power law functions (Taborda *et al.*, 2014)

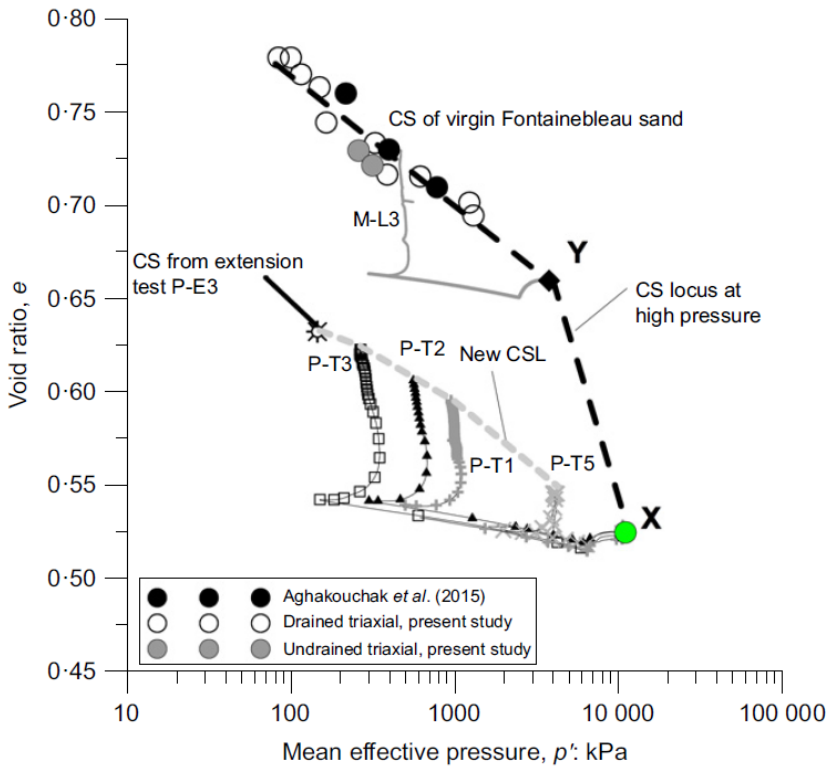

Figure 6-3 Relocation of critical state line of siliceous Fontainebleau NE34 sand due to particle crushing (Altuhafi *et al.*, 2017)

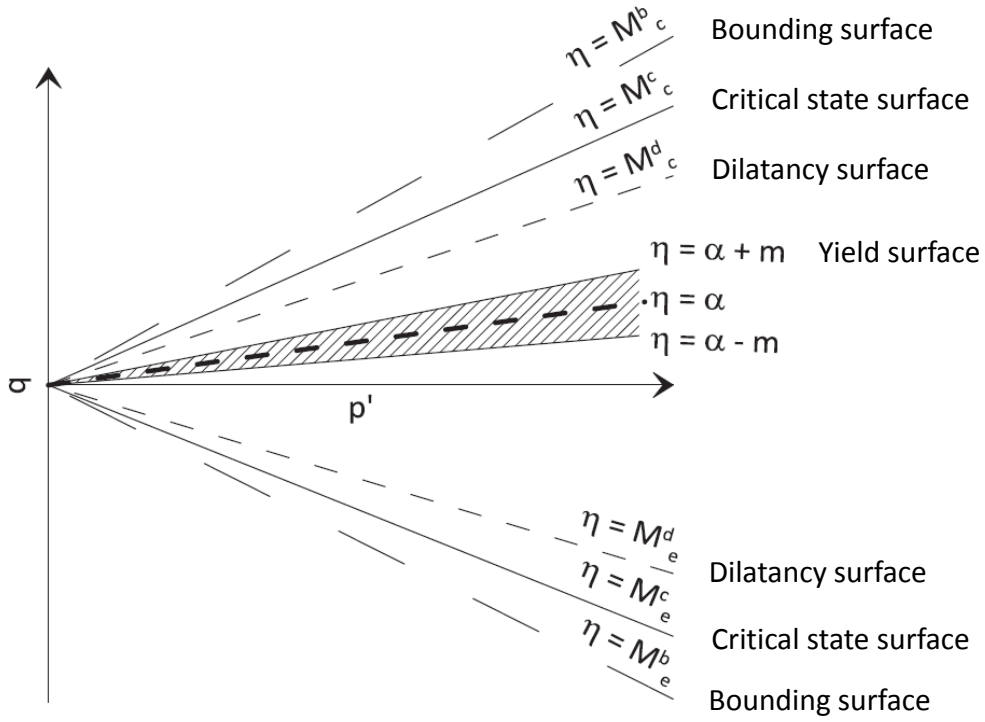

Figure 6-4 Representation of the multiple bounding surface model adopted in the PISA simulation of Dunkirk pile tests (Taborda *et al.*, 2014)

6.3 Assumptions and corrections applied in analysing large-strain triaxial shearing tests

Area corrections

While specimen deformation measurements obtained from local strain sensors are crucial to establishing the behaviour of sands under small strain static or cyclic test conditions, their response often becomes unrepresentative after large strains have developed. Global measurements made by external axial displacement transducers and volume-gauges were therefore adopted as being more representative when considering the specimens' overall large strain deformations.

Alternative approaches for correcting the specimens' cross-sectional areas were also considered. As summarised by Germaine & Ladd (1988), the options include:

$$A_c = A_0\left[\frac{1-\varepsilon_{vol}}{1-\varepsilon_a}\right] \quad \text{right-cylinder} \tag{6.9}$$

$$A_c = A_0\left[-\frac{1}{4}+\frac{\sqrt{25-20\varepsilon_a-5\varepsilon_a^{\,2}}}{4(1-\varepsilon_a)}\right]^2 \quad \text{parabolic} \tag{6.10}$$

$$A_c = A_0\left[\frac{1-\varepsilon_{vol}}{1-a\varepsilon_a}\right] \quad \text{bulging} \tag{6.11}$$

Where A_0 is specimen cross sectional area at the beginning of shearing. ε_{vol} and ε_a are respectively specimen volumetric strain and axial strain during shearing. The parameter a is an experimental constant, defined as the ratio of the length of the specimen to the length of bulging zone and was found to be normally between 1 and 2.

The right-cylinder assumptions is the most commonly adopted form and may be most applicable to tests performed with lubricated plattens. The Author's specimens could not retain truly right-cylinder shapes after 10-15% axial strains and failed with some degree of bulging, regardless of the platten configuration used. However, the implementation of bulging correction required precise and case-by-case determination of bulging length and the parameter a, which was found practically difficult and subjective under the varied testing conditions and strain levels considered (up to 40% axial strain). The right-cylinder area correction was therefore retained throughout the Author's interpretation as a consistent, even if not fully precise, measure.

Corrections for membrane constraints

Membrane restraint corrections are required when testing sands under low stress or large strain conditions. The elastic membrane corrections proposed by Hellings (1988) were employed to correct the axial (σ_a) and radial stress (σ_r) through the following formulations.

$$\sigma_a = \sigma_{a0} - 2\alpha\beta(2\varepsilon_a + \varepsilon_r) \tag{6.12}$$

$$\sigma_r = \sigma_{r0} - \alpha\beta(\varepsilon_a + 2\varepsilon_r) \tag{6.13}$$

with

$$\alpha = 4E_m t_0 / (3D_0) \tag{6.14}$$

$$\beta = \frac{1}{(1-\varepsilon_r)^2(1-\varepsilon_a)} \tag{6.15}$$

Where the σ_{a0} and σ_{r0} are the uncorrected axial and radial stresses, respectively, ε_a and ε_r represent recorded axial and radial strain, and t_0 and D_0 denote the membrane's initial thickness and diameter. E_m is the Young's modulus for latex rubber, which was adopted as 1100 kPa for tests with ≈ 10 days duration that involved large axial straining (ε_a > 20%).

6.4 Shear stress-strain response and volumetric behaviour

Following the interpretation of the (Batch 2) Dunkirk sand's pre-failure stiffness behaviour presented in Chapter 5, the following sections discuss the sand's large strain behaviour to failure. Detailed descriptions of the testing methodology and programme are given in Section 5.3 and Table 5-2.

Before moving on to examine the four hypotheses posed in Section 6.1, it is worth considering the test outcomes that concern the sand's (normalised) shear stress-strain response and volumetric behaviour under various testing conditions. The key influences of specimen density, stress level and stress history (*OCR*) on large strain behaviour are highlighted below, considering an initial set of experiments.

The initial set of tests was performed with standard size semi-rough (SR) or fully-rough (FR) plattens (see descriptions in Section 5.3.3). Further discussion is presented in the following sub-section on the effects of end-restraint, drawing on later experiments performed with over-sized fully lubricated (OL) plattens.

6.4.1 Shear stress-strain response

Effects of effective stress level and specimen density

Figures 6-5 and 6-6 summarise the typical triaxial compression and extension stress-strain (q-ε_a) responses of the dense (relative density R_d = 79%, e_0 = 0.640) and medium dense (R_d = 50%, e_0 = 0.740) specimens that had been normally consolidated to a range of isotropic initial mean effective stress levels (p_0'). Most of the specimens mobilised relatively stable final shear strengths after 25-35% axial compression strains, although fully steady trends were not reached in some cases due to apparatus travel limits. In contrast, the extension tests exhibited clear necking failures after around 11% axial strain, corresponding to the onset of severe strain localisation. The latter stress-strain data are regarded as providing nominal trends, as indicated with dashed lines in Figure 6-6.

Figure 6-7 demonstrates how the normalised shear stress-strain responses (q/p') vary with effective stress and strain levels for the dense (R_d = 79%, e_0 = 0.640) specimens. The peak q/p' ratios generally decreased with increasing p_0' and the three higher p_0' tests trended towards similar ultimate q/p' ratios of 1.3, which corresponds to ϕ_{ult}' = 32.3˚.

The effects on shear strength of specimen density are evident in Figure 6-8, which compares the trends for specimens prepared at three densities (R_d = 50%, 79% and 95%) and under two stress levels (p_0' = 100 kPa and 400 kPa). As expected, the dense specimens exhibited higher peak q/p' and ϕ_{peak}' values, and at earlier axial strain levels, but their ultimate trends converged with those of the less dense specimens. Similarly evolving patterns were observed in the normalised q/p' trends of these tests, as plotted in Figure 6-9, which also indicates the combined effects of specimen density and mean effective stress level.

Effects of over-consolidation

The important effects of effective stress history (*OCR*) on pre-failure stiffness behaviour were addressed in Section 5.5.1. It was shown that while the normalised initial (Y_1) linear elastic stiffness levels may not be unduly influenced by *OCR*, an over-consolidated stress history could extend the linear range and enhance the sands' non-linear stiffness characteristics considerably. Positive effects on shear strengths are also evident, as shown in Figure 6-10. The over-consolidated specimens (*OCR* = 4) mobilised higher peak q/p' and ϕ' than the normally consolidated specimens that persisted up to around 10% axial strain, although thereafter their trends converged towards common ultimate conditions.

Although the sand conditions are largely normally consolidated at the Dunkirk PISA test site, any in-situ over-consolidation should be accounted for when designing site-specific laboratory testing programmes and performing numerical analyses for other cases. The effects of *OCR* are most important over the non-linear strain range from 0.001% to 1% that most affects the outcomes from analyses of practical geotechnical engineering problems; including cases involving piles driven in sands, see Jardine (2013).

6.4.2 Volumetric response

The specimens sheared from isotropic stress states manifested invariably contractive volume changes in their early stage of shearing, before transforming to dilatant patterns up to failure.

Examples are shown in Figure 6-11 of ε_{vol}-ε_a trends for a set of medium dense (R_d = 50%, e_0 = 0.740) specimens, indicating clear effects of effective stress level on the

volumetric response. Only the test performed under p_0' = 600 kPa (a relatively high stress level) appeared to reach constant volume (critical state) ultimate conditions, while tests performed under lower stresses showed dilation continuing, even after axial strains of 30-35%, even though the q/p' responses showed more stable trends (see Figure 6-9). As discussed later, the volumetric responses were affected significantly by sample end restraint, particularly in the tests on less dense specimens.

Figure 6-12 demonstrates further effects of over-consolidation on volumetric behaviour. The *OCR* = 4 specimens manifested less initial contraction and greater ultimate dilation. Their overall ε_{vol}-ε_a trends were located below those of the normally consolidated specimens.

The above presented axial (ε_a) and volumetric (ε_{vol}) datasets from external axial displacement and volume-gauge measurements allow further calculation of triaxial shear strains ε_s (calculated as $2/3\times(\varepsilon_a - \varepsilon_r)$ or $(\varepsilon_a - \varepsilon_{vol}/3)$) and total dilation ($D^t = d\varepsilon_{vol}^t/d\varepsilon_s^t$), which are essential in the interpretation of stress-dilation correlations, as detailed in Section 6.7.

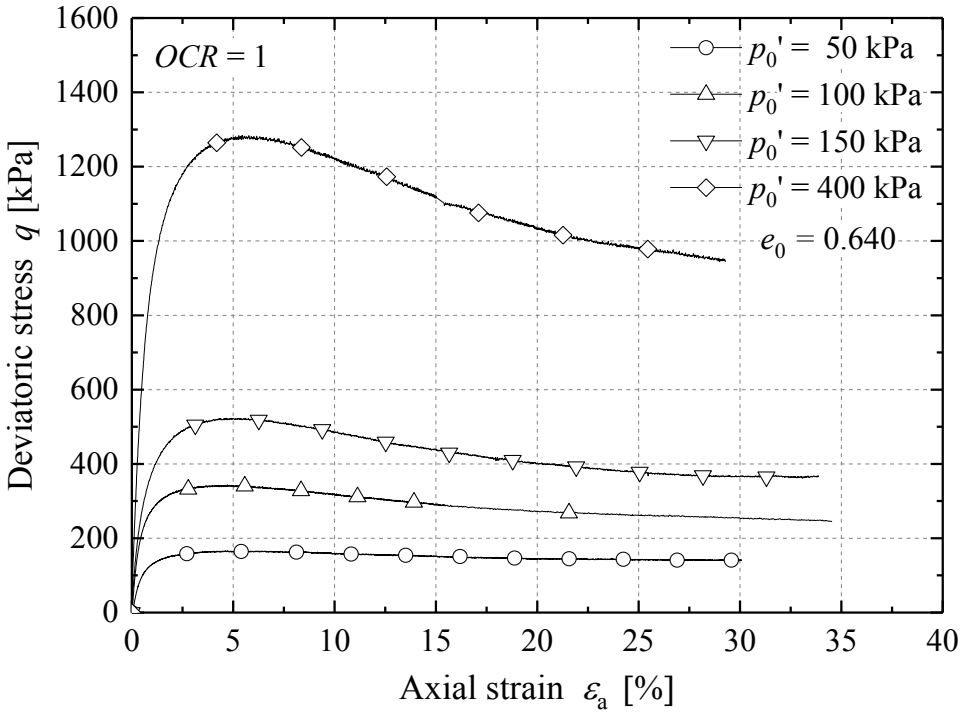

Figure 6-5 Stress-strain response of normally consolidated dense (R_d = 79%, e_0 = 0.640) samples under triaxial compression employed semi-rough plattens

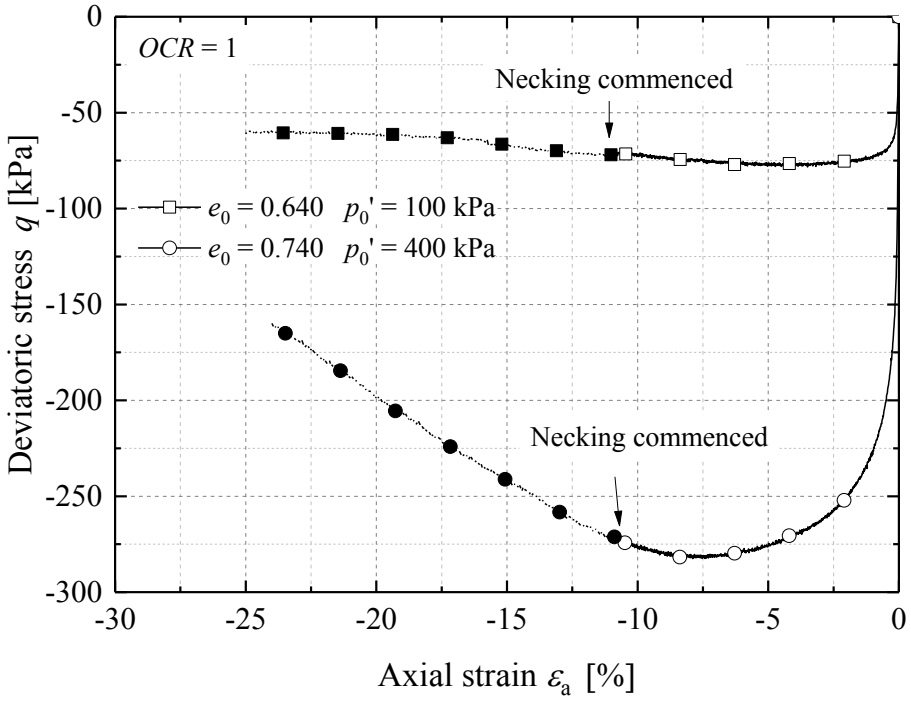

Figure 6-6 Stress-strain response of normally consolidated dense (R_d = 79%, e_0 = 0.640) and medium dense (R_d = 50%, e_0 = 0.740) samples under triaxial extension

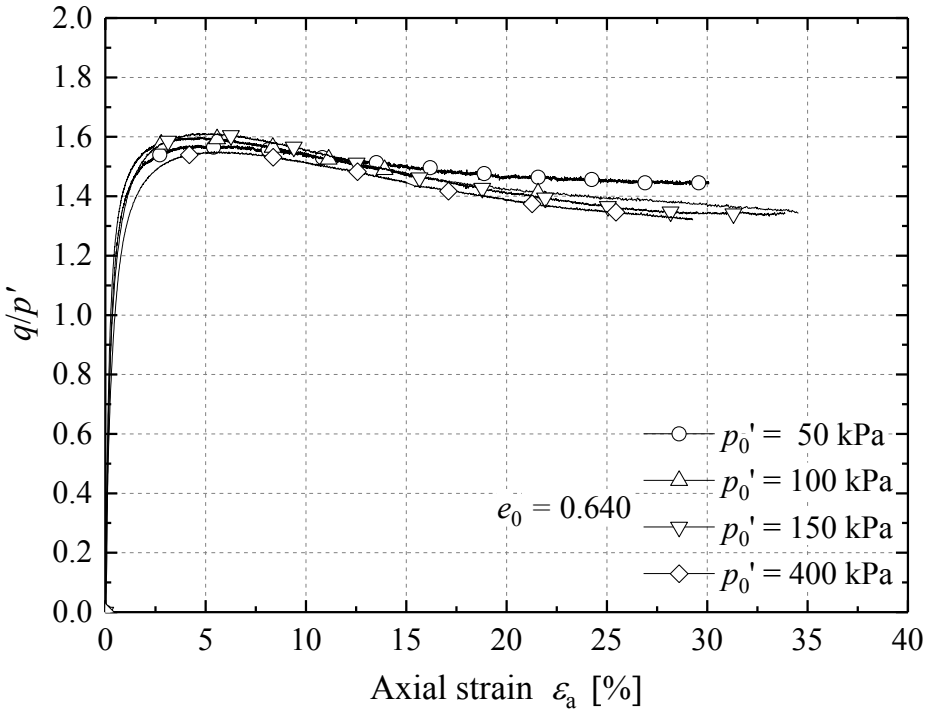

Figure 6-7 Normalised stress-strain response of the dense (R_d = 79%, e_0 = 0.640) specimens (OCR = 1) adopting semi-rough plattens

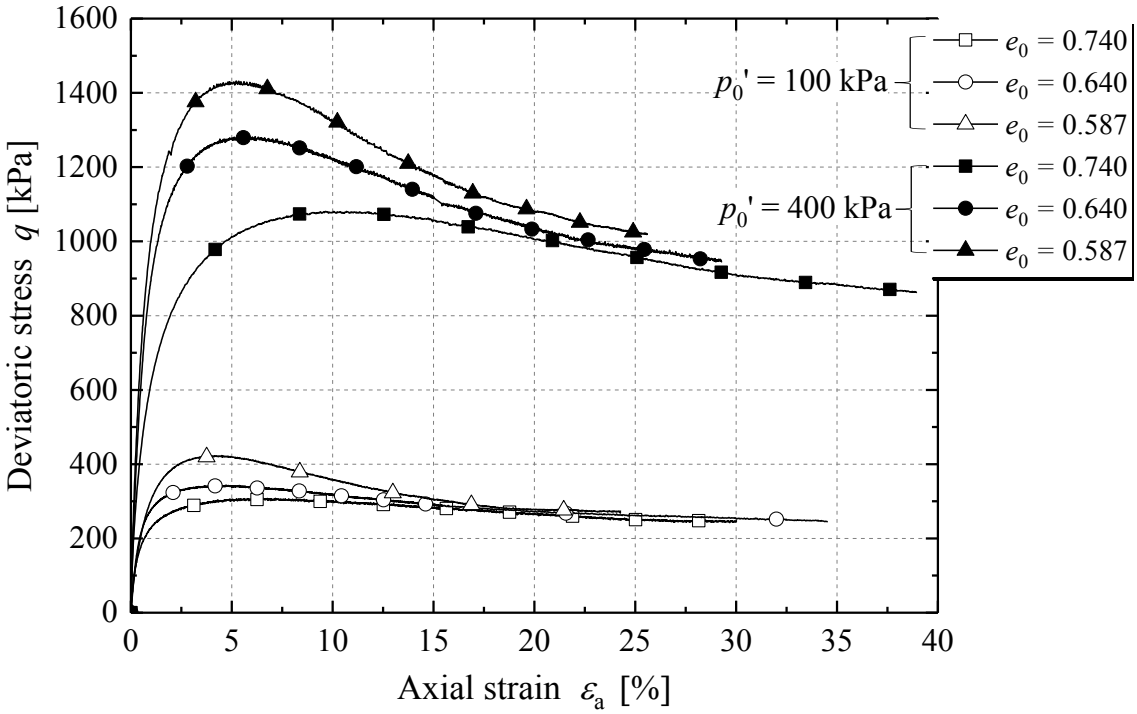

Figure 6-8 Effects of specimen density on shear strength (OCR = 1) (fully-rough plattens for e_0 = 0.740 samples, others with semi-rough plattens)

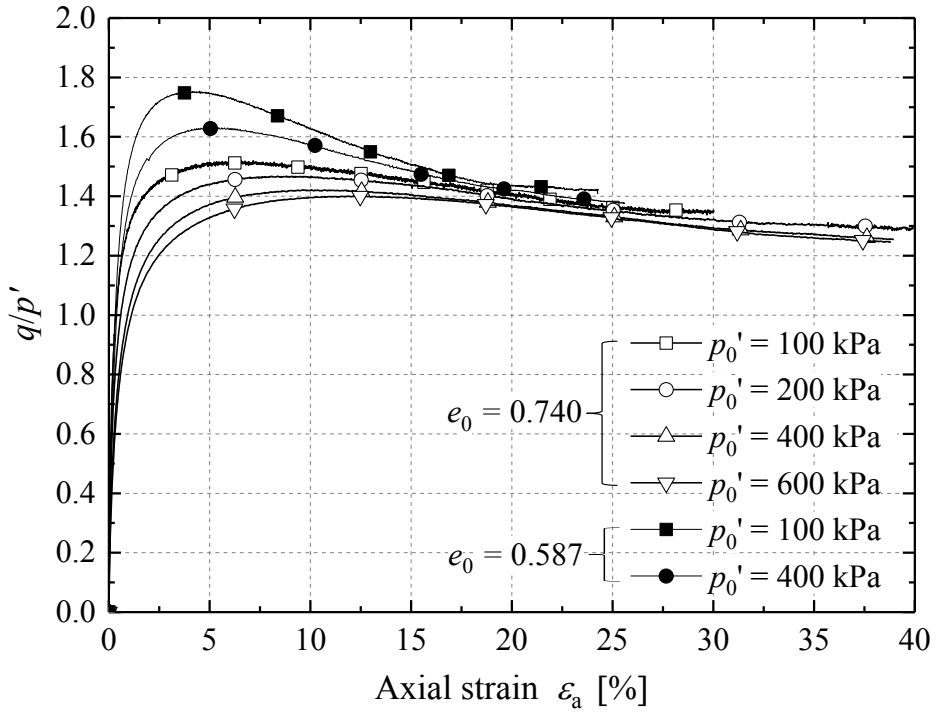

Figure 6-9 Normalised stress-strain response of the very dense (R_d = 95%, e_0 = 0.587) and medium dense (R_d = 50%, e_0 = 0.740) samples with semi-rough and fully-rough plattens respectively

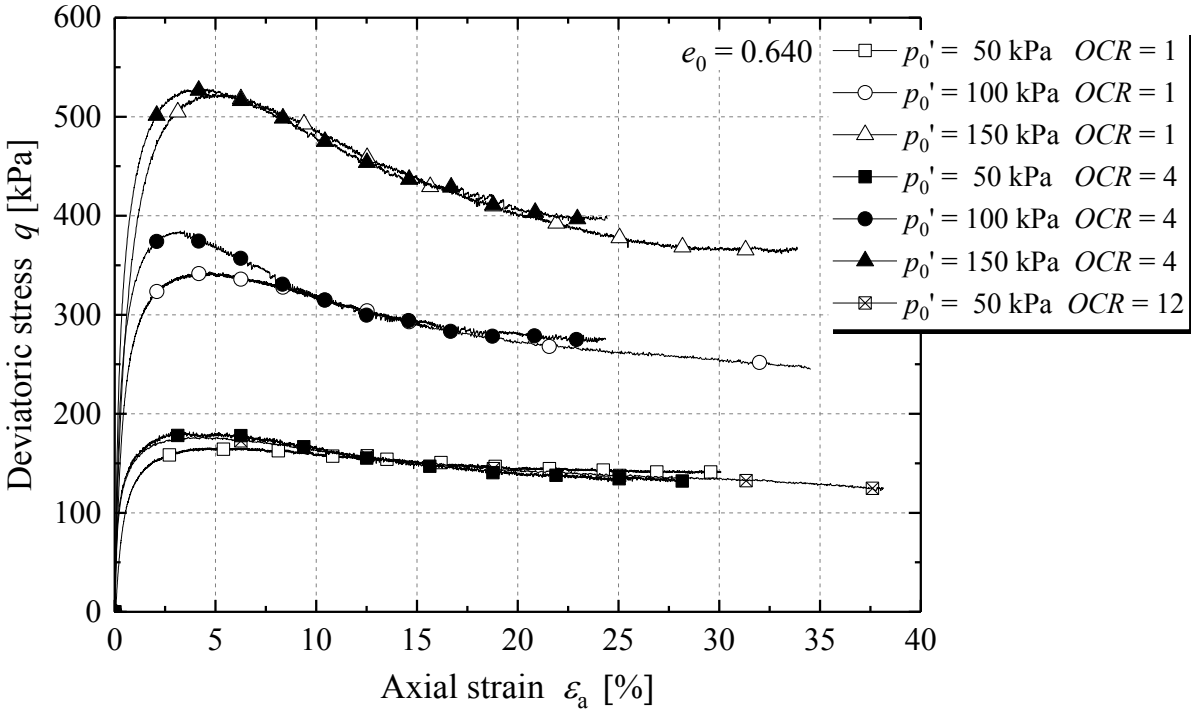

Figure 6-10 Effects of over-consolidation on shear strength of dense (R_d = 79%, e_0 = 0.640) specimens under three effective stress levels (all tested with semi-rough plattens)

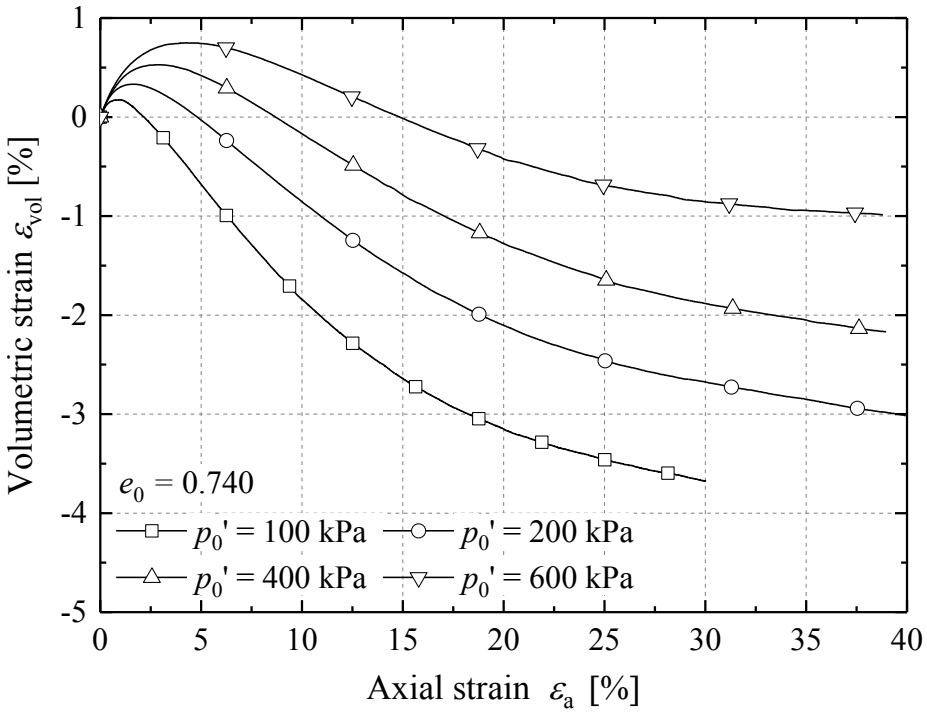

Figure 6-11 Volumetric response of the medium dense (R_d = 50%, e_0 = 0.740) specimens tested with fully-rough plattens

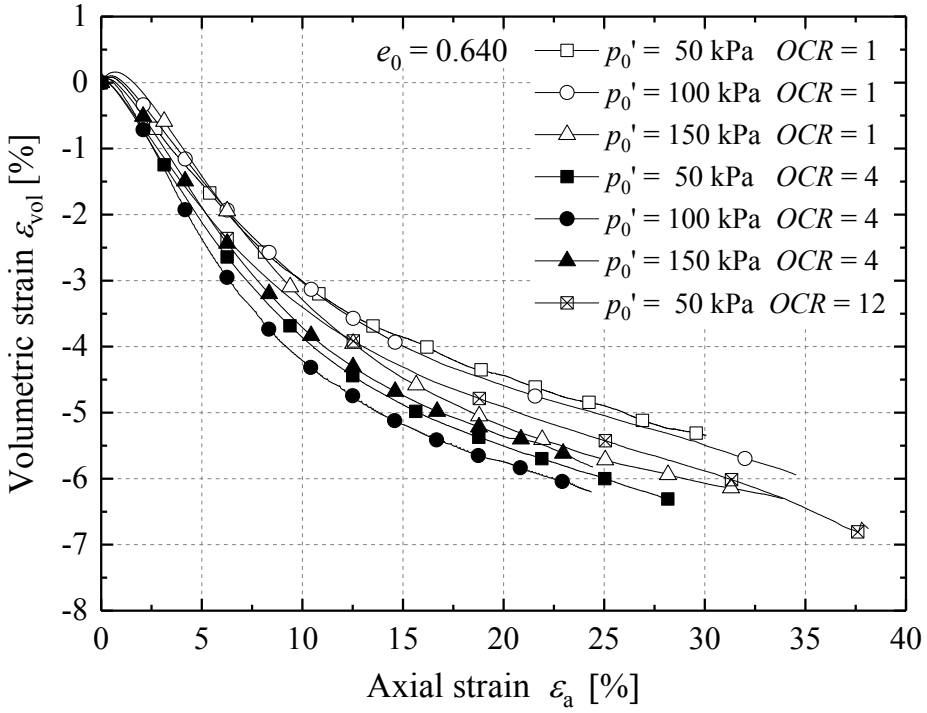

Figure 6-12 Effects of over-consolidation on the volumetric response of the dense (R_d = 79%, e_0 = 0.640) specimens tested with semi-rough plattens

6.5 Effects of end constraints on large strain behaviour

The effects of end restraint on pre-failure stiffness were outlined in Section 5.6. The discussion extends in this section to cover the impact of end conditions on shear stress-strain and volumetric response, allowing the hypothesis #4 posed in Section 6.1 to be tested.

The three types of platten configurations considered: standard size semi-rough (SR), standard size fully-rough (FR) and over-sized (enlarged) fully lubricated, are described Section 5.3.3. The tests on very dense (R_d = 95%, e_0 = 0.587) and dense (R_d = 50%, e_0 = 0.740) specimens were performed with the semi-rough plattens, while the medium dense (R_d = 50%, e_0 = 0.740) tests employed the fully-rough plattens. Parallel tests on specimens of three densities were performed adopting the fully lubricated plattens under selected effective stress levels.

Effects on shear strength

Figures 6-13 to 6-15 demonstrate how platten conditions affected the normalised shear stress-strain (q/p') responses of the medium dense, dense and very dense specimens, respectively for samples taken to p' levels of 100-600 kPa. The tests adopting over-sized fully lubricated plattens showed consistently softer shearing responses and normalised q/p' trends that fell below the (semi- or fully-) rough platten tests.

The differences appeared to be most significant in the medium dense specimen tests and the q/p'-ε_a trends indicated ultimate values that depended on the platten restraint. In contrast, the effects of platten conditions on the dense and medium dense specimens were only discernible over the first of 15% axial strain, thereafter the tests performed with different platten conditions trended towards similar q/p' ratios.

Effects on volumetric behaviour

The effects of end restraint on volumetric response were also prominent, as demonstrated in Figures 6-16 to 6-18. The most notable differences were again observed in the medium dense (R_d = 50%) specimen tests where the use of fully-rough plattens led to less initial contraction, followed by significantly higher dilation rates. The fully lubricated plattens led to more stable ultimate ε_{vol}-ε_a trends. The differences were less significant with the dense (R_d = 79%) and very dense (R_d = 95%) samples, although end restraint also led to higher ultimate dilation rates in these experiments.

Overall, the sample restraint provided by rough ends led the specimens to behave virtually as if they were 'denser', manifesting higher peak strengths and greater dilation.

Further discussion on end restraint

The mechanisms proposed for explaining the higher small strain stiffnesses seen in the rough platten tests discussed in Section 5.6 also apply to the specimens' large strain responses. The over-sized fully lubricated plattens allowed the granular assemblies to deform more freely in the radial direction, facilitating lateral buckling of the contact force chains and leading to lower shear strength and stiffness under compression. Permitting the particles more freedom to rotate and rearrange also explained the higher contractive volume responses seen in the tests with lubricated ends, and why the volumetric contraction transformed to dilation after larger axial strains.

It is also not surprising that the differences in volumetric response were most pronounced in the less dense samples and became more marginal as specimen density increased. Specimens of high density developed significant dilation upon shearing, compared to which the additional 'dilation' imposed by end restraint may become minimal.

The experimental evidence supports the hypothesis that, even with specimen height to diameter ratio greater than 2:1, end constraints effects cannot be overlooked in the characterisation of pre-failure stiffness, shear stress-strain response, volumetric behaviour and consequently critical states through triaxial testing. Although the constraints applied at the sample ends, their effects on global behaviour were significant. The effects also varied with specimen density and effective stress level, and were found most remarkable in less dense tests.

Results from the triaxial tests performed with standard size (fully- or semi-) rough plattens were employed in the sand model calibration and numerical analyses of PISA Dunkirk pile tests. As described in Section 2.2.2, the Dunkirk site profile includes layers of high relative density sands (100% in the top 3 m and average 75% over 3 m to 30 m depth) over the longest pile embedded depth (10 m). The calibration of the model was primarily performed against the test results of dense (R_d = 79%) specimens, which were less affected by end restraint.

Taborda *et al.* (2018) discuss and demonstrate that adjustments to the yield surface

locations and model parameters that are required to cover the sand states of the top 3 m hydraulic fill with high relative density (100%), over low effective stresses that could not be achieved reliably in laboratory tests. It is believed that the end restraint effects, although notable in element scale tests, only affected the calibration outcomes marginally. The potential impact on the modelling of the large scale PISA piles' behaviour is unlikely to be unduly significant.

Further evidence is provided in later discussions that distinguish the impact of end conditions on critical state behaviour, shear strength envelopes and the characterised state parameters.

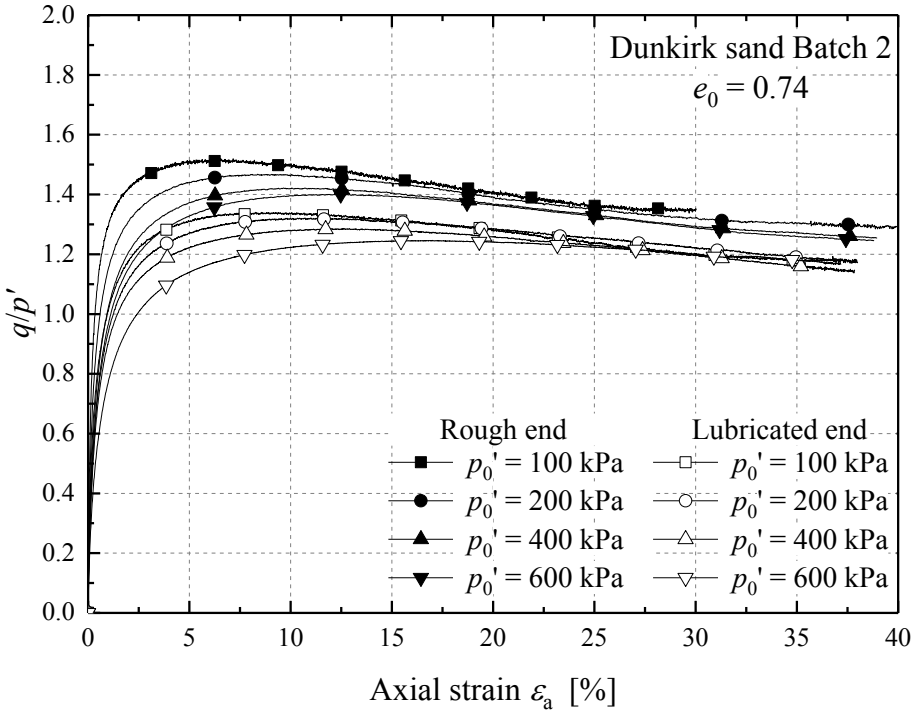

Figure 6-13 Normalised stress-strain trends for medium dense (R_d = 50%, e_0 = 0.740) samples performed with fully-rough and fully lubricated plattens

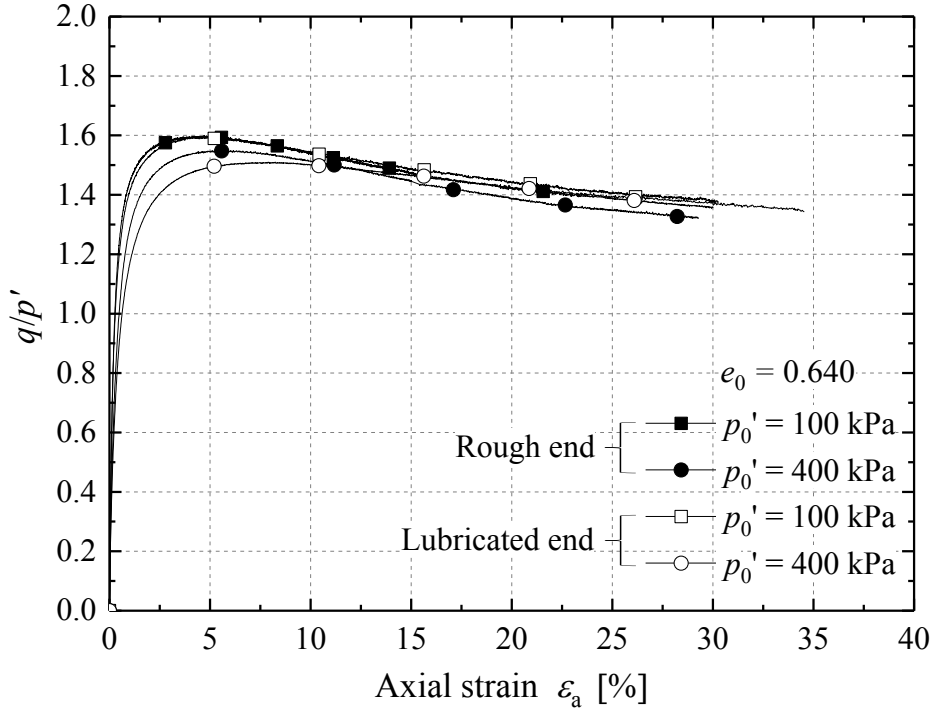

Figure 6-14 Normalised stress-strain trends for the dense (R_d = 79%, e_0 = 0.640) samples performed with semi-rough and fully lubricated plattens

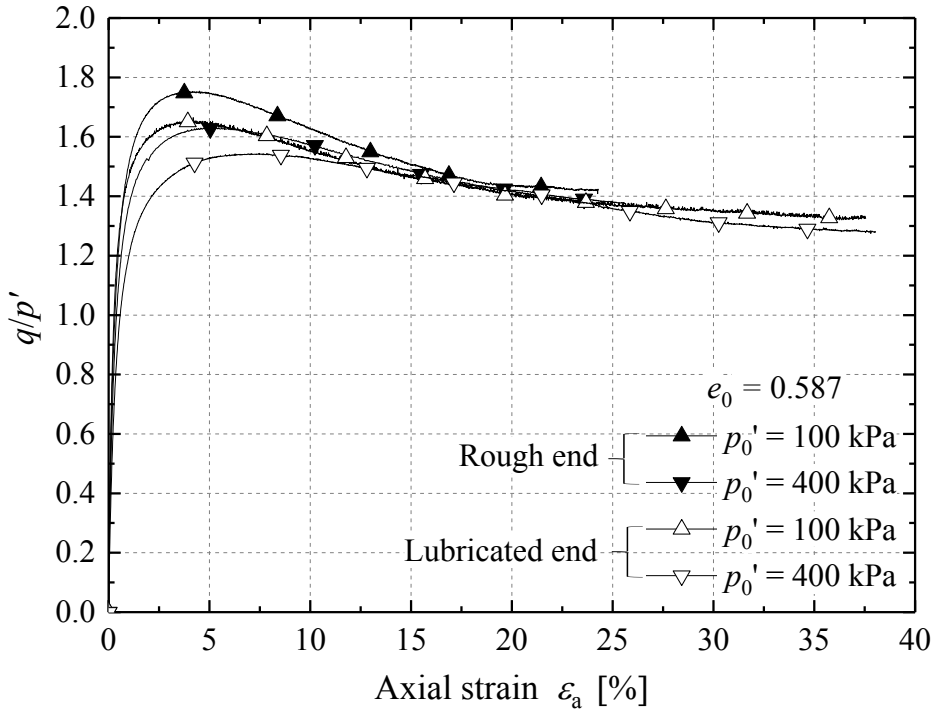

Figure 6-15 Normalised stress-strain trends for the very dense (R_d = 95%, e_0 = 0.587) samples performed with semi-rough and fully lubricated plattens

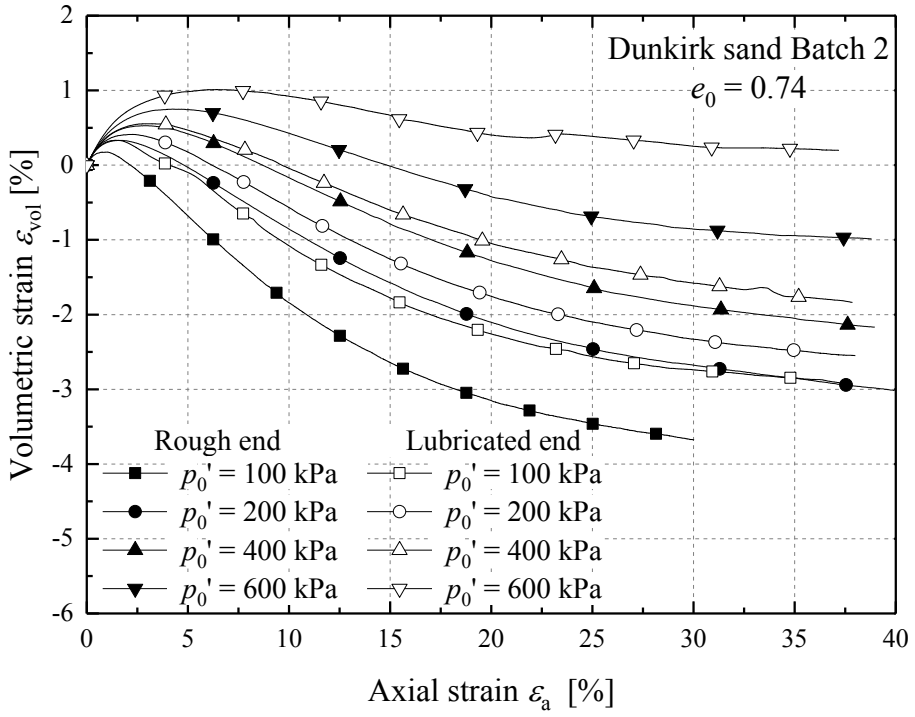

Figure 6-16 Comparison of volumetric behaviour of the medium dense (R_d = 50%, e_0 = 0.740) samples carried out with fully-rough and fully lubricated plattens

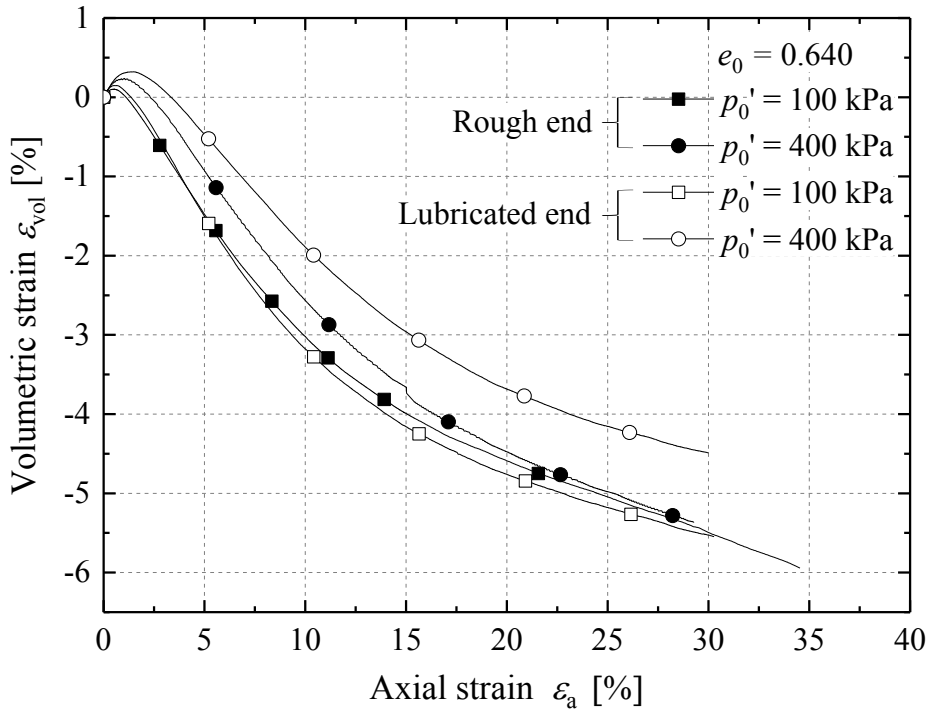

Figure 6-17 Comparison of volumetric behaviour of the dense (R_d = 79%, e_0 = 0.640) samples carried out with semi-rough and fully-lubricated plattens

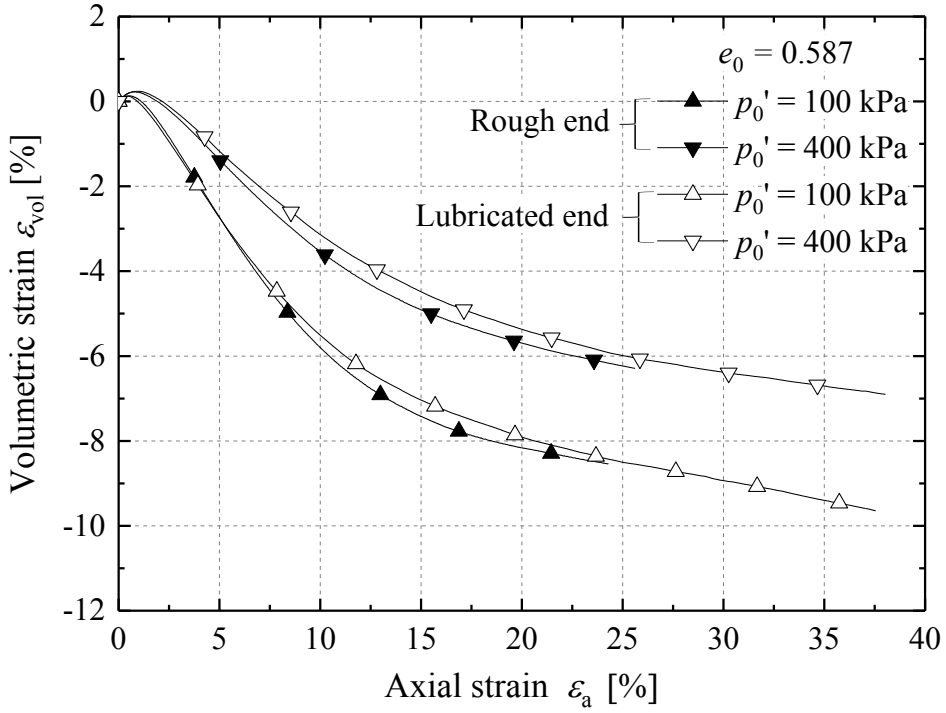

Figure 6-18 Comparison of volumetric behaviour of the very dense (R_d = 95%, e_0 = 0.587) samples carried out with semi-rough and fully lubricated plattens

6.6 Critical state behaviour of Dunkirk sands

Sands' critical state lines (CSL) provide a key reference state for the numerical modelling such as that conducted for the PISA piles' monotonic loading response, which was conducted with a 'state parameter' constitutive model (Taborda *et al.*, 2014). The stress levels considered in the PISA modelling mostly fell in the < 1 MPa range over which grain crushing was expected to be negligible. This allowed the single power law type CSL expressed in Equation (6.2) to be applied to the Dunkirk sand layers.

Determined CSL based on dense (R_d = 79%) specimen tests

Aghakouchak (2015) characterised the critical state behaviour of Dunkirk sand from drained monotonic triaxial compression tests on dense (R_d = 79%, e_0 = 0.64) anisotropically consolidated specimens under three initial p_0' conditions (as listed in Table 5-3) that employed standard size semi-rough plattens and were sheared up to 25% axial strains. He noted that fully stabilised volume changes were not achieved due to the apparatuses' limited axial travel. Extrapolation approaches were applied to the measured final sections of volumetric strain data to derive an ultimate set of constant-volume void ratios, from which he constructed a critical state line expressed in power law function as

$$e = 0.91 - 0.135\left(\frac{p'}{101.33}\right)^{0.179} \tag{6.16}$$

The reference value of 0.91 for p' = 0 kPa condition represents the sand's e_{max}.

Aghakouchak (2015)'s final experimental data points and the critical state line he derived from them (while taking account for a need for his curve to converge to e_{max} at p' = 0 kPa) are plotted in Figure 6-19. The Author's tests, which were sheared from isotropic stress states to larger axial strains of 30-35%, showed very similar e-logp' response to Aghakouchak (2015)'s anisotropically consolidated specimens, and their ultimate states match well.

Characterisation of CSL based on medium dense (R_d = 50%) specimens

The Author's tests on medium dense (R_d = 50%) specimens were sheared to more than 35% axial strain in tests that employed both rough and over-sized lubricated plattens

helped to check for possible effects on the interpreted critical state line related to differences in specimen initial density and platten configuration.

The test results are plotted in the e-logp' plane as shown in Figure 6-20, also indicating the CSL expressed in (6.16). It is clear that, regardless of the platten conditions, the e-logp' trends for the R_d = 50% specimens trended invariably beyond the CSL defined by Aghakouchak (2015) from tests on dense specimens (R_d = 79%) that employed semi-rough plattens.

The tests on medium dense (R_d = 50%) specimens performed with over-sized fully lubricated plattens reached final void ratios that were consistently lower than those from the tests employing rough plattens, reflecting the differences in volumetric response as seen in Figure 6-16. However, the void ratio differences were within 0.003, excluding the tests with p_0' = 100 kPa. The set of (e, p') points at the end of the tests could be reasonably drawn through with a single power law fitting CSL as

$$e = 0.91 - 0.100\left(\frac{p'}{101.33}\right)^{0.262} \tag{6.17}$$

Comparisons of the two sets of critical state line established from dense (R_d = 79%) and medium dense (R_d = 50%) expressed in Equations (6.16) and (6.17) revealed the major difference in the lines' curvature. Both lines were constructed based on dilatant samples and specimens with relatively lower density (higher e_0) are more likely to reach or approach the sand's 'true' critical state.

CSL adopted in the PISA FE simulations

The critical state line based on the Author's and Aghakouchak's (2015) dense (R_d = 79%) specimens expressed in Equation (6.16) was adopted in the PISA FE simulations of Dunkirk pile tests. Although the CSL expressed in Equation (6.17) may characterise the sand's critical state behaviour more accurately, Taborda *et al.* (2018) demonstrate that extrapolation of the laboratory test data was required to cover the low effective stress and high relative density (≈ 100% at top 3 m) in-situ sand states. Any such extrapolation may be carried out with higher accuracy and more certainty when based on laboratory element tests whose initial states fall close to those expected in-situ. To this extent the curve adopted for the FE analysis (Equation (6.16)) could be considered equally appropriate to that given by Equation (6.17).

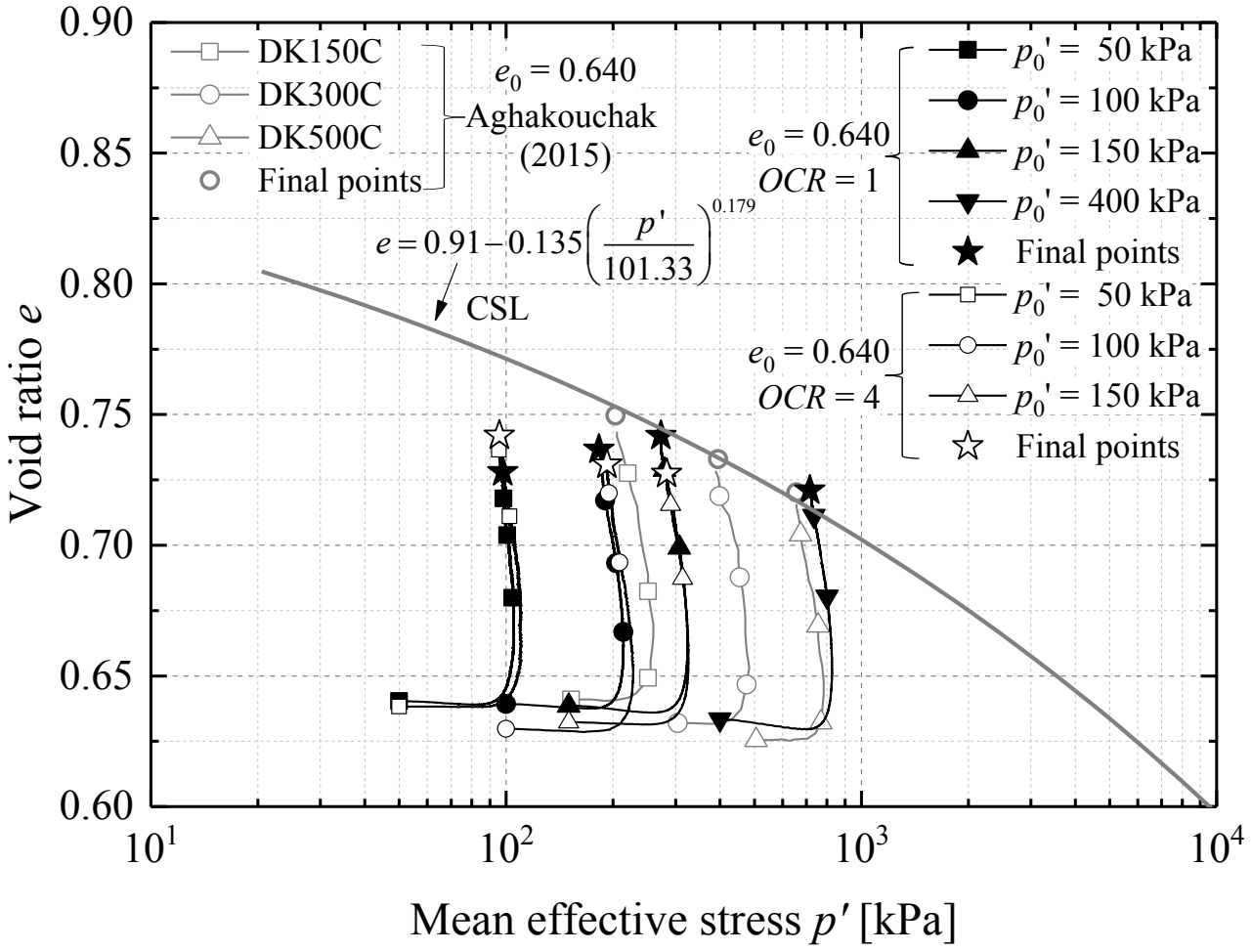

Figure 6-19 *e*-*p′* trends for the dense (R_d = 79%, e_0 = 0.640) Batch 2 Dunkirk sands and the CSL proposed by Aghakouchak (2015) that was adopted for PISA numerical simulation of Dunkirk pile tests (Taborda *et al.*, 2018) (note: all tests performed with semi-rough platten)

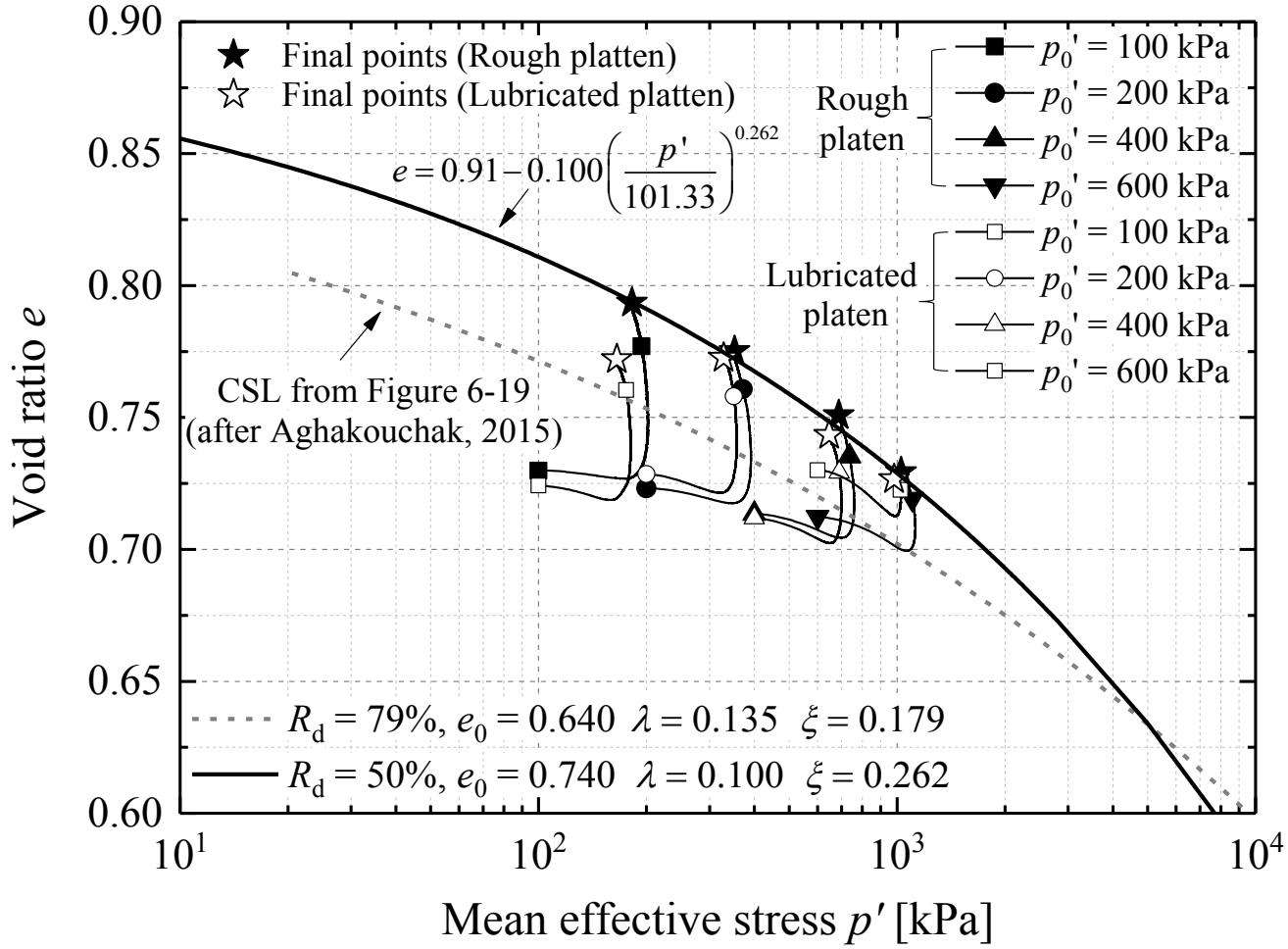

Figure 6-20 e-p' trends for the medium dense (R_d = 50%, e_0 = 0.740) Batch 2 Dunkirk sand and the determined CSL, in comparison with the "dense" CSL characterised by Aghakouchak (2015)

6.7 State parameter-based interpretation of sand behaviour

The monotonic shearing behaviour of Dunkirk sand may be interpreted further and applied in numerical modelling through the unified state parameter-based approach set out by Been & Jefferies (1985). The interpretive methodology adopted is that outlined by Manzari & Dafalias (1997), Papadimitriou & Bouckovalas (2002), Taborda (2011), Taborda *et al.* (2014) and Azeiteiro *et al.* (2017).

Before proceeding, it is important to recall from Section 6.2.2 that the framework adopted was developed considering isotropic behaviour without considering the anisotropic features of stiffness that were demonstrated over the linear, non-linear and fully plastic ranges of behaviour in tests on Dunkirk sand. The components of elastic volumetric strains (ε_{vol}^{e}) and shear strains (ε_{s}^{e}) are linked to soils' effective stress states (p' and q) through globally defined maximum shear stiffness (G_{max}) and bulk modulus (K_{max}) without separating the contribution of stress components, as commonly considered in the cross-anisotropic linear elasticity framework (see Sections 3.2.1 and 5.9) or in plastic models that capture anisotropic yielding and shear strength characteristics.

Peak strength envelopes and peak stress ratio states $(q/p')_{peak}$

Referring to Figure 6-4, the peak stress ratio state $(q/p')_{peak}$ defines within the modelling approach the outer bounding surface, which is dependent on initial soil state. Figures 6-21 and 6-22 plot the peak stress states reached under triaxial compression and extension conditions, differentiating the employed platten conditions and sample densities. It is evident that higher $(q/p')_{peak}$ values were reached in tests on higher density specimens of R_d = 79% and 95%, and the tests performed with lubricated ends developed lower peak q/p' ratios, which is expected from the normalised stress-strain trends seen in Figures 6-13 and 6-15. The peak strength envelope in triaxial extension was defined based on tests employing isotropically consolidated samples and rough plattens, leading to $(q/p')_p^{TXE}$ = 0.93, which is lower than the $(q/p')_p^{TXE}$ value of 0.99 reported by Aghakouchak (2015) from his anisotrpically (K_o) consolidated triaxial extension tests.

Critical state envelope M_{cs}

A similar approach was employed to locate the critical state envelope, by plotting the

stress states ultimately reached in the triaxial tests, as shown in Figures 6-23 and 6-24. The envelopes defined for the medium-density (R_d = 50%) and higher density specimens exhibited moderate differences, regardless of the platten conditions employed, indicating that fully stable q/p' trends were not reached in some tests. Nevertheless, critical state ratios (M_{cs}^{TXC}) of 1.30 and 1.23 were obtained for testing with rough plattens and lubricated plattens, respectively, corresponding to inter-particle friction angles (ϕ_{cs}') of 32.3˚ and 30.7˚, respectively. Triaxial extension tests performed with rough plattens exhibited critical state ratios (M_{cs}^{TXE}) of 0.90 and ϕ_{cs}' of 32˚.

Determination of dilatancy coefficient D^p

Phase transformation conditions may be characterised from drained tests by the transition from plastic contraction to plastic dilation. Assumptions have to be made to determine the plastic dilatancy coefficient D^p, which is defined as the ratio between plastic volumetric strain ($\Delta\varepsilon_{vol}^p$) and plastic shear strain (ε_s^p). Taborda (2011) employed the following equations to define the maximum shear stiffness G_{max} and maximum bulk modulus K_{max} based on isotropic linear elastic assumptions, and D^p was calculated according to Equation (6.20).

$$G_{max} = B\frac{p_{ref}}{0.3+0.7e^2}\sqrt{\frac{p_{ref}}{101.3}} \tag{6.18}$$

$$K_{max} = \frac{2(1+\nu)}{3(1-2\nu)}G_{max} \tag{6.19}$$

$$D^p = \frac{\Delta\varepsilon_{vol}^p}{\Delta\varepsilon_s^p} = \frac{\Delta\varepsilon_{vol}^t - \Delta\varepsilon_{vol}^e}{\Delta\varepsilon_s^t - \Delta\varepsilon_s^e} \approx \frac{\Delta\varepsilon_{vol}^t - \Delta p'/K_{max}}{\Delta\varepsilon_s^t - \Delta q'/(3G_{max})} \tag{6.20}$$

Where B is an elastic material (non-dimensional) shear stiffness parameter and ν is Poisson's ratio. The superscripts 't' and 'e' represent total and the elastic component of volumetric strain or shear strain. For simplicity, the constant Poisson's ratio ν = 0.17 reported by Kuwano (1999) from purely axial compression tests, was applied for all the stress and strain conditions involved. Close value of ν = 0.18 was obtained from the Author's tests (see Section 5.5.1).

Figures 6-25 and 6-26 plot the plastic dilatancy trend against stress ratio q/p' for triaxial tests on medium dense specimens (R_d = 50%) employing fully-rough and fully lubricated plattens. The D^p-q/p' traces showed largely linear trends over the intermediate

stress ratio range of $0.6 < q/p' < 1.2$. Regression analyses led to the (positive) slopes that determined the dilatancy constants A_d in Equation (6.8). The stress ratios at which the D^p decreased to below zero (onset of dilation) was characterised as phase transformation stress ratios $(q/p')_{PPT}$.

Derivation of state parameter constants

The final key step of applying the state parameter approach is to determine the state parameter constants k_c^b and k_c^d (referring to Equations (6.6) and (6.7)), with 'c' representing triaxial compression conditions, 'b' denoting bounding surface or peak stress ratio state and 'd' indicating dilatancy surface.

Figures 6-27 and 6-28 plot the trends for peak and phase transformation stress ratios $(q/p')_{peak}$ and $(q/p')_{PPT}$ against the corresponding state parameter ψ_{peak} (= e_{peak} - e_{cs}) and ψ_{PPT} (= e_{PPT} - e_{cs}). Linear regressions of the $(q/p')_{peak}$-ψ_{peak} and $(q/p')_{PPT}$-ψ_{PPT} data led to determine $k_c^b = 2.58$ and $k_c^d = 0.84$ for the tests performed with rough plattens, and $k_c^b = 2.78$ and $k_c^d = 0.44$ for the tests carried out with lubricated plattens.

Taborda *et al.* (2018) employed k_c^b and k_c^d values of 2.70 and 0.88 for the PISA modelling of Dunkirk pile tests, after accounting for the nominal differences in the site's elastic shear stiffness (G_{vh}) profile characterised from in-situ seismic CPT (SCPT) measurements and equivalent isotropic G_{max} values interpreted from drained laboratory tests on isotropic consolidated specimens. The adjusted values provided a close match with the parameters derived here.

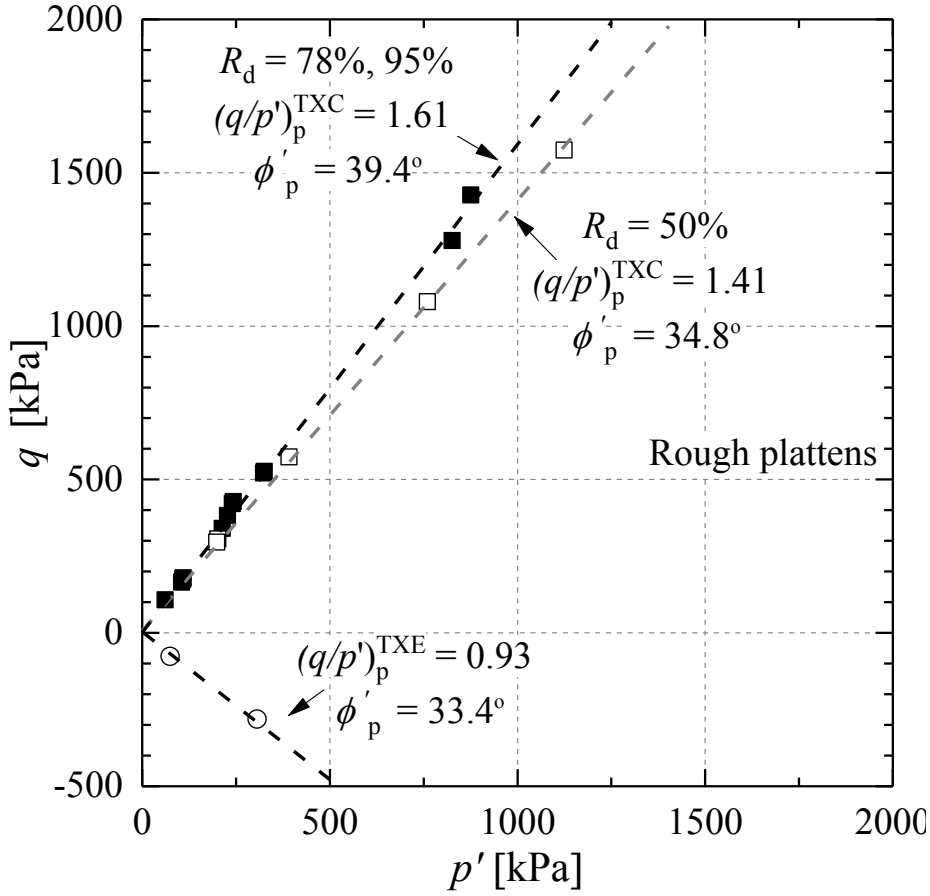

Figure 6-21 Peak strength envelopes defined for triaxial tests performed with (semi- or fully-) rough plattens

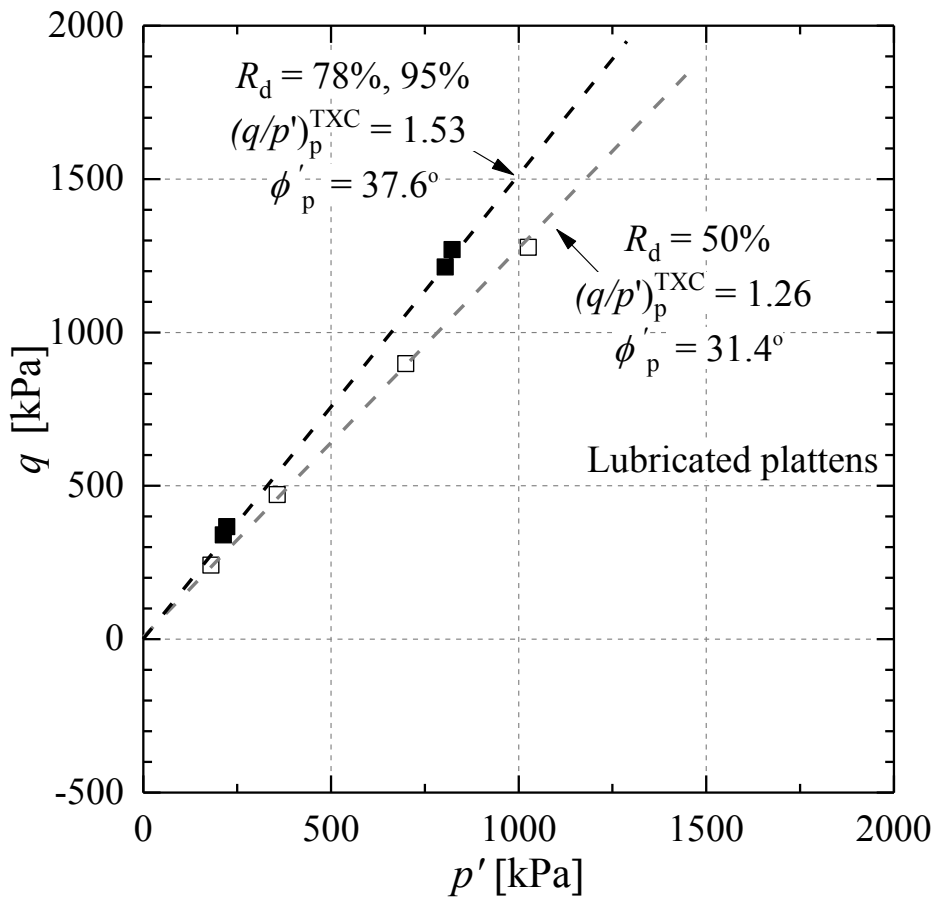

Figure 6-22 Peak strength envelopes defined for triaxial tests performed with fully lubricated plattens

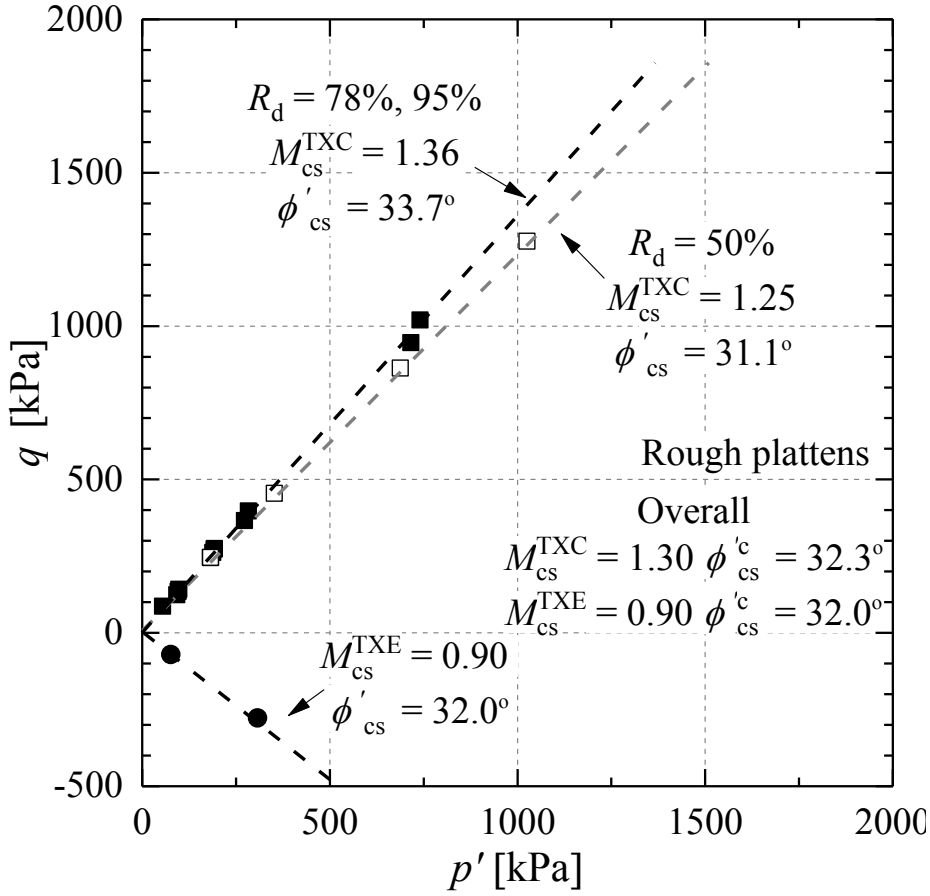

Figure 6-23 Critical state strengths defined for triaxial tests performed with (semi- or fully-) rough plattens

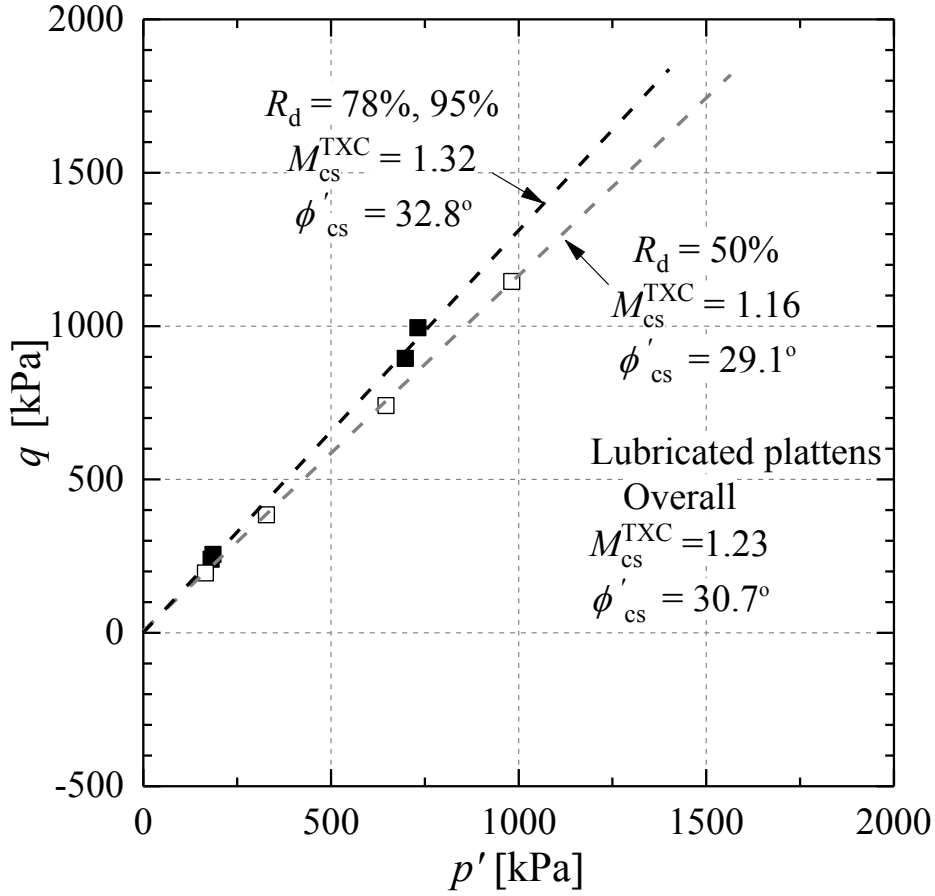

Figure 6-24 Critical state strengths defined for triaxial tests performed with fully lubricated plattens

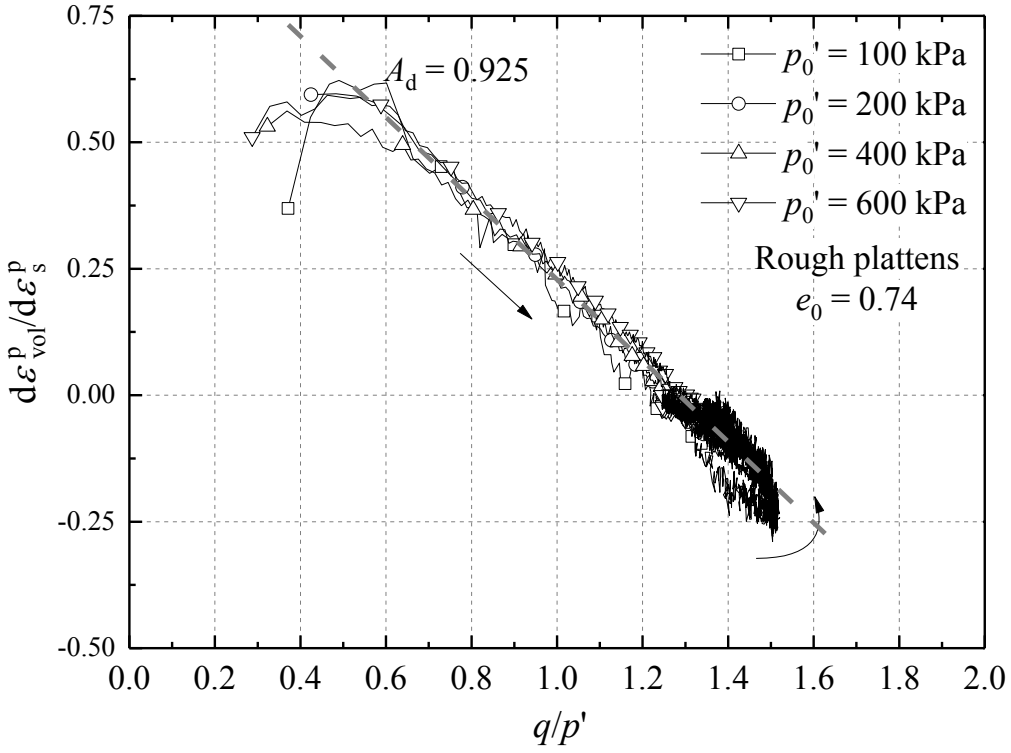

Figure 6-25 Stress-dilation correlation determined for medium dense specimens (R_d = 50%, e_0 = 0.740) in triaxial tests employed (semi- or fully-) rough plattens

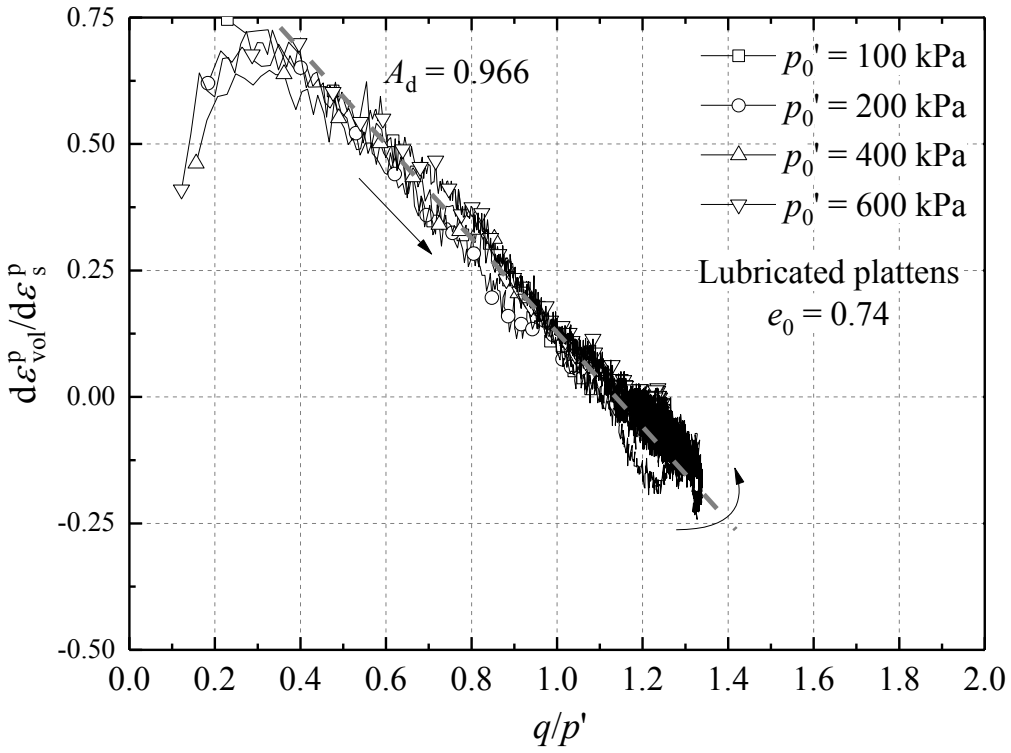

Figure 6-26 Stress-dilation correlation determined for medium dense specimens (R_d = 50%, e_0 = 0.740) in triaxial tests employed fully lubricated plattens

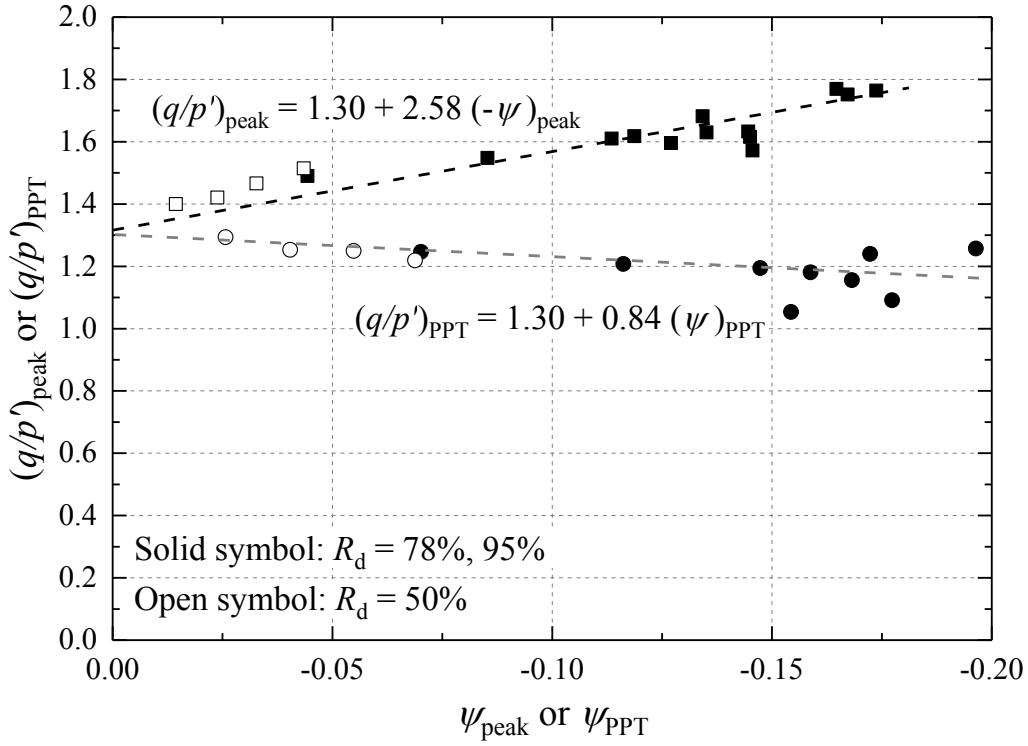

Figure 6-27 Derivation of state parameter constants k_c^b and k_c^d from triaxial tests employed (semi- or fully-) rough plattens

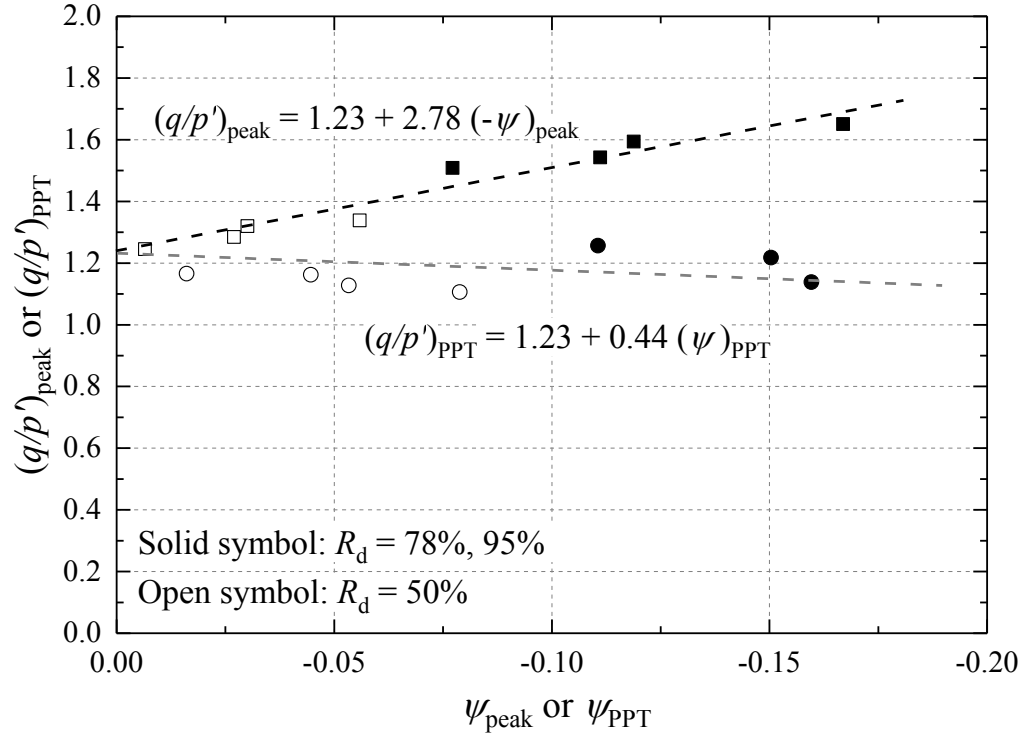

Figure 6-28 Derivation of state parameter constants k_c^b and k_c^d from triaxial tests employed fully lubricated plattens

6.8 Comparison of Dunkirk sand Batch 2 and Batch 3 in terms of large strain behaviour

The previous discussion on Dunkirk sand's large strain behaviour focused on the Author's triaxial tests on Batch 2 sand samples. However, as mentioned earlier, sample availability limitations meant that, the study of cross-anisotropic linear elastic stiffness behaviour described in Section 5.9 and the long-term cyclic loading behaviour that is reported in the next Chapter 7 had to be carried out with Batch 3 material.

Similar to the comparisons presented in Section 5.8 on the pre-failure stiffnesses between these two batches of sands, this section clarifies any differences between shear strength and volumetric behaviour of the two batches as well as their critical state lines, drawing on parallel triaxial tests on Batch 3 samples by Vinck (2016). Comparisons of the grading and limiting void ratios between these two batches are detailed in Sections 2.2.2 and 5.3.2.

Shear stress-strain behaviour

Figure 6-29 compares the normalised stress-strain (q/p') trends for specimens prepared to similar e_0 around 0.64 and sheared under triaxial compression conditions from isotropic stress states of p_0' = 100 and 400 kPa, all employing the over-sized lubricated plattens. It can be observed that the Batch 3 sand exhibited a softer response over the first 5% of axial strain and lower peak q/p' stress ratios compared to the Batch 2 sand. The Batch 3 tests also showed lower ultimate q/p' values and the overall traces did not seem to converge clearly at large strains.

Volumetric behaviour

The corresponding volumetric trends of the above tests are summarised in Figure 6-30. Overall, the Batch 3 sand developed significantly higher initial contraction and lower ultimate dilation than Batch 2 sample, indicating generally more contractive behaviour.

Recalling that the two batches of sands have very similar (dry) gradings (see Figure 2-9), the variations in the two Batches' volumetric response may indicate differences in: (i) grain characteristics, as the Batch 2 sand contains a greater proportion of $CaCO_3$ shell fragments; (ii) the inclusion of more fines in Batch 3 that seemed to adhere to grains under dry conditions (see the microscopic observations in Figure 4-20) but tended to be 'dissolved' and separated during water pluviation.

Critical state behaviour

A tentative critical state line was established for the Batch 3 sand based on three tests on less dense specimens ($e_0 > 0.725$) from isotropic states of $p_0' = 100$, 400 and 600 kPa, as shown in Figure 6-31. Also plotted for comparison are the two critical state lines for the Batch 2 sand that were discussed in Section 6.6.

It is expected that the Batch 3 sand was less dilative when sheared from identical initial states and the resultant final (e, p') states were located below those of the Batch 2 material of identical initial void ratios. A critical state line was constructed using a similar approach of fitting a power law function through final (e, p') data points, and the reference void ratio e_{cs_ref} adopted the e_{max} value of 0.98, as included in Table 5-1. As shown in Figure 6-31, the critical state line of the Batch 3 sand is situated below that of the Batch 2 sand proposed by the Author over the 10 to 1000 kPa pressure range but passes above that defined by Aghakouchak (2015).

As later discussed in Section 7.5, the critical state line established for the Batch 3 Dunkirk sand under monotonic loading provided a reference line for characterising sand volume change under long-term cyclic loading and examining whether stable ultimate state(s) equivalent to the critical state line for monotonic loading can also be found for cyclic loading.

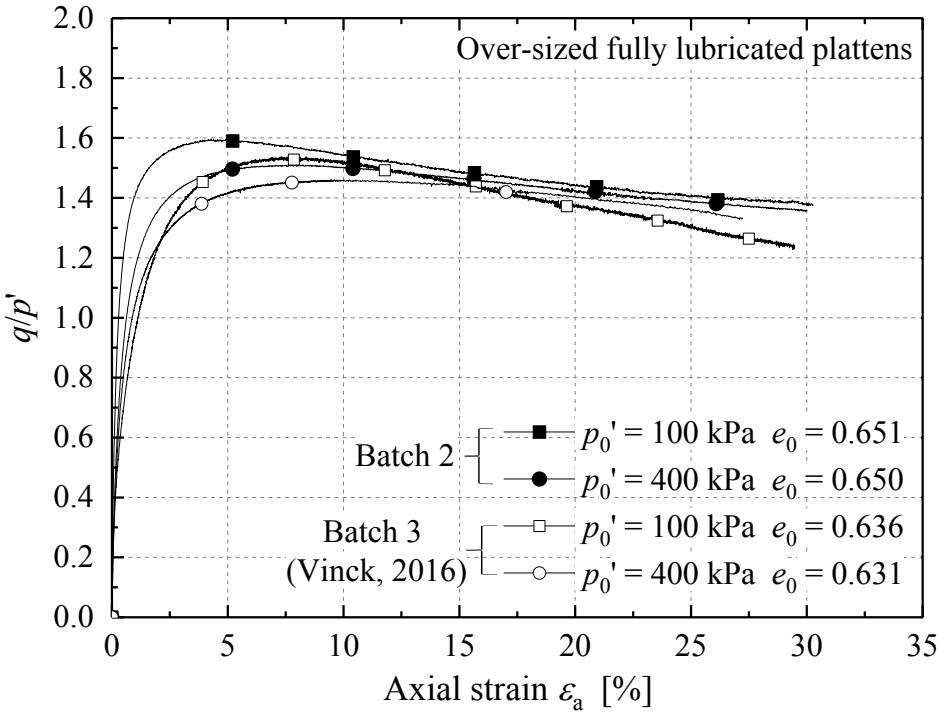

Figure 6-29 Normalised shear stress-strain trends for Batch 2 and Batch 3 Dunkirk sands with e_0 ≈ 0.64 (all tested with fully lubricated plattens)

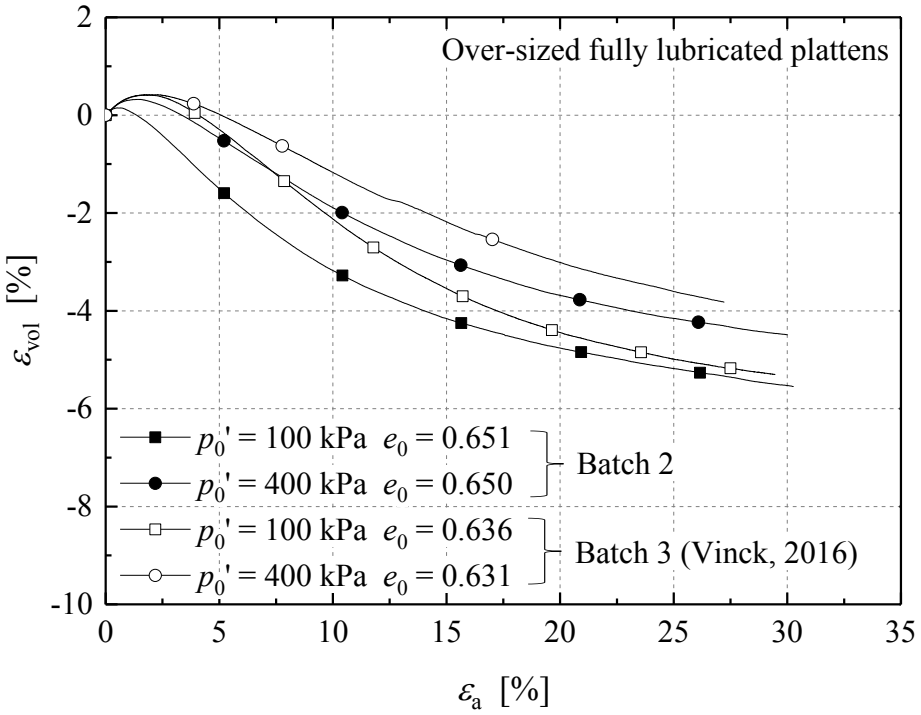

Figure 6-30 Volumetric trends for Batch 2 and Batch 3 Dunkirk sands with e_0 ≈ 0.64 (all tested with fully lubricated plattens)

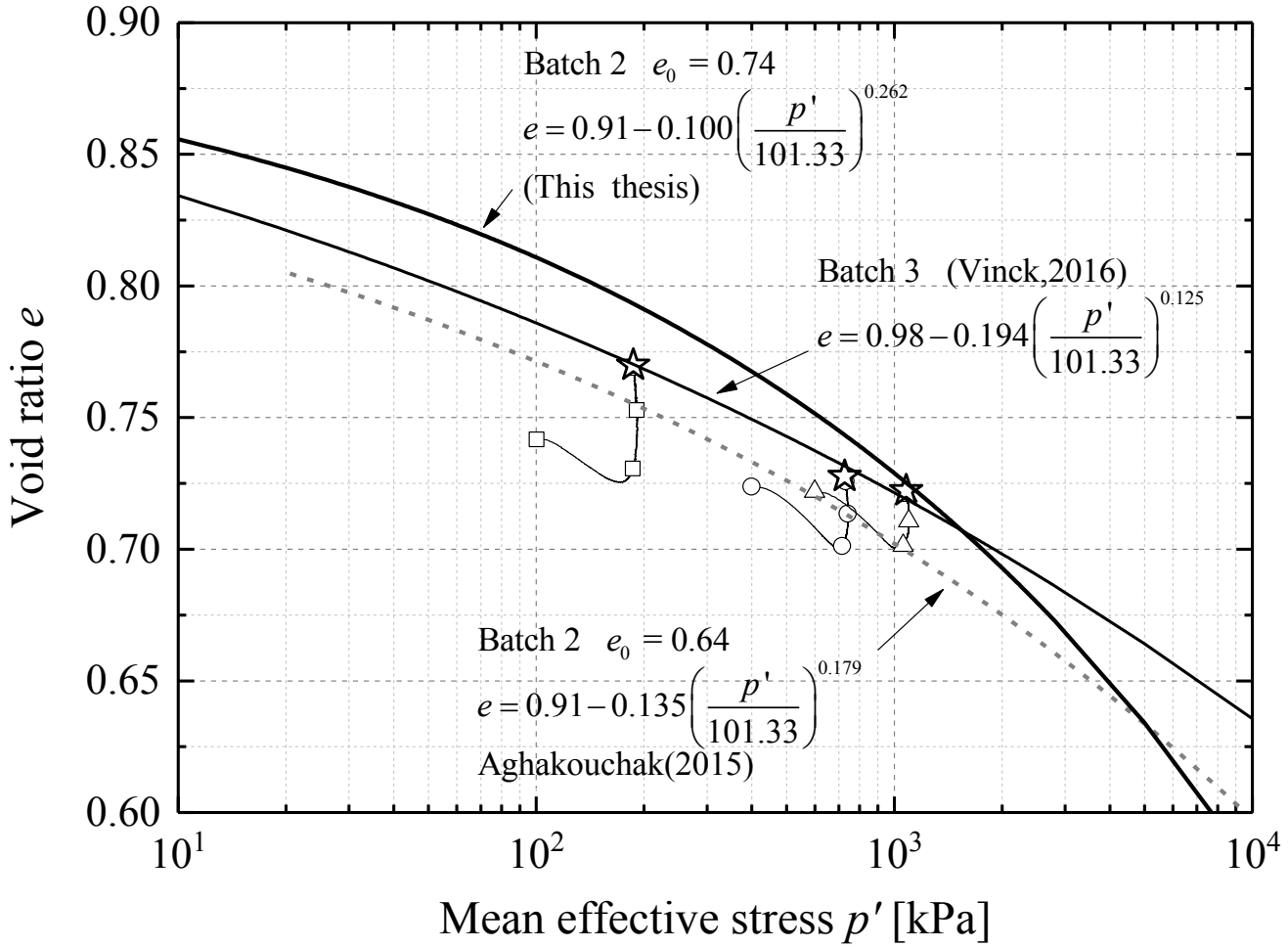

Figure 6-31 Critical state line established for Batch 3 Dunkirk sand by Vinck (2016), in comparison with CSLs for the Batch 2 sand

6.9 Summary and conclusions

This chapter was concerned with the large strain behaviour of Dunkirk sand under monotonic loading, drawing on test outcomes from the research programme set out in Chapter 5 by Tables 5-2 to 5-4. The data interpretation and discussion was structured to test the four hypotheses posed in the introduction. The main conclusion drawn are as follows.

1. The attained hierarchy of (normalised) shear stress-strain trends (q-ε_a and q/p'-ε_a) and volumetric strain trends (ε_{vol}-ε_a) reflected systematically the combined effects of specimen initial density and effective stress level on Dunkirk sand's shear strength and dilatancy behaviour.

2. The over-consolidated specimens developed higher peak shear strengths and mobilised q/p' or ϕ' values up to 10% axial strains, and more dilatant volumetric behaviour than the normally consolidated specimens. Such positive gains tended to diminish as shearing progressed to even higher strain levels.

3. End restraint led the sand specimens to exhibit higher apparent stiffness, peak strengths, less initial contraction and greater ultimate dilation. Standard size rough plattens restrained lateral buckling of the contact force chains under compression and permitted less freedom for the sand grains to rotate and rearrange, leading to significant overall effects on the sand samples' global strength and volumetric response, even when the specimens fulfilled the recommended geometrical criterion of initial height to diameter ratio greater than 2:1.

4. The effects of end restraint varied with specimen density and effective stress level, and were found to be most significant in tests on the Author's less dense (R_d = 50%) samples.

5. Regardless of the platten configurations employed, medium dense specimens (R_d = 50%, e_0 = 0.740) that were sheared to large axial strains (30-40%) reached largely stable volume response exhibited e-logp' trends that exceeded the critical state line estimated from similar tests on denser specimens (R_d = 79%, e_0 = 0.640).

6. Triaxial tests on medium dense specimens (R_d = 50%) are believed to give a more accurate representation of the sand's true critical state behaviour. A fit through the final (p', e) datasets led to the adopted characterisation of the Dunkirk sand's

critical state line, as expressed by a power law function.

7. The critical state, bounding and dilatant surfaces of the sand were characterised for numerical analysis using the state parameter-based approach. Linear state parameter-dependent correlations between the sand's density and stress states were established in terms of state parameter constants, which were modestly affected by the platten type and end restraint conditions.
8. The outcomes of the state parameter-based interpretation of Dunkirk sand monotonic were applied to calibrate Taborda *et al.*'s (2014) bounding surface plasticity constitutive model that was employed for the successful modelling of PISA lateral loaded pile tests at Dunkirk (Taborda *et al.*, 2018).
9. In comparison with the Batch 2 Dunkirk sand, which was the main focus of this chapter, the Batch 3 sand showed a softer monotonic shearing response and less dilatant volumetric straining, leading to a critical state curve located below that proposed for the Batch 2 sample by the Author when considering engineering (< 1 MPa) effective stress range.

CHAPTER 7
Behaviour of Dunkirk sand under long-term cyclic loading

7.1 Introduction

Many geotechnical structures are subject to long-term dynamic or quasi-static cyclic loading over their operational lives. Offshore piled foundations experience cyclic loads ranging from those induced by relatively gentle tidal, diurnal or seasonal temperature changes, through to significant operational loads imposed by machinery (especially with wind turbines), storm winds and waves, or earthquakes and tsunami. While undrained or constant volume cycling can cause collapse, the undesirable potential consequences of drained cyclic loading are more often manifested as the accumulation of irrecoverable foundation movements and the degradation of stiffness. However, scope also exists for full foundation failure to result from high level drained repetitive loading.

Rational assessment of the performance of foundation response to repetitive loads requires information on the cyclic shearing behaviour of the relevant soils. Extensive research has been carried out to examine undrained soil behaviour under rapid earthquake loading, with many studies investigating soil liquefaction potential under extreme seismic events involving short cyclic loading periods. With sandy soils, lower frequency repetitive loading under offshore wind and wave loads are more often associated with substantially drained conditions. If the drainage conditions allow liquefaction to be eliminated, then strain accumulation and stiffness alternation often become the main concerns. This is generally assumed to be the case for piles driven in sands when subjected to lateral loads, although some excess pore pressures may be generated around large monopiles under storm conditions. However, axial failure can be generated under drained cyclic loading as near constant volume conditions applying close to the shafts due to the particular kinematic constraints imposed, see Jardine *et al.* (2012) and Tsuha *et al.* (2012).

This chapter presents a laboratory research programme that addressed the drained cyclic shearing behaviour of Dunkirk sand under long-term relatively, low frequency, repetitive loading. The main focus was on the lateral loading cases examined in the PISA pile tests at the Dunkirk site. The outcomes are applicable to the ongoing interpretation and modelling of the cyclic PISA pile tests at Dunkirk, and will also be useful for validating constitutive models for other offshore sand sites as well as application in a wider range of onshore and offshore cyclic loading cases.

The testing programme consisted of constant cell pressure (CCP) cyclic triaxial tests on reconstituted Dunkirk sand specimens. Large numbers (up to 10^4) of sinusoidal loading cycles were applied with cyclic periods of two minutes. Most specimens survived the long-term cycling and these were subsequently sheared monotonically to failure under drained conditions.

The main questions and hypotheses examined in this chapter include:

#1. How sand behaviour is affected under drained cyclic loading by soil density (R_d), static effective stress level (p_0'), effective stress history (OCR), mean cyclic loading stress ratio ($\eta = q_{mean}/p_0'$) as well as the cyclic amplitude stress ratio ($CSR = q_{cyc}/p_0'$);
#2. Whether the trends for permanent cyclic strain (ε^{acc}) accumulation with the number of cycles (N) are described better by power law, semi-logarithmic or other functions of N;
#3. Whether cyclic strain flow rules and dilation trends depend critically on effective stress (p_0') and mean cyclic loading stress (q_{mean}/p_0') levels, as proposed by Wichtmann *et al.* (2005), and whether they can be expressed by dilation models that consider the stress ratio (q_{mean}/p_0') as the main variable;
#4. If a 'cyclic' critical state or ultimate state line exists towards which the state paths of sand elements of varying density converge after experiencing a range of cyclic loading conditions;
#5. Whether cyclic thresholds and kinematic yield surfaces can be identified on the basis of the accumulated cyclic strain and cyclic stiffness trends;
#6. If drained cyclic shearing history affects the stiffness, shear strength and kinematic yielding behaviour that applies to monotonic shearing imposed after cyclic loading.

7.2 Review: Behaviour of granular materials under long-term cyclic loading

Soil behaviour under cyclic loading is both a fundamental aspect of soil behaviour and a potentially critical issue in engineering practice. Cyclic loads can be broadly categorised into those involving (i) dynamic loading or (ii) quasi-static loading. Dynamic loadings, typically seen in earthquake or impact loading cases and involve inertial components of response that are significant compared to the static terms. Dynamic loading is usually applied at high frequencies and can induce potentially abrupt failures.

Quasi-static cyclic loading is imposed at lower frequencies and its impact is often manifested as gradual geotechnical or structural deformation or stiffness changes over time. This type of cyclic loading is critical to the fatigue design and long-term serviceability of a wide range of infrastructure elements, such as pavements, railway tracks and offshore supporting structures (Byrne, 2011, Jardine *et al.*, 2012, Kallehave *et al.*, 2015, Cai *et al.*, 2017). However, such loading can also lead to failure in cases where the boundary conditions impose kinematic constraints that have a similar effect to maintaining undrained conditions, as applying around pile shafts under axial cycling (Aghakouchak, 2015).

Fully drained conditions are often assumed to apply to spread foundations under long-term, low-frequency quasi-static loading, and these conditions may be matched in laboratory tests. However, it is possible that when large volumes of soils are excited more rapidly, as for example around very large monopiles driven in silty sands under lateral cyclic storm loads, the response may not be fully drained.

This section first introduces a categorisation of cyclic stress-strain response into five general ranges that involve distinct sets of cyclic stress thresholds. The characteristics of cyclic stress-strain behaviour in each range are further correlated with an interpretive framework of cyclic multiple kinematic yield surfaces. The review then moves on to summarise laboratory studies of how granular materials behave under long-term drained cyclic loading conditions. The effects of several influential factors are discussed.

7.2.1 Cyclic stress-strain response and interpretive frameworks

The theorems of plastic shakedown and ratcheting (Melan, 1936, Koiter, 1960, Brown,

1974) are often employed to characterise the stress-strain responses of soils or structures subjected to cyclic loading, as shown in Figure 7-1. Five categories of material responses can be distinguished (Collins & Boulbibane, 2000, Alonso-Marroquin & Herrmann, 2004, García-Rojo & Herrmann, 2005).

- **Elastic response** When the applied cyclic stresses are maintained within a truly elastic range, the soils respond linearly and all deformations are fully recoverable, without generating or accumulating any plastic strains. As shown in Chapter 5, this range may be very small for soils such as Dunkirk sand.
- **Elastic shakedown** In the cases where the applied cyclic stresses exceed the elastic limit but stay below a certain limit (termed 'elastic shakedown limit'), the soils generate plastic strains over a finite number of stress or strain excursions, after which the soil adapts to the applied cyclic stresses and the response becomes purely elastic.
- **Plastic shakedown** After the imposed stress level exceeds the elastic shakedown limit, the material generates significant plastic straining, but ultimately reaches a long-term steady state where plastic strains cease to accumulate. The hysteretic stress-strain loop covers a constant area and the energy dissipated is bounded per cycle (García-Rojo & Herrmann, 2005). The upper limit of cyclic stress level generating shakedown behaviour is termed 'shakedown' limit, which is a critical criterion in engineering practice, for example in pavement design (Collins & Boulbibane, 2000).
- **Plastic ratcheting** Once the shakedown limit is exceeded, the soils or structures can no longer accommodate the imposed cyclic loads and the plastic straining continues, albeit at a decreasing rate. The hysteretic stress-strain loops do not close and permanent plastic shear strains continue to accumulate in every cycle. If the amplitudes of cyclic stress or strain do not exceed a certain limit, the rate of straining accumulating may gradually decrease to a negligible value and the soil state may ultimately converge towards asymptotic conditions where terminal states (Narsilio & Santamarina, 2008) are reached. Although no catastrophic failure is induced by the ratcheting type of cyclic response, the accumulated permanent strains may exceed the permissible strain and deformation limits applying to the structure or its foundations. Structural serviceability or fatigue requirements may no longer be satisfied.
- **Incremental collapse** In contrast to the ratcheting phenomena, incremental

collapse occurs when asymptotic strain states cannot be held and the soils produce uncontrollable plastic flow that develops after a certain number of cycles.

Cyclic kinematic yield surfaces

The degree to which the general cyclic thresholds discussed above apply to soils can be determined by performing stress- or strain-controlled cyclic DSS, triaxial or HCA tests covering a range of stress or strain amplitudes. The cyclic responses are often interpreted by reference to conceptual or numerical models originally developed for interpreting soil behaviour under monotonic loading. Table 7-1 summarises findings from recent stress-controlled undrained cyclic triaxial or HCA testing programmes on two silica sands (Dunkirk and Fontainebleau NE34 sand, Aghakouchak (2015)), heavily over-consolidated stiff glacial Cowden till (Ushev, 2018) and lightly over-consolidated soft Wenzhou clay (Guo *et al.*, 2017) and also strain-controlled DSS tests on reconstituted kaolinite and kaolinite-bentonite clays (Mortezaie & Vucetic, 2016). The identified cyclic thresholds are also indicated.

Aghakouchak (2015) interpreted the undrained cyclic behaviour he observed in triaxial and HCA tests on Dunkirk and Fontainebleau NE34 sands using the concepts of *stable, metastable* and *unstable* cyclic response that were adopted by Jardine & Standing (2012)'s and Tsuha *et al.* (2012)'s analyses of the cyclic response of axially loaded pile foundations under drained, but highly kinematically constrained, conditions. The three categories of undrained cyclic shearing behaviour were identified based on criteria of mean effective stress drift, permanent cyclic strain accumulation and cyclic stiffness degradation. A similar interpretation was attempted by Guo *et al.* (2017) (as shown in Figure 7-2) who identified from undrained cyclic triaxial and HCA tests on Wenzhou soft clay ranges for the cyclic stress ratio (*CSR*) under which *stable, metastable* and *unstable* cyclic responses were interpreted based on the criteria of permanent vertical strain, resilient modulus and damping ratio.

Aspects of the cyclic shearing behaviour can also be analysed through the framework of kinematic yield surfaces outlined by Jardine (1992, 2013). The soils could remain fully stable under very low level cycling that remained within the elastic Y_1 limits. Larger perturbations could also allow the elements to stay within *stable* zone when cyclic stress or strain is within the Y_2 yield surface and the cyclic stress-strain

response is similar to elastic shakedown. The soils could manifest *metastable* responses when their cyclic stress states engage the Y_2 yield surface and gradually adjust its size and relocate its position as cycling evolves. The soils gradually accommodate the cyclic shearing and achieve a more stable response to continued cycling. Cyclic behaviour in this *metastable* zone corresponds to plastic shakedown or ratcheting. In the third category of *unstable* response, the cyclic stress path engages the outer Y_3 yield surface. The soils fail in a certain number of cycles and manifest incremental collapse.

Undrained triaxial and hollow cylinder cyclic loading experiments on NE34 and Dunkirk sands by Aghakouchak (2015) verified that the limits or thresholds of cyclic response are dependent on factors such as specimen density, effective stress history (*OCR*) and cyclic pre-conditioning. Ushev (2018) further demonstrated that the undrained cyclic thresholds of the Cowden till, in which half of the PISA pile tests took place, were also dependent of mean deviatoric stress (q_{mean}) level and reduced markedly as the q_{mean} levels caused the cyclic stress paths to approach the outer (Y_3) yielding surfaces.

The undrained cyclic behaviours of sands and clays have been interpreted with reference to widely accepted conceptual frameworks, such as multiple kinematic yield surfaces and critical state soil mechanics. However, it appears from the Author's review that less attention has been given to examining the long-term drained cyclic behaviour of granular materials within the same frameworks.

López-Querol & Coop (2012) examined the existence (or otherwise) of a 'dynamic' critical state or ultimate state line for their loose Dogs Bay sand specimens (e_0 = 1.2~1.4, D_{50} = 0.2 mm) after undergoing thousands of drained cyclic stress cycles from isotropic stress states. Correlations between the change of state parameter ($\Delta\psi$) and initial state parameter (ψ) were established as shown in Figure 7-3, which indicated broadly linear $\Delta\psi$- ψ trends with the slopes increasing with cyclic stress ratio β ($=q_{cyc}/p_0'$). The loose specimens developed prominently contractive volume changes that varied with imposed cyclic stress ratio and did not lead to any unique ultimate state line equivalent to the CSL interpreted for monotonic loading. However, the authors argued that further studies were required considering varied conditions of specimen density, effective stress level and states, before more general conclusions could be drawn.

The Author's research programme set out to examine some of the aspects discussed above, providing further insights into characterising any cyclic thresholds and kinematic yield surfaces that might apply to drained cyclic and post-cycling monotonic shearing.

Table 7-1 Cyclic thresholds and features of cyclic kinematic yield surfaces summarised from recent laboratory programmes on a range of soils

Reference	Soils & characteristics	Test type	Cyclic thresholds	Kinematic yield surfaces
Aghakouchak (2015)[2]	Water-pluviated siliceous fine Dunkirk and Fontainebleau NE34 sand (OCR = 4)	Stress-controlled triaxial and HCA tests	1. *Stable* zone, $CSR \leq 0.25$; elastic or elastic shakedown behaviour. 2. *Metastable* zone, $0.30 < CSR < 0.45$ (Dunkirk), $0.30 < CSR < 0.55$ (NE34); plastic shakedown or ratcheting behaviour. 3. *Unstable* zone, $CSR > 0.5$ (Dunkirk) $CSR > 0.6$ (NE34), incremental collapse behaviour.	Interpretation using the multiple kinematic yield surface framework by Jardine (1992, 2013) 1. *Stable* zone, within Y_2 yield locus. 2. *Metastable* zone, Y_2 yield locus engaged and re-located with cycles. 3. *Unstable* zone, engaged Y_3 yield surface
Ushev (2018)	Heavily over-consolidated stiff glacial Cowden till	Stress-controlled triaxial tests	Thresholds varied with initial mean deviatoric stress (q_m) level and reduced markedly as stress path approached Hvorslev surface	
Guo *et al.* (2017)	Lightly over-consolidated intact soft Wenzhou clay	Stress-controlled triaxial and HCA tests	*Stable* zone, $CSR \leq 0.03$; *Metastable* zone, $0.03 < CSR < 0.16$; *Unstable* zone: $CSR \geqslant 0.16$, shown in Figure 7-2	
Mortezaie & Vucetic (2016)	Reconstituted normally (NC) and overly (OC) consolidated kaolinite and kaolinite-bentonite clays	Strain-controlled DSS tests	NC kaolinite, γ_{td} [3] range: 0.012-0.014%, γ_{tp} [3] range: 0.014-0.034%; NC kaolinite-bentonite, γ_{td} range: 0.013-0.016%, γ_{tp} range: 0.052-0.078%. γ_{tp} and γ_{td} ranges varied with OCR with γ_{tp} typically higher than γ_{td}	

Notes:

1. All the test series were performed under undrained shearing condition.
2. Threshold ranges shown were from triaxial tests. Threshold ranges from HCA tests were slightly different.
3. γ_{td}: threshold of shear strain amplitude for cyclic stiffness degradation below which no degradation would occur; γ_{tp}: threshold of shear strain amplitude for cyclic pore water pressure below which no permanent pore water pressure would be generated (Mortezaie & Vucetic, 2016).

7.2.2 Laboratory investigations of sand behaviour under long-term cyclic loading

This subsection summarises some of the main findings gained from earlier laboratory research reported in the literature that involved drained long-term cycling in sands. The key factors dominating strain accumulation patterns and directions are reviewed and the various functions describing the rates and 'terminal' states of strain development are summarised. Discussions is also presented on cyclic stiffness evolution and the effects of cyclic loading history (or 'memory') and irregular cycles.

Laboratory research into long-term drained cyclic loading and dominant factors

Extensive research into long-term drained cyclic behaviour has been carried out in triaxial apparatus, by for example Tatsuoka & Ishihara (1974), Marr & Christian (1981) and Sun *et al.* (2017). Triaxial tests involving constant cell pressures (CCP) apply stress-controlled cycling by superimposing deviatoric stress cycles q_{cyc} often in combination with an initial mean deviatoric stress q_{mean}, as shown in Figure 7-4. The loading characteristics are described by normalised ratios of the mean deviatoric stress q_{mean} and the cyclic (half peak-to-trough) amplitude q_{cyc}. The mean cyclic stress ratio η, and the cyclic stress amplitude ratio CSR, are defined here as:

$$\eta = \frac{q_{mean}}{p_0'} \tag{7.1}$$

$$CSR = \frac{q_{cyc}}{p_0'} \tag{7.2}$$

The strain development patterns observed in drained cyclic tests are generally markedly different to those seen in undrained cyclic loading, where no volume straining can occur (Seed & Lee, 1966, Ishihara *et al.*, 1975).

Under drained conditions, cyclic straining is often most marked over the first few "conditioning" cycles, involving both significant strain amplitudes (ε^{ampl}) and rates of strain accumulation (ε^{acc}), as shown in Figure 7-5. Plastic strain accumulation continues as shearing evolves, but often with reducing rates of strain accumulation and changes in cyclic stiffness, until an ultimate strain equilibrium state is reached, where the unrecoverable plastic strain component (ε^{acc}) reaches or approaches an asymptotic

value with a recoverable strain component that oscillates around the permanent accumulated strain with a constant amplitude. The cyclic shear stress-strain behaviour manifested after a large number of cycles is often termed shakedown or ratcheting (Brown, 1974). The ultimate equilibrium state where continuing strain accumulation becomes negligible and plastic strain components reach asymptotic values is referred as the terminal state (Narsilio & Santamarina, 2008, Chong & Santamarina, 2016).

The permanent strain accumulation trends of sandy materials under drained cyclic shearing have also been investigated through cyclic direct simple shear (DSS) tests, see for example Silver & Seed (1971), Youd (1972) and Nikitas *et al.* (2017), and Hollow Cylinder Apparatus (HCA) experiments, as exemplified by Tong *et al.* (2010), Cai *et al.* (2015) and Yu *et al.* (2016). These laboratory studies have examined the effects of a wide range of factors, including initial relative density, effective stress level and history, cyclic shear stress or strain amplitude, loading characteristics (one-way or two-way, uniaxial or multi-axial shearing in a generalised stress space), cycling frequency and number of cycles. The effects of some of the key factors are briefly discussed below.

Initial void ratio or relative density Sandy materials often manifest continuous compaction or densification when subjected to drained repetitive shearing cycles. Many researchers have demonstrated that the rates of densification or volume straining depend critically on the initial relative density or void ratio of the specimens. Wichtmann *et al.* (2005), for example, demonstrated how the magnitudes of accumulated permanent strains increased significantly with decreases in initial relative density of specimens subjected up to 10^5 cycles, as shown in Figure 7-6, whereas the cyclic strain amplitudes were less dependent on initial relative density.

Effective stress ratio and level Effective stress ratio has been recognised as one of the dominant factors affecting the direction of cyclic permanent strain or cyclic dilatancy. Chang & Whitman (1988) extended the energy approach used by Roscoe & Burland (1968) in developing the modified Cam clay model and proposed a relationship between the cumulative (or residual) strain ratio and effective stress states as.

$$\frac{\varepsilon_{\mathrm{v}}^{\mathrm{acc}}}{\varepsilon_{\mathrm{s}}^{\mathrm{acc}}} = \frac{(M^2 - \eta_0^2)}{2\eta_0} \tag{7.3}$$

Where ε_v^{acc} and ε_s^{acc} are accumulative volumetric strain and deviatoric strain, respectively, which are expressed as $\varepsilon_v^{acc} = \varepsilon_a^{acc} + 2\varepsilon_r^{acc}$ and $\varepsilon_s^{acc} = 2/3(\varepsilon_a^{acc} - \varepsilon_r^{acc})$ with accumulated axial (ε_a^{acc}) and radial (ε_r^{acc}) strain in a triaxial space. η_0 and M are initial static stress ratio and stress ratio at critical state, respectively. The critical state stress ratio M was regarded as a characteristic threshold in the q-p' stress space below which contractive volumetric strain was accumulated while dilative volumetric strains developed above this limit.

Chang & Whitman (1988) and later Wichtmann *et al.* (2005) defined the ratio $\varepsilon_v^{acc}/\varepsilon_s^{acc}$ as a cyclic strain accumulation direction, which was argued to be dependent only on stress ratio; largely independent of relative density and effective stress level; and to change slightly with the number of shearing cycles, as shown in Figure 7-7. Figure 7-8 indicates good match between their experimental trends and the dilation model predictions (Equation (7.3)). However, the tests reported were performed predominantly on medium-dense specimens (I_{D0} or R_d: 0.57-0.69) under a single cyclic stress ratio (ζ or CSR = 0.3). It remained unclear how cyclic strains would develop in looser or denser specimens and under a wider range of stress conditions. These aspects are further examined in the Author's study.

Cyclic loading characteristics A range of cyclic loading styles may be imposed in testing, depending on the test apparatus type and its performance. As demonstrated in Figure 7-4, one-way or two-way purely axial load cycling can be readily achieved in triaxial testing with constant cell pressures (CCP). Although restricted to triaxial stress space, this configuration requires only relatively simple cyclic stress controls and enables accurate measurements of strain components, particularly if local strain sensors are deployed. Cyclic stiffness and damping ratios can then be determined with a high level of accuracy.

More sophisticated cyclic stress or strain paths may involve simultaneously varying triaxial cell pressure or employing other type of apparatus, such as constant p' triaxial, Direct Simple Shear (DSS) or Hollow Cylinder Apparatus (HCA) equipment. Wichtmann *et al.* (2007a) identified three types of In-Phase (IP) and Out-of-Phase (OP) cyclic stress cycles that can be applied in cyclic triaxial and multi-directional DSS tests, as illustrated in Figure 7-9. Triaxial tests on granular materials involving variable cell pressure (VCP) were reported by Brown & Hyde (1975), Rondón *et al.* (2009) and Sun

et al. (2017), and it appears that the relative amount of cumulative strains generated in VCP tests in comparison with CCP tests depend on the cyclic stress amplitude and cyclic stress path inclination. The stress components in the out-of-phase type of cyclic stress cycles oscillate around certain baseline values with a phase shift, forming stress path loops that encompass measurable areas. Wichtmann *et al.* (2007a) demonstrated that the characteristics of cyclic strain accumulation varied with the inclination (or polarisation) of the stress loop applied. The out-of-phase loops generated higher strain accumulation rates than the in-phase cycles, although it is arguable that the shear strain measured in multi-directional DSS apparatus is not fully representative of field behaviour due to the significant stress and strain non-uniformity within the specimens, especially when testing sands.

Other type of out-of-phase cyclic stress paths can be applied through hollow cylinder testing. Tong *et al.* (2010) investigated strain accumulation characteristics and flow rules under tests involving cyclic rotation of principal stress axes and addressed the effects of the level of intermediate principal stress on plastic volumetric straining. Cai *et al.* (2015) generated cardioid shaped incremental $\Delta\tau_{z\theta} - \Delta(\sigma_z\text{-}\sigma_\theta)/2$ cyclic stress paths in HCA testing to represent idealised traffic loading and demonstrated a significant dependency of the vertical permanent deformations on the cyclic torsional stress ratio (shown in Figure 7-10). HCA testing offers two further degrees of freedom in applying representative cyclic stress paths and provides an opportunity to track and investigate separately the effects of principal stress axis direction and intermediate principal stress level, which cannot be achieved in conventional triaxial or DSS tests.

Cyclic shear stress or strain amplitude Cyclic shearing (stress or strain) amplitude is one of the predominant factors affecting cyclic stress-strain response and stiffness. Many researchers have investigated the effects of cyclic stress ratio (*CSR*) on the rate and magnitude of permanent strain developing and the amplitude of the 'recoverable' shear strain. Wichtmann *et al.* (2005) verified that cumulative permanent strains, rates of accumulation and the amplitudes of shear strain increase remarkably with the increase of cyclic stress amplitude. Cai *et al.* (2015) reported cyclic drained HCA tests incorporating cyclic shearing stress in the vertical (σ_z) and torsional ($\tau_{z\theta}$) direction, and demonstrated that the cyclic stress components generated similarly positive effects on the magnitudes of permanent vertical strain accumulated, as shown in Figure 7-10.

Cyclic shearing frequency and number of cycles Investigating the influence of frequency in long-term cyclic tests requires special measures, including:

a. Apparatus that is capable of imposing (ideally relatively fast) cycling while maintaining accurate stress control quality and suitably frequent data logging;

b. Measuring sensors with very good drift and compliance characteristics that are insensitive to variations of testing environment (diurnal or seasonal temperature fluctuations in particular);

c. The ability to ensure full drainage in the tested soils considering grain size, fines content and specimens dimension as well as drainage boundary conditions;

d. The ranges of cyclic stress or strain amplitudes that may be applied;

e. Loading frequencies that are appropriate in relation to those encountered in the potential problems that the element tests aim to represent (for example, offshore wind or wave loading, traffic loading);

f. Constraints regarding time and apparatus availability, particularly in testing programmes that aim to apply 10^4-10^5 or more cycles per test.

The potential effects of cycling frequency on accumulative strain development were investigated by Wichtmann *et al.* (2005), for example, who reported parallel triaxial tests performed on a quartz sand (D_{50} = 0.55 mm) with a single cyclic deviatoric stress (q_{cyc}) of 60 kPa and loading frequencies ranging from 0.05 Hz to 2 Hz (corresponding to cycle period of 0.5 s to 20 s) on medium-dense cylindrical specimens (200 mm height, 100 mm diameter). The results indicated only minor differences in accumulated strain amplitudes and strain ratios. However, López-Querol & Coop (2012) raised concerns regarding possibly incomplete drainage in their triaxial tests on loose (76 mm height, 38 mm diameter) specimens of fine Dogs Bay sand (D_{50} = 0.20 mm), that applied two-way cycling with q_{cyc} up to 240 kPa, and concluded that, although time-consuming, 90 s periods (up to 180 times longer than employed by Wichtmann *et al.* (2005)) may be required for the applied step-shaped stress cycles to attain fully drained conditions.

The issue of non-uniform excess pore water pressure development has been examined in undrained cyclic testing on lower permeability clays. Ushev (2018) deployed multiple pore water pressure probes in his cyclic triaxial tests on Cowden till to investigate pore water pressure distribution trends under undrained cyclic shearing, and concluded that uniformly distributed pore water pressures and reliable sample end

measurements could only be achieved with his stiff low plasticity till 200 mm high, 100 mm diameter specimens under very slow shearing, with cyclic periods larger than 30 minutes. However, employing mid-height pore water probes allowed representative pore pressure measurements over individual cycles at far higher frequencies. Ushev (2018) ran his main cyclic programme successfully with 5 minute periods by employing such probes. Few similar verification exercises have been reported, although cyclic triaxial or DSS testing studies involving relatively high shearing frequencies (> 0.5 Hz) have been conducted on a wide range of soils.

It is worthwhile pointing out that due to the non-linear and strain-rate dependent nature of geo-materials (Tatsuoka, 2011, Jardine, 2013), soils do not respond instantaneously to the imposed cyclic stresses and that the stress and strain waveforms are not synchronic, particularly when shearing cycles involve large amplitudes or high frequencies. The tendency for deformation to lag behind stress changes is best captured and studied by employing local strain instruments, rather than external displacement or volume measurements. This is further discussed in Section 7.3.2, drawing observations from the current testing programme.

As noted earlier, granular materials commonly generate relatively high rates of non-recoverable plastic straining over the early stages of drained shearing tests ($N < 10^2$-10^3) that gradually slow down until permanent strains or volume change approach asymptotic terminal states or densities (Narsilio & Santamarina, 2008). The rates at which the asymptotic states are approached depend on material type, specimen density and shearing amplitude. Wichtmann *et al.* (2005) observed 'over-proportional' trends of accumulated strain after 10^4 cycles in which the slope of the ε^{acc}-log(N) trends ascended over time, suggesting that any final equilibrium could only be approached after very large N with their medium-dense silica sand (with $R_d \approx 60\%$, $D_{50} = 0.55$ mm). However, tests on fine loose Dogs Bay sand (with $e_0 = 1.2$~1.4, $D_{50} = 0.2$ mm) by López-Querol & Coop (2012) approached asymptotic trends after only 10^2-10^3 cycles.

Strain accumulation pattern and functions

Empirical correlations have been proposed to fit experimental relationships between accumulative permanent strains and the number of imposed cycles, providing the basis for simple methods for predicting long-term cyclic deformation in soils. Chong & Santamarina (2016) summarised five types of generalised functions for describing

permanent strain patterns and accumulating rates, as shown in Table 7-2. The factors *b*, *c*, *d* employed in the formulations are fitting parameters that aim to match the (usually axial) strain accumulation characteristics and asymptotic conditions (shakedown or ratcheting) seen under usually moderate-to-large number of loading cycles. Similar formulations have been adopted to describe the global accumulation of pile head deflections, body rotations or the degradations of soil reaction moduli or stiffnesses against number of loading cycles, see for example the review by Jardine *et al.* (2012).

However, determining asymptotic conditions after long-term cyclic loading is a subtle process that requires very accurate and reliable strain or volume measurements to capture the generally small residual strain rates. Extrapolation approaches may be required in tests in which only limited numbers of loading cycles were applied. The applicability of these functions in fitting the Author's test outcomes is examined later in this chapter.

Table 7-2 Summary of generalised plastic strain accumulation functions for sandy materials subjected to long-term repetitive loading (modified from Chong & Santamarina (2016))

Type	Plastic strain accumulation function	Plastic strain accumulation rate
Exponential function	$\varepsilon_N^{acc} = \varepsilon_1 + b\{1-\exp[-c(N-1)]\} + d(N-1)$	$\frac{d\varepsilon_N^{acc}}{dN} = bc\exp[-c(N-1)] + d$
Hyperbolic function	$\varepsilon_N^{acc} = \varepsilon_1 + b\frac{N^c-1}{N^c+b} + d(N-1)$	$\frac{d\varepsilon_N^{acc}}{dN} = \frac{bcN^c(b+1)}{N(b+N^c)^2} + d$
Polynominal function	$\varepsilon_N^{acc} = \varepsilon_1 + b(1-N^c) + d(N-1)$	$\frac{d\varepsilon_N^{acc}}{dN} = bcN^{-(1+c)} + d$
Power function	$\varepsilon_N^{acc} = \varepsilon_1 + b(N^c-1) + d(N-1)$	$\frac{d\varepsilon_N^{acc}}{dN} = bcN^{c-1} + d$
Log-linear function	$\varepsilon_N^{acc} = \varepsilon_1 + b\log(N) + d(N-1)$	$\frac{d\varepsilon_N^{acc}}{dN} = \frac{b}{\ln(10)}\frac{1}{N} + d$

Notes:

1. N: number of cycles; b, c, d: fitting parameters;
2. d: rate of ratcheting at $N \gg 1$; $d = 0$ suggesting shakedown behaviour;
3. Sources of the functions refer to the summary by Chong & Santamarina (2016).

Stiffness evolution in large number of low to high amplitude cycling

Tracking the changes in soils' stiffness and damping characteristics is important when studying long-term cyclic soil behaviour for fatigue assessment and other aspects of soil-structure system response.

The evolution of granular materials' static shear stiffness while undergoing large numbers of small amplitude perturbations has been investigated through bender element and stress probing tests. Escribano & Nash (2015) tracked the shear stiffness (G_{vh}, G_{hv}, G_{hh}) of Hostun sand in cyclic triaxial tests by means of bender element tests, and identified no consistent trends of elastic shear stiffness change with evolving shearing cycles.

Tests that apply very small shear stress and strain amplitudes that that remain within the soils' linear elastic (Y_1) range do not develop significant strain accumulation or changes in stiffness over time. Cycles that exceeded this limit, even though invoking relatively small straining, were investigated by Nikitas *et al.* (2017) and Cui *et al.* (2017) through strain-controlled cyclic direct simple shear experiments and discrete element modelling (DEM) approaches. General trends were found for shear modulus to increase under these conditions with the number of cycles, effective stress level and specimen density.

The soils' cyclic stiffnesses are likely to be stress- and strain-dependent, particularly over the non-linear range, as with the static stiffnesses as previously discussed in Chapters 4 and 5. The deployment of high resolution local strain sensors enables individual stress-strain loops and cyclic stiffnesses to be characterised with significantly greater accuracy than is available conventionally. These aspects are presented and discussed later on the basis of the Author's experiments.

Effects of loading history

Other effects of loading history that affect the monotonic and cyclic shearing behaviour of sands have been addressed in earlier research. López-Querol & Coop (2012) reported that the volumetric straining (or change of state parameter) of loose Dogs Bay sand appeared to be unaffected by the sequence of cyclic stress packages being applied, as illustrated in Figure 7-11. They further reported that samples subjected to a certain amplitude of cycling would retain the 'memory' from the previous loading stage with same amplitude, manifesting as smoothly continuing volumetric strain, regardless of any intervening stages occurring in-between the two loading stages. However, the cyclic straining 'memory' would be overwritten if equilibrium conditions (developing negligible strain increments) had been reached in any subsequent stage that involved a higher cycling amplitude than the preceding

loading stage.

Aghakouchak *et al.* (2015) demonstrated that both the 'monotonic' effective stress history (*OCR*) and drained pre-conditioning stress cycles affected significantly the undrained cyclic shearing behaviour of siliceous Dunkirk and NE34 sands, with his over-consolidated (*OCR* = 4) and pre-cycled "conditioned" specimens exhibiting notably higher cyclic shearing resistance than normally consolidated specimens. Extended ageing had an equally marked impact. These features are of crucial importance to the modelling of the axial cyclic response of driven piles whose installation process involves both extreme pre-loading (as the pile tip passes) and multiple shear and normal stress cycles imposed by hammer blows at points located close to pile shafts. The potential effect of 'monotonic' over-consolidation (*OCR*) on the subsequent drained cyclic shearing responses was investigated in the Author's programme.

Irregular cycling

While regular cycling employing uniform amplitudes and frequencies is adopted for most laboratory, model and field testing studies, irregular non-uniform cycling with mixed amplitudes is more common in practical engineering cyclic loading cases, especially those applied to offshore piles. A common approach for dealing with such randomly distributed cyclic loads is to adopt so-called "cycle-counting" or "rainflow" schemes to decompose recorded load spectra into ordered load packages containing a give number of cycles with constant values of average and cyclic loads (see examples by Puech *et al.* (2012) and Jardine *et al.* (2012)). This approach effectively assumes that the damage rules proposed by Miner (1945) are valid and that the cumulative effects from these decomposed idealised stress cycles are equivalent to the original irregular cyclic loads.

A superposition approach of this type was set out formally by Stewart (1986). He derived permanent strains from variable-amplitude loads from uniform-amplitude cyclic triaxial tests, following the procedures illustrated in Figure 7-12 for tests that showed steady trends with log(*N*). The denotations ε_{Ni} and ε_{Nj} represent permanent strains generated after *N* cycles in two uniform cyclic tests with stress amplitude cases of *i* and *j*. In the original derivation, Stewart (1986) assumed a constant coefficient of strain accumulation rate, *C* for different cycling stress amplitudes. Taking the case of

stress amplitude j as a reference, the equivalent number of cycles (N_j^*) under the j stress amplitude cycling to generate the permanent strain ε_{Ni} under the i stress amplitude cycling is defined as

$$N_j^* = \exp\left[\frac{2.3}{C}\left(\frac{\varepsilon_{Ni}}{\varepsilon_{1j}} - 1\right)\right] \tag{7.4}$$

The superposed strain found after N_i cycles of the stress amplitude i and N_j applications of the stress amplitude j can be determined by

$$\varepsilon_{N(i+j)} = \varepsilon_{1j}\left[1 + C\log(N_j + N_j^*)\right] \tag{7.5}$$

While the above equations apply only to linear ε_N-log(N) correlations, the basic concept has been extended to cycling scenarios with varied amplitude levels and accumulation rates and also other types of ε_N-N correlations, see the example for the application of power law correlation by Merritt *et al.* (2012), Wichtmann & Triantafyllidis (2017) or Rattley *et al.* (2017).

Post-cycling monotonic shearing behaviour

Aghakouchak (2015) reported that his pre-loaded and pre-cycled Dunkirk sand specimens exhibited higher undrained cyclic shearing resistance than normally consolidated or previously uncycled "virgin" specimens, indicating that pre-cycling enhances the soils' micro-fabrics. Nicolai *et al.* (2017) recently reported from 1-G and multiple gravity centrifuge model tests remarkable increases of moment capacity of monopiles in sands due to prior cyclic loading, and concluded that such increases were related to the magnitude of the prior cyclic load, the number of loading cycles and cyclic loading symmetry.

Laboratory element tests that incorporate cyclic loading and post-cycling monotonic shearing stages, in conjunction with tests on "virgin" specimens (as those presented in Chapters 5 and 6), could enable comprehensive characterisation of cycling effects and post-cycling monotonic behaviour. This approach was employed in the Author's research programme, as described in the following section.

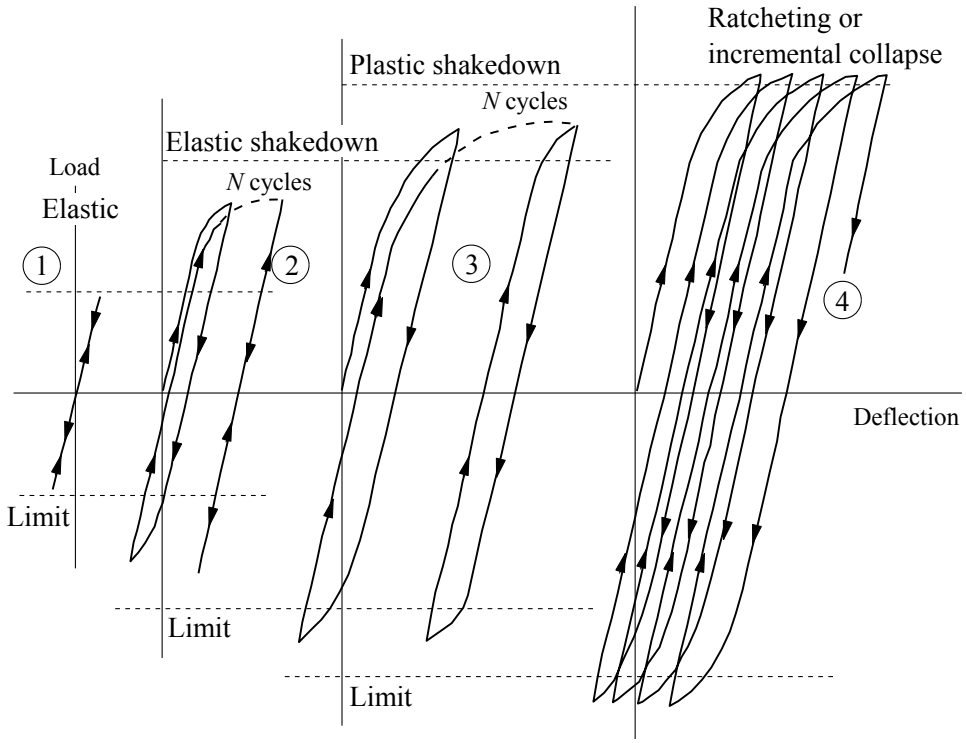

Figure 7-1 Characteristics of stress-strain loop and strain pattern of soils subjected to repetitive loading cycles, distinguishing: (1) purely elastic behaviour; (2) elastic shakedown; (3) plastic shakedown; (4) ratcheting or incremental collapse
(modified from Collins & Boulbibane (2000))

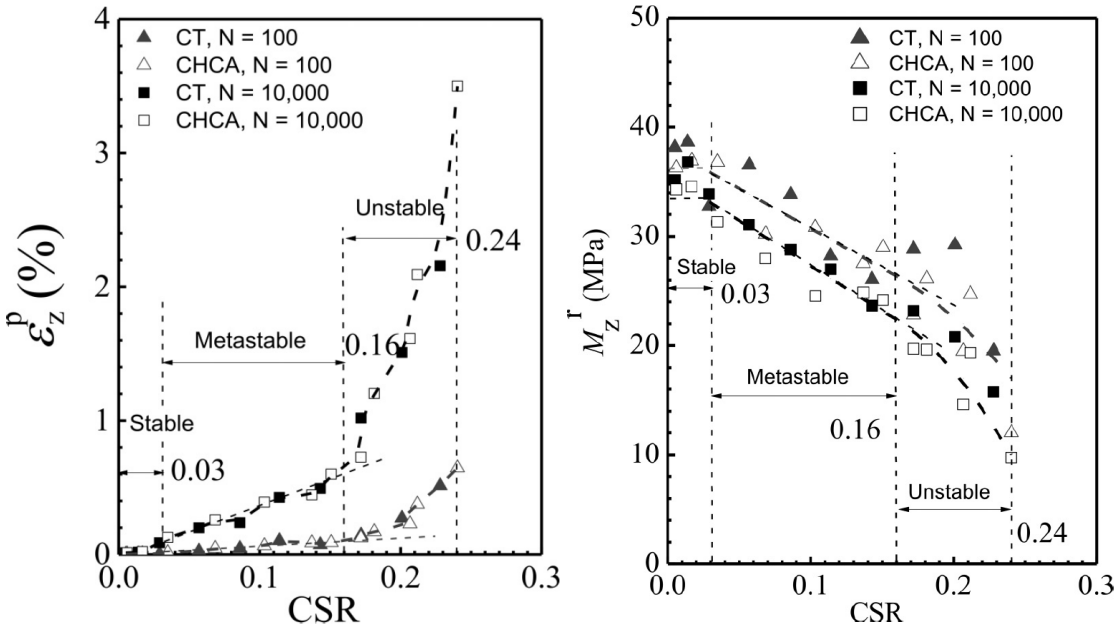

Figure 7-2 Identification of cyclic stress ratio (*CSR*) range of *Stable*, *Metastable*, *Unstable* cyclic response of soft clays subjected to undrained cyclic loading based on the criteria of vertical permanent strain (ε_z^p) and resilient modulus (M_z^r) (Guo *et al.*, 2017)

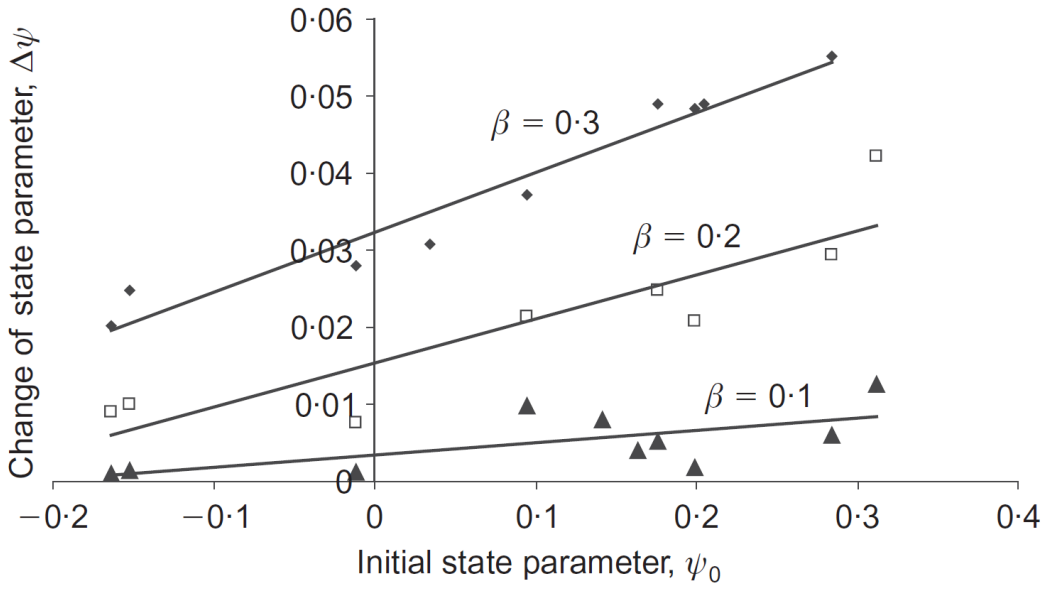

Figure 7-3 Correlation trends between the change of state parameter ($\Delta\psi$) and initial state parameter (ψ) of loose isotropically consolidated Dogs Bay sand subjected to drained cyclic shearing of different cyclic stress ratio β (=q_{cyc}/p_0') (López-Querol & Coop, 2012)

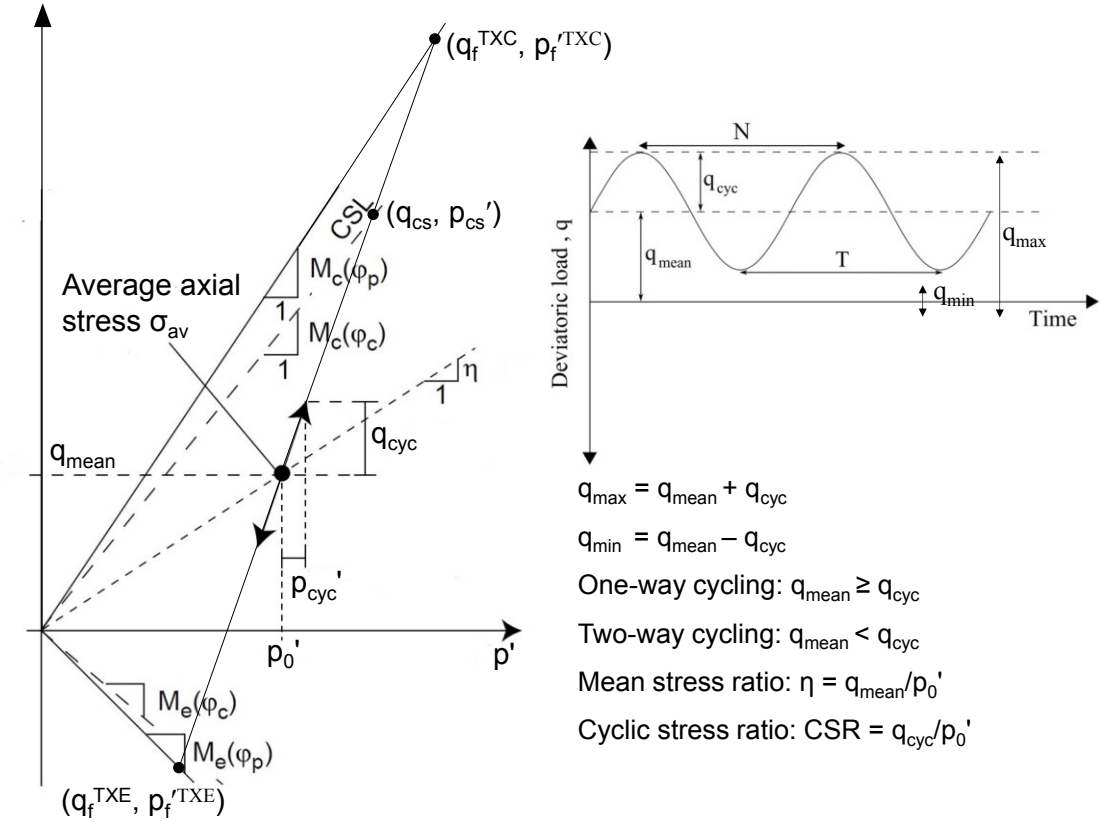

Figure 7-4 Cyclic loading definitions in triaxial stress space and the failure envelopes, considering drained Constant Cell Pressure (CCP) conditions

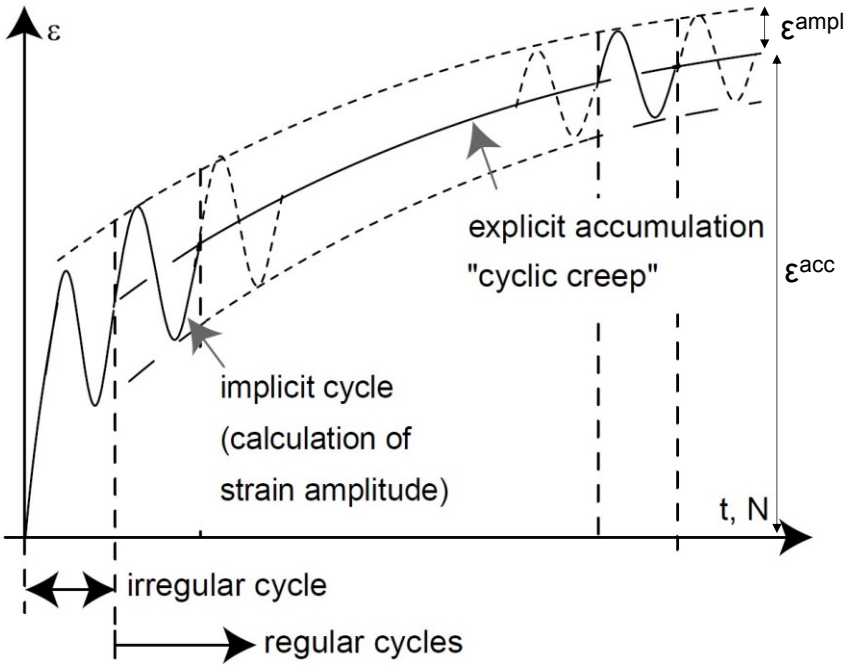

Figure 7-5 Typical strain accumulating patterns in drained cyclic tests, identifying rapid strain generation over initial conditioning cycles and decreasing accumulating rates over high number of shearing cycles (modified from Wichtmann *et al.* (2005))

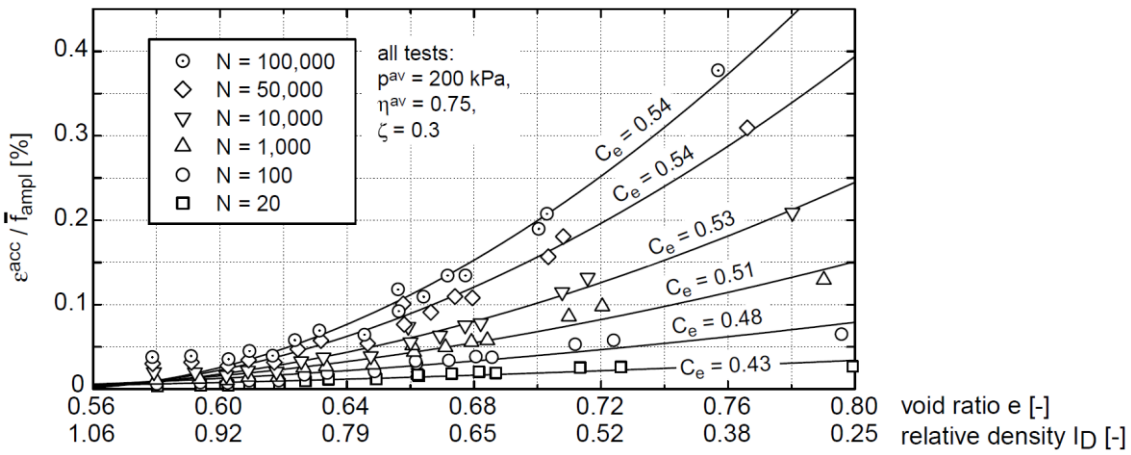

Figure 7-6 Dependence of permanent strain accumulation on sample initial relative density (C_e: material constant; ε^{acc}: accumulated permanent strain; f_{ampl}: amplitude function, see Wichtmann *et al.* (2005))

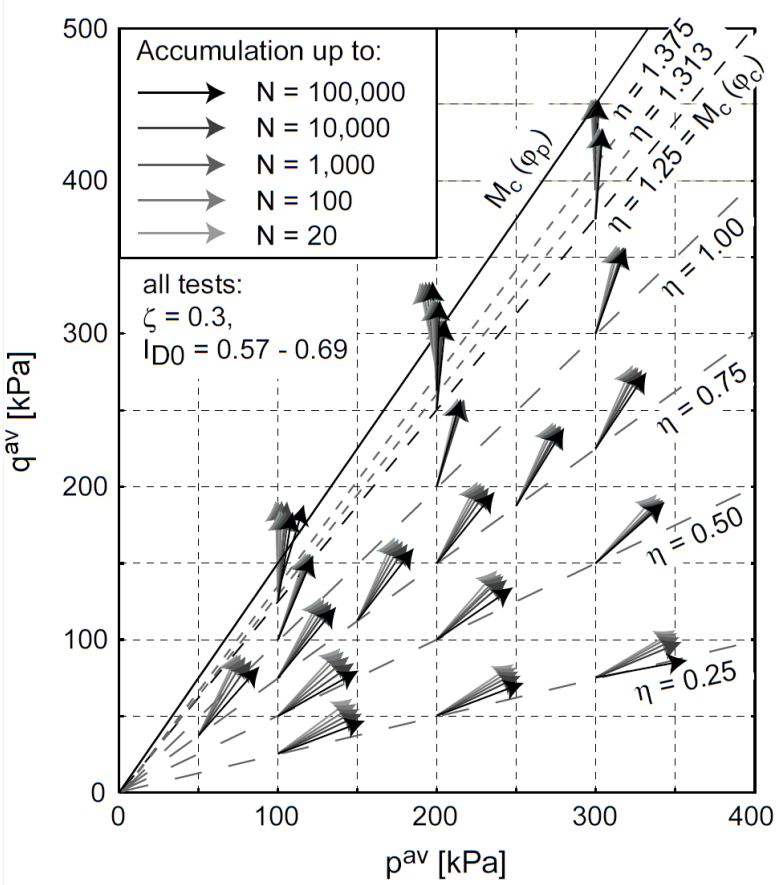

Figure 7-7 Cyclic flow determined in triaxial compression condition (Wichtmann *et al.*, 2005)
(I_{D0}: relative density; ζ: cyclic stress ratio, q_{cyc}/p_0'; sand D_{50} = 0.55 mm, C_u = 1.8)

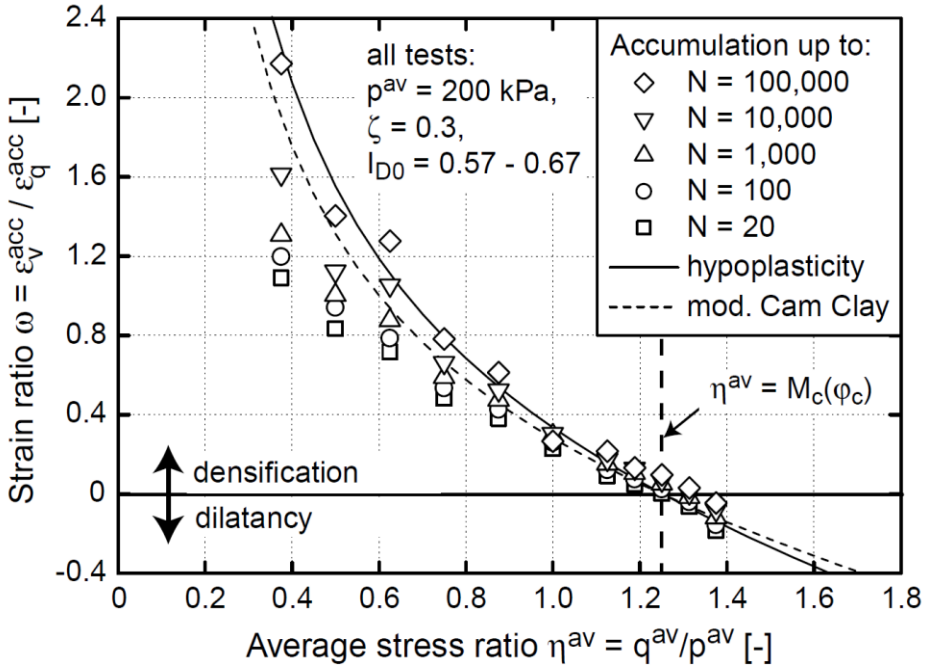

Figure 7-8 Experiment trends for permanent cyclic strain ratio and average stress ratio fitted by theoretical predictions (Wichtmann *et al.*, 2005)

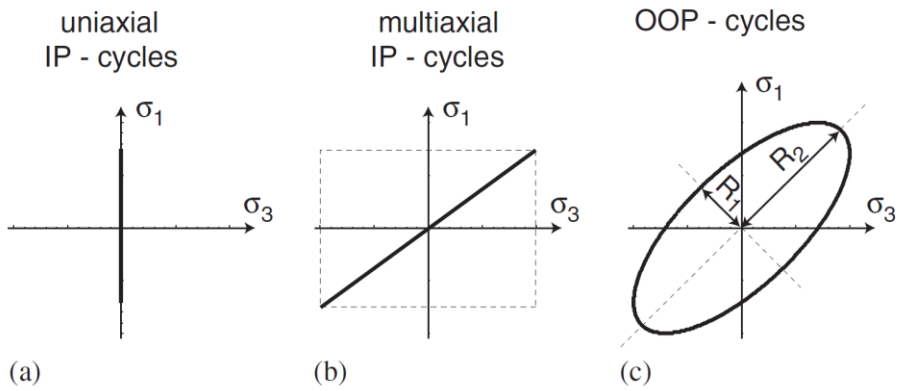

Figure 7-9 In-phase (IP) and out-of-phase stress cycles that can be applied in cyclic triaxial and multi-directional direct simple shear tests (Wichtmann *et al.*, 2007a)

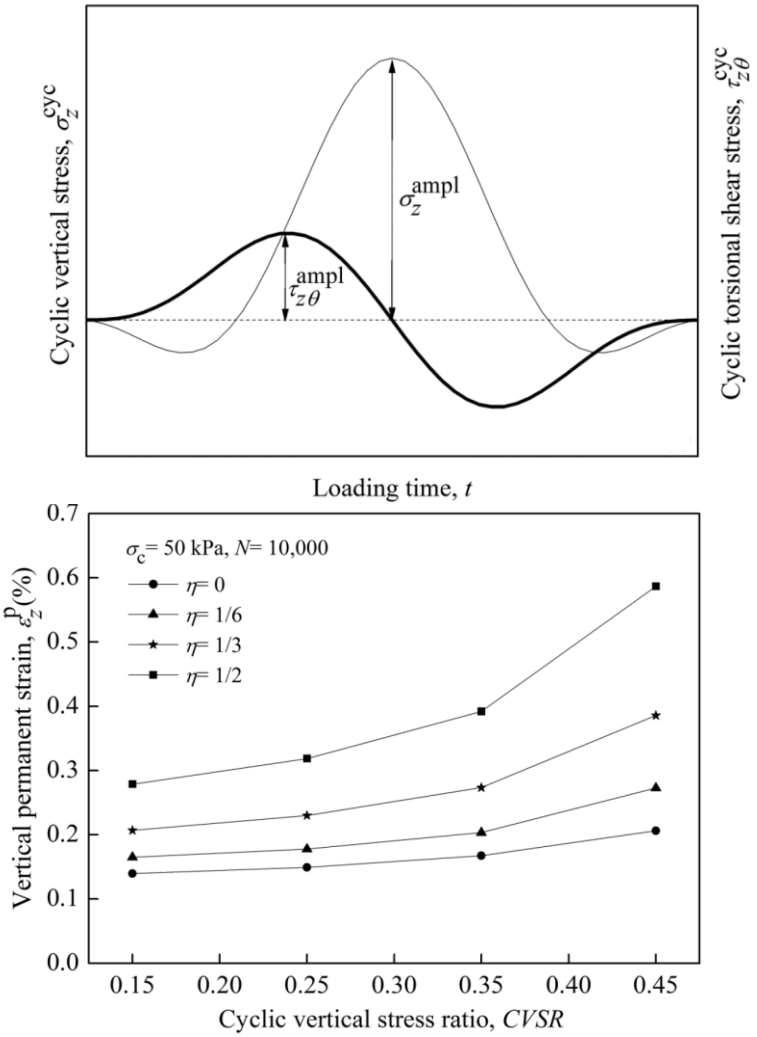

Figure 7-10 Effects of cyclic vertical and torsional stress ratio on vertical permanent strain observed in HCA tests reproducing idealised traffic loading stress cycles (Cai *et al.*, 2015) (Cyclic vertical stress ratio, $CVSR = \sigma_z^{ampl}/2p_0'$, cyclic torsional stress ratio, $\eta = \tau_{z\theta}^{ampl}/\sigma_z^{ampl}$)

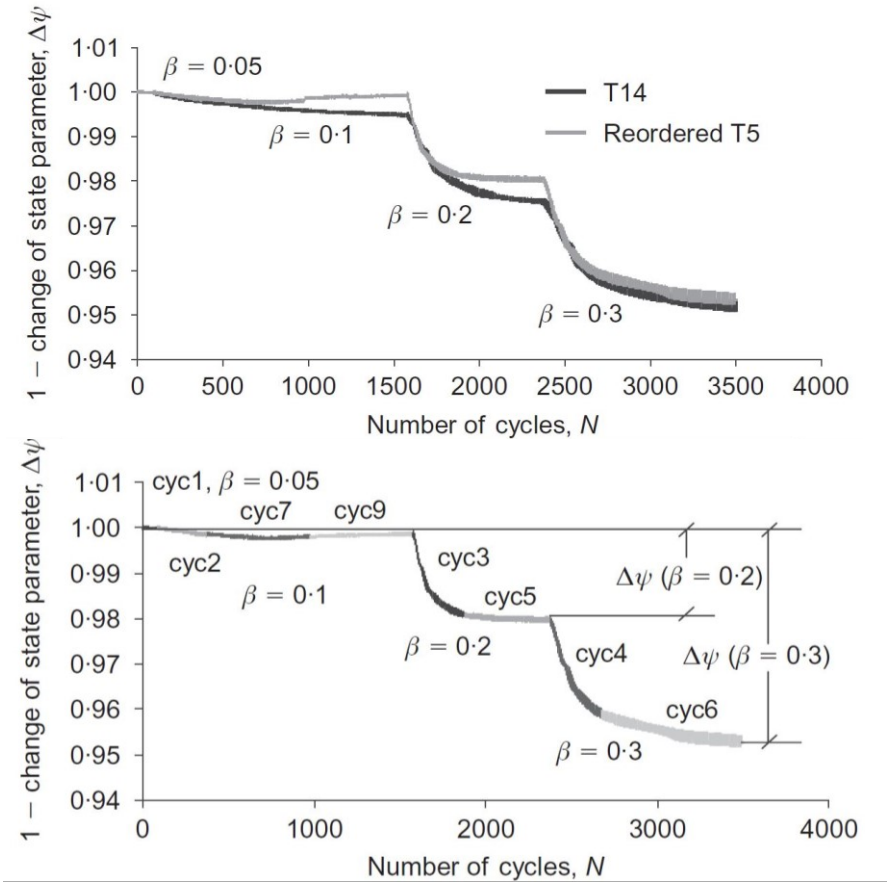

Figure 7-11 Changes of state parameter ($\Delta\psi$) of loose Dogs Bay sand subjected to cyclic loading packages of varied cyclic stress ratios β ($=q_{cyc}/p_0'$) (López-Querol & Coop, 2012)

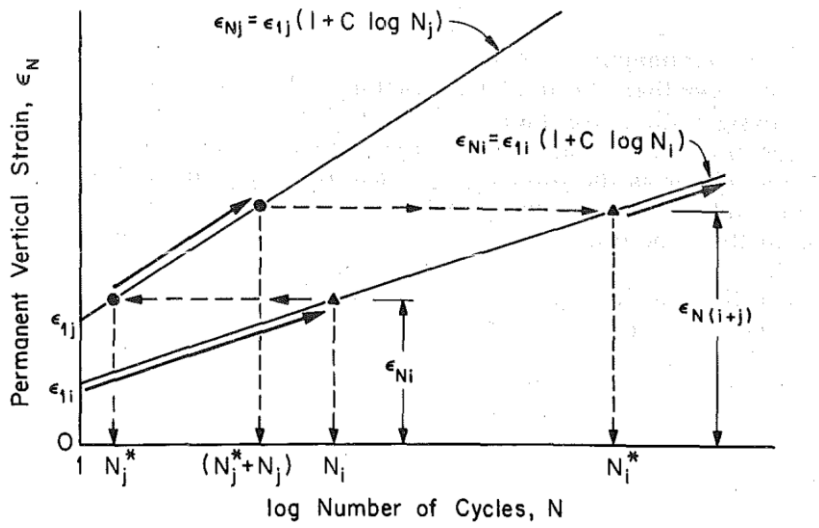

Figure 7-12 Superposition approach proposed by Stewart (1986) for calculating accumulative strains from variable-amplitude cyclic shearing

7.3 Research methodology and programme

The Author's testing programme was developed to test the hypotheses proposed in Section 7.1. The research methodology, together with some key technical considerations regarding strain determinations, are presented below, followed by detailed descriptions of the research programme completed.

7.3.1 Research methodology

The research programme consisted of suites of Constant Cell Pressure (CCP) drained cyclic triaxial tests performed on reconstituted Dunkirk sand specimens of 38 mm diameter and around 80 mm heights.

Although more variable cyclic shearing paths could be applied through HCA testing, or triaxial testing with Variable Cell Pressure (VCP), CCP triaxial testing has the merit of enabling straightforward cyclic control that could accommodate a wide range of loading amplitudes with the systems available to the Author. Additionally, by deploying local strain instruments, the strain components developed under CCP triaxial testing were determined with much higher accuracy than is possible with conventional external strain or volume measurements, enabling more reliable characterisation of ratcheting, damping and cyclic stiffness properties. Testing larger 100 mm diameter specimens offers some advantages, as discussed by Ushev (2018). However, consideration of the volume of the Dunkirk sand available for testing indicated that smaller specimen sizes were required for the intended comprehensive investigation to be completed.

It was not feasible to model the specific in-situ stress histories imposed by monopile installation or match cycling patterns that soil elements might experience around laterally loaded pile foundations. Lateral loading of offshore piles in the field engages a large mass of soil within which the initial and imposed stress conditions vary considerably with radial distance from the pile axis, circumferentially around the axis and with depth.

This is in contrast to Aghakouchak's (2015) laboratory element programme that investigated directly the cyclic performance of axially loaded driven piles. Concentrating on the near shaft conditions that control the axial capacity allowed the problem to be simplified into definable 4-D stress conditions as set out by Jardine *et al.* (2012) and Aghakouchak *et al.* (2015). Aghakouchak's programme highlighted the

importance when considering elements located close to pile shaft (as shown in Figure 1-4) of reproducing the driving stress cycling, intense pre-loading and subsequent relaxation associated with pile installation and also of imposing extended ageing periods to reproduce the in-situ conditions applying before imposing cyclic loading.

In contrast, the response of laterally loaded large diameter rigid monopiles is predominantly affected by the stiffness and strength of the far larger soil volumes that are involved in developing the passive, active and side shear force components identified in Figure 1-5. While Aghakouchak (2015) tested over-consolidated, pre-cycled and aged samples, the Author's testing programme focused primarily on normally consolidated conditions, with a small number of additional checks on over-consolidated specimens. The main masses of sand encountered around the Dunkirk PISA piles are normally consolidated.

Rather than attempting to consider the full range of stress conditions around the PISA Dunkirk piles as they underwent cyclic testing, the Author aimed to produce a benchmark dataset against which models proposed to represent the drained cyclic shearing behaviour of Dunkirk sand can be calibrated and to cover an appropriate range of relative density, effective stress conditions and cyclic stress amplitudes. Validated and calibrated constitutive models may then be employed in cyclic analyses of the long-term cyclic behaviour of the monopiles and other structures experiencing comparable conditions.

The quasi-static cyclic tests were performed with stress-controlled sinusoidal waves and fixed periods of two minutes, i.e. $f = 0.0083$ Hz. The slow shearing motion imposed ensured that shearing cycles could be controlled precisely with the available equipment, even when shearing amplitudes were large (q_{cyc} up to 200 kPa). Uniform pore water pressure conditions were assured and enough data points could be recorded to fully characterise each cycle. Around 14 days of cycling were required for the repetitive loading stage of each 10^4 cycle test and most tests took 28 days to complete.

All the experiments were performed in Lab 1 (see Section 2.3.7) which is equipped with upgraded temperature controlled systems. The low degree of temperature fluctuation (±0.3 ˚C) minimised thermal impacts on strain measurements to levels that were considered negligible in the testing programme.

7.3.2 Strain determination approaches

Two sets of strains can be determined in the three Bishop-Wesley triaxial apparatuses employed, through the local vertical and radial strain sensors, in addition to external vertical displacement and volume measurements.

Strain data from local strain sensors are in principle more accurate and representative of the cyclic deformation of the specimens. The measurements from local axial and radial strain sensors, which are mounted in the central height of the specimen, are largely immune from system compliance and bedding errors, and are therefore more representative of the specimen cyclic deformation.

Upgraded radial-belt systems (as described in Section 2.3.4 and shown in Figure 2-21) were used throughout the testing and the cyclic volumetric strains were determined directly from the local axial and radial strains. Over-sized fully lubricated plattens described in Section 5.3.1 were employed to alleviate end constraints and facilitate uniform stress distribution and radial deformation within the specimens.

The strains calculated from the external displacement and volume measurement systems were only adopted in the tests which developed large cyclic strains. In all other cases, the external strains were regarded as giving only reference data. As described in Section 2.3.7, the triaxial systems' volume-gauges and pore water pressure drainage systems were subject to low but measurable levels of short- and long-term compliance error. These errors could affect significantly the cyclic volumetric strains in long duration cyclic shearing tests where the overall changes of specimen volume decreased to very low values after large numbers of cycles. As illustrated in Figure 7-13, the cyclic volumetric strains determined from external volume-gauge measurements exhibited stable or curved trends over large shearing cycles, resulting in unrepresentative 'terminal' state or cyclic dilation trends. The volume-gauge measurements were susceptible to even minor temperature fluctuations, leading to sometimes "wavy" volumetric strain trends.

The effects of system compliance were found to be more pronounced in tests conducted at high effective stress level (corresponding to high specimen stiffness) that imposed large stress amplitudes. Figure 7-14 demonstrate full cycle permanent strain trends in a test under (q_{mean}, p_0') = (300, 400) (in kPa) and cycled with q_{cyc} = 200 kPa. The strain trends over the first 10 cycles are later shown in Figure 7-24. The external

axial strains from the displacement transducer were higher than those from local strain sensors due to axial compliance. Dilatant (negative) volume changes were noted from the local strain sensors over the first 20 cycles, followed by a contractive trend, whereas the volume-gauge measurements indicated constantly contractive (positive) volumetric strains. The latter may reflect compliances at the lubricated ends caused by compression of latex membrane disks and grain penetrations under high axial stresses (σ_v') that were cycled in the range between 400 and 800 kPa.

7.3.3 Test material and research programme

Test material and specimen density

The material tested in the programme was Batch 3 Dunkirk sand. Vinck (2016) reported on the material's small to large strain monotonic shearing behaviour after isotropic consolidation, which differs marginally from the Batch 2 material's behaviour that was reported in Chapters 5 and 6. Additional monotonic tests on Batch 3 samples from anisotropic stress states similar to those employed in the Author's cyclic tests were carried out to establish the monotonic behaviour of specimens that had not experienced any cyclic shearing.

The tested specimens were prepared to form dense and very dense states with initial void ratios (e_0) around 0.710 and 0.640, corresponding to relative density (R_d) of 73% and 92%, respectively, adopting the e_{max} and e_{min} values reported by Vinck (2016), as summarised in Table 5-1.

Test code and programme

Table 7-3 provides a detailed summary of the individual tests' void ratio, stress path and conditions, applied cyclic stress ratio (*CSR*) and number of shearing cycles. Each test is denoted using a unique test code in the form of 'AI(100)73', 'AI(100)92-0.1' or 'AI(100)92-OC-0.1', indicating the follow meaning.

(a) The first letter, A to G, denotes the group number and stress state as shown in Figures 7-15 to 7-18;
(b) The second letter or letter/number, I, K, A0.43, A1.07 or A1.2, indicates the stress conditions of Isotropic, *K*o-consolidated ($q_{mean}/p_0' = 0.75$) or Anisotropic condition with q_{mean}/p_0' equals to 0.43, 1.07 or 1.2;

(c) The number in brackets, (100) or (156), represents the effective stress level p_0' in kPa;

(d) The following number, 73 or 92, indicates the specimen relative density of 73% ($e_0 \approx 0.71$) and 92% ($e_0 \approx 0.64$);

(e) The last number, such as -0.1, -0.3, -0.4, indicates the imposed cyclic stress amplitude ratio ($CSR = q_{cyc}/p_0'$);

(f) The Over-Consolidated tests ($OCR = 4$) included in Group A are distinguished by using the letters -OC before the last set of numbers.

Full details of the testing scheme and the aspects intended to investigate are presented below, following the several main testing stages.

Specimen preparation, consolidation/creep and stress states

A consistent water-pluviation method was adopted to reconstitute the Batch 3 Dunkirk sand specimens. The testing outcomes from the static tests presented in the previous chapters have largely confirmed the method's features in producing uniform sand specimens with well-controlled initial densities (void ratios).

The main programme was designed to cover a reasonably wide range of stress levels and ratios. Figures 7-15 to 7-18 plot the consolidation effective stress paths in triaxial q-p' space, where stress-controlled constant cell pressure drained cyclic shearing was imposed at initial mean cyclic effective stress points A to H.

As shown in Figure 7-15, the mean cyclic loading stress points A and B are situated on the isotropic axis and the cyclic loading involved symmetric two-way shearing. A group of over-consolidated ($OCR = 4$) specimens was sheared cyclically at the stress point A, as shown in Figure 7-16. Their consolidation paths are explained latter.

The other samples' initial (mean loading) stress points were offset and their applied cyclic shearing paths kept $q = (\sigma_v'-\sigma_h')$ or $(\sigma_z'-\sigma_r')$ positive at all stages. Figure 7-17 plots the consolidation paths for the cyclic tests performed at initial mean stress points C, D and E, corresponding to three effective stress levels ($p_0' = 133.3$, 266.7 and 400 kPa) with identical stress ratios ($\sigma_v'/\sigma_h' = 2$, $\eta = q_{mean}/p_0' = 0.75$), which is close to the K_o (= 0.5) condition.

Figure 7-18 summarises the consolidation paths applied for suites of tests performed at anisotropic stress states of F, G and H, also indicating their mean cyclic

stress ratios (η). Group F imposed more strongly anisotropic mean stress conditions with $\sigma_v'/\sigma_h' = 3$, $\eta = 1.2$ that approached the sand's peak ($(q/p')_{peak} = 1.50$) and critical state ($M_{cs} = 1.31$) failure envelopes. The initial stress points G and H are aligned with stress points C and F on the effective stress path for drained monotonic shearing from point A, holding constant $\sigma_h' = 100$ kPa, representing different offsets from the isotropic axis.

As detailed in Table 7-3, most of the anisotropically consolidated specimens involved two-stage consolidation stress paths. All commenced from an initial isotropic state O and progressed to an initial anisotropic state O′ (or O″) with constant $\sigma_h' = 20$ kPa and, after a creep stage of at least 48 hours, continued the consolidation to the designated stress states following stress paths of constant stress ratio with σ_h' stress change rates of 1 kPa/min.

Another set of specimens (CK(133)92-0.375, FA1.2(167)92-0.3, GA0.43(117)92 -0.43 and HA1.07(156)92-0.32) was first isotropically consolidated to $\sigma_h' = 100$ kPa, followed by a constant σ_h' consolidation (or pre-shearing) at a rate of $\Delta\sigma_v'/\Delta t = 1$ kPa/min to the target q values. Given that the specimens were allowed at least 48 hours for creep straining to slow to negligibly low rates (below 0.002%/day) after each consolidation stage, it is believed that the impacts of the precise consolidation paths on the following cyclic shearing response were small or negligible. Therefore their consolidation paths are not distinguished from other constant stress ratio stress paths in the Figures 7-17 and 7-18. This group of tests all imposed equal cyclic shearing amplitudes, with $q_{cyc} = 50$ kPa, to examine in particular the effects of mean cyclic stress ratio (q_{mean}/p_0') on cyclic volumetric behaviour, while fixed sets of cyclic stress amplitude ratio (CSR, q_{cyc}/p_0') were applied to the Author's other suites of tests.

Detailed discussion of consolidation and creep strains and strain rates is not included in this Chapter. Illustrative strain trends and the interpretive strain rates for isotropically ($\eta = 0$) consolidated Batch 2 Dunkirk sand were presented in Section 5.4. Table 7-3 summarises specimen void ratios after setting-up (under 20 kPa suction) and creeping (for at least 48 hours) at the targeted mean cyclic stress points. However, detailed consideration of the residual creep rates was essential to interpreting long-term cycling tests, as discussed later in Sections 7.3.5 and 7.4.2.

Long-term drained cyclic shearing stage

The above cyclic stress conditions are plotted in a normalised q_{cyc}/p_0'-q_{mean}/p_0' (CSR-η) diagram in Figure 7-19. Their points form a square grid with $\eta = q_{mean}/p_0' \geq 0$ for all the Author's tests. Recalling the cyclic triaxial stress space illustrated in Figure 7-4, the peak and critical state envelopes can be defined for drained constant cell pressure (CCP) cyclic triaxial tests on the compression and extension side, assuming $(q/p')_p^{TXC} = 1.5$, $M_{cs}^{TXC} = 1.31$ and $(q/p')_p^{TXE} = -1.0$, $M_{cs}^{TXE} = -0.9$, respectively. Note that in the following formulations, the extension stress ratios $(q/p')_p^{TXE}$ and M_{cs}^{TXE} adopt negative signs to be compatible with those for compression.

These failure points can be redefined in the CSR-η stress space shown in Figure 7-19 by noting that at failure

$$q_f = q_{mean} \pm q_{cyc}$$

$$\frac{q_f}{p_0'} = \frac{q_{mean} \pm q_{cyc}}{p_0'} = \eta \pm CSR \tag{7.6}$$

$$\frac{q_f}{p_0'} = \frac{q_f}{p_f'} \cdot \frac{p_f'}{p_0'} = (q/p)_{peak} \cdot \frac{p_f'}{p_0'} \quad \textbf{or} \quad M_{cs} \cdot \frac{p_f'}{p_0'}$$

Then from the geometry shown in Figure 7-4, it is easy to know that the CCP stress paths lead to

$$\begin{aligned} \frac{p_f'}{p_0'} &= \frac{p_0' + q_{cyc}/3}{p_0'} = 1 + \frac{1}{3} CSR \quad \textbf{(compression)} \\ \frac{p_f'}{p_0'} &= \frac{p_0' - q_{cyc}/3}{p_0'} = 1 - \frac{1}{3} CSR \quad \textbf{(extension)} \end{aligned} \tag{7.7}$$

So the failure lines can be drawn in Figure 7-19 as limits to q_f/p_0' that are given by

$$\begin{aligned} \left(\frac{q_f}{p_0'} \right)_{peak}^{TXC} &= \eta + CSR = (q/p)_{peak}^{TXC} \cdot (1 + \frac{1}{3} CSR) \quad \textbf{(compression)} \\ \left(\frac{q_f}{p_0'} \right)_{peak}^{TXE} &= \eta - CSR = (q/p)_{peak}^{TXE} \cdot (1 - \frac{1}{3} CSR) \quad \textbf{(extension)} \end{aligned} \tag{7.8}$$

The resulting failure criteria applying in compression and extension and at peak (failure) and critical state are plot in Figure 7-19. Because the CCP path is inclined and different q_f/p_f' ratios apply in compression and extension, the failure criteria are not

symmetric but skew very significantly towards the positive η side.

The trough stress states of the $\eta = 0$ tests (Group A and B) therefore fall far closer to the extension failure envelope than the peaks do those in compression. The specimens are more prone to develop negative axial or shear strains and would fail under extension if their trough stress points approach the extension failure criteria under high *CSR*s. In contrast, the stress states of the two tests performed under high η of 1.2 and cycled under $CSR = 0.4$ and 0.5 exceeded the critical state M values at the peak of each cycle and approached the peak envelope on the compression side. As demonstrated later, these specimens could not sustain 10^4 shearing cycles and failed in compression after certain numbers of cycles (N_f).

As mentioned in Section 7.2.2, sands may not respond instantaneously to the imposed cyclic stress or strain waveforms due to the effects of their non-linear and time-dependent nature, as well as the possible impact of system compliance. Figure 7-20 illustrates the cyclic deviatoric and strain trends observed in test DK(266)92-0.3, and indicates delayed, although not overly significant, local axial straining over the first 1-4 deviatoric stress cycles. The divergence became negligible after 1000-1004 cycles, as the specimen's micro-fabrics gradually aligned to sustain the applied style of cyclic loading.

The degree of cyclic stress-strain mismatch varied with factors including specimen density, effective stress level, loading frequency, cyclic amplitude and number of shearing cycles. The external strain measurements, which are often made by displacement transducers fixed close to the loading ram or the cell chamber, may not capture these delayed strain patterns as well and so reflect the true cyclic strains occurring in the specimens, particularly under relatively rapid shearing motions.

Effects of specimen density

As set out in Table 7-3, most of the Author's specimens were prepared to very dense state with $e_0 = 0.64$, $R_d = 92\%$, while three tests were performed on less dense specimens ($e_0 \approx 0.71$, $R_d = 73\%$) at anisotropic stress states of C, D and E with $CSR = 0.3$.

The specimens' initial void ratios were determined under 20 kPa isotropic suction, following the approach described in Section 5.3.2. The mass of fines that was left suspended in sand-water mixture and could not be transported fully into the specimen

mould was determined carefully for each test and was accounted for in the determination of initial void ratios. An average of 1% of fine soil was lost in the course of forming the specimens by water pluviation.

Effects of OCR

The potential effects of 'static' effective stress history (*OCR*) on drained cyclic shearing behaviour were examined in a set of three over-consolidated specimens in the Group A-OC(4) tests. As shown in Figure 7-16, these specimens were first anisotropically consolidated to stress point D ($\sigma_v' = 400$ kPa, $\sigma_h' = 200$ kPa), before being swelled to A ($\sigma_v' = \sigma_h' = 100$ kPa), leading to an over-consolidated condition with $OCR = 4$. The swelling stage employed a linear effective stress path, which led to small (-0.004%) radial strains in comparison with the -0.11% axial 'swelling' strain.

Post-cycling drained static shearing

Most of the specimens sustained their imposed long-term cyclic stages without developing excessive strains or failure. The cyclic stages were followed by drained monotonic shearing at an axial strain rate of 5%/day to characterise post-cyclic stiffness and shear strength behaviour, and allow comparison with the outcomes of the monotonic tests (which involved $CSR = 0$).

As shown in Table 7-3, the only tests in Group F that failed were those taken q_{cyc}/p_0' and q_{mean}/p_0' condition that exceeded the critical state limits and approached the compression peak failure envelope.

7.3.4 Illustrative deviatoric stress-axial strain trends over full testing stages

The above testing procedures and typical shear stress-strain responses are illustrated in Figure 7-21, taking a test from Group C (CK(133)92-0.3, $e_0 = 0.640$) as an example. The test included two stages of consolidation (O to O′ and O′ to C, as shown in Figure 7-17), each followed by a creep period of 48 hours. Stress-controlled drained cyclic shearing was imposed over 10^4 cycles between $q_{max} = 140$ kPa and $q_{min} = 60$ kPa, with the fixed period $T = 2$ minutes. The sample was finally sheared monotonically until axial strains of up to 35% had been achieved. Details of the behaviour seen in each stage of cyclic shearing and post-cycling monotonic shearing are presented and discussed in the following sections.

7.3.5 Residual strain rates and background creeping

The importance of allowing sufficient time for soil samples to creep and age when assessing their mechanical behaviour under monotonic and cyclic loading has been emphasised by, for example, Tatsuoka (2011) and Jardine (2013). In long-term cyclic tests that in particularly concern permanent cyclic straining and strain rates, extended period of creep is also of great significance. When assessing long-term straining rates over cycling, any prior cycling residual creep rates should also be accounted for and distinguished from the nominal cyclic strain rates.

Figure 7-22 plots residual axial creep strain rates (%/$\log_{10}N$) defined as axial creep strains (%) accumulated over one log cycle of 200-2000 shearing cycle (N) range, which took 60 hours to complete. The average length of creep period (in hours) allowed for each Group of test is denoted by the number in brackets. It was assumed that, as a simplified measure, the creep strain rate (%/hour) calculated over the last hour of the creep stage persisted over the long-term drained cycling and combined with any strain accumulation developed due to cycling. The 200-2000 cycle creep rates were calculated as: (%/$\log_{10}N$) = [residual rate pre-cycling %/hour]×60.

As shown in Figure 7-22, the residual creep rates generally increased with the applied η ratio. As shown later in Section 7.4.2, the residual creep rate magnitudes were comparable to the total strain rates observed (when $N > 200$) in many of the cyclic tests performed at relatively low *CSR*s.

Table 7-3 Drained cyclic triaxial testing programme on Dunkirk sand Batch 3

Test code	Group	Stress condition		e_0	Cyclic shearing			e^*
		Stress path	η		*CSR*	q_{cyc} [kPa]	*N*	
AI(100)73	A	OA	0	0.686	0			
AI(100)92				0.636	0			0.632
AI(100)92-0.1				0.632	0.1	10	6287	0.630
AI(100)92-0.3				0.643	0.3	30	11333	0.630
AI(100)92-0.5				0.645	0.5	50	10692	0.603
AI(100)92-OC-0.1	A-OC	OO′DA		0.645	0.1	10	11522	0.637
AI(100)92-OC-0.3				0.647	0.3	30	10587	0.631
AI(100)92-OC-0.5				0.637	0.5	50	10549	0.598
BI(400)73	B	OB	0	0.699	0			0.682
BI(400)92				0.631	0			0.619
BI(400)73-0.1				0.686	0.1	40	5038	0.668
BI(400)92-0.1				0.642	0.1	40	10545	0.628
BI(400)92-0.3				0.637	0.3	120	10231	0.617
BI(400)92-0.5				0.640	0.5	200	12076	0.588
CK(133)73	C	OO′C	0.75	0.707	0			0.695
CK(133)92-0.1				0.659	0.1	13.3	11713	0.653
CK(133)92-0.3				0.637	0.3	40	10723	0.630
CK(133)73-0.3				0.716	0.3	40	10630	0.701
CK(133)92-0.5				0.644	0.5	66.7	10697	0.631
CK(133)92-0.375		OAC		0.642	0.375	50	10466	0.631
DK(266)92-0.1	D	OO′D	0.75	0.645	0.1	26.7	11211	0.634
DK(266)92-0.3				0.643	0.3	80	10812	0.626
DK(266)73-0.3				0.714	0.3	80	10656	0.685
DK(266)92-0.5				0.643	0.5	133.3	10778	0.615
EK(400)92	E	OO′E	0.75	0.651	0			0.638
EK(400)92-0.1				0.643	0.1	40	10821	0.629
EK(400)92-0.3				0.641	0.3	120	11446	0.621
EK(400)73-0.3				0.701	0.3	120	10616	0.676
EK(400)92-0.5				0.644	0.5	200	11501	0.621

Continued Table 7-3 Drained cyclic triaxial testing programme on Dunkirk sand Batch 3

Test code	Group	Stress condition		e_0	Cyclic shearing			e^*
		Stress path	η		*CSR*	q_{cyc} [kPa]	*N*	
FA1.2(167)92-0.1	F	OO″F	1.2	0.654	0.1	16.7	10212	0.650
FA1.2(167)92-0.3		OAF		0.644	0.3	50	10781	0.654
FA1.2(167)92-0.4		OO″F		0.644	0.4	66.7	N_f = 4468	
FA1.2(167)92-0.5				0.647	0.5	83.3	N_f = 954	
GA0.43(117)92-0.43	G	OAG	0.43	0.658	0.428	50	10799	0.639
HA1.07(156)92-0.32	H	OAH	1.07	0.649	0.321	50	10204	0.649

Notes:

1. Enlarged lubricated plattens and upgraded local radial strain instruments were used throughout the programme;
2. The reconstituted sand specimens were prepared with water pluviation method;
3. e_0: void ratio after setting-up (before consolidation stages), being determined under 20 kPa suction; e^*: void ratio after cyclic-shearing or before monotonic shearing;
4. The specimen's relative density is indicated in the test code as the numbers followed the bracket, 92 or 73 (%).
5. Cyclic shearing cycles were applied with a period of 2 minutes, i.e. T = 2 minutes, f = 0.0083 Hz;
6. A constant rate of 5%/day was used for the post-cycling monotonic shearing stage under drained conditions.

7.3.6 Figures

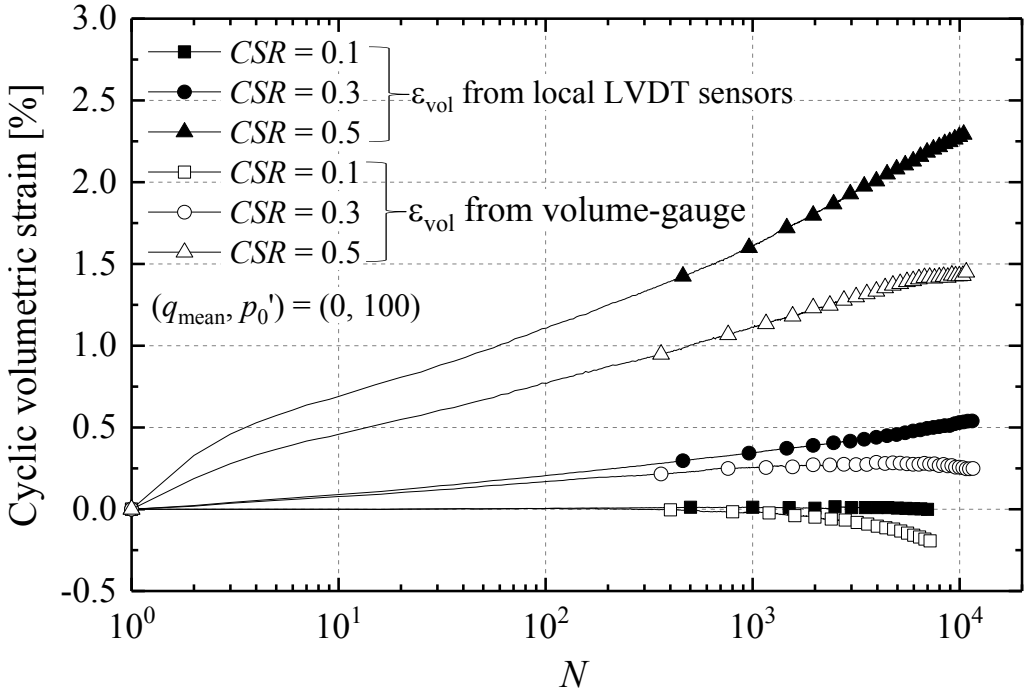

Figure 7-13 Accumulated volumetric strain trends (at beginning of each cycle) for Group A tests (q_{mean} = 0, p_0' = 100 kPa) determined from local strain sensors and external volume-gauge

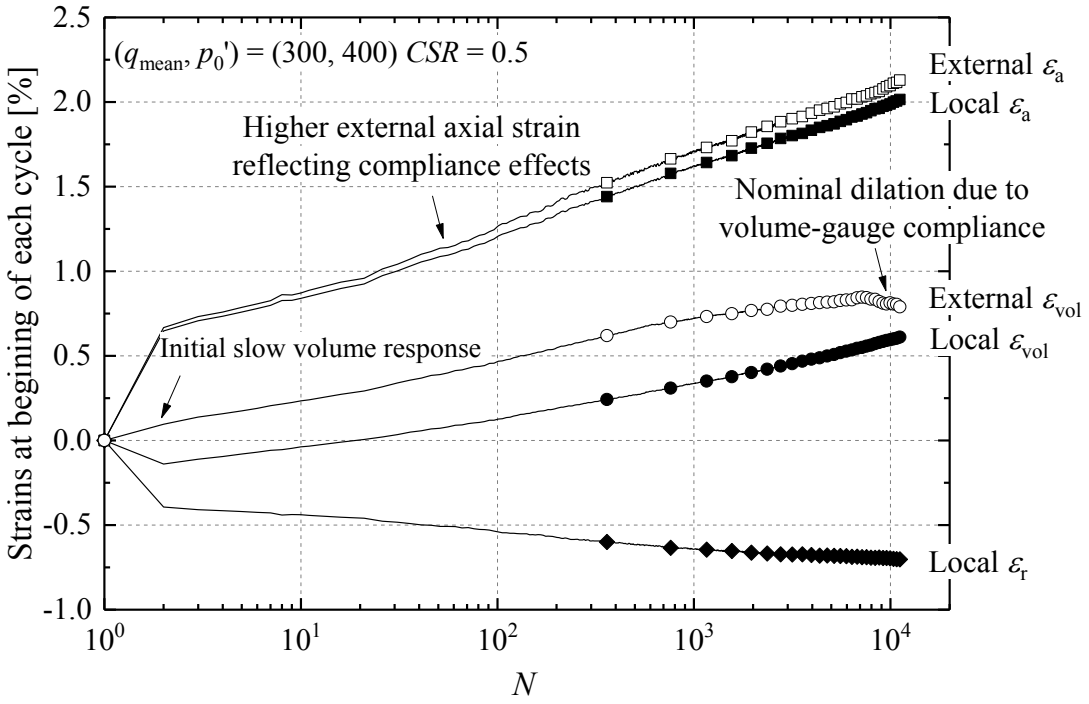

Figure 7-14 Accumulated cyclic strain trends for test EK(400)92-0.5 comparing local and external strain measurements (initial 10 cycle strain trends see Figure 7-24)

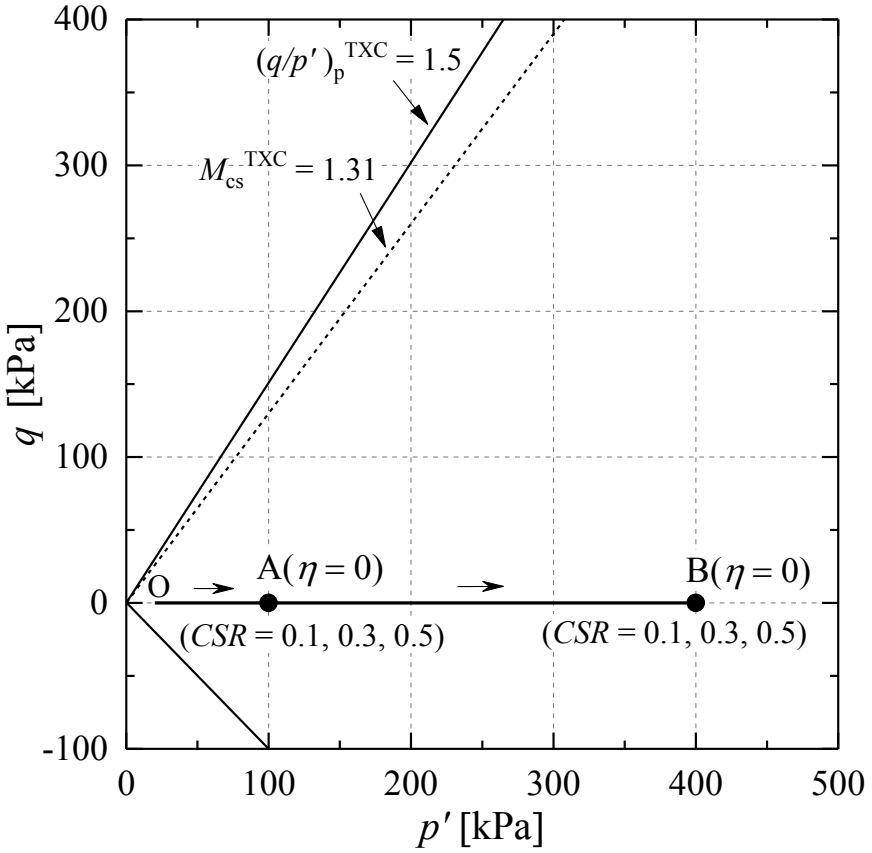

Figure 7-15 Consolidation stress paths for Group A and B tests ($\eta = 0$)

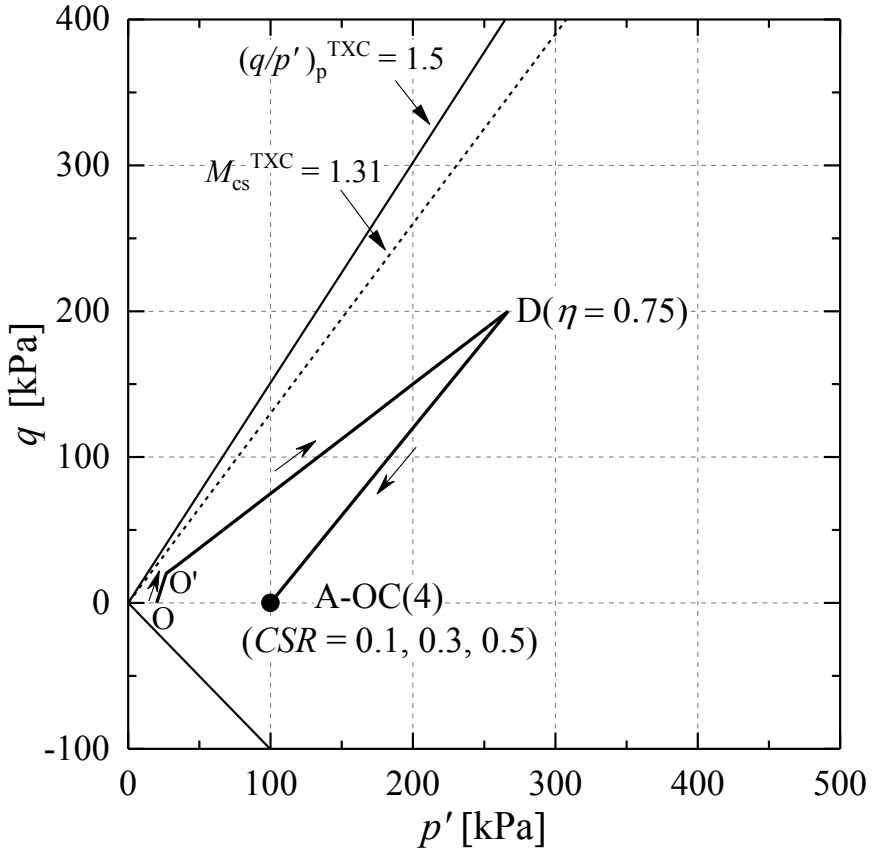

Figure 7-16 Consolidation stress paths for over-consolidated Group A tests

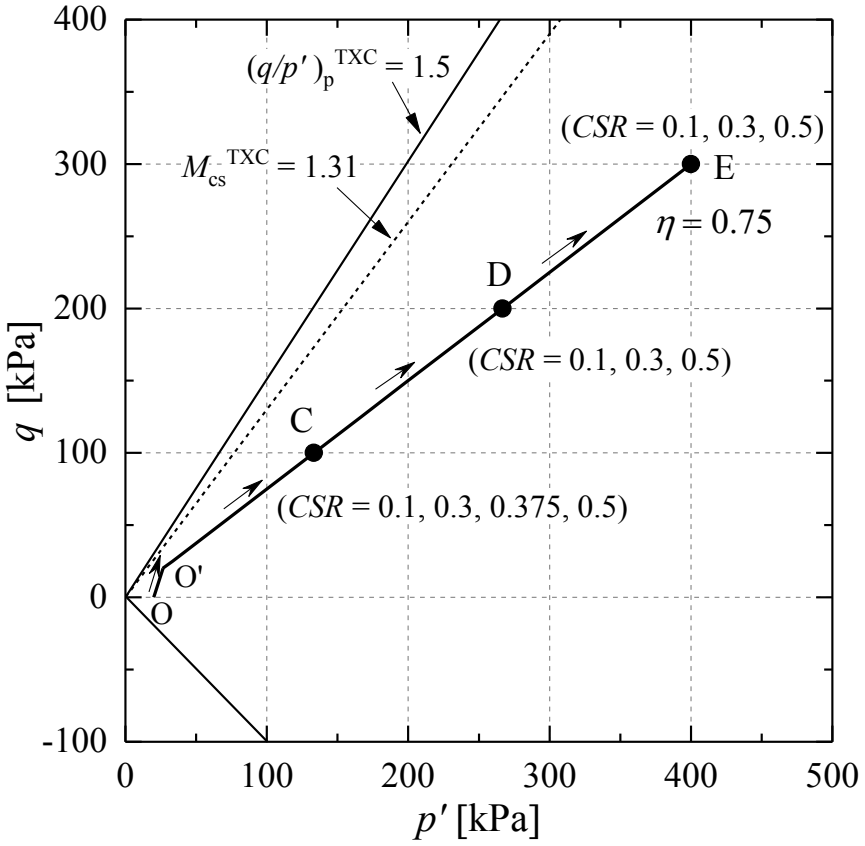

Figure 7-17 Consolidation stress paths for K_o consolidated Group C, D and E tests

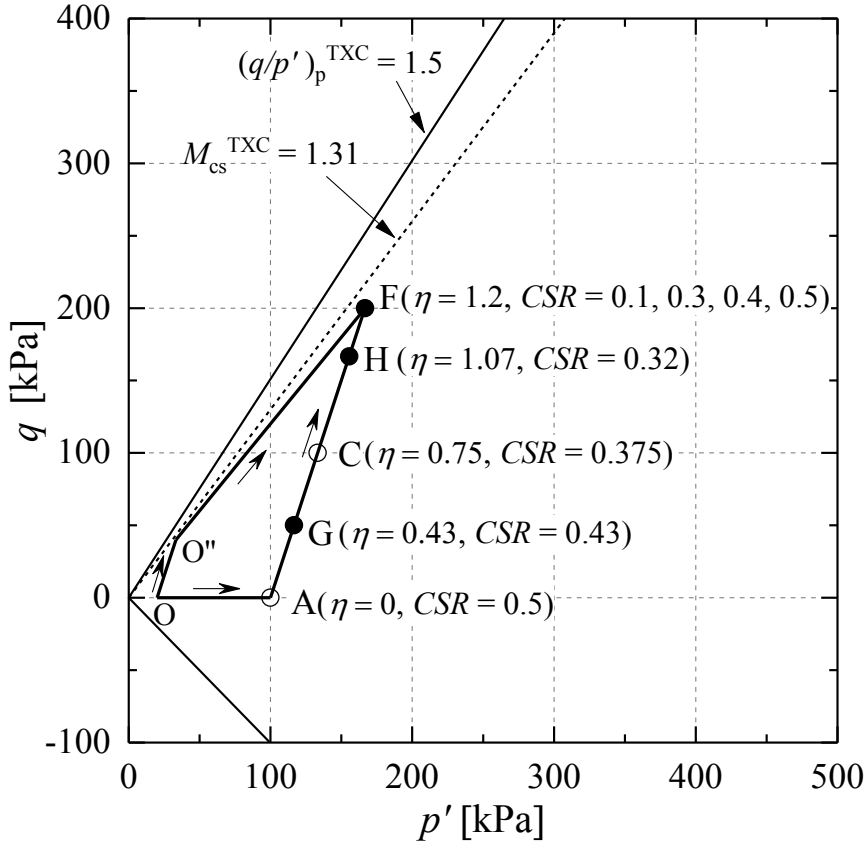

Figure 7-18 Consolidation stress paths for anisotropically consolidated Group F, G and H tests

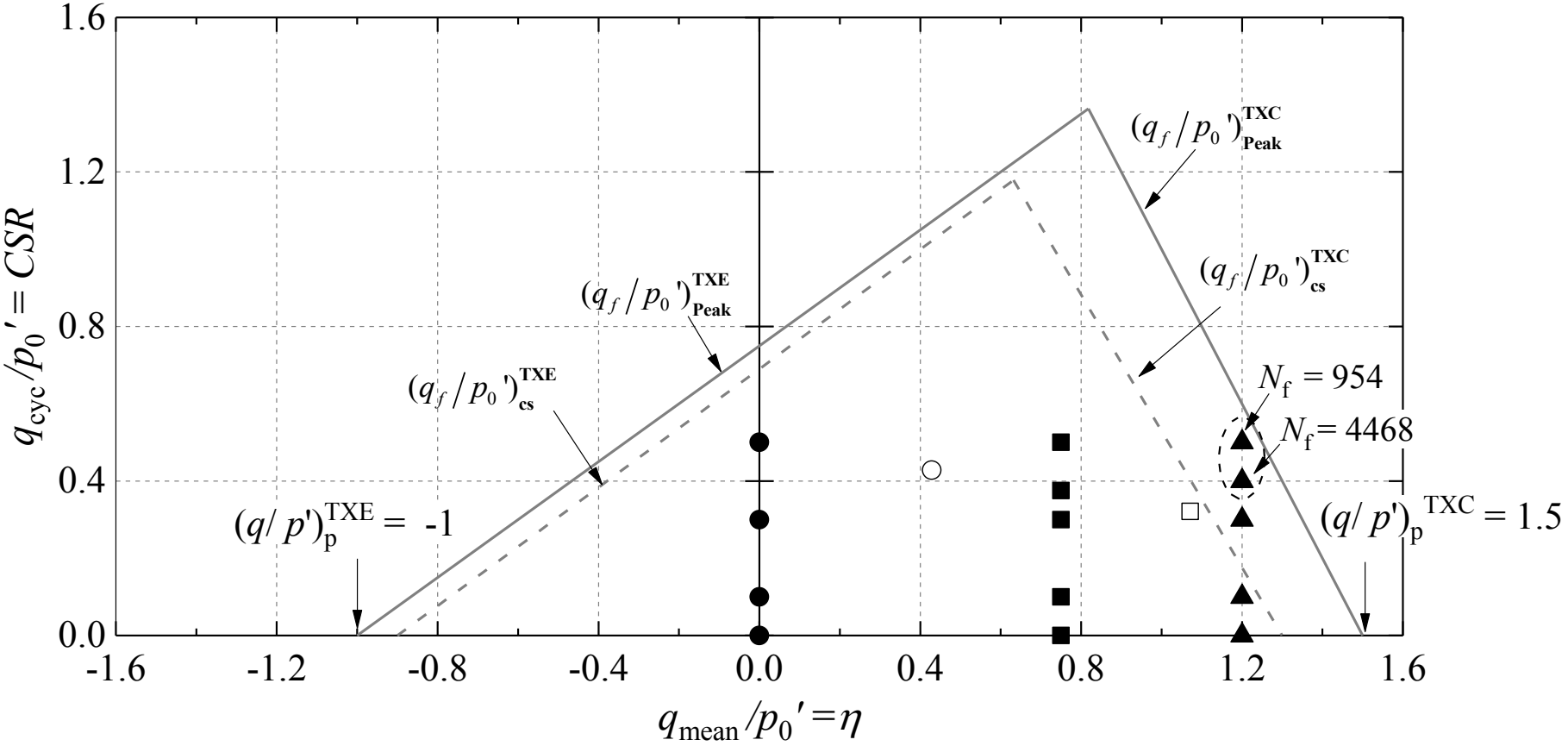

Figure 7-19 Normalised q_{cyc}/p_0'-q_{mean}/p_0' (*CSR*-η) stress states with reference to peak and critical state envelopes

(Note $(q/p')_p^{TXC} = 1.5$, $M_{cs}^{TXC} = 1.31$, $(q/p')_p^{TXE} = -1$ and $M_{cs}^{TXE} = -0.9$)

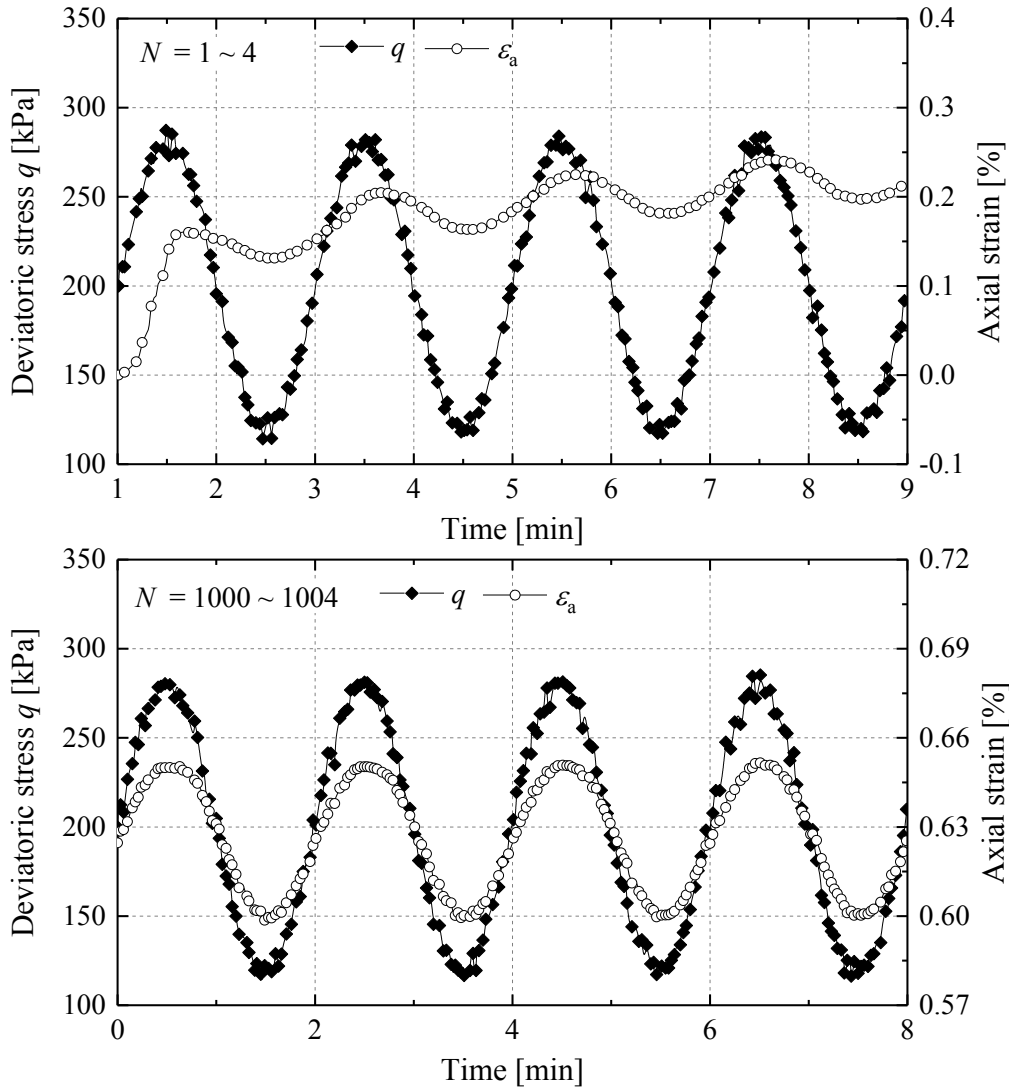

Figure 7-20 Example of cyclic deviatoric and strain trends from test DK(266)92-0.3, noting the delayed peak axial strains in the first 1~4 cycles and the fully 'matched' stress-strain peaks and troughs in the 1000~1004 shearing cycles

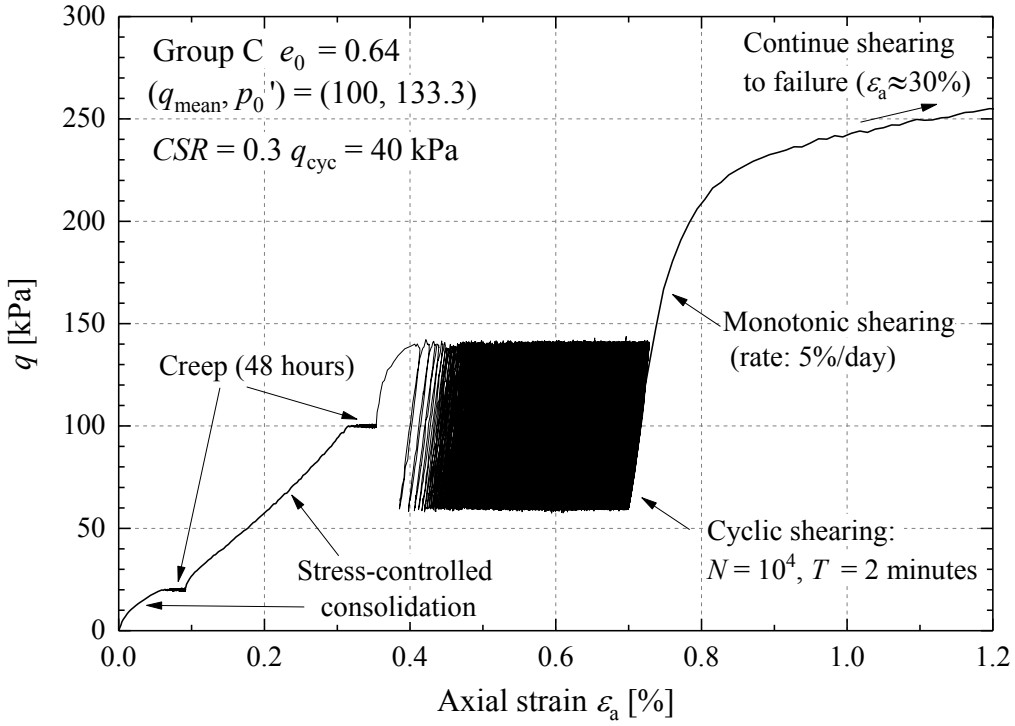

Figure 7-21 Illustrative overall stress-strain (q-ε_a) trends of test CK(133)92-0.3

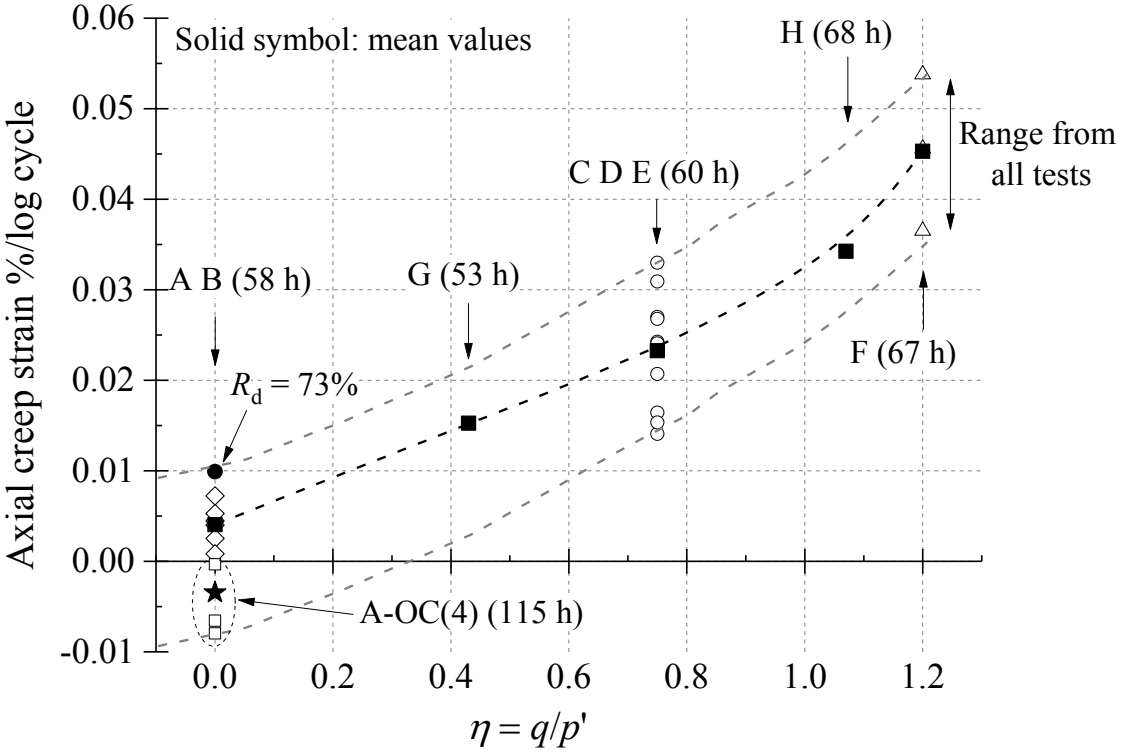

Figure 7-22 Residual axial creep strain rates (%/log$_{10}$(N)) calculated over 200-2000 loading cycles, also indicating the mean values against stress ratios (q/p') for the R_d = 92% specimens (the number in the brackets indicate creep time prior to cyclic shearing)

7.4 Characteristic patterns of cyclic strains and deformation

This section summarises the extensive cyclic strain datasets attained from the Author's testing before offering a detailed characterisation of the patterns of accumulative straining developed under the conditions explored. The data are presented in terms of both the individual strain components (ε_a^{acc} and ε_r^{acc}) sensed by local strain devices, and the corresponding strain invariants (ε_s^{acc} and ε_{vol}^{acc}) that identify the possible cyclic flow rules in triaxial space, as reviewed in Section 7.2.2.

The experimental results regarding cyclic strain amplitudes and changes of void ratio are presented and discussed in the subsequent sections with reference to the sand's critical state line (CSL) (referring to Sections 6.6 and 6.8).

7.4.1 Accumulation patterns of strain components

The following discussion considers how the cumulative trends of cyclic strain components (ε_a^{acc} and ε_r^{acc}) varied with number of loading cycles (N). Semi-logarithmic scales are adopted as these allow direct comparisons of positive (compression) and/or negative (extension) strain components and automatically helps the visualisation of the often rapidly evolving strain trends developed over the initial shearing cycles. The strains recorded from the beginning of each shearing cycles were adopted as the key measures to track permanent cyclic strain development, with all plots starting from zero with the first cycle ($N = 1$).

However, it is important to note that plotting the strain data with semi-logarithmic scales does not necessarily imply that the cyclic strain trends (ε^{acc}-N) follow log-linear functions ($\varepsilon^{acc} = b\log(N)$, see Table 7-2), as suggested by several researchers (see the review by Chong & Santamarina (2016)). As explained later in Section 7.4.4, in many cases the cyclic strain trends were found to be better fitted by power law functions. The ε^{acc}-$\log_{10}(N)$ curves show variable gradients over the first stages of cycling but trend to approximately log-linear long-term strain trends once $N > 200$, as demonstrated below.

Before discussing the overall strain accumulation datasets, two examples are given in Figures 7-23 and 7-24 from tests BI(400)92-0.5 and EK(400)92-0.5 to demonstrate how cyclic patterns can be affected significantly by the effective stress states. Under identical conditions of p_0' (= 400 kPa) and CSR (= 0.5), the isotropically consolidated specimen developed significant extensional axial strain and compressional radial strain

under two-way cyclic shearing, while the anisotropically consolidated specimen showed the opposite strain signs under one-way cycling, where the deviatoric stresses remained constantly on the positive side of the isotropic axis. The fundamental reason for this difference in response is the asymmetric q_f/p_0' failure envelopes identified in Figure 7-19 that result from both the inclined q/p' stress path followed and the difference between the $(q/p')_{peak}$ values applying in compression and extension.

Nevertheless, the two exemplar tests exhibited some commonly observed straining patterns. All tests that applied high *CSR*s developed significant straining over their first few shearing cycles. In some such tests, the strain trends 'reversed' as the specimens gradually 'recovered' from their dramatic initial shearing cycles.

Figures 7-23 and 7-24 also demonstrate that the axial strains determined from the local strain sensors exhibited generally smaller amplitudes than those deduced from the external displacement transducers, although the patterns were largely comparable, leading to the latter measurements underestimating cyclic stiffnesses.

Cyclic strain accumulation: normally consolidated Groups A and B with η = 0

Let us start from the normally consolidated Groups A and B specimens, which were isotropically consolidated to p_0' = 100 kPa or 400 kPa and then subjected to cyclic loading with *CSR*s of 0.1, 0.3 and 0.5. The loading was applied in a two-way cycling manner that led to higher absolute stress ratios $|q/p'|$ on the negative deviatoric stress side (axial extension) because of the inclined constant σ_h' stress path directions with $dq/dp' = 3$. In all cases, the cyclic perturbation exceeded the limits of the sand's elastic ranges (see Section 5.5.1) and plastic straining was expected to develop. Figures 7-25 and 7-26 plot the axial and radial cumulative strains observed in these two sets of tests on the standard semi-logarithmic scales.

The results indicate that significant straining occurred in the first few shearing cycles. However, the ε_a^{acc}-$\log_{10}(N)$ and ε_r^{acc}-$\log_{10}(N)$ trends developed over larger numbers of cycles gradually trended towards the linear semi-log patterns summarised in Table 7-2, showing almost constant slopes when $N > 200$. Regressions were undertaken over these ranges to give slopes Δ (= $d\varepsilon_a^{acc}/d\log_{10}(N)$) that are denoted in the plots. The regression slopes Δ and the corresponding R^2 values are summarised in Table 7-4.

The strain trends in Figures 7-25 and 7-26 demonstrate a clear dependency of the

cyclic strains on the levels of effective stress (p_0') and cyclic stress ratio (*CSR*). The magnitudes of the ultimate accumulated strains are compared in later discussion, but a general tendency is evident for the cyclic radial strains to increase very significantly with p_0' and *CSR* from the minimal (positive or negative) values observed under *CSR* = 0.1. The axial cyclic strains also grew with *CSR* level up to 0.3. Raising the *CSR* to 0.5 led the specimens to develop more significant negative (extensional) axial strains after the first shearing cycles, followed by gradual accumulation towards the positive strain side. The ultimate axial strains were significantly lower than the corresponding radial strains, and in the test with p_0' = 400 kPa, the axial strains remained tensile after 10^4 cycles.

The axial strain trends reflected the inherently anisotropic nature of the isotropically consolidated specimens that, as granular assemblies, are more susceptible to extensional loading in the axial direction, as outlined in Chapter 5. Significant negative axial straining occurred in the first half-cycle unloading as the stress ratio η (q/p') decreased from 0.43 to -0.6. The unloading stage was also accompanied by large compressional strains in the radial direction, indicating clear reductions in cyclic stiffnesses over the initial cycles. However, as cycling continued, the specimens appeared to gradually recover and gain stiffness, leading to the observed reversed axial strains trending towards the positive side.

Figure 7-27 plots the cyclic volumetric strain trends for the two groups of tests. The specimens developed predominantly contractive volume changes that increased with the level of mean effective stress (p_0') and *CSR*. Little dilative cyclic volumetric straining occurred, with only minimal dilation occurring in one Group A test conducted under *CSR* = 0.1.

Cyclic strain accumulation: over-consolidated (OCR = 4) Group* A-OC(4) *tests

As illustrated in Figure 7-16, the over-consolidated specimens followed anisotropic consolidation and swelling stress paths that can be expected to lead to higher stiffnesses and Y_3 yielding points under drained and undrained axial compression loading than the equivalent normally consolidated specimens. Conversely these over-consolidated specimens are likely to yield at lower Y_3 points under axial extension stress paths than isotropically consolidated specimens (see Section 5.7 or Kuwano & Jardine (2007)).

This feature was evident in the cyclic loading outcomes presented in Figure 7-28, comparing the axial and radial cyclic strains over the first 10 cycles of the two *OCR* = 1 and *OCR* = 4 specimens, both cycling with *CSR* = 0.5. The *K*-consolidated *OCR* = 4 specimen generated lower axial strains in the first-quarter of its compression cycle, reflecting its higher axial compression stiffness than the isotropically consolidated *OCR* = 1 specimen. The former, however, developed clearly higher (negative) axial tensile straining over the first half-cycle of unloading, leading to an overall axial strain trend that stayed below that of the *OCR* = 1 specimen but with smaller amplitudes. It is also interesting to note that, despite the clear differences in the specimens' axial strains, closely comparable trends were observed for their cyclic radial strains.

Extending to the full cyclic duration range, Figure 7-29 plots the axial and radial cyclic strains of the *OCR* = 4 specimens. The cumulative radial strains exhibited increasing patterns with increasing *CSR* as with the *OCR* = 1 specimens. Opposite trends, however, were observed with the axial strains that accumulated consistently towards the negative (extension) side as *CSR* increased, although the slopes (Δ) of the ε_a^{acc}-$\log_{10}(N)$ trends were positive over 200-10^4 cycles, reflecting the *K*-consolidated samples' lower Y_3 yield stress under extension conditions.

The above trends are illustrated further in separate comparisons of the axial and radial cyclic strain trends, as presented in Figures 7-30 and 7-31, respectively. Unlike the isotropically consolidated *OCR* = 1 specimens that developed compressional axial strains that increased with *CSR*, the cyclic axial strains of the *K*-consolidated *OCR* = 4 specimens stayed constantly on the negative (extension) side and decreased with *CSR*. The cyclic radial strains of the two sets of specimens showed comparable trends over full shearing cycles, suggesting no significant effect of the predominantly axial effective stress history on the radial cyclic strains.

The above cyclic strain trends for the anisotropically over-consolidated *OCR* = 4 tests reflected combined effects of changes in effective stress level and stress ratio (q/p_0' from 0.75 to 0). Different strain trends may be expected for isotropic over-consolidation stress path that maintains constant stress ratio $q/p_0' = 0$ but varies the effective stress components (σ_v' and σ_h'). However, these tests remain to be performed.

Strain accumulation in one-way cyclic shearing of test Groups C, D and E

Test Groups C, D and E were consolidated to anisotropic stress states with different effective stress levels (p_0' = 133.3, 266.7 and 400 kPa) but identical mean cyclic stress ratios ($\eta = q_{mean}/p_0' = 0.75$), as shown in Figure 7-17.

Figures 7-32 to 7-34 plot the cumulative axial and radial strain trends for the three groups of tests on semi-logarithmic scales. Also indicated are the ultimate cyclic strains and the slopes of linear-logarithmic regressions fitting the ε^{acc}-$\log_{10}(N)$ trends for $N > 200$. The magnitudes of the cumulative strains varied systematically with the mean effective stress and *CSR* levels. A consistent straining pattern could be observed in which the specimens developed compressional (positive) strains in the axial direction and extensional (negative) strains in the radial direction under drained cycling, and their magnitudes invariably increased with the *CSR* level.

It is also evident that the slopes of cumulative strain trends (ε^{acc}-$\log_{10}(N)$) are higher for axial than radial strains under identical *CSR*s.

Accumulated cyclic volumetric strains were determined directly from the axial and radial strain components, and the trends are compared in Figure 7-35. For clarity, only the trends for the low and high effective stress Group C (p_0' = 133.3 kPa) and E (p_0' = 400 kPa) are plotted. The volumetric strains trended towards contraction in all cases, and this tendency increased mildly as p_0' and *CSR* increased. However, the volume changes were significantly lower than those of the isotropically consolidated Groups A and B tests, as shown in Figure 7-27, reflecting the effects of mean cyclic stress ratio (q_{mean}/p_0') on cyclic volume change.

The cyclic volumetric strains accumulated in the dense (R_d = 73%) and very dense (R_d = 92%) specimens under intermediate *CSR* level of 0.3 are plotted in Figure 7-36 for comparison. The R_d = 73% specimens exhibited higher volume change during cycling, also accompanied by higher slopes of the ε^{acc}-$\log_{10}(N)$ trends.

Strain accumulation of test Group F with η = 1.2

As shown in Figure 7-18, the Group F tests employed more markedly anisotropic initial stress states with q_{mean}/p_0' = 1.2 and σ_v'/σ_h' = 3. Four cyclic tests were performed in this group, of these the *CSR*s of 0.4 and 0.5 experiments could not sustain 10^4 cycles and failed after 4468 and 954 cycles, respectively.

Starting with the two specimens tested with low *CSR*s of 0.1 and 0.3 that sustained over 10^4 shearing cycles, Figure 7-37 plots the accumulation trends for axial, radial and volumetric strains, also denoting the slopes of the ε^{acc}-$\log_{10}(N)$ fitting trends. The specimens developed significant compressive axial strains and extensional radial strains that were higher than those observed in Groups C, D and E tests under equivalent *CSR* conditions, although the straining patterns were similar. The strain trends appear to follow linear ε-$\log_{10}(N)$ correlations reasonably well, even over their initial cycles. However, the overall volumetric strains were negative, indicating a dilative cyclic responses, in contrast to the above cyclic tests, which were performed at lower stress ratios and manifested predominantly cyclic contraction and densification.

Incremental collapse was encountered in the Group F tests performed with high *CSRs* of 0.4 and 0.5, corresponding to trough-to-peak stress ratio (q/p') ranges of 0.92-1.41 and 0.84-1.46, respectively, that exceeded the critical state stress ratio (M_{cs} = 1.31) and approached the compression peak strength envelope ($(q/p')_{peak}$ = 1.50). Figure 7-38 plots the trends for cyclic axial and volumetric strains, based on external axial and volume-gauge measurements. The two failures involved axial collapses with significant bulging. As with the lower *CSR* Group F tests, negative volumetric strains accumulated during cycling, indicating dilative trends.

***Strain accumulation of samples with identical σ_3' and q_{cyc}* but varied q_{mean} levels**

As listed in Table 7-3 and indicated in Figures 7-17 and 7-18, tests AI(100)92-0.5, CK(133)92-0.375, FA1.2(167)92-0.3, GA0.43(117)92-0.43 and HA1.07(156)92-0.32) were consolidated to stress states that were aligned on the drained monotonic shearing path from an isotropic state of p_0' = 100 kPa, and sheared under identical cyclic deviatoric stress (q_{cyc}) of 50 kPa.

Figures 7-39 and 7-40 plot respectively the axial and radial strain accumulation trends for this set of specimens. The axial strains were compressive and accumulated more markedly as the q_{mean} level increased, despite the fact that the corresponding *CSR*s were decreasing. The cyclic radial strains exhibited a consistent pattern that accumulated on the compression side at low q_{mean} values (0 and 50 kPa) and reverted to extension as q_{mean} increased. A similar pattern was noted in the cyclic volumetric strains, as shown in Figure 7-41, which showed dilative trends under higher q_{mean} (or high cyclic mean stress ratio q_{mean}/p_0') conditions.

7.4.2 Characteristics of long-term ($N > 200$) strain rates

As demonstrated in the above ε^{acc}-$\log_{10}(N)$ plots, the strain accumulation trends could be reasonably well approximated by linear-logarithmic functions after the first 100-200 stress cycles. Further interpretation is presented below regarding the strain rates over full-cycle range. However, it is important to note that the overall ε^{acc}-$\log_{10}(N)$ slopes determined from N = 200 up to 10^4 cycles include the long-term creep contributions. Correction is made for the residual creeping in the discussion given below.

Table 7-4 summarises the slopes (%/$\log_{10}(N)$) of the linear ε-$\log_{10}(N)$ fitting trends, also listing the corresponding R^2 values. Encouragingly good fitting with R^2 exceeding 0.95 in most cases confirmed that the long-term strain trends can be reasonably well represented by linear ε^{acc}-$\log_{10}(N)$ correlations.

One case that deviated from this trend was the over-consolidated Group A test consolidated to p_0'= 100 kPa and cycled under CSR = 0.3 (test AI(100)92-OC-0.3). As shown in Figure 7-30, this over-consolidated specimen developed axial strains that were initially biased towards the negative (extension) side, followed by a reversed trend after a certain number of cycles. The test cycled under the intermediate CSR level of 0.3 commenced to accumulate axial strains towards the positive side after around 1500 cycles, leading to the nominal low R^2 value from linear regression.

Figures 7-42 and 7-43 demonstrate how the long-term axial and radial strain rates (%/$\log_{10}(N)$) varied with the applied CSRs. The absolute values of the axial and radial strain rates increased consistently with CSR. However, as the stress ratio (η) increased, the axial strain rates increased towards the axial compression side, while the radial strain rates decreased towards the radial extension side. The tests involving the high stress ratio (η) of 1.2 manifested clearly higher long-term strain rates in both directions compared with those of the low stress ratio tests. Backward extrapolation of the trends as shown in Figures 7-42 and 7-43 allows the CSR thresholds below which the long-term strain rates decrease to zero to be estimated.

However, accounting for the background axial creep rates outlined in Section 7.3.5 and Figure 7-22, Figure 7-44 demonstrates the corrected trends for the long-term strain rates against CSR. The strain rates developed under cycling with CSR = 0.1 remained close to zero under all three mean cyclic stress ratios (η) considered, suggesting that negligible axial strains accumulated under this CSR due to cycling alone.

Table 7-4 Slopes (%/$\log_{10}(N)$) and R^2 of fitted linear ε-$\log_{10}(N)$ strain trends with correlations over shearing cycles of $N \geq 200$, before considering background creeping

Test code	Cyclic shearing			Strain rate (%/$\log_{10}(N)$	
	CSR	q_{cyc} **[kPa]**	***N***	$d\varepsilon_a/d\log_{10}(N)$ (R^2)	$d\varepsilon_r/d\log_{10}(N)$ (R^2)
AI(100)92-0.1	0.1	10	6287	0.0048 (0.98)	-0.0066 (0.91)
AI(100)92-0.3	0.3	30	11333	0.0184 (0.99)	0.0297 (0.97)
AI(100)92-0.5	0.5	50	10692	0.0557 (1.00)	0.1136 (1.00)
AI(100)92-OC-0.1	0.1	10	11522	-0.0014 (0.90)	0.0015 (0.98)
AI(100)92-OC-0.3	0.3	30	10587	0.0015 (0.39)	0.0358 (0.99)
AI(100)92-OC-0.5	0.5	50	10549	0.0352 (0.97)	0.1148 (0.95)
BI(400)73-0.1	0.1	40	5038	0.0099 (0.98)	0.0037 (0.95)
BI(400)92-0.1	0.1	40	10545	0.0072 (0.98)	0.0012 (0.72)
BI(400)92-0.3	0.3	120	10231	0.0218 (0.98)	0.0419 (0.96)
BI(400)92-0.5	0.5	200	12076	0.0253 (0.92)	0.0959 (0.99)
CK(133)92-0.1	0.1	13.3	11713	0.0168 (1.00)	-0.0118 (0.99)
CK(133)92-0.3	0.3	40	10723	0.0498 (0.98)	-0.0180 (0.97)
CK(133)92-0.375	0.375	50	10466	0.0900 (0.99)	-0.0283 (0.99)
CK(133)92-0.5	0.5	66.7	10697	0.1358 (0.99)	-0.0235 (0.98)
CK(133)73-0.3	0.3	40	10630	0.1291 (0.99)	-0.0462 (0.99)
DK(266)92-0.1	0.1	26.7	11211	0.0171 (0.98)	-0.0080 (0.93)
DK(266)92-0.3	0.3	80	10812	0.0949 (0.99)	-0.0231 (0.98)
DK(266)92-0.5	0.5	133.3	10778	0.2051 (0.99)	-0.0325 (0.94)
DK(266)73-0.3	0.3	80	10656	0.1714 (0.98)	-0.0354 (0.98)
EK(400)92-0.1	0.1	40	10821	0.0162 (0.99)	-0.0045 (0.95)
EK(400)92-0.3	0.3	120	11446	0.0757 (0.99)	-0.0127 (0.99)
EK(400)92-0.5	0.5	200	11501	0.1635 (1.00)	-0.0264 (0.97)
EK(400)73-0.3	0.3	120	10616	0.1385 (1.00)	-0.0290 (0.99)
FA1.2(167)92-0.1	0.1	16.7	10212	0.0329 (0.99)	-0.0251 (0.98)
FA1.2(167)92-0.3	0.3	50	10781	0.2412 (1.00)	-0.1765 (1.00)
FA1.2(167)92-0.4	0.4	66.7	4468	Incremental collapse during cycling	
FA1.2(167)92-0.5	0.5	83.3	954		
GA0.43(117)92-0.43	0.428	50	10799	0.0877 (0.98)	0.0168 (0.95)
HA1.07(156)92-0.32	0.321	50	10204	0.1141 (0.99)	-0.0620 (0.99)

7.4.3 Strain rates applying over the full range of cycles

The paragraphs above discussed the long-term strain rates observed once $N > 200$. Although informative, these trends do not capture or represent the significant straining that developed over the first few cycles. An approach for considering the tangential strain rates ($d\varepsilon/dN$-N) applying over the full test durations is introduced below, before presenting the cyclic strain data on double-logarithmic scales, demonstrating trends that are fitted better by power law functions for many tests.

Full-cycle range strain accumulation rates

The trends for cyclic strain accumulation against number of shearing cycles (ε^{acc}-N) cannot be represented accurately for all cases by one single polynomial function and fitting parameter. In order to derive the tangential strain rates ($d\varepsilon^{acc}/dN$) applying over the full range of cycles for each test, a three-section fitting approach was adopted employing high-order polynomial functions to fit the cumulative cyclic strain trends.

The ε^{acc}-N data were divided into three overlapping sections. The first started from the first or second cycle, and usually extended to $N = 100$ or 200. In the cases where significant straining occurred in the first cycle, the cyclic strain rate was calculated manually and the fitting was instead initiated from the second cycle to improve overall fitting quality. High order (> 6) polynomial functions were adopted to fit each section until good fit ($R^2 > 0.99$) was obtained. The fitted ε^{acc}-N curves were then joined and differentiated to obtain strain rate curves ($d\varepsilon^{acc}/dN$-N).

The outcomes are illustrated below taking examples from test Groups A, C and F, as shown in Figures 7-45 to 7-47, respectively. The $d\varepsilon^{acc}/dN$-N trends are plotted on double-logarithmic scales, and therefore the strain rates' absolute values are presented. As N approached 10^4, the strain rates diminished down to minimal levels of 10^{-6}-10^{-5} %/cycle, resulting in the slightly 'wavy' trends noted in the figures.

The $d\varepsilon^{acc}/dN$-N trends could be reasonably approximated by a suite of power law functions ($d\varepsilon^{acc}/dN = A(N)^n$) that expressed as straight lines on double-logarithmic scales. The fitting parameters A and n are denoted in the above plots. Note that for a cyclic strain trace that follows log-linear function ($\varepsilon^{acc} = k \times \log_{10}(N)$), its strain rate should fit a power law function with partial power -1, i.e. $d\varepsilon^{acc}/dN = kN^{-1}$. Higher values of fitting exponent n, however, were observed in most cases, as shown in

Figures 7-45 to 7-47, indicating full-cycle range cyclic strain trends (ε^{acc}-N) are deviated from log-linear correlations. The Group F test cycled with CSR = 0.3 gave the closest match to log-linear function, which is evident as seen in Figure 7-37 that both strain components followed approximately linear trends on a semi-logarithmic scale.

Slow strain rate reductions were noted in several low CSR tests, and were most pronounced in the Group F test with CSR = 0.1 as shown in Figure 7-47. The trend reflected the sample's tendency to generate significant strain accumulation rates before manifesting sharp reduction in rates after a certain number of cycles.

Influential factors affecting cyclic strain rates

The cyclic strain rates are critically dependent on the CSR level. The isotropically and normally consolidated Group A specimens developed higher strain rates in the radial direction, as shown in Figure 7-45, in contrast to the anisotropically consolidated Groups C and F tests that exhibited higher strain rates in axial compression than in radial extension. The Group F tests performed under higher stress ratio of η = 1.2 developed clearly higher strain rates than those of the lower stress ratio Groups A and C tests.

Figure 7-48 highlights the potential dependency of cyclic strain rates on effective stress level (p_0'). Cyclic strains were accumulated at higher rates in the tests under higher p_0' of 400 kPa, conforming to the observations made in the ε^{acc}-$\log_{10}(N)$ trends compared in Figure 7-35.

The impact of specimen density on cyclic axial strain rates is illustrated in Figure 7-49, comparing the outcomes from the set of dense ($e_0 \approx 0.71$, R_d = 73%) and very dense ($e_0 \approx 0.64$, R_d = 92%) specimens under equivalent p_0' and CSR conditions. The $d\varepsilon^{acc}/dN$-N curves show virtually parallel patterns, and the trends for the R_d = 73% specimens were located above those for the R_d = 92% ones.

7.4.4 Cyclic strain accumulation functions

Accumulated cyclic strains on double-logarithmic scales

The above trends for cyclic strain rates ($d\varepsilon^{acc}/dN$-N) suggested that the cumulative cyclic strains can be represented by power functions in cases where no change in the sign of straining developed. To verify this, the cyclic axial and radial strains of the

Group B (η = 0, (q_{mean}, p_0') = (0, 400)) and C tests (η = 0.75, (q_{mean}, p_0') = (0, 400)) are replotted on double-logarithmic scales, as shown in Figures 7-50 to 7-53, corresponding to the ε^{acc}-$\log_{10}(N)$ trends shown in Figure 7-26 and Figure 7-32 respectively for these two test groups, noting that the strain trends of these tests stayed constantly either on the positive or negative side without crossing zero .

As mentioned in Section 7.4.1, the ε^{acc}-$\log_{10}(N)$ traces were defined as starting from zero to facilitate comparison by indicating strains accumulated at the beginning of the N^{th} cycle, whereas the current $\log_{10}(\varepsilon^{acc})$-$\log_{10}(N)$ plots represent strains that were generated at the end of the N^{th} cycle. The strain traces on double-logarithmic scales were fitted by power law functions expressed as $\varepsilon^{acc}(N) = mN^n$, with m representing strain generated after the first cycle. Positive m values suggest positive (compressional) strains and positive n values indicate positive slopes of the absolute strain $|\varepsilon^{acc}(N)|$ trends in double-logarithmic scales.

As demonstrated in Figures 7-50 and 7-51, the strain trends of the Group B tests can be reasonably well represented by power law functions, particularly for the high *CSR* (0.3 and 0.5) conditions. Greater deviations were noted in the *CSR* = 0.1 test, which developed minimal negative radial strains in the first 30 cycles. Encouraging good fitting was reached in the Group C tests with R^2 values exceeding 0.95 for both the axial and radial strain components, as shown in Figures 7-52 and 7-53. The negative m and positive n fitting values for the radial strains implied straining towards radial extension and increased as cycling continued.

Fitting parameters for $\varepsilon^{acc}(N) = mN^n$ functions

Applying the above approach for other tests, Table 7-5 summarises the power law fitting parameters obtained for axial and radial strain components, also indicating the R^2 values as established over full cycle range. Strain traces that reversed direction could not be expressed by a single set of parameters. This was seen in several low η tests (0 or 0.43) and in the over-consolidated Group A-OC(4) tests. Nevertheless, overall good fitting with high R^2 values was attained in the other testing cases, and the straining trends were implied from the parameter signs.

Derivation of cyclic strains as strain rates integrals

An alternative approach to derive accumulated cyclic strains is to perform power law

fitting exercises on the full-cycle range strain rate trends and express the accumulation trends as strain integrals. The difficulty of expressing strains across the zero strain conditions can be resolved using this approach.

Referring to Table 7-2, the strain rate data were first fitted using power law function, $d\varepsilon^{acc}/dN = mN^m + d$, employing the approach as described above. The parameter d represents the rate of ratcheting and is set as zero for the current discussion. The full-cycle cumulative cyclic strain trends can be expressed using power law functions in the form of

$$\varepsilon_{\mathbf{N}}^{\mathbf{acc}} = \varepsilon_{N=1} + b(N^{\mathbf{c}} - 1) \tag{7.9}$$

Where $b = m/(n+1)$ and $c = n+1$; $\varepsilon_{N=1}$ is the strain generated in the first shearing cycle. Taking the test Groups A ($\eta = 0$, (q_{mean}, p_0') = (0, 100)) and C ($\eta = 0.75$, (q_{mean}, p_0') = (100, 133.3)) as examples, Figures 7-54 to 7-57 compare the measured and fitted axial and radial strain trends over full cycle ranges in semi-logarithmic scales, indicating a generally good match. The strain trends that crossed zero can also be expressed.

However, unlike the above $\varepsilon^{acc}(N) = mN^m$ formulation in which the first cycle's strain is indicated implicitly, it is generally difficult to determine the first cycle strain $\varepsilon_{N=1}$ accurately from the strain rate integration approach, particularly in the cases where significant straining occurs over the first few cycles. The $\varepsilon^{acc}(N) = mN^m$ formulation is therefore regarded as a more direct way of characterising long-term cyclic strains.

There is also scope to correlate the above fitting parameters m and n with the mean cyclic stress ratio (q_{mean}/p_0') and cyclic amplitude stress ratio (q_{cyc}/p_0') that may allow predictions of cyclic strains to be made under more general stress conditions. This approach was outlined by Ushev (2018) for his interpretation of undrained cyclic behaviour of Cowden till. Further investigation is required to develop a similar treatment for the Author's Dunkirk drained cyclic tests.

Table 7-5 Summary of parameters for fitting cyclic axial and radial strains with power law functions ($\varepsilon^{acc}(N) = mN^n$)

Test code	Axial strains			Radial strains		
	***m* [%]**	***n***	R^2	***m* [%]**	***n***	R^2
AI(100)92-0.1	0.001	0.346	0.928	Reversed to negative at $N = 540$		
AI(100)92-0.3	0.028	0.186	0.912	0.025	0.219	0.980
AI(100)92-0.5[(a)]	0.019	0.307	0.911	0.273	0.141	0.997
AI(100)92-OC-0.1	-0.001	0.317	0.907	0.002	0.201	0.813
AI(100)92-OC-0.3[(b)]	-0.057	-0.008	0.034	0.036	0.204	0.997
AI(100)92-OC-0.5[(b)]	-0.563	-0.135	0.804	0.260	0.143	0.985
BI(400)73-0.1	0.003	0.250	0.890	0.005	0.291	0.920
BI(400)92-0.1	0.002	0.315	0.946	0.002	0.219	0.623
BI(400)92-0.3	0.016	0.241	0.882	0.056	0.182	0.979
BI(400)92-0.5	-0.520	-0.189	0.902	0.593	0.089	0.977
CK(133)92-0.1	0.009	0.263	0.948	-0.003	0.322	0.985
CK(133)92-0.3	0.065	0.184	0.994	-0.016	0.207	0.985
CK(133)92-0.375	0.289	0.123	0.997	-0.136	0.098	0.995
CK(133)92-0.5	0.333	0.139	0.998	-0.189	0.073	0.986
CK(133)73-0.3	0.213	0.168	0.990	-0.095	0.152	0.996
DK(266)92-0.1	0.005	0.312	0.966	-0.001	0.351	0.991
DK(266)92-0.3	0.224	0.145	0.985	-0.073	0.125	0.985
DK(266)92-0.5	0.571	0.132	0.993	-0.258	0.078	0.948
DK(266)73-0.3	0.257	0.173	0.997	-0.103	0.125	0.997
EK(400)92-0.1	0.006	0.295	0.969	-0.001	0.304	0.993
EK(400)92-0.3	0.162	0.151	0.980	-0.047	0.114	0.986
EK(400)92-0.5	0.772	0.104	0.980	-0.445	0.050	0.929
EK(400)73-0.3	1.423	0.058	0.990	-0.884	0.023	0.924
FA1.2(167)92-0.1	0.011	0.303	0.900	-0.005	0.339	0.929
FA1.2(167)92-0.3	0.634	0.148	0.890	-0.491	0.143	0.900
FA1.2(167)92-0.4	Incremental collapse during cycling					
FA1.2(167)92-0.5						
GA0.43(117)92-0.43	0.145	0.167	0.986	Reversed trend at $N = 865$		
HA1.07(156)92-0.32	0.269	0.144	0.989	-0.211	0.121	0.988

Notes: [(a)]: axial strain reversed to positive, fitting only for $N > 24$;

[(b)]: relatively poor fit for axial strain due to straining reversals, see Figure 7-29.

7.4.5 Cyclic strain ratios and cyclic dilation

As reviewed in Section 7.2.2, researchers including Chang & Whitman (1988) and Wichtmann *et al.* (2005) have attempted to correlate the cyclic strains accumulated by sands (usually represented by ε_s^{acc} and ε_{vol}^{acc}) with their mean cyclic stress states (p_0', q_{mean}). Chang & Whitman (1988) argued that the cyclic dilation-stress ratio ($\varepsilon_v^{acc}/\varepsilon_s^{acc}$-$\eta$) correlations could be expressed by stress-dilation models, such as those defined by Rowe (1962) and Roscoe & Burland (1968), that were initially established for monotonic loading conditions. Experimental studies by Wichtmann *et al.* (2005) and Wichtmann *et al.* (2007b) found that Chang & Whitman's (1988) cyclic dilation model (see Equation (7.3)) fitted well with the measured cyclic dilation-stress ratio data (as demonstrated in Figure 7-7).

The Author's tests provided an opportunity to examine whether the above stress-dilation models can be applied to fine Dunkirk sand specimens with R_d of 73% and 92%, and explore the potential effects of effective stress level, cyclic stress ratio (CSR) and number of shearing cycle (N), which were believed to be of only minor importance in the previous studies.

The direction of cyclic strains, defined as the ratio between the cyclic deviatoric and volumetric strains ($\varepsilon_s^{acc}/\varepsilon_{vol}^{acc}$), are denoted in Figures 7-58 to 7-60 as a set of unit vectors starting from the (q_{mean}, p_0') point of each test group. The volumetric (ε_{vol}^{acc}) and deviatoric strain (ε_s^{acc}) were calculated as $\varepsilon_{vol}^{acc} = \varepsilon_a^{acc} + 2\varepsilon_r^{acc}$ and $\varepsilon_s^{acc} = 2/3(\varepsilon_a^{acc} - \varepsilon_r^{acc})$, with ε_a^{acc} and ε_r^{acc} being the accumulated axial and radial strains. The slope of the vector with respect to the positive ε_{vol}^{acc} axis is defined by the angle θ^{acc}, indicating any deviation of cyclic straining from the conditions of zero deviatoric strain and pure contractive volumetric strains. Strain vectors are shown for N values of 10, 300 and 10^4 in the plots to track any changes of θ^{acc} during cycling.

Effects of effective stress ratio (η)

Focusing first on the specimens cycled under intermediate (CSR = 0.3-0.43) and high (CSR = 0.5) cyclic stress ratios that generated significant cyclic straining. Their strain vector outcomes are shown in Figure 7-59 and Figure 7-60, respectively. A consistent pattern emerges for the strain vectors to rotate gradually towards the $+\varepsilon_{vol}^{acc}$ axis as N increases.

The influence of mean cyclic effective stress ratio q_{mean}/p_0' (η) on cyclic straining pattern is evident as η increased. The ultimate cyclic strain ratios deviated further from the θ^{acc} = 0 condition, showing greater deviatoric straining compared to volumetric strains under high η conditions. The overall pattern was found similar to that reported by Wichtmann *et al.* (2007b), as previously shown in Figure 7-7.

Cyclic straining under zero mean cyclic stress conditions (q_{mean} = 0) was dominated by significant contractive volumetric strains ($+\varepsilon_{vol}^{acc}$), accompanied by minor "negative" deviatoric strains ($-\varepsilon_s^{acc}$). As discussed earlier, the $-\varepsilon_s^{acc}$ strains and small "negative" θ^{acc} values indicated the sand's inherently anisotropic behaviour and greater susceptibility to high *CSR* two-way cycling that extended to significant q values. The specimens cycled under anisotropic stress condition from q_{mean}/p_0' = 0.75 developed both positive volumetric and deviatoric straining, indicating predominantly axial compressional strains and minor radial extension strains. The specimens under high η values of 1.07 and 1.2 manifested significant deviatoric strains and relatively minor dilatant (negative) volumetric strains.

The observations summarised above from high *CSR* tests were broadly reflected in the low *CSR* tests, as shown in Figure 7-58. However, the low *CSR* tests performed at low effective stresses (p_0') tended to develop slightly different cyclic strain patterns, suggesting additional effects of *CSR* and p_0', as discussed below.

***Effects of cyclic stress ratio* (*CSR*)**

Considering both the q_{mean}/p_0' = 0 and 0.75 conditions as shown in Figures 7-59 and 7-60, the specimens cycled with the highest *CSR* (0.5) generated higher θ^{acc} angles than those under intermediate *CSR*s, suggesting more deviatoric strain accumulation developed under higher *CSR*.

The tests performed under the low *CSR* of 0.1, as shown in Figure 7-58, indicated a different pattern of generating positive deviatoric strains under low amplitude cycling. The straining patterns were clearly shown in Figures 7-25 and 7-26 that compressional (positive) axial cyclic strains and relatively minor (positive and negative) radial strains were generated under *CSR* = 0.1.

However, the low *CSR* tests also exhibited a tendency to dilate part-way through their cycling, with the θ^{acc} increasing with N from certain stages. The latter was clear in the low p_0' and low *CSR* Group A test (shown in Figure 7-27) and Group C test (shown

in Figure 7-35). The results suggested that unlike the high *CSR* tests that tended to generate predominantly contractive volumetric straining, the soil subjected to low amplitude cyclic perturbation could develop cyclic dilation upon shearing or after a certain number of contractive shearing cycles.

Kuwano & Jardine (2007) argued that when travelling along effective stress paths of fixed inclination dq/dp', the strain increment directions developed under initial elastic loading persisted until the onset of Y_2 yielding. The strain increment vectors could then rotate progressively. The features were clearly seen in Section 5.7 in relation to the Author's monotonic tests. The Author's cyclic loading tests also support this conclusion and indicate that Y_2 yielding is likely to apply to Dunkirk sand in cyclic tests that impose *CSR* levels greater than or equal to the minimum of 0.1 applied in the Author's tests.

***Effects of effective stress level* (p_0')**

The influence of effective stress level on the cyclic strain ratios depended also on the *CSR* and mean cyclic effective stress ratio ($\eta = q_{mean}/p_0'$). Under the low *CSR* conditions shown in Figure 7-58, the delayed dilation phenomenon was only observed under low p_0' conditions, confirming that dilation was repressed under high effective stresses. Similar effects were found in the high *CSR* tests with $\eta = 0.75$ as the strain vectors aligned closer to the constant stress ratio line under higher p_0' conditions, leading to lower positive θ^{acc} values, as shown in Figures 7-59 and 7-60.

The exhibition in high *CSR* tests with $\eta = 0$ of lower negative θ^{acc} values under high effective stresses reflected their anisotropic large strain yielding and failure characteristics.

***Effects of number of shearing cycles* (N)**

The above results also indicated clear trends for the cyclic strain ratios to evolve as the cycling continued. Under high *CSR*s, the strain ratio vector rotated gradually towards the horizontal $+\varepsilon_{vol}^{acc}$ axis as cycling continued, while the reverse trend applied in the low p_0' tests when cycled at low *CSR*s.

***Cyclic dilation-stress ratio trends* ($\varepsilon_{vol}^{acc}/\varepsilon_s^{acc}$-$\eta$)**

As under monotonic loading conditions, the cyclic dilation can be expressed as

$d\varepsilon_{vol}^{acc}/d\varepsilon_s^{acc}$, the reciprocal of the above cyclic strain ratios employed above.

Figure 7-61 plots the cyclic dilation-stress ratio trends identified for anisotropically consolidated tests cycled with high *CSRs* (0.3-0.5). General trends can be observed for cyclic dilation to increase as cycling continued and trend towards negative values as stress ratio η increased. Also indicated is the trend predicted by Chang & Whitman (1988)'s cyclic dilation model (Equation (7.3) assuming $M_{cs} = 1.31$).

The Dunkirk cyclic tests commenced to manifest dilative (negative $\varepsilon_{vol}^{acc}/\varepsilon_s^{acc}$) strains at lower stress ratios than are predicted from Equation (7.3), with dilation from $\eta = 1.07$ (shown in Figure 7-41), significantly below the critical state stress ratio $M_{cs} = 1.31$. The divergent trends might reflect the effects of specimen density. Most of the specimens tested in the current studied were prepared with higher relative densities of 92%, than those tested by Chang & Whitman (1988) and Wichtmann *et al.* (2005), which fell in the 57%-67% range.

Figure 7-62 identifies the cyclic dilation-stress ratio trends for the low *CSR* (=0.1) tests at three η levels. The low *CSR* specimens developed significant less cyclic volumetric straining, and the $\varepsilon_{vol}^{acc}/\varepsilon_s^{acc}$-$\eta$ trends identified were much flatter than those of high *CSR* tests. The low *CSR* tests also trended towards negative $\varepsilon_{vol}^{acc}/\varepsilon_s^{acc}$ asymptotes, reflecting enhanced cyclic dilation as shearing evolved.

Figure 7-63 includes the outcomes from the $\eta = 0$ tests, which clearly deviated from the above trends. The cyclic straining of the istropically consolidated specimens under two-way cycling was affected markedly by the levels of p_0' and *CSR*, and their cyclic dilation pattern could not be reconciled with the Chang & Whitman (1988) dilation model.

7.4.6 Figures

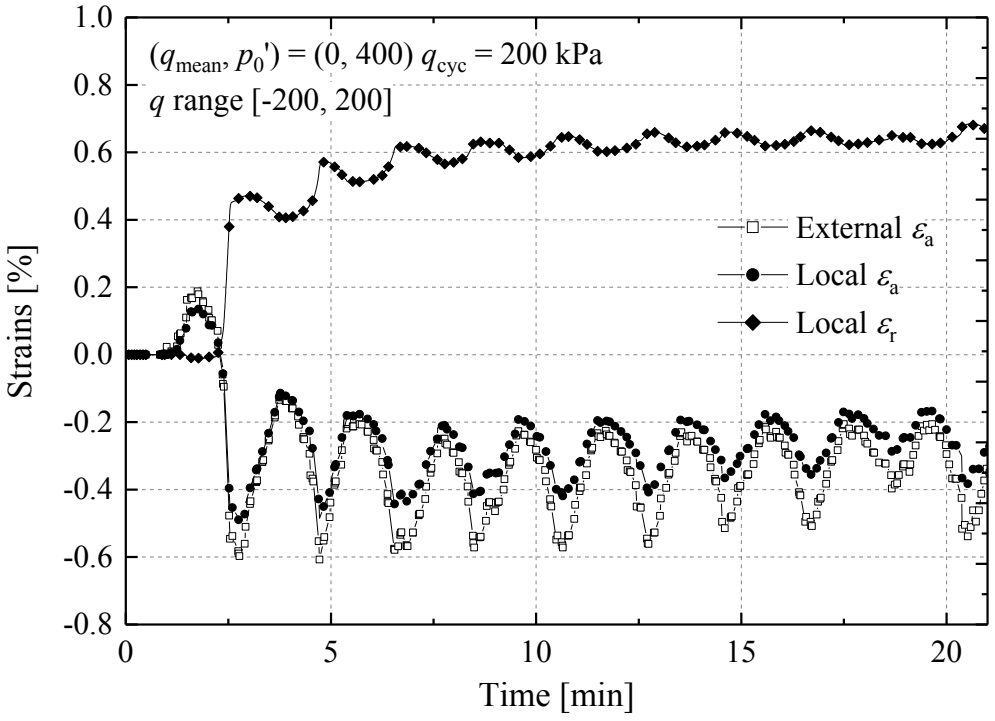

Figure 7-23 Measured cyclic strains in the first 10 cycles of test BI(400)92-0.5, with isotropic mean effective stress conditions

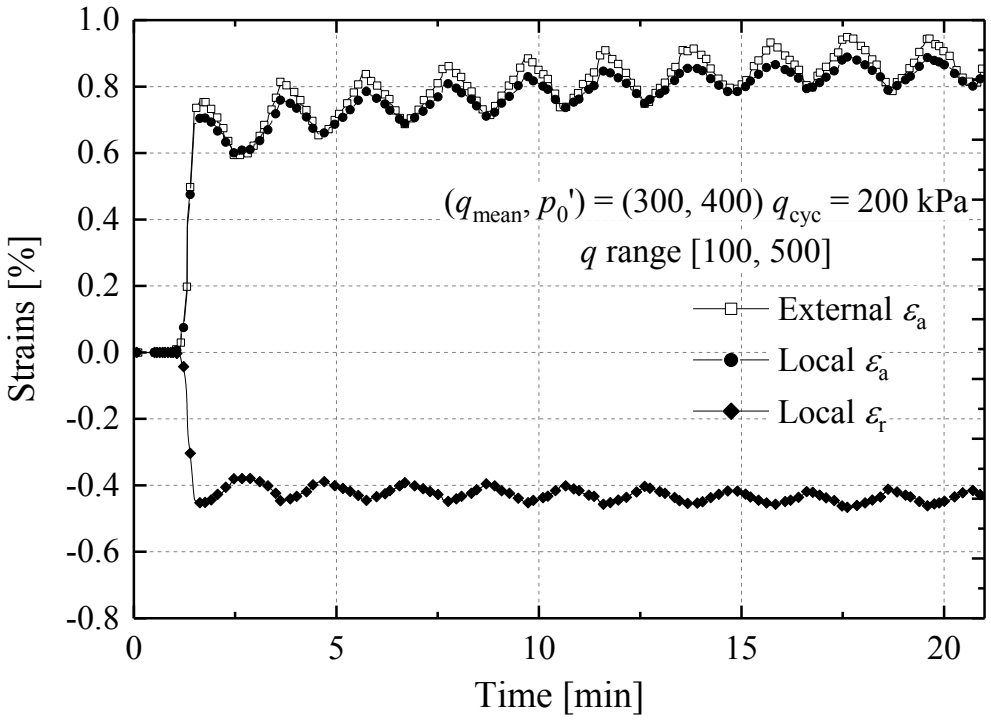

Figure 7-24 Measured cyclic strains in the first 10 cycles of test EK(400)92-0.5, with anisotropic (K_o = 0.5) mean effective stress conditions

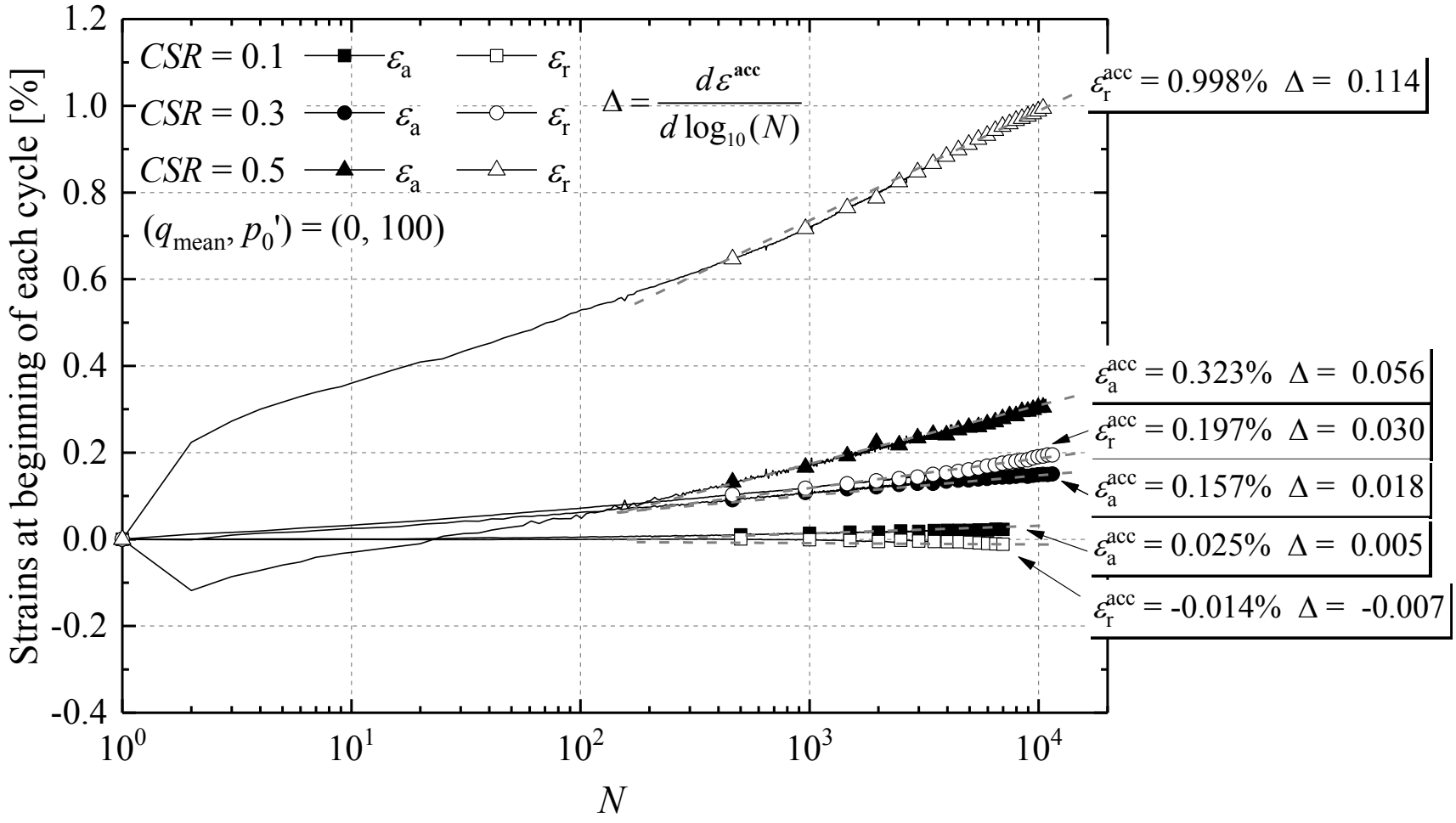

Figure 7-25 Axial and radial strain accumulation trends for the Group A tests ($\eta = 0$, (q_{mean}, p_0') = (0, 100) (kPa)) (Note: consolidation stress path see Figure 7-15)

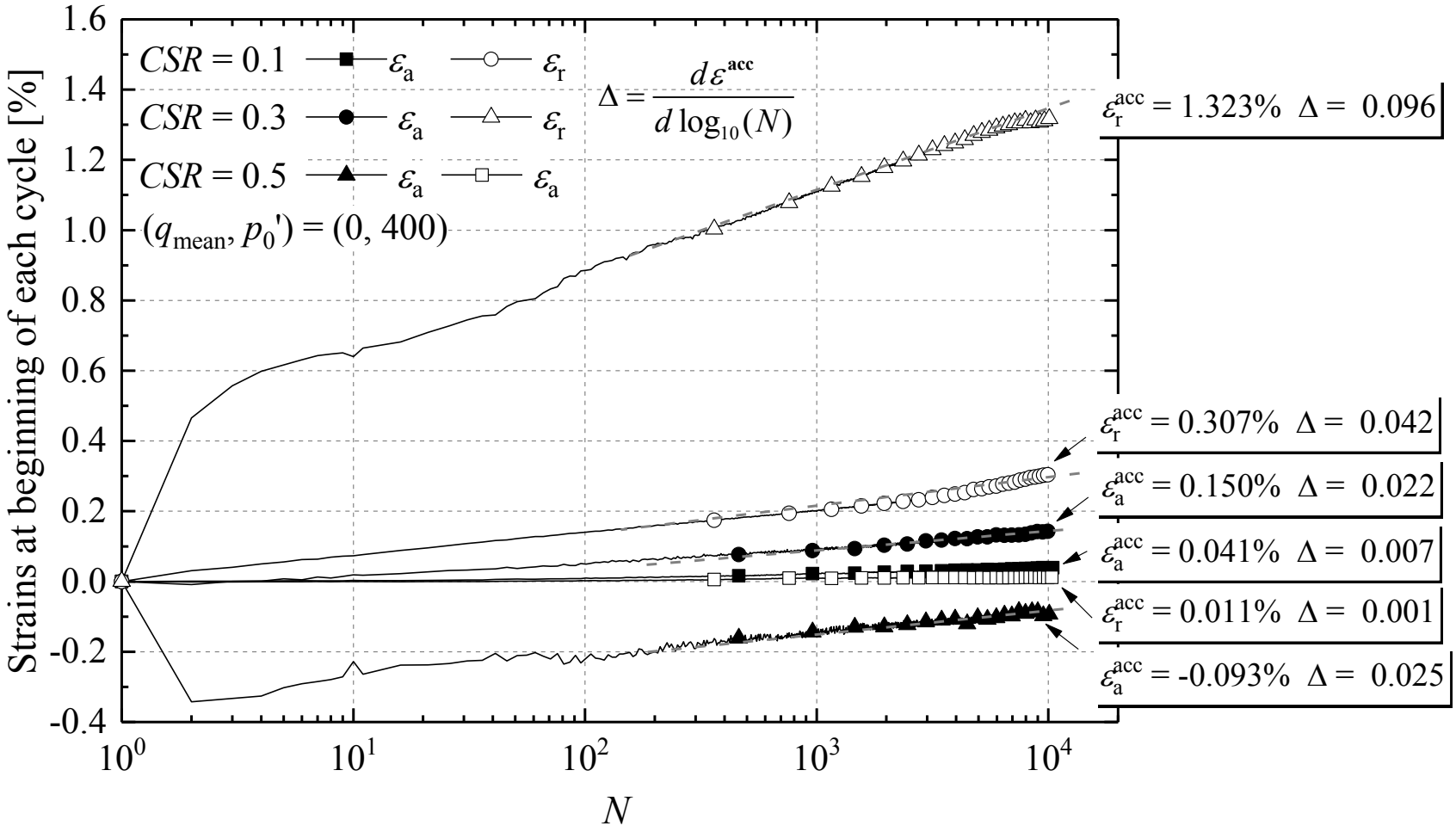

Figure 7-26 Axial and radial strain accumulation trends for the Group B tests (η = 0, (q_{mean}, p_0') = (0, 400) (kPa)) (Note: consolidation stress path see Figure 7-15)

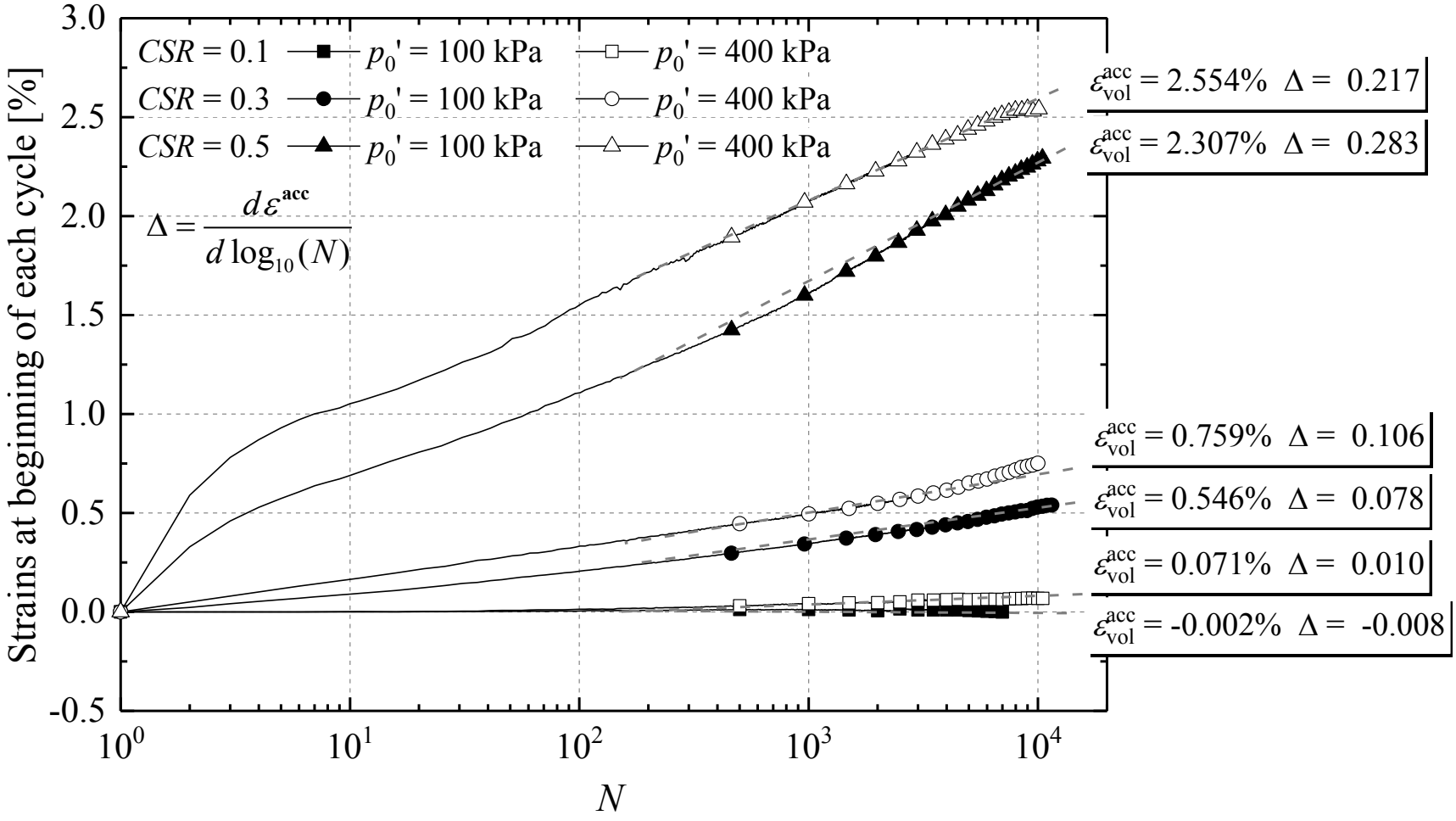

Figure 7-27 Cyclic volumetric strains for the Group A tests (η = 0, (q_{mean}, p_0') = (0, 100) (kPa)) and B tests (η = 0, (q_{mean}, p_0') = (0, 400) (kPa))

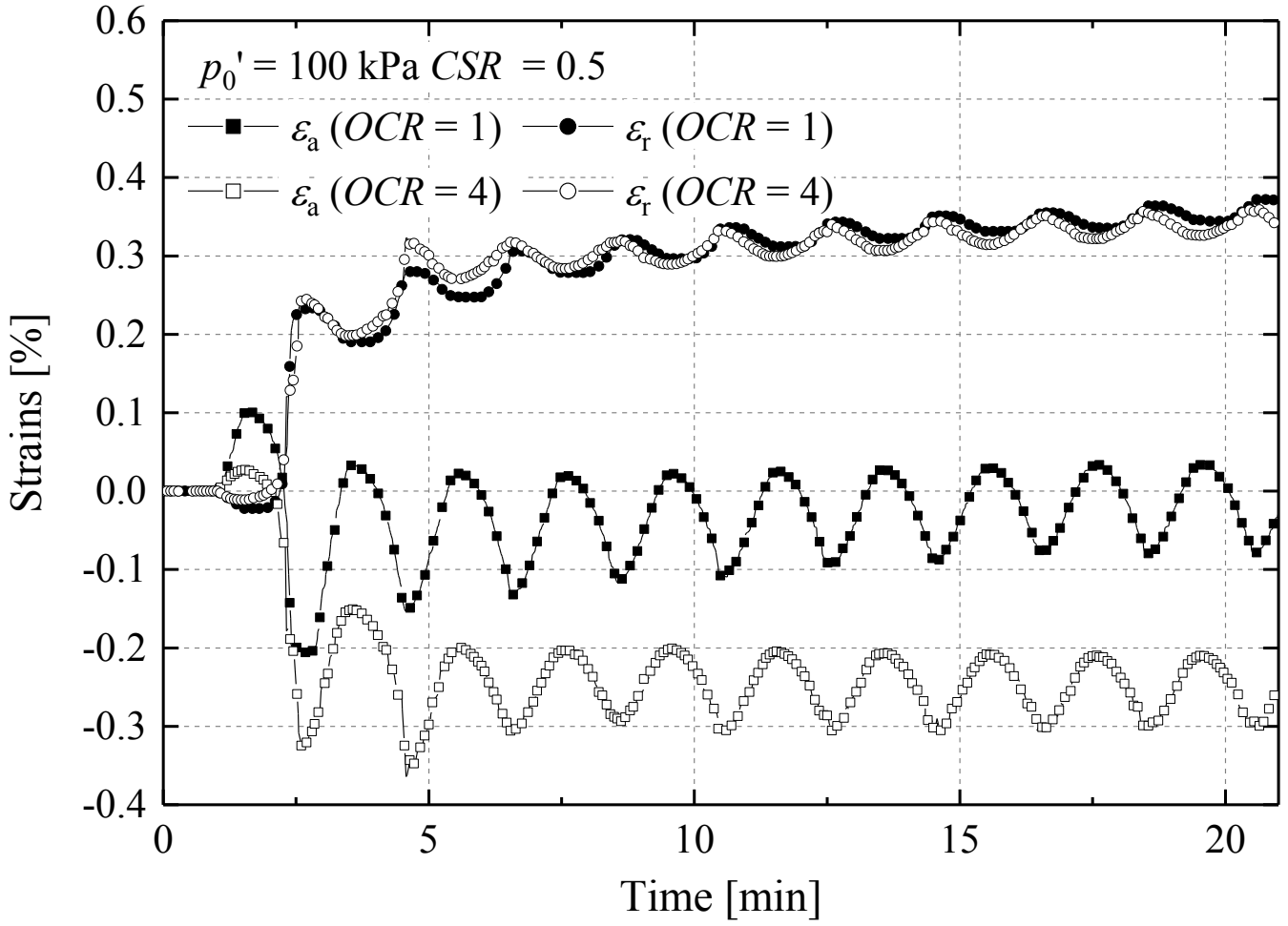

Figure 7-28 Local axial and radial strains generated in the first 10 shearing cycles of the normally consolidated Group A and over-consolidated Group A-OC(4) tests (η = 0, (q_{mean}, p_0') = (0, 100) (kPa)) under CSR = 0.5

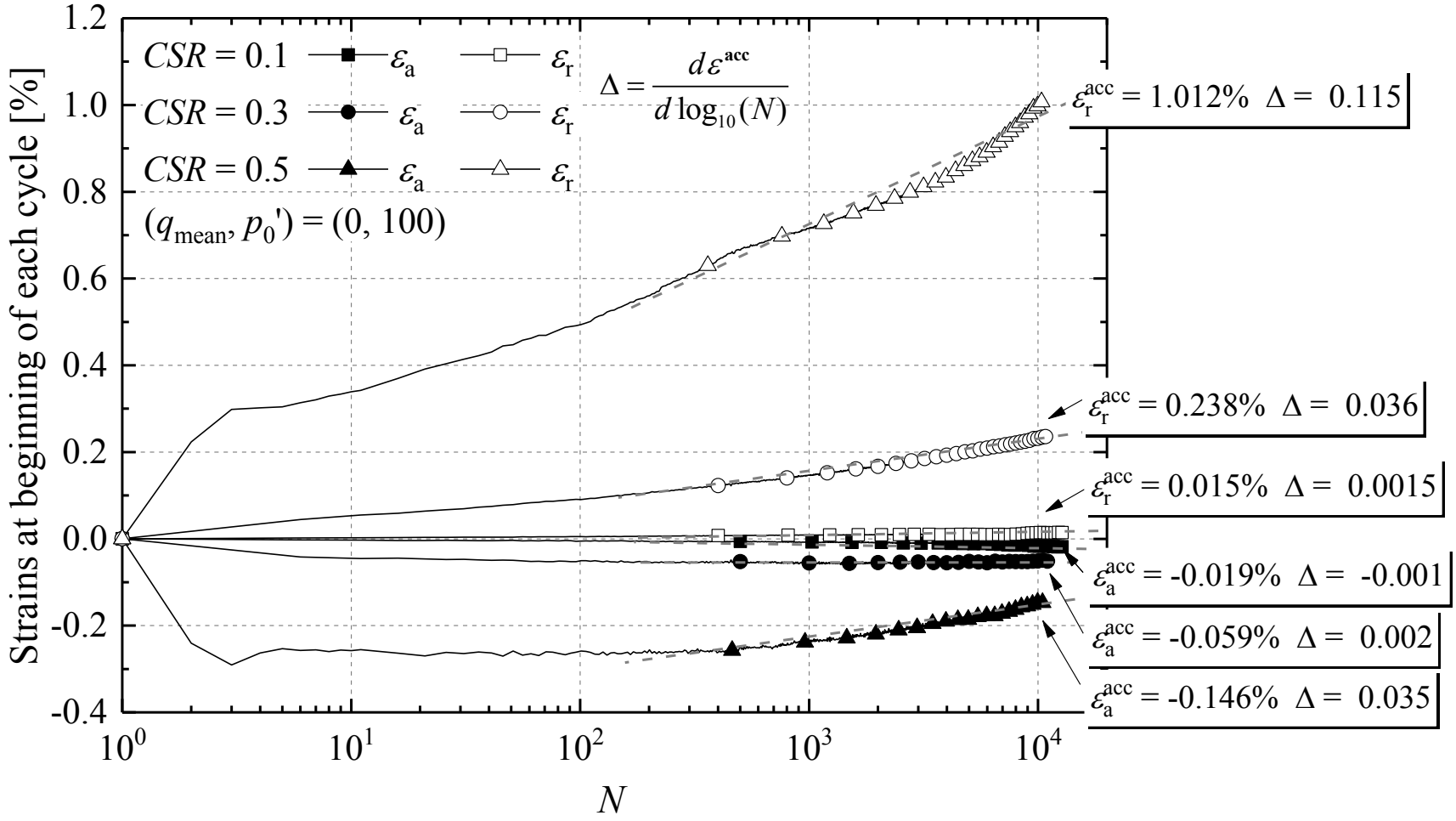

Figure 7-29 Strain trends for the over-consolidated Group A-OC(4) tests (η = 0, (q_{mean}, p_0') = (0, 100) (kPa)) (Note: consolidation stress path see Figure 7-16)

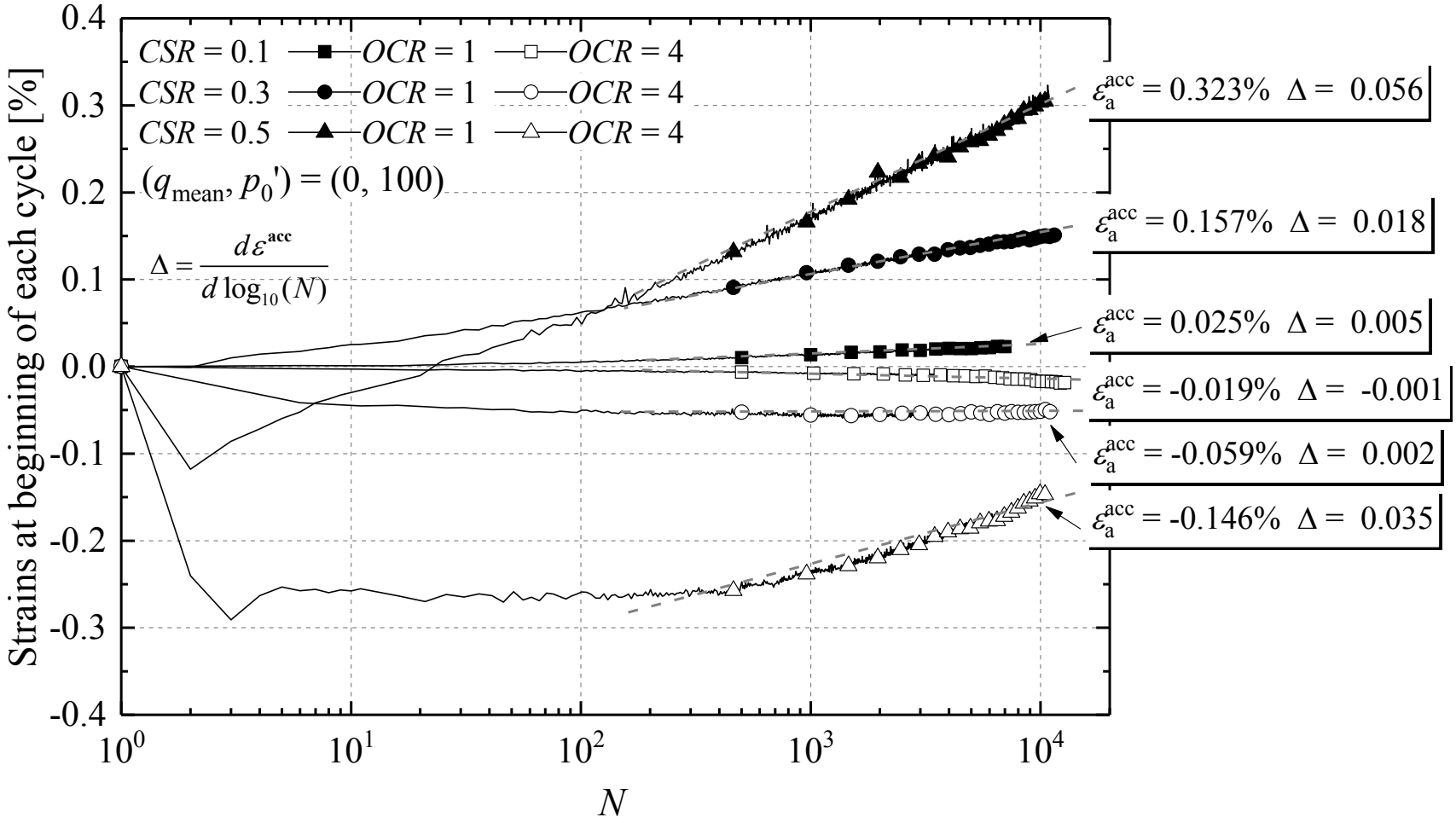

Figure 7-30 Local axial strains for the normally consolidated Group A and over-consolidated Group A-OC(4) tests (η = 0, (q_{mean}, p_0') = (0, 100) (kPa))

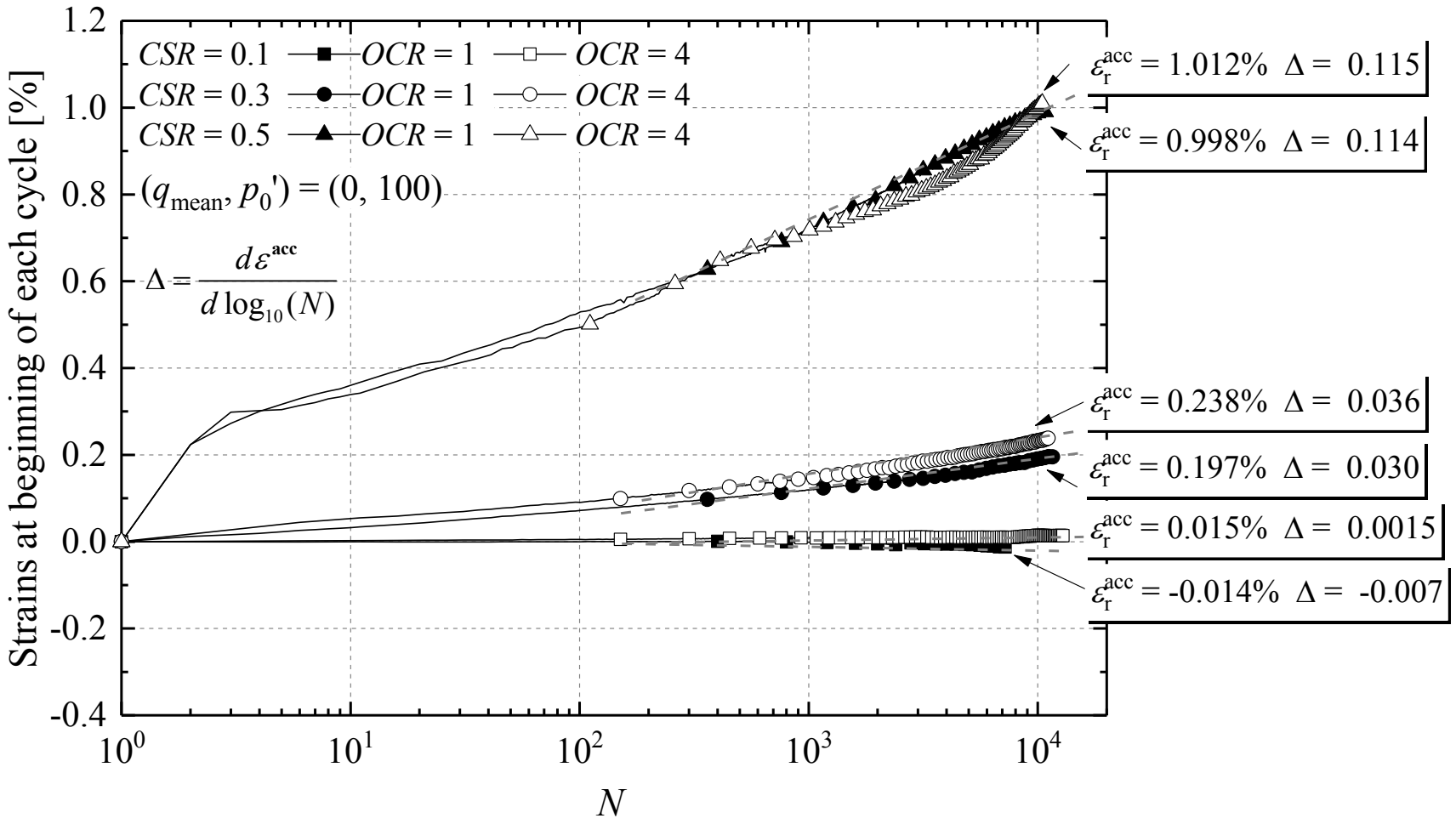

Figure 7-31 Local radial strains for the normally consolidated Group A and over-consolidated Group A-OC(4) tests ($\eta = 0$, (q_{mean}, p_0') = (0, 100) (kPa))

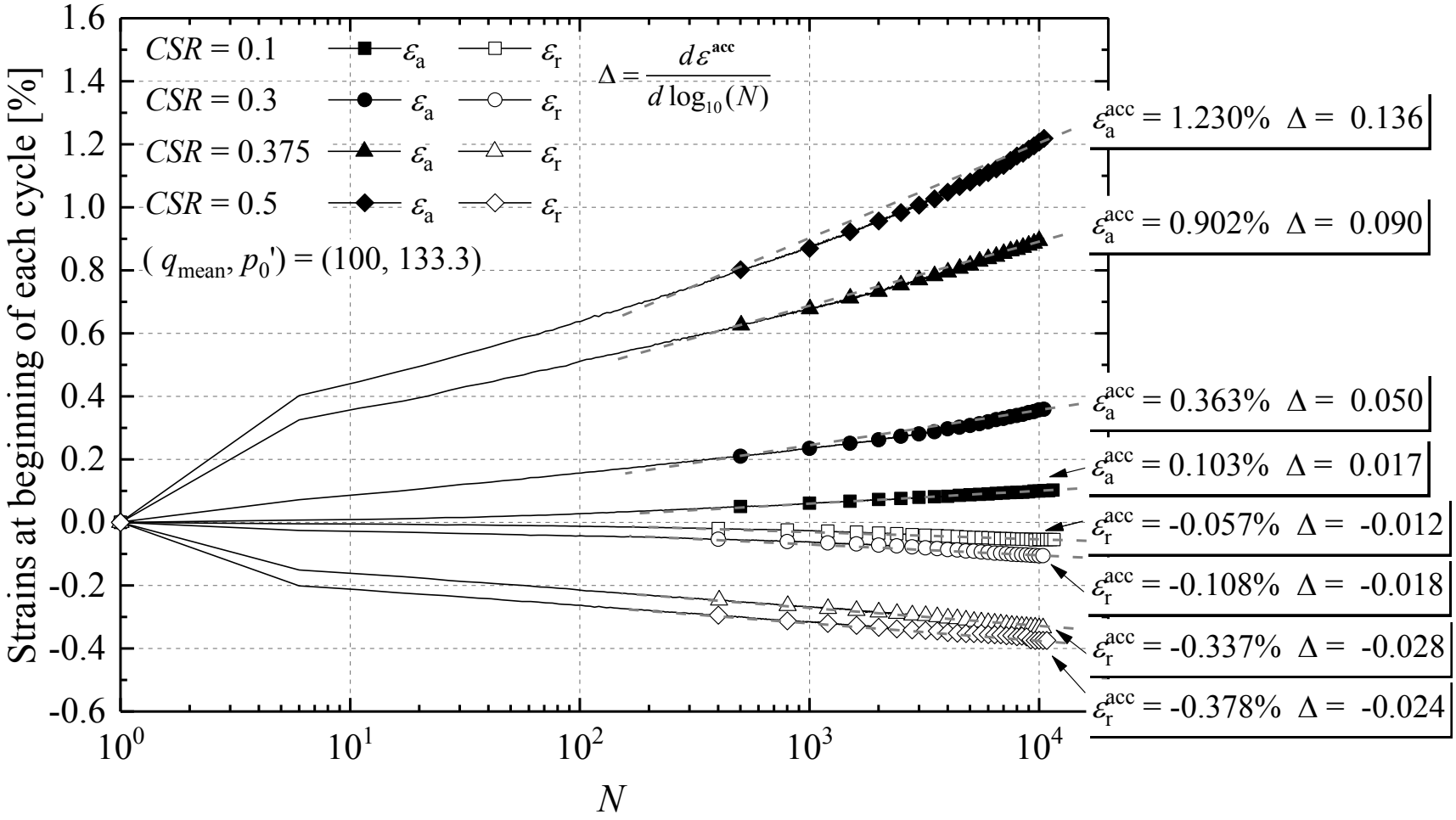

Figure 7-32 Local axial and radial strain accumulation trends for very dense (R_d = 92%, $e_0 \approx 0.640$) Group C tests (η = 0.75, (q_{mean}, p_0') = (100, 133.3) (kPa))
(Note: consolidation stress path see Figure 7-17)

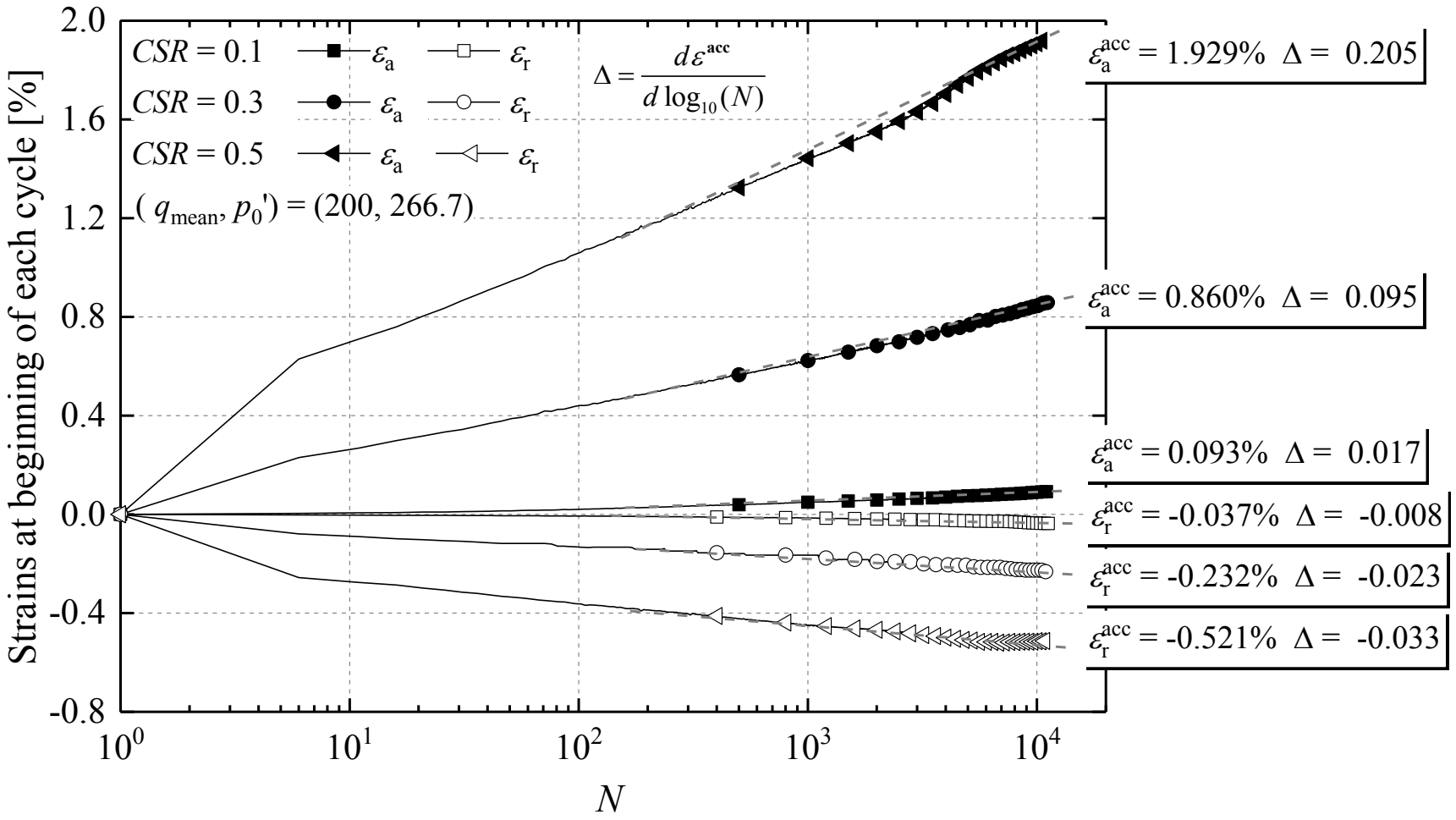

Figure 7-33 Local axial and radial strain accumulation trends for very dense (R_d = 92%, $e_0 \approx 0.640$) Group D tests (η = 0.75, (q_{mean}, p_0') = (200, 266.7) (kPa))
(Note: consolidation stress path see Figure 7-17)

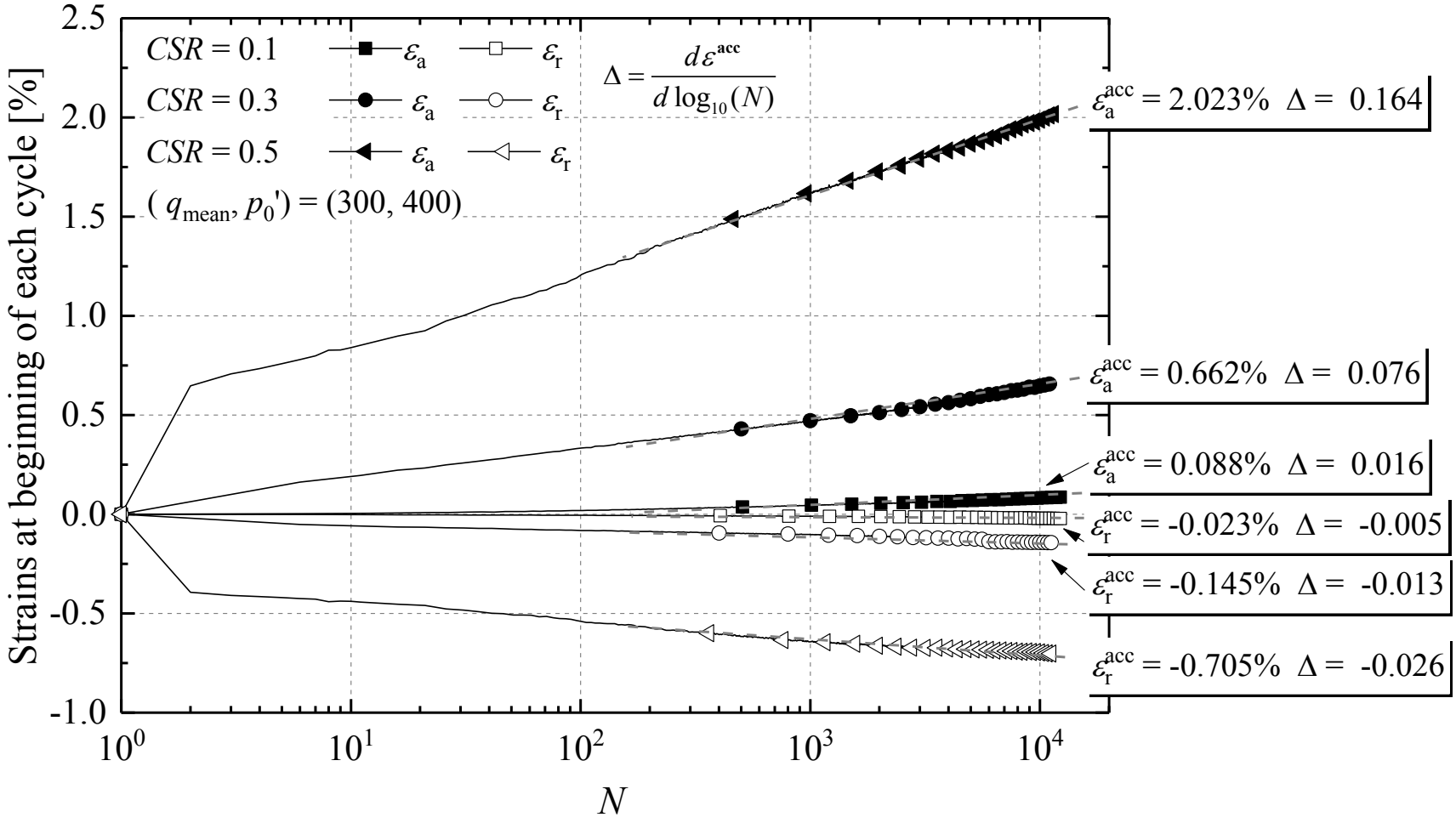

Figure 7-34 Local axial and radial strain accumulation trends for very dense (R_d = 92%, e_0 ≈ 0.640) Group E tests (η = 0.75, (q_{mean}, p_0') = (300, 400) (kPa))
(Note: consolidation stress path see Figure 7-17)

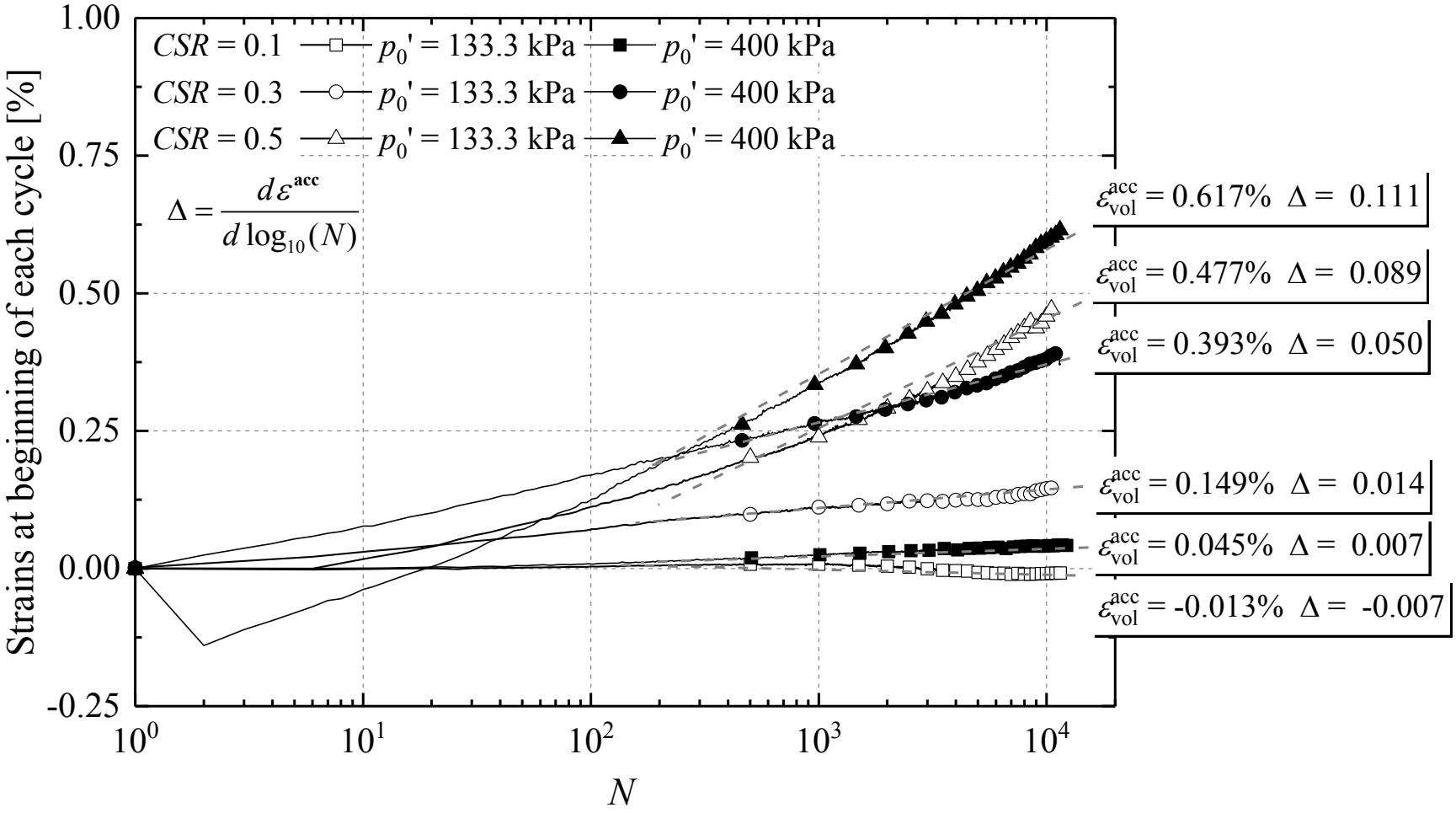

Figure 7-35 Cyclic volumetric strains for very dense (R_d = 92%, $e_0 \approx 0.640$) Group C tests (η = 0.75, (q_{mean}, p_0',) = (100, 133.3) (kPa)) and E tests (η = 0.75, (q_{mean}, p_0') = (300, 400) (kPa))

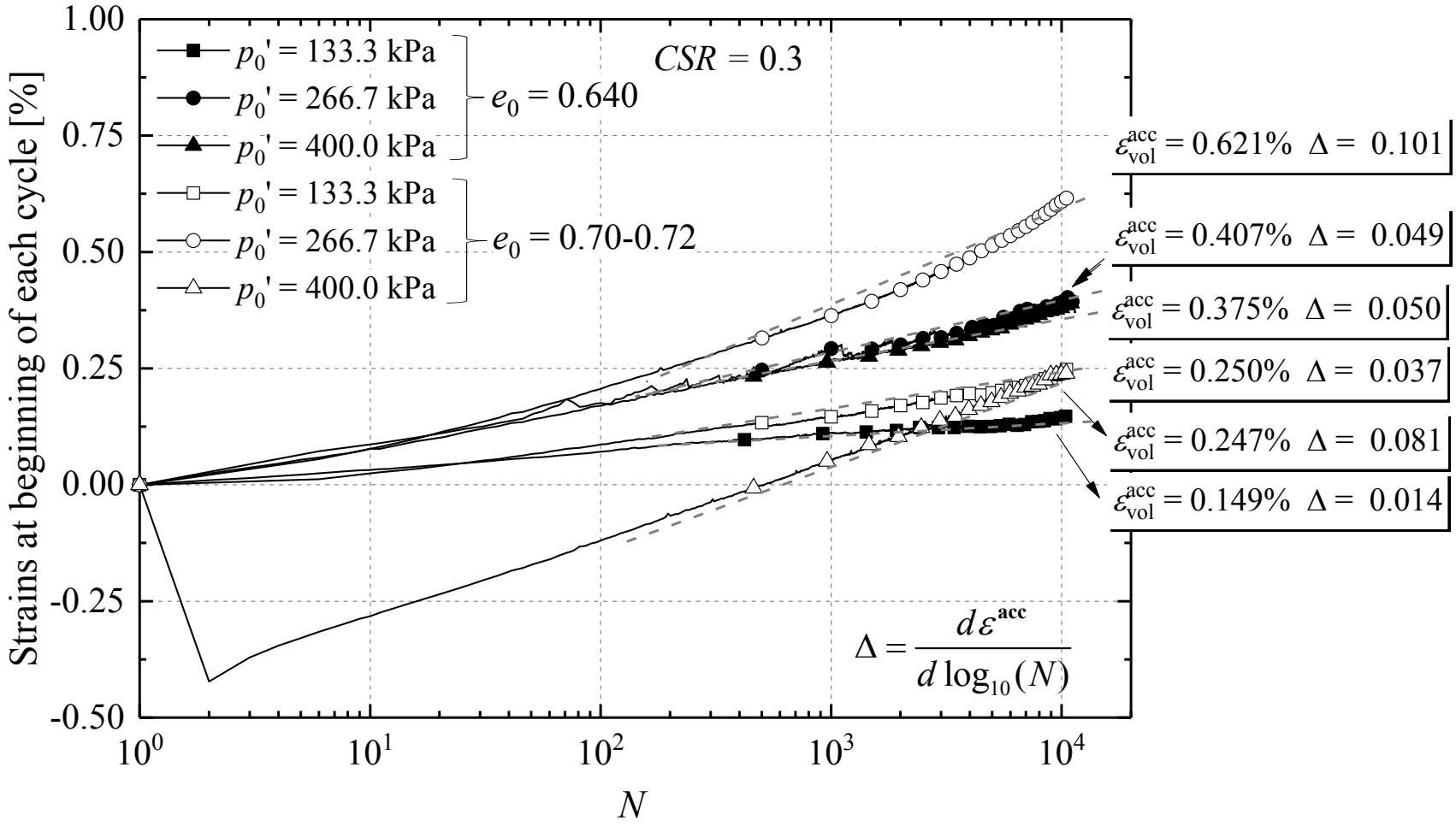

Figure 7-36 Accumulated volumetric strains for the very dense ($e_0 \approx 0.640$) and dense ($e_0 \approx 0.710$) Group C, D and E specimens ($\eta = q_{mean}/p_0' = 0.75$) under $CSR = 0.3$

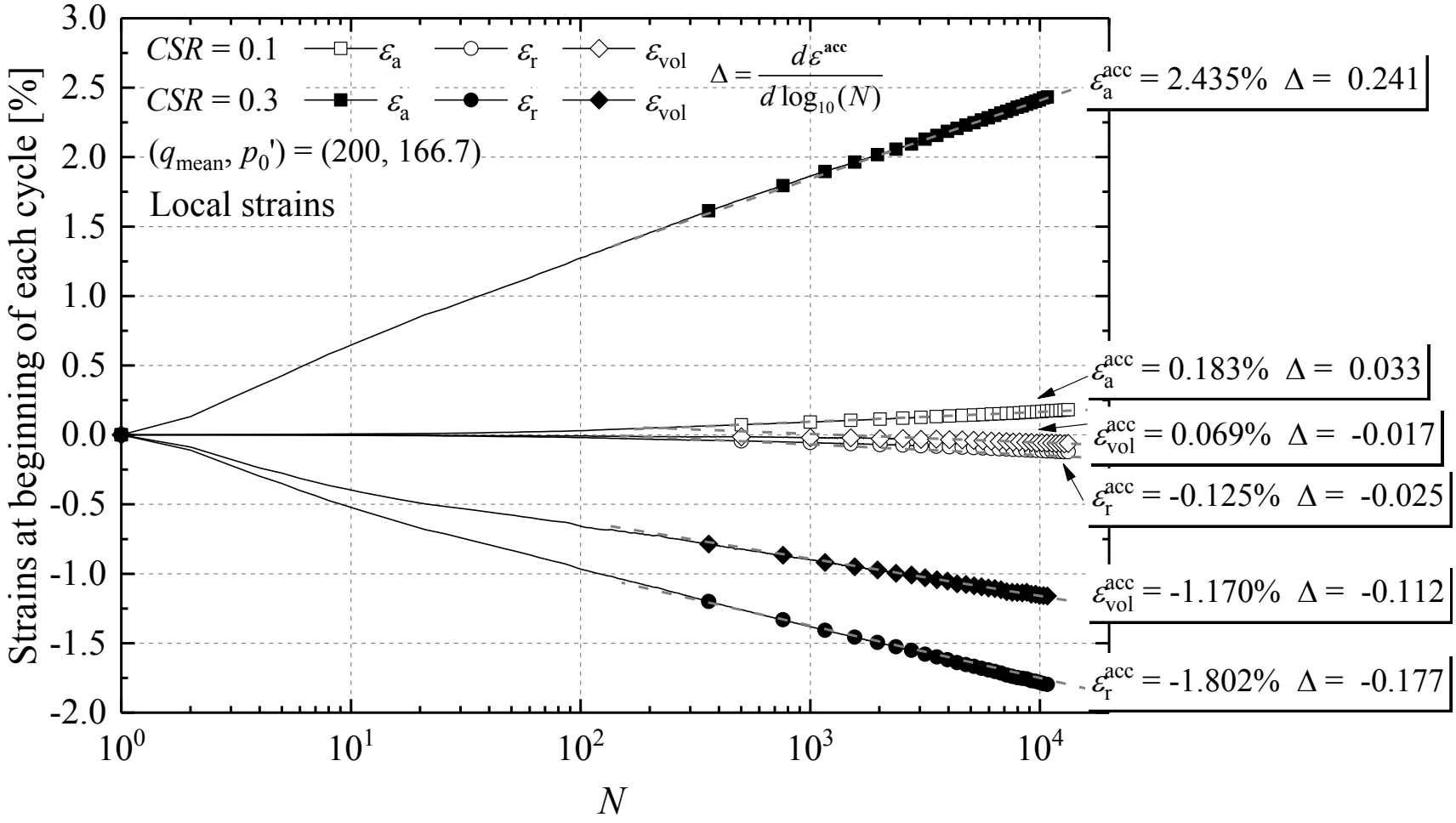

Figure 7-37 Local strain trends for the Group F tests (η = 1.2, (q_{mean}, p_0') = (200, 166.7) (kPa)) tests under low *CSR*s of 0.1 and 0.3 (Note: consolidation stress path see Figure 7-18)

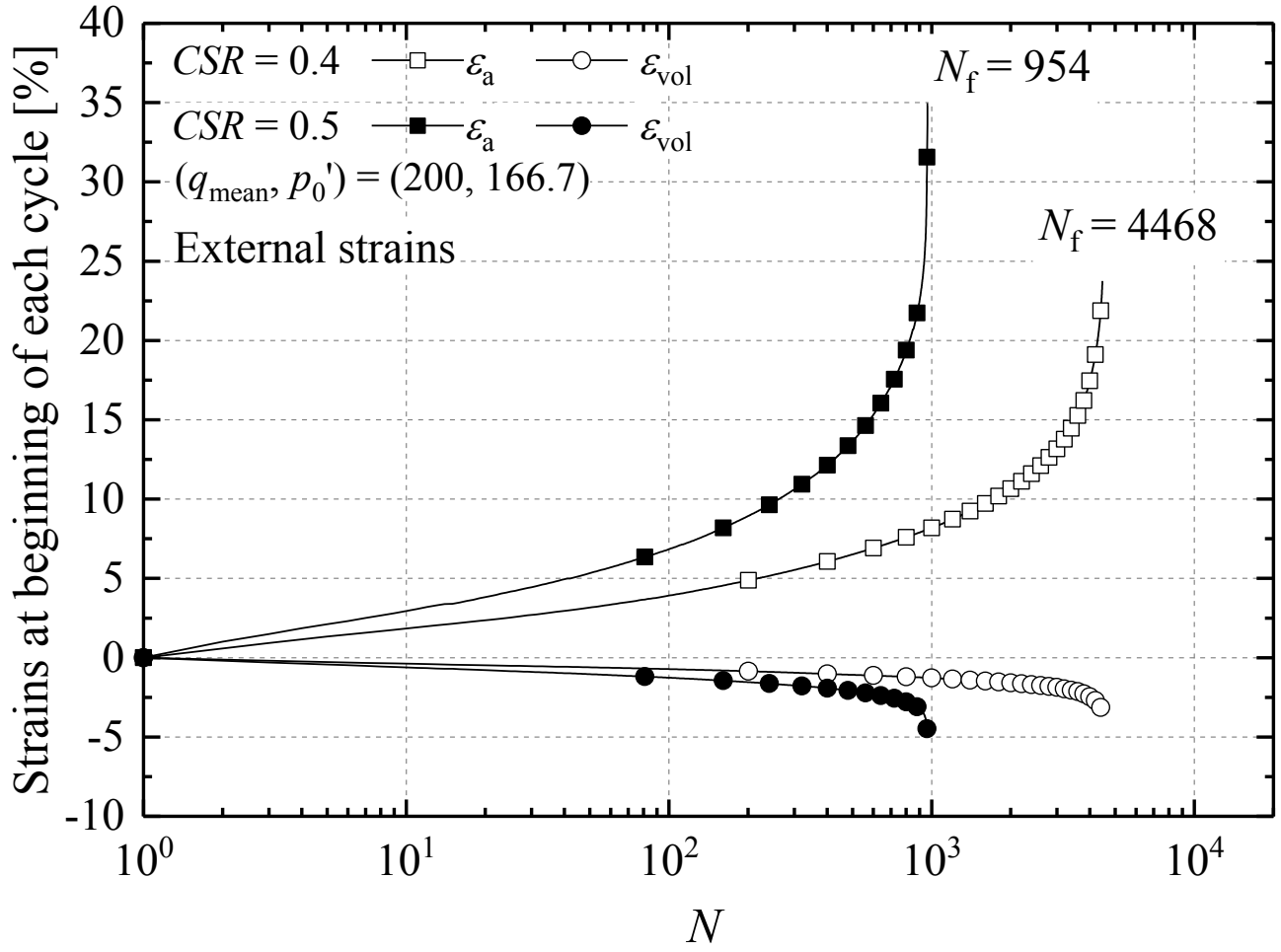

Figure 7-38 External strain trends for the Group F tests (η = 1.2, (q_{mean}, p_0') = (200, 166.7) (kPa)) tests under high *CSR*s of 0.4 and 0.5

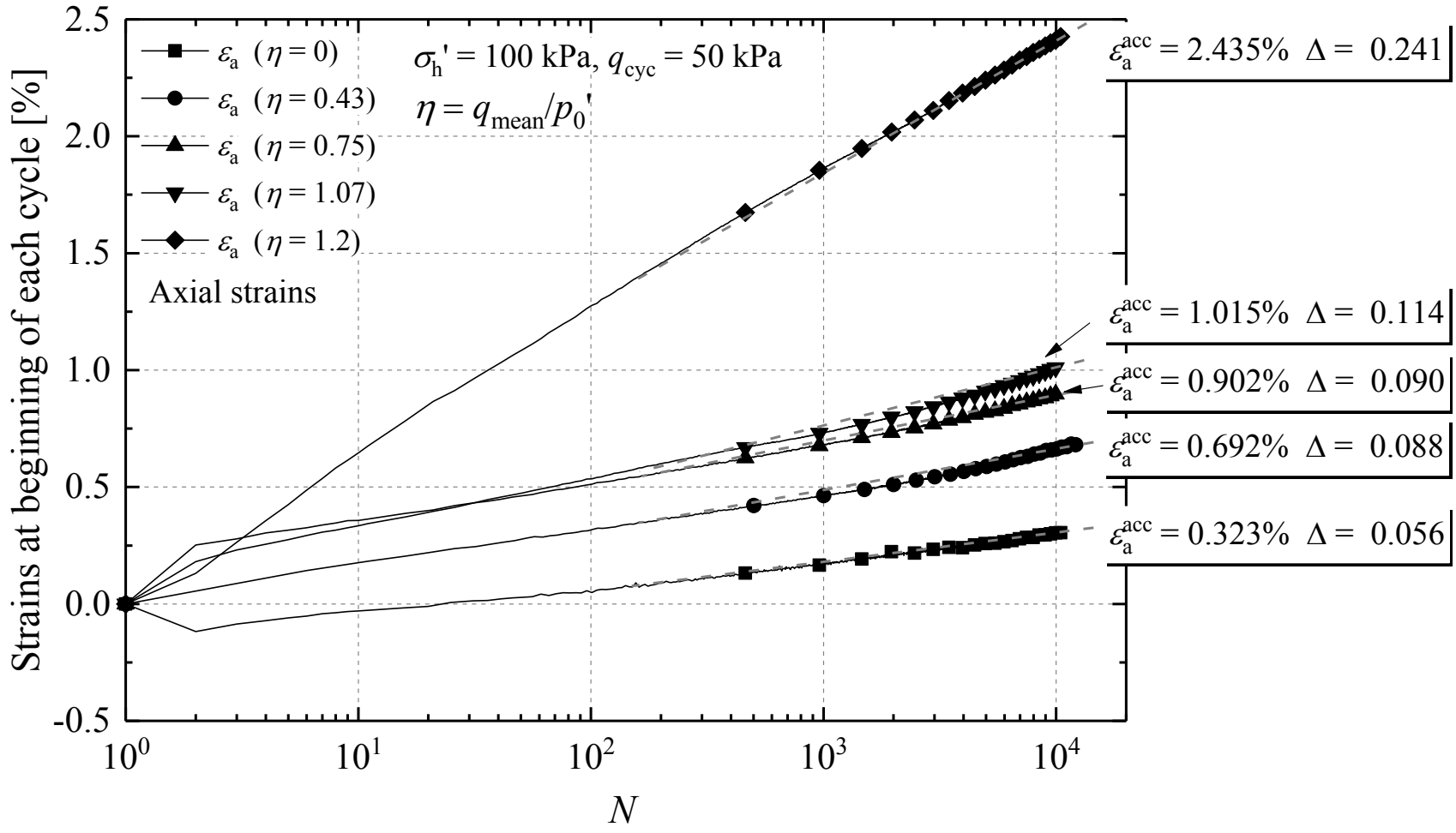

Figure 7-39 Axial strain accumulation trends for the set of samples in test with identical σ_h' and q_{cyc} but varied q_{mean} levels (Note: consolidation stress paths see Figure 7-18)

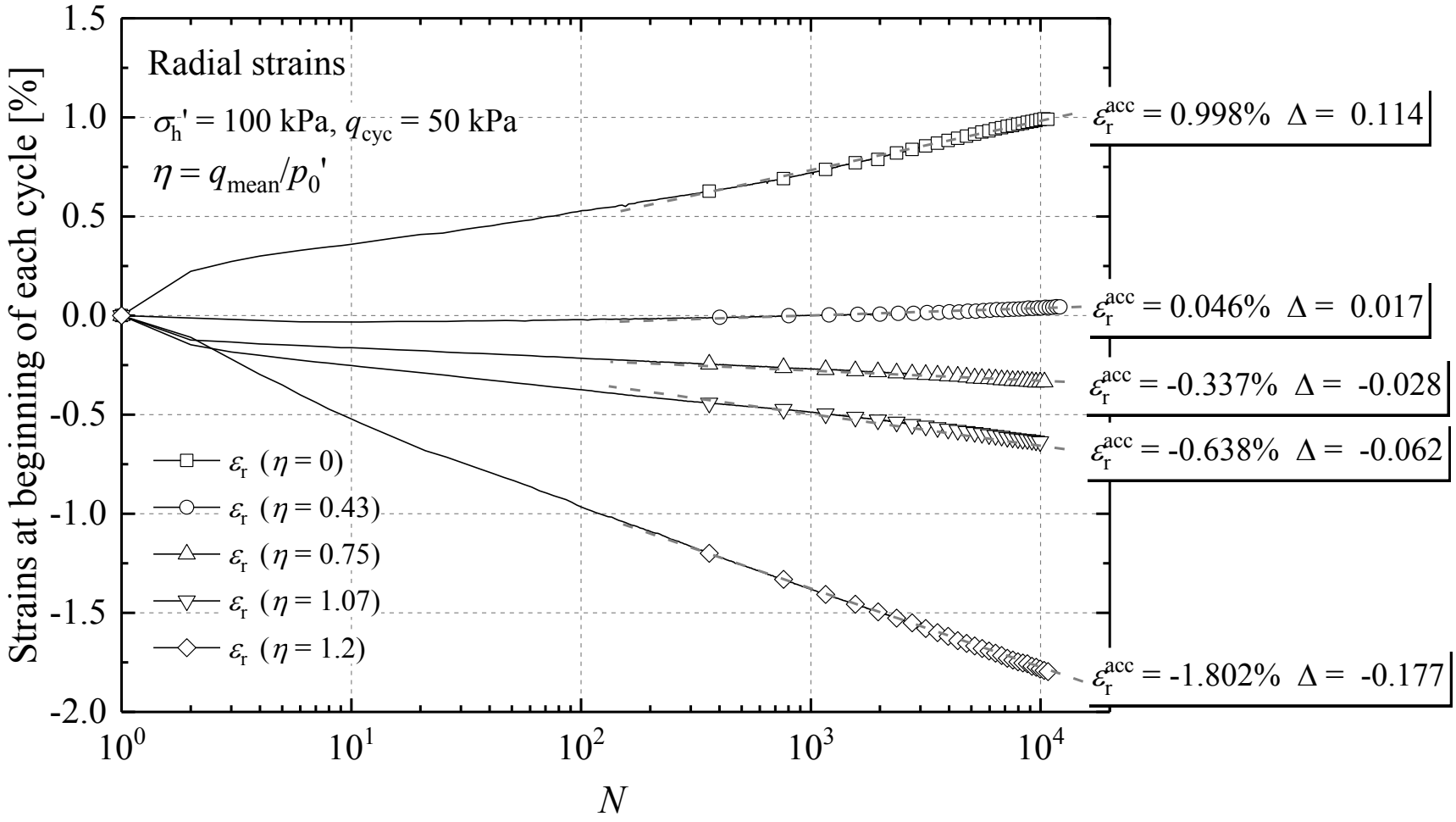

Figure 7-40 Radial strain accumulation trends of the set of samples with identical σ_h' and q_{cyc} but varied q_{mean} levels (Note: consolidation stress paths see Figure 7-18)

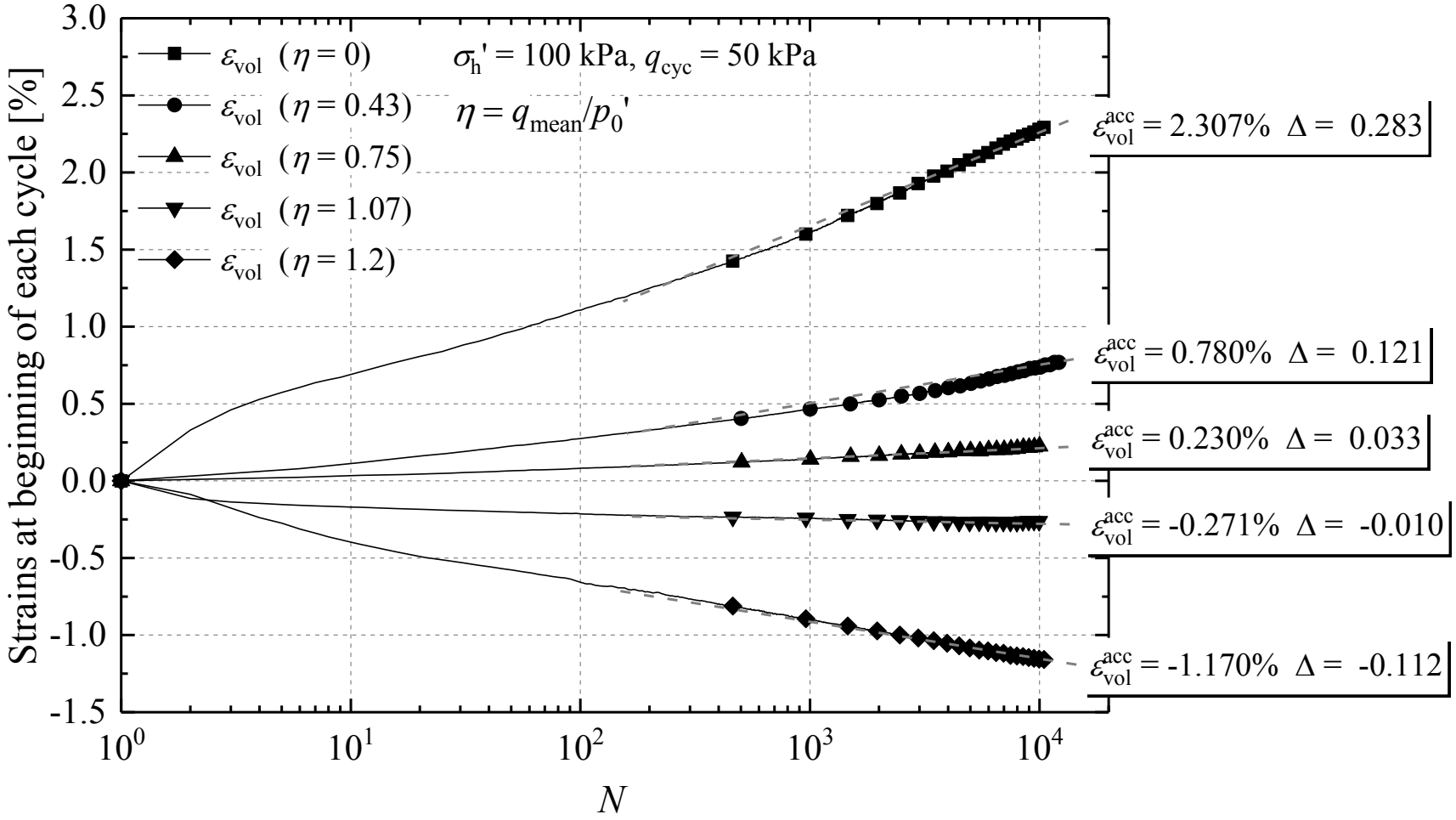

Figure 7-41 Volumetric strain trends for the set of samples with identical σ_h' and q_{cyc} but varied q_{mean} levels (Note: consolidation stress paths see Figure 7-18)

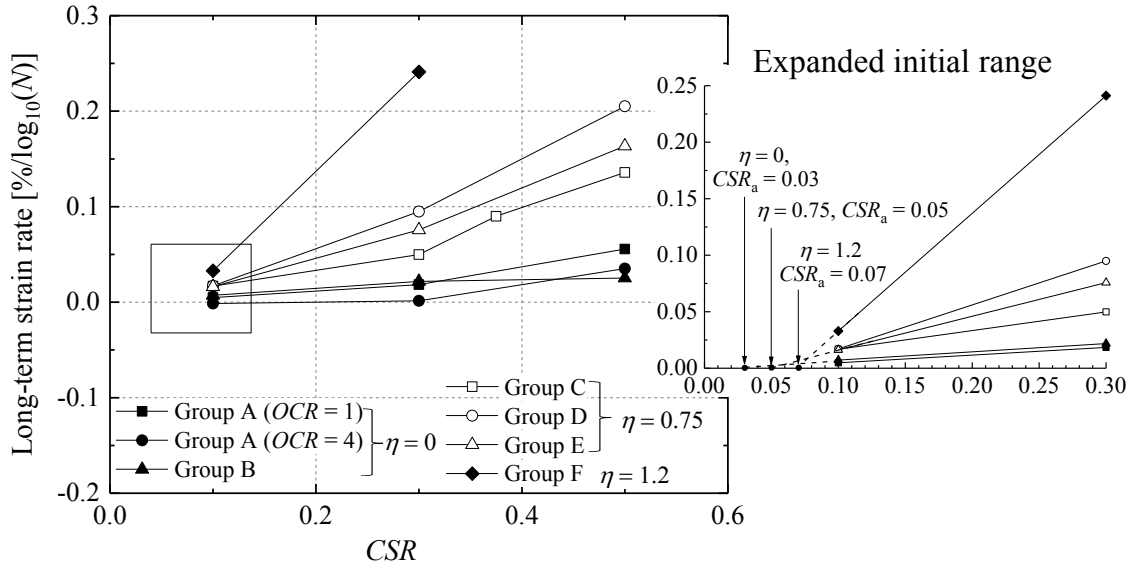

Figure 7-42 Nominal Long-term axial strain rates of the very dense (e_0 = 0.64, R_d = 92%) specimens and the identification of *CSR* level of zero axial strain rate, before correcting for background creep

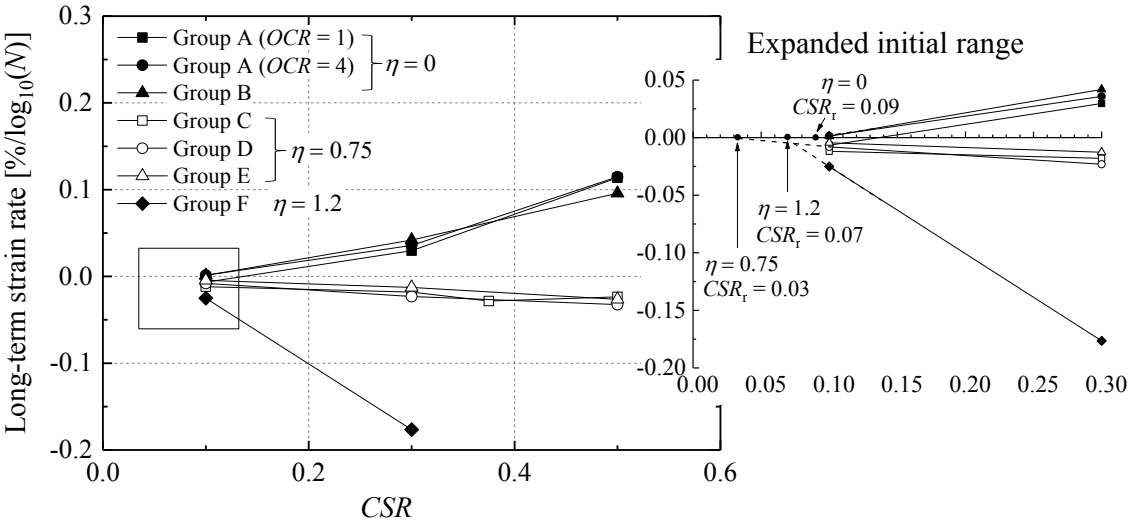

Figure 7-43 Nominal long-term radial strain rates of the very dense (e_0 = 0.64, R_d = 92%) specimens and the identification of *CSR* level of zero radial strain rate, before correcting for background creep

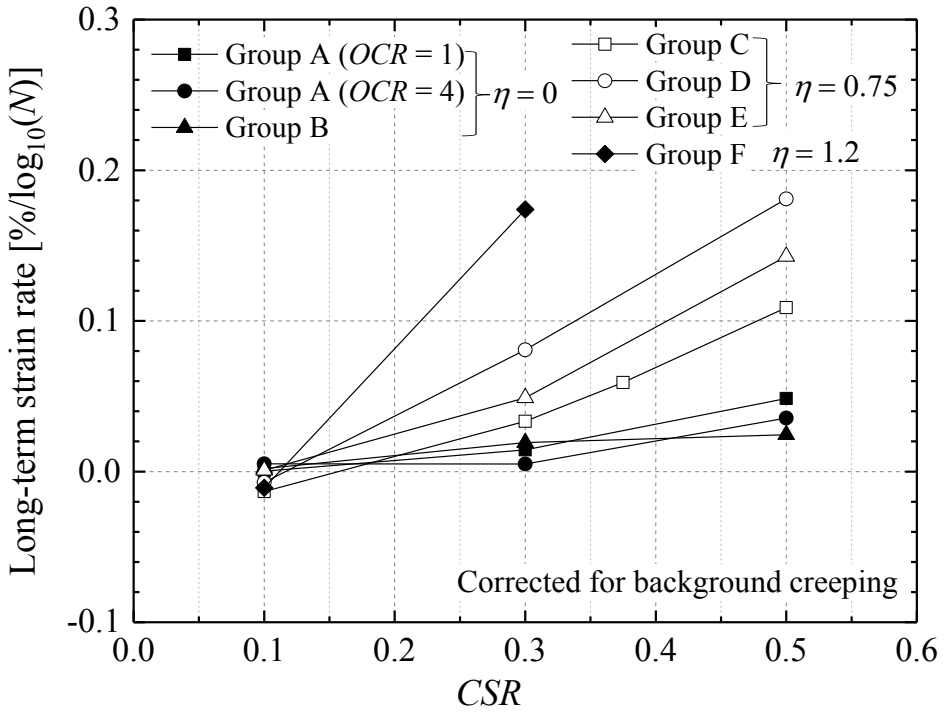

Figure 7-44 Long-term axial strain rates of the very dense (e_0 = 0.64, R_d = 92%) specimens after correcting for background creeping

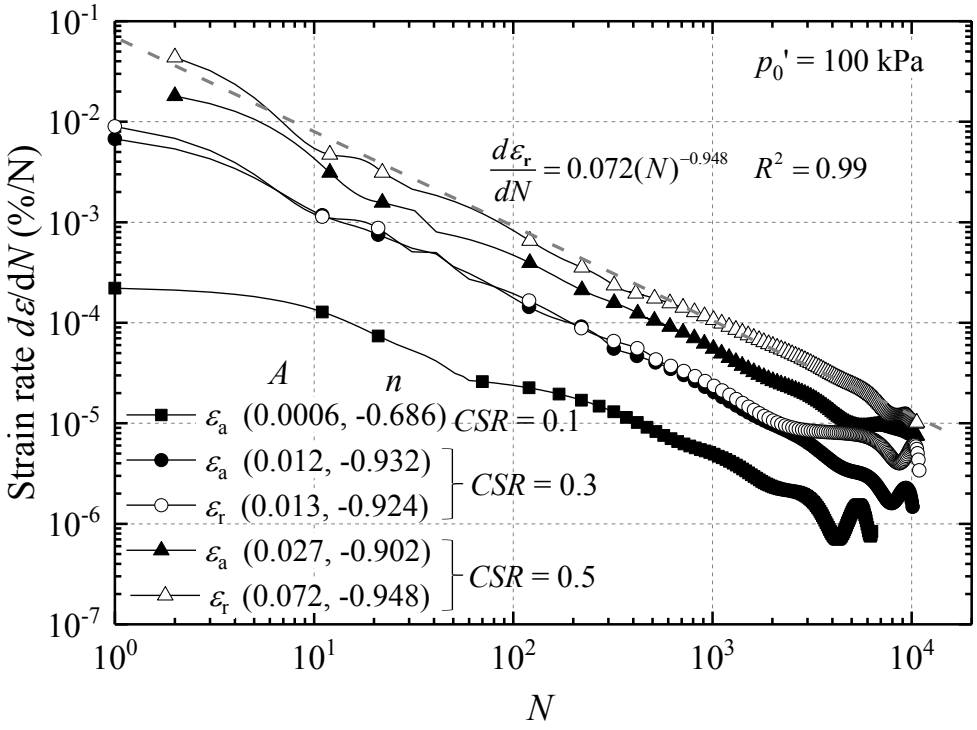

Figure 7-45 Strain accumulation rates of the very dense (R_d = 92%, e_0 ≈ 0.640) Group A tests (η = 0, (q_{mean}, p_0') = (0, 100) (kPa)), also indicating parameters A and n for best fitting $d\varepsilon^{acc}/dN = A(N)^n$ trends

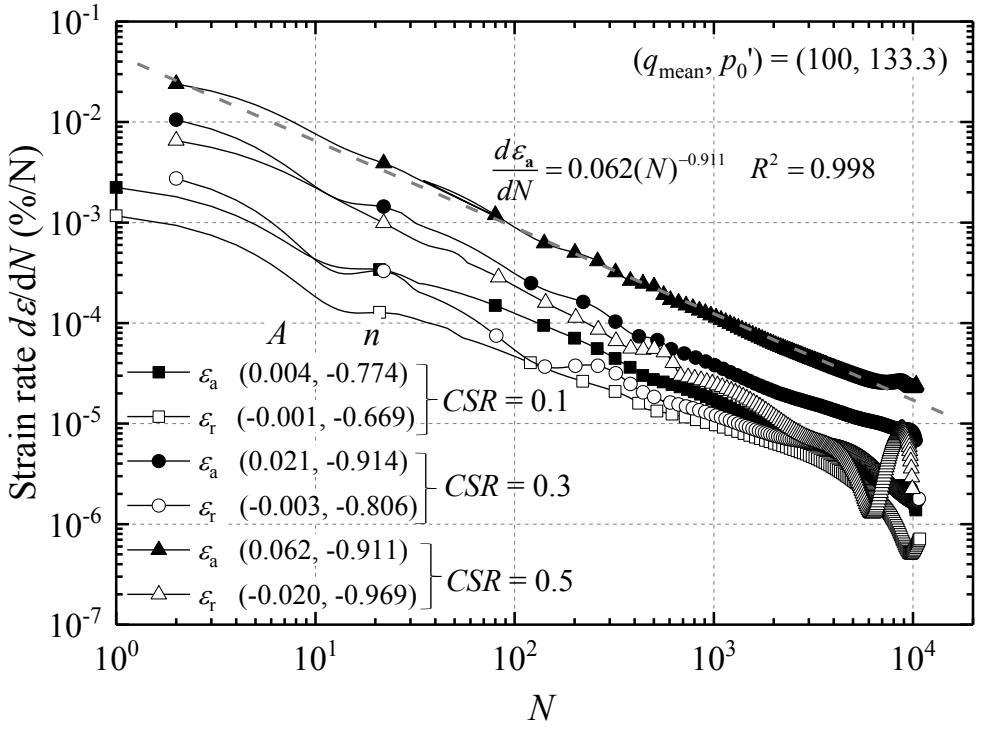

Figure 7-46 Absolute strain accumulation rates of the very dense (R_d = 92%, e_0 = 0.64) Group C tests (η = 0.75, (q_{mean}, p_0') = (100, 133.3) (kPa)), also indicating parameters A and n for best fitting $d\varepsilon^{acc}/dN = A(N)^n$ trends

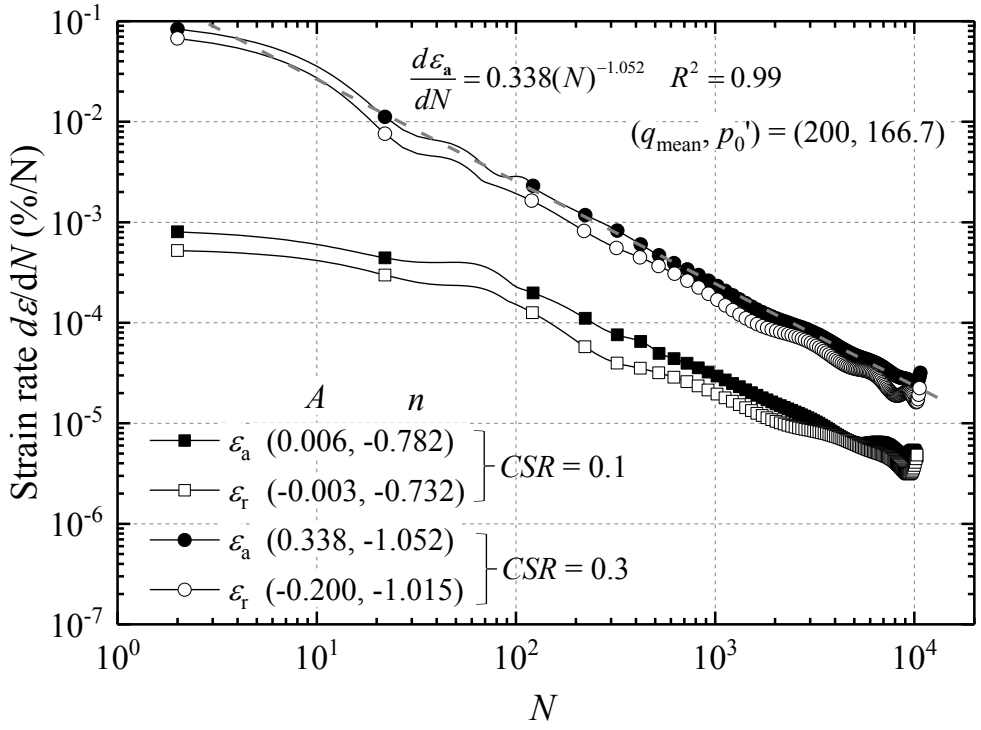

Figure 7-47 Strain accumulation rate of the very dense (R_d = 92%, e_0 = 0.64) Group F tests (η = 1.2, (q_{mean}, p_0') = (200, 166.7) (kPa)), also indicating parameters A and n for best fitting $d\varepsilon^{acc}/dN = A(N)^n$ trends

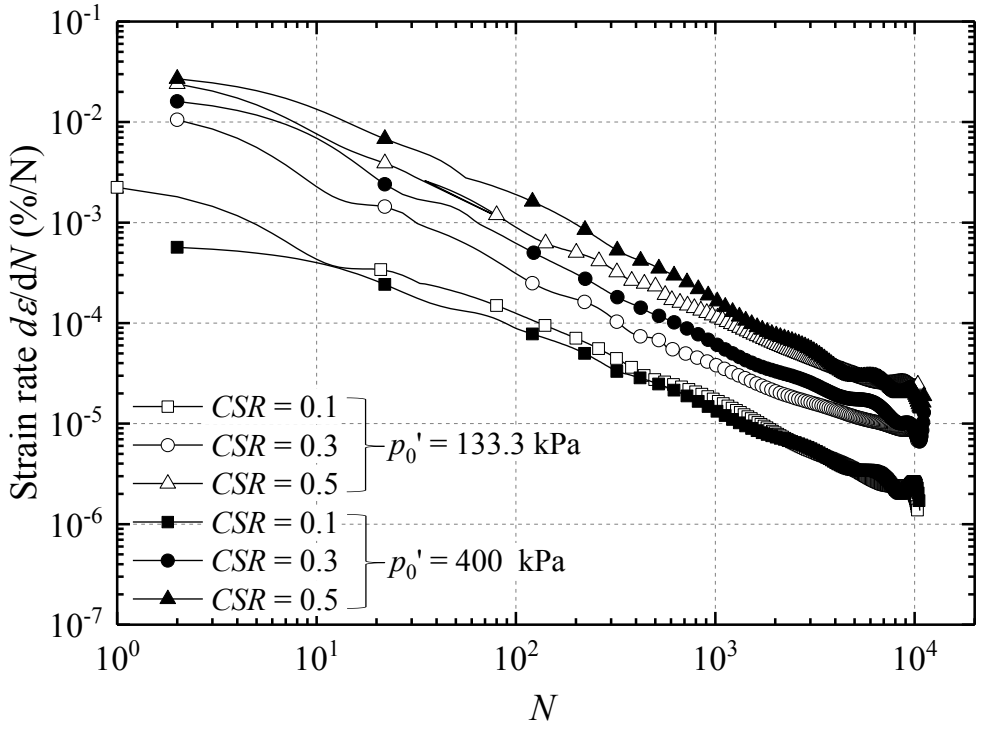

Figure 7-48 Axial strain accumulation rates of very dense Groups C and E specimens (R_d = 92%, e_0 = 0.64) (η = 0.75)

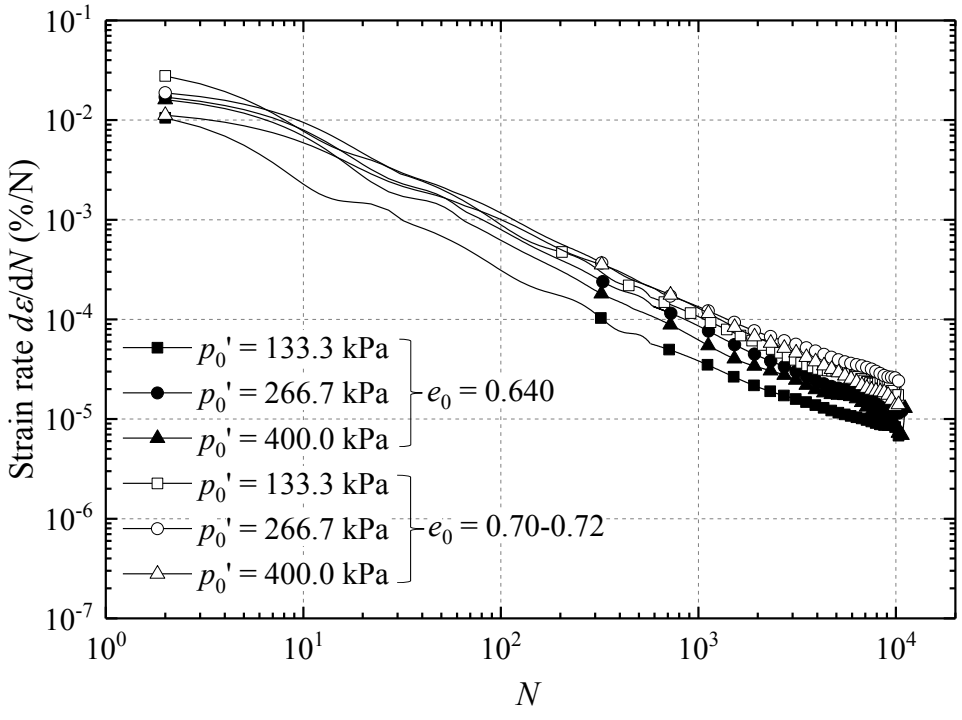

Figure 7-49 Effects of specimen density on cyclic axial strain rates (tests from Groups C, D and E with η = 0.75, CSR = 0.3)

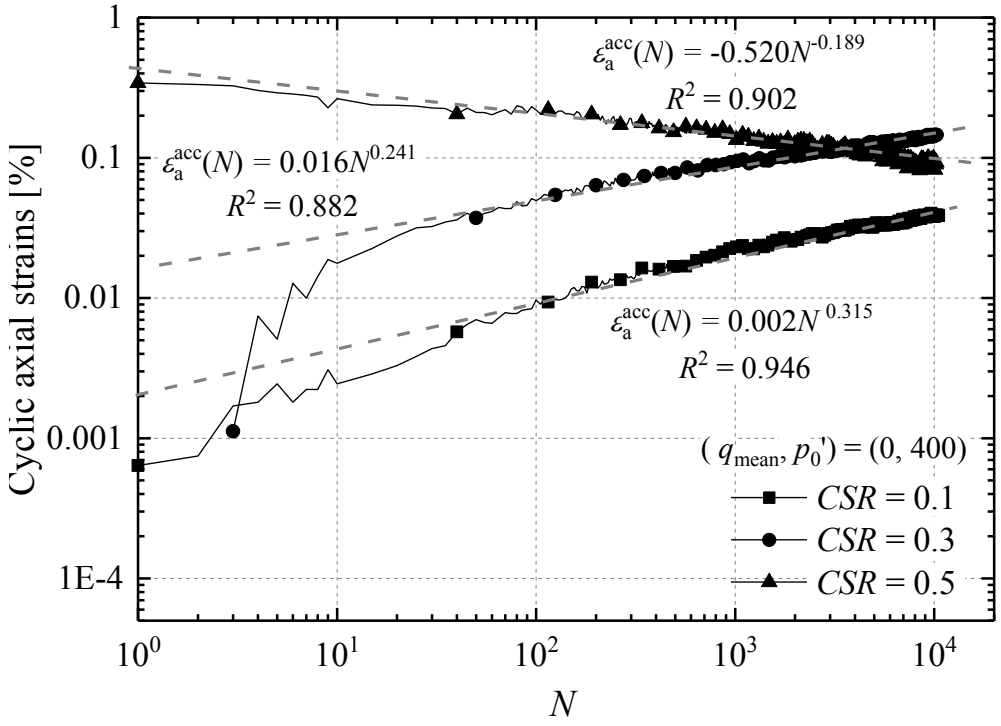

Figure 7-50 Cyclic axial strain trends for very dense (R_d = 92%) Group B ((q_{mean}, p_0') = (0, 400)) (kPa) tests on double-logarithmic scale

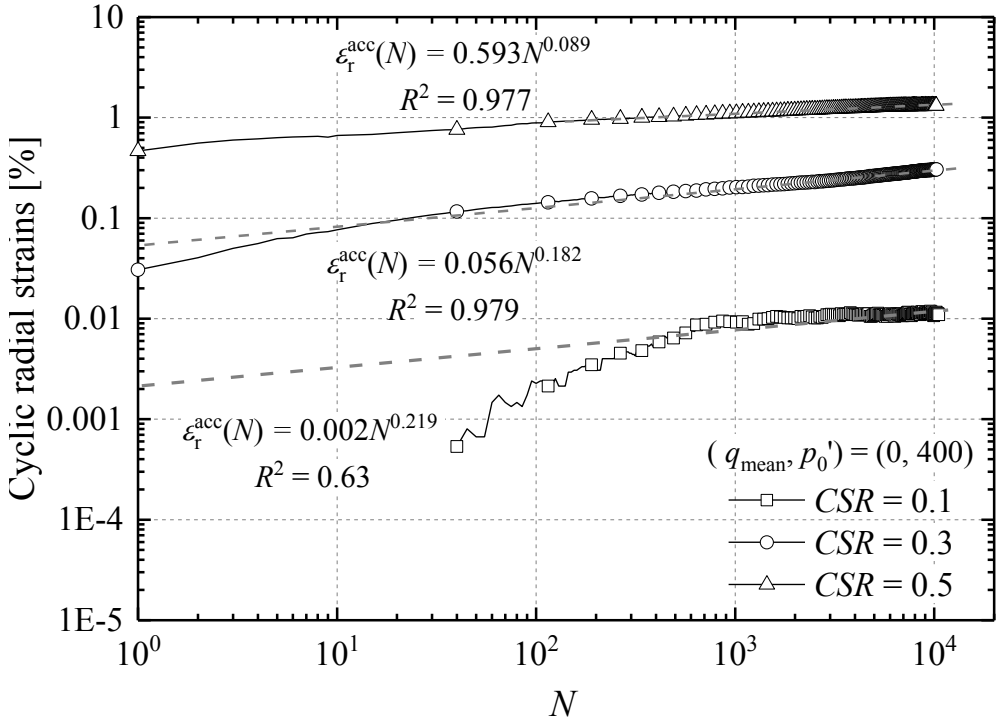

Figure 7-51 Cyclic radial strain trends for very dense (R_d = 92%) Group B ((q_{mean}, p_0') = (0, 400)) (kPa) tests on double-logarithmic scale

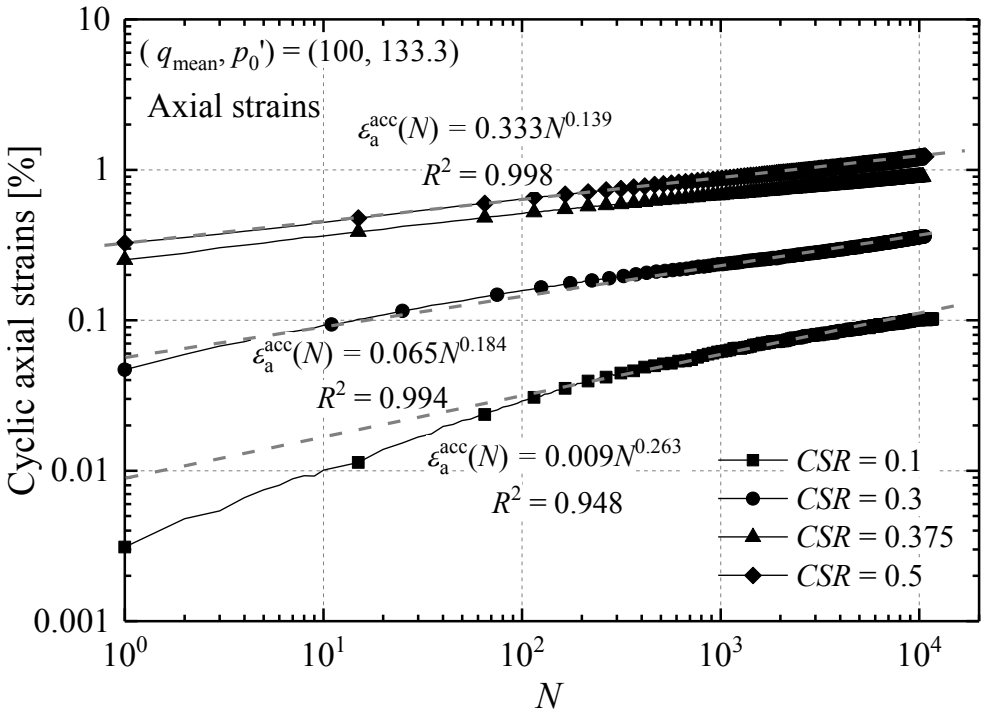

Figure 7-52 Cyclic axial strain trends for very dense (R_d = 92%) Group C ((q_{mean}, p_0') = (100, 133.3)) (kPa) tests on double-logarithmic scale

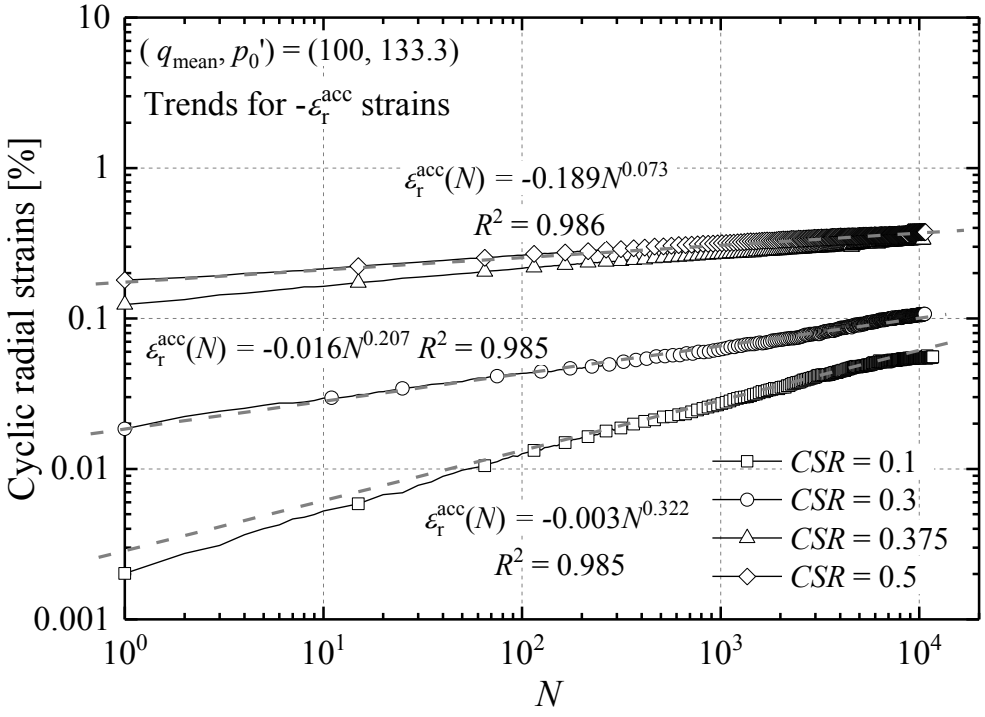

Figure 7-53 Cyclic radial strain trends for very dense (R_d = 92%) Group C ((q_{mean}, p_0') = (100, 133.3)) (kPa) tests on double-logarithmic scale

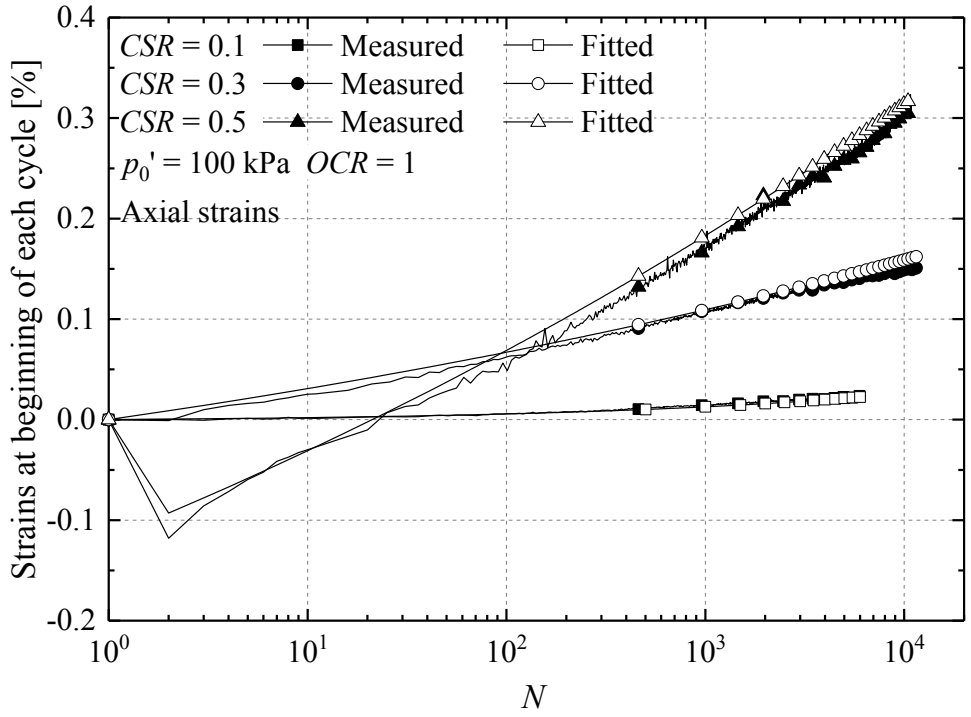

Figure 7-54 Comparison of the measured and fitted axial strains for Group A tests ($\eta = 0$, (q_{mean}, p_0') = (0, 100))

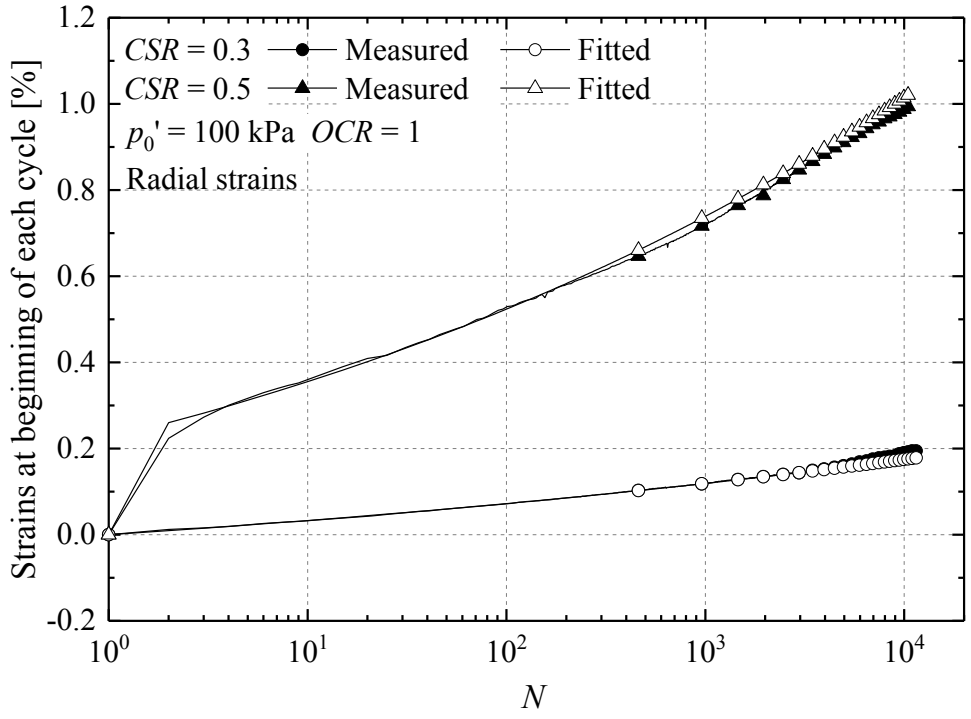

Figure 7-55 Comparison of the measured and fitted radial strains for Group A tests ($\eta = 0$, (q_{mean}, p_0') = (0, 100))

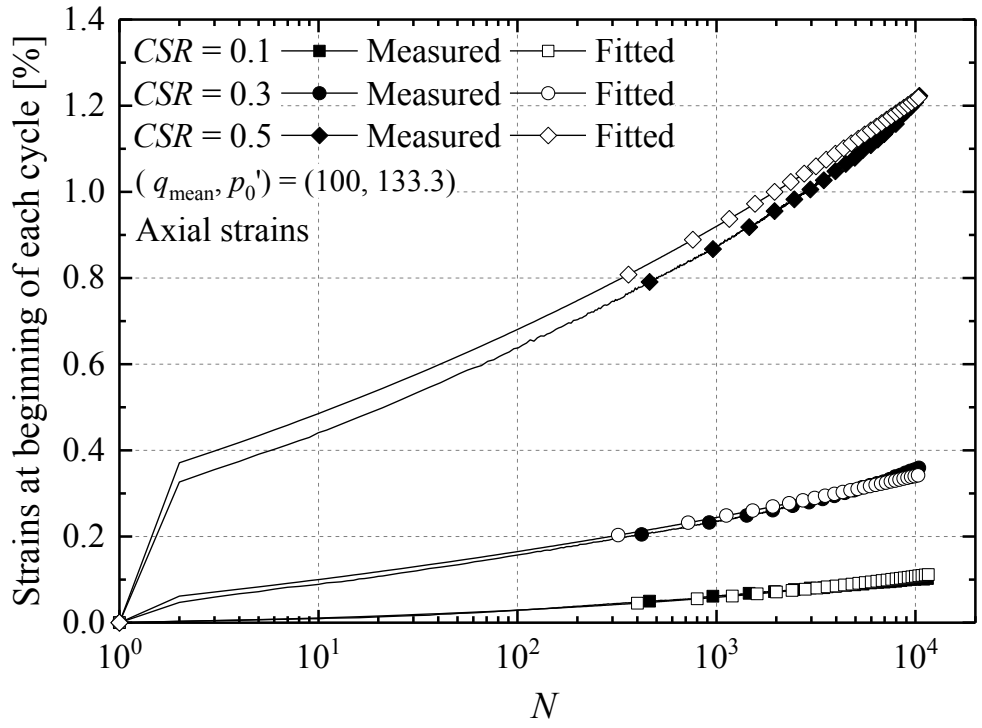

Figure 7-56 Comparison of the measured and fitted axial strains for Group C tests (η = 0.75, (q_{mean}, p_0') = (100, 133.3))

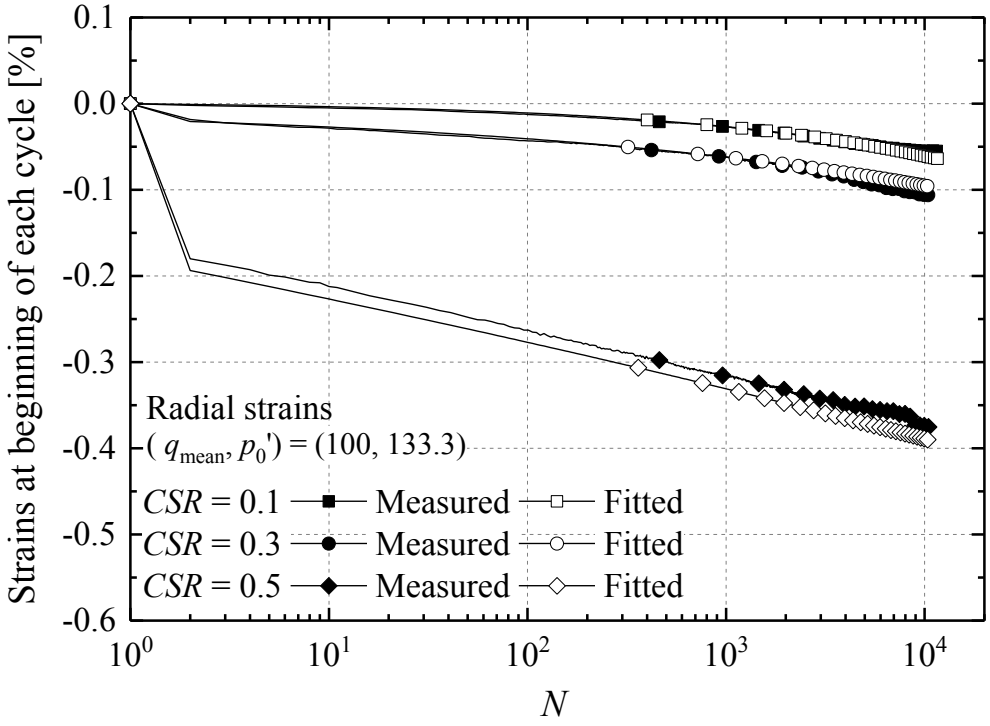

Figure 7-57 Comparison of the measured and fitted radial strains for Group C tests (η = 0.75, (q_{mean}, p_0') = (100, 133.3))

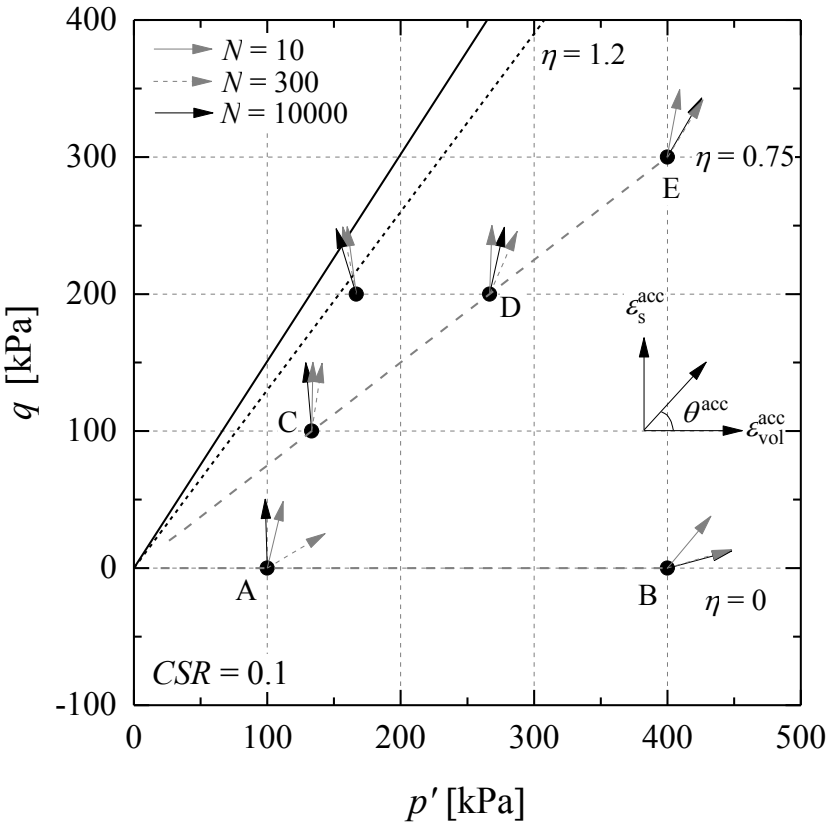

Figure 7-58 Directions of cyclic strain ratio of the specimens cycled with *CSR* = 0.1

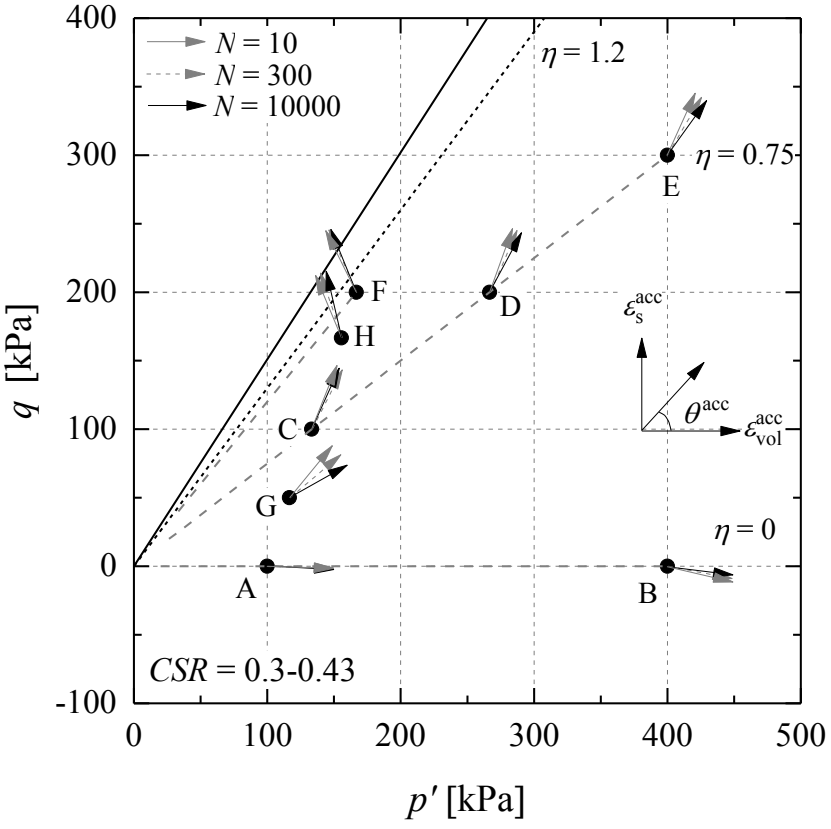

Figure 7-59 Directions of cyclic strain ratio of the specimens cycled with intermediate *CSR*s

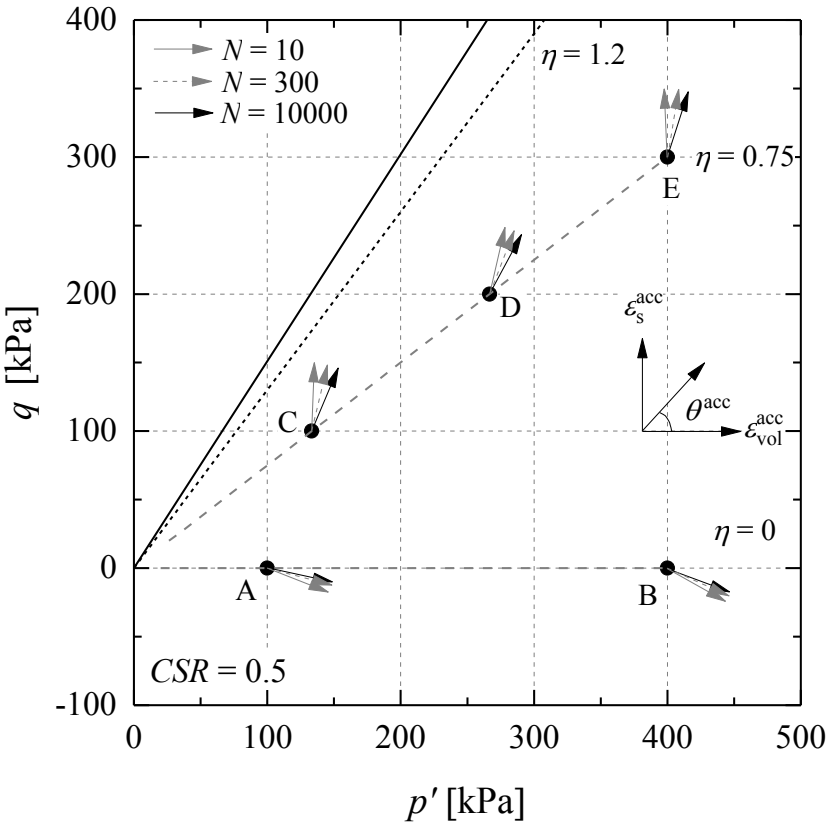

Figure 7-60 Directions of cyclic strain ratio of the specimens cycled with *CSR* = 0.5

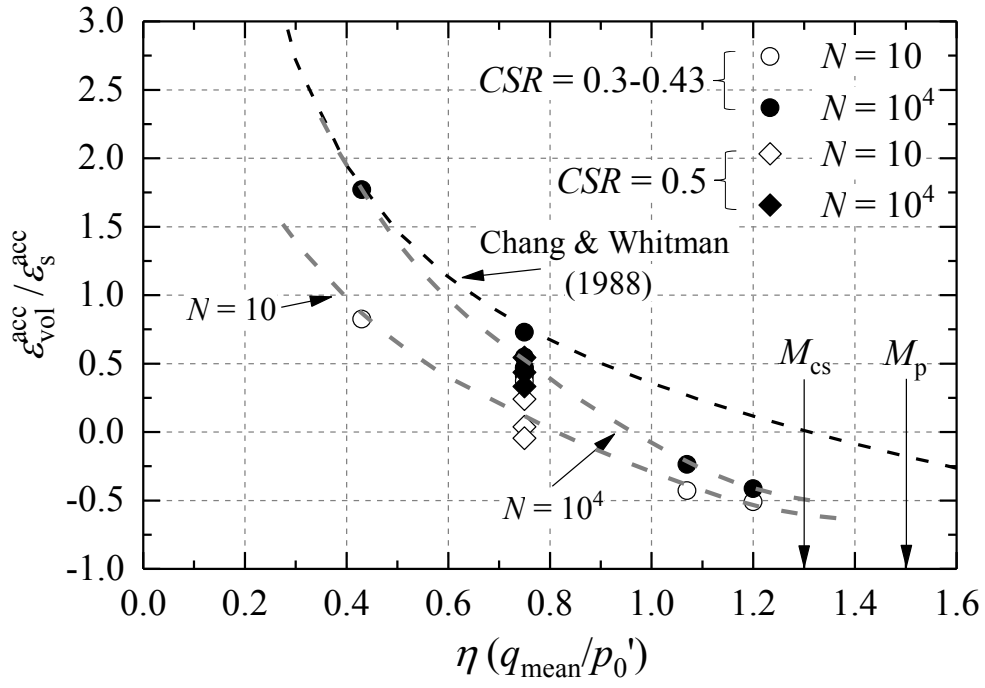

Figure 7-61 Cyclic dilation-stress ratio trends identified for high *CSR* tests

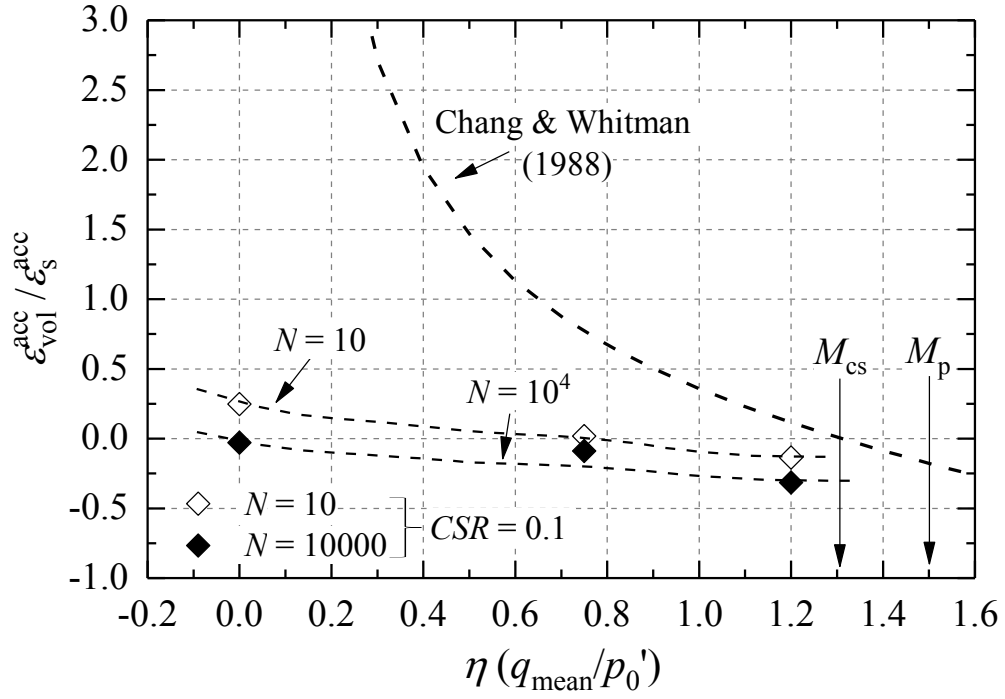

Figure 7-62 Cyclic dilation-stress ratio trends identified for low *CSR* tests

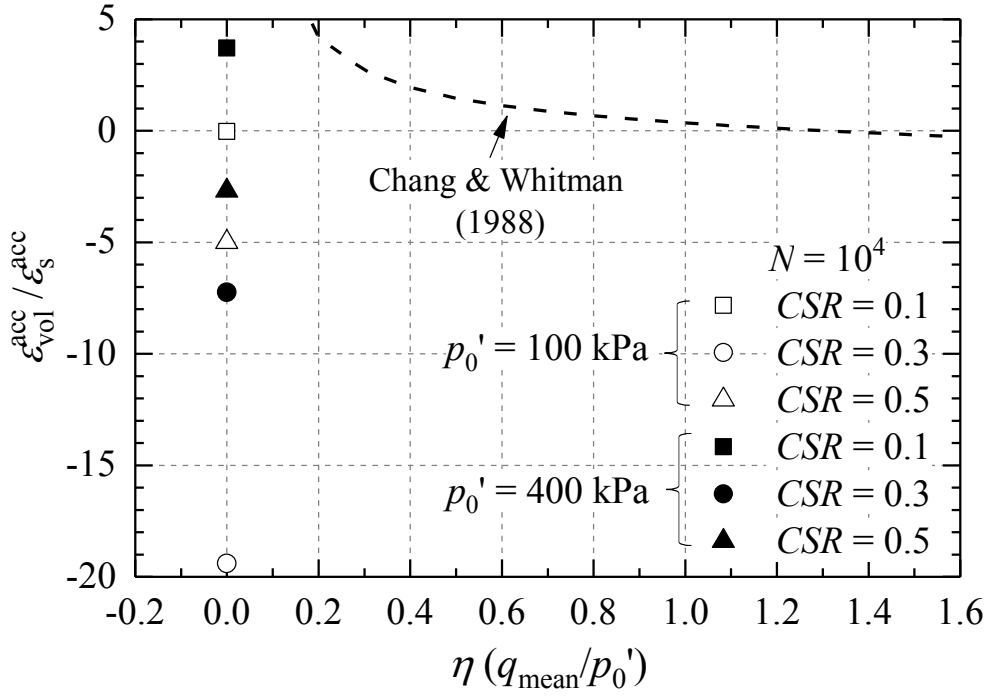

Figure 7-63 Cyclic dilation of the isotropically consolidated specimens ($\eta = 0$) after 10^4 shearing cycles

7.5 Void ratio changes generated by drained cyclic loading and their relationship to the CSL

The Dunkirk sand's volume change characteristics under long-term cyclic loading were further examined within the critical state framework established from monotonic experiments on the Batch 3 sand, which was discussed in Section 6.8.

Taking examples from test Groups A ($\eta = 0$, $p_0' = 100$ kPa), C ($\eta = 0.75$, $p_0' = 133.3$ kPa) and F ($\eta = 1.2$, $p_0' = 167$ kPa), Figures 7-64 to 7-66 plot the evolving trends of specimen void ratio change against number of shearing cycles under a range of loading *CSRs*. Figure 7-64 demonstrates how the specimen void ratios determined from local strain instruments and external volume-gauge compare, and highlights the potential errors in volume-gauge measurements due to long-term compliance issues, which led to the external data indicating nominally more dilatant trends. As discussed earlier, the mean cyclic stress ratio ($\eta = q_{mean}/p_0'$) affects the invariant strain vector $\varepsilon_s/\varepsilon_{vol}$. Significant contractive volume strains were generated under $\eta = 0$ conditions, while dilative straining occurred in the high η tests. The cyclic straining varied greatly with *CSR* levels, without showing any clear sign of reaching any convergent final volume trend.

Figure 7-67 plots the void ratio changes of the specimens cycled under sufficiently high *CSR*s for significant void ratio changes to develop. The start (open symbols) and end (solid symbols) of the tests performed under different mean cyclic stress ratio ($\eta = q_{mean}/p_0'$) ranges. The $\eta = 0$ specimens' void ratios trended sharply downwards from the CSL while the high η (= 1.2) tests dilated towards the CSL. Specimens tested under $\eta = 0.75$ showed relatively minor void ratio reductions compared to those of $\eta = 0$ tests. Overall, it appeared unfeasible to construct any steady state curve in e-p' space towards which the void ratios of the cyclic tests trended under the ranges of cyclic loading conditions applied by the Author.

Following the approach of López-Querol & Coop (2012), the changes of state parameter $\Delta\psi$ (= e_0 - e_{final}) (as defined in Section 6.2.2) of the $\eta = 0$ and 0.75 tests are plotted against initial state parameters ψ_0 (= e_0 - e_{cs}), as shown in Figures 7-68 and 7-69, respectively. Fitting trends are suggested tentatively to reflect the effects of mean cyclic stress ratio and *CSR* level.

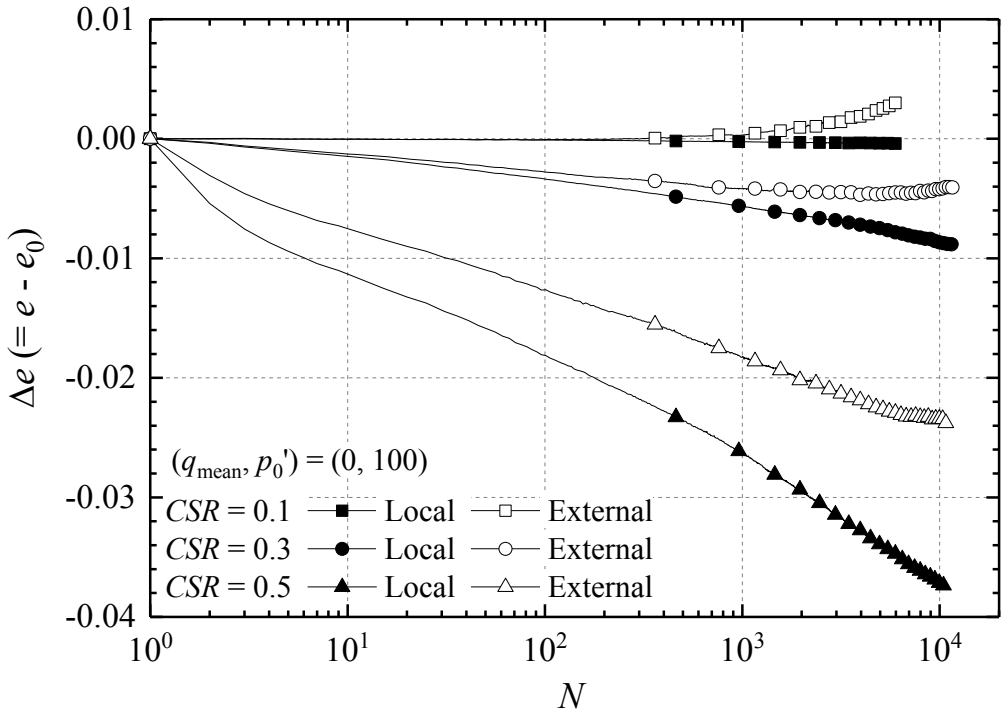

Figure 7-64 Void ratio change against cycle number for very dense (R_d = 92%, e_0 = 0.640) Group A tests (η = 0, (q_{mean}, p_0') = (0, 100) (kPa))

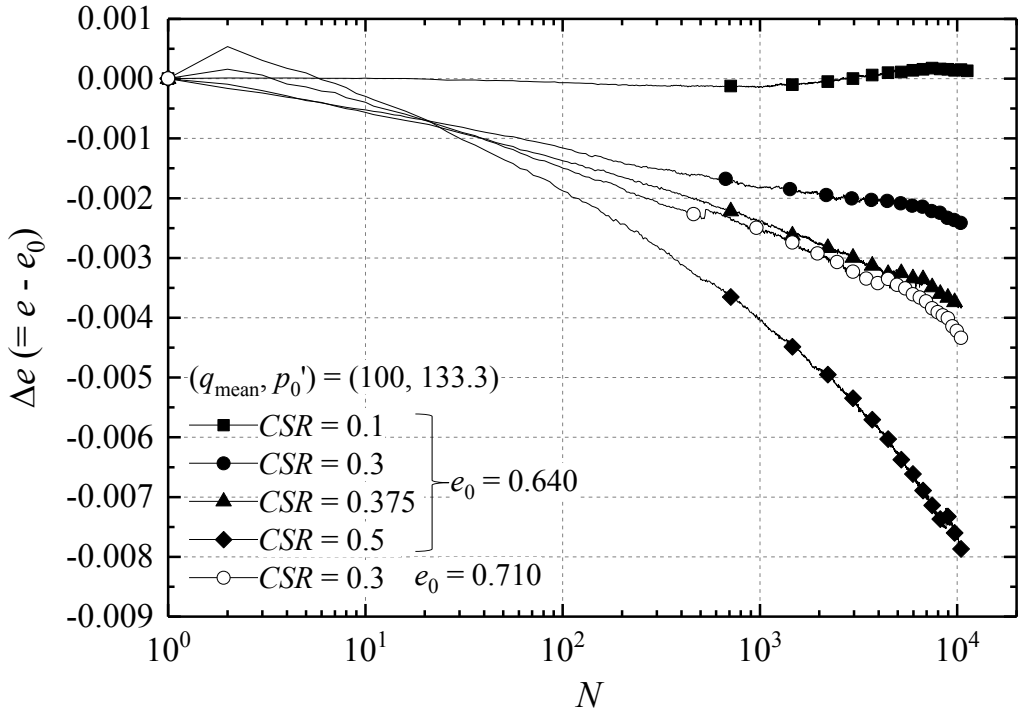

Figure 7-65 Void ratio change against cycle number for Group C tests (η = 0.75, (q_{mean}, p_0') = (100, 133.3) (kPa))

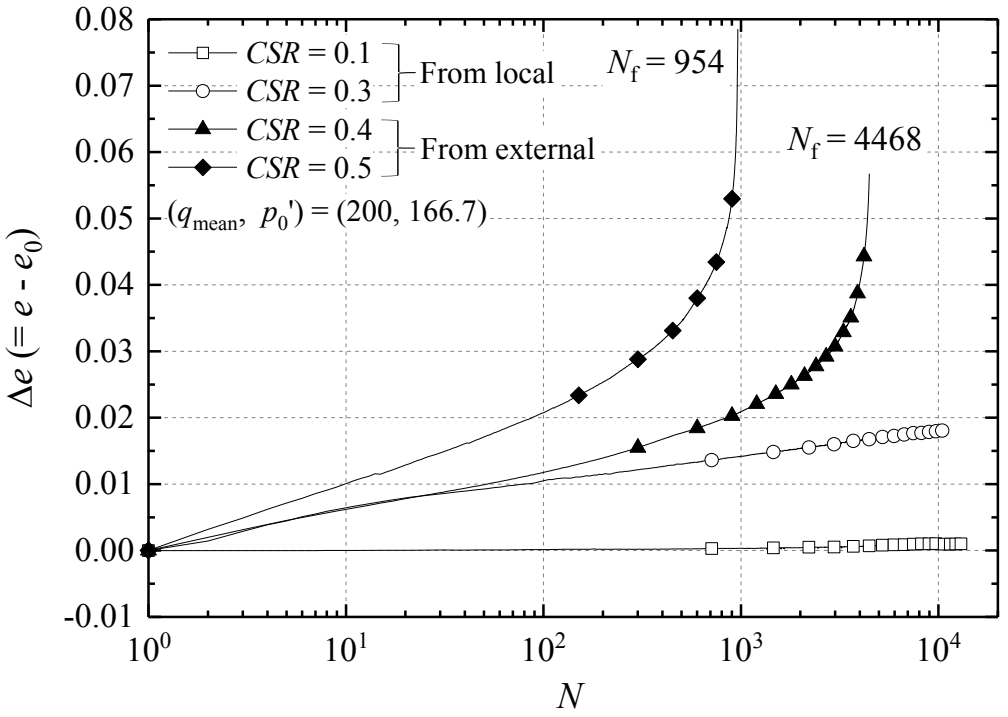

Figure 7-66 Void ratio change against cycle number for very dense (R_d = 92%, e_0 = 0.640) Group F tests (η = 1.2, (q_{mean}, p_0') = (200, 166,7) (kPa))

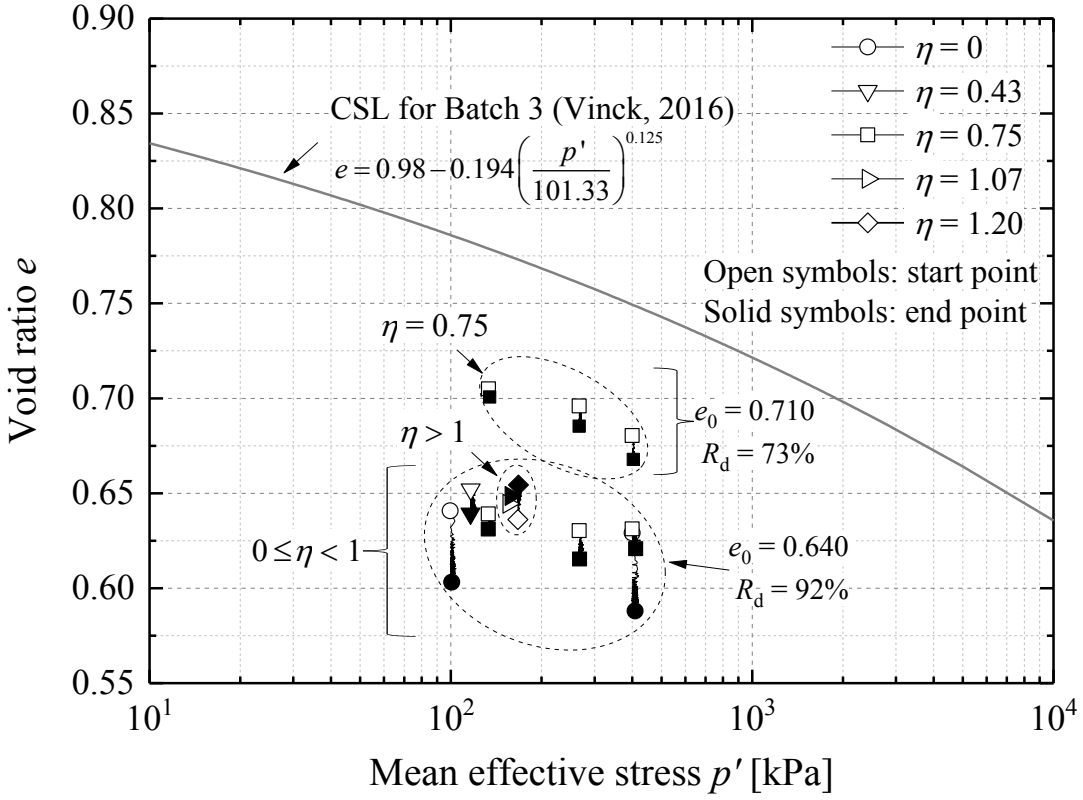

Figure 7-67 Void ratio change of sand specimens cycled with high *CSR*s

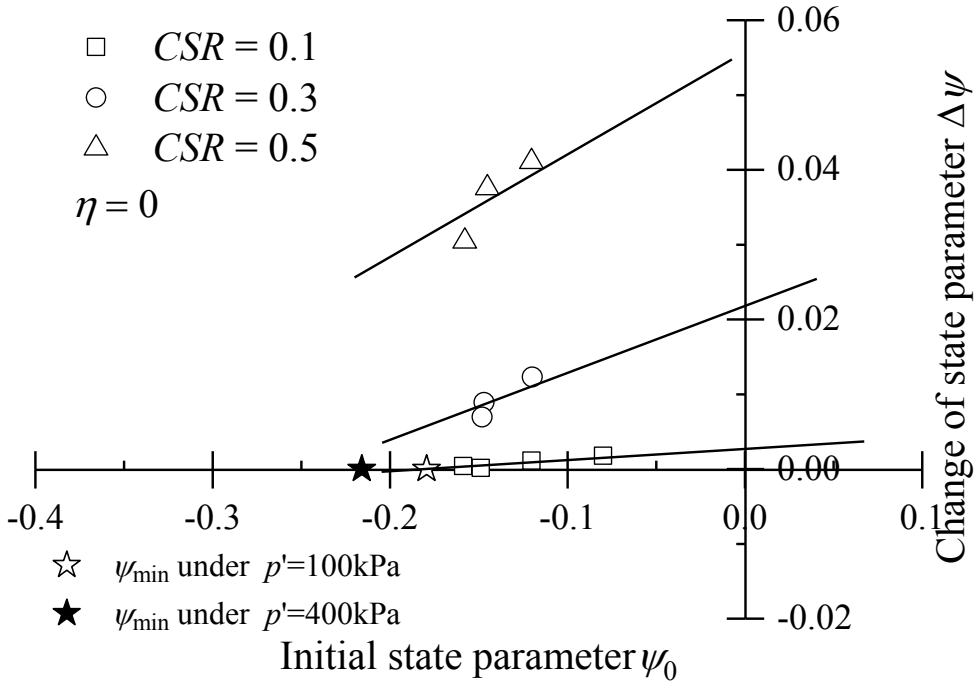

Figure 7-68 State parameter changes of the η = 0 tests (R_d = 92%, e_0 = 0.640)

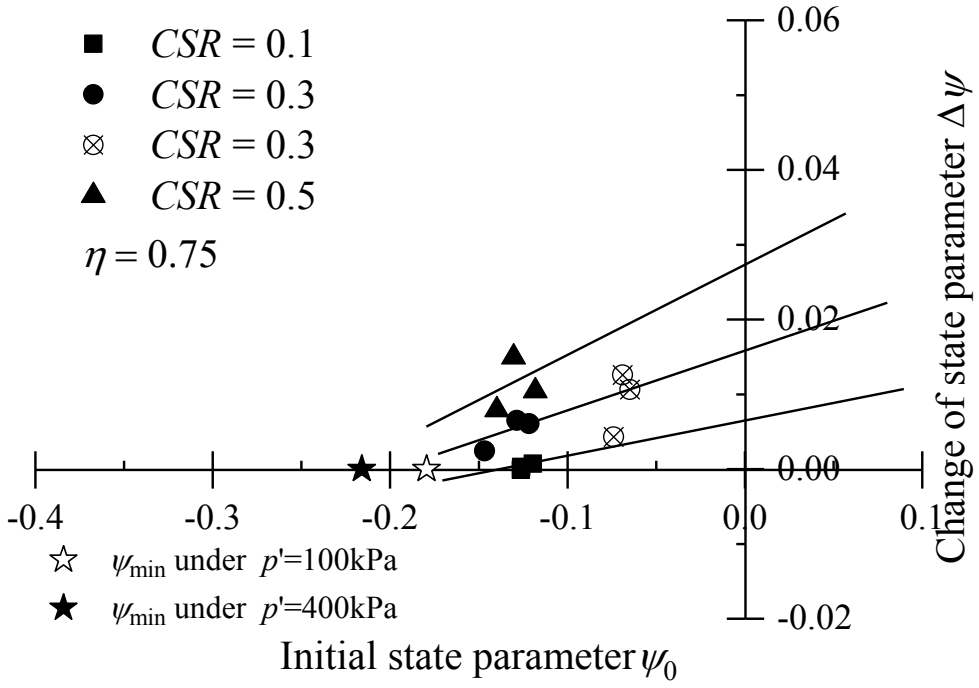

Figure 7-69 State parameter changes of the η = 0.75 tests (R_d = 73% or 92%)

7.6 Cyclic strain amplitude observations

The discussion in the previous two sections centred on permanent strain accumulation. Characterisation of the cyclic strain amplitudes is also important. The peak (ε^{peak}) and trough (ε^{trough}) axial and radial strains for each shearing cycle were identified and their differences (ε_a^{peak}- ε_a^{trough}, ε_r^{peak}- ε_r^{trough}) were considered as double the cyclic strain amplitudes (or peak-to-trough amplitudes).

Taking the outcomes from test Groups A (η = 0, p_0' = 100 kPa), B (η = 0, p_0' = 400 kPa) and C (η = 075, q_{mean} = 100 kPa, p_0' = 133.3 kPa) as examples, Figures 7-70 to 7-72 demonstrate how strain amplitudes varied with the number of cycles.

The strain amplitudes are highly dependent of the stress ratio and *CSR* level. Naturally, tests cycled with higher *CSR*s exhibited consistently higher strain amplitudes than those of the lower *CSR* tests. Unlike the cyclic average strain accumulation rates which degraded constantly during shearing, the strain amplitudes mostly tended to decrease markedly and reach stable plateaux after 10-100 shearing cycles. The cyclic radial strain amplitudes were consistently lower than the axial equivalents.

The cyclic strain amplitudes were also affected by specimen density, *OCR* and effective stress level. Figure 7-73 demonstrates the expected trend for the denser (R_d = 92%) specimens to develop lower strain amplitudes, while the axial strain amplitudes of the over-consolidated specimens were consistently lower than those observed with the normally consolidated specimens, as shown in Figure 7-74, confirming that the over-consolidation (as well as prior *K*-consolidation) enhanced stiffness in the axial direction. Figure 7-75 further reveals the dependency of cyclic strain amplitude on effective stress levels, with higher p_0' invariably resulting in greater strain amplitudes under equivalent *CSR* conditions, which is inevitable if soil stiffness rises with $(p')^n$ and $n < 1$, as is usually the case with sands.

The deviator stress-strain response seen in each cycle of the stress-controlled cyclic tests provided sufficient data to characterise stress-strain loops and cyclic stiffness behaviour. As detailed in the next section, it is convenient to consider the axial cyclic strains through the corresponding variations of cyclic stiffness that was observed in each experiment.

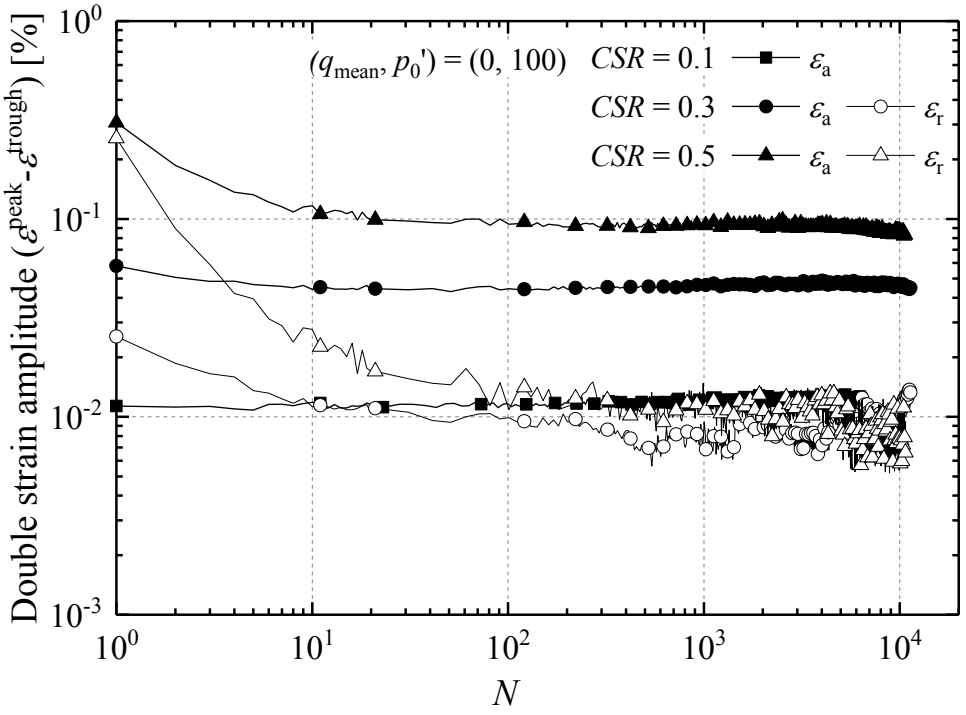

Figure 7-70 Double cyclic strain amplitude (ε^{peak}-ε^{trough}) against number of cycles of the Group A tests (R_d = 92%, e_0 = 0.640) (η = 0, (q_{mean}, p_0') = (0, 100) (kPa))

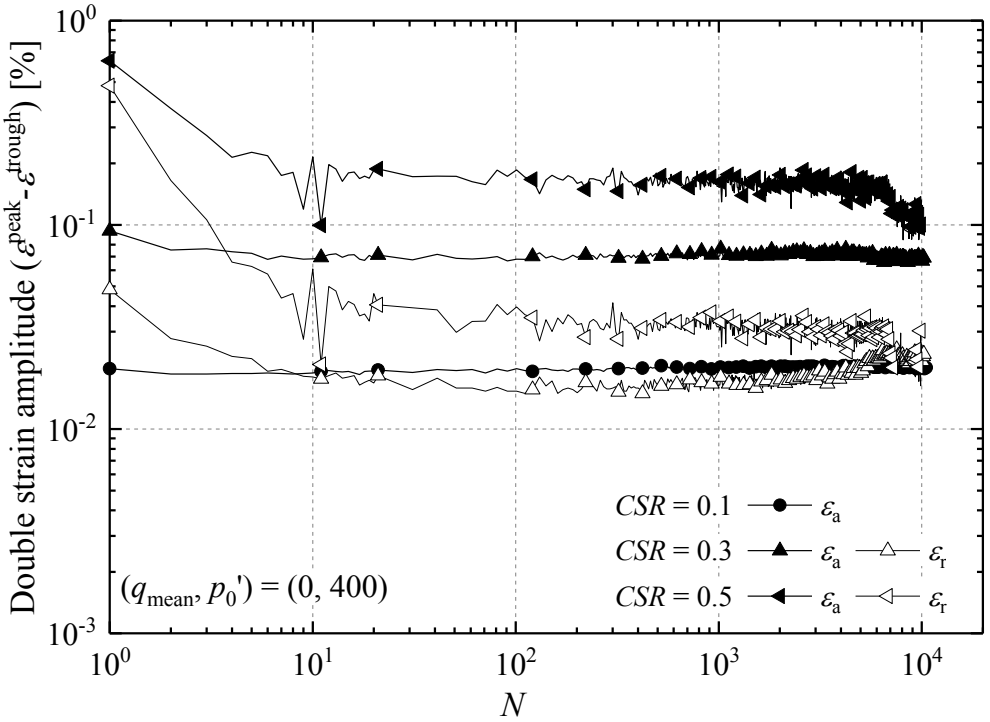

Figure 7-71 Double cyclic strain amplitude (ε^{peak}-ε^{trough}) against number of cycles of the Group B tests (R_d = 92%) (η = 0, (q_{mean}, p_0') = (0, 400) (kPa))

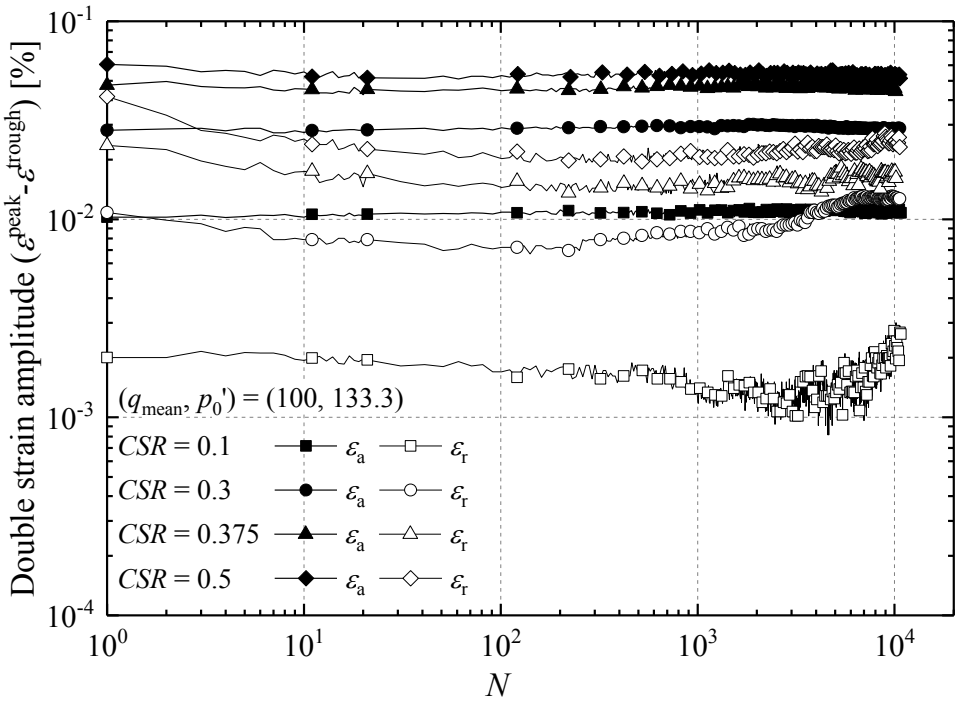

Figure 7-72 Double cyclic strain amplitude (ε^{peak}-ε^{trough}) against number of cycles of the Group C tests (R_d = 92%, e_0 = 0.640) (η = 0.75, (q_{mean}, p_0') = (100, 133.3) (kPa))

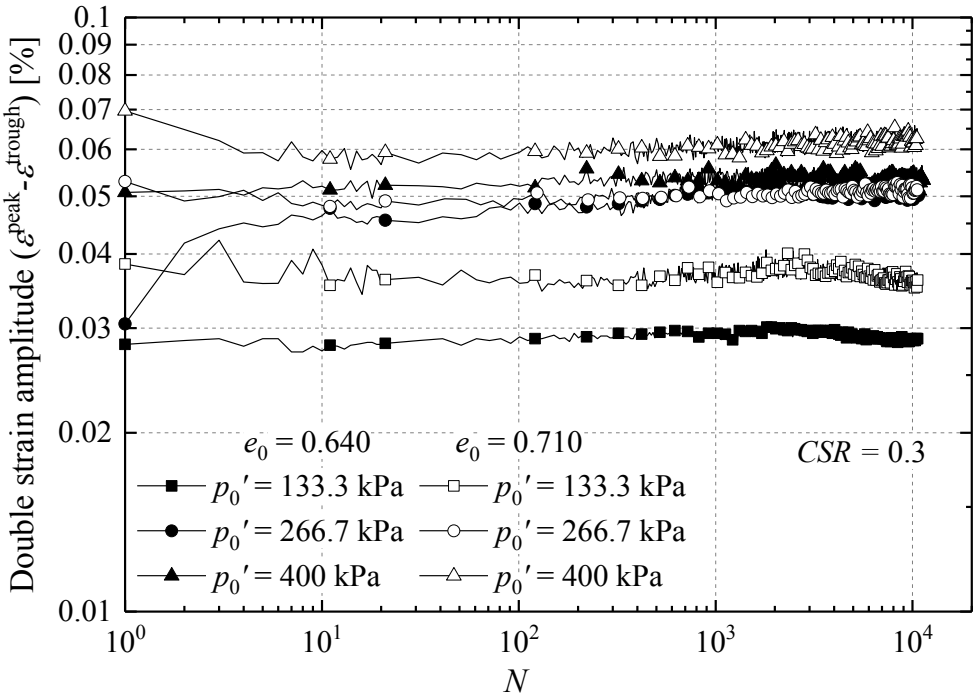

Figure 7-73 Effects of specimen density on cyclic axial strain amplitudes (tests from Group C, D and E with η = 0.75 and CSR = 0.3)

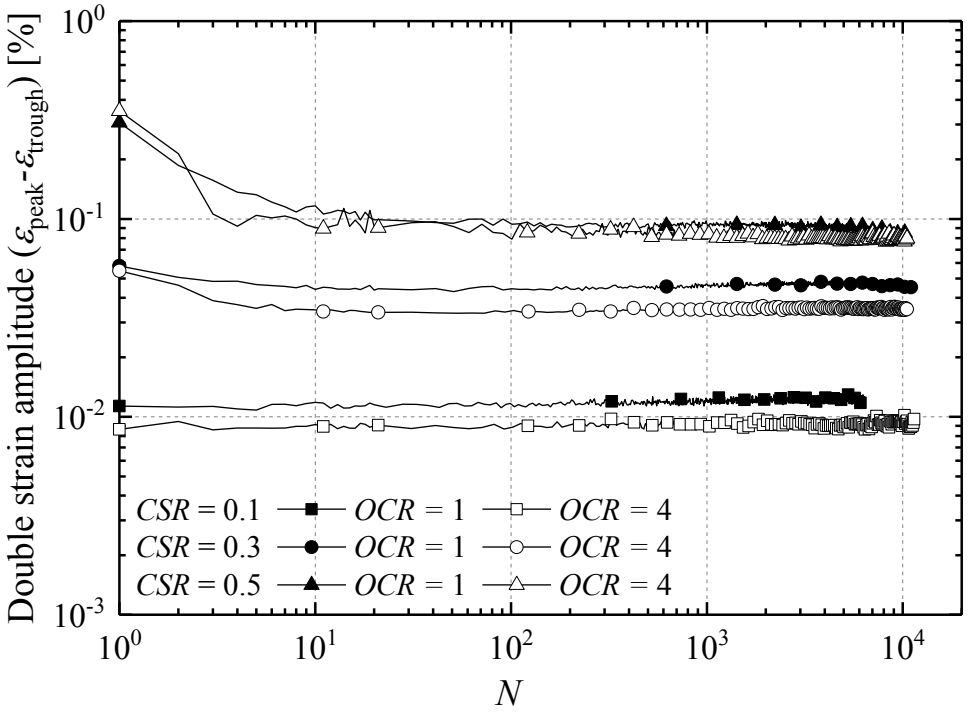

Figure 7-74 Double axial strain amplitudes of the normally consolidated Group A and over-consolidated Group A-OC(4) specimens (R_d = 92%) (η = 0, (q_{mean}, p_0') = (0, 100) (kPa))

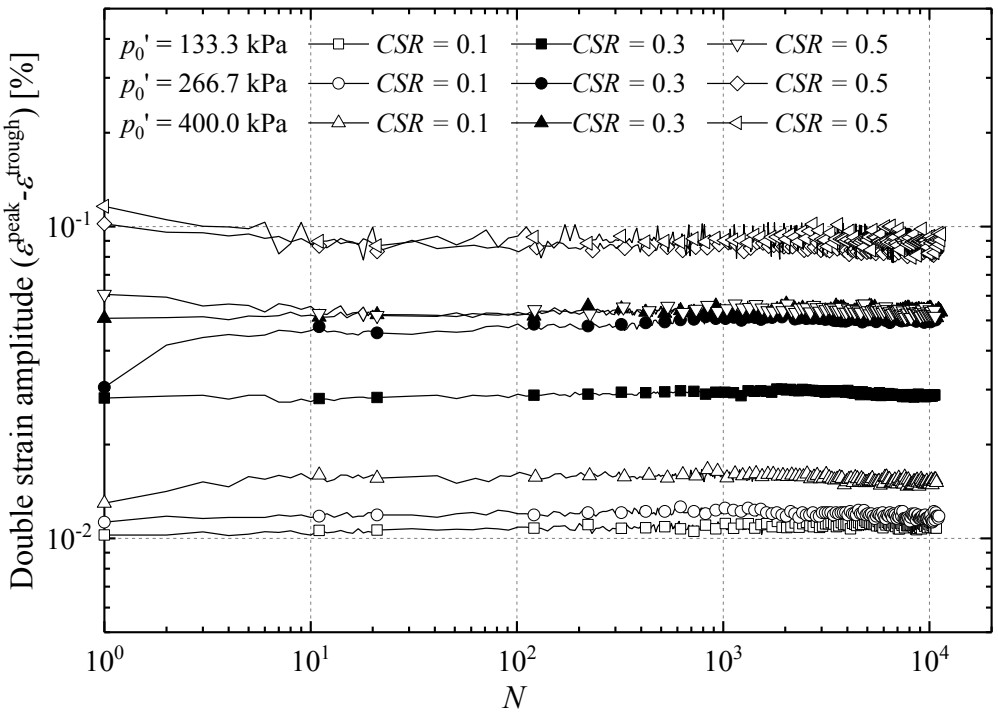

Figure 7-75 Effects of effective stress level (p_0') on axial strain amplitude of Group C, D and E tests (R_d = 92%, e_0 = 0.640) ($\eta = q_{mean}/p_0'$ = 0.75)

7.7 Cyclic stiffness evolution and cyclic thresholds

The following paragraphs summarise the cyclic stress-strain and stiffness behaviour observed in the Author's tests. Cyclic thresholds are identified based on both cyclic stiffness and the accumulated axial cyclic strain trends discussed in Section 7.4.

7.7.1 Cyclic shear stress-strain response

Taking as an example one Group A (η = 0, (q_{mean}, p_0') = (0, 100)) experiment that imposed CSR = 0.3 (q_{cyc} = 30 kPa), Figure 7-76 shows the individual stress-strain loops recorded over the N = 1, 30, 100, 300, 1000, 3000 and 10000 cycles. In this particular case, both the axial and radial strains showed compressive trends as cycling progressed. The stress-strain loops inscribed their largest area over the first cycle and this area gradually decreased in width as shearing evolved, but did not reduce to zero. Nor did the strain loops close or converge fully after up to 10000 cycles, demonstrating continuingly plastic aspect of stress-strain response and ratcheting behaviour.

As discussed by Ushev (2018) in relation to the parallel tests on Cowden till, the recorded stress-strain data also provide sufficient information to investigate the energy dissipation and damping characteristics of the sand during long-term cycling, although this has yet to be implemented for the Dunkirk sand.

7.7.2 Secant cyclic stiffness and evolving trends

Secant vertical cyclic stiffness (E_v^{cyc}) can be defined as the stiffness developed over the half cycles of unloading and loading, as illustrated in Figure 7-77 by the following measures.

$$E_{N,sec}^{unloading} = \frac{q_{max}^{N} - q_{min}^{N}}{\varepsilon_{q,max}^{N} - \varepsilon_{q\_min}^{N}} \tag{7.10}$$

$$E_{N,sec}^{loading} = \frac{q_{min}^{N} - q_{max}^{N+1}}{\varepsilon_{q,min}^{N} - \varepsilon_{q,max}^{N+1}} \tag{7.11}$$

Where $\varepsilon_{q,max}$ and $\varepsilon_{q,min}$ are the axial strains at the maximum and minimum deviatoric stress in each stress cycle, respectively. It should be noted that, as illustrated in Figure 7-20, due to the non-linear and viscous nature of the soils, the $\varepsilon_{q,max}$ and $\varepsilon_{q,min}$ at shearing cycle N might not correspond simultaneously to the peak and trough axial strains ($\varepsilon_{a,peak}$, $\varepsilon_{a,trough}$) in that stress cycle. Stiffnesses determined from the maximum

and minimum deviatoric stresses (q_{max} and q_{min}) and the corresponding axial strains ($\varepsilon_{q,max}$ and $\varepsilon_{q,min}$) are denoted as $E_{v,q}^{cyc}$. The $\varepsilon_{a,peak}$ and $\varepsilon_{a,trough}$ of each cycle and the corresponding deviatoric stresses ($q_{a,peak}$ and $q_{a,trough}$) were recorded, and the secant stiffnesses over the largest axial strain range (i.e. strain amplitude range) are denoted as $E_{v,\varepsilon}^{cyc}$.

Figure 7-78 demonstrates how the trends of secant cyclic stiffnesses vary according to the approaches adopted, particularly over the initial 100 shearing cycles. Remarkable differences can be noted between the unloading and loading stiffnesses that the unloading trends are located above the loading trends and degrade with shearing cycles, contrasting with the loading stiffnesses that increase over the initial shearing cycle. As cycling continues, the strain increments developed between consecutive shearing cycles decrease and the unloading and loading trends tend to converge, as noted earlier by Ushev (2018) in his cyclic tests on Cowden till.

The differences between the cyclic stiffnesses based on deviatoric stresses ($E_{v,q}^{cyc}$) and axial strains ($E_{v,\varepsilon}^{cyc}$) varied with effective stress level and *CSR*. The results and interpretation presented below are based on the $E_{v,q}^{cyc}$ stiffness measure.

***Cyclic secant stiffness evolution of the test Groups A and B* ($q_{mean} = 0$)**

The trends of cyclic secant stiffness against number of cycles are summarised in Figures 7-79 to 7-81 for test Groups A, A-OC(4) ($\eta = 0$, (q_{mean}, p_0') = (0, 100)) and B ($\eta = 0$, (q_{mean}, p_0') = (0, 400)). A general trend can be observed that cycling at *CSR* of 0.1 led to the secant cyclic stiffness remaining almost constant up to $N = 100$, followed by only slightly decreases as shearing continued. In the cases of *CSR* of 0.3 and 0.5, the initial cyclic secant stiffnesses were lower than seen at *CSR* = 0.1, reflecting the non-linear behaviour explored for monotonic test conditions in Chapter 5. However, the stiffness gradually rose as cyclic shearing continued, reflecting enhanced fabrics formed within the specimens.

The comparison between the normally and over-consolidated samples on Figure 7-80 also highlights the effects of effective stress history. The *K*-consolidated *OCR* = 4 samples present consistently higher cyclic stiffnesses than the isotropically and normally consolidated equivalent specimens over the *CSR*s considered.

Axial cyclic stiffness depends primarily on vertical effective stress level and specimen density, as shown by comparing the Group A tests at p_0' = 100 kPa and those

from Group B with p_0' = 400 kPa. At equivalent *CSR*s, the initial secant cyclic stiffnesses of the Group B samples were around double those of the Group A samples, indicating that broadly, cyclic stiffness grows in proportion to $(\sigma_v'/p_r)^{0.5}$.

Cyclic secant stiffness evolution of the test Groups C, D and E ($\eta = q_{mean}/p_0' = 0.75$)

The cyclic secant stiffness evolution trends of test Groups C, D and E are shown in Figures 7-82 to 7-84. For clarity, only the loading stiffness trends are presented. The general evolving patterns are similar to those in the above Groups A and B: relatively stable cyclic secant stiffness trends were reached after the initial 10-100 shearing cycles.

The very dense (R_d = 92%, $e_0 \approx 0.640$) Group C tests with (q_{mean}, p_0',) = (100, 133.3) showed less dependency on *CSR* with the trends condensing into a relatively narrow stiffness range of 250-300 MPa, although only the *CSR* = 0.1 test showed stable stiffnesses over the first 10 to 100 cycles. The cyclic stiffness of the less dense samples (R_d = 73%, $e_0 \approx 0.710$) was located below those of the very dense samples. In test Groups D and E, the cyclic stiffnesses under the *CSR* = 0.1 condition were clearly higher than those under *CSR*s = 0.3 and 0.5, while again no clear differences were observed under the two higher *CSR* conditions.

Cyclic secant stiffness evolution of the test Groups F ($\eta = q_{mean}/p_0' = 1.2$)

Figure 7-85 summarises the loading cyclic stiffnesses from test Group F (η = 1.2, (q_{mean}, p_0') = (200, 167)). Here, the cyclic stiffnesses were more strongly affected by *CSR*, with the *CSR* = 0.1 test again being the only case that was stable over the first 100 cycles. It is interesting to note that the stiffnesses shown in the high *CSR* tests, which failed before reaching 10^4 cycles, remained broadly steady until shortly before failure occurred through an incremental collapse mechanism. The latter differs from that seen in undrained cyclic tests, which often manifest still more abrupt sample deformation and stiffness loss as they approach failure.

Cyclic secant stiffness trends of tests with different stress ratio

The stiffness trends of the tests involving identical σ_h' (=100 kPa) and q_{cyc} (= 50 kPa) levels but a range of mean cyclic stress ratios ($\eta = q_{mean}/p_0'$) from 0 to 1.2 are summarised in Figure 7-86. The stiffness trends reflected the combined effects of axial stress (σ_v') and *CSR* level, leading to secant stiffnesses that increased with the increase

of η.

Normalised cyclic stiffness

It is useful to assess the cyclic stiffnesses $E_{v,q}^{cyc}$ in normalised terms. The cyclic stiffnesses developed during loading stages were considered as they were in accordance with the direction of axial cyclic strain accumulation. The normalisation involves first dividing by the void ratio function $f(e)$ (=$(2.17\text{-}e)^2/(1+e)$. In a second stage the $E_{v,q}^{cyc}$ data were normalised by the linear elastic Young's moduli (E_{v0}') observed in monotonic tests conducted or extrapolated for the corresponding mean cycling points, employing the $E_{v,tan}/f(e)\text{-}C_v\times(\sigma_v'/p_r)^{a_v}$ relationships established in Chapter 5 for Batch 3 sand. Both the void ratio variations and differences in σ_v' were accounted for in these treatments.

However, it is important to recall that, as discussed in Section 5.9, the constant stress ratio (q/p') triaxial probing tests on Batch 3 Dunkirk sand revealed a moderate dependency of the axial elastic stiffness constants (C_v and a_v) on q/p' ratio, showing that the assumptions implicit in Equation (5.1) and (5.2) are not completely validated. C_v increased from 143.0 MPa under isotropic condition ($q/p' = 0$) to 170 MPa under quasi-K_o condition ($q/p' = 0.75$), while the corresponding a_v decreased from 0.54 to 0.45. As no probing tests were performed under ($q/p' = 1.2$) conditions, the corresponding E_{v0}' values over relatively lower p' range were likely to have been underestimated if were derived based on the stiffness constants obtained for $q/p' = 0.75$ conditions.

Considering first the normalised stiffness trends over first 1000 cycles, Figures 7-87 and 7-88 plot respectively the trends for the $\eta = 0$ tests and higher η (0.75 and 1.2) tests cycled with the lowest $CSR = 0.1$. The very dense $\eta = 0$ tests exhibited $E_{v,q}^{cyc}/E_{v0}'$ trends that stayed largely stable below 1. The high η tests mostly exhibited close $E_{v,q}^{cyc}$ and E_{v0}' values, while the $\eta = 1.2$ test showed $E_{v,q}^{cyc}/E_{v0}'$ trends slightly above 1, which may reflect the E_{v0}' value possible being slightly underestimated, as discussed above.

Extending to consider ultimate cycling states, Figures 7-89 to 7-90 plot the trends for normalised ultimate cyclic stiffnesses against CSR level after 10^4 loading cycles. As expected, a general pattern is indicated for cyclic stiffnesses to decrease markedly with CSR. $E_{v,q}^{cyc}/E_{v0}'$ values fell below unity in most of the intermediate CSR (= 0.3) tests, while the K-consolidated $OCR = 4$ specimen cycled with $CSR = 0.1$ manifested clearly

higher cyclic stiffness than the isotropically and normally consolidated the OCR = 1 specimen. Under cycling to large N values, the $E_{v,q}^{cyc}/E_{v0}'$ ratios remained below 1 for the η = 0 test and slightly above 1 for high η (0.75 and 1.2) tests, excepting the η = 0.75 specimen cycled from the relatively lower p_0' of 133.3 kPa.

7.7.3 Cyclic thresholds and kinematic yielding behaviour

The kinematic yielding surface framework set out in Section 5.2.2 and applied to monotonic loading in Section 5.7 can also be applied to the cyclic experiments. The first linear elastic Y_1 limit is readily established as the point where cyclic tests started to show non-linear behaviour. Recalling Figure 5-24, Dunkirk sand sheared monotonically from isotropic stresses exhibited linear and elastic response (within Y_1) when the axial perturbations $\Delta q/p'$ fell below around 0.06, and the corresponding Y_1 yielding surfaces were largely symmetric around the q = 0 axis. This condition was reached in all the Author's cyclic tests.

Potential further cyclic thresholds corresponding to the second Y_2 condition may be considered in terms of two strain-based criteria: (i) the onset of cyclic axial strain (ε_a^{acc}) accumulation; and (ii) shifts in trends for the secant cyclic stiffnesses ($E_{v,q}^{cyc}$), as normalised by the linear elastic Young's moduli (E_{v0}') at the corresponding cycling stress states.

Accumulated cyclic axial strain (ε_a^{acc}) criterion

Cumulative axial strain provides a direct measure of the threshold CSR below which the long-term axial strain rates are close to zero under axial cycling and the soil manifests a fully stable response. It was shown in Figure 5-27 that the Batch 2 Dunkirk sand's monotonic Y_2 yielding surface was not completely symmetric about the origin for isotropically consolidated state, and any two-way cyclic loading that applied q_{cyc} equally to the compression and extension side tended to lead the specimen to engage Y_2 yielding earlier at the extension side. The magnitudes of the Y_2 region grew with increasing R_d, OCR and p_0' levels and diminished as stress ratio (η) varied from 0 (isotropic) in tests conducted away from the isotropic axis. However, tests conducted at p_0' = 400 kPa from η = 0 on specimens with e_0 = 0.640 (R_d = 79%) showed the Y_2 region as extending vertically to q/p_0' = 0.5 above the axis and 0.31 below it.

Figures 7-42 and 7-43 showed how the nominal long-term axial and radial strain

rates varied under cyclic loading with *CSR* levels under three mean stress ratio (η = 0, 0.75 and 1.2) conditions. Extrapolating the trends towards zero strain rate led to the determination of intercepts that all fell below *CSR* = 0.1. However, the treatment did not consider the specimens background creeping. As noted in Section 7.3.5, all specimens showed finite, although small, creep rates before the axial cycling was applied. Figure 7-22 showed the ranges of rates observed in the Author's tests after a range of creep pause periods imposed after consolidating to η values between 0 and 1.2. As shown in Figure 7-44, deducing these background creeping from the cyclic strain trends led to 'net' axial strain rates that were minimal (practically zero) for the tests performed with *CSR* up to and including 0.3 for the η = 0 condition and around 0.2 for η = 0.75 and lower again ($\approx$ 0.1) for η = 1.2, and so satisfy the elastic shakedown or Y_2 criterion described in Section 7.2.1.

The *CSR* level at which the net axial strain rates rose significantly above zero (i.e. Y_2 yielding threshold) depended on the stress ratio (η) and also the *OCR* conditions. The strain rate for the anisotropic and over-consolidated Group A(OC) specimens remained minimal ($< 0.01\%/\log_{10}(N)$) as *CSR* increased to 0.3. The high η (= 1.2) Group F specimens exceeded Y_2 threshold at *CSR* level just above 0.1, while interpolation between behaviour of the specimens cycled from lower η of 0 or 0.75 suggested that *stable* cyclic responses persisted up to a slightly higher *CSR* level of around 0.20. These observations show that the inferred Y_2 surfaces changed in shape and reduced in size as η increased, as described earlier from the monotonic tests reported by Kuwano & Jardine (2007).

U*nstable* responses, associated with Y_3 yielding, were identified in the *CSR* = 0.3 and 0.4 tests conducted from η = 1.2. The specimen cycled with *CSR* = 0.3 (FA1.2(167)92-0.3) sustained 10^4 shearing cycles, while the *CSR* = 0.4 sample (FA1.2(167)92-0.4) exhibited incremental collapse and failed after 4468 drained cycles, as its stress state further approached the failure envelope (shown in Figure 7-19). *Unstable* thresholds were not engaged in the Author's tests cycled from η = 0 and 0.75 conditions even under maximum *CSR* of 0.5. As shown in Figure 7-19, there is clear tendency for specimens cycled under η = 0 conditions with higher *CSR*s to move towards Y_3 yielding under extension condition.

Cyclic stiffness criterion

The variations in cyclic stiffness trends with *CSR* level offer an alternative perspective for considering how kinematic yielding was engaged during the drained cyclic tests on Dunkirk sand.

The threshold for assessing the *stable* response expected for paths that within the Y_2 kinematic yield surface could be also defined as the cyclic level below which cyclic stiffnesses $E_{v,q}^{cyc}$ remained largely stable. As indicated in Figures 7-87 to 7-90, the $E_{v,q}^{cyc}/E_{v0}'$ ratios identified for the first 1000 cycles under *CSR* = 0.1 persisted as shearing continued to large number of cycles. The cyclic stiffnesses remained largely stable over the long-term cycling, as seen in Figures 7-79 to 7-85. The stiffness trends indicate that all subject to cycling with *CSR* = 0.1 were kept within their Y_2 yielding, which supports the observations made above regarding the specimens' long-term axial cyclic strain accumulation behaviour.

Tests involving the next higher *CSR* = 0.3 led the specimens to develop significant stiffness losses (see Figures 7-79 to 7-85), and the ultimate $E_{v,q}^{cyc}/E_{v0}'$ ratios were clearly lower than those under *CSR* of 0.1, suggesting the threshold for the *stable* response falls between the *CSR* 0.1 and 0.3 levels. The gradually 'recovering' trends of loading cyclic stiffnesses ($E_{v,q}^{cyc}$) shown in the above plots and the decreasing areas of the cyclic stress-strain loops (shown in Figure 7-76), however, suggested that the samples' Y_2 yielding surface were slowly relocated and extended as the specimens gradually adapted to the imposed constant amplitude cycling.

Abrupt stiffness degradation was observed in the η = 1.2 tests under the higher *CSR*s of 0.4 and 0.5, confirming the *unstable* response that eventually led to cyclic failure. The overall steeper reduction trends of $E_{v,q}^{cyc}/E_{v0}'$ seen in the η = 1.2 tests suggested the *CSR* range for *stable* and *metastable* response is smaller under this η than with the lower η conditions of 0 and 0.75.

Overall, the *CSR* levels at which Y_2 yielding is indicated to have occurred by the two criteria discussed above are broadly compatible and also in keeping with those determined from analyses of the monotonic tests on the Batch 2 Dunkirk sand material presented in Section 5.7. However, slight differences can be expected between the kinematic yielding behaviour of the two batches employed for the monotonic and cyclic test programmes.

7.7.4 Figures

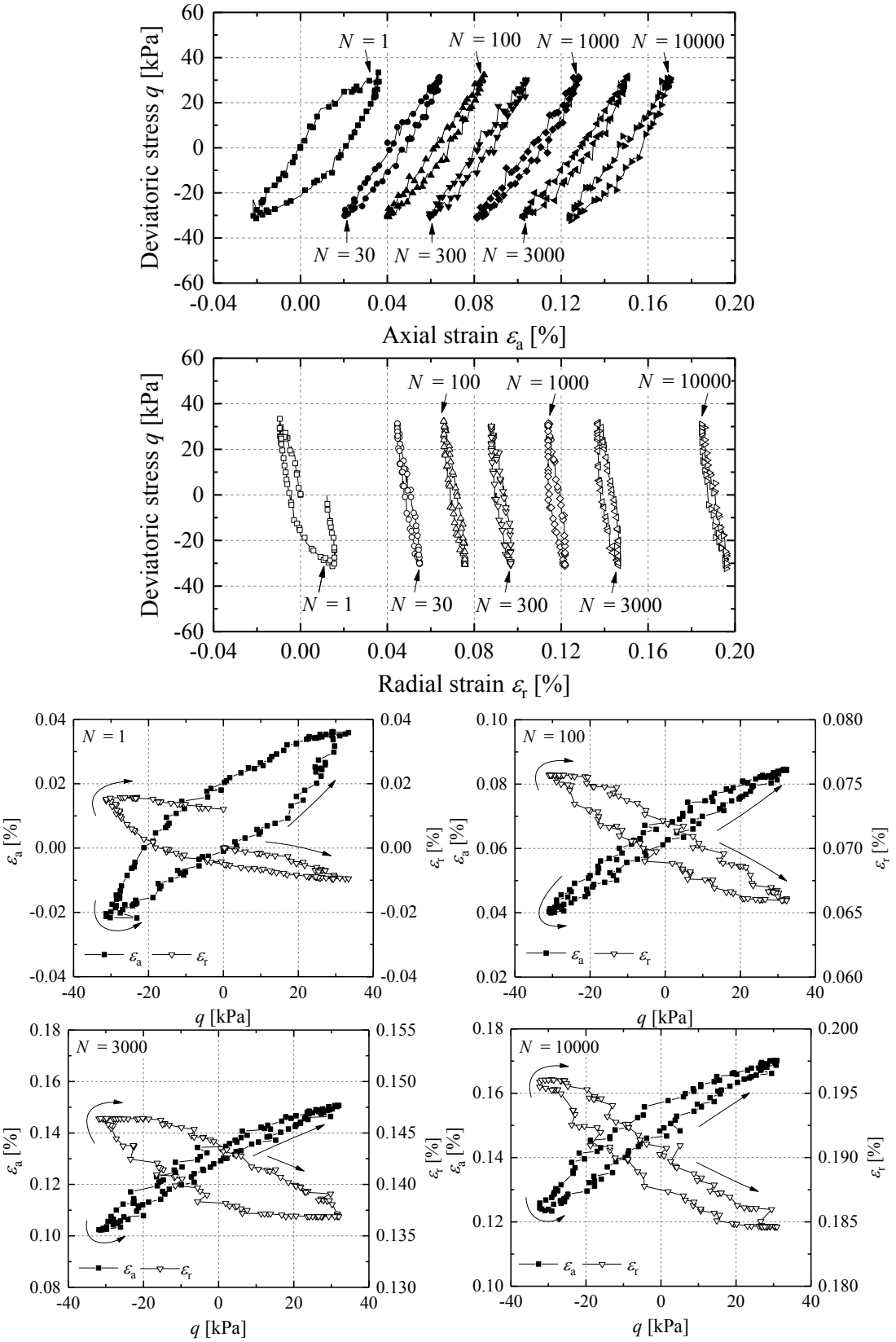

Figure 7-76 Axial and radial strain-stress loops of a Group A (η = 0, (q_{mean}, p_0') = (0, 100) (kPa)) test with q_{cyc} = 30 kPa (CSR = 0.3)

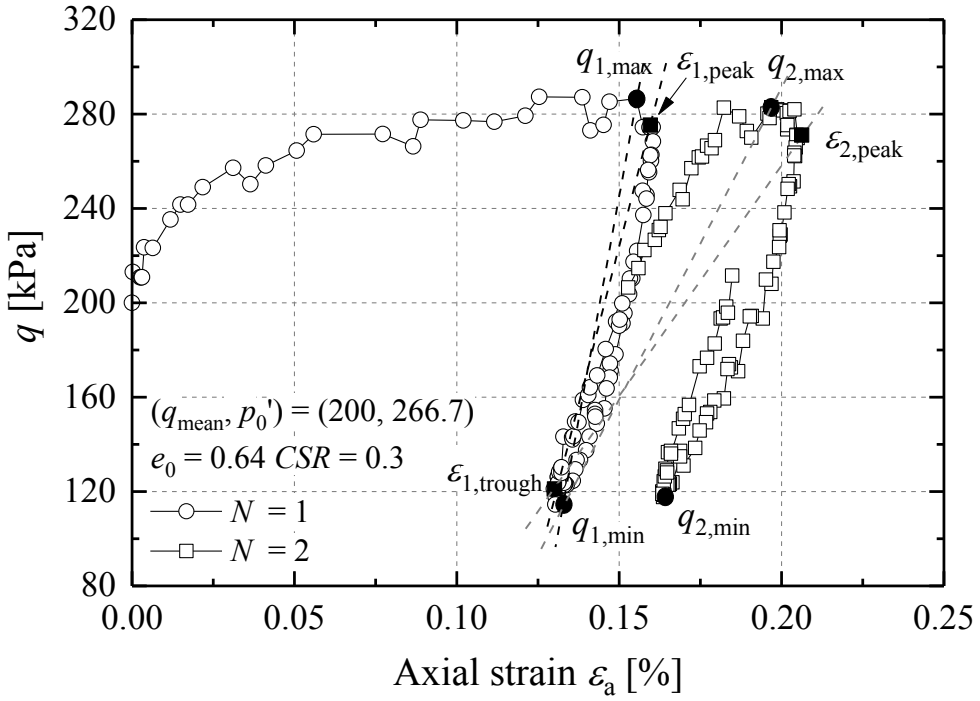

Figure 7-77 Example of stress-strain response (first two shearing cycles), identifying maxima and minima deviatoric stresses and peak and trough axial strains in each cycle

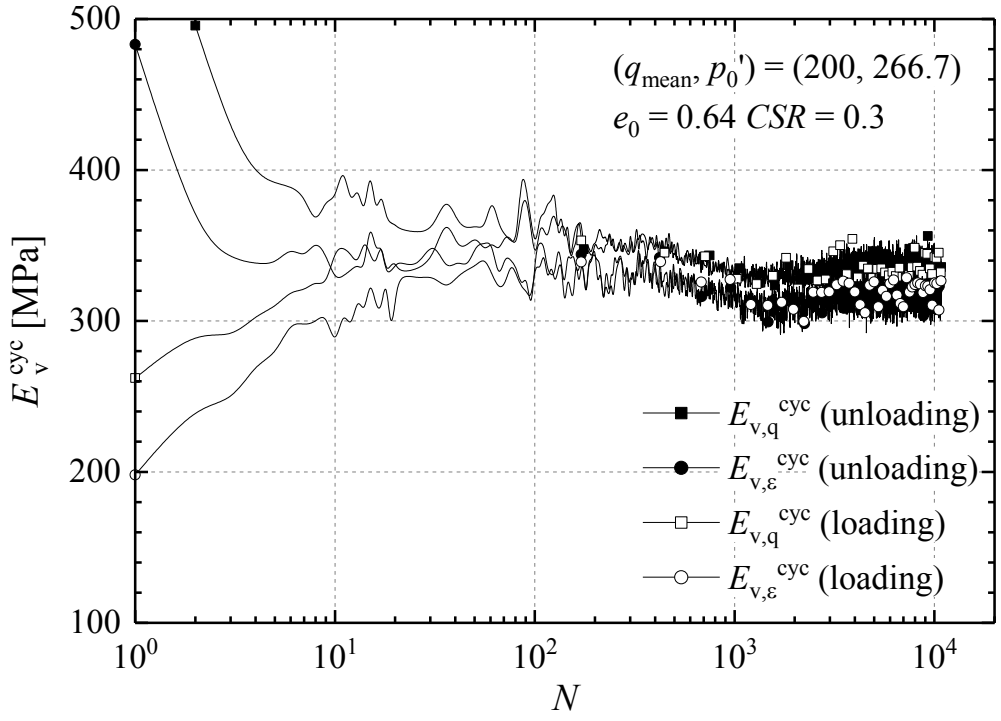

Figure 7-78 Secant cyclic stiffness trends established from different methods for a *CSR* = 0.3 test

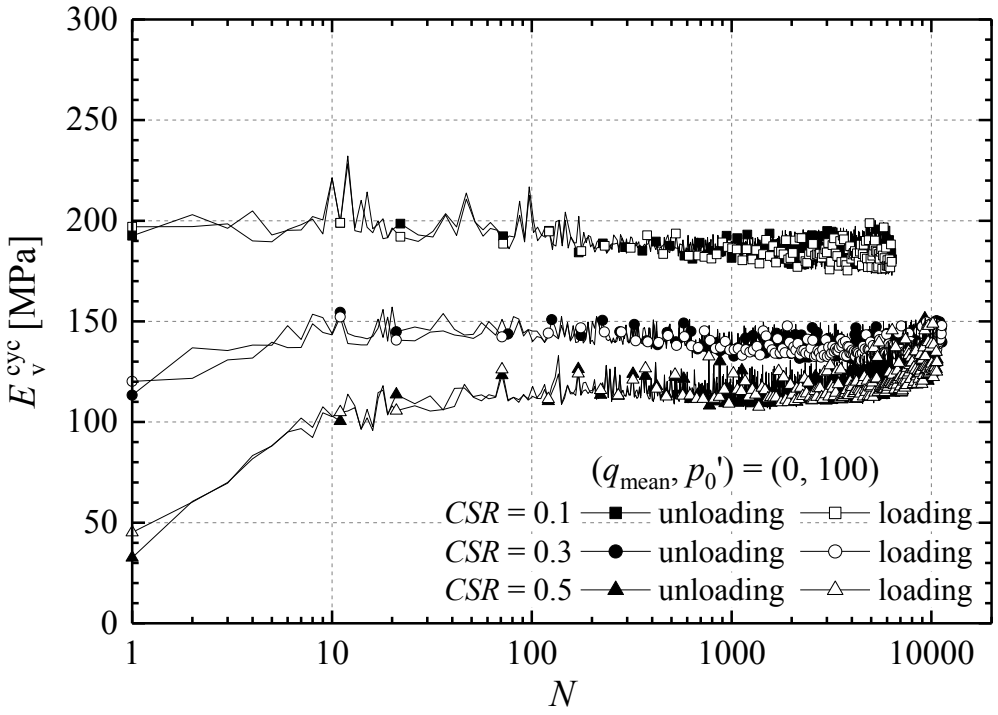

Figure 7-79 Loading and unloading axial cyclic secant stiffness of the Group A tests (R_d = 92%, e_0 = 0.640) (η = 0, (q_{mean}, p_0') = (0, 100) (kPa))

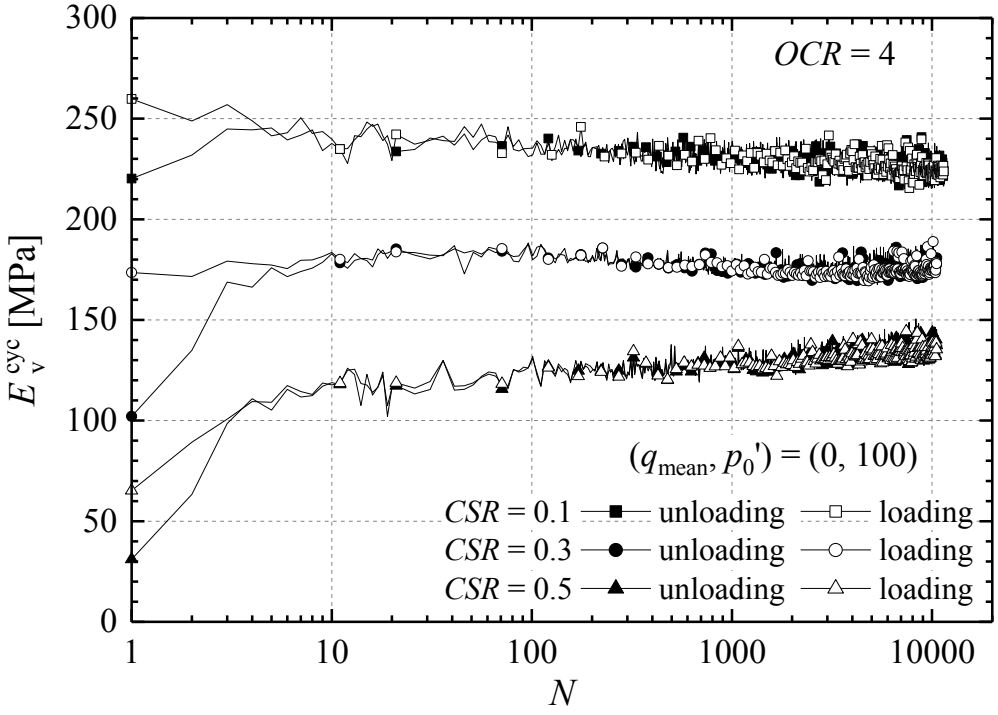

Figure 7-80 Loading and unloading axial cyclic secant stiffness of the over-consolidated Group A-OC(4) tests (R_d = 92%, e_0 = 0.640) (η = 0, (q_{mean}, p_0') = (0, 100) (kPa))

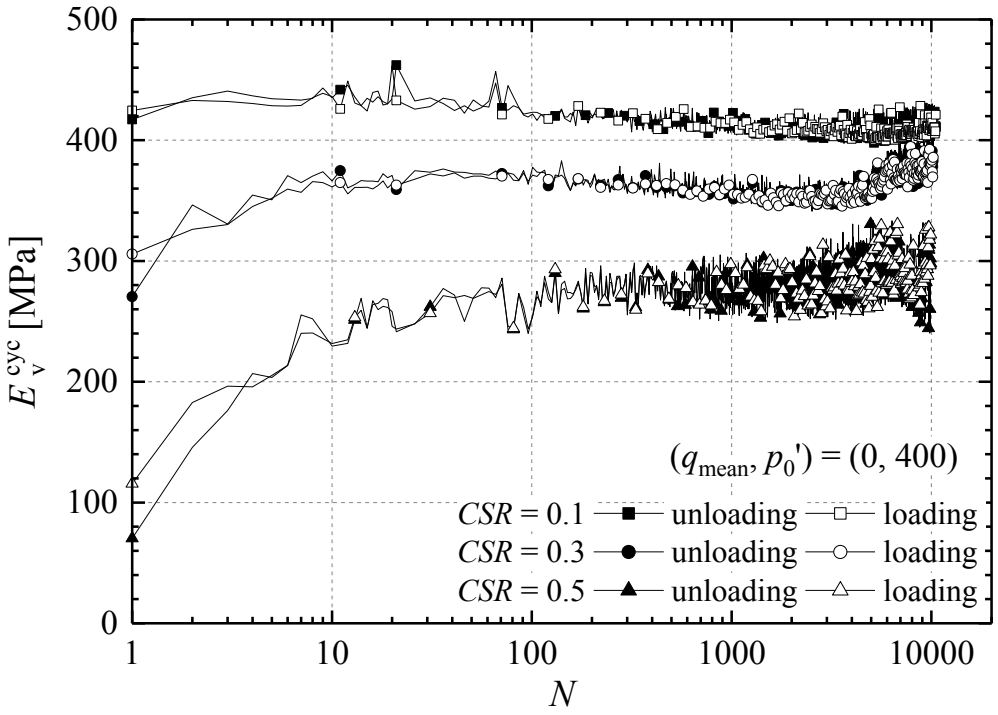

Figure 7-81 Loading and unloading axial cyclic secant stiffness of the Group B tests (R_d = 92%, e_0 = 0.640) (η = 0, (q_{mean}, p_0') = (0, 400) (kPa))

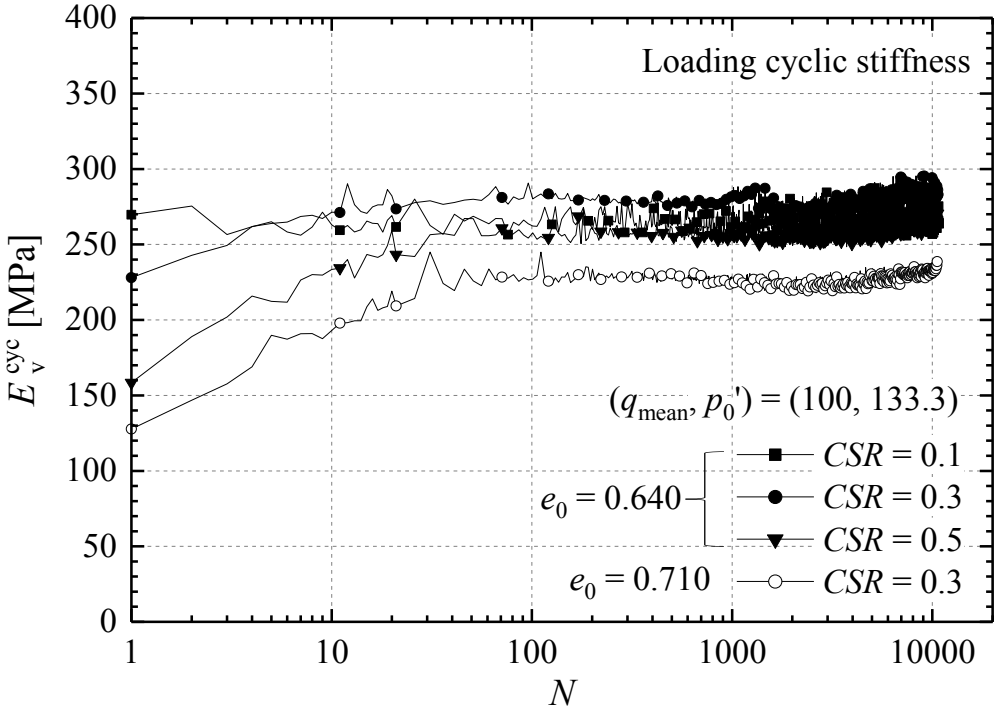

Figure 7-82 Loading axial cyclic secant stiffness of the Group C tests (η = 0.75, (q_{mean}, p_0') = (100, 133.3) (kPa))

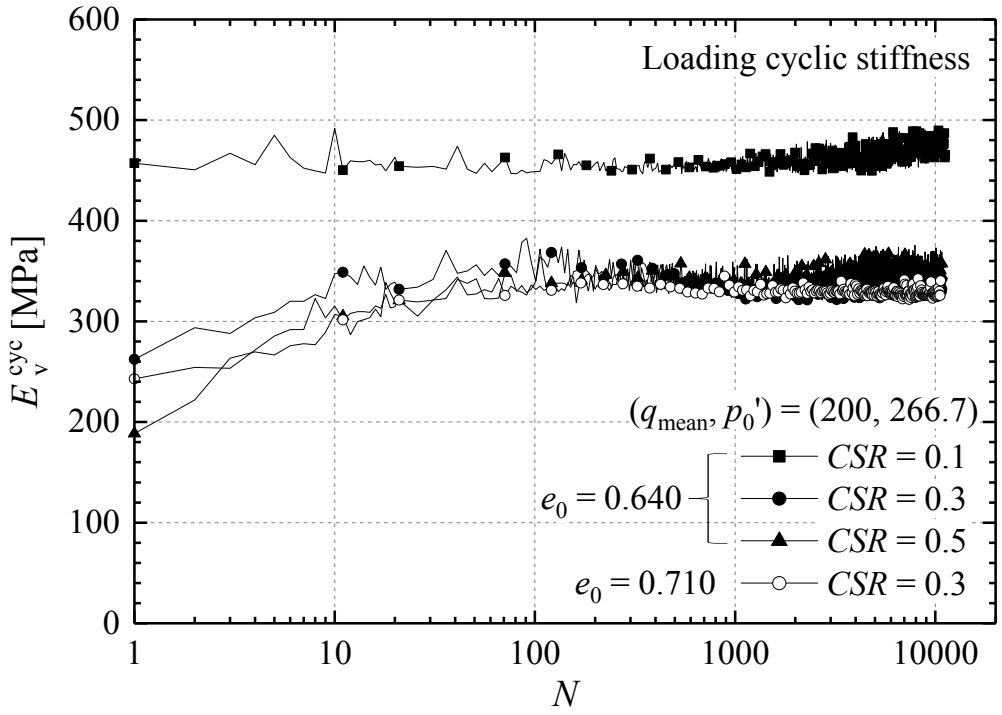

Figure 7-83 Loading axial cyclic secant stiffness of the Group D tests ($\eta = 0.75$, (q_{mean}, p_0') = (200, 266.7) (kPa))

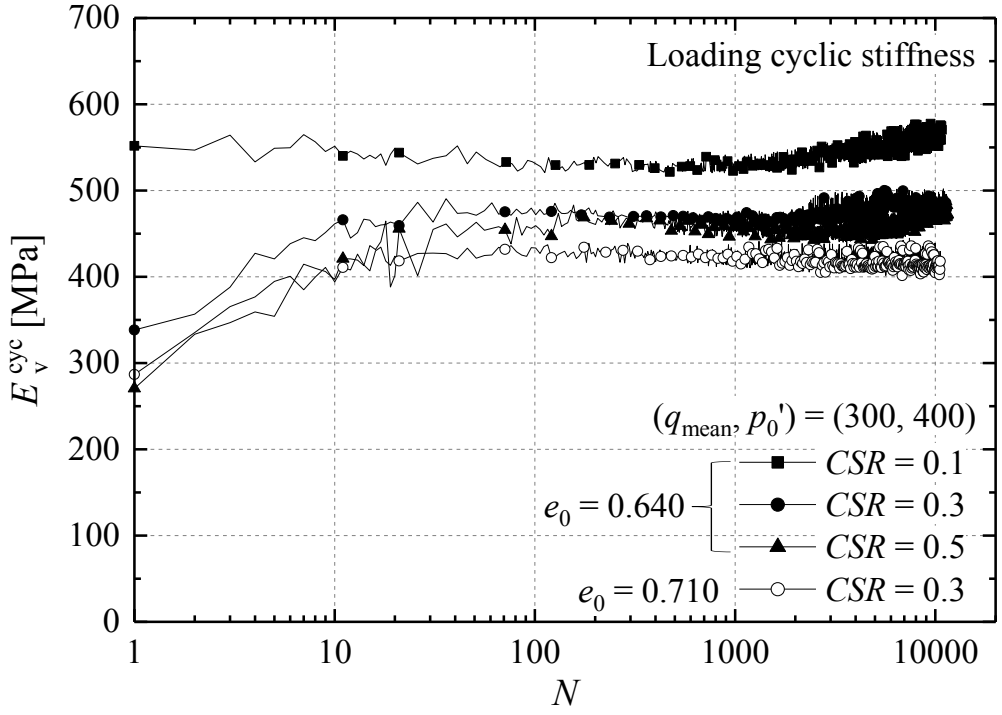

Figure 7-84 Loading axial cyclic secant stiffness of the Group E tests ($\eta = 0.75$, (q_{mean}, p_0') = (300, 400) (kPa))

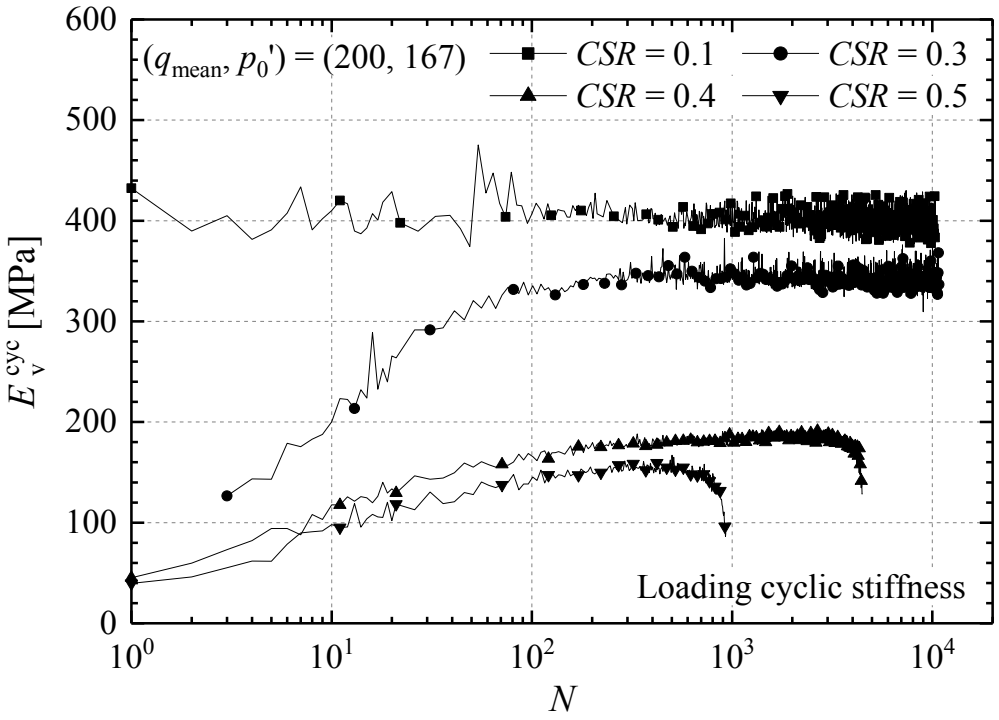

Figure 7-85 Loading axial cyclic secant stiffness of the Group F samples (R_d = 92%, e_0 = 0.640) (η = 1.2, (q_{mean}, p_0') = (200, 167) (kPa)), noting that external axial strains were used for calculation in the cases of *CSR*s = 0.4 and 0.5

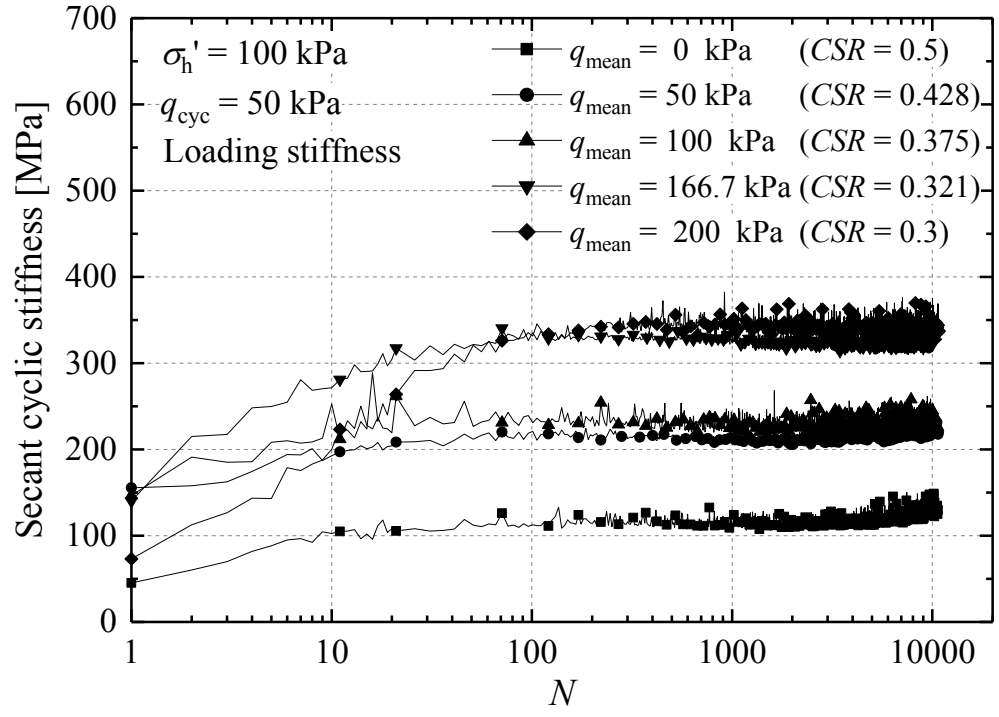

Figure 7-86 Comparison of loading axial cyclic secant stiffness of the samples with identical σ_h' and q_{cyc} (Note: consolidation stress paths see Figure 7-18)

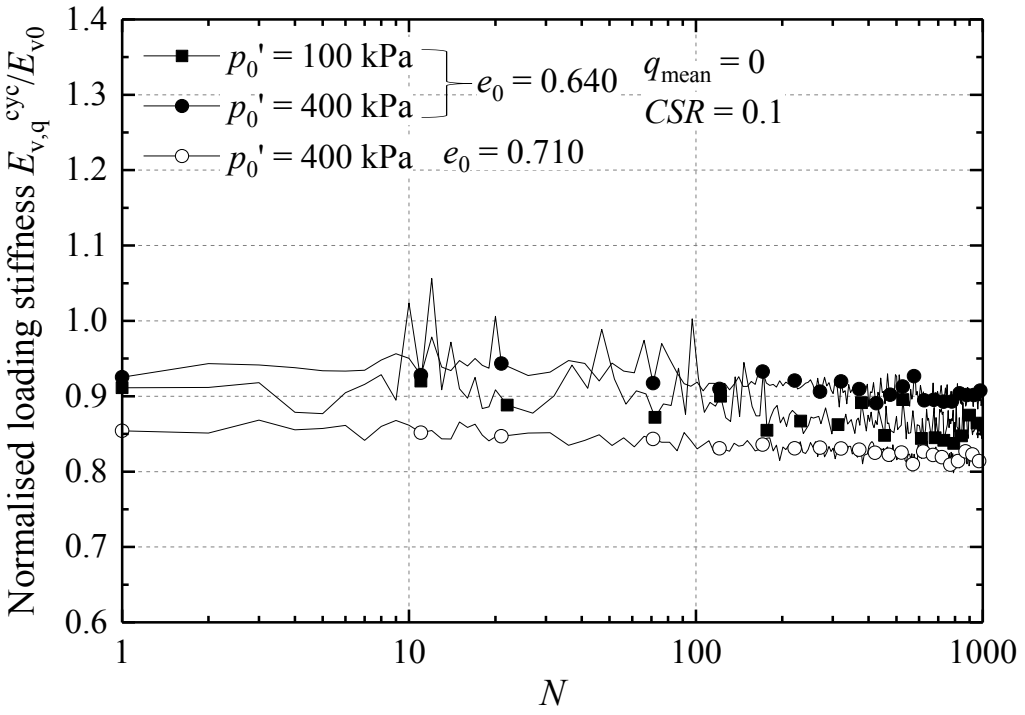

Figure 7-87 Trends for normalised cyclic loading stiffness of the η = 0 tests over initial 1000 cycles under CSR = 0.1

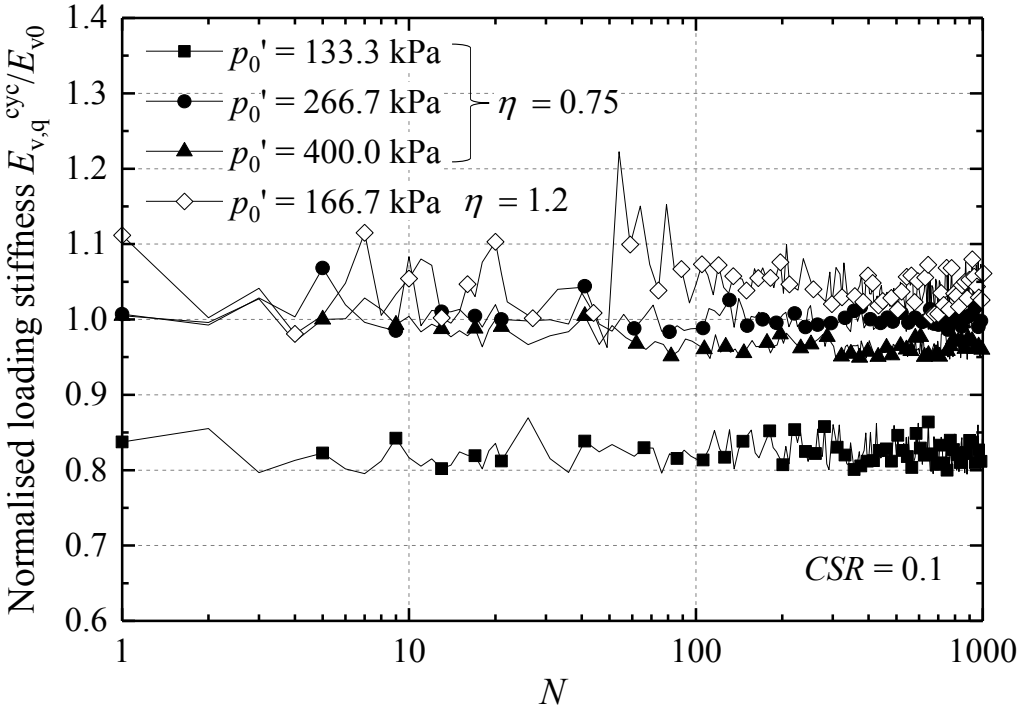

Figure 7-88 Trends for normalised cyclic loading stiffness of the η = 0.75 and 1.2 tests over initial 1000 cycles under CSR = 0.1

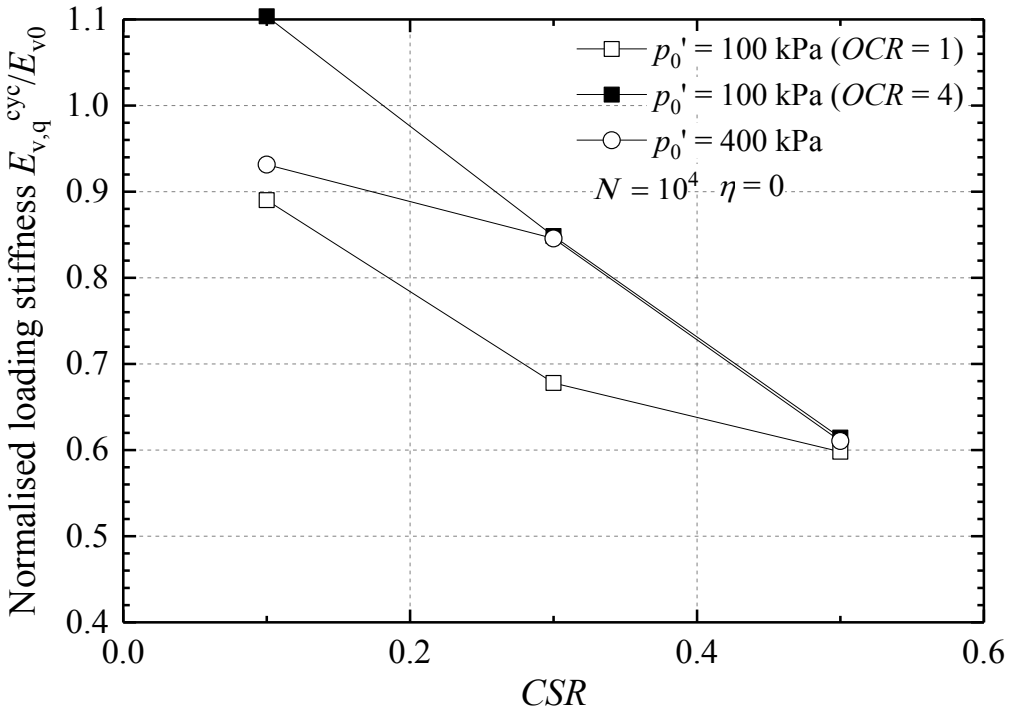

Figure 7-89 Trends for normalised cyclic stiffness against *CSR* of the $\eta = 0$ tests after 10^4 loading cycles

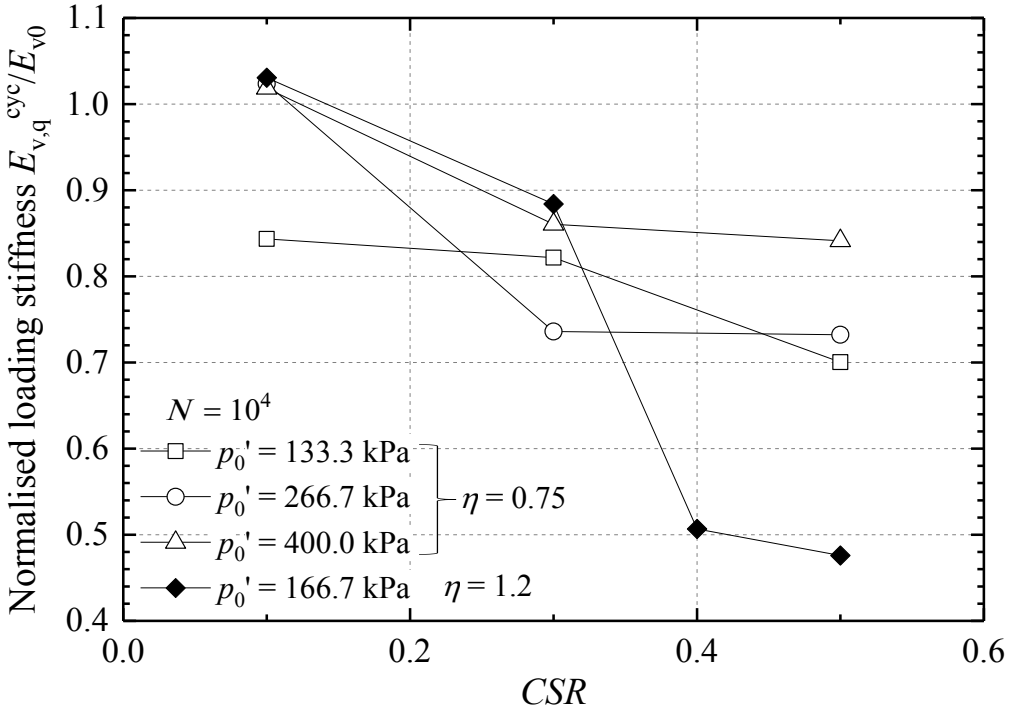

Figure 7-90 Trends for normalised cyclic stiffness against *CSR* of the $\eta = 0.75$ and 1.2 tests after 10^4 loading cycles

7.8 Post-cycling monotonic stiffness and strength behaviour

Cyclic shearing under fully drained conditions led to significant volumetric straining without, in most cases, cyclic failure developing. It was considered important to investigate the soils' post-cycling stiffness, yielding, strength and dilation behaviour to help assess how cycling might affect subsequent soil-structure performance under monotonic loading, such as those highlighted by for example, Nicolai *et al.* (2017).

As mentioned in Section 7.2.2, the specimens were sheared to failure after the cyclic loading stages under drained conditions at a constant axial strain rate of 5%/day.

7.8.1 Post-cycling stiffness characteristics

The post-cycling small strain stiffness characteristics are conveniently represented by stiffness degradation trends of vertical Young's moduli (E_v') against axial strains normalised by void ratio function. The Hardin & Richart (1963) void ratio function $f(e) = (2.17\text{-}e)^2/(1+e)$ was employed to account for the void ratio variations and to exclude the sample density effects on stiffnesses. The secant vertical Young's moduli ($E_{v,sec}'$) were adopted as direct representation of soils' stiffness characteristics

The degradation trends of normalised secant vertical Young's moduli ($E_{v,sec}'/f(e)$) against axial strain of the test Groups A to F are summarised in Figures 7-91 to 7-97. Linear regression were performed over the initial 10^{-4}-2×10^{-3}% axial strain range to attain linear elastic stiffnesses. The $E_{v,sec}'/f(e)$-ε_a trends show clear differences from the equivalent "CSR = 0" tests on "virgin" uncycled specimens. The previously cycled specimens exhibited higher initial stiffness and longer plateaux combined with delayed stiffness degradation; the specimens had become stiffer through cycling. Given that the curves were normalised for void ratio, the beneficial effects must reflect micro-fabric optimisation under cycling, rather than specimen density variations.

The plots presented in Figures 7-91 to 7-97 demonstrate that the gains in small strain Young's moduli increase remarkably with the prior cyclic stress ratio (CSR). Long-term repetitive loading results in significantly better organised particle chains and contacts in the axial direction. These processes relocate and expand the sand's Y_1 and Y_2 kinematic yield surfaces.

Effects of specimen density

The gains in axial stiffness that resulted from cycling were noted to be more

pronounced in the less dense specimens with $e_0 \approx 0.71$ and $R_d = 73\%$. As shown in Figures 7-94 and 7-96, the stiffness trends of the $R_d = 73\%$ specimens matched generally well with those of the very dense specimens ($e_0 \approx 0.64$, $R_d = 92\%$) after they had experienced equivalent *CSR* cycling.

Effects of effective stress history

The post-cycling axial stiffness were also found to be affected significantly by the specimens' earlier effective stress history, as demonstrated in Figure 7-92. Clear differences of the axial stiffness of the over-consolidated specimens can be noted over the <0.01% strain range, where the stiffness increased with *CSR* level. However, the stiffness trends started to converge after 0.04% axial strains with the effects of prior *CSR* levels becoming eventually negligible. The stiffness trends of the normally consolidated samples were all located beneath those of the *K*-consolidated over-consolidated samples, suggesting that the preferred micro-structure developed by the latter specimens remained significant even after the long-term cycling.

Effects of effective stress level

Figures 7-98 and 7-99 highlight the effects of effective stress level on post-cycling axial shear stiffness with identical stress ratio ($\eta = q_{mean}/p_0'$), comparing results from Groups A and B ($\eta = 0$) and Groups C, D and E ($\eta = 0.75$). The axial stiffnesses increased clearly with rising effective stress level. Further investigation is required to establish $[E_{v,tan}'/f(e)]$-$[\sigma_v'/p_r]$ correlations for the post-cycling stiffnesses that incorporate the pre-imposed cyclic stress ratios, q_{mean}/p_0' and *CSR*, as additional variables.

Similar observations were also noted in the set of tests subjected to $q_{cyc} = 50$ kPa at identical σ_h' but different q_{mean} levels, as plotted in Figure 7-100. The normalised stiffnesses increased with q_{mean} values. It is also noted that the stiffness plateaux of the tests with higher q_{mean} were shorter and the stiffness decayed at earlier strain ranges than the lower q_{mean} tests, probably due to the fact that the tests at higher stress ratio were closer to the peak strength and critical state envelopes and therefore significant stiffness degradation occurred at earlier strains. As also noted in Figure 7-100, the degradation trends of the cycled tests converged after around 0.1% strain.

7.8.2 Post-cycling shear strength behaviour

Figures 7-101 to 7-106 show the stress ratios σ_1'/σ_3' mobilised in the post-cycling shear tests to help identify any effects on the large strain shearing behaviour. The axial strains were determined from the external displacement transducer and membrane corrections were applied as described in Section 6.3.

Figure 7-101 shows the σ_1'/σ_3'-ε_a trends for the normally consolidated Group A and the over-consolidated Group A-OC(4) tests, also plotted is the trend of the equivalent CSR = 0 "virgin" test. The σ_1'/σ_3'-ε_a trends for the cycled specimens fell into two narrow bands, and the trends for the over-consolidated specimens are located higher than the normally consolidated specimens. The "virgin" sample, however, showed a clearly weaker response. Although direct comparison of peak stress ratio would also require consideration of the void ratios, the results clearly demonstrated the positive impacts of the static and cyclic loading histories (represented by OCR and CSR) on the large strain shearing behaviour.

The general trend was for the pre-cycled specimens to achieve higher peak stress ratios (σ_1'/σ_3') and at earlier stages, by degrees that increased with CSR. The Group D tests, as shown in Figure 7-104, represent 'unusual' cases where the peak stress ratio decreased with CSR and where the highest CSR = 0.5 case reached its peak σ_1'/σ_3' at a much lower strain of 0.3%.

Figure 7-106 plots the trends from the set of tests conducted at identical σ_h' but different q_{mean} levels. It is clear that the peak stress ratios and stiffnesses of these pre-cycled specimens also increased systematically with the q_{mean} level.

Taking the results from the test Group B (η = 0, (q_{mean}, p_0') = (0, 400) as examples, Figure 7-107 compares the pre-cycled and "virgin" tests' volumetric strain and dilation trends. While the volumetric deformation of the less dense (R_d = 73%, e_0 = 0.71) specimens was less affected by the prior cyclic shearing, the R_d = 92% specimens showed remarkable increases in dilation which increased with CSR level, and mirrored the shear stress-strain trends noted in Figure 7-102.

7.8.3 Figures

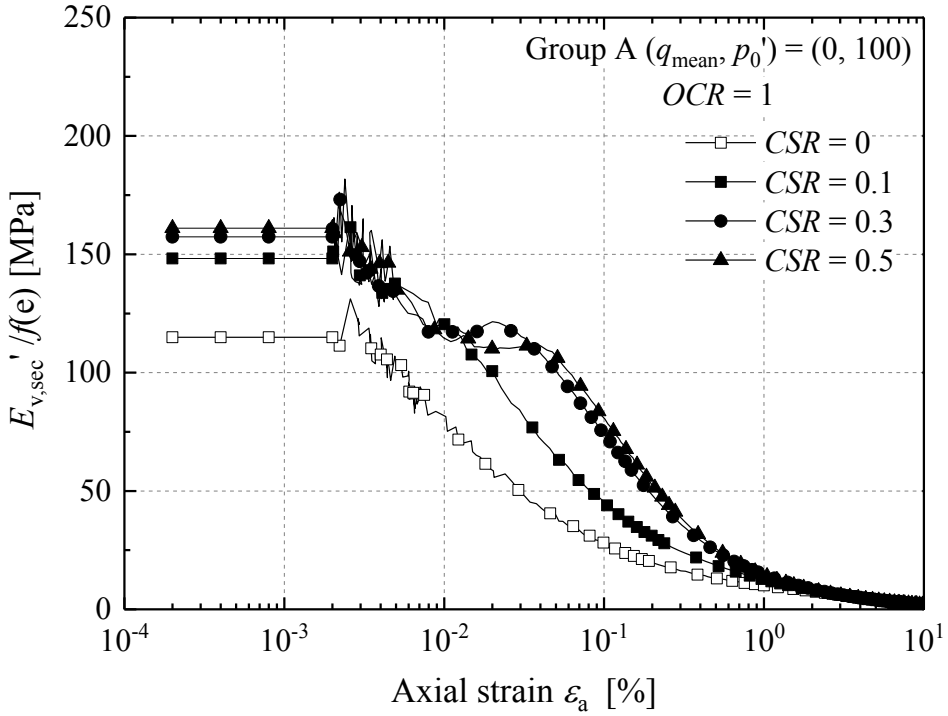

Figure 7-91 Degradation of normalised vertical secant stiffness against axial strain of the Group A tests (η = 0, (q_{mean}, p_0') = (0, 100) (kPa))

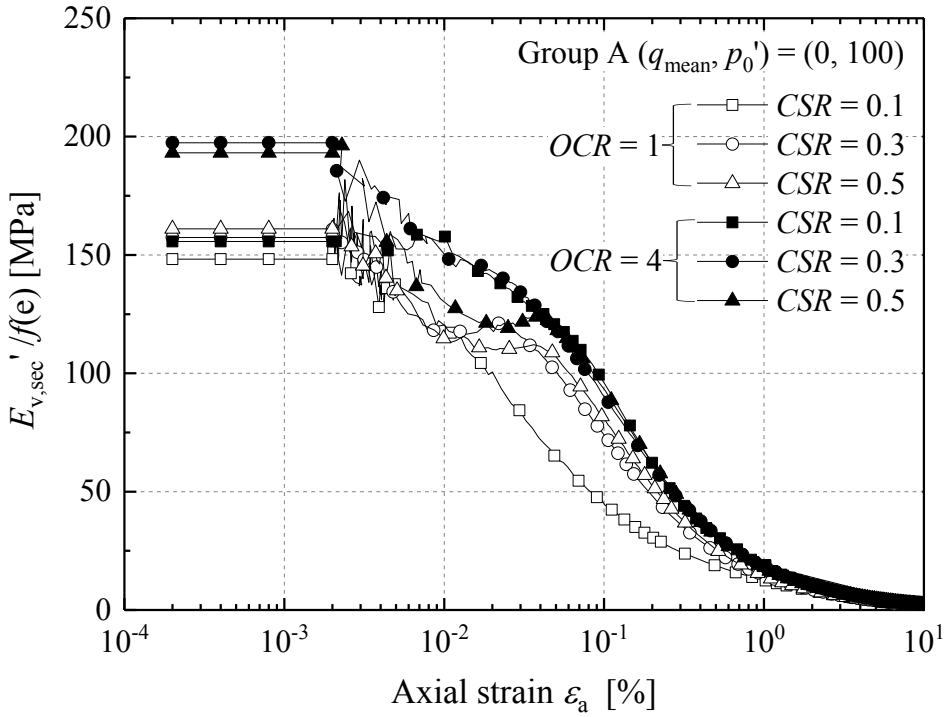

Figure 7-92 Degradation of normalised vertical secant stiffness against axial strain of the normally consolidated Group A and over-consolidated Group A-OC(4) tests

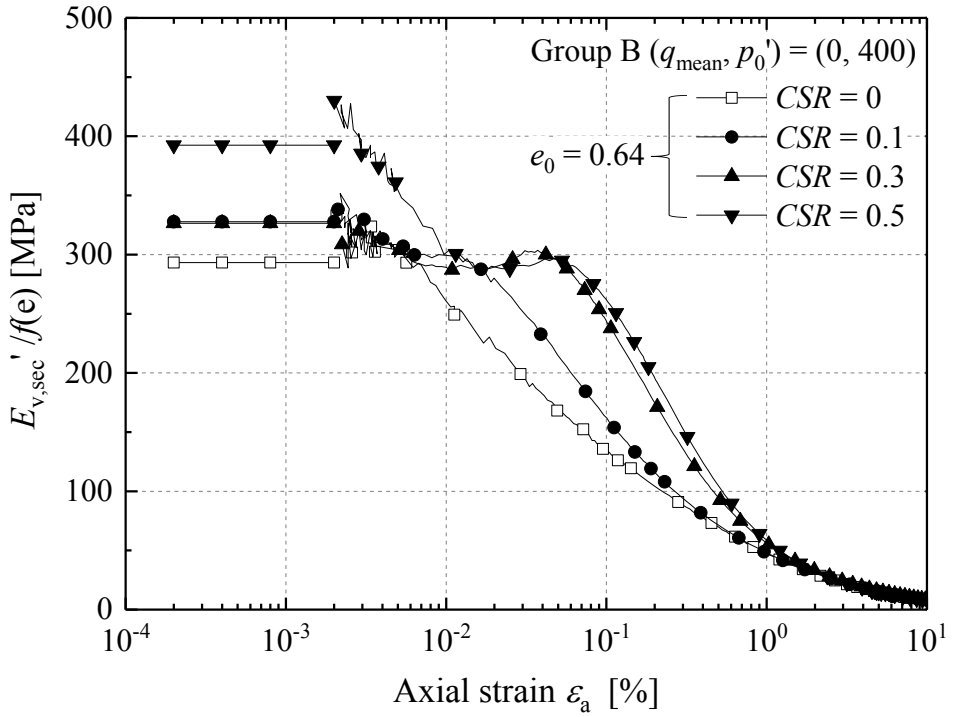

Figure 7-93 Degradation of normalised vertical secant stiffness against axial strain of the Group B tests (η = 0, (q_{mean}, p_0') = (0, 400) (kPa))

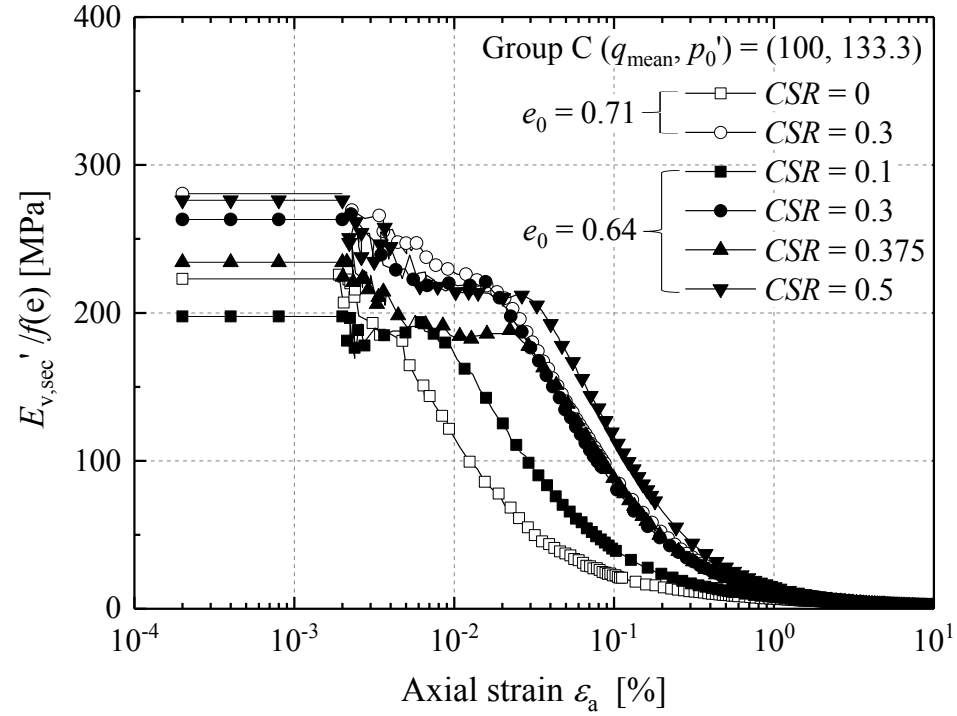

Figure 7-94 Degradation of normalised vertical secant stiffness against axial strain of the Group C tests (η = 0.75, (q_{mean}, p_0') = (100, 133.3) (kPa))

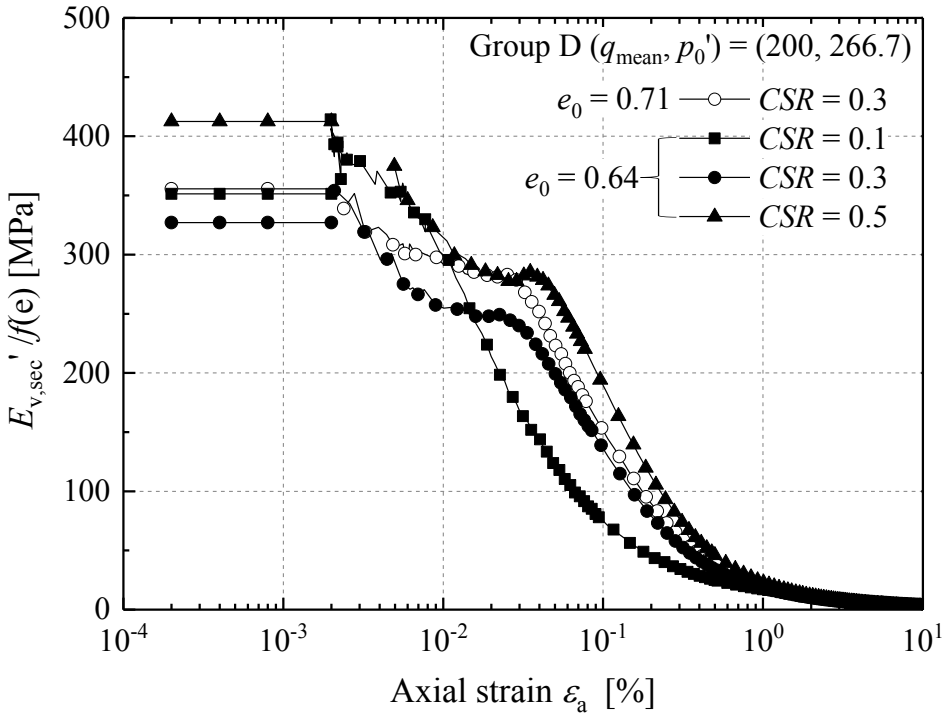

Figure 7-95 Degradation of normalised vertical secant stiffness against axial strain of the Group D tests (η = 0.75, (q_{mean}, p_0') = (200, 266.7) (kPa))

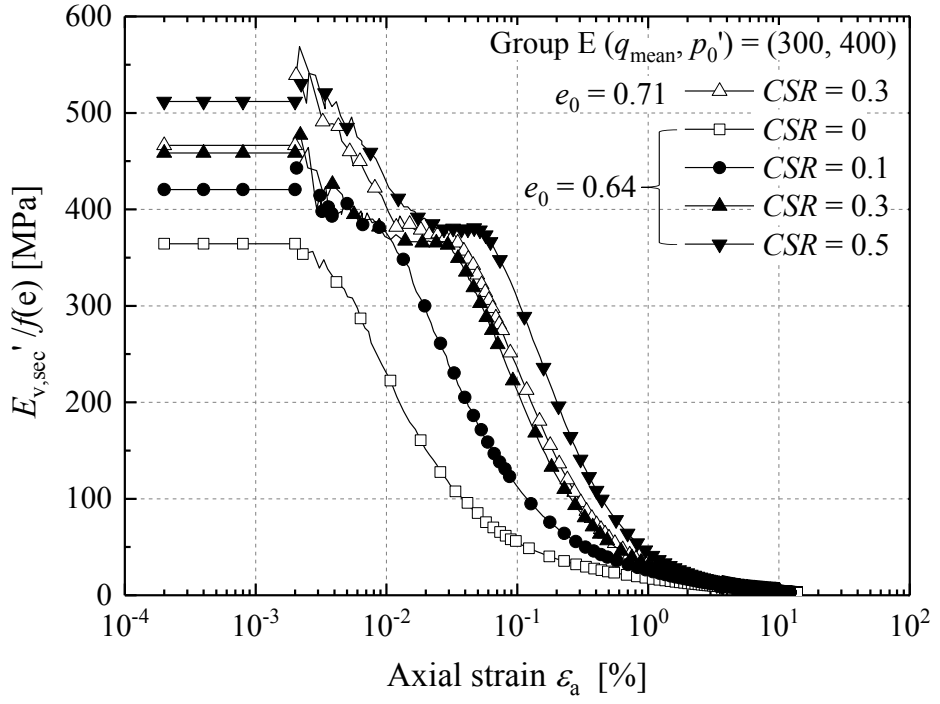

Figure 7-96 Degradation of normalised vertical secant stiffness against axial strain of the Group E tests (η = 0.75, (q_{mean}, p_0') = (300, 400) (kPa))

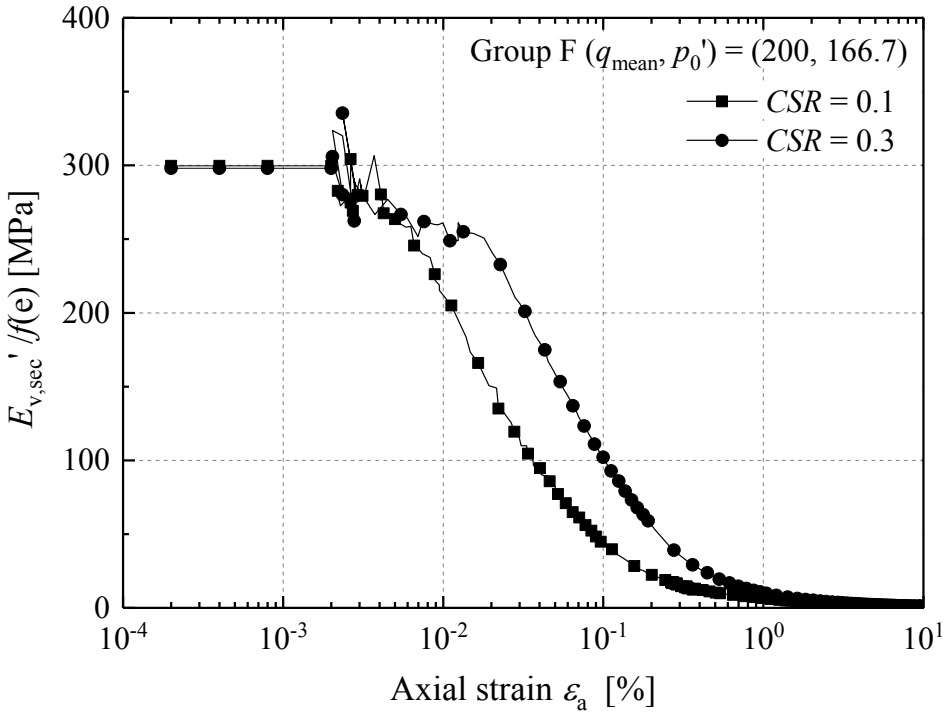

Figure 7-97 Degradation of normalised vertical secant stiffness against axial strain of the Group F tests (η = 1.2, (q_{mean}, p_0') = (200, 167) (kPa))

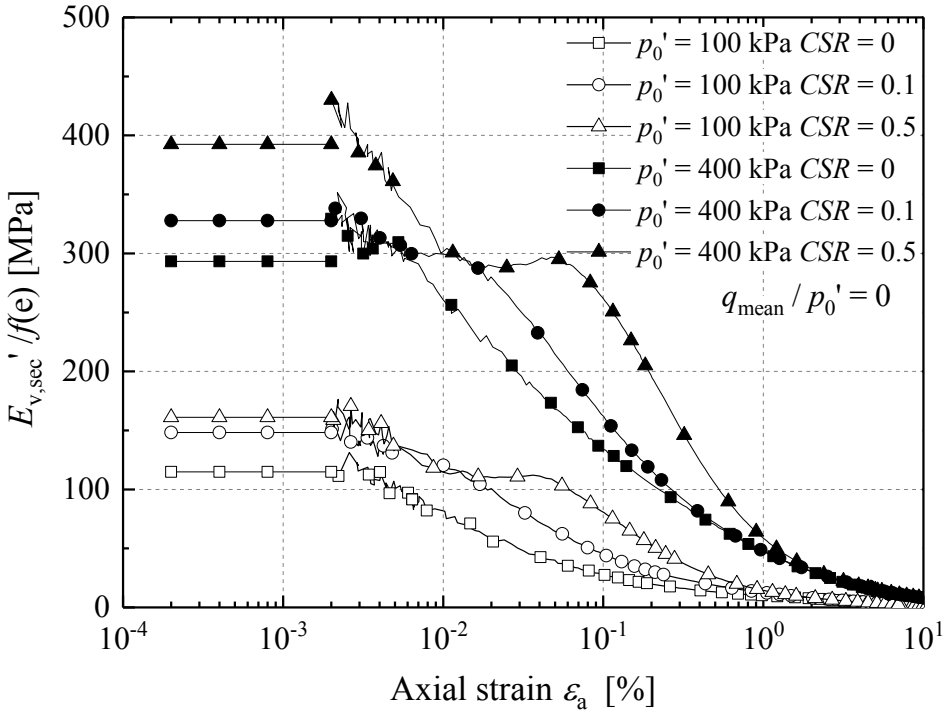

Figure 7-98 Effects of mean effective stress (p_0') and cyclic amplitude stress ratio (CSR) on normalised vertical stiffness of the tests with $q_{mean}/p_0' = 0$

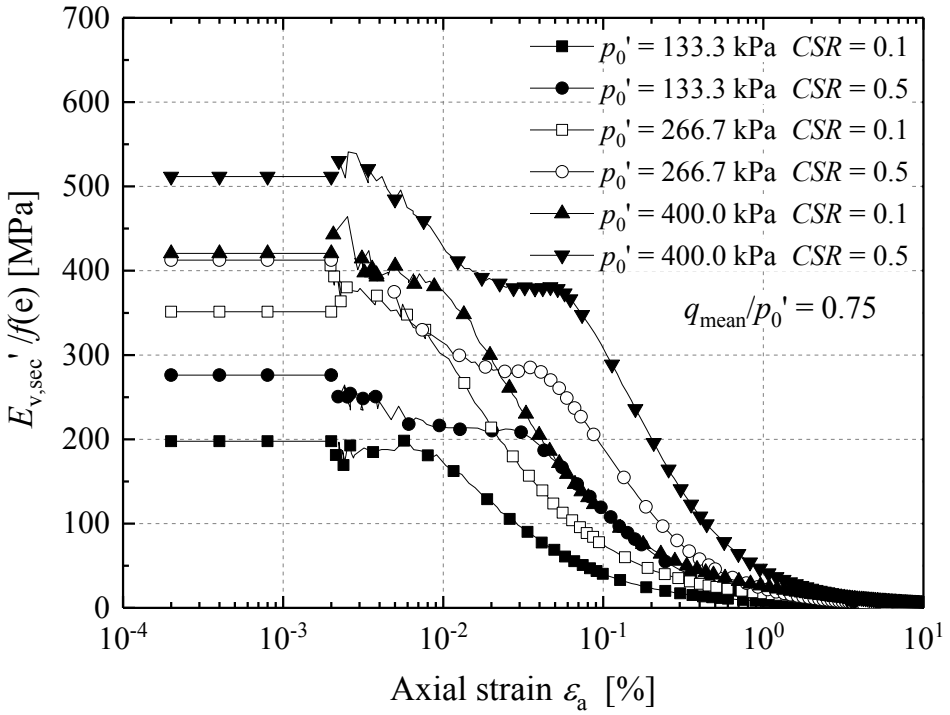

Figure 7-99 Effects of mean effective stress (p_0') and cyclic amplitude stress ratio (CSR) on normalised vertical stiffness of the tests with $q_{mean}/p_0' = 0.75$

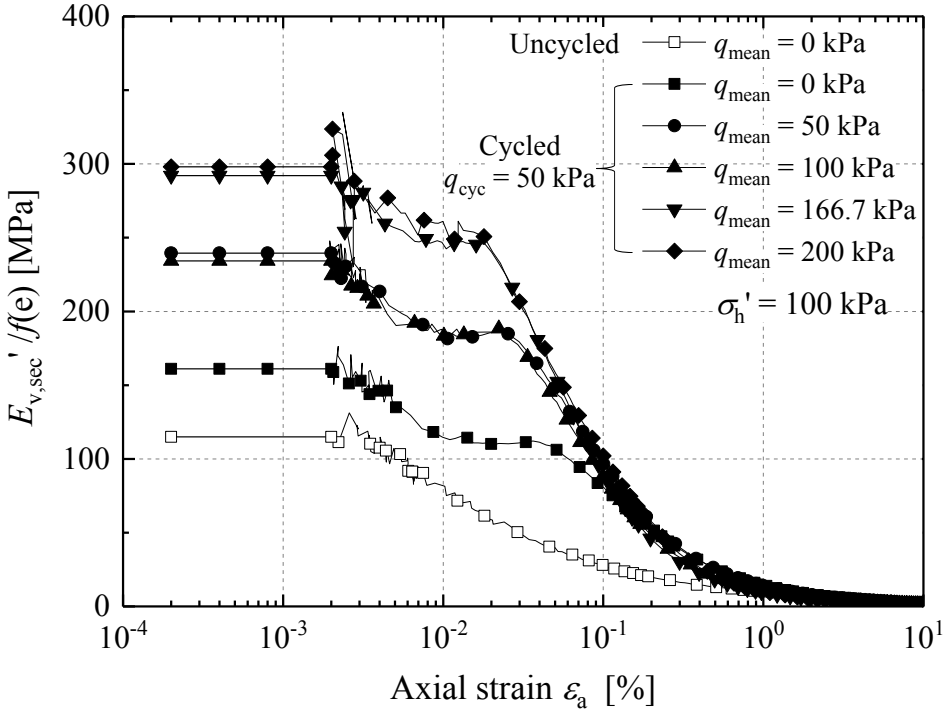

Figure 7-100 Degradation of normalised vertical secant stiffness against axial strain of the set of tests with identical σ_h'

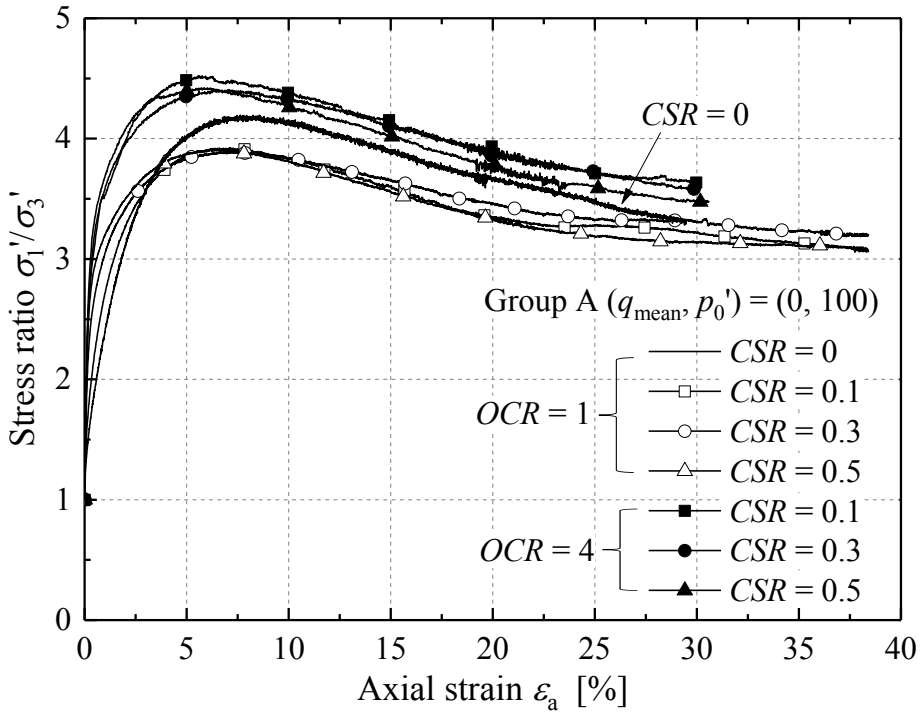

Figure 7-101 Normalised shear stress-strain trends of the normally consolidated and over-consolidated Group A tests (η = 0, (q_{mean}, p_0') = (0, 100) (kPa))

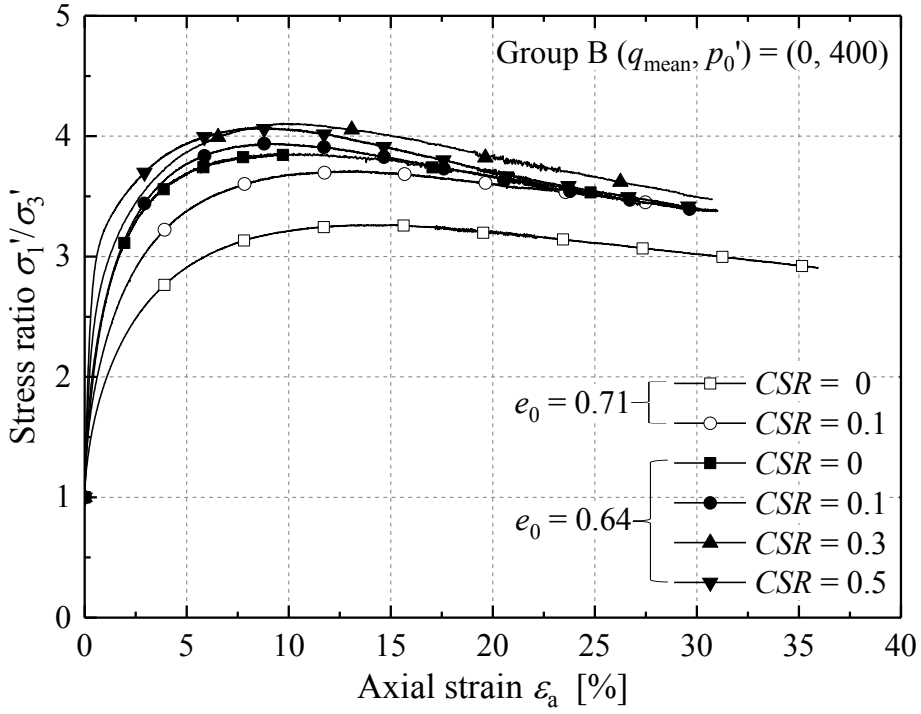

Figure 7-102 Normalised shear stress-strain trends of the Group B tests (η = 0, (q_{mean}, p_0') = (0, 400) (kPa))

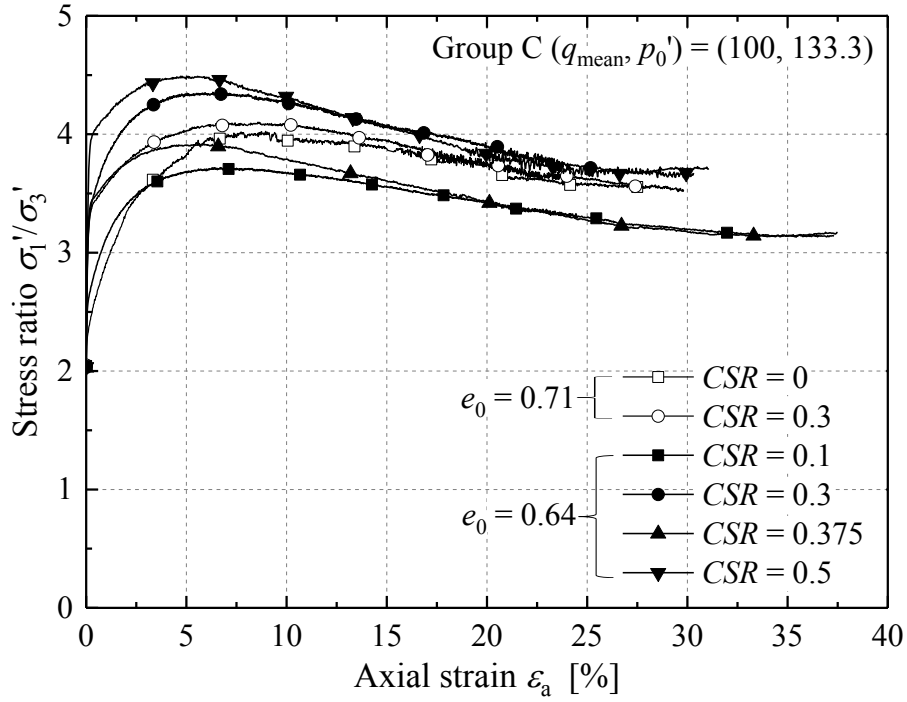

Figure 7-103 Normalised shear stress-strain trends of the Group C tests (η = 0.75, (q_{mean}, p_0') = (100, 133.3) (kPa))

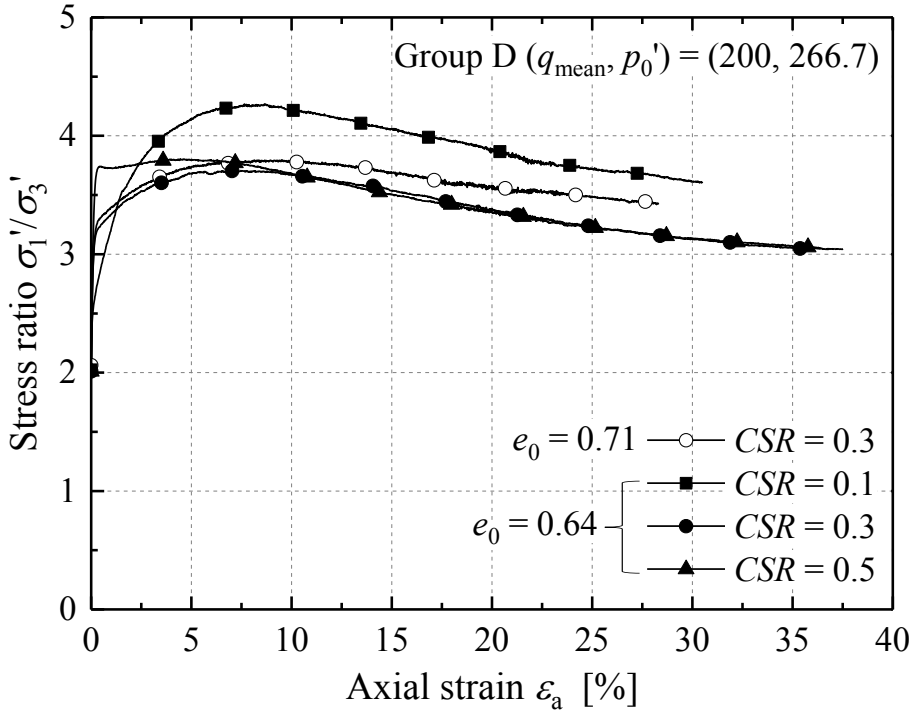

Figure 7-104 Normalised shear stress-strain trends of the Group D tests (η = 0.75, (q_{mean}, p_0') = (200, 266.7) (kPa))

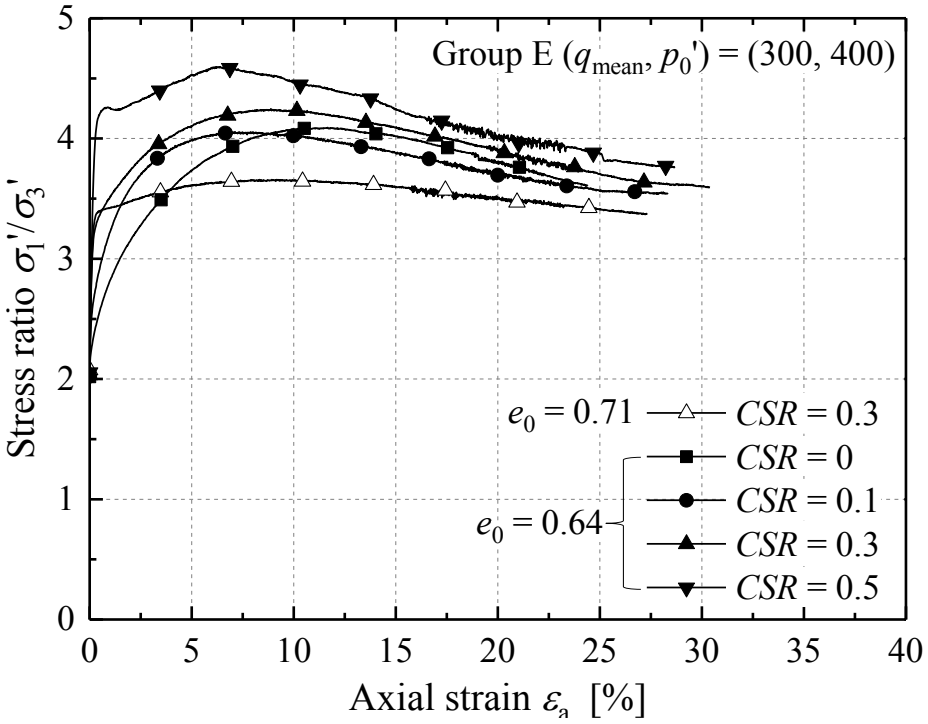

Figure 7-105 Normalised shear stress-strain trends of the Group E tests (η = 0.75, (q_{mean}, p_0') = (300, 400) (kPa))

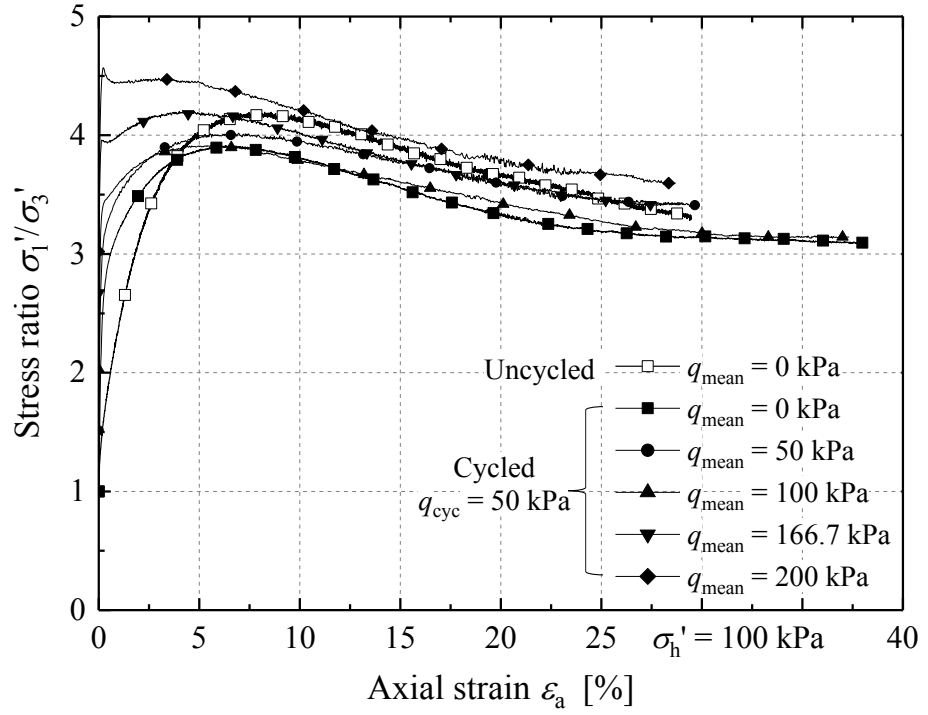

Figure 7-106 Normalised shear stress-strain trends of the set of tests with identical σ_h' and q_{cyc}

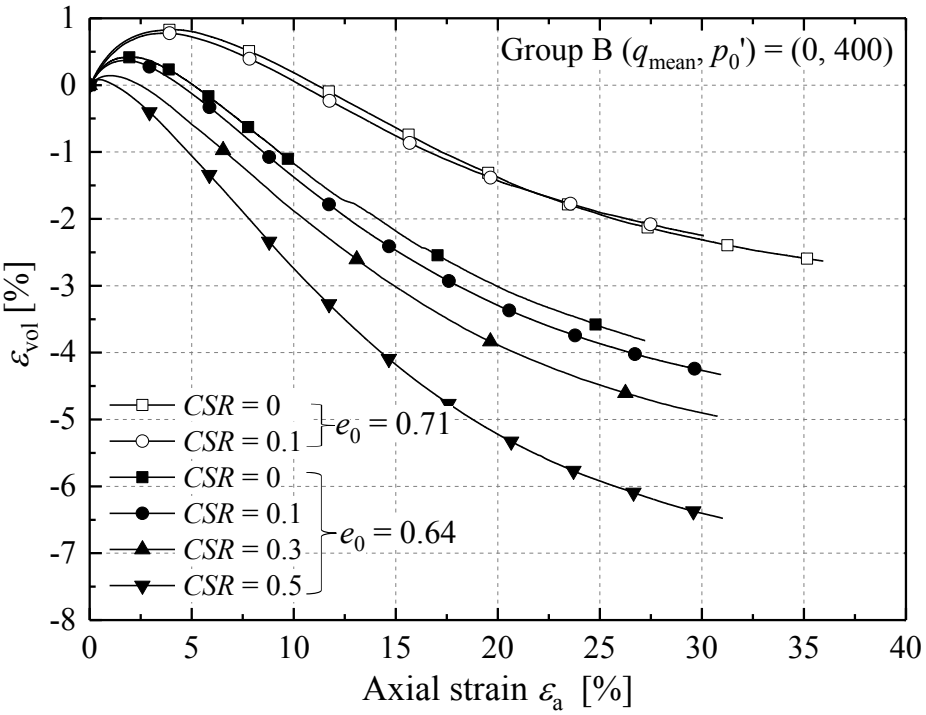

Figure 7-107 Characteristics of volumetric strain and dilation of the Group B tests (η = 0, (q_{mean}, p_0') = (0, 400) (kPa))

7.9 Summary and conclusions

This last main chapter reported a cyclic triaxial programme designed to investigate the long-term cyclic shearing, and post-cycling monotonic shearing, behaviour of Dunkirk sand under drained conditions. The test programme focused primarily on normally consolidated very dense (R_d = 92%, e_0 = 0.640) water-pluviated specimens, and considered how effective stress (p_0'), mean cyclic stress ratio ($\eta = q_{mean}/p_0'$) and cyclic amplitude stress ratio (CSR) affected the outcomes observed in 30 tests that extended to 10,000 cycles. Parallel checks were also carried out on dense (R_d = 73%, e_0 = 0.710) and anisotropically over-consolidated (OCR = 4) specimens. The interpretation was focused on exploring the validity, or otherwise, of the key hypotheses posed in Section 7.1. The following main conclusions can be drawn.

1. Upgraded high-resolution local strain instruments provided the accurate and representative cyclic strain measurements that are essential to characterising cyclic strain and stiffness behaviour. External displacement and volume-gauge measurements were susceptible to errors from system compliance and generated less accurate, and in some cases significantly misleading, strain measurements over the long-term (2-week) tests that imposed up to 10^4 cycles.

2. The patterns of permanent cyclic strain accumulation depended on the mean cyclic stress ratio (η) and cyclic amplitude stress ratio (CSR). The specimens generated significant compressive radial straining under high CSR two-way symmetric cycling at isotropic (η = 0) states, reflecting both the inclination (dq/dp') of the imposed constant σ_h' stress paths and the sand's anisotropic fabric, which is inherently more susceptible to axial extension. Under higher η (0.75 or 1.2) conditions, the sand developed axial compressional strains and radial extensional strains that increased invariably with the increase of CSR.

3. Significant contractive cyclic volumetric strains accumulated under loading from η = 0, which reduced markedly in tests that imposed higher η and reversed fully to develop cyclic dilation under cycling with η values of 1.07 and 1.2.

4. The cyclic straining patterns for the OCR = 4 specimens that followed anisotropic stress paths indicated the sand's enhanced micro-structure under axial compression but reduced ability to sustain cycling in extension, reflecting the combined effects pre-loading and prior pattern of consolidation stresses.

5. Power law functions gave the best fits for the accumulated cyclic strains and strain rates over the full-cycle ranges of tests that showed only one sign of straining. Correlations were established between the derived fitting parameters and the imposed cycling conditions as well as the observed cyclic straining patterns.

6. All experiments manifested quasi log-linear ε^{acc}-$\log_{10}(N)$ trends once $N > 200$, whose slopes indicated measures of the long-term rates of strain development under cycling.

7. The cyclic flow directions, as quantified by the strain ratio $\varepsilon_s^{acc}/\varepsilon_{vol}^{acc}$, were found to vary with a range of factors. Specimens tested from low p_0' and under low *CSR* manifested greater cyclic dilation, with the strain vector trending towards $\theta^{acc} > 90°$ as cycling evolved. The strain vectors of the specimens subjected to high *CSR* cycling trended towards the constant η-axes.

8. The cyclic dilation-stress ratio trends ($\varepsilon_v^{acc}/\varepsilon_s^{acc}$-$\eta$) of the high *CSR* tests fell below the trend predicted by Chang & Whitman (1988)'s cyclic dilation model, which focuses on the effects of η alone.

9. The Cyclic volumetric strains or void ratio changes varied with a range of influential factors, but did not show any trend to converge towards any cyclic steady state equivalent to the critical state line established for monotonic shearing.

10. Secant cyclic stiffnesses tended to vary over the early stages of cycling and then tend towards stable trends. Even the specimens that eventually experienced incremental collapse showed stable stiffness trends until shortly before failure. As expected, the ultimate cyclic stiffnesses decreased as *CSR* increased.

11. All of the Author's cyclic tests imposed perturbations that engaged the Dunkirk sand's initial linear elastic, Y_1, kinematic yield surface. However, stable cyclic responses were observed well beyond these elastic limits.

12. The cyclic thresholds below which *stable* responses were observed were determined as $CSR = 0.3$ for $\eta = 0$, $CSR = 0.2$ for $\eta = 0.75$ conditions, and $CSR = 0.11$ for higher η of 1.2, respectively, based on the permanent net axial strain rate criterion and the alternative cyclic stiffness criterion. These limits were associated with the onset of Y_2 yielding.

13. Prior drained cycling imparted significant positive effects on the post-cycling

monotonic shear stiffnesses and shear strengths of Dunkirk sand that could not be explained solely by soil densification. The most significant gains in monotonic vertical stiffnesses and shear strengths were seen in the higher *CSR* tests, which is interpreted as being due to micro-fabric changes that optimised the sand's ability to carry vertical drained loading.

14. The *OCR* = 4 specimens appeared to retain their 'memory' of pre-cycling anisotropic and over-consolidated stress history over the long-term cycling by manifesting higher stiffnesses and shear strengths than the uncycled and cycled *OCR* = 1 specimens when undergoing post-cycling monotonic shearing to failure.

CHAPTER 8
Conclusions and recommendations for future research

8.1 Overall summary

The Author's laboratory-based research programme was motivated by two recent piling research projects: a field micro-pile study with NGI/UC Dublin and Grenoble-Tech into the ageing of piles driven in sands (Carroll *et al.*, 2017, 2018), and the recent PIle Soil Analysis (PISA) joint industry project (2013-2016) (Byrne *et al.*, 2015b, Zdravković *et al.*, 2015, Byrne *et al.*, 2017) that aimed to develop new design methods for large diameter monopiles under lateral and moment loading.

The Author contributed to the first phase of the PISA project by providing laboratory experiments to support the design and numerical modelling of the PISA monotonic pile tests that were conducted in Dunkirk sand. The Author's research scope was substantially extended, in conjunction with the parallel initial study on Cowden till completed by Ushev (2018), to form an integrated programme of advanced laboratory characterisation for Cowden till and Dunkirk sand that covered four further relevant aspects of the mechanical behaviours of the PISA test site soils:

#1. Soil-soil/steel interface shearing and residual strengths;
#2. Shear strength anisotropy;
#3. Anisotropy of the stress-strain-stiffness behaviour observed from the linear elastic range (Y_1) up to failure;
#4. The response to large numbers of loading cycles, considering undrained conditions for Cowden till and the drained response of Dunkirk sand;

The Author's research on interface shearing was further extended to help characterise the Blessington and Larvik sands encountered in the joint micro-pile field study conducted with NGI, UC Dublin and Grenoble-Tech.

The overall experimental programme employed several classical and some

newly-developed advanced laboratory apparatuses and techniques. Significant effort was expended by the Author and his colleagues to upgrade and optimise technical aspects of the equipment to achieve the capabilities that were essential for the current research.

The main conclusions drawn from the research programme are summarised below. Those aspects that require further research are also identified.

8.2 Main conclusions

The main conclusions that may be drawn from the Author's laboratory-based research can be summarised under five headings.

8.2.1 High pressure compression and sand-steel interface shearing behaviour

The Author conducted high pressure oedometer compression tests (σ_v' up to 100 MPa) and sand-steel interface shearing experiments to help establish the behaviour of the highly mutated soils generated by driven pile installation in sands that are found in thin bonds around their shafts after driving. The most significant findings were:

1. The Dunkirk and Fontainebleau NE34 sand manifested highly non-linear and time-dependent compression behaviour, which was quantified through compression and creep indices (C_c and C_α) that were related to normal stress level and the sands' different minerologies, particle size distribution, shapes and uniformity characteristics.

2. Bishop interface ring shear tests were conducted on fresh samples of Dunkirk, Blessington and Larvik sands that imposed large-displacement (5 m) pre-conditioning shear displacements and revealed significant increases in interface friction angles (δ_{cv}') with normal effective stress level, regardless of the interfaces' steel material grade or surface roughnesses. No such stress-dependency was found in the parallel direct shear sand-steel interface tests.

3. Ring shear interface experiments that involved rough mild steel interfaces and one month ageing periods (under submerged conditions) showed remarkable increases over time in shearing resistances and rates of vertical dilation. Still more pronounced age rated changes were noted in the parallel direct shear interface tests involving submerged Dunkirk sand.

4. No such ageing effects were observed in tests with inert stainless steel interfaces, so physicochemical reactions are concluded to be the central to the ageing process.

5. Case-specific interface testing involving appropriate soil media, water chemistry, interface materials, stress levels, pre-conditioning stages, ages and displacement levels may be conducted to derive fully representative interface frictional angles for practical applications.

8.2.2 Stiffness and shear strength anisotropy of low-plasticity stiff Cowden till

Hollow Cylinder (HCA) and triaxial probing tests performed on intact Cowden till specimens identified significant aspects of the till's potential stiffness and shear strength anisotropy that have implications for the interpretation and modelling of the PISA field test piles' response to lateral and moment loadings, as well as future practical analysis of monopile behaviour in glacial till.

1. HCA experiments posed considerable challenges when working with stony, fissured, tills.

2. The $\alpha_{d\sigma}$-controlled constant b (= 0.5) undrained HCA tests revealed the till's anisotropic small strain stiffness behaviour. Undrained Young's and shear moduli developed in horizontal planes (E_{h0}^{u} and G_{hh0}) were 60-70% higher than those in the vertical planes (E_{v0}^{u} and G_{vh0}). These differences extended into the non-linear strain ranges, although the degree of stiffness anisotropy reduced with increasing strain level.

3. Advanced triaxial probing and multi-directional bender element tests also confirmed that the ratios between horizontal to vertical drained and undrained linear elastic stiffnesses (G_{hh0}/G_{vh0}, E_{h0}^{u}/E_{v0}^{u}, E_{h0}'/E_{v0}') were invariably greater than unity, regardless of the interpretation method implemented.

4. Stiffness anisotropy was most prominent in the top 6 m of the Cowden glacial deposit but persisted to below the 10 m tip depths of the longest PISA test piles.

5. Cowden till exhibited a notably ductile shear stress-strain response when sheared to failure and manifested significant shear strength anisotropy in HCA tests conducted with b = 0.5. The till mobilised its minimum and maximum shear strengths under vertical compression (α = 0˚) and lateral compression (α = 90˚) modes, respectively.

The torsional shear mode ($\alpha \approx 45^{\circ}$) led to shear strengths between these limits.

6. The Cowden till's pattern of stiffness anisotropy was comparable to that seen in earlier studies on older, higher *OCR*, plastic marine clays. However, it showed a milder and different form of shear strength anisotropy, which was also varied markedly from the patterns seen in young, low *OCR* clays and sands.

8.2.3 Pre-failure stiffnesses and yielding behaviour of Dunkirk sands

The Author's programmes of primarily drained monotonic experiments on reconstituted Dunkirk sands employed local strain and bender element sensors that allowed the sands' behaviour to be characterised over the full strain ranges that can be applied in triaxial testing. The outcomes contributed directly to the interpretation and numerical modelling of PISA field pile tests at Dunkirk. The main conclusions drawn are as follows.

1. The water pluviated reconstituted Dunkirk sand specimens manifested clear inherent anisotropy over their small linear elastic ranges (Y_1). Stiffnesses in the horizontal planes (E_h' and G_{hh}) were inherently higher than on the vertical planes (E_v' and G_{vh}) when tested from isotropic stress conditions. However, these stiffness characteristics were modified significantly by imposing further isotropic or anisotropic effective stress changes to the sand specimens.

2. The vertical and horizontal Young's moduli were found to depend principally on σ_v' and σ_h' respectively, raised to fractional powers, although the empirically found material parameters were found to be mildly dependent on the σ_h'/σ_v' stress ratio (K). In the same way, the G_{vh} and G_{hh} shear moduli were found to depend principally on (σ_v', σ_h') respectively, raised to fractional powers. In both cases, account also had to be taken of void ratio changes through a $f(e)$ function.

3. After exceeding its Y_1 elastic limit, Dunkirk sand developed highly non-linear stiffnesses that depended critically on void ratio, strain level, current stress states and effective stress history (*OCR*). Over-consolidated specimens developed notably longer Y_1 plateaux and higher non-linear stiffnesses. These aspects of the sand's stiffness may not be captured by procedures that rely only on body wave velocity measurements (made in the laboratory or in-situ) and generic normalised stiffness-strain decay curves.

4. Two kinematic yielding surfaces, Y_1 and Y_2, were located and explained in detail for the isotropically consolidated specimens. The sizes of the surfaces in q-p' space varied with specimen density and effective stress level, and their vertical scales could be represented by power law functions of p'.
5. It was shown that the end restraint implicit in conventional triaxial testing led to nominally higher stiffnsses with Dunkirk sand than were observed with equivalent tests employing fully lubricated plattens. The most pronounced impact was seen when testing low relative density specimen tests under low effective stress levels.

8.2.4 Large strain and critical state behaviour of Dunkirk sands

Dunkirk sand's stress-strain-dilatancy behaviour was investigated over large strains and up to failure in triaxial tests. The main outcomes, as interpreted within the critical state framework, in conjunction with the state parameter-based approach were:

1. Critical state lines could be established for Dunkirk sands as power law functions in e-p' space, with most credence being given to tests on specimens having the lowest densities that were achievable with the Author's water pluviation sample formation method.
2. The effects of end restraint noted above in relation to small strain behaviour persisted into the large strain range. End restraint affected the sample's global responses, leading to higher peak strengths and greater dilation.
3. The sand's failure behaviour could be characterised through the bounding surface approach of Manzari & Dafalias (1997) where the latter were characterised in terms of the current state parameter. Model fitting parameters were determined that correlated the sand's density and stress states with simple linear state parameter-dependent relationships.
4. The state parameter-based interpretation was central to calibrating and validating Taborda *et al.*'s (2014) multiple bounding surface plasticity constitutive model, which was employed in the successful modelling of the multiple PISA lateral loading pile tests performed at Dunkirk on piles up to 2 m diameter (Taborda *et al.*, 2018).

8.2.5 Long-term cyclic shearing and post-cycling behaviour of Dunkirk sand

A suite of benchmarking drained cyclic triaxial tests was also conducted that applied long-term (up to 10^4 cycles) cyclic loading to Dunkirk sand specimens, covering a range of factors including initial specimen density (R_d) and *OCR* as well as the mean cyclic stress ratio ($\eta = q_{mean}/p_0'$) and the cyclic amplitude ratio ($CSR = q_{cyc}/p_0'$). The main findings are:

1. The cyclic strain measurements made with highly accurate and upgraded local strain instruments were largely immune from system compliance and temperature fluctuation (±0.3°) effects, generating the good-quality and representative datasets required for characterising permanent cyclic strain trends, strain flow rules and cyclic stiffness behaviour.
2. Consistent cyclic straining patterns were observed that varied systematically with the considered influential factors.
3. The trends observed for permanent cyclic strains (ε^{acc}) and strain accumulation rates ($d\varepsilon_{acc}/dN$) were best fitted by power law functions, although these could only be applied to cases where the strain accumulation trends did not change sign as cycling progressed. Quasi-linear ε^{acc}-$\log_{10}(N)$ trends were observed in all cases over the $N > 200$ range, which also provided indications of the sand's long-term cycling response.
4. The interpretation of the long term cyclic strain rates trends had to take account of the very slow residual rates of creep straining that applied prior to the start of cycling, even after creep pauses of up to 80 hours duration.
5. Close analysis of the patterns of permanent strain development showed cyclic flow rules and dilation trends that varied distinctively with η, *CSR* and *N*. These could not be depicted accurately with simple cyclic dilation models that consider η as the only influential factor.
6. The cyclic volumetric strains and void ratio changes varied with a range of influential factors, but did not show any trend to converge towards any cyclic steady state equivalent to the critical state line established for monotonic shearing.
7. The Y_1 and Y_2 kinematic yield surface framework was applied successfully to help interpret cyclic thresholds for fully *stable* responses. The latter were identified as

CSR = 0.15 for samples cycled from η = 0 and 0.75 conditions and *CSR* = 0.11 for the tests with higher η values, based on both permanent cyclic strain accumulation and cyclic stiffness criteria. The conditions under which drained cyclic failure could occur were also identified.

8. Monotonic tests conducted after extended drained cyclic loading developed higher stiffness and peak shear strengths than "virgin" specimens, indicating that enhanced micro-fabrics had developed under cycling that optimised the sand's ability to carry drained vertical loading.

8.3 Recommendations for future research

The Author's research addressed important aspects of soil behaviours of both Cowden clay till and Dunkirk (and other) sands that may have important implications for practical piling engineering, particularly with offshore applications. The studies were necessarily limited in several regards and a number of questions may be identified as topics for possible future research. These include:

1. Further studies into the kinematic yielding behaviour of sands appear to be desirable. These should integrate a wider range of drained/undrained monotonic, and cyclic, triaxial or HCA tests and cover a wider range of q, p', b, α, *OCR* and void ratio conditions.

2. The Author's triaxial probing tests demonstrated a greater-than-expected sensitivity in the uniaxial stiffness fitting function terms to the K ratios applied in the triaxial tests that explored the linear elastic stiffness behaviour. Further experimental or numerical studies may be required to provide further evidence on these aspects of the stress-induced anisotropy of sands.

3. The Author's triaxial studies into cyclic loading behaviour of Dunkirk sand revealed several important features of the granular material's response to long-term cyclic loading, considering fully drained conditions. Further analysis of the Author's tests is required to:
   (1) investigate how permanent cyclic strain patterns evolve;
   (2) characterise the individual cycles' stress-strain and damping behaviour;
   (3) establish correlations between cyclic strain development parameters and the

imposed cyclic stress conditions, as quantified for example by the mean cyclic stress ratio η, and cyclic amplitude stress ratio CSR.

4. The Author's cyclic triaxial study focused on axial cyclic loading under uniform cyclic amplitude conditions. Further research could fruitfully consider more general and variable cyclic stress paths in triaxial or HCA experiments by applying variable-amplitude (non-uniform) cyclic loading conditions.

References

Ackerley, S. K., Standing, J. R. & Kamal, R. H. (2016) A system for measuring local radial strains in triaxial apparatus. *Géotechnique* **66(6)**:515-522.

Addenbrooke, T. I., Potts, D. M. & Puzrin, A. M. (1997) The influence of pre-failure soil stiffness on the numerical analysis of tunnel construction. *Géotechnique* **47(3)**:693-712.

Agarwal, K. B. (1968) *The influence of size and orientation of sample on the undrained strength*, PhD thesis, Imperial College (University of London).

Aghakouchak, A. (2015) *Advanced laboratory studies to explore the axial cyclic behaviour of driven piles*, PhD thesis, Imperial College London.

Aghakouchak, A., Sim, W. W. & Jardine, R. J. (2015) Stress-path laboratory tests to characterise the cyclic behaviour of piles driven in sands. *Soils and Foundations* **55(5)**:917-928.

Airey, D. W. & Wood, D. M. (1987) An evaluation of direct simple shear tests on clay. *Géotechnique* **37(1)**:25-35.

Airey, D., Al-Douri, R. & Poulos, H. (1992) Estimation of pile friction degradation from shearbox tests. *Geotechnical Testing Journal* **15(4)**:388-392.

Airey, D. W. & Kelly, R. B. (2010) Interface behaviours from large diameter ring shear tests. In *Characterization and Behaviour of Interfaces*. (Frost, J. D. (ed)) IOS press, Atlanta, Georgia, USA.

Al-Haj, K. (2014) *Mechanical response of two plastic clay soils from Sudan*, PhD thesis, Imperial College London.

Al-Haj, K. M. A. & Standing, J. R. (2016) Soil water retention curves representing two tropical clay soils from Sudan. *Géotechnique* **66(1)**:71-84.

Al-Tabbaa, A. & Muir Wood, D. (1989) An experimentally based "bubble' model for clay. In *3rd International Conference on Numerical Models in Geomechanics*. Niagara Falls, Canada, pp. 91-99.

Alonso-Marroquin, F. & Herrmann, H. (2004) Ratcheting of granular materials. *Physical Review Letters* **92(5)**:054301.

Altuhafi, F. N. & Coop, M. R. (2011) Changes to particle characteristics associated with the compression of sands. *Géotechnique* **61(6)**:459-471.

Altuhafi, F. N., O'Sullivan, C. & Cavarretta, I. (2013) Analysis of an image-based method to quantify the size and shape of sand particles. *Journal of Geotechnical and Geoenvironmental Engineering* **139(8)**:1290-1307.

Altuhafi, F. N., Coop, M., R. & Georgiannou, w. V., N. (2016) Effect of particle shape on the mechanical behavior of natural sands. *Journal of Geotechnical and Geoenvironmental Engineering* **142(12)**:04016071.

Altuhafi, F. N., Jardine, R. J., Georgiannou, V. N. & Moinet, W. W. (2017) Effects of particle breakage and stress reversal on the behaviour of sand around displacement piles. *Géotechnique* **68(6)**:546-555.

Alvarado, G. & Coop, M. R. (2012) On the performance of bender elements in triaxial tests. *Géotechnique* **62(1)**:1-17.

Andresen, A. & Kolstad, P. (1979) The NGI 54 mm sampler for undisturbed sampling of clays and representative sampling of coarser materials. In *State of the art on current practice of soil sampling, International Symposium of Soil Sampling*. Japanese Society of Soil Mechanics and Foundation Engineering, Tokyo, Japan, Vol. 1, pp. 13-21.

Antonyuk, S., Tomas, J., Heinrich, S. & Mörl, L. (2005) Breakage behaviour of spherical granulates by compression. *Chemical Engineering Science* **60(14)**:4031-4044.

Arthur, J. R. F. & Menzies, B. K. (1972) Inherent anisotropy in a sand. *Géotechnique* **22(1)**:115-128.

Ashmawy, A. K. & Drnevich, V. P. (1994) General dynamic model for the resonant column/quasi-static torsional shear apparatus. *Geotechnical Testing Journal* **17(3)**:337-348.

Atkinson, B. K. (1979) A fracture mechanics study of subcritical tensile cracking of quartz in wet environments. *Pure and Applied Geophysics* **117(5)**:1011-1024.

Azeiteiro, R. J. N., Coelho, P. A. L. F., Taborda, D. M. G. & Grazina, J. C. D. (2017) Critical state-based interpretation of the monotonic behaviour of Hostun sand. *Journal of Geotechnical and Geoenvironmental Engineering* **143(5)**.

Barmpopoulos, I., Ho, T., Jardine, R. & Anh-Minh, N. (2010) The large displacement shear characteristics of granular media against concrete and steel interfaces. In *Proceedings of the Research Symposium on Characterization and Behavior of Interfaces*. (Frost, J. (ed)) IOS press, Atlanta, USA.

Baudet, B. & Stallebrass, S. (2004) A constitutive model for structured clays. *Géotechnique* **54(4)**:269-278.

Been, K. & Jefferies, M. G. (1985) A state parameter for sands. *Géotechnique* **35(2)**:99-112.

Been, K., Jefferies, M. G. & Hachey, J. (1991) The critical state of sands. *Géotechnique* **41(3)**:365-381.

Bellotti, R., Jamiolkowski, M., Lo Presti, D. C. F. & O'Neill, D. A. (1996) Anisotropy of small strain stiffness in Ticino sand. *Géotechnique* **46(1)**:115-131.

Bishop, A. W. & Green, G. E. (1965) The influence of end restraint on the compression strength of a cohesionless soil. *Géotechnique* **15(3)**:243-266.

Bishop, A. W. (1966) The 6th Rankine lecture: The strength of soils as engineering materials. *Géotechnique* **16(2)**:91-130.

Bishop, A. W., Green, G. E., Garga, V. K., Andresen, A. & Brown, J. D. (1971) A new ring shear apparatus and its application to the measurement of residual strength.

Géotechnique **21(4)**:273-328.

Bishop, A. W. & Wesley, L. D. (1975) A hydraulic triaxial apparatus for controlled stress path testing. *Géotechnique* **25(4)**:657-670.

Blaker, Ø., Lunne, T., Vestgården, T., Krogh, L., Thomsen, N. V., Powell, J. J. M. & Wallace, C. F. (2015) Method dependency for determining maximum and minimum dry unit weights of sands. In *3rd International Symposium on Frontiers in Offshore Geotechnics*. (Meyer, V. (ed)) Leiden, Netherlands: CRC Press/Balkema, Oslo, Norway.

Bromhead, E. (1979) A simple ring shear apparatus. *Ground Engineering* **12(5)**:40-44.

Brosse, A. M. (2012) *Study of the anisotropy of three British mudrocks using a Hollow Cylinder Apparatus*, PhD thesis, Imperial College London.

Brosse, A., Jardine, R. J. & Nishimura, S. (2015) Undrained stiffness anisotropy from Hollow Cylinder testing of four Eocene-to-Jurassic stiff clays. *Canadian Geotechnical Journal* **54(3)**:313-332.

Brosse, A., Kamal, R. H., Jardine, R. J. & Coop, M. R. (2016) The shear stiffness characteristics of four Eocene-to-Jurassic UK stiff clays. *Géotechnique* **67(3)**:242-259.

Brosse, A. M., Jardine, R. J. & Nishimura, S. (2017) The undrained shear strength anisotropy of four Jurassic to Eocene stiff clays. *Géotechnique* **67(8)**: 653-671.

Brown, S. (1974) Repeated load testing of a granular material. *Journal of the Geotechnical Engineering Division-ASCE* **100(7)**:825-841.

Brown, S. & Hyde, A. (1975) Significance of cyclic confining stress in repeated-load triaxial testing of granular material. *Transportation research record* **(537)**.

Brucy, F., Nauroy, J.-F., Le Tirant, P. & Meunier, J. (1991) Comparison of static and dynamic tests of piles in sand, In *Proceedings of Conf. Fondations Profondes*, pp. 369-378.

Buckley, R. (2018) *The axial behaviour of displacement piles in chalk*, PhD thesis, Imperial College London.

Burd, H. J., Byrne, W. B., McAdam, R. A., Houlsby, G. T., Martin, C. M., Beuckelaers, W. J. A. P., Zdravković, L., Taborda, D. M. G., Potts, D. M., Jardine, R. J., Gavin, K., Doherty, P., Igoe, D., Skov Gretlund, J., Pacheco Andrade, M. & Muir Wood, A. (2017) Design aspects for monopile foundations. In *Proceedings of the 19th International Conference on Soil Mechanics and Geotechnical Engineering (ICSMGE 2017): Unearth the Future, Connect Beyond*. (Lee, W., Lee, J.-S., Kim, H.-K., and Kim, D.-S. (eds)), Seoul, Republic of Korea.

Burland, J. (1989) The 9th Laurits Bjerrum Memorial Lecture: "Small is beautiful"—the stiffness of soils at small strains. *Canadian Geotechnical Journal* **26(4)**:499-516.

Burland, J. B. (1990) The 30th Rankine Lecture: On the compressibility and shear strength of natural clays. *Géotechnique* **40(3)**:329-378.

Byrne, B. (2011) Future design for offshore wind turbines: Géotechnique Lecture 2011.

Byrne, B. W., McAdam, R., Burd, H. J., Houlsby, G. T., Martin, C. M., Zdravković, L.,

Taborda, D. M. G., Potts, D. M., Jardine, R. J., Sideri, M., Schroeder, F. C., K. Gavin, Doherty, P., Igoe, D., Wood, A. M., Kallehave, D. & Gretlund, J. S. (2015a) Field testing of large diameter piles under lateral loading for offshore wind applications. In *XVI European Conference on Soil Mechanics and Geotechnical Engineering*. (Winter, M., Smith, D., Eldred, P., and Toll, D. (eds)) ICE Publishing, Edinburg, UK.

Byrne, B. W., McAdam, R., Burd, H. J., Houlsby, G. T., Martin, C. M., Zdravković, L., Taborda, D. M. G., Potts, D. M., Jardine, R. J., Sideri, M., Schroeder, F. C., K. Gavin, Doherty, P., Igoe, D., Wood, A. M., Kallehave, D. & Gretlund, J. S. (2015b) New design methods for large diameter piles under lateral loading for offshore wind applications. In *3rd International Symposium on Frontiers in Offshore Geotechnics*. (Meyer, V. (ed)) Leiden, Netherlands: CRC Press/Balkema, Oslo, Norway.

Byrne, B., McAdam, R., Burd, H., Houlsby, G., Martin, C., Beuckelaers, W., Zdravkovic, L., Taborda, D., Potts, D., Jardine, R., Ushev, E., Liu, T., Abadias, D., Gavin, K., Igoe, D., Doherty, P., Gretlund, J. S., Andrade, M. P., Wood, A. M., Schroeder, F., Turner, S. & Plummer, M. (2017) PISA: New design methods for offshore wind turbine monopiles. In *8th International Conference on Offshore Site Investigation & Geotechnics*. The Society for Underwater Technology, London, UK, Vol. 1, pp. 142-161.

Cai, Y., Sun, Q., Guo, L., Juang, C. H. & Wang, J. (2015) Permanent deformation characteristics of saturated sand under cyclic loading. *Canadian Geotechnical Journal* **52(6)**:795-807.

Cai, Y. Q., Guo, L., Jardine, R. J., Yang, Z. X. & Wang, J. (2017) Stress–strain response of soft clay to traffic loading. *Géotechnique* **67(5)**:446-451.

Carraro, J. & Prezzi, M. (2008) A new slurry-based method of preparation of specimens of sand containing fines. *Geotechnical Testing Journal* **31(1)**:1-11.

Carroll, R., Carotenuto, P., Dano, C., Salama, I., Silva, M., Gavin, K. & Jardine, R. (2017) Field studies on the axial capacity of small diameter piles and ageing effects in sands. In *8th International Conference on Offshore Site Investigation & Geotechnics*. The Society for Underwater Technology, London, UK, Vol. 2, pp. 1160-1169.

Carroll, R., Carotenuto, P., Dano, C., Salama, I., Silva, M., Gavin, K. & Jardine, R. (2018) Field experiments at three sites to investigate the effects of age on steel piles driven in sand. *Under review by Geochnique*.

Cavarretta, I. & O'Sullivan, C. (2012) The mechanics of rigid irregular particles subject to uniaxial compression. *Géotechnique* **62(8)**:681-692.

Cavarretta, I., O'Sullivan, C. & Coop, M. R. (2017) The relevance of roundness to the crushing strength of granular materials. *Géotechnique* **67(4)**:301-312.

Chandler, R. & Gutierrez, C. (1986) The filter-paper method of suction measurement. *Géotechnique* **36(2)**:265-268.

Chang, C. & Whitman, R. (1988) Drained permanent deformation of sand due to cyclic

loading. *Journal of Geotechnical Engineering* **114(10)**:1164-1180.

Chaudhary, S. K. & Kuwano, J. (2003) Anisotropic multiple yielding of dense Toyoura sand in p'-constant shear plane. *Soils and Foundations* **43(4)**:59-69.

Chen, H. (2017a) *Soil-steel interface testing on three sands*, MSc thesis, Imperial College London.

Chen, S. (2017b) *Temperature-controlled interface shear box testing of a sand for pipeline design*, MSc thesis, Imperial College London.

Chong, S.-H. & Santamarina, J. C. (2016) Sands subjected to repetitive vertical loading under zero lateral strain: accumulation models, terminal densities, and settlement. *Canadian Geotechnical Journal* **53(12)**:2039-2046.

Chow, F. C. (1997) *Investigations into the behaviour of displacement piles for offshore foundations*, PhD thesis, Imperial College London (University of London).

Chow, F. C., Jardine, R. J., Nauroy, J. F. & Brucy, F. (1997) Time-related increases in the shaft capacities of driven piles in sand. *Géotechnique* **47(2)**:353-361.

Chow, F. C., Jardine, R. J., Brucy, F. & Nauroy, J. (1998) Effects of time on capacity of pipe piles in dense marine sand. *Journal of Geotechnical and Geoenvironmental Engineering* **124(3)**:254-264.

Ciantia, M. O., Arroyo, M., Butlanska, J. & Gens, A. (2016) DEM modelling of cone penetration tests in a double-porosity crushable granular material. *Computers and Geotechnics* **73(2016)**:109-127.

Ciantia, M. O., Piñero, G., Zhu, J. & Shire, T. (2017) On the progressive nature of grain crushing. In *Powders and Grains 2017 – 8th International Conference on Micromechanics on Granular Media*. (Radjai, F., Nezamabadi, S., Luding, S., and Delenne, J. Y. (eds)) EPJ Web of Conferences, Montpellier, France, Volume 140 (2017).

Ciantia, M. O., Arroyo, M., Sullivan, C. O., Gens, A. & Liu, T. (2018) Grading evolution and critical state in a discrete numerical model of Fontainebleau sand. *Géotechnique in print*.

Clayton, C. R. I. (2011) Stiffness at small strain: research and practice. *Géotechnique* **61(1)**:5-37.

Collins, I. F. & Boulbibane, M. (2000) Geomechanical analysis of unbound pavements based on shakedown theory. *Journal of Geotechnical and Geoenvironmental Engineering* **126(1)**:50-59.

Coop, M. (1990) The mechanics of uncemented carbonate sands. *Géotechnique* **40(4)**:607-626.

Coop, M. R. & Lee, I. K. (1993) The behaviour of granular soils at elevated stresses. In *Proceedings of the C. P. Wroth Memorial Symposium: Predictive soil mechanics*. London: Thomas Telford, London, pp. 186-198.

Coop, M. R. & Lee, I. K. (1995) The influence of pore water on the mechanics of granular

soils. In *Proceedings of the XIth European regional conference on SMFE*. Copenhagen, Denmark, Vol. 1, pp. 63-73.

Coop, M., Sorensen, K., Freitas, T. B. & Georgoutsos, G. (2004) Particle breakage during shearing of a carbonate sand. *Géotechnique* **54(3)**:157-164.

Cui, L., Bhattacharya, S., Nikitas, G. & Vimalan, J. (2017) Predicting long term performance of OWT foundation using cyclic simple shear apparatus and DEM simulations. In *8th International Conference on Offshore Site Investigation & Geotechnics*. The Society for Underwater Technology, London, UK, Vol. 2, pp. 1132-1139.

CUR (2001) Bearing capacity of steel pipe piles, Report 2001-8. Gouda, The Netherlands, Centre for Civil Engineering Research and Codes.

Daramola, O. (1978) *The influence of stress history on the deformation of sand*, PhD thesis, Imperial College London (University of London).

DeJong, J. T. & Frost, J. D. (2002) A multisleeve friction attachment for the cone penetrometer. *Geotechnical Testing Journal* **25(2)**:111-127.

Dejong, J. T., Randolph, M. F. & White, D. J. (2003) Interface load transfer degradation during cyclic loading : A microscale investigation. *Soils and Foundations* **43(4)**:81-93.

DeJong, J. T. & Westgate, Z. J. (2009) Role of initial state, material properties, and confinement condition on local and global soil-structure interface behavior. *Journal of Geotechnical and Geoenvironmental Engineering* **135(11)**:1646-1660.

Dixon, N. & Spriggs, M. (2007) Quantification of slope displacement rates using acoustic emission monitoring. *Canadian Geotechnical Journal* **44(8)**:966-976.

Doherty, P., Kirwan, L., Gavin, K., Igoe, D., Tyrrell, S., Ward, D. & O'Kelly, B. C. (2012) Soil properties at the UCD geotechnical research site at Blessington. In *Bridge and Concrete Research in Ireland*., Dublin, Ireland.

Dominguez-Quintans, C., Quinteros, V. S., Carraro, J. A. H., Zdravkovic, L. & Jardine, R. J. (2018) An innovative in-mould slurry deposition technique for triaxial reconstitution of sands and silty soils specimens. BGA annual conference (poster presentation).

Dove, J. & Frost, J. (1999) Peak friction behavior of smooth geomembrane–particle interfaces. *Journal of Geotechnical and Geoenviron. Engineering* **125(7)**:544-555.

Drnevich, V. P. (1978) Resonant-column testing–Problems and solutions. *Dynamic Geotechnical Testing, Special Technical Publication 654, ASTM*:384-398.

Escribano, D. E. & Nash, D. F. T. (2015) Changing anisotropy of G_0 in Hostun sand during drained monotonic and cyclic loading. *Soils and Foundations* **55(5)**:974-984.

Escribano, D. L. (2014) *Evolution of stiffness and deformation of hostun sand under drained cyclic loading*, PhD thesis, University of Bristol.

Fakharian, K. & Evgin, E. (1996) An automated apparatus for three-dimensional monotonic and cyclic testing of interfaces. *Geotechnical Testing Journal,* **19(1)**:22-31.

Fakharian, K. & Evgin, E. (1997) Cyclic simple-shear behavior of sand-steel interfaces under

constant normal stiffness condition. *Journal of Geotechnical and Geoenvironmental Engineering* **123(12)**:1096-1105.

Farhadi, B. & Lashkari, A. (2017) Influence of soil inherent anisotropy on behavior of crushed sand-steel interfaces. *Soils and Foundations* **57(1)**:111-125.

Fernandes, F., Syahrial, A. & Valdes, J. (2010) Monitoring the oedometric compression of sands with acoustic emissions. *Geotechnical Testing Journal* **33(5)**.

Fonseca, J. (2011) *The evolution of morphology and fabric of a sand during shearing*, PhD thesis, Imperial College London.

García-Rojo, R. & Herrmann, H. (2005) Shakedown of unbound granular material. *Granular matter* **7(2-3)**:109-118.

Garga, V. & Infante Sedano, J. (2002) Steady state strength of sands in a constant volume ring shear apparatus. *Geotechnical Testing Journal* **25(4)**:414-421.

Gasparre, A. (2005) *Advanced laboratory characterisation of London clay*, PhD thesis, Imperial College London.

Gasparre, A., Nishimura, S., Coop, M. R. & Jardine, R. J. (2007a) The influence of structure on the behaviour of London Clay. *Géotechnique* **57(1)**:19-31.

Gasparre, A., Nishimura, S., Minh, N. A., Coop, M. R. & Jardine, R. J. (2007b) The stiffness of natural London Clay. *Géotechnique* **57(1)**:33-47.

Gasparre, A., Hight, D. W., Coop, M. R. & Jardine, R. J. (2014) The laboratory measurement and interpretation of the small-strain stiffness of stiff clays. *Géotechnique* **64(12)**:942-953.

Gavin, K. G., Igoe, D. J. P. & Kirwan, L. (2013) The effect of ageing on the axial capacity of piles in sand. *Proceedings of the Institution of Civil Engineers - Geotechnical Engineering* **166(2)**:122-130.

Gavin, K., Jardine, R., Karlsrud, K. & Lehane, B. M. (2015) The effects of pile ageing on the shaft capacity of offshore piles in sand. In *Proceeding of International Symposium Frontiers in Offshore Geotechnics (ISFOG)*. (Meyer, V. (ed)) CRC Press, London, Oslo, Noway, Vol. 1, pp. 129-152.

GDS GDSIST: GDS Interface Shear Tester.

Germaine, J. & Ladd, C. (1988) Triaxial testing of saturated cohesive soils. In *Advanced Triaxial Testing of Soil and Rock, ASTM STP 97*. (Donagh, R. T., Chaney, R. C., andSilver, M. L. (eds)) American Society for Testing and Materials, Philadelphia, pp. 421-459.

Ghionna, V. N. & Mortara, G. (2002) An elastoplastic model for sand–structure interface behaviour. *Géotechnique* **52(1)**:41-50.

Gibson, R. E. (1974) The 14th Rankine Lecture: The analytical method in soil mechanics. *Géotechnique* **24(2)**:115-140.

Graham, J. & Houlsby, G. T. (1983) Anisotropic elasticity of a natural clay. *Géotechnique*

33(2):165-180.

Gu, X., Yang, J., Huang, M. & Gao, G. (2015) Bender element tests in dry and saturated sand: Signal interpretation and result comparison. *Soils and Foundations* **55(5)**:951-962.

Guo, L., Cai, Y., Jardine, R. J., Yang, Z. & Wang, J. (2017) Undrained behaviour of intact soft clay under cyclic paths that match vehicle loading conditions. *Canadian Geotechnical Journal* **55(1)**:90-106.

Hardin, B. O. & Blandford, G. E. (1989) Elasticity of particulate materials. *J. Geotech. Engng Div., ASCE* **115(GT6)**:788-805.

Hardin, B. O. & Richart, F. (1963) Elastic wave velocities in granular soils. *Journal of Soil Mechanics & Foundations Div* 89(Proc. Paper 3407).

Hardy, H. R., Jr. (2005) *Acoustic emission/microseismic activity: volume 1: principles, techniques and geotechnical applications.* CRC Press.

Hellings, J. E. (1988) *The strength and stiffness of soils associated with excavations*, PhD thesis, Imperial College (University of London).

Hidalgo, R. C., Grosse, C. U., Kun, F., Reinhardt, H. W. & Herrmann, H. J. (2002) Evolution of percolating force chains in compressed granular media. *Physical review letters* **89(20)**:1-5.

Hight, D. W., Gens, A. & Symes, M. J. (1983) The development of a new hollow cylinder apparatus for investigating the effects of principal stress rotation in soils. *Géotechnique* **33(4)**:355-383.

Hight, D. W. & Jardine, R. J. (1993) Small strain stiffness and strength characteristics of hard London Tertiary clays. In *Geotechnical engineering of hard soils–soft rocks*. (Anagnostopoulos, A., Schlosser, F., Kalteziotis, N., and Frank, R. (eds)) Balkema, Rotterdam, the Netherlands, Vol. 1, pp. 533–552.

Ho, T., Jardine, R. & Anh-Minh, N. (2011) Large-displacement interface shear between steel and granular media. *Géotechnique* **61(3)**:221.

HongNam, N. & Koseki, J. (2005) Quasi-elastic deformation properties of Toyoura sand in cyclic triaxial and torsional loadings. *Soils and Foundations* **45(5)**:19-37.

Hosseini Kamal, R. (2012) *Experimental study of the geotechnical properties of UK mudrocks*, PhD thesis, Imperial College London.

Hosseini Kamal, R. l., Coop, M. R., Jardine, R. J. & Brosse, A. (2014) The post-yield behaviour of four Eocene-to-Jurassic UK stiff clays. *Géotechnique* **64(8)**:620-634.

Ibraim, E., Christiaens, P. & Pope, M. (2011) Development of a hollow cylinder torsional apparatus for pre-failure deformation and large strains behaviour of sand. *Geotechnical Engineering Journal of the South-east Asian Geotechnical Society (SEAGS) & Association of Geotechnical Societies in South-East Asia (AGSSEA), Special Issue on Soil Behaviour* **42**:58-68.

Ibraim, E., Luo, S. & Diambra, A. (2017) Particle soil crushing: passive detection and

interpretation. In *19th International Conference on Soil Mechanics and Geotechnical Engineering*. (Lee, W., Lee, J.-S., Kim, H.-K., and Kim, D.-S. (eds)) ISSMGE, Seoul, Korea.

Ishihara, K., Tatsuoka, F. & Yasuda, S. (1975) Undrained deformation and liquefaction of sand under cyclic stresses. *Soils and Foundations* **15(1)**:29-44.

Ishihara, K. (1993) The 33rd Rankine Lecture: Liquefaction and flow failure during earthquakes. *Géotechnique* **43(3)**:351-451.

Jamiolkowski, M., Leroeuil, S. & Lo Presti, D. C. F. (1991) Design parameters from theory to practice. In *Proceedings of Geo-coast '91 International Conference*. Yokosuka, Japan, vol. 2, pp. 877-917.

Jardine, R. J., Symes, M. J. & Burland, J. B. (1984) The measurement of soil stiffness in the triaxial apparatus. *Géotechnique* **34(3)**:323-340.

Jardine, R. J. (1985) *Investigations of pile-soil behaviour, with special reference to the foundations of offshore structures*, Imperial College London (University of London).

Jardine, R. J., Potts, D., Fourie, A. & Burland, J. (1986) Studies of the influence of non-linear stress–strain characteristics in soil–structure interaction. *Géotechnique* **36(3)**:377-396.

Jardine, R. J. (1992) Some observations on the kinematic nature of soil stiffness. *Soils and Foundations* **32(2)**:111-124.

Jardine, R. J., Lehane, B. M. & Everton, S. J. (1992) Friction coefficients for piles in sands and silts. In *Offshore Site Investigation and Foundation Behaviour*. (Ardus, D. A., Clare, D., Hill, A., Hobbs, R., Jardine, R. J., and Squire, J. M. (eds)) Society for Underwater Technology, Dordrecht, pp. 661-677.

Jardine, R. J. (1996) *Preliminary report on the design and manufacture of equipments*. Imperial College London.

Jardine, R. (2002) Stability and Instability: Soft clay embankment foundations and offshore continental slopes In *International Symposium on Coastal Geotechnical Engineering in Practice*. Balkema, Rotterdam, pp. 99-118.

Jardine, R. J., Gens, A., Hight, D. W. & Coop, M. R. (2004) Developments in understanding soil behaviour. In *Advances in geotechnical engineering: The Skempton conference*. Thomas Telford, vol. 1, pp. 103.

Jardine, R. J., Chow, F. C., Overy, R. F. & Standing, J. R. (2005) *ICP design methods for driven piles in sands and clays.* London, Thomas Telford.

Jardine, R. J., Standing, J. R. & Chow, F. C. (2006) Some observations of the effects of time on the capacity of piles driven in sand. *Géotechnique* **56(4)**:227-244.

Jardine, R. J., Puech, A. & Andersen, K. H. (2012) Cyclic loading of offshore piles: Potential effects and practical design In *Proceedings of 7th International conference on offshore site investigations and geotechnics*. Society of Underwater Technology, SUT, pp. 59-100.

Jardine, R. J. & Standing, J. R. (2012) Field axial cyclic loading experiments on piles driven in sand. *Soils and Foundations* **52(4)**:723-736.

Jardine, R. J., Zhu, B. T., Foray, P. & Yang, Z. X. (2013a) Interpretation of stress measurements made around closed-ended displacement piles in sand. *Géotechnique* **63(8)**:613-627.

Jardine, R. J., Zhu, B. T., Foray, P. & Yang, Z. X. (2013b) Measurement of stresses around closed-ended displacement piles in sand. *Géotechnique* **63(1)**:1-17.

Jardine, R. J. (2013) The 2nd Bishop Lecture Advanced laboratory testing in research and practice.. In *18th International Conference on Soil Mechanics and Geotechnical Engineering*. (Delage, P., Desrues, J., Frank, R., Puech, A., and Schlosser, F. (eds)) des Ponts, Paris, vol. 1, pp. 33-55.

Jardine, R. J. (2018) The 56th Rankine Lecture: Geotechnics, energy and climate change. *Geochnique in press*.

Jardine, R. J., Buckley, R. M., Kontoe, S., Barbosa, P. & Schroeder, F.C. (2018) Behaviour of piles driven in chalk. In *Proceedings of the Chalk 2018 Conference* (Lawrence, J.A., Preene, M., Lawrence, U.L. & Buckely, R.(eds)) London, UK.

Jeanjean, P., Zhang, Y., Zakeri, A., Andersen, K., Gilbert, R. & Senanayake, A. (2017) A framework for monotonic p-y curves in clays. In *8th International Conference on Offshore Site Investigation & Geotechnics*. The Society for Underwater Technology, London, UK, Vol. 1, pp. 108-141.

Jefferies, M. & Bean, K. (2006) *Soil liquefaction a critical state approach*. Taylor & Francis.

Jiang, Y., Wang, G. & Kamai, T. (2017) Acoustic emission signature of mechanical failure: Insights from ring-shear friction experiments on granular materials. *Geophysical Research Letters* **44(6)**:2782-2791.

Kallehave, D., Byrne, B. W., LeBlanc Thilsted, C. & Mikkelsen, K. K. (2015) Optimization of monopiles for offshore wind turbines. *Philosophical Transactions of the Royal Society A: Mathematical, Physical and Engineering Sciences* **373(2035)**.

Karlsrud, K., Jensen, T. G., Wensaas Lied, E. K., Nowacki, F. & Simonsen, A. S. (2014) Significant ageing effects for axially loaded piles in sand and clay verified by new field load tests. In *Proceedings of the Offshore Technology Conference*, Houston, TX, USA, pp. paper OTC-25197-MS.

Kelly, R., Airey, D. & Tabucanon, J. (2003) Design and performance of a 1 m diameter ring shear apparatus. *Geotechnical Testing Journal* **26(4)**.

Ketcham, R. A. & Carlson, W. D. (2001) Acquisition, optimization and interpretation of X-ray computed tomographic imagery: applications to the geosciences. *Computers & Geosciences* **27(4)**:381-400.

Kirkgard, M. M. & Lade, P. V. (1993) Anisotropic three-dimensional behavior of a normally consolidated clay. *Canadian Geotechnical Journal* **30(5)**:848-858.

Kishida, H. & Uesugi, M. (1987) Tests of the interface between sand and steel in the simple

shear apparatus. *Géotechnique* **37(1)**:45-52.

Klotz, E. & Coop, M. (2002) On the identification of critical state lines for sands. *Geotechnical Testing Journal* **25(3)**:289-302.

Koerner, R. M., Lord Jr, A. E., McCabe, W. M. & Curran, J. W. (1976) Acoustic emission behavior of granular soils. *Journal of the Geotechnical Engineering Division-ASCE* **103**:1460-1461.

Koiter, W. T. (1960) *General theorems for elastic-plastic solids.* North-Holland, Amsterdam.

Kovacevic, N., Hight, D. W. & Potts, D. M. (2007) Predicting the stand-up time of temporary London Clay slopes at Terminal 5, Heathrow Airport. *Géotechnique* **57(1)**:63-74.

Kuwano, R. (1999) *The stiffness and yielding anisotropy of sand*, PhD thesis, Imperial College London.

Kuwano, R., Connolly, T. & Jardine, R. (2000) Anisotropic stiffness measurements in a stress-path triaxial cell. *Geotechnical Testing Journal* **23(2)**:141-157.

Kuwano, R. & Jardine, R. J. (2002a) On measuring creep behaviour in granular materials through triaxial testing. *Canadian Geotechnical Journal* **39(5)**:1061-1074.

Kuwano, R. & Jardine, R. J. (2002b) On the applicability of cross-anisotropic elasticity to granular materials at very small strains. *Géotechnique* **52(10)**:727-749.

Kuwano, R. & Jardine, R. (2007) A triaxial investigation of kinematic yielding in sand. *Géotechnique* **57(7)**:563-579.

Lade, P. V. & Kirkgard, M. M. (2000) Effects of stress rotation and changes of *b*-values on cross-anisotropic behavior of natural *K*o consolidated soft clay. *Soils and Foundations* **40(6)**:93-105.

Lee, D. M. (1992) *The angles of friction of granular fills*, PhD thesis, University of Cambridge.

Lehane, B. (1992) *Experimental investigations of pile behaviour using instrumented piles*, PhD thesis, Imperial College (University of London).

Lemos, L. J. L. (1986) *The effect of rate on residual strength of soil*, PhD thesis, Imperial College London (University of London).

Li, X. S. & Wang, Y. (1998) Linear representation of steady-state line for sand. *Journal of Geotechnical and Geoenvironmental Engineering* **124(12)**:1215-1217.

Lings, M. L. (2001) Drained and undrained anisotropic elastic stiffness parameters. *Géotechnique* **51(6)**:555-565.

Lings, M. L. & Dietz, M. S. (2005) The peak strength of sand-steel interfaces and the role of dilation. *Soils and Foundations* **45(6)**:1-14.

López-Querol, S. & Coop, M. R. (2012) Drained cyclic behaviour of loose Dogs Bay sand. *Géotechnique* **62(4)**:281-289.

Lunne, T., Robertson, P. K. & Powell, J. J. M. (1997) *Cone penetration testing in geotechnical practice.* New York, Blackie Academic/Routledge Publishing.

Luo, S., Diambra, A. & Ibraim, E. (2016) Application of acoustic emission on crushing monitoring of individual soil particles in uniaxial compression test. 1st IMEKO TC4 International Workshop on Metrology for Geotechnics, MetroGeotechnics

Lupini, J. F., Skinner, A. E. & Vaughan, P. R. (1981) The drained residual strength of cohesive soils. *Géotechnique* **31(2)**:181-213.

Mair, R. J. (1993) Developments in geotechnical engineering research: Application to tunnels and deep excavations. Unwin Memorial Lecture 1992. *Proceedings of the Institution of Civil Engineers - Civil Engineering* **97(1)**:27-41.

Manzari, M. T. & Dafalias, Y. F. (1997) A critical state two-surface plasticity model for sands. *Géotechnique* **47(2)**:255-272.

Marinho, F. A. M. (1994) *Shrinkage behaviour of some plastic soils*, PhD thesis, Imperial College (University of London).

Marr, W. & Christian, J. (1981) Permanent displacements due to cyclic wave loading. *J Geotech Eng Div ASCE* **107(GT8)**:1129-1149.

Martinez, A., Frost, J. & Hebeler, G. (2015) Experimental study of shear zones formed at sand/steel interfaces in axial and torsional axisymmetric tests. *Geotechnical Testing Journal* **38(4)**:409-426.

Martinez, A. & Frost, J. D. (2018) Undrained behavior of sand–structure interfaces subjected to cyclic torsional shearing. *Journal of Geotechnical and Geoenvironmental Engineering* **144(9)**.

McDowell, G. R., Bolton, M. D. & Robertson, D. (1996) The fractal crushing of granular materials. *Journal of the Mechanics and Physics of Solids* **44(12)**:2079-2101.

McDowell, G. R. & Bolton, M. D. (1998) On the micromechanics of crushable aggregates. *Géotechnique* **48(5)**:667-679.

McDowell, G. & Bolton, M. (2001) Micro mechanics of elastic soil. *Soils and Foundations* **41(6)**:147-152.

McDowell, G. R. (2002) On the yielding and plastic compression of sand. *Soils and Foundations* **42(1)**:139-145.

McDowell, G. R. & De Bono, J. P. (2013) On the micro mechanics of one-dimensional normal compression. *Géotechnique* **63(11)**:895-908.

Melan, E. (1936) *Theorie statisch unbestimmter Systeme aus ideal-plastischem Baustoff.* Hölder-Pichler-Tempsky in Komm.

Menkiti, O. C. (1995) *Behaviour of clay and clayey-sand, with particular reference to principal stress rotation*, PhD thesis, Imperial College London (University of London).

Merritt, A., Schroeder, F. C., Jardine, R. J., Stuyts, B., Cathie, D. & Cleverly, W. (2012) Development of pile design methodology for an offshore wind farm in the North Sea. In *7th International Conference on Offshore Site Investigation & Geotechnics*. The Society for Underwater Technology, London, UK, pp. 439-448.

Mesri, G. & Vardhanabhuti, B. (2009) Compression of granular materials. *Canadian Geotechnical Journal* **46(4)**:369-392.

Michalske, T. A. & Freiman, S. W. (1982) A molecular interpretation of stress corrosion in silica. *Nature* **295(5849)**:511.

Michlmayr, G., Cohen, D. & Or, D. (2012) Sources and characteristics of acoustic emissions from mechanically stressed geologic granular media - A review. *Earth-Science Reviews* **112(3)**:97-114.

Miner, M. (1945) Cumulative damage in fatigue. *Trans Am Soc Mech Eng* **67**:A159-164.

Minh, N. A. (2006) *An investigation of the anisotropic stress-strain-strength characteristics of an Eocene clay*, PhD thesis, Imperial College London.

Molenkamp, F. (1998) Principle of axial shear apparatus. *Géotechnique* **48(3)**:427-431.

Mortara, G., Mangiola, A. & Ghionna, V. N. (2007) Cyclic shear stress degradation and post-cyclic behaviour from sand–steel interface direct shear tests. *Canadian Geotechnical Journal* **44(7)**:739-752.

Mortezaie, A. & Vucetic, M. (2016) Threshold shear strains for cyclic degradation and cyclic pore water pressure generation in two clays. *Journal of Geotechnical and Geoenvironmental Engineering* **142(5)**:04016007.

Mróz, Z. (1967) On the description of anisotropic workhardening. *Journal of the Mechanics and Physics of Solids* **15(3)**:163-175.

Muir Wood, D. (2007) The magic of sands – the 20th Bjerrum Lecture. *Canadian Geotechnical Journal* **44(11)**:1329-1350.

Muir Wood, D. & Maeda, K. (2008) Changing grading of soil: effect on critical states. *Acta Geotechnica* **3(1)**:3-14.

Najjar, S. S., Gilbert, R. B., Liedtke, E., McCarron, B. & Young, A. G. (2007) Residual shear strength for interfaces between pipelines and clays at low effective normal stresses. *Journal of Geotechnical and Geoenvironmental Engineering* **133(6)**:695-706.

Nakata, Y., Kato, Y., Hyodo, M., Hyde, A. F. L. & Murata, H. (2001) One-dimensional compression behaviour of uniformly graded sand related to single particle crushing strength. *Soils and Foundations* **41(2)**:39-51.

Narsilio, A. & Santamarina, J. (2008) Terminal densities. *Géotechnique* **58(8)**:669.

Nguyen, H., O'Sullivan, C. & Otsubo, M. (2018) Discrete element method analysis of small-strain stiffness under anisotropic stress states. *Géotechnique Letters* **8**:1-7.

Nicolai, G., Ibsen, L. B., O'Loughlin, C. D. & White, D. J. (2017) Quantifying the increase in lateral capacity of monopiles in sand due to cyclic loading. *Géotechnique Letters* **7(3)**:245-252.

Nikitas, G., Arany, L., Aingaran, S., Vimalan, J. & Bhattacharya, S. (2017) Predicting long term performance of offshore wind turbines using cyclic simple shear apparatus. *Soil Dynamics and Earthquake Engineering* 92(Supplement C):678-683.

Nishimura, S. (2006) *Laboratory study on anisotropy of natural London clay*, PhD thesis, Imperial College London.

Nishimura, S., Minh, N. & Jardine, R. (2007) Shear strength anisotropy of natural London Clay. *Géotechnique* **57(1)**:49-62.

Nishimura, S. (2014a) Assessment of anisotropic elastic parameters of saturated clay measured in triaxial apparatus: Appraisal of techniques and derivation procedures. *Soils and Foundations* **54(3)**:364-376.

Nishimura, S. (2014b) Cross-anisotropic deformation characteristics of natural sedimentary clays. *Géotechnique* **64(12)**:981-996.

O'Donovan, J. (2014) *Micromechanics of wave propagation through granular material*, PhD thesis, Imperial College London.

Oda, M. (1972) Initial fabrics and their relations to mechanical properties of granular material. *Soils and Foundations* **12(1)**:17-36.

Oda, M., Koishikawa, I. & Higuchi, T. (1978) Experimental study of anisotropic shear strength of sand by plane strain test. *Soils and Foundations* **18(1)**:25-38.

Orsi, T. H. & Anderson, A. L. (1999) Bulk density calibration for X-ray tomographic analyses of marine sediments. *Geo-Marine Letters* **19(4)**:270-274.

Otsubo, M. (2017) *Particle scale analysis of soil stiffness and elastic wave propagation*, PhD thesis, Imperial College London.

Otsubo, M. & O'Sullivan, C. (2018) Experimental and DEM assessment of the stress-dependency of surface roughness effects on shear modulus. *Soils and Foundations*.

Oumarou, T. A. & Evgin, E. (2005) Cyclic behaviour of a sand-steel plate interface. *Canadian Geotechnical Journal* **42(6)**:1695-1704.

Papadimitriou, A. G. & Bouckovalas, G. D. (2002) Plasticity model for sand under small and large cyclic strains: a multiaxial formulation. *Soil Dynamics and Earthquake Engineering* **22(3)**:191-204.

Parker, E. J., Jardine, R. J., Standing, J. R. & Xavier, J. (1999) Jet grouting to improve offshore pile capacity. In *Proceeding of Offshore Technology Conference*. Houston, pp. 415–420, OTC 10828.

Pickering, D. J. (1970) Anisotropic Elastic Parameters for Soil. *Géotechnique* **20(3)**:271-276.

PISA Academic Work Group (2017) *PISA final report*.

Porovic, E. (1995) *Investigation of soil behaviour using a resonant-column torsional shear hollow-cylinder apparatus*, PhD thesis, Imperial College London (University of London).

Potts, D. M. & Zdravković, L. (1999) *Finite element analysis in geotechnical engineering: theory.* London, Thomas Telford.

Potts, D. M. & Zdravković, L. (2001) *Finite element analysis in geotechnical engineering:*

application. London, Thomas Telford.

Potyondy, J. G. (1961) Skin friction between various soils and construction materials. *Géotechnique* **11(4)**:339-353.

Powell, J. & Butcher, A. (2003) Characterisation of a glacial clay till at Cowden, Humberside. In *Proceedings of the International Workshop on Characterisation and Engineering Properties of Natural Soils*. (Tan, T. S., Phoon, K. K., Hight, D. W., and Leroueil, S. (eds)) CRC Press, London, vol. , pp. 983-1020.

Puech, A., Canou, J., Bernardini, C., Pecker, A., Jardine, R. & Holeyman, A. (2012) SOLCYP: a four year JIP on the behaviour of piles under cyclic loading. In *Proceedings of 7th Offshore Site Investigation and Geotechnics: Intergrated Geotechnologies - Present and Future*. Society for Underwater Technology, London, UK.

Puzrin, A. M. & Burland, J. B. (1998) Non-linear model of small-strain behaviour of soils. *Géotechnique* **48(2)**:217-233.

Quinteros, V. S., Dyvik, R. & Mortensen, N. (2017) Interface friction angle from ring shear tests on offshore North Sea sands. In *Geotechnical Frontiers 2017*. (Brandon, T. L., and Valentine, R. J. (eds)) ASCE, Orlando, USA, Vol. GSP 280.

Ramsey, N., Jardine, R., Lehane, B. & Ridley, A. (1998) A review of soil-steel interface testing with the ring shear apparatus. In *Offshore Site Investigation and Foundation Behaviour*. Society of Underwater Technology, London, UK.

Rattley, M. J., Costa, L., Jardine, R. J. & Cleverly, W. (2017) Laboratory test predictions of the cyclic axial resistance of a pile driven in North Sea soils. In *8th International Conference on Offshore Site Investigation & Geotechnics*. The Society for Underwater Technology, London, UK, Vol. 2, pp. 636-643.

Rimoy, S., Silva, M., Jardine, R., Yang, Z. X., Zhu, B. T. & Tsuha, C. H. C. (2015) Field and model investigations into the influence of age on axial capacity of displacement piles in silica sands. *Géotechnique* **65(7)**:576-589.

Roesler, S. K. (1979) Anisotropic shear modulus due to stress anisotropy. *J. Geotech. Engng Div., ASCE* **105(GT7)**:871-880.

Rolo, R. (2004) *The anisotropic stress - strain - strength behaviour of brittle sediments*, Imperial College London (University of London).

Rondón, H., Wichtmann, T., Triantafyllidis, T. & Lizcano, A. (2009) Comparison of cyclic triaxial behavior of unbound franular material under constant and variable confining pressure. *Journal of Transportation Engineering* **135(7)**:467-478.

Roscoe, K. H. & Burland, J. B. (1968) On the generalised stress-strain behaviour of 'wet' clay In *Proceedings of Engineering Plasticity* (Heyman, J., and Leckie, F. A. (eds)). Cambridge University Press.

Rowe, P. & Barden, L. (1964) Importance of free ends in triaxial testing. *Journal of the Soil Mechanics and Foundations Division* **90(1)**:1-28.

Rowe, P. W. (1962) The stress-dilatancy relation for static equilibrium of an assembly of particles in contact. *Proc. of the Royal Society of London* **Series A(269)**:500-527.

Saada, A. S. (1970) Testing of anisotropic clay soils. *Journal of Soil Mechanics and Foundation Division, ASCE* **96(SM5)**:1847-1852.

Saada, A. & Townsend, F. (1981) State of the art: Laboratory strength testing of soils. In *Laboratory shear strength of sois*. American Society for Testing and Materials,, Philadelphia, USA, pp. 7-77.

Saada, A. (1988) State-of-the-art paper: Hollow cylinder torsional devices: their advantages and limitations. In *Advanced Triaxial Testing of Soil and Rock*. (Donaghe, R. T., Chaney, R. C., and Silver, M. L. (eds)) American Society for Testing and Materials, Philadelphia, USA, pp. 766-795.

Sadrekarimi, A. & Olson, S. M. (2010) Particle damage observed in ring shear tests on sands. *Canadian Geotechnical Journal* **47(5)**:497-515.

Sassa, K., Fukuoka, H., Wang, G. & Ishikawa, N. (2004) Undrained dynamic-loading ring-shear apparatus and its application to landslide dynamics. *Landslides* **1(1)**:7-19.

Sau, N., Arroyo, M., Pérez, N. & Pineda, J. A. (2015) Using CAT to obtain density maps in Sherbrooke specimens of silty soils. In *Geomechanics from Micro to Macro*. (Al., S. E. (ed)) 2015 Taylor & Francis Group, London, Cambridge, UK.

Schofield, A. N. & Wroth, C. P. (1968) *Critical state soil mechanics*. London: McGraw-Hill.

Schutt, D. (2015) *Laboratory testing of Cowden till*, MSc thesis, Imperial College London.

Seed, H. B. & Lee, K. L. (1966) Liquefaction of saturated sands during cyclic loading. *J. Soil Mech. Found. Div. ASCE* **92(SM6)**:105-134.

Shibuya, S. (1985) *Undrained behaviour of granular materials under principal stress rotation*, Imperial College London (University of London).

Silver, M. & Seed, H. (1971) Volume changes in sands during cyclic loading. *J Soil Mech Found Div ASCE* **97(SM9)**:1171-1182.

Sim, W. W., Aghakouchak, A. & Jardine, R. J. (2013) Cyclic triaxial tests to aid offshore pile analysis and design. *Proceedings of the ICE - Geotechnical Engineering* **166(GE2)**:111-121.

Simpson, B., O'Riordan, N. J. & Croft, D. D. (1979) A computer model for the analysis of ground movements in London Clay. *Géotechnique* **29(2)**:149-175.

Smith, P. R., Jardine, R. J. & Hight, D. W. (1992) The yielding of Bothkennar clay. *Géotechnique* **42(2)**:257-274.

Stark, T. D. & Vettel, J. J. (1992) Bromhead ring shear test procedure. *Geotechnical Testing Journal* **15(1)**:24-32.

Stark, T. D., Williamson, T. A. & Eid, H. T. (1996) HDPE geomembrane/geotextile interface shear strength. *Journal of Geotechnical Engineering* **122(3)**:197-203.

Stewart, H. E. (1986) Permanent strains from cyclic variable-amplitude loadings. *Journal of*

Geotechnical Engineering **112(6)**:646-660.

Rao, K. S. S., Allam, M. M. & Robinson, R. G. (1996) A note on the choice of interfacial friction angle. *Proceedings of the Institution of Civil Engineers - Geotechnical Engineering* **119(2)**:123-128.

Sun, Q., Cai, Y., Chu, J., Dong, Q. & Wang, J. (2017) Effect of variable confining pressure on cyclic behaviour of granular soil under triaxial tests. *Canadian Geotechnical Journal*:1-10.

Symes, M. J. P. R. (1983) *Rotation of principal stresses in sand*, Imperial College London (University of London).

Sze, H. Y. & Yang, J. (2014) Failure modes of sand in undrained cyclic loading: Impact of sample preparation. *Journal of Geotechnical and Geoenvironmental Engineering* **140(1)**:152-169.

Taborda, D. M. G. (2011) *Development of constitutive models for application in soil dynamics*, PhD thesis, Imperial College London.

Taborda, D. M. G., Zdravković, L., Kontoe, S. & Potts, D. M. (2014) Computational study on the modification of a bounding surface plasticity model for sands. *Computers and Geotechnics* **59**:145-160.

Taborda, D. M. G., Zdravković, L., Potts, D. M., Burd, H. J., Byrne, B. W., Gavin, K., Houlsby, G. T., Jardine, R. J., Liu, T., Martin, C. M. & McAdam, R. A. (2018) Numerical analysis of laterally loaded pile tests in sand. *Under review by Geotechnique*.

Tan, S. A., Chew, S. H. & Wong, W. K. (1998) Sand–geotextile interface shear strength by torsional ring shear tests. *Geotextiles and Geomembranes* **16(3)**:161-174.

Tapias, M., Alonso, E. E. & Gili, J. (2016) Compressibility, grain breakage and time-dependent behavior of gap-graded aggregates of sugar cubes. *Soils and Foundations* **56(5)**:805-817.

Tastan, E. & Carraro, J. (2013) A new slurry-based method of preparation of hollow cylinder specimens of clean and silty sands. *Geotechnical Testing Journal* **36(6)**:811-822.

Tatsuoka, F. (2011) Laboratory stress-strain tests for the development of geotechnical theories and practice. In *Bishop lecture, Proceedings of the Fifth International Symposium on Deformation Characteristics of Geomaterials, IS-Seoul 2011*. (Chung, C. K., Kim, H. K., Lee, J. S., Jung, Y. H., and Kim, D. S. (eds)), Seoul, Korea, pp. 3-50.

Tatsuoka, F. & Ishihara, K. (1974) Drained deformation of sand under cyclic stresses reversing direction. *Soils and Foundations* **14(3)**:51-65.

Tatsuoka, F., Molenkamp, F., Torii, T. & Hino, T. (1984) Behavior of lubrication layers of platens in element tests. *Soils and Foundations* **24(1)**:113-128.

Tatsuoka, F., Ochi, K., Fujii, S. & Okamoto, M. (1986) Cyclic undrained triaxial and torsional shear strength of sands for different sample preparation methods. *Soils and Foundations* **26(3)**:23-41.

Taylor, H. (2016) *Assessing the potential for suffusion in sands using x-ray micro-CT images*, PhD thesis, Imperial College London.

Tika, T. E., Vaughan, P. R. & Lemos, L. J. L. J. (1996) Fast shearing of pre-existing shear zones in soil. *Géotechnique* **46(2)**:197-233.

Todisco, M. C., Wang, W., Coop, M. R. & Senetakis, K. (2017) Multiple contact compression tests on sand particles. *Soils and Foundations* **57(1)**:126-140.

Todisco, C., Coop, M. & Pereira, J. M. (2018) Fabric characterisation in transitional soils. *Granular Matter* **20(2)**.

Toll, D. G. (2002) TRIAX user manual Version 4. *Geotechnical Systems Group, Durham University, Durham*.

Tong, Z.-X., Zhang, J.-M., Yu, Y.-L. & Zhang, G. (2010) Drained deformation behavior of anisotropic sands during cyclic rotation of principal stress axes. *Journal of Geotechnical and Geoenvironmental Engineering* **136(11)**:1509-1518.

Tsiampousi, A., Zdravkovic, L. & Potts, D. M. (2013) A new Hvorslev surface for critical state type unsaturated and saturated constitutive models. *Computers and Geotechnics* **48**: 156-166.

Tsuha, C. H. C., Foray, P. Y., Jardine, R. J., Yang, Z. X., Silva, M. & Rimoy, S. (2012) Behaviour of displacement piles in sand under cyclic axial loading. *Soils and Foundations* **52(3)**:393-410.

Uesugi, M. & Kishida, H. (1986) Influential factors of friction between steel and dry sands. *Soils and Foundations* **26(2)**:33-46.

Uesugi, M., Kishida, H. & Tsubakihara, Y. (1989) Friction between sand and steel under repeated loading. *Soils and Foundations* **29(3)**:127-137.

Uesugi, M., Kishida, H. & Uchikawa, Y. (1990) Friction between dry sand and concrete under monotonic and repeated loading. *Soils and Foundations* **30(1)**:115-128.

Ushev, E. (2018) *Laboratory investigation of the mechanical properties of Cowden till under static and cyclic conditions*, PhD thesis, Imperial College London.

Vaid, Y. P. & Rinne, N. (1995) Geomembrane coefficients of interface friction. *Geosynthetics International* **2(1)**:309-325.

Vaid, Y. P., Sayao, A., Hou, E. & Negussey, D. (1990) Generalized stress-path-dependent soil behaviour with a new hollow cylinder torsional apparatus. *Canadian Geotechnical Journal* **27(5)**:601-616.

Vaughan, P. R., Lovenbury, H. T. & Horswill, P. (1975) The design, construction and performance of Cow Green embankment dam. *Géotechnique* **25(3)**:555-580.

Vinck, K. P. A. (2016) *Laboratory testing of Dunkerque sand*, MSc dissertation, Imperial College London.

Wang, W. & Coop, M. R. (2016) An investigation of breakage behaviour of single sand particles using a high-speed microscope camera. *Géotechnique* **66(12)**:984-998.

Whittle, A., J., DeGroot, D., J., Ladd, C., C. & Seah, T. H. (1994) Model prediction of anisotropic behavior of Boston Blue clay. *Journal of Geotechnical Engineering* **120(1)**:199-224.

Wichtmann, T., Niemunis, A. & Triantafyllidis, T. (2005) Strain accumulation in sand due to cyclic loading: drained triaxial tests. *Soil Dynamics and Earthquake Engineering* **25(12)**:967-979.

Wichtmann, T., Niemunis, A. & Triantafyllidis, T. (2007a) On the influence of the polarization and the shape of the strain loop on strain accumulation in sand under high-cyclic loading. *Soil Dynamics and Earthquake Engineering* **27(1)**:14-28.

Wichtmann, T., Niemunis, A. & Triantafyllidis, T. (2007b) Strain accumulation in sand due to cyclic loading: Drained cyclic tests with triaxial extension. *Soil Dynamics and Earthquake Engineering* **27(1)**:42-48.

Wichtmann, T. & Triantafyllidis, T. (2017) Strain accumulation due to packages of cycles with varying amplitude and/or average stress – On the bundling of cycles and the loss of the cyclic preloading memory. *Soil Dynamics and Earthquake Engineering* **101**:250-263.

Wood, D. M. (1990) *Soil behaviour and critical state soil mechanics.* Cambridge university press.

Wood, D. M. & Belkheir, K. (1994) Strain softening and state parameter for sand modelling. *Géotechnique* **44(2)**:335-339.

Yamamuro, J., Bopp, P. & Lade, P. (1996) One-dimensional compression of sands at high pressures. *Journal of Geotechnical Engineering* **122(2)**:147-154.

Yamashita, S., Kawaguchi, T., Nakata, Y., Mikami, T., Fujiwara, T. & Shibuya, S. (2009) Interpretation of international parallel test on the measurement of G_{max} using bender elements. *Soils and Foundations* **49(4)**:631-650.

Yang, J. & Gu, X. Q. (2013) Shear stiffness of granular material at small strains: does it depend on grain size? *Géotechnique* **63(2)**:165-179.

Yang, Z. X., Li, X. S. & Yang, J. (2007) Undrained anisotropy and rotational shear in granular soil. *Géotechnique* **57(4)**:371-384.

Yang, Z. X., Li, X. S. & Yang, J. (2008) Quantifying and modelling fabric anisotropy of granular soils. *Géotechnique* **58(4)**:237-248.

Yang, Z. X., Jardine, R. J., Zhu, B. T., Foray, P. & Tsuha, C. H. C. (2010) Sand grain crushing and interface shearing during displacement pile installation in sand. *Géotechnique* **60(6)**:469-482.

Yoshimi, Y. & Kishida, T. (1981) A ring torsion apparatus for evaluating friction between soil and metal surfaces. *Geotechnical Testing Journal* **4(4)**:145-152.

Youd, T. L. (1972) Compaction of sands by repeated shear straining. *Journal of the Soil Mechanics and Foundations Division, ASCE* **98(SM7)**:709-725.

Yu, H. S., Yang, L. T., Li, X. & Wanatowski, D. (2016) Experimental investigation on the

deformation characteristics of granular materials under drained rotational shear. *Geomechanics and Geoengineering* **11(1)**:47-63.

Zdravkovic, L. (1996) *The stress-strain-strength anisotropy of a granular medium under general stress conditions*, Imperial College London.

Zdravkovic, L. & Jardine, R. (1997) Some anisotropic stiffness characteristics of a silt under general stress conditions. *Géotechnique* **47(3)**:407-437.

Zdravković, L., Potts, D. M. & Jardine, R. J. (2001) A parametric study of the pull-out capacity of bucket foundations in soft clay. *Géotechnique* **51(1)**:55-67.

Zdravković, L. & Jardine, R. (2001) The effect on anisotropy of rotating the principal stress axes during consolidation. *Géotechnique* **51(1)**:69-83.

Zdravković, L., Potts, D. & Hight, D. (2002) The effect of strength anisotropy on the behaviour of embankments on soft ground. *Géotechnique* **52(6)**:447-457.

Zdravkovic, L. & Potts, D. M. (2005) Finite element investigation of non-uniformities in hollow cylinder experiments. In *11th International Conference on Computer Methods and Advances in Geomechanics*. (Barla, B. G. (ed)), Balkema, Vol. 2, pp. 251-258.

Zdravković, L., Taborda, D. M. G., Potts, D. M., Jardine, R. J., Sideri, M., Schroeder, F. C., Byrne, B. W., McAdam, R., Burd, H. J., Houlsby, G. T., Martin, C. M., K. Gavin, Doherty, P., Igoe, D., Wood, A. M., Kallehave, D. & Gretlund, J. S. (2015) Numerical modelling of large diameter piles under lateral loading for offshore wind applications. In *3rd International Symposium on Frontiers in Offshore Geotechnics*. (Meyer, V. (ed)) Leiden, Netherlands : CRC Press/Balkema, Oslo, Norway.

Zhang, G. & Zhang, J. (2006) Large-scale apparatus for monotonic and cyclic soil-structure interface test. *Geotechnical Testing Journal* **29(5)**:401-408.

Zhang, G. & Zhang, J. (2009) State of the art: Mechanical behavior of soil–structure interface. *Progress in Natural Science* **19(10)**:1187-1196.

Zhang, J., Feng, D. & Hou, W. (2018) An automated large-scale apparatus for 3-D cyclic testing of soil-structure interfaces. *Geotechnical Testing Journal* **41(3)**:459-472.

Zhao, B., Wang, J., Coop, M. R., Viggiani, G. & Jiang, M. (2015) An investigation of single sand particle fracture using X-ray micro-tomography. *Géotechnique* **65(8)**:625-641.

Zhu, J. (2016) *One-dimensional high-pressure compressions on granular materials of varying crushability*, MSc thesis, Imperial College London.

Ziogos, A., Brown, M., Ivanovic, A. & Morgan, N. (2017) Chalk–steel interface testing for marine energy foundations. *Proceedings of the Institution of Civil Engineers - Geotechnical Engineering* **170(3)**:285-298.